1st International Conference of the
International Journal of Structural Integrity

Faculty of Engineering, University of Porto, Portugal
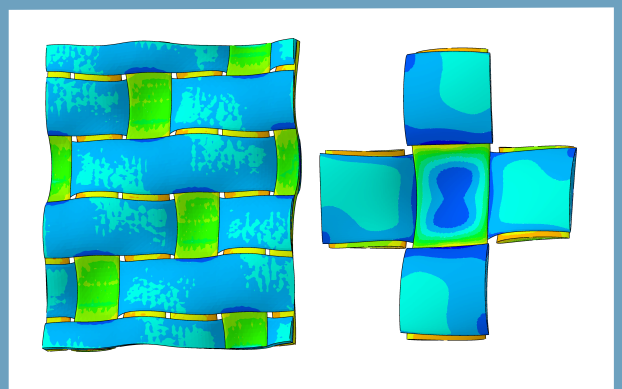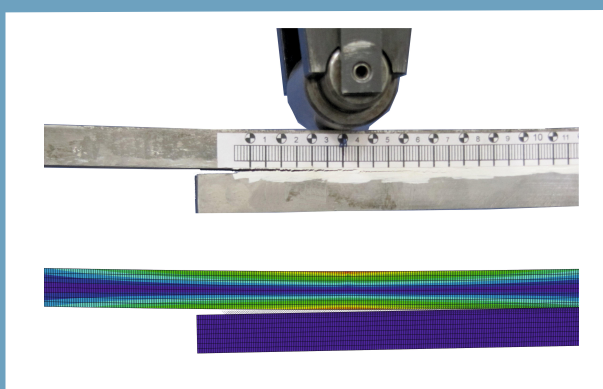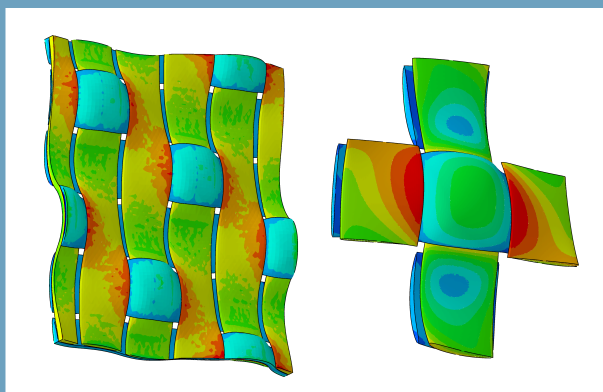
June 25-28, 2012

Proceedings

blank

1st International Conference of the International Journal of Structural Integrity

Faculty of Engineering, University of Porto, Portugal

June 25-28, 2012

Organizing Committee:
Chris Rodopoulos, Monash University, Australia, and IJSI editor-in-chief
Fernanda Fonseca, FEUP, Portugal
Lucas F.M. da Silva, FEUP
Paulo M. S. T. de Castro, FEUP, Chairman of Organizing Committee
Pedro M.G.P. Moreira, INEGI
Pedro P. Camanho, FEUP

Local Organizing Committee:
Paulo M. S. T. de Castro, FEUP, Chairman of Organizing Committee
Fernanda Fonseca, FEUP, Portugal
Pedro M.G.P. Moreira, INEGI, Portugal
Sérgio M.O. Tavares, FEUP, Portugal
Valentin Richter-Trummer, FEUP, Portugal

Scientific Committee:
A. Navarro, University of Seville, Spain
Ali Yousefiani, The Boeing Company, USA
B. Farahmand, Technical Horizon Inc, USA
C. Soutis, University of Sheffield, UK
Chris Rodopoulos, Monash University, Australia
Claudio DalleDonne, EADS Deutschland GmbH, Germany
Daniel Kujawski, Western Michigan University, USA
G. Labeas, University of Patras, Greece
Geng Sheng Wang, FOI, The Swedish Defence Research Agency, Sweden
Hamid Saghizadeh, The Boeing Company, USA
J. N. Bandyopadhyay, Indian Institute of Technology, India
Jaime Tupiassú Pinho de Castro, PUC-Rio, Brazil
Kotoji Ando, Yokohama National University, Japan
L. Marsavina, Universitatea Politehnica Timişoara, Romania
L. Wagner, Technische Universität Clausthal, Germany
Leslie Banks-Sills, Tel-Aviv University, Israel
M. M. I. Hammouda, Al-Azhar University, Egypt
Madabhushi Janardhana, Directorate General Technical Airworthiness, RAAF, Australia
Paulo M. S. T. de Castro, Universidade do Porto, Portugal
Peter Horst, Technische Universität Carolo-Wilhelmina zu Braunschweig, Germany
R. Ritchie, University of California, Berkley, USA
Simon Barter, DSTO, Australia
Spiros Pantelakis, University of Patras, Greece
Stephen Reed, Ministry of Defence, Defence Science and Technology Laboratory, UK
V. Troshchenko, National Academy of Sciences, Ukraine
Y. H. Huh, KRISS, Korea

Sponsors

http://www.easn.net

http://www.fct.pt

http://www.emeraldinsight.com/products/journals/journals.htm?id=ijsi

http://www.up.pt

http://www.spmateriais.pt

http://www.icf-wasi.org

http://www.fe.up.pt

Contents

Index

Conference Overview

HE INTERNATIONAL JOURNAL OF STRUCTURAL INTEGRITY - IJSI was launched in 2010 and is published in partnership with the European Aeronautics Science Network - EASN. The ISJI aims at a broad coverage of structural integrity issues, including material characterizations from the fracture and fatigue points to view, numerical modelling of those phenomena in materials and real structures, failure analysis methodologies and structural integrity evaluation criteria. The journal provides a forum for the key players in this broad area of science and technology, as universities, research institutes, manufacturing industry, legislative bodies and government agencies, SMEs, consultancy and maintenance companies. Occasionally scientific meetings are sponsored or even organized by the journal, as this 1st International Conference which will take place in Porto, Portugal. The conference aims at being a forum for discussion of current trends of research in structural integrity, in aeronautics and space, but also in other sectors of engineering where structural integrity is a key concern.

The conference topics are aligned with the IJSI coverage, and include but are not limited to:

- Advances in fracture analysis
- Coating technology and structural performance
- Design and structural assessment of metallic and composite structures
- Durability of metallic and composite structures
- Environmental effects and structural performance
- Evaluation of joining technologies
- Examination of computational codes for stress analysis and damage tolerance
- Nanomechanics and nanomaterials
- Non-destructive testing
- Probabilistic approach to damage tolerance
- Repair technologies
- Scale effects
- Structural ageing
- Structural health monitoring
- Structural integrity
- Structural performance evaluation of metals, composites, hybrids and polymers
- Surface engineering and structural performance

Plenary Invited Lectures

Claudio Dalle Donne, EADS Innovation Works

Metallic Technologies and Surface Engineering
EADS Innovation Works
81663 München
Germany

Lighter, Faster, Greener - Additive Layer Manufacturing for Aerospace Structures

with co-authors Jon Meyer, Frank Palm, Erhard Brandl, Laetitia Kirschner and Katja Schmidtke, EADS Innovation Works

ADDITIVE LAYER MANUFACTURING (ALM) is a revolutionary concept by which components are grown from the ground up, rather than machined from a larger block. Very complex geometries can be produced rapidly and directly from computer-aided design (CAD) information without the need for dies, form tools or molds. Additionally, ALM utilises significantly less raw material for any given component and produces negligible levels of waste in comparison to traditional machining processes, in which up to 90% of the material is removed. In this overview the Additive Layer Manufacturing is described and some examples of actual and potential applications are given. Furthermore key technology drivers are discussed and a special focus is given to the fundamental understanding of additive manufactured material properties, which is still at an early stage. For example, there is only little experience in predicting the effect of defects on the fatigue behavior. Such understanding of damaging mechanisms will be key to developed design rules for future primary structures applications.

Claudio Dalle Donne was born in Karlsruhe in 1965. He studied Mechanical Engineering at the Karlsruhe University of Technology and was awarded a doctorate there in 1996. From 1991 to 2004 he worked at the Institute of Materials Research of the German Aerospace Centre (DLR) in Cologne in various functions and departments (fatigue, fracture mechanics, friction stir welding). In 2004 he moved to the EADS Corporate Research Centre Germany (now EADS Innovation Works) as head of the "Metallic Structure" department. Since 2007 he has headed the transnational department "Metallic Technologies and Surface Engineering". Author or co-author of a large number of scientific papers and reports, Dr. Dalle Donne is currently the ICAF National Delegate for Germany, and member of the editorial board of the International Journal of Structural Integrity.

Jerzy Komorowski, NRC Institute for Aerospace Research

General Manager, NRC Institute for Aerospace Research
National Research Council Canada
1200 Montreal Road, M-3, Ottawa, ON K1A 0R6
Canada

The Age for Reason

with co-author Nicholas C. Bellinger

IN THE PAST, three design paradigms have been used to determine the life of aircraft structures; no-life, safe-life and damage tolerance.

The no-life paradigm was used to design the earliest commercial jet aircraft. Due to the fact that little information was available regarding the material systems used to fabricate aircraft, large safety factors were applied to the static strength of the different materials. In addition, the materials were assumed to be ideal continuous, homogeneous and isotropic. Not surprisingly, as aircraft entered into service, cracks formed in some components, which occasionally fractured resulting in the complete loss of an aircraft and in turn, fatalities. To improve aircraft design, a new paradigm was developed known as the safe-life methodology, which is currently used to design "safety" critical components, such as landing gears, in aircraft. Although this methodology assumes that all materials are ideal continuous, homogeneous and isotropic as in the no-life method, safety factors are applied to the fatigue (or endurance) limit to take into account material scatter. To reduce the risk of aircraft flying with unknown cracks, the damage tolerance methodology was developed, which assumes that all fatigue critical components contain growing cracks. In this methodology, the crack growth life is estimated, which drives directed in-service inspections allowing undamaged components to remain in service. Investigations that have been carried out over the years on failed components have revealed that these methodologies do not adequately take into account complex damage scenarios (such as wide-spread fatigue damage), environmental and age degradation modes (such as corrosion and fretting), improper damage repair and usage variability. In addition, as new material systems (such as fibre-metal laminates) and fabrication technologies (such as resin transfer moulding) are introduced into new aircraft designs, unanticipated failure mechanisms will develop due to cyclic and environmental loading. To address these concerns a new life management methodology, known as the Holistic Structural Integrity Process (HOLSIP), is being developed by an international consortium to augment and enhance traditional safe-life and damage tolerance methodologies in order to provide a powerful design and sustainment tool. This presentation will provide examples of the deficiencies of the current life methodologies and the need to move toward a physics-based method.
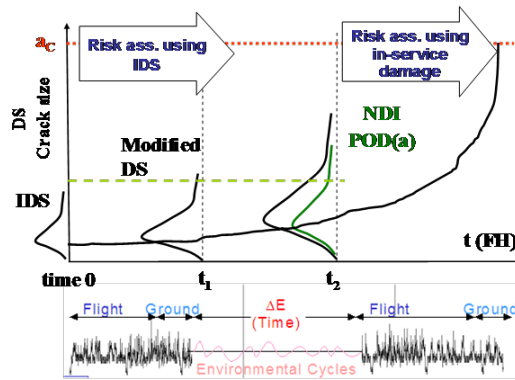
Figure: Holistic Structural Integrity Process.

On January 17, 2012, Jerzy Komorowski was appointed General Manager of NRC's Aerospace portfolio. Since April 2012, he has also served as the Interim GM for the Energy, Mines and Environment portfolio. Previously, Mr. Komorowski was Director General of the NRC Institute for Aerospace Research (IAR 2005-2012); Director of the Structures, Materials and Propulsion Laboratory at IAR (2002-2005); and leader of IAR's Structures Group (1998 to 2002). He joined IAR - formerly known as the National Aeronautical Establishment - in 1982.

Mr. Komorowski received his ME in applied mechanics from the Warsaw Technical University, Poland, in 1976. During his career, he has published more than 100 reports, journal and conference papers. His early research was focused on experimental strain analysis, as well as environmental effects in composite and metallic materials. In the 1990s, he was active in the field of non-destructive inspection, developing new optical inspection methods and pioneering models of the impact of corrosion on the integrity of aircraft structures. As Director of the Structures, Materials and Propulsion Laboratory, Mr.

Komorowski helped it to become one of the leading research centres for holistic structural integrity design.

Mr. Komorowski is a graduate of NRC's LEAD Executive Challenge program. He is also a member of the Canadian Aeronautics and Space Institute; the Canadian voting member of the NATO Research and Technology Organization Advanced Vehicles Technology Panel (AVT); and Chair of the AVT Support Committee. He serves as the Canadian National Resource Specialist at the Aerospace Engineering Group of the Technical Cooperation Program.

As General Manager of NRC's Aerospace portfolio, Mr. Komorowski serves on the boards of directors of the Consortium for Research and Innovation in Aerospace in Quebec; Aéro Montréal - an industry cluster organization; EnviroTREC - the Canadian Environmental Test Research and Education Centre; and the Green Aviation Research & Development Network. He is also Deputy Chair of the Steering Committee of the Canadian Aerospace Environmental Technology Road Map.

Chris Rodopoulos, Monash University

Monash University
Victoria 3800
Australia

Fatigue damage discrepancies and the multiple stages of the similitude concept

THE WORK demonstrates how the theory of the fatigue damage map (FDM) can be used in order to define a closed form locus where fatigue crack growth can be sought. The Intrinsic FDMLocus depending only on readily material properties represents a tool able to accurately predict crack growth of polycrystals. If the Locus is expressed in terms of a surface plot after triangulation of the data, it concludes into visualization of the potential for multiple similitude stages. The stages are defined as a function of the maximum far field stress and ΔK. Multiple similitude stages are found to dominate the short and near threshold area (Stage I growth) and represent direct result of the effect of polycrystalline behaviour to flow resistance. The work concludes that interrogation of the points defining the Intrinsic FDM Locus and related to the three thresholds can provide potential characteristics in the quest for an ideal damage tolerance material.

Chris Rodopoulos was born in Athens, Greece in 1967. In 1991 he received his Dipl.-Eng. in Mechanical Engineering from the University of Patras. In 1992 he received an MSc in Advanced Materials from Nottingham University. In 1996 he completed his PhD from the University of Sheffield. His research interests are focused on Surface Engineering Treatments, Fatigue Damage Tolerance Analysis, Theoretical Stress Analysis and Thermomechanical Fatigue of Metal Matrix Composites. He is the editor-in-chief of the International Journal of Structural Integrity, and the author of more than 120 papers and four books. Since 2002 he has led the Interest Group Surface Engineering Treatments with the European Aeronautics Science Network. He is a member of several professional organizations, including ASME, AIAA, ESIS and IMechE. During his career so far he has received 5 awards for research papers. He has strong collaborations with a number of key research institutes and industrial bodies including, EADS, Airbus UK, Boeing, Rolls-Royce, Hyundai, NRC-CNRC, NASA Langley, Applied Ultrasonics, Metal Improvement Company, CLFA, DLR, NLR, SIKA, Penetron, LAGARGE, etc.

Mário A. P. Vaz, Faculty of Engineering, University of Porto

Faculty of Engineering, University of Porto
Porto
Portugal

Experimental techniques for stress/strain assessment and structural monitoring

MECHANICAL design is basically an exercise of creativity, triggered by specific needs. However, a deep understanding of materials behaviour and Solid Mechanics methods is necessary to achieve good project solutions. The engineering community continues to cross the boundaries of known practices in design and manufacturing techniques, looking for new materials and more efficient mechanical systems, new energy sources and their effects upon the environment, and so, the opportunities for structural failure will inevitably increase.

Nowadays, different tools are available to optimize any engineering solution, among which Experimental Mechanics has always played a most prominent role. It is related to such diverse disciplines as physical and mechanical sciences, engineering (mechanical, aeronautical, civil, automotive, nuclear, etc.), materials, electronics, medicine and biology, and uses experimental methodologies to test and evaluate the behaviour and performance of all kinds of materials, structures and mechanical systems. Quality control, safety, destructive and non-destructive testing of materials and components, analysis of prototypes and even fundamental research are some of the possible applications of Experimental Mechanics. During the last few decades the development of computer based techniques, as well as laser-optics methods, nanotechnologies and nanomaterials, among many other technological advances, added new dimensions and perspectives to Experimental Mechanics and Testing.

The experimental techniques may be used to access the distribution of stresses or strains in the surface of diffuse materials. Imaging techniques used with structured or coherent illumination allow operating without contact to perform high resolution measurements. Likewise it is possible to obtain complex three-dimensional geometry of objects and analyzing its deformation in real time. With these techniques is thus possible to understand the behavior of structures and components under complex loading conditions even when they are constructed on new materials. These techniques have also shown themselves useful in the design and construction of structural monitoring systems. If the structural behavior of a component is previously known sensors can use to record continuously its stress level and prevent catastrophe situations, or, as well, to predict its service life.
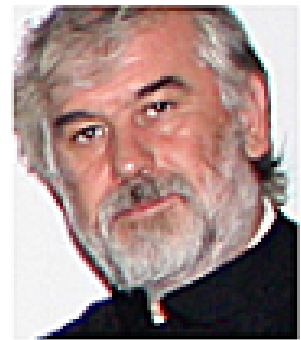
Mário Augusto Pires Vaz was born in Bragança, northeast of Portugal, in August 1961. He studied Mechanical Engineering at the Faculty of Engineering of University of Porto (FEUP), where he received his PhD in Mechanical Engineering in 1995. He is Professor of the Department of Mechanical Engineering of FEUP and Director of the Laboratory of Optics and Experimental Mechanics of INEGI/FEUP. His main research interests are: Solid Mechanics, Experimental mechanics, laser metrology and, more recently, Experimental Biomechanics. He is member of the National committee for Experimental Mechanics and holds the position of president of the Portuguese Society of Biomechanics.

He is member of the following organizations: Portuguese Association of Experimental Stress Analysis (APAET), Portuguese Society of Biomechanics (SPB), Associação Portuguesa de Mecânica Teórica, Aplicada e Computacional (APMTAC), SPIE - The International Society for Optical Engineering, DYMAT- European association for the promotion of research into the dynamic behaviour of materials and its applications and is the Portuguese member of the European Society for Experimental Mechanics (EURASEM) and Society for Experimental Mechanics (SEM) councils. He was involved in more than two hundred papers published in international journals and conferences with peer review.

Articles and Abstracts

Life Management Aspects of Composite Airframe Structures in the ADF Environment

Madabhushi Janardhana[1] and Paul Callus[2]

[1]*Aircraft Structural Integrity Section, Directorate General Technical Airqorthiness, RAAF Williams, L474 B-2-South, Laverton, Victoria, 3027, AUSTRALIA, madabhushi.janardhana@defence.gov.au*

[2]*Defence Science Technology Organisation, 506 Lorimar Street, Fishermans Bend, Victoria, 3207, AUSTRALIA, paul.callus@dsto.defence.gov.au*

Abstract. In both military and commercial aviation, a focused life management program for airframe structures is required once the aircraft start operating in service. The discipline of holistic airframe management is commonly known as Aircraft Structural Integrity (ASI) management. The increased use of composite structures in the primary and secondary structure of Military aircraft has created a need to consider the life management (LM) aspects that are specific to these structures. This paper provides a brief review of current state addressing the deficiencies and limitations in regulations and standards dealing with LM of composite structures – as relevant to airframe applications. In providing this review, this paper also briefly discusses numerous damage mechanisms and defect characterization with a view to address their relevance to LM of composite structures. A future program plan on Damage and Life Management (D-LM) approaches for composite structures is briefly outlined.

Keywords: Airframe Structural Integrity, Composite Structures, Life management

Structural damage evaluation using PZT sensors and guided waves

M. Santos [1] and J.Santos [1]

[1]*University of Coimbra's Mechanical Engineering Research Center, Department of Electrical Engineering and Computers, Polo II, 3030-290 Coimbra, Portugal, marioj@deec.uc.pt*

Abstract This work deals with the evaluation of the applicability of bonded PZT sensors for the detection and classification of different artificial defects in aluminum plates as well as impact defects in fiber glass composite plates. First, the sensors have been designed and bonded on different plates. It was observed that the experimental behavior of sensors is according to theoretical predictions. Fundamental symmetrical (S0) and anti-symmetrical (A0) modes were identified in our experiments. These modes were proved by solving the Rayleigh-Lamb frequency equations. Some holes and slits with different dimensions were drilled in the aluminum plates and the laminate composites were impacted with different energy levels. Using a pitch and catch configuration, the signals have been collected after interaction with defects. Three different approaches of signal processing techniques have been used for defect detection: time, frequency and integrated time-frequency analysis. Simple amplitude measurements were accomplished in time domain analysis. In the frequency domain, the use of the Fast Fourier Transform (FFT) allowed the detection of deviations from the original benchmark spectrum. The time-frequency analysis, which combines time and frequency information, has given rise to the so-called spectrogram, based on two different approaches: Short-time Fourier Transform (STFT) and Wavelet Transform (WT). The best results are provided by the time domain method, probably due to the high tuned behavior of the PZT sensors, which hide small spectrum variations. Based on the experimental measurements, it is possible to establish empirical relations in an attempt to describe signal amplitude behavior with defect dimensions. The presented results, due to their empirical character need to be confirmed with other experimental configurations, namely: plate dimensions, type of material, defect geometries or coupling. However, it was demonstrated the applicability of PZT sensors, when defect evaluation in plates is demanded.

1   Introduction

Vibration-based techniques for structural health monitoring (SHM) have been extensively studied for several years in order to evaluate damages, which usually produce changes in the vibrational characteristics of the structure, such as natural frequencies, mode shapes and modal damping. Recently, damage detection through ultrasonic guided waves, such as Lamb waves, has been gained increasing importance due to the possibility of inspecting large structures. Once excited, the Lamb waves can propagate all over considerable distances. Thus, a receiver positioned on the structure at a remote position can collect the propagation signals observed along with the path between transmitter and receiver, providing information about eventual surface defects or internal cracks. The generation of Lamb waves by conventional transducers has some limitations because they are relatively large and expensive. An emerging technique based on piezoelectric lead zirconate titanate (PZT) sensors has the potential to improve significantly the SHM. These sensors are small, lightweight, inexpensive, and can be produced in different geometries. They can be bonded on the structures surface, mounted inside built-in structures and can even be embedded between the structural and non-structural layers of a complete construction.

2   PZTs for generate and collect Lamb waves

Many authors have considered the use of Lamb waves for non-destructive testing. Rose have summarized the potential of these waves in terms of damage detection and characterization [1], that are mainly: the possibility of inspection of entire cross sectional area of a structure with a single direction displacement, inspection of large insulated or coated structures, no necessity of using complex motion devices, good sensitivity, low energy consumption and low cost. However complications that are encountered include the existence of multiple modes and the dispersive character of these modes, and also the waves reflected in boundaries, which could mask the signal of interest. Normally the fundamental symmetric (S_0) and anti-symmetric (A_0) are preferred to use in practice due to their better time discrimination when compared with higher order modes.

PZT ceramics deliver excellent performance in Lamb wave generation and acquisition. They are also called active sensors due to its dual sensing and excitation characteristics. Typically when working in kHz range is possible to obtain around an hundred of mV or more in sensing, using as excitation signal a tone burst with 10 V of amplitude. The resonant frequency of the PZT is given by [2]

$$f = \frac{v}{L}\left(n + \frac{1}{2}\right) \quad (n = 0,1,2,...) \tag{1}$$

where L is the length of the PZT and v is the Lamb wave velocity of the propagating mode in the material. The thickness selection have to take in account the maximum voltage allowed by the PZT without depolarizing, that is around 250-300 V/mm [3].

3   Processing techniques

The most important signal processing and damage identification techniques, when using guided waves generated by PZT ceramics can be divided in time, frequency and integrated time-frequency analysis. Time domain analysis usually uses time of flight or amplitude variations measurements associated to triangulation techniques and artificial neural networks. Normally this analysis, except for few successful applications, needs a benchmark signal for comparison [2]. In frequency domain is possible to get additional information about the signals behavior than in time analysis. Fast Fourier transform (FFT) and its two-dimensional variant (2D-FFT) [4,5] are widely used when spectrum information is demanded. With 2D-FFT is possible to isolate different propagation modes, which could exist in the original signal, and present them in frequency-wavenumber domain. The main drawback of this method is the need of a great number of collected signals, which, in some cases, makes it difficult to put into practice. Finally the integrated time-frequency analysis combines the two previous techniques, giving rise to 2D representations. Practical implementation of one of this techniques is the Short-time Fourier transform (STFT), that is obtained by applying a FFT to a small piece of the time signal (time window). After, a continuous movement of this time window along the time axis gives rise to a time-frequency representation. Another recent tools used in PZT guided waves signal processing is the Wavelet transform (WT). This transform uses a special signal called wavelet, which has a limited time duration and average amplitude equal to zero. Continuous Wavelet transform (CWT) and discrete Wavelet transform (DWT) are the typical forms of WT. CWT is used for 2D frequency-time analysis. Applied to an analog signal is possible to obtain directly in a scale-time domain and the scale variable can be connected with frequency in an easier way. The difference from STFT in that the resolution depends on the scale. The CWT modifies the length of the wavelet at different

scales (frequency) to analyze adaptively signals with localized information. DWT is widely useful in signal de-noising, filtering and compression.

4   Experimental work
4.1 Guided wave propagation with PZTs

PZT generation of Lamb waves were initial perform in an aluminium plate with 330x250x1 mm. From bar type PZ29 (50x20x0.4 mm) from Ferroperm Piezoceramics, several pieces of 7x7 mm were cut. For excitation an arbitrary waveform generator Tektronix AFG3022 was used to produce a 3-cycle toneburst with a Hanning window, that was previous synthesized in Matlab. This windowing technique is used to narrow the signal bandwidth and to focus the maximum amount of energy into the desired frequency with a minimum spreading to neighbor frequencies. The signal as 10 V of amplitude. The received signal is collected by a digital oscilloscope and transferred by USB to further processing. The PZTs were mounted 100 mm apart on the surface of the aluminium plate, using high density grease as a coupling agent. For making electrical connections to PZTs, standard soldering of 50 μm section wire was done in the top surface. In the bottom surface, a flattened wire (10 μm), obtained by a mechanical process, was lightly soldered to minimize perturbation in the coupling process. In Fig. 1 is shown the complete experimental setup. After a frequency sweep was verified that the maximum signal in the receiver is obtained for 320 kHz. In Fig.4 is presented the signals obtained for that frequency. The first signal is the direct wave and the second is the reflection from the end of the plate. From Rayleigh-Lamb dispersion equations [5] is possible to obtain the existing propagation modes in the aluminium plate. Using time of flight, it can easily be proved that both waves in Fig. 2 correspond to the S_0 fundamental mode, which for this frequency has a phase velocity of 5400 m/s.
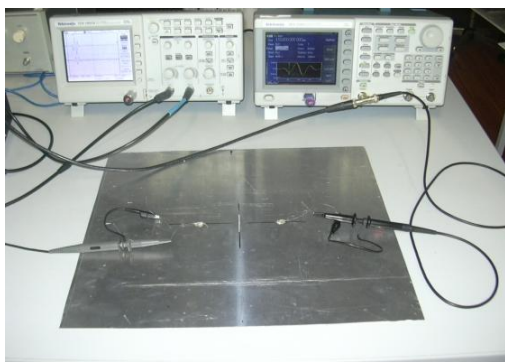
Fig. 1 - Experimental setup   Fig. 2 - PZT signals propagating in
                                    1mm thickness aluminium plate.
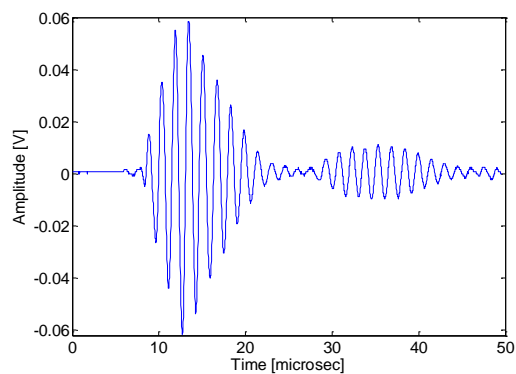
4.2 Pitch and catch evaluation of simulated damages using PZTs
4.2.1 Holes and slits in aluminium plates

Pitch and catch method, also known as transmission method, is used to detect structural changes in a certain material, between a transmitter transducer and a receiver transducer. Using this technique and the previous section experimental setup, through holes and slits of different dimensions, conceived in the same type of 1 mm thickness aluminium plate, were analyzed. In this experiment silicone glue was used as coupling between the PZTs and plate in an attempt to avoid the previous coupling problems. Starting from the lower dimension, amplitude signals were collected for each defect. The diameter holes analyzed was: 1, 2, 3, 4,

5, 6, 8, 10, 12 and 14 mm and the length slits analyzed was from 6 to 34 mm, with 2 mm step. The minimum slit dimension was 6 mm due to limitations of the available tools. A frequency sweeping was also performed to analyze the influence of this parameter in the study. The normalized results are presented in Fig. 3 (a) and (b). The data regarding the zero dimensions defects were obtained for reference defect-free plates. For both types of defects is visible a generally decay with the defect dimensions increasing. This behavior is consistent with the expectations: as the defects dimensions increase, it's like an increasing of a shadow zone where no direct transmission occurs, so the received signal decreases. The decaying is almost monotonous except for the first dimension point analyzed after the reference plate. For these points some additional resonance phenomena should exist, which conducts to this out of pattern behavior (decreasing for 1 mm hole and increasing for 6 mm slit). In a generally way, with the frequency variation, there are not great changes in the presented curves, except for previous referred 6 mm slit resonance. In this case the resonance effect is more pronounced for low frequencies, while for higher frequencies is almost inexistent. A detailed analytical evaluation of the presented plots is behind the scope of this work.

(a)   (b)
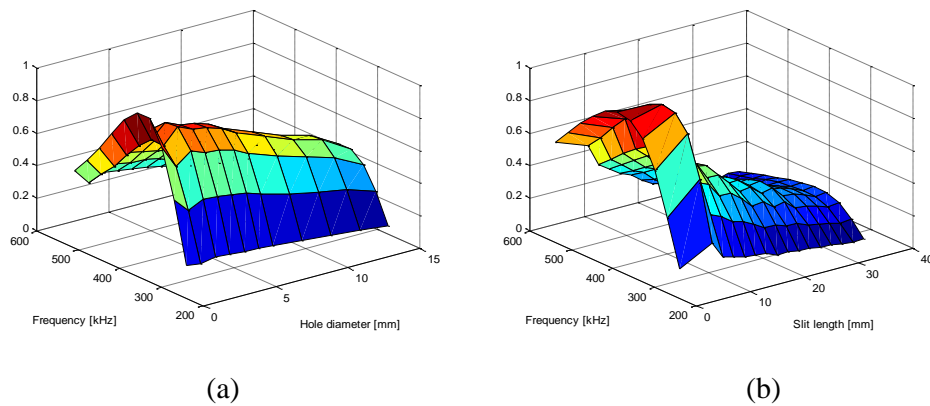
Fig. 3 Normalized experimental amplitude measurements for simulated defects in aluminium plates: (a) holes; (b) slits.

Nevertheless, based in the experimental measurements, is possible to establish empirical relations in an attempt to describe its behavior. Using fitting tools was possible to verify that in Fig. 4 (a) (holes) the best fit is linear and in Fig. 4 (b) (slits) the best fit is negative exponential. In the first case, the data has very weak frequency dependence, so using an average value for all frequencies the coefficient R^2 is 0.926. If the first point (1 mm) is neglected, R^2 goes up to 0.995. In the second case for lower frequencies $R^2=0.90$ and for higher frequencies $R^2=0.95$. Again if the first point (6mm) is neglected, the average value of R^2 for lower and higher frequency goes up to 0.92 and 0.98, respectively.

Frequency and time-frequency domain processing techniques previous mentioned, don't give quantitative results regarding the potential evaluation of defects, probably due to the high tuned behavior of the PZT sensors, which hide small spectrum variations. As examples, STFT and WT obtained for one of the analyzed signals are shown in Fig. 5 (a) and (b).

(a)   (b)
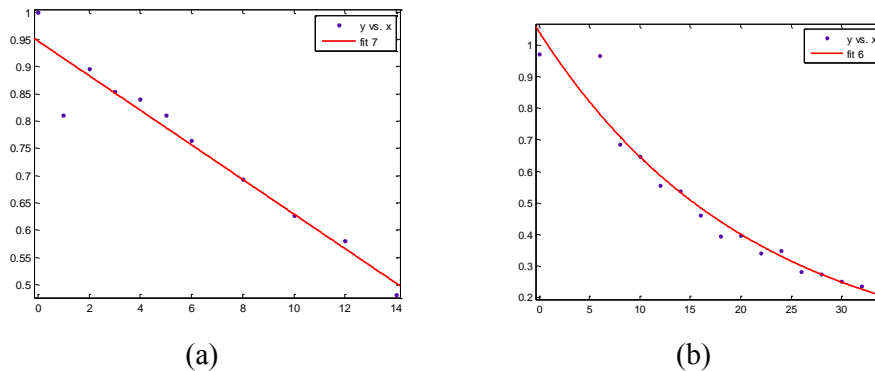
Fig. 4 Fitting curves for central frequency experimental data of Fig 3: (a) holes; (b) slits.

(a)   (b)
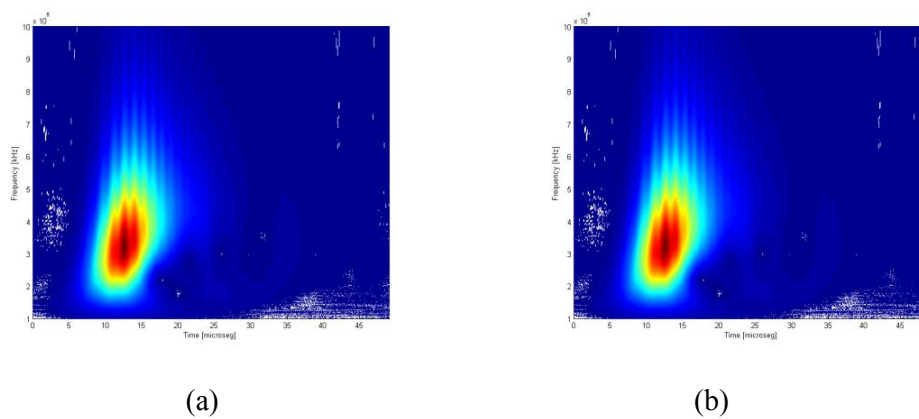
Fig. - 5 Processing transforms: (a) STFT; (b) WT.

4.2.1 Impacts in fiber glass composite laminates

In our first experiments four 300x300 mm fiber glass composite laminates are considered and described in Table 1. Samples A and B have unidirectional fiber structure and samples C and D have cross fiber structure. The fiber glass plates were cut from their original dimensions (300x300mm) in 150x150mm plates, giving rise to four samples of each type.

Table 1 – *Fiber glass composite plates*

	Type	Thickness (mm)	Average signal decreasing after impact
A	$[0]_{24}$	3.4	45%
B	$[0]_{16}$	2.1	8%
C	$[0_2/90_2]_s$	1	40%
D	$[0_2/90_2]_{2s}$	2.1	60%

Low velocity impact tests were performed using a drop weight-testing machine Instron Ceast model 9340. The impact energy used was proportional to the ply number of each plate. For the plate C: 1J, for the plates B and D: 2J and for the plate A: 3J. The detection technique used was the same as previous for holes and slits. For samples A the tests were done in fiber

direction and for samples B in cross direction. For all samples was verified a decaying in signals amplitude after impact. Three samples of each type were analyzed and was seen that the repeatability among different measurements was poor, probably due to local anisotropy in the plates after impacts. Maximum variations around 15% were found for the same set of values. The average results are presented in Table 1. The main quantitative conclusion to be drawn is related to the different impact influence in the collected signal. While in samples A, C and D the signal amplitude decreasing is very much pronounced, in sample B the decreasing is very small. The explanation must be related with the fiber orientation. Sample B is the only one where the propagation is preformed in the fibers direction, so the influence of broken fiber due to the impact, is not so severe as in the other samples. As in the last section, frequency analysis techniques don't give any conclusive results related to the impact detection.

5   Conclusions

In the presented work it was shown the applicability of PZT sensors when defect detection in plates are demanded. With a correct designing and with a simple experimental setup, is possible to excite and collect guided waves in the plates. The existing propagation guided wave modes were identified and its propagation parameters were according to theory. PZT sensors, which are small, lightweight, inexpensive, and can be produced in different geometries avoids the use of conventional transducers. These characteristics make also possible to bond them on the surface or inside built-in structures. Experimental tests were performed in aluminium plates with drilled holes and slits and in laminate fiber glass composites impacted with different energy levels. The pitch and catch configuration was used to collect signals after interaction with defects. For aluminium plates defects it was observed a monotonous decreasing behavior with the increasing of its dimensions and empirical relations were established. For impacted fiber glass plates the influence of defects in signal amplitude was also confirmed. Frequency or time-frequency analysis techniques reveal that are not appropriate when working with these high tuned sensors. The presented results, due to empirical character need to be confirmed with other experimental configurations, namely: plate dimensions, type of material, defect geometries or coupling. In impacted plates further studies could be done, namely multiple impact effects and the use of better performance materials like carbon fiber composites.

6   References

[1]   J.L. Rose, "*A vision of ultrasonic guided wave inspection potential*", Proceedings of the Seventh ASME NDE Topical Conference NDE, Vol. 20, pp.1–5, 2001.

[2]   Z. Su, L. Ye, Y. Su, "*Guided Lamb waves for identification of damage in composite structures: A review*", Journal of Sound and Vibration, 295, pp. 753–780, 2006.

[3]   C.S. Wang, F. K. Chang, "*Diagnosis of impact damage in composite structures with built-in piezoelectrics network*", Proceedings of SPIE 3990, pp.13–19, 2000.

[4]   Alleyne, D., Cawley, P., "*A two-dimensional Fourier transform for the measurement of propagating multimode signals*", *J. Acoust. Soc. Am.,* 89, pp.1159-1168, 1991.

[5]   Viktorov, I., "*Rayleigh and Lamb Waves –Physical Theory and Applications*", Plenum Press, New York, 1967.

Structural Integrity Assessment of Components with Defects and Safety Factors against Fracture

Yu.G. Matvienko

*Mechanical Engineering Research Institute of the Russian Academy of Sciences,
4 M. Kharitonievsky Per., 101990 Moscow, Russia; e-mail: ygmatvienko@gmail.com*

Abstract To substantiate the structural integrity and acceptable states of damaged components, safety factors against fracture and plastic collapse are included in basic equations of fracture mechanics. The safety factors against fracture are calculated by demanding that the applied critical stress should not be less than the yield stress of material for a component with a crack or a notch of the acceptable size. Basic equations have been presented to calculate the safety factor against fracture for critical values of the stress intensity factor, crack tip opening displacement, the J-integral and the failure assessment diagram as well as to estimate an acceptable (safe) region for an engineering component with a crack- or notch-like defect of the acceptable size.

Structural integrity assessment of the engineering components damaged by crack- or notch-like defects is discussed from view point of the failure assessment diagram. It was shown that the safety factor against fracture for a notch-like defect is a function of the yield stress as well as the elastic stress concentration factor and the safety factor against plastic collapse. For the special case of a notch the failure assessment diagrams are transferred to the failure assessment diagram for component with a sharp crack, and the safety factor becomes the safety factor against fracture of cracked component. The methodology of the failure assessment diagram has been employed for the structural integrity analysis and assessment of acceptable sizes of throw-thickness notch in a plate under tension and surface longitudinal notch-like defects in a pressure vessel.

1 Introduction

Structural integrity assessment methods play an important role in the industrial realization of fracture mechanics applications. If the engineering component is defect-free, the applied stresses are compared with a limit stress such as the yield stress of the material. As long as the yield stress exceeds the applied stress, the component is regarded as safe. If the component contains a crack or crack-like defect, fracture mechanics approach has to be employed. Therefore, the comparison between the applied crack driving force and the material's fracture toughness has to be carried out on the basis of crack tip parameters such as the stress intensity factor, the J-integral, the crack tip opening displacement or etc. Two types of the structural integrity assessment are made: a probabilistic assessment or a deterministic assessment. It is obvious that the following parameters must be known when the structure reliability is analyzed: load, crack length, fracture toughness and yield stress of materials according to the FAD. The principle of establishing a probabilistic approach has been considered in details [1-3]. But the reliability analysis is more complex and costly compared with a deterministic analysis, and is not convenient for common engineers to utilize it. Moreover, probabilistic fracture mechanics is relatively new in the area of structural integrity safety case and there are often too few data to have sufficient confidence in the results of the calculations to rely on them for decisions on permission for plant to operate. That is why the deterministic method is the basis of reliability assessment. Therefore, in engineering, most assessment of component reliability are made deterministically so that failure is avoided by including safety factors on

each of the different equation inputs. In this case, safety factors against fracture and plastic collapse have been considered [4, 5]. The safety factors are set to unity for the evaluation of critical conditions.

The aim of this paper is to give basic principles of deterministic fracture mechanics for a component with a crack- or notch-like defect and its application in the structural integrity analysis.

2   General aspects of structural integrity assessment

General principles of structural integrity assessment in a frame of deterministic fracture mechanics is illustrated by the notch failure assessment diagram. To determine an acceptable (safe) region, it should be reasonable to introduce safety factors (e.g. [4, 5]) in the failure criterion. The following condition should be fulfilled if detected or assumed notch-like defect of a certain size should be assessed as acceptable [6]

$$K_{1notch} \leq \frac{K_{1C}}{SF_K} \sqrt{1 - \left(\frac{\sigma}{\sigma_0}\right)^2} \left[1 - \left(\frac{\sigma_0}{\sigma}\right)^2 \frac{1}{K_t^2}\right]^{-1/2} \tag{1}$$

where SF_K is safety factor against fracture, K_{1C} is the fracture toughness, K_t is the elastic stress concentration factor, σ_0 is the local strength ahead of the notch tip. The stress intensity factor at the notch tip is denoted as K_{1notch}. The acceptable applied stress σ is suggested to be not more than σ_Y / SF_Y, i.e.

$$\sigma \leq \frac{\sigma_Y}{SF_Y}, \tag{2}$$

where SF_Y is safety factor against plastic collapse.

The safety factor SF_K can be calculated by making an assumption that the applied acceptable stress should be not less than the yield stress σ_Y (Eq. (2)) of material for an engineering component with a notch-like defect of the acceptable size [4]. In this case, the failure criterion for a notch-like defect of the acceptable size on the boundary of fracture and plastic collapse can be given by

$$\frac{1}{2}\sqrt{\pi\rho}\,\sigma_Y K_t = K_{1C} \sqrt{1 - \left(\frac{\sigma_Y}{\sigma_0}\right)^2} \left[1 - \left(\frac{\sigma_0}{\sigma_Y}\right)^2 \frac{1}{K_t^2}\right]^{-1/2}. \tag{3}$$

Here, the stress intensity factor at the notch-like defect tip is assumed to be as given by the relationship

$$K_{1notch} = \frac{1}{2}\sqrt{\pi\rho}\,\sigma K_t. \tag{4}$$

The safety factor SF_Y against plastic collapse corresponding to Eq. (2) is introduced in the failure criterion (1) to determine the acceptable defect as

$$\frac{1}{2}\sqrt{\pi\rho}\,\frac{\sigma_Y}{SF_Y} K_t = \frac{K_{1C}}{SF_K} \sqrt{1 - \left(\frac{\sigma_Y / SF_Y}{\sigma_0}\right)^2} \left[1 - \left(\frac{\sigma_0}{\sigma_Y / SF_Y}\right)^2 \frac{1}{K_t^2}\right]^{-1/2}. \tag{5}$$

Combining Eqs. (3) and (5), the safety factor SF_K against fracture can be presented as

$$SF_K = SF_Y \frac{\sqrt{1 - \left(\dfrac{\sigma_Y / SF_Y}{\sigma_0}\right)^2} \sqrt{1 - \left(\dfrac{\sigma_0}{\sigma_Y}\right)^2 \dfrac{1}{K_t^2}}}{\sqrt{1 - \left(\dfrac{\sigma_Y}{\sigma_0}\right)^2} \sqrt{1 - \left(\dfrac{\sigma_0}{\sigma_Y / SF_Y}\right)^2 \dfrac{1}{K_t^2}}} . \tag{6}$$

Here, the local strength can be defined taking as follows

$$\frac{\sigma_0}{\sigma_Y} = -\frac{\beta}{2 SF_Y} + \sqrt{\frac{1}{4}\left(\frac{\beta}{SF_Y}\right)^2 - \frac{(1 + v^2 - v)(\beta / SF_Y)^2 - 1}{(1 - 2v)^2}} \tag{7}$$

for plane strain and

$$\frac{\sigma_0}{\sigma_Y} = -\frac{\beta}{2 SF_Y} + \sqrt{1 - \frac{3}{4}\left(\frac{\beta}{SF_Y}\right)^2} . \tag{8}$$

for plane stress. The value $\beta(a/W)$ is a dimensionless parameter (so-called biaxiality ratio) which depends on geometry and loading mode. Values of $\beta(a/W)$ can be considered as a normalized measure of the crack tip constraint and have been tabulated for various geometries in literature.

It can be seen from Eq. (6) that the safety factor against fracture is a function of the yield stress as well as the elastic stress concentration factor and the safety factor against plastic collapse.

Thus, the right-hand side of Eq. (1) defines the acceptable region in the notch failure assessment diagram. If the assessment point falls within this region, the component with a notch-like defect is acceptable, i.e. it fulfils the required safety demands. For the special case of a crack ($K_t \to \infty$) the notch failure assessment diagrams are transferred to the failure assessment diagram for component with a sharp crack [6-9], and the safety factor (6) becomes the safety factor against fracture of cracked component

$$SF_K = SF_Y \frac{\sqrt{1 - \left(\dfrac{\sigma_Y / SF_Y}{\sigma_0}\right)^2}}{\sqrt{1 - \left(\dfrac{\sigma_Y}{\sigma_0}\right)^2}} . \tag{9}$$

To demonstrate the structural integrity assessment procedure, an infinite plate with a notch-like defect under uniform remote tensile stress has been considered. Equation (5) gives the approximate relation for a notch-like defect of the acceptable size $[a]$ as follows [6]

$$[a] = \frac{1}{\pi} \frac{K_{1C}^2}{SF_K^2} \frac{SF_Y^2}{\sigma_Y^2} \left[1 - \left(\frac{\sigma_Y}{\sigma_0 SF_Y}\right)^2\right] + \frac{\rho}{4}\left(\frac{\sigma_0 SF_Y}{\sigma_Y}\right)^2 . \tag{10}$$

The elastic stress concentration factor is assumed to be equal to the acceptable factor $[K_t]$, i.e. $K_t = [K_t] \approx 2\sqrt{[a]/\rho}$. The following mechanical properties of the material and the safety

factor against plastic collapse for plane strain were used: $K_{1C} = 102\,\mathrm{MPa}\sqrt{\mathrm{m}}$, $\sigma_Y = 340\,\mathrm{MPa}$, $\beta = -1$, $\nu = 0.3$, $SF_Y = 1.5$. Calculation of the safety factor against fracture from Eq. (9) gives $SF_K = 1.59$. It is seen that the acceptable size of a notch-like defect decreases with the increase of the elastic stress concentration factor tending to its limiting value, i.e. the acceptable size of a sharp crack (Fig. 1).

An acceptable (safe) region for an engineering component with a notch-like defect of the acceptable size can be represented from Eq. (1) by Fig. 2.
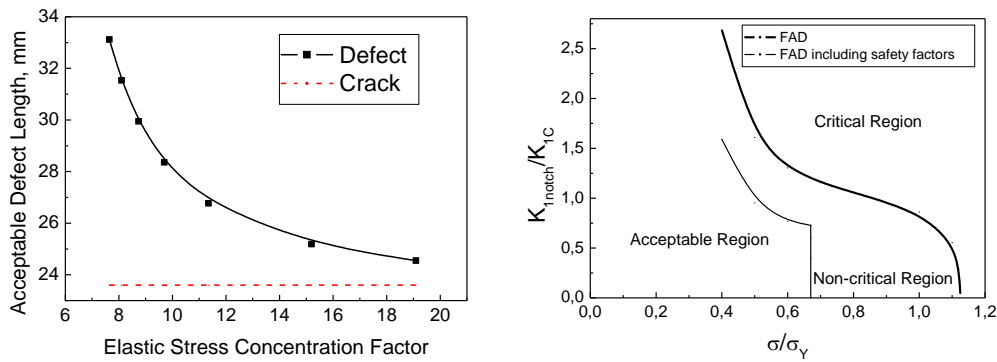
Figure 1 - *Acceptable defect length in an infinite plate as a function of the elastic stress concentration factor*

Figure 2 - *Notch failure assessment diagram including safety factors against fracture and plastic collapse ($SF_K = 1.59$, $SF_Y = 1.5$, $K_t = 8$)*

3   Acceptable notch-like defect in a pressure vessel

An assessment of the acceptable surface longitudinal notch-like defects in a pressure vessel is based on the notch failure assessment diagram described by Eq. (5). Substituting Eq. (6) into Eq. (5), the acceptable elastic stress concentration factor $[K_t]$ can be written as follows

$$[K_t] = \sqrt{\frac{4}{\pi\rho}\frac{K_{1C}^2}{\sigma_Y^2}\left[1 - \left(\frac{\sigma_T}{\sigma_0}\right)^2\right] + \left(\frac{\sigma_0}{\sigma_Y}\right)^2}\ .\tag{11}$$

Thus, acceptable state of the damaged pressure vessel has been presented by the following criterion

$$K_t \leq [K_t],\tag{12}$$

where K_t is the elastic stress concentration factor for the surface notch-like defect under consideration.

The pressure vessel/defect geometry is described by the wall thickness *t*, vessel outer diameter *D*, defect depth *l*, and defect tip radius ρ. In the analysis presented below a wall thickness of 30 mm and a diameter of 1200 mm are applied. The notch-like defect length is assumed to be an infinite value. To determine the elastic stress concentration factor for the surface external defect, the 2D finite element simulations of steel pressure vessels were

carried out using the ANSYS code. The following mechanical properties of the steel and the safety factor against plastic collapse for plane strain were used: $K_{1C} = 100\,\text{MPa}\sqrt{\text{m}}$, $\sigma_Y = 285\,\text{MPa}$, $v = 0.3$, $SF_Y = 1.5$. In this case, the acceptable depth of a surface notch-like defect in the pressure vessel amounts to 10.23 mm.

4   Some safety factors against fracture

Typical expressions for the calculation of safety factors against fracture in criteria approaches of liner and non-linear fracture mechanics can be obtained following general principles, which are given in the section 2, and taking into account formulae for fracture mechanics parameters under consideration, namely,

(i)   The energy J-integral [10] for a nonlinear material

$$J = 2\pi \frac{n}{1+n}\alpha\sigma_Y\varepsilon_Y a\left(\frac{\sigma}{\sigma_Y}\right)^{1+n}, \quad SF_J = \left(SF_Y\right)^{1+n}; \tag{13}$$

(ii) Stress intensity factor for a linear elastic material

$$K_I = \sqrt{JE}, \qquad\qquad SF_K = \left(SF_Y\right); \tag{14}$$

(iii) Crack tip opening displacement δ

$$\delta = \frac{8\sigma_Y a}{\pi E}\ln\sec\left(\frac{\pi}{2}\frac{\sigma}{\sigma_0}\right), \qquad SF_\delta = \frac{\ln\sec\dfrac{\pi}{2}\dfrac{\sigma_Y}{\sigma_0}}{\ln\sec\dfrac{\pi}{2}\dfrac{\sigma_Y}{(SF_Y)\sigma_0}}. \tag{15}$$

The local strength σ_0 is treated according to von Mises yield criterion as a property of both the yield stress and the *T*-stress which quantifies constraint in different geometries and type of loading [6, 9]. Here, σ_Y is the reference stress, $\varepsilon_Y = \sigma_Y/E$ is the associated elastic strain, E is the Young's modulus, α is the constant and n is the strain hardening exponent in the Ramberg-Osgood model of the material.

5   Conclusions

The deterministic method is recommended to be based on including safety factors against fracture and plastic collapse in criteria equations of fracture mechanics. Basic equations have been presented to calculate the safety factor against fracture for critical values of the stress intensity factor, crack tip opening displacement, the J-integral and the notch failure assessment diagram as well as to estimate an acceptable (safe) region for an engineering component with a crack- or notch-like defect of the acceptable size. Structural integrity assessment of the engineering components damaged by crack- or notch-like defects is discussed from view point of the failure assessment diagram. The effect of crack tip constraint has been expressed by biaxiality ratio $\beta(a/W)$ and it is incorporated into criteria equations for the calculation of safety factors against fracture.

6   References

[1]   W.Q. Wang, C.J. Liu, S.J. Zhou, *"On the probabilistic failure assessment diagram"*, Int. J. Pres. Ves & Piping, Vol. 76, pp. 653-662, 1999.

[2]   J.P. Tronskar, M.A. Mannan, M.O. Lai, G. Sigurdsson, K.O. Halsen, *"Crack tip constraint correction applied to probabilistic fracture mechanics analyses of floating production, storage and off-loading vessels"*, Eng. Fract. Mech., Vol. 70, pp. 1415-1446, 2003.

[3]   R. Bullough, F.M. Burdekin, O.J.V. Chapman, V.R. Green, D.P.G. Lidbury, J.N. Swingler, R. Wilson, *"The demonstration of incredibility of failure in structural integrity safety cases"*, Int. J. Pres. Ves. & Piping, Vol. 78, pp. 539-552, 2001.

[4]   Yu.G. Matvienko, N.A. Makhutov, *"Strength and survivability analysis in engineering safety for structures damaged by cracks"*, Int. J. Pres. Ves & Piping, Vol. 76, pp. 441-444, 1999.

[5]   B. Brickstad, M. Bergman, P. Andersson, L. Dahlberg, I. Sattari-Far, F. Nilsson, *"Procedures used in Sweden for safety assessment of components with cracks"*, Int. J. Pres. Ves. Piping, Vol. 77, pp. 877-881, 2000.

[6]   Yu.G. Matvienko, *"Failure Assessment Diagrams in Structural Integrity Analysis"*, In: Damage and Fracture Mechanics / eds.: T. Boukharouba, M. Elboujdaini and G. Pluvinage. Springer, Netherlands, pp. 173-182, 2009.

[7]   Yu.G. Matvienko, *"Local fracture criterion to describe failure assessment diagrams for a body with a crack/notch"*, Int. J. Fracture, Vol. 124, pp. 107-112, 2003.

[8]   Yu.G. Matvienko, *"Erratum: Local fracture criterion to describe failure assessment diagrams for a body with a crack/notch"*, J. Fracture, Vol. 131, p. 309, 2005.

[9]   Yu.G. Matvienko, *"Development of models and criteria of notch fracture mechanics"*, Structural Integrity and Life**,** Vol. 11, No1, pp. 3-7, 2011.

[10]   Yu.G. Matvienko, *"J-estimation formulas for nonlinear crack problems"*, Int. J. Fracture, Vol. 68, pp. R15-R18, 1994.

Comparing an Extended Kalman Filter with a Hopfield Neural Network

for on-line damage detection in Euler-Bernoulli beams

Almeida, J.[1] , Alonso, H.[2,3], Rocha, P.[1,2]

[1]*Faculdade de Engenharia da Universidade do Porto, Portugal*
[2]*Centro de Investigação e Desenvolvimento em Matemática e Aplicações, Universidade de Aveiro, Portugal*
[3]*Universidade Lusófona do Porto, Portugal Departamento de Matemática, Universidade de Aveiro, Portugal*

Abstract In this paper two identification methods are used to detect online damage in an Euler-Bernoulli beam. The damage is simulated by a change in some of the model parameters and is detected by an Extended Kalman Filter and by a Hopfield Neural Network. For tuning the identification methods different scenarios of damage were considered. Both methods track the changes in the beam parameters and the results obtained are very satisfactory.

1   Introduction

With the development of engineering structures (e.g. aircrafts, bridges and off-shore platforms) a greater attention with cracks that endanger the whole structure is necessary. The detection of this damage is an important point to avoid the total crashing of the structure and mainly to repair the cracks in the their early growth state to minimize the costs. In order to detect beam damage, identification methods have been used to identify the beam parameters [6] and monitor their variation. Indeed recent studies show that the beam damage can be represented by a change in the parameters involved in the EB model [6]. Hence, detecting damage is the same of detecting a parameter change.

In this paper two identification methods are presented to identify the beam parameters of a damped Euler-Bernoulli (EB) model representing the time evolution of the transverse displacement along a vibrating beam. Due to its simplicity this model is often used in structural and mechanical engineering [5]. The first method is an Extended Kalman Filter (EKF) [9] and the second one is a Hopfield Neural Network (HNN) [1]. Both identification methods rest on the choice of an initial tuning that influences the quality of the parameter estimates. Here these methods are evaluated for different tunings and the best one is chosen taking into account the mean error between the real parameters and their estimates.

The EKF and the HNN are used to track parameter changes based on simulated vibration data in different scenarios. The tuning chosen for each identification method is applied to three other damage scenarios in order to validate the methods proposed here.

2   Computational model for the Euler-Bernoulli beams

This section describes the computational model for the Euler-Bernoulli model for the deflection of a beam. The method of separation of variables is applied in order to write this model as a state-space system that will serve as basis for the identification procedure.

2.1   Problem formulation

$$\mu \frac{\partial^2}{\partial t^2} w(t,x) + c \frac{\partial}{\partial t} w(t,x) + EI \frac{\partial^4}{\partial x^4} w(t,x) = q(t,x) \qquad (1)$$

where $q(t, x)$ is the transverse excitation at location x and at instant t, m is the mass per unit length, c is the damping coefficient, E is the elastic modulus and I is the second moment of area. Here these parameters are considered to be constant along the beam, and the excitation $q(t, x)$ is taken to be zero (free vibration). Moreover the beam is taken to be simply-supported at both ends, which is translated by the following boundary conditions,

$$w(t,x)|_{x=0,L} = 0 \text{ and } \frac{\partial^2}{\partial x^2}w(t,x)\bigg|_{x=0,L} = 0$$

2.2   First order model

In this subsection the method of separation of variables is applied to the Euler-Bernoulli model to rewrite the model as a first order state-space model. The separation of variables consists in considering that the solution, $w(t, x)$, of (1) is given by, $w(t,x) = f(t)g(x)$. Here $g(x)$ is taken as $g(x) = \sin\left(\frac{\pi}{L}x\right)$ and the function $f(t)$ is the solution of,

$$f''(t) + \frac{c}{\mu}f'(t) + \frac{EI}{\mu}f(t) = 0, \tag{2}$$

with the following initial conditions, $f(0) = \gamma_0$ and $f'(0) = \gamma_1$ .This   is   corresponds   to considering $w(0,x) = \gamma_0 \sin\left(\frac{\pi}{L}x\right)$ and $\frac{\partial}{\partial t}w(0,x) = \gamma_1 \sin\left(\frac{\pi}{L}x\right)$.

Taking a spatial discretization interval of Δx, a vector $\overline{W}$ is constructed with the values of g(x) at the discretization points, i.e.,

$$\overline{W} = \begin{bmatrix} g(0) \\ g(\Delta x) \\ \vdots \\ g(L) \end{bmatrix} \epsilon \mathbb{R}^{\frac{L}{\Delta x}+1}. \tag{3}$$

This yields $W(t) = f(t)\overline{W}$ as corresponding spatial discretization of *w(t,x)*. The time evolution of *W(t)* is then described by the ODE:

$$f''(t)\overline{W} + \frac{c}{\mu}f'(t)\overline{W} + \frac{EI}{\mu}f(t)\overline{W} = 0, \tag{4}$$

Defining $X_1(t) = f(t)\overline{W}$ and $X_2(t) = f'(t)\overline{W}$ the following first order model is obtained:

$$\begin{cases} X'(t) = F(\theta)X(t), \\ W(t) = CX(t) \end{cases} \tag{5}$$

with $F(\theta) = \begin{bmatrix} 0 & I \\ -\theta_1 I & -\theta_2 I \end{bmatrix}$, where I is the identity matrix with dimension $\frac{L}{\Delta x} + 1$ and X(t) = $\begin{bmatrix} f(t)\overline{W} & f'(t)\overline{W} \end{bmatrix}^T$. Moreover $\theta = [\theta_1 \quad \theta_2]^T$ with $\theta_1 = \frac{EI}{\mu}$ and $\theta_2 = \frac{c}{\mu}$ is the parameter vector. The initial conditions for this model X(0) = $\begin{bmatrix} \gamma_0 \overline{W} & \gamma_1 \overline{W} \end{bmatrix}^T$ with $\gamma_0 = f(0)$ and $\gamma_1 = f'(0)$.

3   Identification methods

Damage in a beam can be detected by a variation in its parameters. Therefore, in order to detect damage it is necessary to identify these parameters and to monitor their evolution in time. In this section two identification methods are described: in the first subsection the Extended Kalman Filter algorithm [9] is explained, and the second subsection presents the Hopfield Neural Networks [1] to be used in the sequel.

3.1   Extended Kalman Filter

In order to identify the beam parameters θ_1 and θ_2, these parameters are incorporated as states whose evolution is constant along time. This originates a nonlinear state-space model with enlarged state to which an Extended Kalman Filter (EKF) is applied. The EKF allows an individualized tuning of the covariance matrix of the process and measurement noise. Here the covariance matrix of the process is taken to be diagonal, since it is assumed that the enlarged states, and in particular the parameters θ_1 and θ_2, are independent. Moreover, the continuous-time representation (8) is discretized by the zero-order hold method [3] using a sampling interval Δt yielding

$$\begin{cases} X(k+1) = \Phi(\theta)X(k), \\ \quad W(k) = CX(k) \end{cases} \tag{6}$$

where $\Phi(\theta) = e^{F(\theta)\Delta t}$ is the sampled system matrix.

The enlarged state vector is given by $\overline{X}(k) = \begin{bmatrix} X(k) \\ \theta(k) \end{bmatrix}$.

Consequently the enlarged state-space model stands as follows:

$$\begin{cases} \overline{X}(k+1) = \underbrace{\begin{bmatrix} \Phi(\theta) & 0_{(2n\times2)} \\ 0_{(2\times2n)} & I_{(2\times2)} \end{bmatrix}}_{h\left(k,\overline{X}(k)\right)} X(k) + v(k) \\ \quad W(k) = \underbrace{\begin{bmatrix} C & 0_{(n\times2)} \end{bmatrix}}_{h\left(k,\overline{X}(k)\right)} X(k) + e(k) \end{cases} \tag{7}$$

Here $v(k)$ and $e(k)$ are mutually independent Gaussian white noise sequences with zero mean and covariances R_1 and R_2, respectively, tuned by an empirical analysis.

3.2   Hopfield Neural Networks

As an alternative identification method, a Hopfield Neural Network (HNN) was applied to the beam vibration data. Similarly what happens in EKF, the HNN produces a time-evolving estimate parameters. The system equations are reduced to the form, $y(t) = A(t)\theta$, where *y(t)* and *A(t)* are a certain vector and a certain matrix, respectively, computed from the system data, and θ is the vector of model parameters to be estimated online.

The HNN to be used here as an online estimator was proposed in [1] and is given by the following dynamics,

$$\frac{d\hat{\theta}}{dt}(t) = \frac{1}{c\beta} D_c\left(\hat{\theta}(t)\right) A(t)^T\left(y(t) - A(t)\hat{\theta}(t)\right) \tag{8}$$

where $c, \beta > 0$ and $\forall\, i \in 1, \dots, N, t \geq t_0, s_i(t) \in \,]-s, s[$ and $D_c(\hat{\theta}(t))$ is a positive definite and invertible matrix defined by,

$$D_c\left(\hat{\theta}(t)\right) = \begin{bmatrix} c^2 - \theta_1(t)^2 & 0 \\ 0 & c^2 - \theta_2(t)^2 \end{bmatrix} \tag{9}$$

In order to apply this HNN, the model (5) is rewritten in the form $y(t) = A(t)\theta$ as,

$$\begin{bmatrix} X_1'(t) - X_2(t) \\ X_2'(t) \end{bmatrix} = \begin{bmatrix} 0 & 0 \\ -X_1(t) & -X_2(t) \end{bmatrix}\begin{bmatrix} \theta_1 \\ \theta_2 \end{bmatrix} \tag{10}$$

where $X_1'(t)$ and $X_1''(t)(= X_2'(t))$ are determined numerically from $X_1(t)$.

3.3 Off-line tunning

In order to tune the EKF and the HNN the beam parameters are assumed to be known and fixed in space and the performance of each identification method is analysed under four different scenarios, namely:

S1 - The beam parameters are fixed in time;

S2 - E suffers a decrease of 10%, 20% and 30% at time t = 0.5s (which implies a decrease of θ_1) [7];

S3 - c suffers a increase of 50%, 100% and 200% at time t = 0.5s (which implies an increase of θ_2) [8];

S4 - μ suffers a decrease of 10%, 20% and 30% at time t = 0.5s (which implies an increase of θ_1 and θ_2) [4].

These scenarios are tested for 8 different tunings of the EKF and 29 different tunings of the HNN. The performance of each tuning is measured in terms of the mean identification error.

Table 1 - *mean error obtained with the application of the EKF and the HNN in each scenario S1, S2, S3 and S4.*

		S1	S2	S3	S4	S1, S2, S3, S4	S1, S3, S4
EKF	Mean id error	1.7×10^{-2}	2.2×10^{-2}	3.1×10^{-2}	2.4×10^{-2}	2.8×10^{-2}	2.2×10^{-2}
	Tuning	6	8	6	8	8	8
HNN	Mean id error	1.7×10^{-2}	1.6×10^{-2}	7.0×10^{-2}	2.5×10^{-2}	4.1×10^{-2}	2.0×10^{-2}
	Tuning	24	28	14	21	17	24

4 Results

This section presents the results obtained in the analysis of the performance of each identification method taking in account the four scenarios described in subsection 3.3. The Euler-Bernoulli model parameters used to simulate the beam vibration data were obtained in [2] as $E = 2 \times 10^{-11} N/m^2$, $I = 2.45 \times 10^{-7} m^4$, $\mu = 23.1\,kg/m$ and $c = 32\,N\,s/m^2$ and in this way $\theta_1 = 2129.5 \frac{m^4}{s^2}$ and $\theta_2 = 1.38\,s^{-1}$. With the aim of normalizing the spatial discretization between 0 and π, the beam length was considered equal to π with 0.1π as spatial sampling interval.

Table 1 shows the mean error obtained with the application of the tuning in the scenarios S1, S2, S3 and S4. As it is possible to see both identification methods have similar results in scenarios S1 and S4. In scenario S2 the HNN has a good performance whereas the EKF presents a good achievement in scenario S3. The EKF is globally the best identification method whereas the HNN presents good results if S2 is not considered. In this case, the best tuning for the EKF is tuning 8, and the best tuning for the HNN (neglecting S2) is 24.

In order to validate these results the EKF and the HNN were applied with tunings 8 and 24, respectively, to the following three scenarios:

S5 - E suffers a decrease of 15% at time t = 0.3s and at time t = 0.7s (which implies a decrease of θ_1) [7];

S6 - c suffers a increase of 50% at time t = 0.3s and at time t = 0.7s (which implies an increase of θ_2) [8];

S7 - μ suffers a decrease of 15% at time t = 0.3s and at time t = 0.7s (which implies an increase of θ_1 and θ_2) [4];

Figure 1 shows the time evolution for the parameters estimates given by the EKF (blue line) and by the HNN (red line) under the conditions of scenario S5. Both identification methods detect the two variations in parameter θ_1.
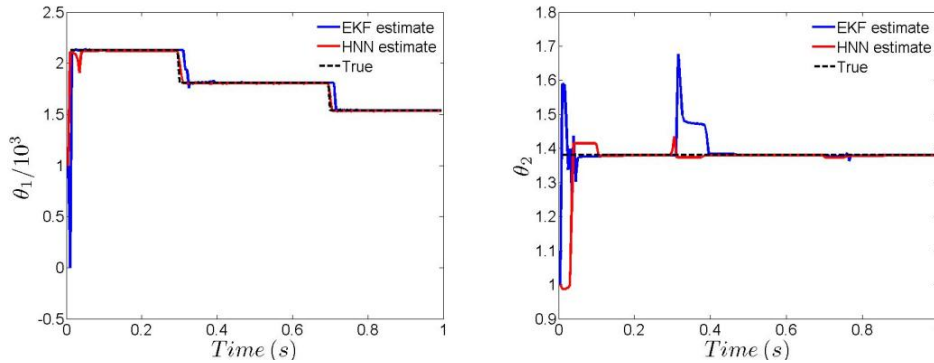
Figure 1 - *Time-evolution of beam parameters under the conditions of S5.*

Figure 2 represents the scenario S6 where both methods detect the beam damage that it is translated by the variation in parameter c but only the EKF converges for the new value of this parameter.
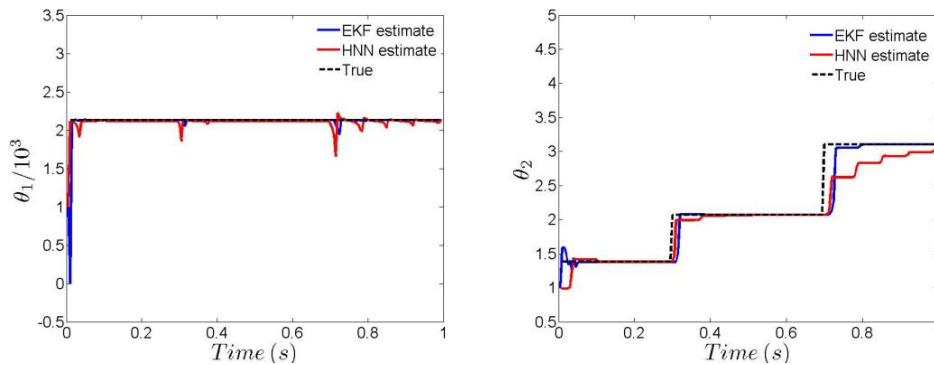
Figure 2 - *Time-evolution of beam parameters under the conditions of S6.*

The variation in parameter μ implies an increase of θ_1 and θ_2 as is shown in Figure 3. Both identification methods detect these changes in parameter values. However the identification of θ_1 is better than the identification of θ_2. For the change in θ_1 the EKF and the HNN have similar results and the HNN method detects almost instantaneously this change. The identification of θ_2 given by the EKF is globally better than the identification given by the EKF.
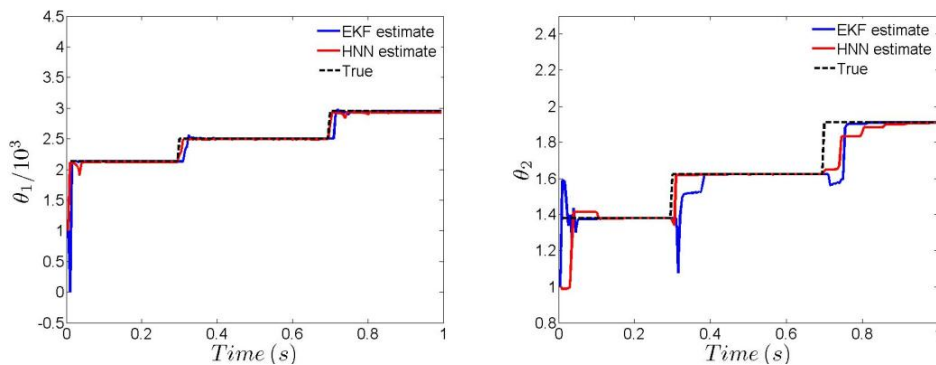
Figure 3 - *Time-evolution of beam parameters under the conditions of S7.*

Table 2 presents the value of the mean error obtained with the application of each identification method in each of the scenarios S5, S6 and S7. The results obtained agree with the results obtained in Figures 1, 2 and 3.

Table 2 - *mean error obtained with the application of the EKF and the HNN in scenarios S5, S6 and S7.*

	S5	S6	S7
EKF	2.5×10^{-2}	4.5×10^{-2}	3.6×10^{-2}
HNN	1.7×10^{-2}	1.2×10^{-2}	3.6×10^{-2}

5   Conclusions

This paper presents a comparison between two identification methods for online damage detection in Euler-Bernoulli beams. The first method is an Extended Kalman Filter and the second one is a Hopfield Neural Network. The damage is represented by a variation in some of the model parameters. Results were obtained under various identification scenarios to find the optimal tuning for each method. In order to validate these tunings both identification methods were applied to three other identification scenarios. The results are very satisfactory for both identification methods and encourage their incorporation in an automatic system for online beam damage detection.

6   Acknowledgements

7   References

[1]   Hugo Alonso, Teresa Mendonça and Paula Rocha. *Hopfield neural networks for on-line parameter estimation.* Neural Netw., 22:450–462, May 2009.
[2]   Hugo Alonso, Pedro Ribeiro, and Paula Rocha. *An automatic system for on-line change detection with application to structural health monitoring.* In Proc. of the 35th Annual Conference of the IEEE Industrial Electronics Society, Porto, 2009.
[3]   K. J. Åström and B. Wittenmark. *Computer-Controlled Systems.* Prentice Hall, Englewood Cliffs, NJ, 1984.
[4]   A. Dixit and S. Hanagud. *Single beam analysis of damage beams verified using a strain energy based damage measure.* International Journal of Solids and Structures, 84, February.
[5]   D. J. Inman. *Engineering Vibration.* Pretince Hall, 1994.
[6]   Samborski S. Manoach, E. and J. Warminski. *Delamination detection of laminated, nonlinear vibrating and thermally loaded beams.* In Proc. of the 10th International Conference on Vibration Problems, pages 67–74.
[7]   P.M. Pawar and R. Ganguli. *Structural Health Monitoring Using Genetic Fuzzy Systems.* Springer, Englewood Cliffs, NJ, 2011.
[8]   D. R. Prasad and D. R. Seshu. *Study on change in modal parameters of RC beams due to faatigue type damage.* Asian Journal of Civil Engineering (Bulding and Housing), 11:521–532, 2010.
[9]   Torsten Söderström. *Discrete-time Stochastic Systems.* Springer-Verlag, London, UK, 2002.

Structural Health Monitoring Based on a Global Optimization Approach

Antunes PJ[1], Guimarães RJ[1], Vaz AI[2], Viana JC[1]

[1]Critical Materials, Lda.,

SpinPark - Centro de Incubação Tecnológica,

Zona Industrial da Gandra, 4806-909 Guimarães, Portugal

pjantunes@crtical-materials.com

[2]Departamento de Produção e Sistemas,

Escola de Engenharia, Universidade do Minho,

Campus de Gualtar, 4710-057 Braga, Portugal

Abstract: SHM-Structural Health Monitoring of critical parts is gradually assuming a relevant role in several engineering fields such as civil, aeronautical and aerospatial. For the particular case of vibration-based SHM techniques, variations in the structure's dynamic response with respect to a healthy baseline (resonance frequencies, mode-shapes and modal damping) are monitored in order to detect the presence of structural damage. Several SHM techniques are able of determining the presence of damage. However, the location and damage severity estimations are variables more difficult to assess. In fact, for the SHM community, this is a very important research field. Critical Materials S.A., of years to this part, is focusing its work in the development of SHM algorithms based on the combination of information retrieved from virtual models (**FE**-Finite Element) with dynamic data obtained from components in service. In this work, a new SHM approach based on global optimization techniques is presented, combining data retrieved from FE models and experimental data. This method is able of, simultaneously, locating, determining the type of damage (stiffness, mass, damping) and outputting its severity (size and variation in material properties). This method demands automated pre/post-processing operations of dynamic FE models, using Abaqus scripting capabilities, and continuous data exchange between Abaqus platform and the external global optimization module. The proposed approach results in a closed loop optimization process, with automated local variation of material and structural properties, driven through the considered objective function. In order to discuss the potentiality of the proposed method several case studies are presented and discussed.

1   Introduction

Mechanical structures subject to vibration loading (deterministic or non-deterministic) are more suitable for failure under normal operative conditions. In fact, the intrinsic nature of vibration loading, associated with loading-unloading effects that can occur at high frequencies, can under some circumstances initiate damage mechanisms that could lead to a catastrophic failure of the structure. The failure during service of mechanical structures must be correctly anticipated in order to avoid accidents that in some cases (automotive, aerospatial) could originate human injuries and equipment loss.

The use of **NDT**-Non Destructive Techniques is nowadays, especially in the aeronautic industry, a common evaluation technique for monitoring the structural integrity of aerostructures. Examples of **NDT** are: Eddy current method, Electromechanical Impedance, Ultrasonic inspection and Lamb Waves. These methods are some of the most used for the inspection of mechanical structures. These techniques are, in concept, off-line methods that are applied when the structure is not in service. They compare the baseline response (undamaged structure) with the current response of the structure. **SHM** techniques, on the other hand, are based on the continuous monitoring of the state of the structure with damage identification (detection/location/severity) in mind. **SHM** involves the integration of sensors and/or actuators, data acquisition and transmission, computational power and processing ability inside the structure, differing from the conventional inspection techniques used in **NDT**.

FEM-Finite Element Method is a very valuable tool for the prediction of the dynamic behavior of structures. In fact, Critical Materials S.A. is developing a **SHM** system that relies on **FE** analysis to identify material damage at the element level. This proposed methodology relies on a good and coherent definition of **FE** models, namely, loading conditions and material constitutive modeling. In fact, the **FE** model should take into account all the mechanical characteristics (elastic and dissipative properties) of the material and the type of loading (deterministic or non-deterministic) that is being applied to the part, in order to allow for a coherent comparison between real and simulated dynamic results.

For the present case-study, in particular, an **SHM** procedure based on a global optimization process is presented. The combination of experimental and simulated dynamic data is the main basis of the proposed method, combining automated pre and post-processing **FE** operations with the execution of optimization loops driven by an external global optimization module.

2   CMT's approach to SHM.

CMT-Critical Materials, of years to this part, is focusing its work in the development of **SHM**-Structural Health algorithms based on the combination of information retrieved from virtual models (**FE**-Finite Element) with dynamic data obtained from components in service. Normally, for damage location and severity estimation procedures, the developed algorithms rely on acceleration or strain data.

The developed algorithms are based on the premise that a change on the dynamic response (considering constant the boundary conditions) of a structure implies a change on the material properties. In fact, the dynamic response of a structure is dependent on several material parameters such as mass, stiffness or damping [1] which has a direct effect on the dynamic response of the structure. Resonance frequencies, modal damping and mode shape are examples of variables that vary in function of the structural state of the analyzed structure.

As an example, is plotted in Figure 1 two spectra (obtained from simulation) correspondent to a baseline (healthy) and damaged (delaminated) structure [2].
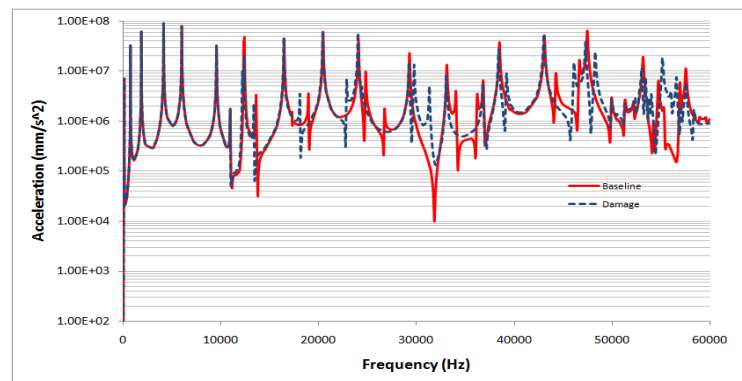
Figure 1 *– Acceleration Spectrum (Baseline Vs. Damaged structure)*

Analysis of experimental data can, by itself, detect if the structure suffer any kind of damage, through, for example, applying signal comparison techniques between the baseline and actual states. However, the location of damage and estimation of its severity it's a more complicated task that demands dedicated and more complex algorithms. In fact, the algorithms developed by **CMT** relies, also, on **FE** data in order to take advantage of the discretized domain that allows localized variation of material and structural properties. With this approach, it is possible to check how variations (in materials properties or others model variables) to the baseline state, influence the dynamic response of the structure. This simulated data when combined with experimental data can improve the capacity of **SHM** algorithms to detect and localize damage and, also, estimate its severity.

In Figure 2, it is plotted a general scheme with the data flow followed by the **SHM** algorithms developed by **CMT** and incorporated in **PRODDIA®**-Structural Systems Health Monitoring Management system.
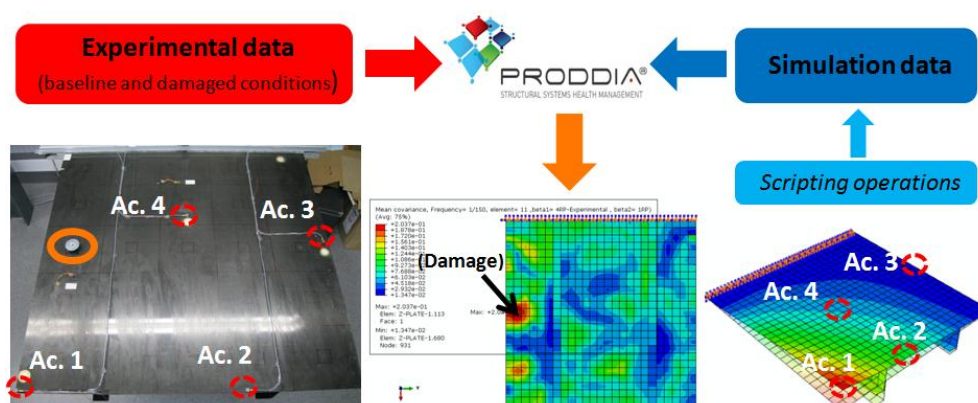
Figure 2 *– Generic data flow implemented in PRODDIA.*

3　Global optimization approach

The proposed method should be able to, simultaneously, locate and quantify damage (variation of Young Modulus, Density and Material/structural damping) based on experimental and simulated data, applying a global optimization approach. This method should rely on intensive automated pre and post-processing **FE** procedures that, in continuous interaction with the external optimization module, drive the process to an optimal solution, corresponding to a damage location and severity.

3.1 Fluxogram

As visible in Figure 3, the fluxogram for the proposed method is divided into four main blocks:

1) *Initial FE operations;*
2) *Optimization;*
3) *FEM Operations;*
4) *Output results.*

The first block is dedicated to the baseline model preparation and simulation of the baseline (healthy) conditions. At this stage, the material and structural properties used are relative to an undamaged (baseline) material.

The optimization block is constituted by the numerical optimization module (optimization code) which, with the proposed method, can be easily replaced by any available (commercial or non-commercial) global optimization module. This characteristic increases the flexibility of the proposed method allowing pre and post-processing operations to be executed using Abaqus scripting capabilities. In fact, these operations are completely automated and executed inside Abaqus platform until an optimal solution is found.

Obtained results are available in *.ODB format, indicating the location of damage (through variation in material properties), its spatial distribution and severity.
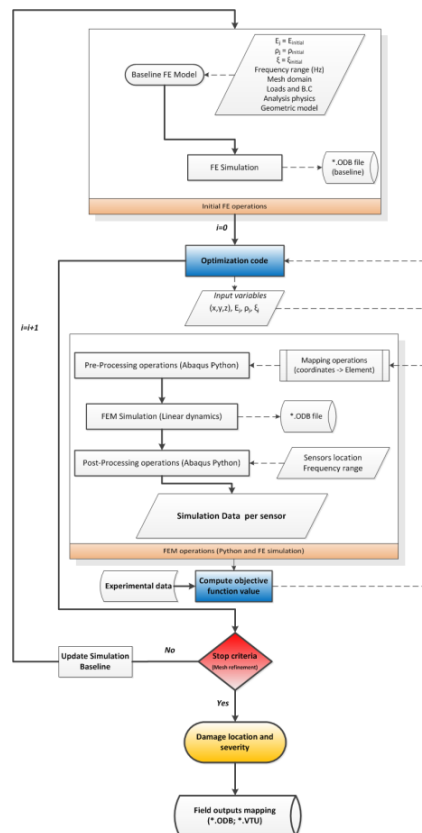
Figure 3 *– Optimization fluxogram.*

3.2 Optimization method

For the present work, the optimization module chosen (PSwarm) is a global nonlinear optimization method, consisting in a direct search method enhanced by particle swarm, which has shown to perform well in a large variety of bound-constrained optimization problems [3] Direct search methods are a popular class of iterative optimization methods that try to minimize a function by comparing objective function values at a finite number of points, where a point, in this context, represents a damage location and severity (see, for example, Con et al., 2009 [4], for additional information about direct search methods).

PSwarm is a population based algorithm, taking advantage in the search for global optima, while it incorporates a direct search strategy to guarantee convergence to local optima. PSwarm is, therefore, a particle swarm algorithm hybridized with a pattern search algorithm. PSwarm is public domain software that can be obtained at http://www.norg.uminho.pt/aivaz/pswarm, providing, among others, an interface to Python (available as a Python module).

As already discussed in Section 3.1, the optimization module, within this framework, treats the objective function as a "black box", as many of its components are obtained by simulation (see Section 3.5). The proposed framework allows other optimization modules to be considered, as long as the global nature of the optimization method is maintained. In fact, we plan to test the use of Evolutionary Strategies or others global optimization algorithms.

3.3 External inputs

The proposed approach is based on the modification of material properties in selected elements of the discretized domain. By so, a base **FE** model that geometrically and dynamically represents the analyzed structure should be defined initially. Special care must be taken in the definitions of loads, boundary conditions and dynamic analysis procedures in order to have a **FE** model representative of the experimental dynamic response. In fact, when experimental signals are used as external inputs, data matching auxiliary operations, between baselines, (experimental/simulation) should be carried on before starting the optimization process

3.4 Optimization variables

Optimization variables are divided into two main categories:

1) *Spatial variables;*
2) *Material variables.*

Spatial variables are coordinates (x,y,z) inputs for the selection of element(s) whose material properties are to be changed in accordance to the optimization flow. In fact, it was implemented a scheme for coordinate-element mapping operations enabling the correspondence between punctual coordinates, obtained from the optimizer, and elements to be affected by changes in material properties.

Material variables, by other hand, are related with the selected material properties to be optimized. Implicitly, damage is accessed, in this procedure, by the monitoring of variation of materials properties to the baseline, as will be discussed in section 5.1.2.

Other **FE** model variables such as dimensions, loads and boundary conditions are considered to be fixed during the optimization process and, therefore, not included in the optimization process.

3.5 Objective function

For damage location procedures, simulated signals, *Y*, can be considered as dependent on material properties such as Young Modulus (*E*), Density (*ρ*), and Material/Structural Damping (*ξ*). These material properties are considered to be local to element *j*. By other hand, experimental signals *X*, are considered as being dependent, only, on the damage location coordinates *x,y,z* (p.ex. spatial coordinates where a mass is positioned in the part). Equations 1 and (2, summarize the dependence of simulated and experimental signals, respectively, where *k* corresponds to the sensor number.

$$Y_k = Y_k\left(E_j, \rho_{j,}\, \xi_j\right) \qquad (1)$$

$$X_k = X_k(x, y, z). \qquad (2)$$

Considering, as an example, the Pearson correlation coefficient as one of the possible correlation metrics to be implemented, we obtain:

$$\phi_k = \frac{\sum_{i=1}^{N}(X_{ik} - \bar{X}_k)(Y_{ik} - \bar{Y}_k)}{\sqrt{\sum_{i=1}^{N}(X_{ik} - \bar{X}_k)^2}\,\sqrt{\sum_{i=1}^{N}(Y_{ik} - \bar{Y}_k)^2}}. \qquad (3)$$

Recalling Equation 3, the objective function *f* can be written by:

$$f = \frac{1}{N}\sum_{k=1}^{N} |\phi_k| - 1 = 0. \qquad (4)$$

For the present case, it was worthy to consider an objective function that compare the two curves (simulated and experimental) and outputs a scalar value of correlation for the considered frequency range and for each experimental sensor. However, other statistical functions can be used, as long as the degree of similarity between experimental and simulated signals can be measured.

4 FE Model

4.1 CFRP Plate

The **FE** model considered for the present case-study is a **CFRP**-Carbon Fibre Reinforced Polymer plate model with approximately 272.5x250mm and 2.5mm thickness.

4.1.1 Material Properties

CFRP material properties were simplified and assumed to be isotropic in order to reduce the number of materials variables to optimize. For this case, and assuming an isotropic behavior, three material variables were considered, namely Young Modulus (*E)*, Density (*ρ)*

and material/structural Damping (ξ). Material properties used in the definition of the **FE** model are summarized in Table 1.

Table 1 - *Material properties*

Material Property	Value
Young Modulus	54 GPa
Density	1380 kgm^{-3}
Poisson's ratio	0.35

4.1.2   Loads and boundary conditions

An Encastre boundary condition was defined at one of the ends of the plate and a unitary load, constant through frequency, was applied at the middle of the right edge simulating an instrumented hammer impact in that zone.

4.1.3   Geometrical domain discretisation

Shell quadratic elements with reduced integration (S8R) were considered for the discretisation of the geometrical domain. In Figure 4, it is displayed a mesh for the CFRP plate considering an element size equal to 10mm. Mass elements were attached to the structure in order to account the self-weight of accelerometers (approximately 11e^{-3}kg) and its influence in the dynamic response of the structure.
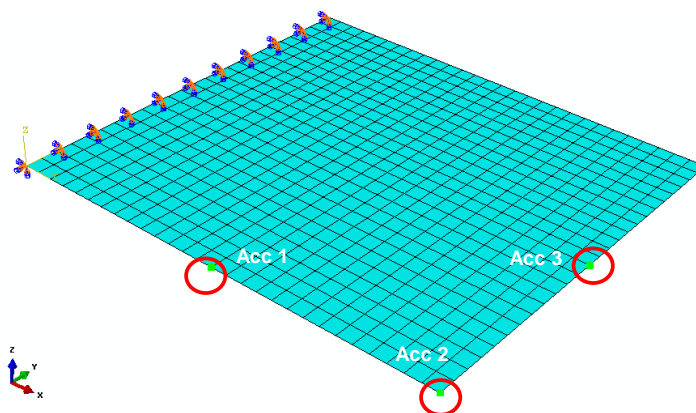
Figure 4 *– Mesh domain.*

4.1.4   Analysis procedure

A mode-base steady-state dynamic analysis procedure was considered for the present **FE** model in the frequency range [0, 1000] Hz. Also, a natural frequency extraction step in the range [0, 1500] Hz, based on the Lanczos Eigensolver, precedes the modal analysis step in order to extract Eigenmodes and Eigenvalues. In order to account the self-weight of the component, a gravity static step was considered as the first step of analysis.

In Table 2 are summarized the main characteristics of the applicable analysis procedures.

***Table 2** - Analysis procedures*

Step	Frequency Range	Frequency Resolution	Damping (modal)
Gravity (self-weight)	N/A	N/A	N/A
Natural Frequency	[0,1500]Hz	N/A	N/A
Modal analysis	[0,1000]Hz	1Hz	0.1%

5 Results

5.1 Simulation Scenario

In this section are summarized the results obtained for damage assessment procedures, replacing experimental signals by signals obtained from simulation. Structural damage, in this procedure, is induced through local (elemental) modification of material properties (see Figure 5 and Figure 6). In practical terms, the simulation of damage scenarios can contribute to study, in more detail, the sensitivity of the proposed method to changes in the dynamic behavior of the structure, without the need of imposing damage to the real structure. Also, the number of damage cases tested and its nature is more easily controlled.

5.1.1 Inputs

a) Signals

As explained above, experimental signals were replaced by simulated signals obtained after elemental affectation of material properties in the **FE** mesh. These simulated signals were obtained by inducing an artificial damage on elements *40, 108, 74* and *4*. As an example, we depict in Figure 5 and Figure 6 the plate model with damage induced in elements *40* and *108*, respectively, considering an element size of 20mm.For the first depicted case (damage in element *40*), the damage is induced through a decrease of 15% in the Young Modulus (E). The damage in element *108* was defined as variation of both Young Modulus and material Density (ρ) equal to 15% and 10%, respectively.

In Table 3, are summarized the levels of damage relative to the four damage cases tested.

***Table 3** - Damage cases*

Case	Young Modulus	Density	Damping (Modal)
1 (Element 40)	-15%	0%	0%
2 (Element *108*)	-15%	-10%	0%
3 (Element *74*)	-15%	0%	0%
4 (Element *4*)	-15%	0%	0%
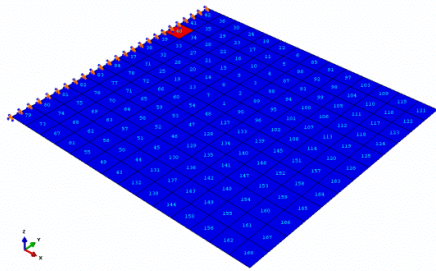
Figure 5 – *Damage applied in element 40*
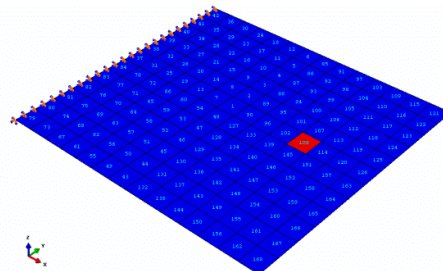
Figure 6 – *Damage applied in element 108*

Acceleration spectra is extracted for the three considered nodes (accelerometers) and used as input for the damage assessment procedure.

b) FE Model

The **FE** model considered as the basis for the damage assessment procedure, has an element size equal to 10mm (see Figure 4), which is different from the element size considered for the **FE** model that originate the input signals (see Figure 5). In fact, the mesh mismatch could introduce more complexity to the optimization process but is interesting to test the capability of algorithm in detecting multi-elemental damage and, therefore, the damage size. In fact, when real signals (experimental) are introduced, the method should be able to detect damage and estimate its severity, independently of the mesh element's initial size.

5.1.2 Damage assessment

In Figure 7, Figure 8, Figure 9 and Figure 10 are plotted the damage field maps obtained for the signals correspondent to damage in elements *40, 108, 74* and *4*, respectively. These damage maps correspond to the optimum material properties distribution in accordance to the considered objective function.

Blue areas in displayed images corresponds to baseline (unchanged) material properties, while, elements colored in red suffer perturbation in the initial materials properties and therefore indicates zones that, most probably are affected by structural damage. A white box indicating the geometrical position (and size) of induced damage (for correspondence see Figure 5 and Figure 6) was inserted in the figure, in order to facilitate the correspondence between discretized domains. Variation of optimized materials properties to baseline (healthy conditions) are summarized in Table 4.

Table 4 - *Optimization results (variations to baseline)*

Case	Young Modulus	Density	Damping (Modal)
1 (Element *40*)	-6.3%	+5.8%	-0.9%
2 (Element *108*)	-7.98%	-5.32%	-4.5%
3 (Element *74*)	-29.1%	-7.3%	-2.5%
4 (Element *4*)	-0.97%	+0.12%	-0.84%
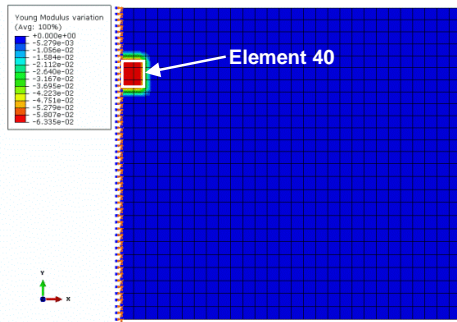
***Figure 7** – Damage map (Damage applied in Element 40)*
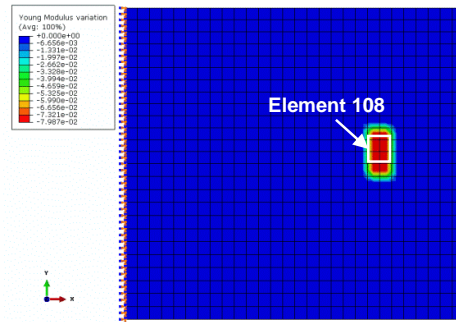
***Figure 8** – Damage map (Damage applied in Element 108)*
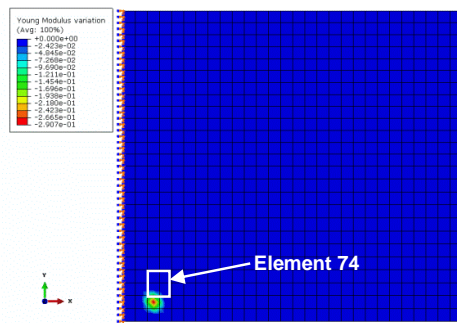
***Figure 9** – Damage map (Damage applied in Element 74)*
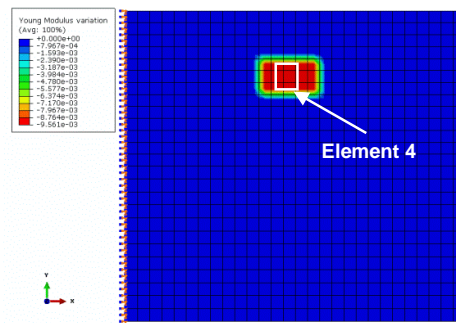
***Figure 10** – Damage map (Damage applied in Element 4)*

6   Discussion

The proposed optimization method was capable to detect variation of material properties (structural damage) in the zones used as input. In fact, for the considered cases, the worst detection capability was found for the case 3 (see Figure 9). Even for this case, the proposed method was capable to detect damage in an element near the damaged zone. However, damage size and severity estimation were not so consistent. In fact, for cases 2 and 4, the damaged area found was greater than the defined as input (see Figure 8 and Figure 10). One of the reasons that can contribute to this effect is the mismatch of meshes that contribute to the selection of elements outside the original damaged area, affecting, consequently, the dynamical behavior of the structure and increasing the difficulty to mimic the input signal. Other reason that can contribute to this effect is the prioritization of optimization variables. In fact, the size of damage (coordinates of element selection window) is the last variable to be optimized that, in conjunction with an inadequate maximum number of simulations, can lead to not so good results

7   Conclusions

The proposed global optimization method, using dynamic simulation data, is capable of detecting damage at multi-elemental level. However, the capability of damage severity and size estimation should be improved. In fact the high number of variables involved (signal variables, model variables and optimization variables), contribute to the complexity of the problem and should be further studied.

The proposed method, in our opinion, has the potentiality to become a commercially valid option for companies interested in **SHM** techniques, namely, for asynchronous structural

damage assessment of parts. Currently, we are embedding this methodology into **PRODDIA®
SHM** platform.

8   Future works

In order to minimize the effect of mesh mismatch and mesh dependence, a mesh refinement process will be included, in the optimization process, in order to further decrease problem's mesh dependence. With this approach, we think it can be possible to improve the capability of damage severity and damage size estimation. However, the refinement process could lead to a more time-consuming process.

Also, it is in the scope of this work, to use experimental data as input for damage assessment procedures. For practical reasons, the damage will be, initially, induced through variation of local mass.

Increasing the number of material variables, through, the inclusion of orthotropy in the definition of material's (CRFP) mechanical behavior will, also, be considered.

The use of different optimization methods, such as Genetic algorithms, is planned for the future and it will be tested in future developments of the proposed method.

9   References

[1] Kim H-Y, "Vibration-based damage identification using reconstructed FRFSs in composite structures", J. Sound Vibr., 259(5), pp. 1131–1146, 2005.

[2] Antunes PJ, Guimarães RJ, Ferreira NJ, Rocha AZ, Baptista MA, Viana JC, Dias GR, "Vibration-based Structural Health Monitoring of composite structures", Proceedings of the 2011 SIMULIA Customer Conference, Barcelona, 2011.

[3] Vaz AIF, Vicente LN, "A particle swarm pattern search method for bound constrained global optimization", Journal of Global Optimization, 39, pp. 197-219, 2007.

[4] Conn AR, Scheinberg K, Vicente LN, "Introduction to Derivative-Free Optimization", MPS-SIAM Series on Optimization, SIAM, Philadelphia, 2009.

Probabilistic assessment of pipelines containing corrosion defect with correlated input parameters based on FITNET FFS procedure

Guian Qian, Markus Niffenegger

Paul Scherrer Institute, Nuclear Energy and Safety Department,
Laboratory for Nuclear Materials, OHSA/06, 5232 Villigen PSI, Switzerland

Abstract   A probabilistic method based on the corrosion module of the FITNET FFS procedure is presented to perform the structural integrity analysis for pipelines by considering plastic collapse. FITNET FFS procedure predicts the same probability as that by the Shell-92 model. The sensitivity analysis of the underlying model shows that the corrosion depth has the most significant contribution to the pipeline failure at an inspection interval of 8 years. The method to allow for the correlations between the input variables is also presented. If the correlation between the initial defect depth and the initial defect length for an individual defect is not considered, the predicted results can be nonconservative.

Nomenclature

D	outer diameter of the pipeline, mm
$d(T)$	time-dependent depth of the defect, mm
d_0	measured depth of the defect at time T_0, mm
k	number of the Monte Carlo simulations for the jth variable
L_0	measured surface length of the defect at time T_0, mm
$L(T)$	time-dependent surface length of the defect, mm
L_{SF}	limit state function, MPa
n	total number of simulation cycles
p_i	rank of the jth variable among the total simulated random variables
p_f	failure pressure of the corroded pipeline, MPa
p_{op}	pipeline operating pressure, MPa
P_F	failure probability of the pipeline
Q	length correction factor
$q_{i,j}$	rank of the output among the total k simulated results for the input p_i
r_j	Spearman rank correlation coefficient for the jth input variable
t	wall thickness of the pipeline, mm
T	elapsed time, years
T_0	time of last inspection, year
$x, x_{2, ...,} x_N, X, Y$	random variables
ΔT_e	pipeline elapsed time since the last inspection date, years
V_r	radial corrosion defect growth rate, mm/year
V_a	axial corrosion defect growth rate, mm/year
$\sigma, \sigma_x, \sigma_y$	standard deviation of random variable
σ_{ys}	yield stress, MPa
σ_{uts}	ultimate tensile strength, MPa
μ, μ_x, μ_y	mean value of random variable
ρ_{XY}	correlation coefficient between X and Y

1   Introduction

Corrosion is recognized as one of the most important degradation mechanisms that affect the long-term reliability and integrity of metallic pipelines. Two basic methodologies are commonly used to predict the remaining lifetime of pipelines. One is the traditional code-based deterministic approach, where the ASME B31G [1], the Modified B31G [2, 3], the Shell-92 [4] models, etc, are used to determine the failure pressure of pipelines. The other is the probabilistic approach, where the stochastic character of random variables is introduced into those models and the failure probability of pipelines is predicted at various operation periods [5-8].

The deterministic approach has received the most attention for the pipeline safety assessment due to the easy application. However, in order to account for the uncertainties in parameters and to achieve a more realistic reuslt, a probabilistic approach should be used.

More recently, the FITNET FFS procedure [9] provides a new failure pressure model in the corrosion module to analyze the plastic collapse failure of pipelines. Therefore, in this paper, a probabilistic method based on the FITNET FFS procedure is presented to predict the failure probability of pipelines with corrosion defect by using the Monte Carlo (MC) simulation method. The result is compared to that obtained from the Shell-92 and Modified B31G models. The model sensitivity is analyzed to identify the most important parameters affecting the safety of corroded pipelines. The impact of the correlated input parameters on the integrity of the pipelines is also presented.

2   Probabilistic model of corroded pipelines

In this study, a longitudinal surface corrosion defect is considered in the pipeline, as shown in Fig. 1. For a quasi-steady corrosion process, the time-dependent depth $d(T)$ and length $L(T)$ can be determined by:

$$\begin{cases} d(T) = d_0 + V_r \left(T - T_0 \right), \\ L(T) = L_0 + V_a \left(T - T_0 \right). \end{cases}$$

$$(1)$$
$$(2)$$

In the FITNET FFS procedure, the failure pressure is expressed as [9]:

$$p_f = \frac{2\sigma_{uts} t \left(1/2 \right)^{\left(65/\sigma_{ys} \right)}}{\left(D - t \right)} \left[\frac{1 - \dfrac{d(T)}{t}}{1 - \dfrac{d(T)}{t} Q^{-1}} \right], \tag{3}$$

where

$$Q = \sqrt{1 + 0.8 \frac{L(T)^2}{Dt}} . \tag{4}$$

The limit state function L_{SF} is defined by the difference between the pipeline failure pressure p_f and the pipeline operating pressure p_{op}, given as:

$$L_{SF} = p_f - p_{op} . \tag{5}$$
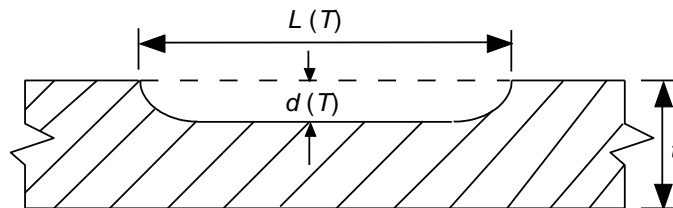
Figure 1 - *Pipeline wall section with an idealized corrosion defect*

The pipeline is considered to operate safely as long as $L_{SF} > 0$ and unsafe when $L_{SF} \leq 0$. The solution of the failure probability of the pipeline is based on the interference model, as shown in Fig. 2.
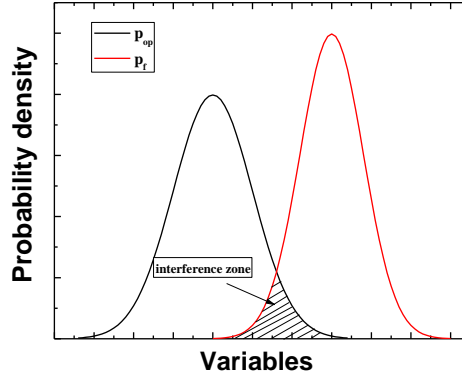
Figure 2 - *Probabilistic assessment model based on the interference model*

The failure probability is given as:

$$P_F = P\left(p_{op} \geq p_f\right) = \int_{-\infty}^{+\infty} f(p_{op})[\int_{-\infty}^{p_{op}} f(p_f)dp_f]dp_{op}. \tag{6}$$

For a general case where $(x_1, x_2, \cdots, x_N)$ are random variables involved, P_F is written as:

$$P_F = \int_{L_{SF}(x_1, \cdots, x_N) \leq 0} f(x_1, \cdots, x_N)dx_1, \cdots, dx_N, \tag{7}$$

where $f(x_1, \cdots, x_N)$ is the joint probability density function of variables $(x_1, \cdots, x_N)$. It is obvious that the integral function is hard to be solved by analytical method due to the complexity. Thus, MC simulation is employed to calculate the multidimensional integral. Random variables $\left(x_1^{(1)}, \cdots, x_N^{(1)}\right), \ldots, \left(x_1^{(n)}, \cdots, x_N^{(n)}\right)$ are generated according to their distributions and the corresponding limit state function $L_{SF}\left(x_1^{(1)}, \cdots, x_N^{(1)}\right), \ldots, L_{SF}\left(x_1^{(n)}, \cdots, x_N^{(n)}\right)$ are calculated. Based on the theory of reliability, the failure probability P_F can be obtained by using the following relation:

$$P_F = \frac{1}{n}\sum_{i=1}^{n}\Omega\left[g(x_1, \cdots, x_N)\right], \tag{8}$$

where

$$\Omega\left[g(x_1, \cdots, x_N)\right] = \begin{cases} 1 & g(x_1, \cdots, x_N) \leq 0 \\ 0 & others \end{cases}. \tag{9}$$

The approximation approaches the exact value of failure probability when the number *n* of MC simulations approaches infinity. The flowchart for computing the failure probability by MC simulation is shown in Fig. 3.

It is possible that there are correlations between different input variables used in Eq. (7). The correlation coefficient ρ_{XY} (-1 $\leq \rho_{XY} \leq$ 1) between two random variables X and Y is defined as:

$$\rho_{XY} = \frac{E\left[(X - \mu_X)(Y - \mu_Y)\right]}{\sigma_X \sigma_Y}, \tag{10}$$

where E is the expected value operator. In order to calculate the failure probability of pipelines by the MC simulation considering the correlated variables, the Nataf transformation

is used in the MC simulation. The correlated random variables generated by the Nataf transformation are used as the input to Eq. (7) to calculate the failure probability of pipelines.
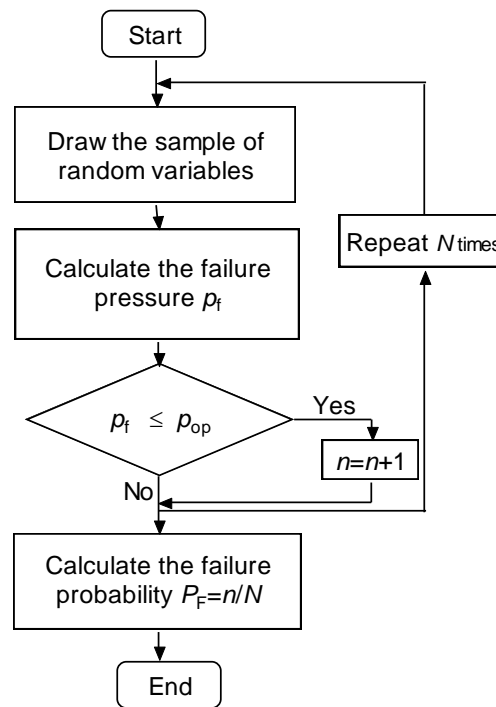
Figure 3 - The flowchart to compute the failure probability

3   Example

In order to demonstrate the applicability of the aforementioned methods, a pipeline described in [5, 6, 7] is chosen in this analysis. The parameters used in this analysis are listed in Table 1 together with their distribution types and statistical values. The failure probability is calculated by the MC method, in which the simulation was repeated 10^5 times.

Table 1 - Random variables used in the assessment (taken from [5, 6, 7])

Parameters	D (mm)	t (mm)	p_{op} (MPa)	σ_{ys} (MPa)	σ_{uts} (MPa)	L_0 (mm)	d_0 (mm)
Mean value	914.4	20.6	7.8	358	455	200	8.24
Standard deviation	18.288	0.412	1.56	25.06	31.85	20	0.824
Distribution	Normal	Normal	Lognormal	Normal	Lognormal	Normal	Normal

4   Results and discussion

4.1 Failure probability

The failure probabilities of the pipeline obtained from the FITNET FFS procedure, the Shell-92 model and the Modified B31G model are compared in Fig. 4. It is shown that the failure probabilities by all the three models increase significantly with the increasing time. The Modified B31G model predicts the lowest failure probability, compared to the FITNET

FFS procedure and the Shell-92 model at the same elapsed time. The FITNET FFS and Shell-92 models predict the same failure probabilities. The failure probabilities at different elapsed times, as well as the trend of failure probability versus elapsed time predicted in this paper are generally in agreement with those in [5] and [6]. This indicates that the presented method for the calculation of failure probability of pipeline is reliable.
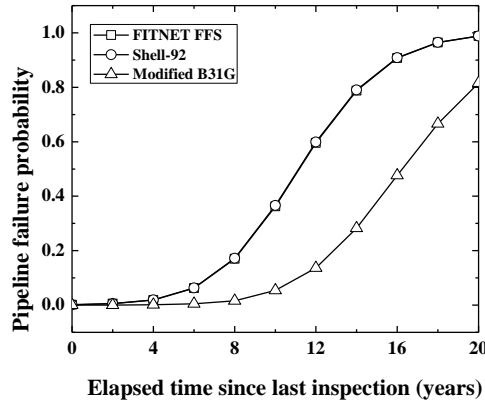
Figure 4 - *Pipeline failure probability by the Modified B31G model, Shell-92 model and FITNET FFS procedure*

4.2 Model sensitivity analysis

Model sensitivity is characterized by the Spearman rank correlation coefficient, which is employed to analyze the joint sensitivity of the random variables and the model. The Spearman rank correlation coefficient is defined as:

$$r_j = 1 - \frac{6 \sum_{i=1}^{n} \left(q_{ij} - p_i \right)^2}{k \left(k^2 - 1 \right)}, \quad r_j \in \left[-1, 1 \right]. \tag{11}$$

The larger the absolute value of the correlation coefficient r_j is, the stronger the dependency of the output on the input variables will be.
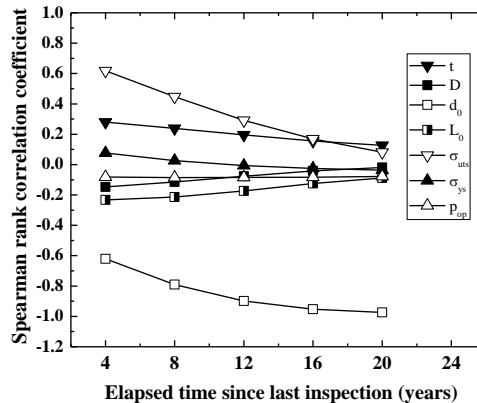
Figure 5 - *Spearman rank correlation coefficient between variable and limit state function at different time*

Fig. 5 shows that the Spearman rank correlation coefficients between the limit state function and every variable at different times. It can be seen that the correlation coefficients

of d_0, σ_{uts}, t and σ_{ys} decrease as the elapsed time increases. For the rest of variables, their correlation coefficients increase with the elapsed time. The Spearman rank correlation is squared for an inspection interval of 8 years to compare their effect on the limit state function. A ranking of the sensitivity of L_{SF} to the variables is given in Table 2. As can be seen, the sensitivity of L_{SF} to d_0 ranks the first, followed by the sequence of σ_{uts}, t, L_0, D, p_{op} and σ_{ys}.

Table 2 - *Ranking degree of sensitivity of variables for T=8 years*

Parameters	d_0	σ_{uts}	t	L_0	D	p_{op}	σ_{ys}
Rate of variation coefficient	65.92%	21.09%	5.97%	4.80%	1.37%	0.78%	0.07%

4.3 Failure probability by considering correlated parameters

In this part, we assume that L_0 and d_0 are correlated with each other because in practice the crack length and depth are controlled by the same defect driving force in the pipeline. Correlation coefficients of 0.3, 0.6 and 0.9 between them are arbitrarily assumed to investigate the effect of the correlation coefficient on the failure probability of the pipeline. Fig. 6 compares the failure probability of the pipeline by considering L_0 and d_0 correlated with the failure probability by assuming them independent (i.e. the correlation coefficient equal to zero). It shows that with a failure probability below 40%, consideration of the correlation between L_0 and d_0 leads to a higher failure probability at the same elapsed time. While when the failure probability is above 40%, the relation reverses. Moreover, the impact of correlation on the failure probability at the same elapsed time increases with the correlation coefficient of the variables. It indicates that without consideration of the correlations, the results are nonconservative under a failure probability of 40% and conservative over a failure probability of 40%. In the real engineering application, the failure probability of the pipelines is supposed to be lower than 40%. Thus, it is important to consider the correlation between L_0 and d_0 in order to achieve a conservative result.
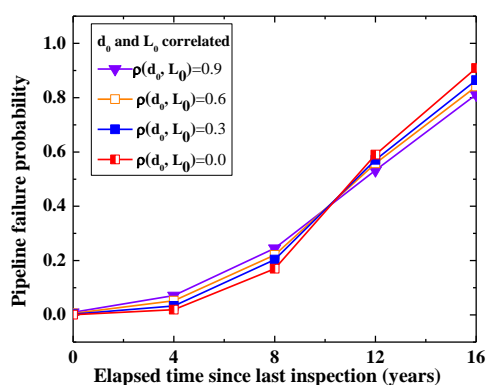
Figure 6 - *Pipeline failure probability by considering L_0 and d_0 are correlated with different correlation coefficients*

5   Conclusions

Based on the presented study, the following conclusions are drawn:
(1) The pipeline failure probability increases with increased elapsed time. The Modified

B31G model predicts the lowest increasing rate of failure probability, whereas the FITNET FFS procedure and the Shell-92 model achieve the same increasing rates at the same elapsed time. It indicates that the Modified B31G model predicts the least conservative result in this study.

(2) Model sensitivity analysis shows that the corrosion defect depth d_0 of the pipeline has the most significant contribution to the pipeline failure probability at an inspection interval of 8 years, followed by σ_{uts}, t, L_0, D, p_{op} and σ_{ys}.

(3) Without consideration of the correlations between L_0 and d_0 will lead to nonconservative results when the failure probability is below 40% and conservative results when the failure probability is above 40%. The impact of the correlated variables on the failure probability increases with the correlation coefficient of the variables.

Acknowledgement

6   References

[1] ASME-B31G, Manual for Determining the Remaining Strength of Corroded Pipelines. A Supplement of ASME B31G Code for Pressure Piping, ASME, New York, 1991.

[2] F. Kiefner, P.H. Vieth, New method corrects criterion for evaluating corroded pipe, Oil Gas J. 6 (1990) 56-59.

[3] ASME-B31G, Manual for Determining the Remaining Strength of Corroded Pipelines. A Supplement of ASME B31G Code for Pressure Piping, ASME, New York, 1995.

[4] N. Leis, D.R. Stephens, An alternative approach to asses the integrity of corroded line pipe, Prat I current status and II alternative criterion, Proceedings of the seventh international Offshore and Polar Engineering Conference, USA, 1997, 624-641.

[5] F. Caleyo, J.L. Gonzalez, J.M. Hallen, A study on the reliability assessment methodology for pipelines with active corrosion defects, Int. J. Press. Vess. Pip. 79 (2002) 77-86.

[6] C.I. Anghel, Risk assessment for pipelines with active defects based on artificial intelligence methods, Int. J. Press. Vess. Pip. 86 (2009) 403-411.

[7] G. Qian, M. Niffenegger, S. Li, Probabilistic analysis of pipelines with corrosion defects by using FITNET FFS procedure, Corros. Sci. 53 (2011) 855-61.

[8] A.K. Sheickh, D.A. Hansen, Statistical modeling of pitting corrosion and pipeline reliability, Corros. Sci.73 (1990) 190-196.

[9] M. Kocak, I. Hadley, S. Szavai, Y. Tkach, N. Taylor, FITNET Fitness-for-Service Procedure-volume 1, GKSS Research Center, 2008.

Analysis of elastic fields in an isotropic medium containing a penny-shaped crack by the Ritz method

A. Tavangari[1], M.T. Kamali[2]

[1]*Main Author, Department of Civil Engineering, Hormozgan University, Bandar-e-Abbas, Hormozgan, Iran, tavangari_a@yahoo.com*
[2]*Department of Civil Engineering, Hormozgan University, Bandar-e-Abbas, Hormozgan, Iran*

Abstract   In the crack growth analysis, the Stress Intensity Factor (SIF) is a fundamental prerequisite. In the present study, the mode I stress intensity factor (SIF) of three-dimensional penny-shaped crack is obtained in an isotropic elastic cylindrical medium with arbitrary dimensions under arbitrary loading at the top of the cylinder, by the semi-analytical method based on the Rayleigh-Ritz method. This method that is based on minimising the potential energy amount of the whole of the system, gives a very close results to the previous studies. Defining the displacements (elastic fields) by hypothetical functions in a defined coordinate system is the base of this research. So for creating the singularity conditions at the tip of the crack the appropriate terms should be found.

Keywords: Three-dimensional cracks; Penny-shaped crack; Stress intensity factor; Fracture mechanics; Ritz method

Optimization of Lattice Structures manufactured by Selective Laser Melting

F. Brenne[1], T. Niendorf[1], H.J. Maier[1,2]

[1]University of Paderborn, Lehrstuhl für Werkstoffkunde (Materials Science), Pohlweg 47-49, 33098 Paderborn, Germany

[2] Direct Manufacturing Research Center (DMRC), Mersinweg 3, 33098 Paderborn, Germany

Abstract In light of shortage of resources, the design and analysis of light-weight structures become increasingly important. Cellular metallic materials produced by direct manufacturing tools are promising candidates to fulfill the upcoming requirements in terms of design flexibility and high specific strengths. Recent studies mainly focus on monotonic mechanical properties of such structures, especially under compressive load. So far, local deformation mechanisms under different loading scenarios have received little attention despite the relevance for actual applications.

Therefore, the objective of the current study was to address the deformation behavior of a lattice structure produced by selective laser melting. A comprehensive in-situ approach was applied using electron back scatter diffraction and digital image correlation (DIC). Samples of Ti-6Al-4V alloy were heat-treated and tested under monotonic and cyclic loading. Results showed that DIC is capable of analyzing the local deformation behavior and detecting failure at an early stage of deformation. This study contributes to understanding the mechanical properties and clarifies the role of local deformation mechanisms. The outcomes allow for subsequent optimization of geometry to design load-adapted structures.

1   Introduction

Currently, great efforts are made in industry and research to reduce fuel consumption and exhaust of emissions by means of consequent light-weight design. Another objective in both fields is to reduce the overall material consumption and therefore to save the shrinking natural resources. Different approaches to fulfill the upcoming requirements can be observed. On the one hand, there is the use of materials of high specific strength, such as aluminum and magnesium alloys, which certainly are most present in public perception [1-3]. On the other hand, there are strategies, which aim at reducing the components' weight using the sandwich design of single components or the integral design of entire structures [3-5]. The latter approach requires geometries of high complexity and therefore presents great challenges to the manufacturing processes.

In this context, the additive manufacturing (AM) techniques, which allow for fabrication of near-net-shaped parts, are of increasing interest, as shown by numerous studies on this subject [e.g. 6-8]. Components manufactured by AM-techniques are built up layer-wise and therefore allow for production of three dimensional parts of high complexity. Depending on the type of the starting materials different function principles are distinguished. Powder bed based techniques include selective laser sintering (SLS), electron beam melting (EBM) and selective laser melting (SLS). Representatives of wire based methods are fused deposition modeling (FDM) and shaped metal deposition (SMD). For each technique certain assets and drawbacks can be observed. In case of SMD, there is a lower contamination of the base material due to a

low surface to volume ratio [9], but also a limited minimum feature size in comparison to SLM. Actual applications of AM products are seen in the fabrication of biomedical parts, e.g. hip prosthesis or dentures, due to the advantage to produce parts adapted to a specific patients' needs. Especially the Ti-6Al-4V alloy is of high importance due to its biocompatibility. An important issue is the adaptation of the stiffness of the replacement to the stiffness of the surrounding tissue. The high design flexibility and the extremely small sized features possible with powder bed AM technologies allow for open or closed cell structures with locally adapted stiffness and optimized compatibility [10]. Further applications are seen in the aerospace sector, where load adapted light-weight structures are increasingly requested in order to reduce the fuel consumption and buy-to-fly ratio [4,11]. Here the Ti-6Al-4V is also a promising candidate due to its balanced and well-studied properties.

Previous studies in the AM field focused on the process parameters, like powder morphology and laser parameters, and their influence on the mechanical properties of the resulting specimens [12,13]. Further investigations envisaged microstructural and mechanical properties of the produced bulk material [14-16]. Studies, which first used the intrinsic advantage of AM technologies, were for instance carried out by [12,17], who investigated the mechanical behavior and failure modes of diverse metallic lattice structures. So far the microstructure of additive manufactured lattice structures has received little attention, despite its crucial importance for the resulting mechanical properties [18]. In case of Ti-6Al-4V the microstructure can be varied by different heat treatments [19], which have a high influence upon the mechanical properties. However, due to layer-wise manufacturing with repeated heat dissipation during the process, traditional heat treatments will not lead to the same microstructural features, as obtained following conventional fabrication methods. Thus, the impact of heat treatment on the microstructure and mechanical behavior for SLMed Ti-6Al-4V lattice structures was investigated in this study.

Another important aspect when increasing the specific loading capacity, is the geometry of the lattice structure itself. As Rehme [12] showed, the relative density as well as the design of the base cell of lattice structures is of high relevance for the resulting mechanical properties. In order to understand the resulting failure mechanisms and to reveal existent weaknesses, the local deformation behavior of one specific lattice structure was examined by means of digital image correlation (DIC). This technique allows for detecting local strains, which serve as indicators for sample failure [18]. The mechanical behavior under tensile and cyclic loading is of high relevance for the envisaged applications, and thus, these loading conditions are employed in this study.

2 Experimental Details

The object of this study was a cubic lattice structure, which was manufactured additively by means of selective laser melting. The cubes had an edge length of 10 mm and consisted of 2 mm x 2 mm x 2 mm star shaped base cells with a mean strut diameter of 0.2 mm. A CAD model of the base cell as well as an image of the entire cube is depicted in Figure 1.
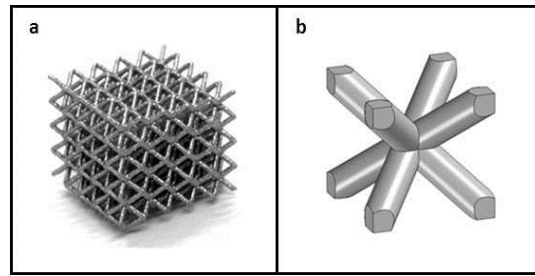
Figure 1 *Image of the cubic lattice structure with an edge length of*
10 mm x 10 mm x 10 mm (a) and CAD model of the base cell with dimensions of
2 mm x 2 mm x 2 mm (b) [18].

For fabrication of the specimens a SLM250HL selective laser melting machine (MTT Technologies GmbH) in combination with MTT AutoFab software Version 1.4 Build 7417 (Marcam Engineering GmbH) was used. The building direction during layer-wise manufacturing was alongside the loading axis of the specimen. An overview of the process parameters is given in *Table 1*.

Table 1 *SLM-process parameters and powder properties*

Laser	Beam energy	Scan velocity	Layer thickness	Average particle size
Yttrium fiber	100 W	450 mm s^{-1}	30 µm	40 µm

Within the same process grip sections were attached to the lattice structure. Thus, a one-piece design of the specimen was achieved, which allowed for mounting the sample directly to the test machine. Previous studies showed that process-related powder particles on the samples' surfaces generate a proper contrast in order to conduct DIC [18]. Therefore, the usually required modification of the surface, e.g. through deposition of an artificial speckle pattern, was not necessary.

Two different microstructural conditions of the titanium alloy were considered. In addition to the as-processed material, samples with a heat treatment in vacuum atmosphere for 2 h at 1050 °C followed by furnace cooling were studied. The characterization of the resulting microstructure was realized by means of electron backscatter diffraction (EBSD). In order to receive a proper surface quality the junctions of the struts were first mechanically polished down to a grid size of 5 µm and then electro-polished utilizing a 5 % perchloric acid solution under a potential of 20 V at -40 °C. Detailed parameters of the EBSD-scans are given in Table 2.

***Table 2** Parameters applied for EBSD scans*

| Material	Acceleration voltage	Working distance	Scanned area	Step size
Ti-6Al-4V	20 kV	19 mm	40 μm x 40 μm	0.3 μm

Mechanical loading was carried out using a MTS servo-hydraulic test rig with a maximum load capacity of ± 15 kN. For the purpose of in-situ characterization of local deformations via DIC a Nikon D60 digital camera with a resolution of 10 megapixels was adapted to the test rig. The camera system was equipped with a macro lens used at a working distance of about 17 mm, while additional spotlights ensured a proper illumination of the samples' surface. During the quasi-static examinations the machine operated in deformation control at a displacement rate of 5 μm/s. The deformation was stopped in regular displacement intervals of 50 μm in order to take images of the samples' surface. Testing terminated when a nominal strain of 30 % was reached (in case of tests under compressive force) or until detachment occurred (under tensile force). In case of cyclic loading, the tests were conducted in force control at a frequency of 10 Hz and an R-ratio of -1. To ensure a fatigue failure, an amplitude of $\Delta \frac{F}{2} = \frac{1}{3} * F_{max}$ was applied, with F_{max} resulting from the compressive deformation test of the as-processed condition. During the first 5000 cycles, images of the samples' surfaces where taken in intervals of 100 cycles, thereafter in intervals of 1000 cycles until sample failure.

The calculation of local deformations was carried out using the commercial VIC-2D software by Limes Messtechnik und Software GmbH. The recorded images were correlated applying a subset size of 100 pixels and a step size of 15 pixels. As high shear forces were assumed to be responsible for sample failure (as previously reported by [18]) the Tresca shear theory was used to calculate the local effective strains.

3   Results and discussion

After processing and heat treatment, the microstructure was analyzed via EBSD. Representative scans are depicted in Figure 2. As shown in Figure 2 (a), the microstructure after the SLM-process consists of α-titanium with lamellar grains of only few micrometers in width. It is supposed that the transformation from the high- to the low-temperature phase occurred diffusionless and therefore resulted in martensitic α'-titanium, since the techniques of additive manufacturing are known for high cooling rates during processing [6,12]. The presence of the martensitic phase after additive manufacturing, especially in case of fabrication of small volume parts by SLM, was already discussed in earlier studies [9,12,13] and is further emphasized by the low EBSD image quality. Further investigations, e.g. by means of transmission electron microscopy, are necessary to find a conclusive proof, since it is not possible to distinguish between the α- and α'-titanium by means of EBSD. From comparison of Figures 2 (a) and (b) a significant change in the microstructure after annealing becomes apparent. The initially fine structure gave way to coarser α-grains and body centered cubic (bcc) β-grains. Furthermore, the residual stress decreased by annealing, which is indicated by the high image quality superimposed in Figure 2 (b). Similar trends were also observed in several other studies [e.g.16,18] and are supposed to root in elevated diffusion rates during annealing above the β-transus, in combination with low temperature gradients due to subsequent furnace cooling [19]. The fraction of the β-phase was significantly higher than after the heat treatment conducted by Gorny et al. [18], what is attributed to the elevated

annealing temperature used in the current study. Still, the overall fraction of this phase remained small, a result of contaminations, i.e. oxygen and nitrogen, which act as α-stabilizers [18]. An equiaxed bimodal structure, which is supposed to reveal the most balanced mechanical properties (as shown by [16] on plate material), could not be achieved in this study. This confirms results by other researchers, who annealed at various temperatures after layer-wise manufacturing and did not obtain a bimodal structure [9,16,18]. Therefore, the absence of bimodal structures is seen to root in a particularly low strain energy after processing (as compared to conventional fabrication methods like rolling).
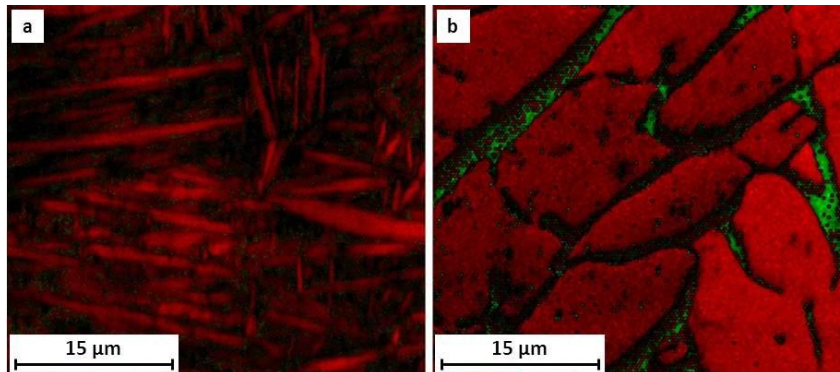
Figure 2 *EBSD scans of titanium samples in the as-processed condition (a) and after heat treatment (b) showing detected phases with superimposed image-quality. The α-phase is depicted in red, the β-phase is shown in green.*

The microstructure's influence on the mechanical behavior of the lattice became evident during subsequent mechanical loading. The resulting compressive force-deformation response of an as-processed as well as of a heat treated sample is depicted in Figure 3 and shows the typical behavior of brittle cellular materials at low degrees of deformation [20]. The minor load drops shown in this graph result from relaxation processes while stopping the testing machine in order to record images for DIC analysis. The as-processed specimen reveals a higher level of the maximum force before an abrupt drop. This drop is related to failure of struts alongside an entire layer of the cube, which became clear by matching the recorded images of the samples with the current state of deformation (not shown). After this first collapse, both samples bear load again with smaller drops in the force signal during further deformation. At this state, the heat treated sample shows higher maximum forces than at the beginning of deformation. However, since the load drops in case of the heat treated condition are not as sharp as of the as-processed condition the ductility is notably improved. The overall energy absorption seems to be almost equal up to a compressive deformation of 3000 μm.
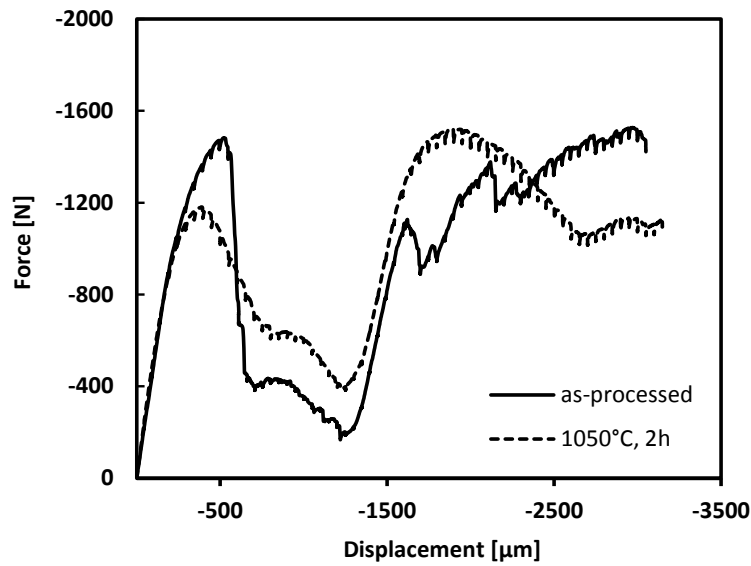
Figure 3 *Compressive deformation behavior of Ti-6Al-4V lattice structures in the as-processed condition and after heat treatment.*

The deformation behavior under tensile force (Figure 4) is different, as the heat treated sample bears higher maximum forces. This sample reveals also a higher ductility, as there are not any steep load drops, as visible in case of the as-processed sample at deformations of about 250 µm and 350 µm. In comparison to the compressive deformation behavior, these load drops are lower. The higher maximum force in case of the heat treated sample is seen to result from the elevated ductility. As the higher ductility allows for alignment of single struts along the loading axis, these struts are able to bear higher forces before failure. These findings additionally support the pivotal role of the geometry regarding the optimization of the structure, as discussed by Rehme [12].
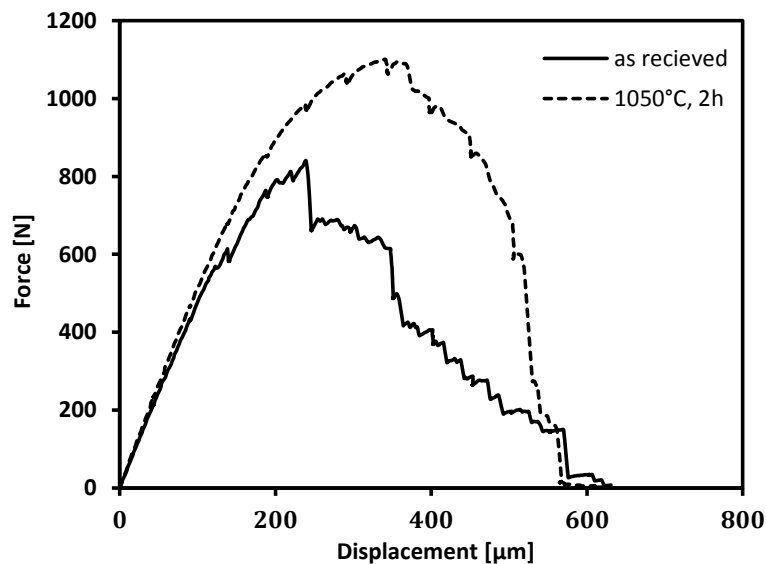
Figure 4 *Deformation behavior under tensile force of Ti-6Al-4V lattice structures following SLM and after heat treatment.*

45

In case of cyclic loading, the heat treated samples reveal improved properties as well, as shown in Figure 5. Although, in both cases there are constantly increasing displacement amplitudes, the overall lifetime is much higher after heat treatment. The softening during the test is supposed to root in failure of single struts and therefore a decreased stiffness of the entire structure. As the as-processed condition is more brittle, single struts show on average an earlier failure, which leads to a reduced overall lifetime.
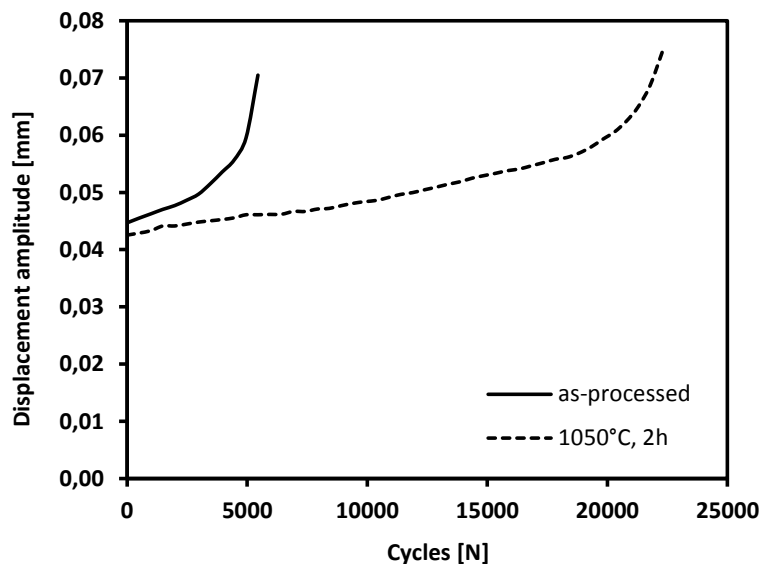
Figure 5 *Displacement response under cyclic loading at ± 210 N, 10 Hz after SLM processing and annealing.*

The differences in the mechanical behavior between the as-processed and the heat treated condition are closely connected with the actual microstructure. In case of the former the extreme fine grain morphology leads to the observed high strength and the low ductility under compressive force. This finding is supported by earlier studies, where a martensitic microstructure led to high strengths and low ductilities [21,22]. After heat treatment the coarser grain morphology and the higher fraction of the β-phase may have led to the improved ductility, as also discussed in [9,18,19]. However, Gorny et al. [18] showed that there is a possibility to raise the ductility at an equal level of strength by a heat treatment at 950°C. The resulting microstructure in their study revealed a lower fraction of the β-phase and an overall finer grain morphology. This emphasizes the importance of the morphology of the grains in addition to the β-phase fraction. The results obtained in the current study, in combination with the results of [18] suggest, that there is an optimum regarding the lath thickness of the α-phase in order to obtain improved ductility and high strength.

The strains calculated for deformation under tensile and cyclic loading are depicted in Figures 6 and 7.
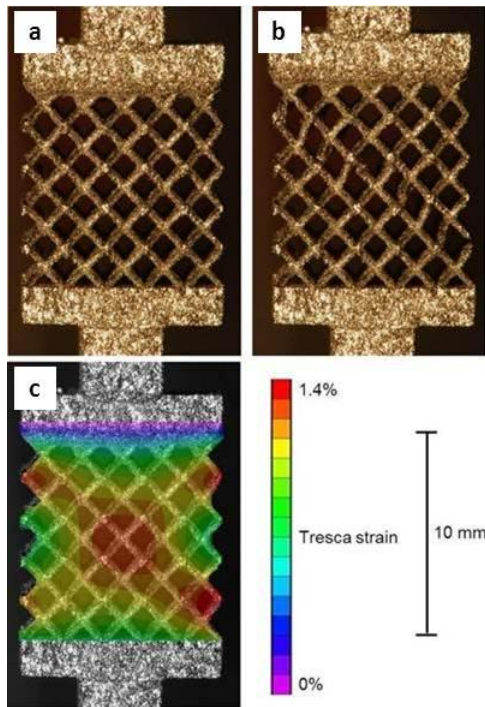
Figure 6 Images of the deformed tensile sample at a displacement of 200 μm (a) and failed sample at 650 μm (b). In (c), the strains calculated at a displacement of 200 μm are superimposed onto the image shown in (a).
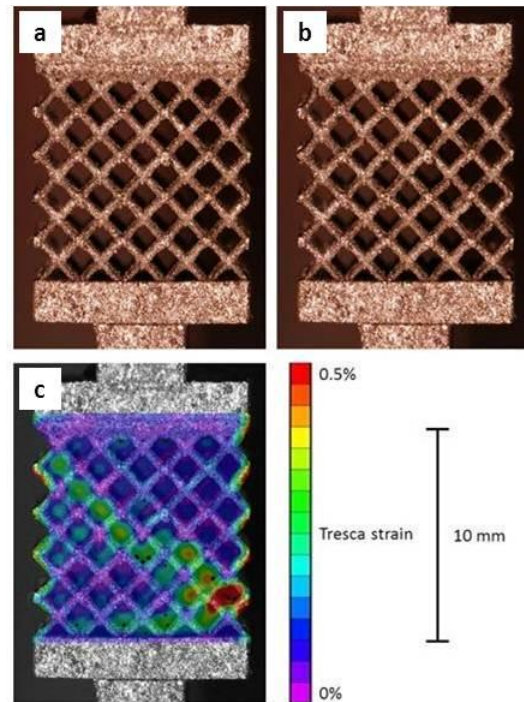
Figure 7 Images of the cyclically loaded specimen at half life (a) and just before failure (b). The strains calculated at the half life are superimposed onto the image in (a).

Since the strain calculation was conducted using a subset size of 100 pixels, deformations are averaged over one base cell and strains in single struts or at the nodes could not be resolved. It has to be noted that high strains over the base cell imply high strains at the nodes [18]. However, the obtained DIC-images clearly show elevated strains at an angle of 45° to the loading axis (Figures 6 (c) and 7 (c)). As the structure is fully symmetric the final failure site depends on the location of inferior defects like pores within single struts. Comparing the elevated strains revealed early by DIC to the images recorded at sample failure (Figures 6 (b) and 7 (b)) it becomes clear, that these are exactly the sites where later failure of the specimens occurred. At the same time the samples exhibit large areas with only low local strains. This demonstrates, that the structure is not evenly loaded and therefore has a high potential for optimization, e.g. through reinforcing the struts in the 45° layers with respect to the loading axis.

While prior studies concentrated on compressive force tests [18] or solely considered the mechanical properties (tensile and ultimate strengths) dependence on cell size [12], the current study sheds light on the deformation behavior under compressive, tensile and cyclic loading. Additionally, the local strains under all loading conditions could be acquired by DIC. As this method reveals minor defects, and thus, highlights the actual deformations within the lattice structure, it is a substantial addition to conventional simulation techniques, such as finite elements method. As the DIC calculations revealed that the strucutre is unevenly loaded and that failure occurred in certain layers of the lattice, the structure can be further optimized in subsequent analyses in order to obtain improved specific mechanical properties.

4 Conclusions

In this study a comprehensive in-situ approach was applied in order to reveal the relationships between the microstructure, the geometry and the mechanical properties of metallic lattice structures manufactured by SLM. Different microstructural conditions of SLMed Ti-6Al-4V were characterized by means of electron backscatter diffraction and related to the mechanical behavior. Additionally, digital image correlation (DIC) was used to determine local strains during deformation with the aim to identify the failure behavior and thereby develop approaches for optimization. The main findings can be summarized as follows:

(1) Annealing of fine SLMed Ti-6Al-4V structures above the β-transus with subsequent furnace cooling leads to disappearance of the initial martensitic α'-titanium at the expense of coarser α-grains and bcc β-grains.

(2) The heat treated samples show improved ductility, which in case of tensile testing leads to higher strengths and under cyclic loading to a higher lifetime. By contrast, under compressive force, the strength is lower than directly after the SLM process.

(3) DIC is capable of detecting the site of failure at an early stage of deformation. As this technique is sensitive to small defects, such as pores, which are not considered by FEM, it is a useful addition to established simulation techniques.

References

[1] W.S. Miller, L. Zhuang, J. Bottema, A.J. Wittebrod, P. De Smet, A. Haszler, A. Vieregge, *"Recent development in aluminium alloys for the automotive industry"*, Materials Science and Engineering A, 280, 37-49, 2000.

[2] D. Brungs, *"Light weight design with light metal castings"*, Materials and Design, 18, 285-291, 1997.

[3] H.P. Degischer, *"Leichtbau – Prinzipien, Werkstoffauswahl und Fertigungsvarianten"*, Wiley-VCH, Weinheim, 2009.

[4] A. Heinz, A. Haszler, C. Keidel, S. Moldenhauer, R. Benedictus, W.S. Miller, *"Recent development in aluminium alloys for aerospace applications"*, Materials Science and Engineering A, 280, 102-107, 2000.

[5] C.A. Steevens, N.A. Fleck, *"Collapse mechanisms of sandwich beams with composite faces and a foam core, loaded three-point bending. Part I: analytical models and minimum weight design"*, International Journal of Mechanical Sciences, 46, 561-583, 2004.

[6] J.-P. Kruth, M.C. Leu, T. Nakagawa, *"Progress in additive manufacturing and rapid prototyping"*, Annals of the CIRP, 47/2, 525-540, 1998.

[7] K. Osakada, M. Shiomi, *"Flexible manufacturing of metallic products by selective laser melting powder"*, International Journal of Machine Tools and Manufacture, 46, 1188-1193, 2006.

[8]   G.N. Levy, R. Schindel, J.P. Kruth, *"Rapid manufacturing and rapid tooling with layer manufacturing (LM) technologies"*, State of the art and future perspectives, CIRP Annals – Manufacturing Technology, 52/2, 589-609, 2003.

[9]   B. Baufeld, E. Brandl, O. van der Biest, *"Wire based additive layer manufacturing: Comparison of microstructure and mechanical properties of Ti-6Al-4V components fabricated by laser-beam deposition and shaped metal deposition"*, Journal of Materials Processing Technology, 211, 1146-1158, 2011.

[10] J. Parthasarathy, B. Starly, S. Raman, A. Christensen, *"Mechanical evaluation of porous (TiAl6V4) structures with electron beam melting (EBM)"*, Journal of the mechanical behavior of biomedical materials, 3, 249-259, 2010.

[11] E. Brandl, V. Michailov, B. Viehweger, C. Leyens, *"Deposition of Ti-6Al-4V using laser and wire, part I: Microstructural properties of single beds"*, Surface and Coatings Technology, 206, 1120-1129, 2011.

[12] O. Rehme, *"Cellular Design for laser freeform fabrication"*, PhD Thesis, Hamburg University of Technology, CuvillierVerlag, Göttingen, 2010.

[13] L.E. Murr, S.M. Gaytan, D.A. Ramirez, E. Martinez, J. Hernandez, K.N. Amato, P.W. Shindo, F.R. Medina, R.B. Wicker, *"Metal fabrication by additive manufacturing using laser and electron beam melting technologies"*, Materials Science and Technology, 28(1), 1-14, 2012.

[14] L.E. Murr, S.A. Quinones, S.M. Gaytan, M.I. Lopez, A. Rodela, E.Y. Martinez, D.H. Hernandez, E. Martinez, F. Medina, R.B. Wicker, *"Microstructure and mechanical behavior of Ti-6Al-4V produced by rapid-layer manufacturing, for biomedical applications"*, Journal of the mechanical behavior of biomedical materials, 2, 20-32, 2009.

[15] S.M. Kelly, S.L. Kampe, *"Microstructural Evolution in Laser-Deposited Multilayer Ti-6Al-4V build: Part I: Microstructural Characterization"*, Metallurgical and Materials Transactions A, 35A, 1861-1867, 2004.

[16] E. Brandl, F. Palm, V. Michailov, B. Viehweger, C. Leyens, *"Mechanical properties of additive manufactured titanium (Ti-6Al-4V) blocks deposited by a solid-state laser and wire"*, Materials and Design, 32, 4665-4675, 2011.

[17] S. McKnown, Y. Shen, W.K. Brookes, C.J. Sutcliffe, W.J. Cantwell, G.S. Langdon, G.N. Nurick, M.D. Theobald, *"The quasi-static and blast loading response of lattice structures"*, International Journal of Impact Engineering, 35, 795-810, 2008.

[18] B. Gorny, T. Niendorf, J. Lackmann, M. Thoene, T. Troester, H.J. Maier, *"In situ characterization of the deformation and failure behavior of non-stochastic porous structures processed by selective laser melting"*, Materials Science and Engineering A, 528, 7962-7967, 2011.

[19] M. Peters, C. Leyens, J. Kumpfert, *"Titan und Titanlegierungen"*, DGM Informationsgesellschaft mbH, Oberursel, Germany, 1996.

[20] L.J. Gibson, M.F. Ashby, *"Cellular Solids – Structure and Properties"*, Pergamon Press GmbH, Kornberg, Germany, 1988.

[21] G. Lütjering, J.C. Williams, *"Titanium"*, Springer Verlag, Berlin, Germany, 2007.

[22] E. Chlebus, B. Kuźnicka, T. Kurzynowski, B. Dybala, *"Microstructure and mechanical behavior of Ti-6Al-7Nb alloy produced by selective laser melting"*, Materials Characterization, 62, 488-495, 2011.

Laser Additive Manufacturing of ScalmalloyRP®: Fracture and Fatigue Behaviour

Katja Schmidtke[1,2], Frank Palm[1], Vitus Holzinger[1], Claus Emmelmann[2]

[1]*EADS Innovation Works, Munich 81663, Germany, Katja.Schmidtke@eads.net*

[2]*Hamburg University of Technology, Hamburg 21073, Germany*

Abstract Modified aluminium alloys containing scandium and magnesium, called ScalmalloyRP®, built up by powder bed based laser additive manufacturing (PB LAM) offer great potential for aerospace applications. ScalmalloyRP® provides an excellent combination of static strength and toughness, but a full material analysis including fracture and fatigue behaviour is essential to validate that it meets the high requirements to become an allowable material for structural aerospace parts. Fracture mechanical characteristics consisting of fracture toughness testing, high cycle fatigue and crack growth behaviour were therefore investigated and are presented in this paper. Samples for each test were manufactured in two different directions (0° and 90°) and tested after artificial aging (4 hours at 325°C). Available alternatives in material choice and manufacturing process are either milling of high strength 7xxx Al-alloys or LAM of medium strength Al-alloys containing silicon and magnesium. Fracture toughness of ScalmalloyRP® was determined for Mode I resulting in K_{IC} values. Both high cycle fatigue (HCF) and crack growth propagation were tested at load ratio R=0.1 whereas crack growth behaviour was additionally tested at a load ratio of R=0.7 to avoid crack closure effects. All investigations show an outstanding material behaviour. Fracture toughness tests result in values presented as combination of yield strength against achievable K_{IC} per aluminium series in Figure 1 a.). A mean value of 39 MPa√m at yield strengths between 500MPa and 515MPa was reached. High cycle fatigue behaviour at load ratio R=0.1 is slightly superior to HCF-behaviour of standard high strength 7075 plate material. The S-N-curves (maximum stress against number of cycles to failure) reveal a run out at $3x10^7$cycles at a maximum stress level of 300MPa, as can be seen in Figure 1 b.). Fatigue-crack growth rate investigations show slow, stable, crack growth for both load ratios investigated (R=0.1 and R=0.7), when compared with high strength 7075 plate material. The results of the testing that was performed demonstrate acceptable fracture and fatigue properties can be achieved with ScalmalloyRP®.
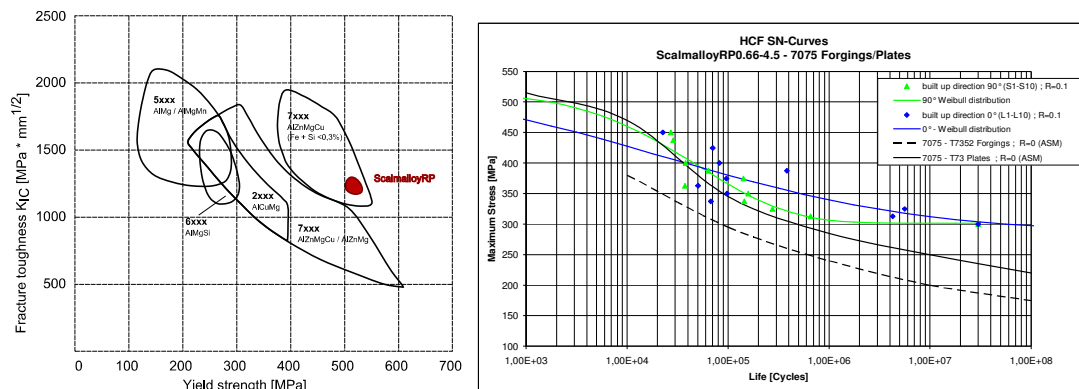
Figure 1 Material behaviour ScalmalloyRP® a.) Fracture toughness K_{IC} b.) S-N curve

Laser heating as approach to retard fatigue crack growth in aircraft aluminium structures

D. Schnubel[1], M. Horstmann[1], P. Staron[2], T. Fischer[2], N. Huber[1]

[1]*Institute of Materials Research, Materials Mechanics, Helmholtz-Zentrum Geesthacht, 21502 Geesthacht, Germany. Contact: dirk.schnubel@hzg.de*

[2]*Institute of Materials Research, Materials Physics, Helmholtz-Zentrum Geesthacht, 21502 Geesthacht, Germany*

Abstract While normally the formation of thermally induced residual stresses is seen mainly as detrimental side effect from production processes like welding or casting, during the last decades some researchers also used the well-directed introduction of thermal residual stresses as tool to retard fatigue crack growth. In the presented study, a defocused laser is used to create a heating line on AA2198-T8 C(T)100 specimens in order to modify the residual stress state. The presented results including thermocouple measurements, residual stress measurements and fatigue crack growth tests show that it is possible to retard fatigue crack growth via laser heating. As next step a quantitative numerical prediction methodology for the resulting fatigue crack growth is developed and validated stepwise on basis of the experimental results. The developed approach couples numerical process simulations for the prediction of the residual stresses with subsequent numerical fracture mechanics analyses. The validated prediction methodology is then used to study the effect of the heating line position on the fatigue crack growth. In conclusion, it is demonstrated that laser heating has the potential to be employed for fatigue crack growth retardation in aircraft aluminium structures.

1 Introduction

One major future challenge for the aircraft industry will be the development of proper strategies for maintenance and life extension of the growing ageing aircraft fleet. In this context, residual stress based life enhancement approaches are believed to have a huge potential for cost efficient solutions [1].

While some researchers used the well directed introduction of thermal residual stresses as tool to retard the fatigue crack growth in thin walled structures during the last decades [2-4], this interesting approach has found so far little attention for aluminium aerospace applications.

The presented work aims to demonstrate that the laser heating process is an interesting new approach for fatigue life enhancement or more specifically for fatigue crack growth retardation and that it is possible to predict the resulting improvements via a FEM based numerical prediction methodology. Furthermore, the developed and validated approach is applied to the optimisation of the positioning of one heating line on a C(T)100 specimen with regard to the total lifetime enhancement in order to demonstrate the capability of the proposed strategy to solve design optimisation problems.

2 Laser heating

A Nd:YAG laser was used for the performed experiments to produce a line of laser heating on the surface of C(T)100 specimens made from the new aircraft alloy AA2198-T8 with a thickness of 5 mm. During the process, the laser travelled at a fixed heating line position $x_h = 55$ mm and with a constant speed of $v_y = 3.33$ mm/s in positive y-direction from one edge of the specimen to the other (Fig. 1). Since the goal was to apply the heating without local melting of the material, a welding optic was used, but the working distance was increased to obtain a laser spot diameter of approximately 5 mm. A layer of silicon carbide powder with a thickness of 0.5 mm was placed on the irradiated surface to ensure an equal absorption of the laser light for all specimens.

Figure 1a shows a photograph of a specimen after laser heating with a schematic of the resulting residual stress state [5]. After heating, tensile longitudinal residual stresses σ_{yy} can be found in the heating area with balancing compressive residual stresses in the remaining part of the specimen. This is similar to the residual stress state after welding.

Figure 1b shows a macrograph of the laser heating area [5]. The depicted vertical structuring is due to the elongated pancake-like grain structure, resulting from the thermo-mechanical treatment during the production. Only beneath the laser-irradiated surface area that is indicated by the white arrows, a slight colour change can be seen in a semi elliptical area. However, no signs of partial melting or surface crack formation can be found.

(a)   (b)
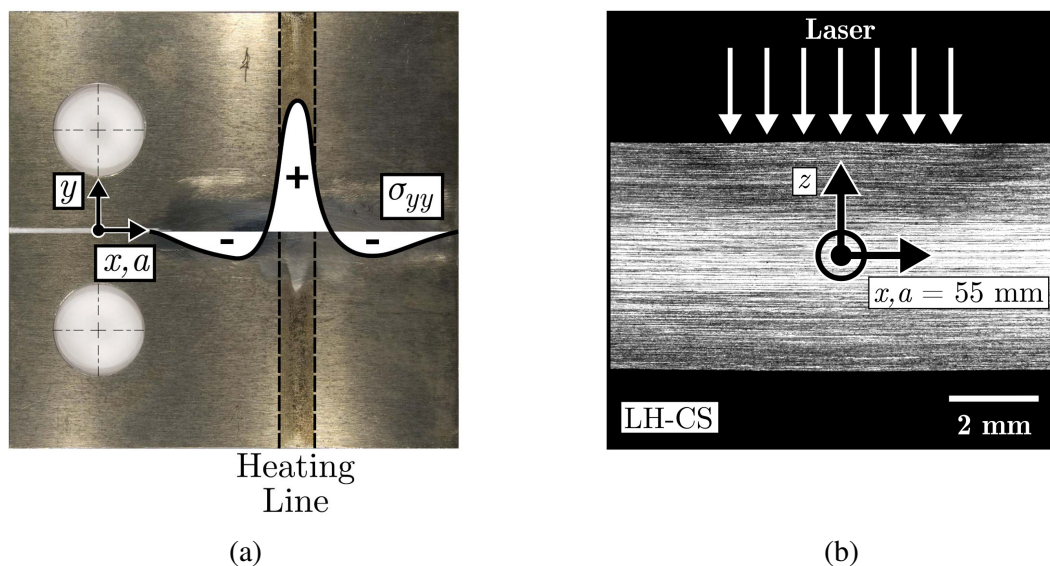
Figure 1 - *(a) Laser heated C(T)100 specimen prepared for FCG testing and (b) cross section macrograph after laser heating [5].*

While the upper graph of Fig. 2 gives a contour plot of the measured micro hardness after laser heating, the lower graph shows the results for $z = 1.8$ mm as line plot [5]. As seen, a significant drop of the micro hardness can be found in the area beneath the laser irradiated surface. For orientation, the lateral extension of the heating zone (HZ) and the heat affected zone (HAZ) are marked light shaded. The remaining part of the specimen shows the hardness of the base material (BM).
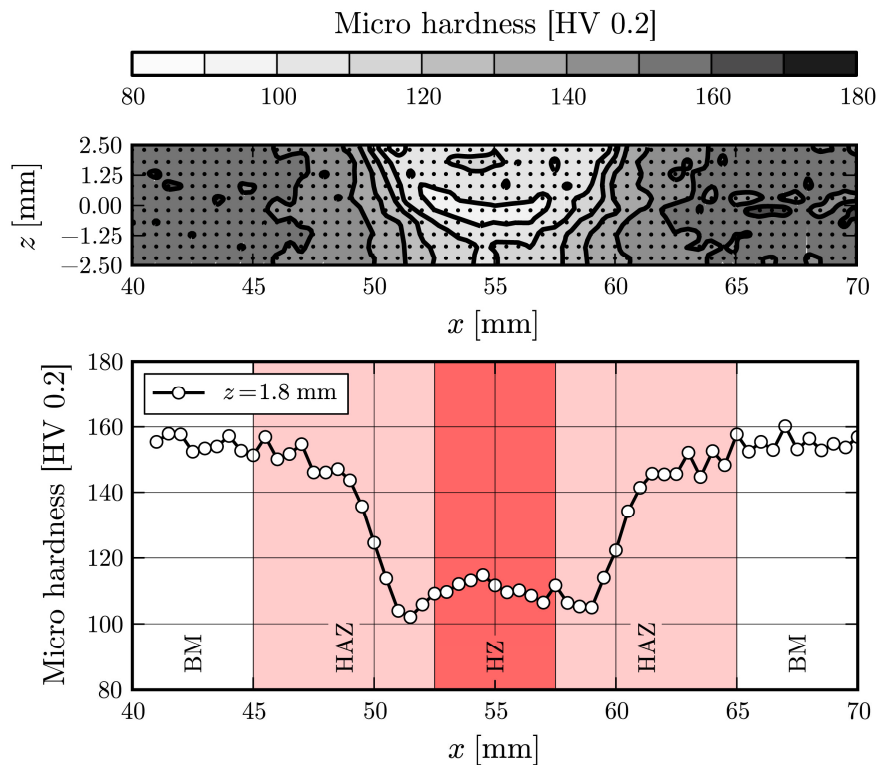
Figure 2 - *Measured micro hardness distribution after laser heating [5].*

Thermocouple measurements were performed to characterise the process temperature field. The heating induced residual stresses were measured for one specimen via synchrotron diffraction using the HARWI II beamline of HZG at DESY, Hamburg. Tests comparing the fatigue crack growth (FCG) of base material and laser heated specimens were performed under constant amplitude loading with $F_{max} = 4.41\pm0.02$ kN and $R = 0.1\pm0.01$; these values are in the typical load range for damage tolerance tests of primary aluminium aircraft structural members. The results of these tests have been published in [5] and are shown later in direct comparison to the numerical prediction results.

3   FCG prediction methodology

The prediction of the fatigue crack growth in structures and components containing residual stresses is a classical fracture mechanics problem and during the last decades the following methodology has found common acceptance [6-9]. In a first step, the residual stress intensity factor K_{res} due to the internal residual stresses is calculated on basis of the measured residual stress component that acts perpendicular to the crack growth direction using for example the finite element method or the weight function method. Then, the total stress intensity $K_{tot} = K_{res} + K_{appl}$ is calculated as the sum of K_{res} and the applied stress intensity K_{appl} using the superposition law. Finally, the fatigue crack growth rate da/dN is calculated by using K_{tot} in an empirical crack growth law, such as the Walker equation.

In general, this approach shows good results. However, with regard to the presented laser heating of C(T)100 specimens there are two major limitations that need to be addressed. Firstly, for cracks growing through compressive residual stress fields, nonlinear contact corrections are needed to ensure a physical sound description of the experimental conditions in the predictions [6,10]. Hence, the superposition law is not valid any more. Secondly,

residual stress measurements are costly, difficult to perform and they normally only deliver specific components of the stress tensor. Additionally, there is a need to perform a large number of measurements, if for example a design parameter like the heating line position shall be examined.

Motivated by these points and adopting the idea presented by Jang et al. [4] to use numerical predictions of heating induced residual stresses as basis for the following fracture mechanics analysis, the extended methodology shown in Fig. 3 was developed, consisting of the following steps:

- Use of a thermal FE analysis to predict the transient heating temperature field.
- Use of a mechanical FE analysis incorporating the thermal expansions and temperature dependent plasticity to predict the full residual stress field after heating.
- Extraction of the total stress intensity factor K_{tot} in a fracture mechanics analysis using the Modified Virtual Crack Closure Technique (MVCCT). In this analysis step the loaded model with the mapped predicted heating residual stresses and distortions is incrementally cut open and a contact condition is added continuously for the newly generated crack faces.
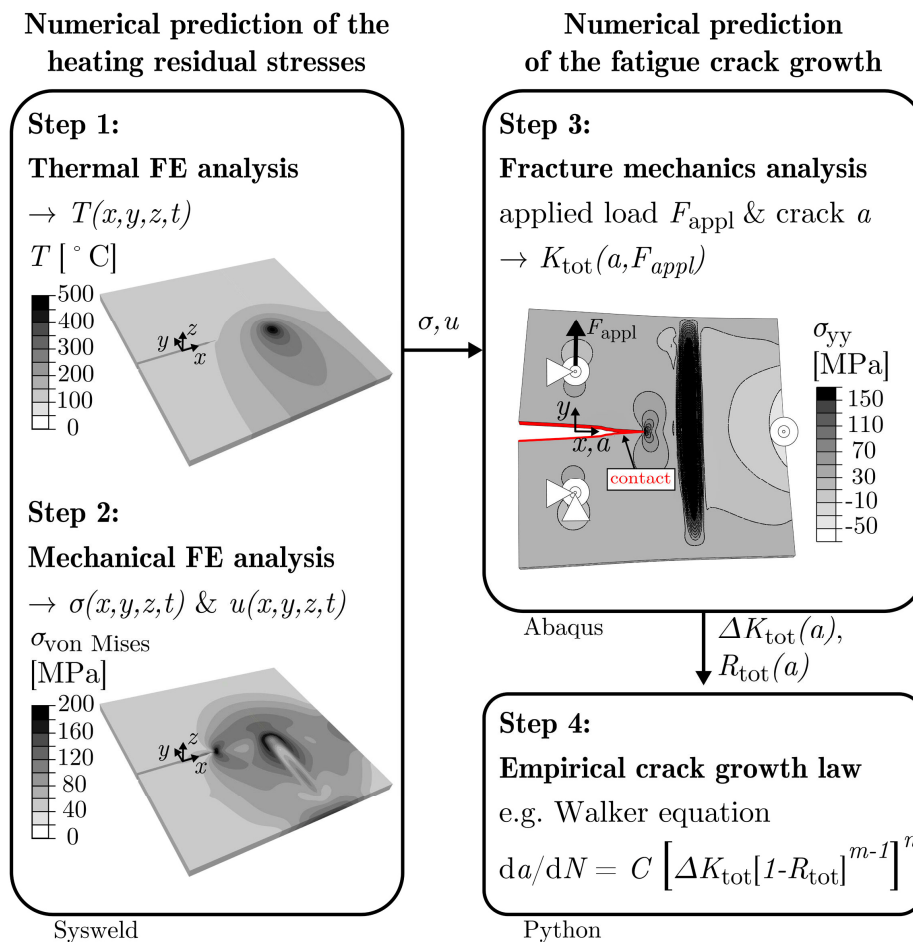- Calculation of the FCG rate da/dN by using the extracted K_{tot} in an empirical crack growth law.

Figure 3 - *Developed numerical prediction approach [11].*

4   Validation of the FCG prediction methodology

This section provides a summary of results published in [11] where also a more detailed description of the used models and boundary conditions is given.

A Goldak ellipsoid volume heat source was used in the thermal analysis for modelling the heat flux into the model. The first step in the thermal analysis is the iterative calibration of this heat source to match the thermocouple measurements. Figure 4a shows the comparison of the measured and numerically predicted peak temperatures T_{max} during the thermo cycle as function of the x-position. As shown, an excellent agreement was achieved with the calibrated heat source.

Figure 4b shows the comparison of the measured and predicted residual stress difference $\Delta\sigma = \sigma_{yy} - \sigma_{xx}$. It can be stated that the mechanical simulation based on the calibrated thermal model delivers a reasonable prediction for the residual stresses, even though slightly higher values of $\Delta\sigma$ are predicted in the HZ compared to the measurements. In addition to the $\Delta\sigma$, the numerically predicted longitudinal stresses σ_{yy} (dotted) and transverse stresses σ_{xx} (dashed) are shown. The amplitude of σ_{xx} is rather small compared to the one of σ_{yy}. Thus, $\Delta\sigma$ is dominated by the contribution of σ_{yy}.

(a)   (b)
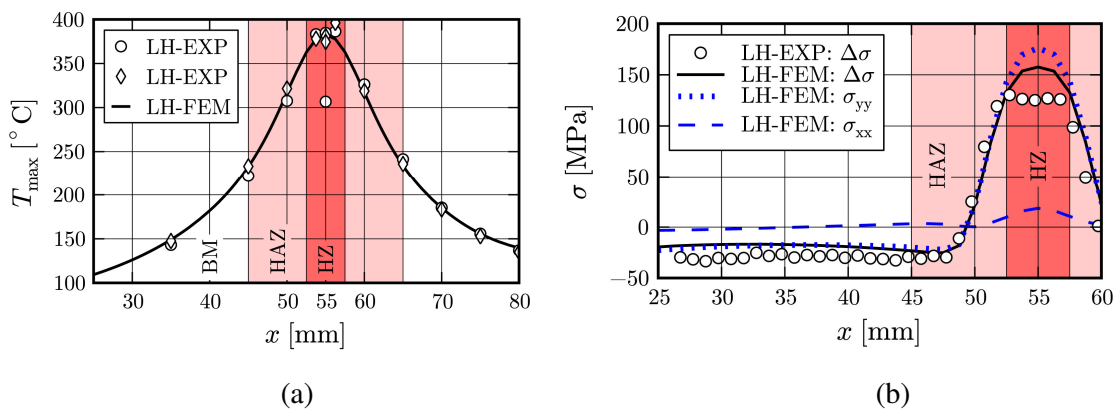
Figure 4 - *(a) Measured (EXP) and predicted (FEM) peak temperatures and (b) measured (EXP) and predicted (FEM) residual stresses [5,11].*

For the fracture mechanics analysis a separate simulation was defined for each crack length a, using the deformed mesh and the full stress field from the last time step of the process simulation after cooling to room temperature. In this mechanical restart simulations pure linear elastic material behaviour with a Young's modulus E = 73 GPa and a Poisson's ratio ν = 0.33 was assumed.

The nodal displacements and forces at the crack tip were extracted and used for the calculation of $K_{tot}(F_{appl}, a)$ via the MVCCT approach. The results for $K_{tot}(F_{max} = 4.41$ kN, a) and $K_{tot}(F_{min} = 0.44$ kN, a) based on the predicted laser heating residual stresses are shown in Fig. 5a (LH-FEM). For comparison, also the results calculated for a model without residual stresses are shown (BM-FEM) what corresponds to base material behaviour.

For a < 49 mm the crack tip is situated in the area of compressive σ_{yy} for the simulation including the laser heating residual stresses. Hence, the $K_{tot}(F_{max})$ is lowered in comparison to the simulations without residual stresses. Under minimum applied load the crack faces at the crack tip stay completely closed as indicated by $K_{tot}(F_{min}) = 0$ MPa√m. In conclusion, this results in a reduction of total stress intensity factor range $\Delta K_{tot} = K_{tot}(F_{max}) - K_{tot}(F_{min})$ for the case LH-FEM.
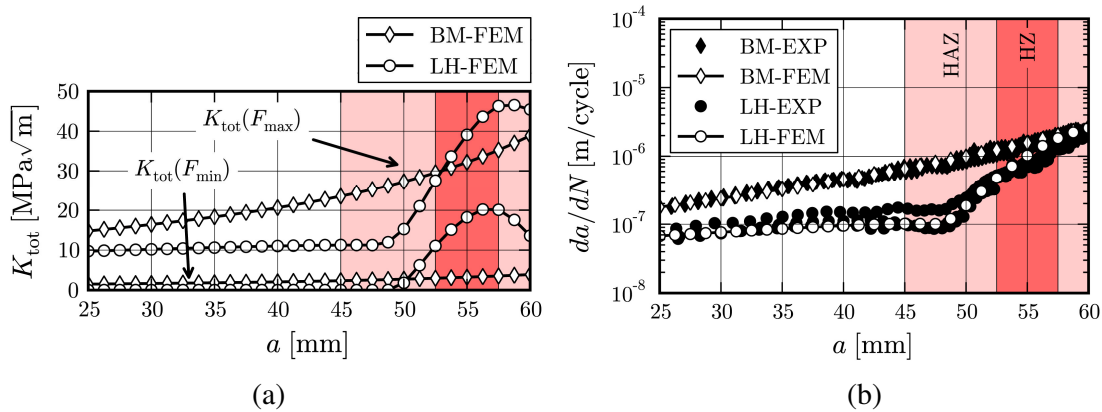
Figure 5 - *(a) Predicted K_{tot} and (b) measured and predicted da/dN for base material specimens (BM) as well as laser heated specimens (LH) [5,11].*

After the crack tip enters the area of tensile residual stresses σ_{yy}, for a > 49 mm, the values of $K_{tot}(F_{min})$ and $K_{tot}(F_{max})$ increase subsequently until both exceed the corresponding values from the simulations without residual stresses, i.e. the total stress intensity factor ratio $R_{tot} = K_{tot}(F_{min}) / K_{tot}(F_{max})$ increases.

For the prediction of da/dN, the calculated K_{tot} were used in the Walker equation (see Fig. 3) with fitted AA2198-T8 material constants [11]. The predicted fatigue crack growth rates for base material specimens (BM-FEM) and laser heated specimens (LH-FEM) are in good agreement with the experimental data (BM-EXP, LH-EXP), as seen from Fig. 5b.

For the base material specimens without residual stresses this is a verification that the fit of the Walker equation constants is reasonable. The agreement of the predictions and the measurement results for the laser heated specimens shows further that the developed approach is able to predict the fatigue crack growth in laser heated specimens with high accuracy.

5   Design optimisation

Figure 6a shows the principle of the design optimisation study on the positioning of one heating line on the C(T)100 specimen. The goal of the optimisation was to identify the heating line position $x_{h,opt}$ leading to a maximum number of load cycles N before a crack with an initial length $a_0 = 25$ mm reaches a final crack length of a = 60 mm.

The model set-up was adopted from the validation case presented in the previous section, including boundary conditions and material properties. However, the applied loads were increased to 150% of the original values. Additionally, the heating line position x_h was varied in steps of 2.5 mm for 25 mm $\leq$ $x_h \leq$ 85 mm.

Figure 6b shows the predicted number of cycles to reach the final crack length N(a = 60 mm) as a function of the heating line position x_h. For the given design optimisation problem, the optimum line position can be identified as $x_h = x_{h,opt} = 45$ mm.

The predicted fatigue crack growth behaviour was experimentally validated for the three heating line positions $x_h = 35$ mm, $x_h = x_{h,opt} = 45$ mm and $x_h = 55$ mm. Due to problems with secondary cracks growing from the fixture holes in a first attempt to perform these tests, for all remaining specimens the initial notch length was extended to a length of x = 30 mm via machining and the fatigue crack growth tests were completed.

(a)   (b)
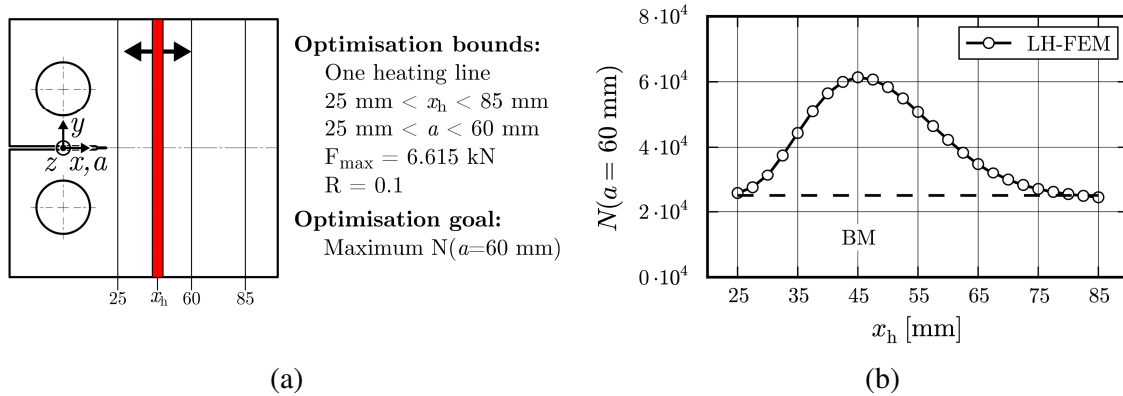
Figure 6 - *(a) Schematic of the performed design optimisation study and (b) predicted number of cycles N(a=60 mm) as a function of the heating line position x_h.*

The fatigue crack growth rates da/dN calculated on basis of the optical crack length measurement data are shown in Fig. 7 in comparison to the predictions. The observed scatter of the experimental data can be explained by small changes of the process conditions during the laser heating. The predictions match the experimental results within the experimental scatter, indicating that the chosen optimisation approach provides correct predictions.
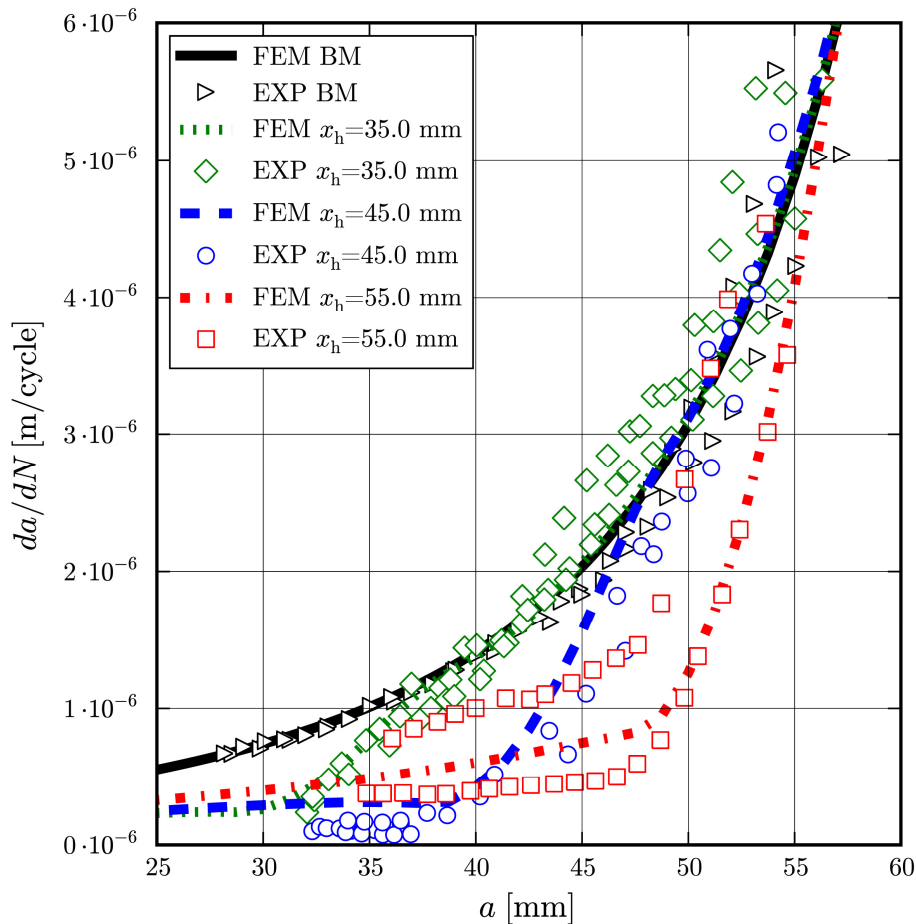
Figure 7 - *Predicted and measured fatigue crack growth rate da/dN as function of the crack length for three selected heating line positions x_h.*

6   Conclusions

In conclusion, it is demonstrated on the laboratory scale that laser heating has the potential to be employed for fatigue crack growth retardation in aircraft aluminium structures. The developed numerical prediction approach is capable to deliver accurate predictions of the fatigue crack growth in laser heated specimens and provides the possibility to be successfully employed for numerically based design optimisation.

7   References

[1]   R. C. McClung, "*A literature survey on the stability and significance of residual stresses during fatigue*", Fatigue & Fracture of Engineering Materials & Structures, Vol. 30, pp. 173-205, 2007

[2]   J. Harrison, "*Exploratory Fatigue Tests on Local Heating as Repair Technique*", British Welding Journal, Vol. 12, pp. 258-260, 1965

[3]   L. W. Tsay, M. C. Young, F. Y. Chou, R. K. Shiue, "*The effect of residual thermal stresses on the fatigue crack growth of laser-annealed 304 stainless steels*", Materials Chemistry and Physics, Vol. 88, pp. 348-352, 2004

[4]   C. D. Jang, H. C. Song, C. H. Lee, " *Fatigue Life Extension of a Through-Thickness Crack Using Local Heating*", In: Proceedings of The Twelfth (2002) International Offshore and Polar Engineering Conference, pp. 224-229, Kitakyushu, Japan, 2002

[5]   D. Schnubel, M. Horstmann, V. Ventzke, S. Riekehr, P. Staron, T. Fischer, N. Huber, "*Retardation of fatigue crack growth in aircraft aluminium alloys via laser heating - Experimental proof of concept*", Materials Science and Engineering A, Vol. 546, pp. 8-14, 2012

[6]   A.P. Parker, "*Stress intensity factors, crack profiles and fatigue crack growth rates in residual stress fields*", In: Residual stress effects in fatigue, ASTM STP 776, pp. 13-31, 1982

[7]   H. Terada, "*Stress intensity factor analysis and fatigue behavior of a crack in the residual stress field of welding*", Journal of ASTM International, Vol. 2, pp. 1-11, 2005

[8]   L. Edwards, "*Influence of residual stress redistribution on fatigue crack growth and damage tolerant design*", Materials Science Forum, Vol. 524-525, pp. 77-82, 2006

[9]   P. Irving, Y. E. Ma, X. Zhang et al., "*Control of crack growth rates and crack trajectories for enhanced fail safety and damage tolerance in welded structures*", In: Proceeding of the 25th ICAF Symposium of the International Committee on Aeronautical Fatigue, pp. 387-405, Rotterdam, Netherlands, 2009

[10] D. Schnubel, N. Huber, "*The influence of crack face contact on the prediction of fatigue crack propagation in residual stress fields*", Engineering Fracture Mechanics, Vol. 84, pp. 15-24, 2012

[11] D. Schnubel, N. Huber, "*Retardation of fatigue crack growth in aircraft aluminium alloys via laser heating - Numerical prediction of fatigue crack growth*", Submitted for publication, 2012

Fatigue Strength of Light Weight Structures produced by Laser Additive Manufacturing in TiAl6V4

Eric Wycisk[1], Jannis Kranz[2], Claus Emmelmann[2]

[1] *Laser Zentrum Nord GmbH (LZN), Am Schleusengraben 14, 21029 Hamburg, Germany*,
eric.wycisk@lzn-hamburg.de
[2] *Institute of Laser and System Technologies (iLAS), Hamburg University of Technology (TUHH), Denickestr. 17, 21073 Hamburg, Germany*

Abstract   Topology optimization and biomimetic methods generate new possibilities in the design of light weight structures. The resulting designs are characterized by their extraordinary specific mechanical strength as well as their individual, load-adapted and highly complex geometries. To exploit the weight saving potential of these approaches to their full extent, manufacturing technologies are needed, which can facilitate the freedom of design entirely. Powder bed-based Laser Additive Manufacturing (LAM) offers these possibilities and therefore gains increasing importance in light weight applications. However before the process will be established in industrial applications entirely there is still extensive research of the dynamic mechanical properties of LAM light weight structures required.

Therefore this paper presents an analysis of the fatigue behavior of LAM optimized, bionic parts. Current research neglects LAM inherent design features such as layer orientation, hollow structures and unfinished surfaces. Therefore the investigations are based on a broader view analyzing different layer orientations as well as surface conditions and their effect on the fatigue strength of LAM TiAl6V4. Due to its corrosion resistance and high specific strength TiAl6V4 is of highest interest for light weight applications and therefore focused on in this study. The results show that the fatigue limit of laser additive manufactured TiAl6V4 compares to conventionally manufactured TiAl6V4 and therefore shows great potential for applications with dynamic loading in the aircraft and automotive industry.

1   Introduction

First established industrial applications of titanium LAM parts are already existing in the medical industry. Due to the charcteristics of medical products such as small part size, individuality, porous structures and biocompatible materials Laser Additive Manufacturing is predestined for an economic production of custom implants and dental restorations [1]. The current improvements of LAM machines regarding part size, building speed and process stability however increase the economic feasibility of larger additive manufactured light weight parts and push them at the brim of industrial production for aeronautic and astronautic applications [2]. Excellent material properties combined with freedom of design allow the use of topology optimization and biomimetic methods to create outstanding lightweight designs with over 50% of weight savings compared to conventional designs [3].

The stepwise process of LAM causes the reduction of complex three dimensional geometries into simple two dimensional manufacturing steps and therefore enables the production of highly complex parts. The individual production steps of the process are shown in Figure 1. During preprocessing a 3D-CAD-model is divided into slices with a thickness corresponding to the layers in the production process. Typical layer thicknesses for TiAl6V4 are hereby 30 μm. Subsequently to the "slicing" operation the prepared data is transmitted to the machine in which the actual manufacturing process occurs in three repeating steps.
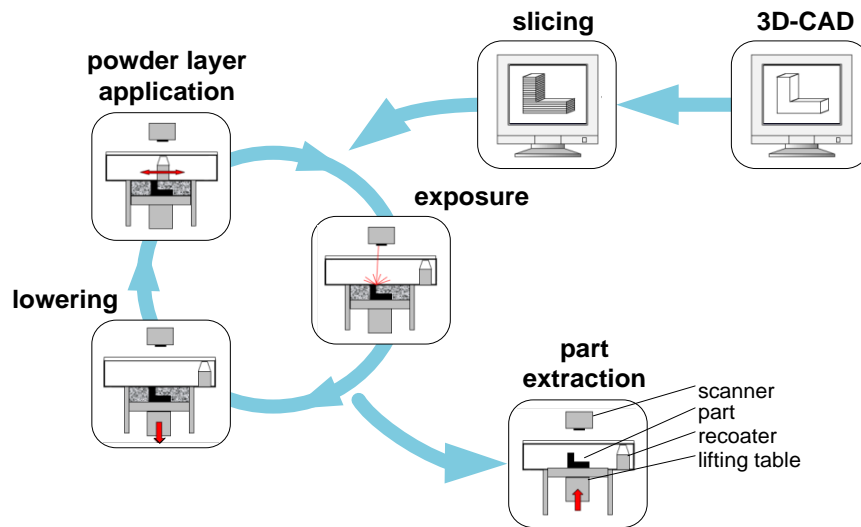
Figure 1 – Production steps of Laser Additive Manufacturing; adapted from [4]

Within the building chamber of the LAM mashine a powder layer is applied onto the building plattform. In the second step the powder is exposed by the laser beam. Due to the energy input of the focused beam the powder melts and solidifies into welding beads after exposure. In every single layer the beam melts the surface area corresponding to the CAD-model slice. Subsequently the base plate is lowered and a new powder layer is applied. After completion of all layers the part can be taken from the powder bed and unmelted powder is recycled for further production [4, 5]. The manufacturing process allows nearly any geometry to be built which facilitates the realization of designs in accordance with the parts stress distribution under load. This permits new design approaches for lightweight structures that were not possible up to now due to the conventional manufacturing processes inherent restrictions (Figure 2). However, due to the layer wise production process LAM parts exhibit characteristic features, whose influences on dynamic properties of parts still have to be investigated. Depending on the orientation of the part during pre-processing and production slicing can results in different layer orientations. The layer orientation within the part therefore corresponds to the building direction. Further characteristics include rough surfaces (approx. Ra = 12 μm) due to adherent powder particles and contour welding beads as well as residual stresses, a particular microstructure and residual porosity.
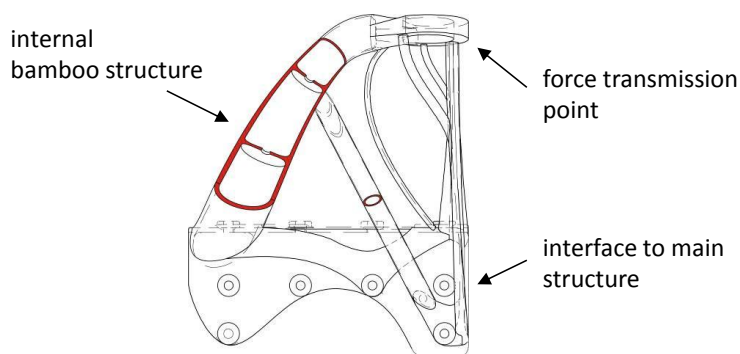
Figure 2 - Optimized bionic LAM lightweight design with hollow bamboo structure
(designed by iLAS and LZN Laser Zentrum Nord)

To substitute conventional designs by LAM parts the fatigue properties of additive manufactured TiAl6V4 light weight structures have to be determined considering above mentioned characteristics. Previous investigations however were only performed with polished specimens and single layer orientation. Results from rotating bending tests (load ratio R = -1) show a fatigue limit of approx. 400 MPa reaching properties of wrought material [6]. In this case to eliminate tensile stresses and alter mechanical properties a heat treatment for 30 min. at 950°C was performed previous to testing. Further studies of the fatigue limit in pulsating tensile stress tests (R = 0.1) show a fatigue limit of approximately 300 MPa and therefore still reach cast properties [7]. Additional pulsating tensile stress tests (R = 0.1) of LAM specimens without surface treatment on the other hand showed a low fatigue limit of 200 MPa [8]. In these cases a heat treatment for 4 h at 843°C was performed.

2   Methods

The dynamic properties of laser additive TiAl6V4 parts were determined in high cycle fatigue (HCF) tests in accordance to DIN 50100 on a servo hydraulic test rig from *MTS*. Hour glass shaped test geometries derived from ASTM E 466 were tested at a load ratio of R = 0.1 with a frequency of 50 Hz. To represent the different characteristics of LAM structures the fatigue limit of specimens built in upright position (90°) and at an angle of 45°, both in polished and untreated "as built" surface conditions, were investigated. In addition, specimens with peened surface were analyzed. The peening process is performed as a combination of abrasive and shot peening with ceramic grit. All specimens were built with a 200 W powder-bed based industrial LAM system with layer thicknesses of 30 μm. For relaxation of residual stresses, essential for the dimensional accuracy of complex light weight structures, a heat treatment for 3h at 650°C in vacuum with argon cooling was performed.

3   Results and Discussion

In correspondence to common density values of LAM TiAl6V4 [5, 6] the manufactured specimens show a high density of > 99.8% measured with Archimedes' principle. The density results are confirmed by light microscopic analysis of polished cross sections showing micro porosity (10 – 30 μm) with few larger pores and defects. After heat treatment the microstructure of all specimens display a typical LAM TiAl6V4 very fine needled, basket-weave structure of α- and β-phase with grain growth in building direction [compare 9]. The static tensile properties of the specimens with yield strength of 1070 MPa, ultimate strength of 1140 MPa and elongation of 10.5% excel the values defined for conventional TiAl6V4 in DIN 17862 and DIN 17865.

Figure 3 shows the fatigue resistances of polished samples with a fatigue limit of 490 MPa reaching properties of wrought material (compare Figure 5). An increase in fatigue limit of about 190 MPa, respectively 60%, compared to earlier results from BRANDL [7] under similar conditions can not only be attributed to the difference in heat treatment. It is suggested that the fast development and improvement of the LAM systems during past years produce superior products with minor defects and account for the large improvement in fatigue strength. Still the data of polished specimens show relatively high scatter of fatigue life at constant stress amplitudes. Subsequent analysis of the crack surfaces under scanning electron microscope show different crack initiation sites for the specimens with early failure. Whereas common failure initiates at the specimen surface the underperforming specimens show crack initiation sites at inside pores larger than 50 μm (see Figure 6).
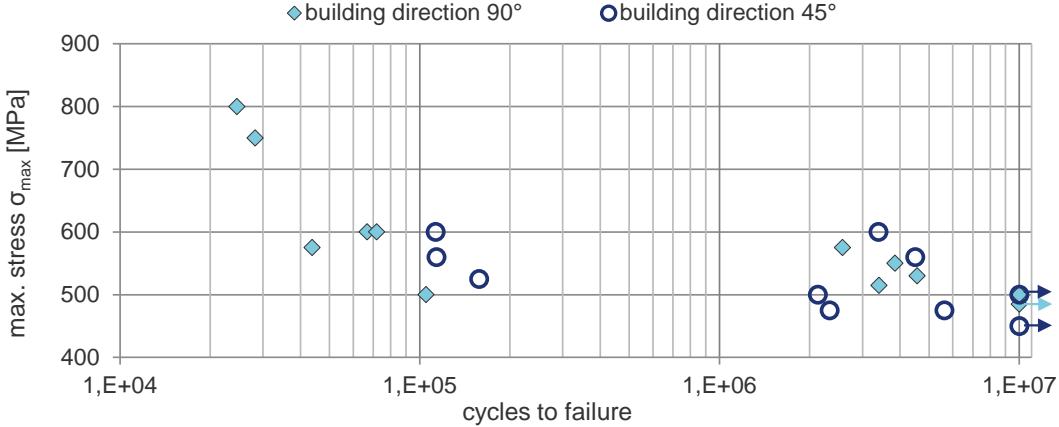
Figure 3 – High cycle fatigue properties of polished specimen at 90° & 45° building angle

To analyze the influence of building direction on the fatigue performance of LAM light weight structures an analysis of covariance for 90° and 45° specimens was performed. With a p-value of 0.57 the results show that at a significance level of 5% no effect of the building direction on the fatigue life can be observed.

Figure 4 shows the fatigue resistance of "as built" samples with a fatigue limit of 220 MPa. As previous research [8, 9] has already suggested, the HCF results of "as build" specimens show low fatigue performance due to multiple crack initiation on the rough surface (see Figure 6). The analysis of covariance for specimen built at 90° and 45° confirm the results from polished specimens with no visible effect from the building direction on HCF performance.
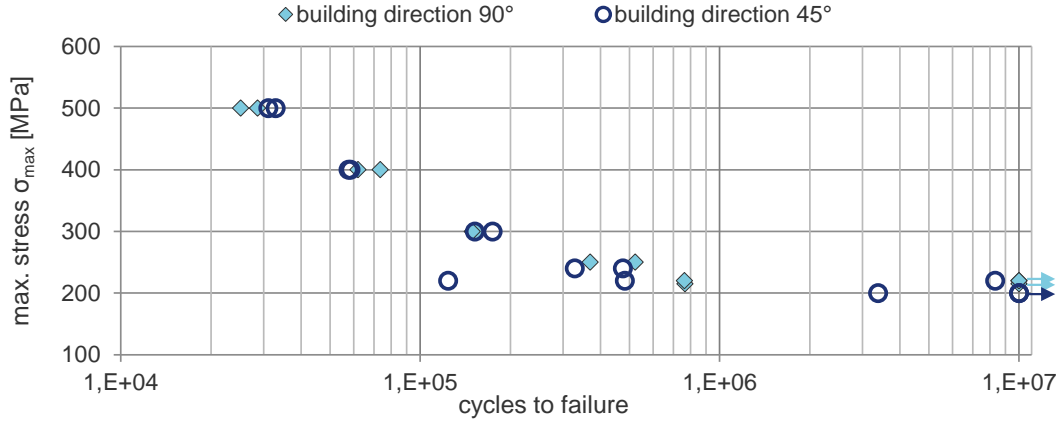
Figure 4 - High cycle fatigue properties of "as built" specimen in 90° & 45° building angle

To account for the fact that LAM light weight structures exhibit complex geometries, with faces which can only be improved by geometrically undefined treatments due to limited accessibility and free-form surfaces, peened samples were tested to analyze the effect of peening on the fatigue performance. Figure 5 shows the fatigue resistance of all tested conditions compared to wrought and cast material.
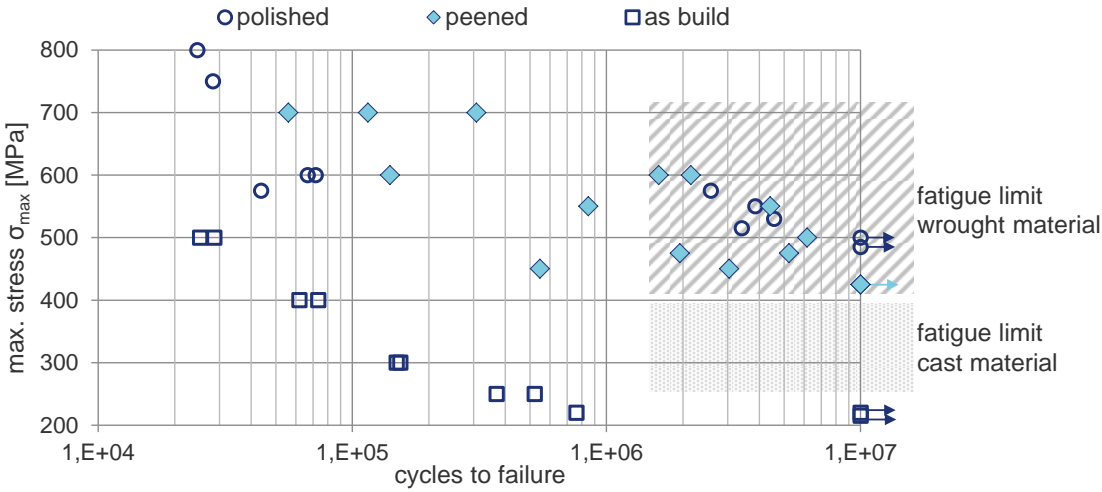
Figure 5 – High cycle fatigue properties of LAM samples with different surface conditions in comparison to wrought and cast material in smooth condition
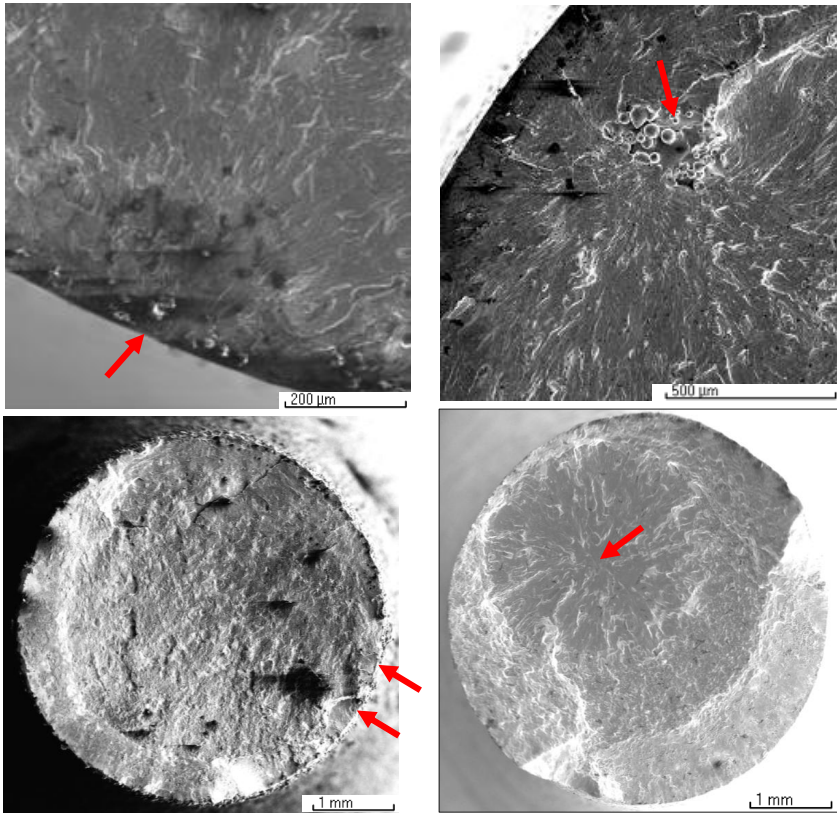
Figure 6 - Fracture surface SEM picture of polished specimen with surface crack initiation (top left) and crack initiation at inside pore (top right), "as built" specimen with multiple surface crack initiation sites (bottom left) and peened specimen with crack initiation site at inside pore (bottom right)

The peened specimens exhibit an increased fatigue limit of 430 MPa, nearly doubling the limit of non-peened specimens and reaching values of wrought material. The performed peening treatment smoothens the surface to an average roughness of Ra = 1.3 µm and additionally introduces compressive stresses into the surface to suppress surface crack initiation [compare 9]. As shown in Figure 6 the crack initiation of peened samples exclusively starts at internal pores with the variation of size and geometry of the crack initiating pore accounting for the high scatter in the data.

4   Conclusions

From the results following conclusions can be drawn:

- − Building direction has no significant influence on the fatigue life of laser additive manufactured TiAl6V4 parts.
- − The surface roughness of untreated samples reduces the fatigue limit significantly due to multiple surface crack initiation.
- − Peening processes can improve the fatigue limit of LAM parts with complex freeform surfaces to values of wrought material in smooth condition.
- − Process inherent residual porosity causes fatigue scatter in HCF data due to variation of pore size and geometry.

The acquired results for the HCF performance emphasize the potential for LAM light weight structures in industrial applications. Due to fatigue strength comparable to conventional material, applications with dynamic load cases do not have to be avoided by LAM parts.

5   References

[1] Emmelmann, C.; Scheinemann, P.; Munsch, M.; Seyda, V., "Laser Additive Manufacturing of modified implant surfaces with osseointegrative characteristics", Physics Procedia, Volume 12, Part A, 2011, Pages 375-384.

[2] Emmelmann, C., Sander, P., Kranz, J., Wycisk, E., "Laser Additive Manufacturing and Bionics: Redefining Lightweight Design", Physics Procedia Volume 12, Part A, 2011.

[3] Emmelmann, C., Petersen, M., Kranz, J., Wycisk, E., (2011) "Bionic lightweight design by laser additive manufacturing (LAM) for aircraft industry", Proc. SPIE 8065, 80650L.

[4] Meiners, W., "Direktes Selektives Laser Sintern einkomponentiger metallischer Werkstoffe", Shaker Verlag, Aachen, 1999.

[5] Over, C., „Generative Fertigung von Bauteilen aus Werkzeugstahl X38CrMoV5-1 und Titan TiAl6V4 mit Selective Laser Melting", Shaker Verlag, Aachen, 2003.

[6] Wirtz, T., „Herstellung von Knochenimplantaten aus Titanwerkstoffen durch Laserformen", Aachen, 2005.

[7] Brandl, E., "Microstructural and mechanical properties of additive manufactured titanium (Ti-6Al-4V) using wire", Shaker Verlag, Aachen, 2010.

[8] Brandl, E., et al., "Wire instead of powder? Properties of additive manufactured Ti-6Al-4V for aerospace applications", in Euro-uRapid2008, Berlin, 2008.

[9] Wycisk, E., Kranz, J., Emmelmann, C., "Influence of surface properties on fatigue strength of lightweight structures produced by Laser Additive Manufacturing in TiAl6V4", Proc. Digital Direct Manufacturing Conference 2012, Berlin, 2012.

Nd:YAG Laser cladding, a suitable tool to improve surface properties of a low nickel maraging steel

M. Cabeza[1], G. Castro[2], P. Merino[1], G. Pena[1], M. Román[2]

[1]*Department of Materials Engineering, Applied Mechanics and Construction. E. E. Industrial, Vigo University, Campus Universitario, Lagoas-Marcosende, 36310, Vigo, Pontevedra, Spain.*
pmerino@uvigo.es

[2]*Technology Centre AIMEN; C/ Relva, 27A. Torneiros, 36410, Porriño, Pontevedra, Spain.*

Abstract

Due to prolonged service lifes and severe working conditions (specially strong thermo-mechanical loads and highly abrasive environments) the surface of tools made in tool steels and high strength alloys may get strongly damaged. This kind of alloys have a very expensive price so that surface repairing processes, such as laser cladding or gas tungsten arc welding (GTAW/TIG), should be welcome in order to increase the service life of the tool, contributing to amortize the made investment.

In this work, the modification of the microestructure and of the surface properties of a Nd:YAG laser cladding processed and later peak-age hardened low nickel (14%) maraging steel are studied. TiN particles were used as reinforcement and laser parameters were optimized to obtain a free-defect overlay.

Laser surface processing impairs the surface properties of the maraging steel, the hardness decreases in the heat affected zone, and so a final age hardening treatment is necessary to obtain the required good combination of high strength and high hardness which is a own characteristic of maraging steels.

1. Introduction

Maraging steels (MS) are low-carbon ultrahigh-strength alloys whose mechanical properties are achieved due to a fine precipitation of intermetallic compounds obtained after an age hardening heat treatment [1, 2, 3]. They offer one of the bests combinations of ultrahigh yield and tensile strength, ductility and fracture toughness of any ferrous materials, which makes them become suitable to use in aircraft landing gears, rocket cases, drive shafts, die casting dies and structural parts [1-4]. Nevertheless, maraging steels show a remarkable disadvantage, their price, caused by the great amount of alloying elements, the great degree of purity (achieved by vacuum melting) [5, 6] and the thermal treatments that are required to get the intermetallic precipitation and thus to achieve the needed combination of good mechanical properties. This makes repair and surface improvement processes become interesting to increase the service life of parts made in this type of alloys, contributing to amortize the investment made on them. Even repairing processes could be carried out with many disposable technics, the high versatility of the laser as a tool among other notable characteristics as the low dilution derived of its use, the excellent process control capability, the high precission obtained, the sharply concentrated heat input and the low distortion generated [7, 8], allow laser cladding turn into a suitable tool to succeed in this kind of processes.

In this case, the surface of a peak-age hardened low nickel (14%) maraging steel has been processed by means of laser cladding and later peak-age hardened again. Hard and high wear resistant particles of TiN were used to improve hardness and wear resistance of the final surface. Visible light (OM) and scanning electron microscopy (SEM) were used to define the microstructure and, together with mechanical profilometry, the quality of the obtained overlays. Vickers hardness test were performed in order to characterize the mechanical behaviour.

After the laser cladding processing, the affected zones of the MS (solidified molten pool and heat affected zone) are clearly softened even hardness values of some zones of the molten pool are clearly higher than those of the age hardened MS. Nevertheless, after the final peak-age heat treatment, the hardness of the heat affected zones is recovered and the hardness of the molten pool increases strongly with respect to the peak-age hardened MS.

2. Experimental procedure

Marlok C1650®, the low nickel (200 grade) maraging steel whose chemical composition is showed in Table 1, is the commercial name of the steel used as substrate. Received in the solution annealed condition, and being so softer than its service life requires, the steel has been hardened following a previously optimized precipitation peak-age hardening treatment [9], which consists on heating to 525ºC and maintaining for 6 hours followed by an air cooling till reach room temperature (20 – 25ºC). Subsequently, the surface of the hardened maraging steel has been processed, by means of laser cladding, with the aim of improve the hardness and the wear resistance. As laser surface processing impairs the properties of the thermal affected zones, a new and final peak-age hardening treatment has to be carried out, in the previously described conditions, to recover them.

A Nd:YAG laser (nominal power 4.4 Kw) and TiN ceramic particles with sizes from 63 to 80 μm were used (feeding rate: 4.16 g/min). Initially, laser surface parameters were chosen taking into account the results obtained after the laser surface melting of this maraging steel in different conditions (solution annealed and peak-age hardened) with the same laser device (to be published as "Nd:YAG laser: A suitable tool to repair damaged surfaces of 14 Ni (200 grade) maraging steel"). Due to the great number of parameters that are involved in such a process, only power and laser traversing speed were modified. Argon has been chosen as shielding (13 l/min) and as carrier gas (3 l/min).The laser cladding has been performed with overlapped passes of 40%.

Samples were grinded, polished to 1 μm, chemically etched with Nital 5% (95 ml ethanol, 5 ml HNO_3) and Kalling's nº1 (33 ml H_2O, 1.5 g $CuCl_2$, 33 ml ethanol, 33 ml HCl) reagents and analysed by means of optical (Olympus GX51) and scanning microscopy (Jeol JSM 5410). Hardness has been measured (Vickers $HV_{0.2}$, Emcotest M1C 010) in the different zones of the samples that were affected by laser cladding and in parent metal.

Table1. Chemical composition of the (200 grade) maraging steel (weight percent).

C	Ni	Mo	Co	Ti	Si	Cr	Mn	S	Fe
<0.005	14.4	4.3	10.7	0.17	0.03	0.02	0.03	<0.002	Bal.

3. Results and discussion

The surface of the laser processed and finally peak-age hardened remains the same as it was after laser cladding. No changes were detected and a good surface quality, smooth and crack-free, with the exception of sample 1, has been achieved with these laser parameters (Table 2). Once etched, it is possible to find a similar fully martensitic microstructure across the transversal sections of all samples, with the solidified molten pool (SMP), the heat affected zone (HAZ) and the parent metal (PM) (Figure 1). No changes were detected in microstructure if the results from light and scanning electron microscopy analysis are compared with those obtained in samples without a post-laser cladding aging heat treatment.

Figure 1. Optical microscopy. Transversal section of the maraging steel after laser cladding (power 2.2 kW and laser traversing speed 8 mm/s) and peak-age hardening treatment (525ºC for 6 hours and then air cooling to room temperature (20 - 25ºC)) showing the different zones that can be found. The solidified molten pool (SMP), a light-etched coarse grain heat affected zone (CGHAZ), a light-etched fine grain heat affected zone (FGHAZ), a dark-etched heat affected zone (DEHAZ) and the parent metal (PM).

Table 2. Nd:YAG Laser cladding of a 14% Ni (200 grade) maraging steel. Laser operation parameters and layer oversizes.

Sample	Power (kW)	Traversing speed (mm/s)	Layer oversize (μm)
1	2.2	5	400
2	2.2	8	300
3	1.8	5	350

After the laser cladding processing, TiN particles are suitably dispersed in the solidified molten pool and there are no remarkable agglomerations. These particles remain perfectly embedded in the maraging steel matrix after the peak age hardening treatment (Figure 2, 3 and 4). No chemical reactivity has been detected among these particles and the maraging steel matrix. At the bottom of the SMP and close to the PM, it can be detected a planar growth (Figure 2), which changes to cellular, cellular dendritic and columnar dendritic with tendency to equiaxic growth in the outermost zones of the SMP (Figures 3 and 4).
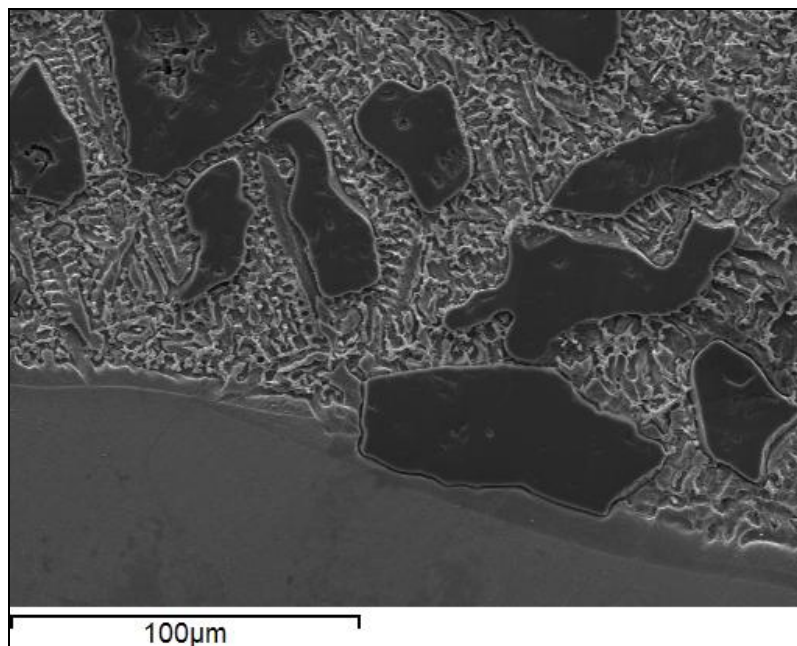
Figure 2. Scanning electron microscopy. Planar growth at the bottom of the solidified molten pool of a 14% Ni (200 grade) maraging steel after being processed by laser cladding (Laser power 2.2 kW and laser traversing speed 5mm/s) and finally peak-age hardened (Heating to 525ºC for 6 hours and then air cooling to room temperature (20 – 25ºC)).
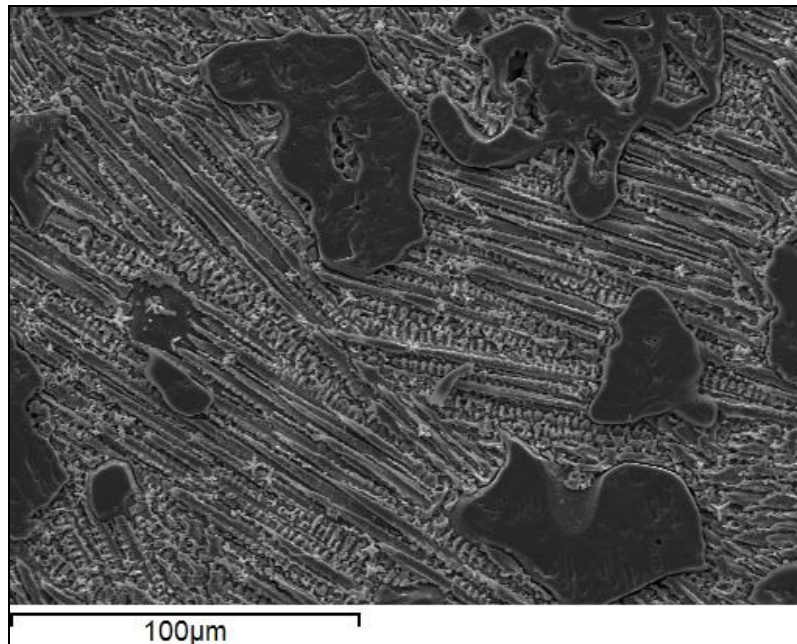
Figure 3. Scanning electron microscopy. Columnar dendritic growth at the middle zone of the solidified molten pool of a 14% Ni (200 grade) maraging steel after being processed by laser cladding (power 2.2 kW and   laser traversing speed 5mm/s) and finally peak-age hardened (Heating to 525ºC for 6 hours and then air cooling to room temperature (20 – 25ºC)).
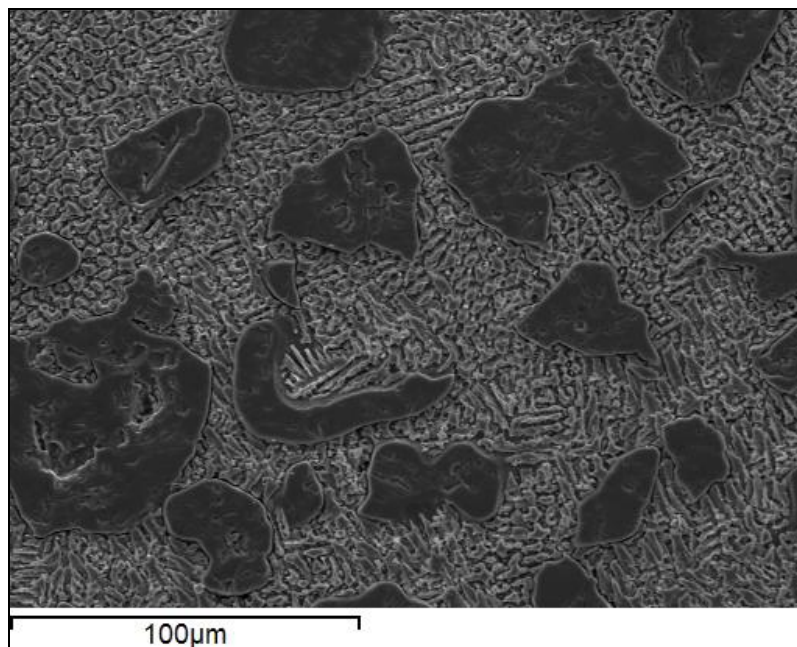
Figure 4. Scanning electron microscopy. Equiaxic and dendritic growth at the upper zone of the solidified molten pool of a 14% Ni (200 grade) maraging steel after being processed by laser cladding (power 2.2 kW and   laser traversing speed 5mm/s) and finally peak-age hardened (Heating to 525ºC for 6 hours and then air cooling to room temperature (20 – 25ºC)).

As it happens after laser cladding, the HAZ is divided into two zones after the final aging heat treatment (Figure 1). Beside the solidified molten pool there is a light etched HAZ. It is formed by a coarse grain zone (CGHAZ) under the SMP and by a fine grain heat affected zone (FGHAZ). Due to laser processing the CGHAZ has been heated to a high temperature where a considerable grain growth has occurred. FGHAZ was heated, but not enough to cause grain growth. Adjacent to the parent metal, there is a dark etched HAZ (DEHAZ) [10].

The main way to achieve a good strength in this kind of alloys is the fine precipitation of intermetallic compounds obtained after an age hardening age treatment [1, 2, 3]. After laser surface processing the properties of the peak-age hardened maraging steel become impaired due to the destruction of these intermetallic precipitates in the melting pool and to their growth in the heat affected zones. Nevertheless it is possible to recover the good properties of the initially peak-aged MS, and even to improve them, by submitting the TiN laser cladded maraging steel to a final peak-age hardening treatment.

Having into account that the hardness of the as-received solution annealed maraging steel was 325 $HV_{0.5}$, that the hardness of the peak-age hardened maraging steel was 525 $HV_{0.5}$ [9] and that the hardness of the laser surface melted maraging steel was of 360 $HV_{0.2}$, a remarkable improvement has been achieved after the last aging heat treatment as can be seen in Figure 5. Now hardness of the heat affected zones are similar to those obtained in the peak-age hardened maraging steel. The effect of the TiN particles in the solidified molten pool has result in a great improvement of the hardness, reaching values of 750 $HV_{0.2}$ (50% higher than those of the peak-age hardened maraging steel).

Figure 5. HV0.2 hardness of the maraging steel after laser cladding (power from 1.8 to 2.2 kW and laser traversing speed from 5 to 8 mm/s) and peak-age hardening treatment (525ºC for 6 hours and then air cooling to room temperature) in the different heat zones that can be found (solidified molten pool (SMP), light-etched coarse grain heat affected zone (CGHAZ), light-etched fine grain heat affected zone, dark-etched heat affected zone and parent metal).
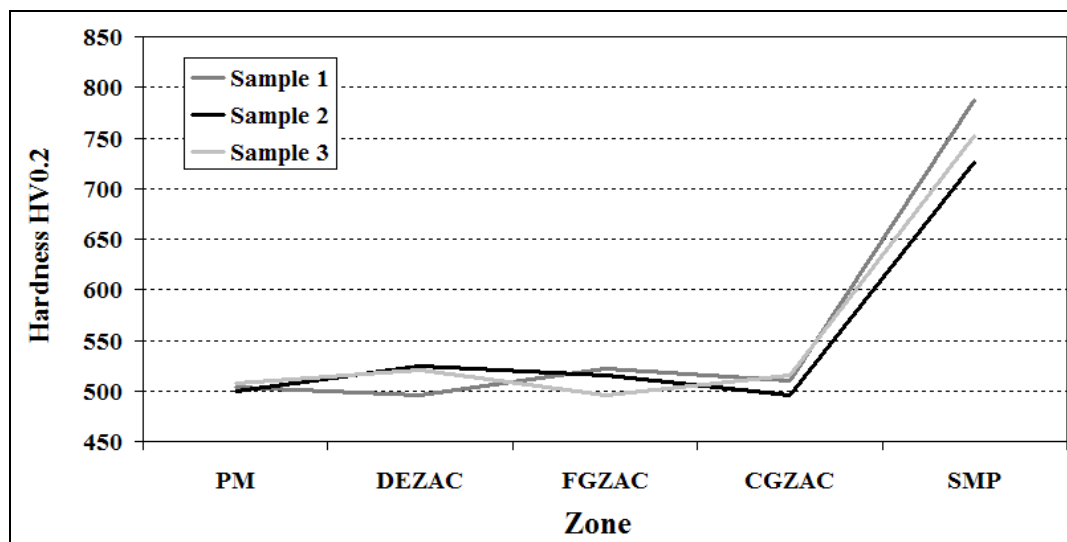
4. Conclusions

♦ It is possible to obtain hard surface coatings of TiN upon a 14% Ni (200 grade) maraging steel substrate by means of Nd-YAG laser cladding (using laser powers from 1,8 to 2,2 kW with traversing speeds of 5 mm/s or a laser power of 2,2 kW with traversing speeds of 8mm/s, always with overlaps of 40%) and after a final peak-age hardening heat treatment (heating to 525ºC for 6 hours and finally air cooling to room temperature).

♦ TiN particles remain perfectly embedded and suitably dispersed after the final peak-age hardening treatment. Non reactivity between matrix and TiC particles has been detected.

♦ Optical and scanning electron microscopy analyses show a fully martensitic microstructure after the final peak-age heat treatment.

♦ After the laser cladding process hardness decreases in the heat affected zones. It can be recovered and even improved if the low nickel maraging steel is submitted again to a final peak-aging heat treatment (heating at 525ºC for 6 hours and then air cooling), reaching hardness values of 500 $HV_{0.02}$ (similar than those obtained in the peak-age hardened maraging steel) in the parent metal and in the heat affected zones. The effect of the TiN particles in the solidified molten pool has result in a great improvement of the hardness, reaching values near to 750 $HV_{0.2}$ (50% higher than those of the peak-age hardened maraging steel).

5. References

[1] "Properties and selection: Irons, steels, and high-performance alloys". Metals Handbook Vol.1, Tenth Edition, ASM International, pp. 792-800, 1990.

[2] A. K. Sinha "Ferrous physical metallurgy", Ed. Butterworths, pp. 597-603, 1989.

[3] W. Sha, A. Cerezo, G.D.W. Smith, "Phase chemistry and precipitation reactions in maraging steels: Part IV. Discussion and conclussions", Metall. Trans. A, Vol. 24 A, pp. 1251-1256, 1993.

[4] M. Sundaresan, M. Manirajan, B. Nageswara Rao, "On the fracture toughness evaluation in weldments of a maraging Steel rocket motor case", Mater. Des., Vol. 31, Issue 10, pp. 4921-4926, (2010).

[5] P. Würzinger, R. Rabitsch, W. Meyer, "Production of maraging steel grades and the influence of specified and nonspecified elements for special applications", J. Mater. Sci., 39, pp. 7295-7302, 2004.

[6] "Tool materials", ASM Specialty Handbook, Second printing, ASM International, pp. 149-153 and 339-346, 1998.

[7] W. M. Steen, J. Mazumder, "Laser material processing", 4ᵀʰ Edition, Ed. Springer, 2010.

[8] E. Toyserkani, A. Khajepour, S. Corbin, "Laser cladding", CRC Press, 2005.

[9] M. Cabeza, G. Castro, P. Merino, G. Pena, M. Román, J. Semiao and P. Vázquez, "Optimization of Ageing Parameters of a Low Nickel Maraging Steel", Mater. Sci. Forum, Vols. 636-637, pp. 471-477, 2010.

[10] V. Venkateswara Rao, G. Madhusudhan Reddy, A. V. Sitarama Raju, "Influence of post-weld heat treatments on microstructure and mechanical properties of gas tungsten arc maraging steel weldments", Mater. Sci. Technol., Vol. 26, nº 12, pp. 1459-1468, 2010.

6. Acknowledgements

Development of advanced techniques for determination of residual stresses

M. E. Fitzpatrick, P. J. Bouchard, J. A. James

Materials Engineering, The Open University, Walton Hall, Milton Keynes MK7 6AA, UK

Abstract Knowledge of residual stresses is key to understanding the structural integrity of safety-critical components and systems. Residual stresses can influence the initiation and growth of fatigue cracks, and influence processes such as creep crack growth at high temperature.

Accurate measurement of residual stresses is therefore required for input to structural integrity calculations. This paper will present recent developments in two complementary techniques: neutron diffraction, and the contour method.

Neutron diffraction can measure stresses deep within complex components, but for complex geometries the set-up time can be considerable and the experimental execution can be difficult. A software simulation system for strain scanning – SScanSS – has been developed whereby a virtual model of the sample is prepared and, by locating the real sample on the instrument by determining fiducial points on its surface, rapid measurement set-up and accurate measurement location is achieved.

The contour method is a relatively new technique for residual stress measurement, where a sample is cut in half and the relaxed surface contours are measured to allow calculation of the pre-existing residual stress. The method has the advantage of providing a complete cross-sectional measurement of the stress normal to the cut surface. There are challenges in identifying the correct cut parameters and the data analysis for smoothing the measured contour.

The paper will present results obtained using these methods from weld residual stresses in applications for the aerospace and nuclear power industries.

Post Weld Rolling Technique Assessment Using the Contour Method

Daniel F. O. Braga[1], Valentin Richter-Trummer[1], Paulo M. S. T. de Castro[1]

[1]*IDMEC-FEUP, Rua Dr. Roberto Frias 4200-465 PORTO, Daniel.Braga@fe.up.pt*

Abstract   Residual stresses play a critical role in several mechanical or structural failure mechanisms, such as fatigue or fracture among others. In order to avoid problems associated with residual stress, post weld treatments may be implemented. In this work measurements obtained with the contour method of both an untreated welded plate specimen as well as an heavily rolled similar specimen are presented. It is possible to observe that not only the nominal values of the residual stresses are lower but also their signal was inverted, i.e., the areas under compression became under tension and the zones under tension became under compression. These facts will have obvious consequences on fatigue crack propagation and this will have to be a consideration in the design of structures subjected to this kind of treatment.

1. Introduction

Residual stress plays a critical role in the failure of mechanical systems due to fatigue, creep, wear, stress corrosion cracking, fracture, buckling, and more. Being able to assess and address the level of these stresses within a body is then of great interest. In this work a post weld treatment was assessed through a new residual stress measuring technique named the contour method. In these situations a trough the thickness characterization of the residual stress field is of interest, this may be required for performing detailed fatigue crack propagation evaluations, for example. However, commonly used residual stress measurement techniques, such as X-ray, or hole drilling, will assess a surface residual stress state, or its trough the thickness distribution but only at very shallow depths, see [1].

The contour method is a destructive residual stress measurement technique based on Bueckner's superposition principle, which is able to deliver the residual stress map perpendicular to a plane of interest within a body, [3; 4]. The methodology for this technique consists in four major steps; cutting, surface topography measurement, data treatment and elastic calculations for obtaining stresses from displacements through FEM (finite elements method), [5; 6].

2. Experimental Procedure

2.1. Material and specimens

The specimens used in this work are three 6 mm thick steel plates with a weld seam at mid width. Figure 1 shows the specimen geometry.

The material used in the specimens studied was S355JR steel according to the EN standard 10025. For the linear elastic FEM calculations involved in the contour method, Young's modulus and Poisson ratio of 210 GPa and 0.3, respectively were used. MIG welding, with V joint surface preparation, was used to produce the weld seam at mid width.

Of the three specimens, two were not subjected to any post-weld treatment, while the other one was treated through post weld rolling technique (PWRT). The rolling force used in PWRT was 150 kN and it was performed in a single pass at a speed of 500 mm/min.

Additional details of the specimens and rolling process used are given in [7].
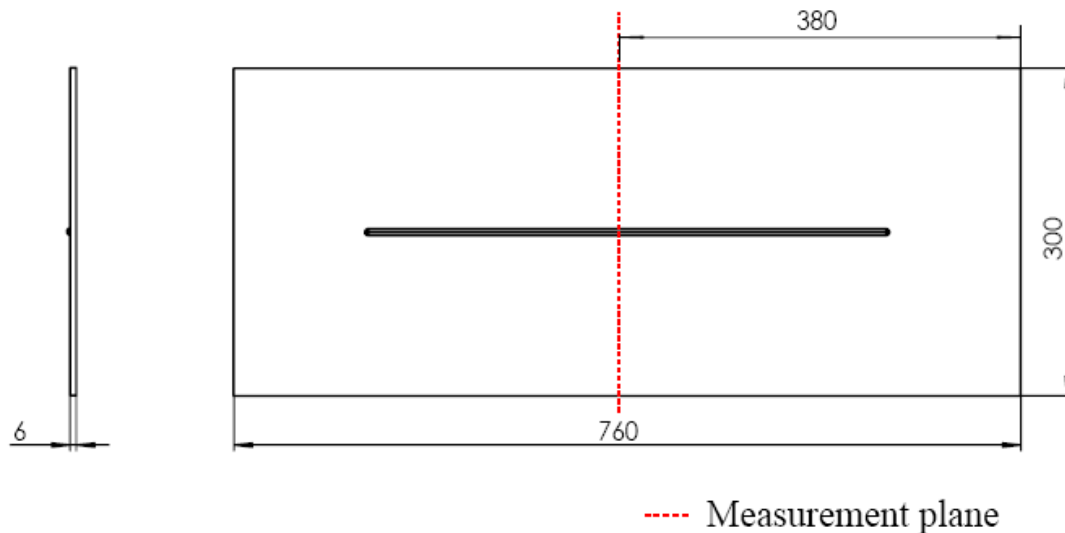
Figure 1 – Specimen's Geometry

2.2. Cutting and measurement of the specimens

Cutting was performed using a Sodick wire electrodischarge machining (wEDM) device with a 0.25 mm diameter hard brass wire at a speed of approximately 5 mm/min. A cleaning operation was executed on the specimen, using sand-blasting, in order to remove the weld slag (to avoid breaking the cut wire with electric non-conductivity problems). As sandblasting is a surface treatment which involves bombarding the component to be treated with small particles, it may induce plasticity and cause residual stress change, in a process similar to shot peening. This superficial residual stress reduction may introduce measurement errors especially in thin specimens, but as it is mentioned around [8] and [9] the penetration of the effect on residual stress of this treatment is very small (0.07 mm in titanium alloys and 0.3 in stainless steel). The specimens were clamped in several positions along their width and in both cutting sides using the purpose made clamping system, seen in Figure 2. This clamping configuration was used with the intention of reducing errors due to plasticity [10], as is suggested by Prime [4].
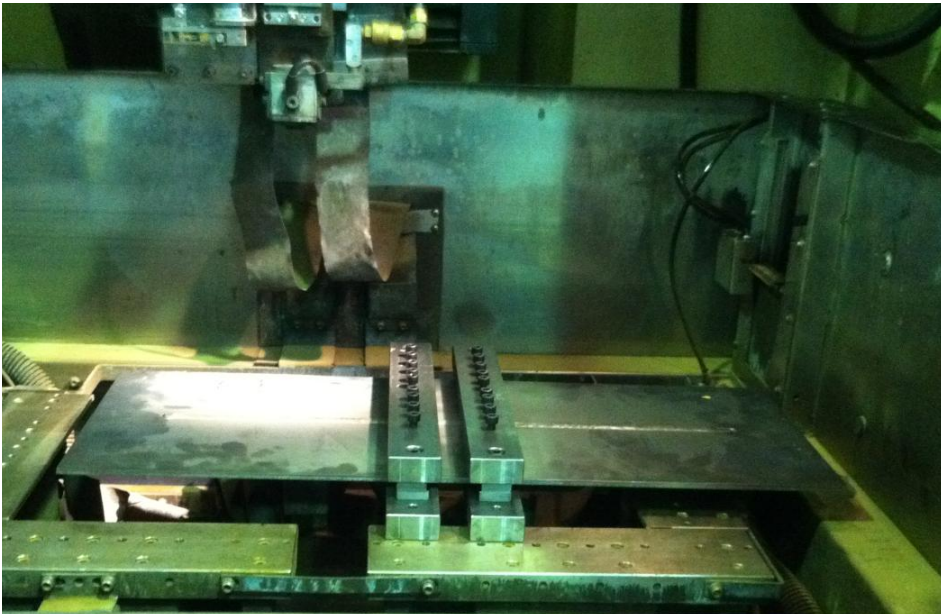
***Figure 2** – wEDM Clamping System*

The topography measurement was performed using a Zeiss UMPC Ultra touch probe based coordinate measuring machine (CMM). A 2 mm x 0.5 mm grid was used for the topography measurement, see Figure 3.
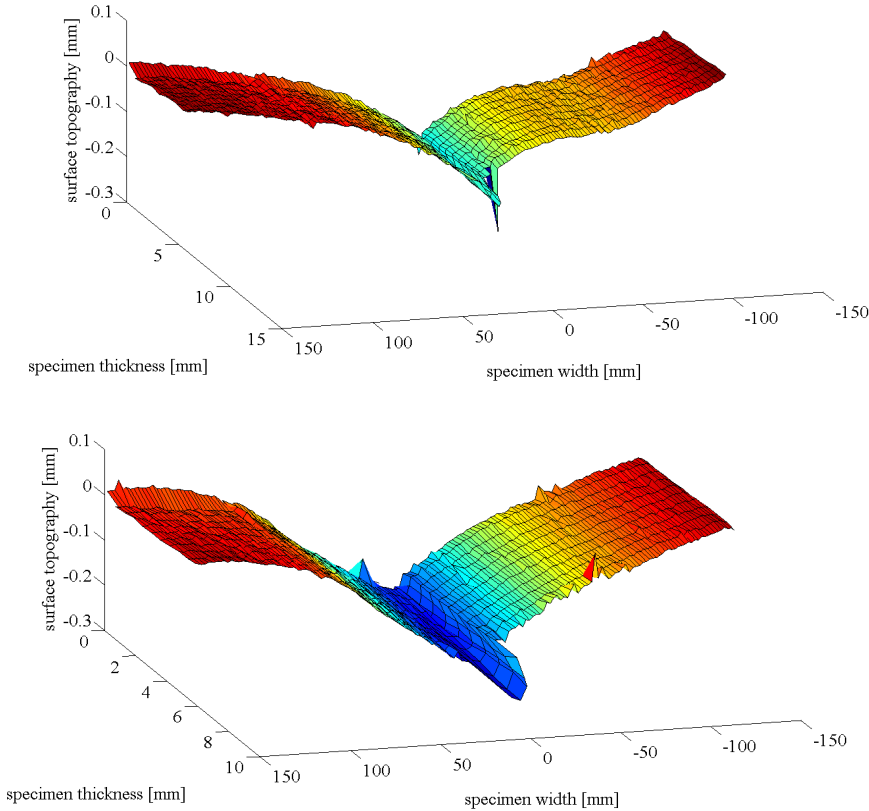
***Figure 3** – CMM Topography Measurement of Both Cut Surfaces for As Welded Specimen*

3. Results

Figure 4 shows the full field maps obtained with contour method for both non-treated and treated specimen.
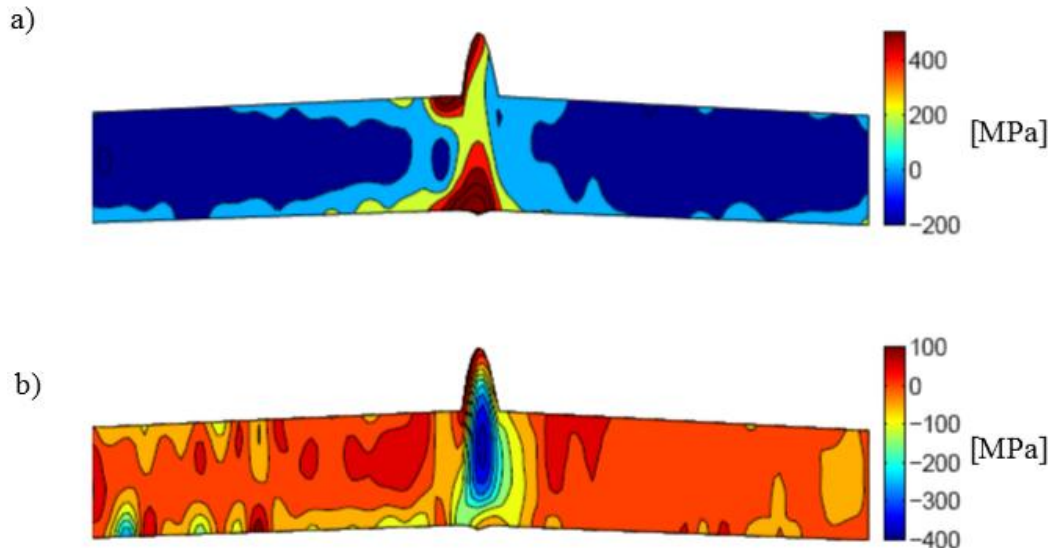
***Figure 4** – Residual Stress Measured Using the Contour Method (a – Non-rolled Specimen, b – Rolled Specimen)*

The maximum tensile residual stress in the as-welded specimen was ~400 MPa (weld) while it was ~100 MPa in the treated specimen (away from the weld). Regarding the compressive residual stress in the as-welded specimen a value of ~200 MPa (away from the weld) was the maximum value reached while in the treated specimen showed ~400 MPa (weld).

An inversion of the residual stress values can be observed for the post weld rolled specimen. This is, the areas under tension in the non-treated specimen are under compression in the treated one and the compressed areas in the non-treated plate are under tension in treated plate. It is likely that the absence of large tensile residual stresses close to the weld specimen will have a beneficial effect on its fatigue performance.

4. Conclusions

Using these rolling parameters the overall values of residual stress are lower than those found for as welded specimens. Furthermore, where before the specimen was subjected to tension, after treatment it becomes subjected to compression. These findings are relevant in fatigue analyses, as the residual stress distribution modifies the crack propagation behavior of the component. Beyond residual stress distribution, factors, such as imperfect microstructure and geometric stress concentrators should also be addressed in order to fully define the crack propagation behavior of the specific component. Taking into account all of the factors mentioned, service life predictions of mechanical components treated with PWRT will be possible.

5. Acknowledgments

6. References

[1]   Philip J. Withers. "*Residual Stress: Definition*", pages 8110–8112, in: Encyclopedia of Materials:Science and Technology. Elsevier, Oxford, 2001.

[2]   V. Richter-Trummer, P.M.G.P. Moreira, P.M.S.T. de Castro, *"Damage Tolerance of Aircraft panels taking into account residual stresses"*, in: P. M. G. P. Moreira et al, eds "Structural Connections for Lightweight Metallic Structures", Springer, 2012, pp. 173-194.

[3]   M. B. Prime,*" Cross-sectional mapping of residual stresses by measuring the surface contour after a cut"*, Journal of Engineering Materials and Technology 123 (2) (2001) 162–168.

[4]   M. Prime, R. Sebring, J. Edwards, D. Hughes, P. Webster, *"Laser surface-contouring and spline datasmoothing for residual stress measurement"*, Experimental Mechanics 44 (2) (2004) 176–184.

[5]   V. Richter-Trummer, Sérgio M. O. Tavares, Pedro M. G. P. Moreira, Miguel A. V. de Figueiredo, and Paulo M. S. T. de Castro, *"Residual stress measurement using the contour and the sectioning methods in a MIG weld: Effects on the stress intensity factor"*, Ciência Tecnologia Materiais, 20:114–119, 2008.

[6]   V. Richter-Trummer and P. M. S. T. de Castro, *"The through-the-thickness measurement of residual stress in a thick welded steel compact tension specimen by the contour method"*, The Journal of Strain Analysis for Engineering Design, 46(4):315–322, 2011.

[7]   H. E. Coules, P. Colegrove, L. D. Cozzolino, S. W. Wen, S. Ganguly and T. Pirling, *"The effect of highpressure rolling on weld-induced residual stresses"*, Science and Technology ofWelding and Joining (2012), in press.

[8]   X. P. Jiang, X. Y. Wang, J. X. Li, D. Y. Li, C. S. Man, M. J. Shepard, T. Zhai, *"Enhancement of fatigue and corrosion properties of pure Ti by sandblasting"*, Materials Science and Engineering: A 429 (1-2) (2006) 30 – 35, doi:10.1016/j.msea.2006.04.024.

[9]   A. Rhouma, H. Sidhom, C. Braham, J. Lédion, M. E. Fitzpatrick, *"Effects of surface preparation on pitting resistance, residual stress, and stress corrosion cracking in austenitic stainless steels"*, Journal of Materials Engineering and Performance 10 (5) (2001) 507–514.

[10]   S. Shin, *"FEM analysis of plasticity-induced error on measurement of welding residual stress by the contour method"*, Journal of Mechanical Science and Technology 19 (10) (2005) 1885–1890.

Fracture Assessment of Thin Films Through Testing of Microbeams

M. Trueba[1], I. Ocaña[1], M.R. Elizalde[1], J.M. Martinez-Esnaola[1], M.T. Hernandez[2], M. Haverty[2], G. Xu[3], D. Pantuso[2]

[1]CEIT and TECNUN (University of Navarra), Manuel Lardizabal 15, 20018 San Sebastián, Spain

[2]Design Technology Solutions, Intel Corporation, Hillsboro 97124 (OR), USA

[3]Logic Technology Q&R, Intel Corporation, Hillsboro 97124 (OR), USA

Abstract: The miniaturization process is the most powerful driving force of the microelectronics industry. New materials and processes are continuously developed. A natural consequence of this process is the need for new techniques and the development of the existing ones for mechanical characterization of thin films. In this paper, we propose an approach to characterize the mechanical behavior of thin films, both brittle (polymeric ILDs) and ductile (Cu). Different kinds of geometries of beams (cantilever beams with or without a pre-notch) have been machined with a FIB (Focused Ion Beam), and tested at the nanoindenter. The experimental results along with the numerical analysis on the stress state at the fracture point are presented.

1. INTRODUCTION

As the microelectronic industry advances, the materials used in integrated circuits are improved from their electronic and optic point of view. But the mechanical properties cannot be disregarded as residual stresses that appear as a consequence of the deposition processes, stresses during packaging and the in-service thermal cycling can make cracks grow and compromise the reliability of the chip.

Thin films are used in many technologies in the microelectronic industry. The traditional mechanical testing techniques are not enough to measure the mechanical properties of the thin films. Many different techniques have been developed to characterize their properties and the properties of their interfaces.

As for characterizing interfaces, two techniques are mainly used in the industry. Four point bending (developed by Dauskardt et al. [1]) is the reference testing method in the industry. In this test, a macroscopic notched sample (10 mm long) is subjected to bending to initiate a crack which kinks and propagates along the interface of interest. The main limitations of this technique are that (i) special specimens involving adhesives are required, thus increasing the throughput time and introducing variability in the results, and (ii) the cracks generated are of the order of millimeters and hence local properties cannot be determined (drawback for patterned structures). As an alternative method, Sánchez et al. [2] developed the cross-sectional nanoindentation (CSN), that was further developed and adapted for characterizing pattern films by Ocaña et al. [3]. In CSN a crack is initiated in the silicon underlying the structures of interest by nanoindentation, and the crack propagation along different interfaces is measured and used to characterize their adhesion energy.

Concerning the fracture characterization of thin films, several efforts have been made. The technique mainly used for this purpose in industry is "channel cracking". Developed by Huang et al. [4] in channel cracking a crack initiated from a scratch is propagated by bending the sample. The film fracture energy is calculated from the stress needed for crack propagation. Even though it is the reference test in industry, this technique gives quite random results and has been proven as extremely sensitive to the operator. Indentation techniques have also been used to measure fracture toughness. A sharp tip (typically a Vickers, a Berkovich or a cube corner diamond) is pushed into bulk brittle materials. If the applied load reaches the critical value, radial cracking can occur. Using the maximum load and the crack length, fracture toughness can be calculated [5,6]. These techniques have been developed in order to obtain the fracture toughness of ceramic materials [7]. Finite element modeling is necessary to describe the complex stress and strain fields that appear under the indenter tip [8]. The main drawback of these techniques is that the crack patterns obtained depend on the system tested (thin film thickness, substrate properties, residual stresses, interfacial properties) which reduces the reproducibility and makes quantification very challenging. Testing of microsamples has been widely used to characterize mechanical properties of small volumes. For instance Matoy et al. [9] used bending of cantilever beams (machined by etching processes) to calculate the fracture toughness of silicon based dielectric materials and found that it increased with decreasing cantilever thickness.

In this work, the ability to obtain fracture properties of metallic and polymeric thin films testing microbeams has been explored. An alternative method to machine samples using FIB is presented. The beams have been tested using a nanoindenter. Cantilever beams have been tested up to fracture. In the case of brittle materials, the maximum load together with the geometrical parameters and the Young's modulus of the materials are used to calculate the fracture stress of the thin films. For ductile materials, the energy introduced during the test and the cracked area are also needed to calculate the fracture toughness.

2. MATERIALS AND EXPERIMENTAL TECHNIQUES

2.1. Material

The samples studied in this work are polymeric and metallic blanket thin films deposited on a {111} Si wafer. Table 1 shows the materials and stacks that have been tested.

Table 1. Materials tested

| Material	Stack	Young's modulus (GPa)
Polymer	750 nm polymer on Si	10
Cu _ A	Cu (0.5 μm) – SiOx (100 nm) – TNT (10 nm)-Si	–
Cu _ B	Cu (1 μm) – SiOx (100 nm) – TNT (10 nm)-Si	–

A Young´s modulus of 155 GPa is assumed for the Si.

2.2. Beam machining

The beams have been machined at the FIB. Sample preparation starts cleaving small pieces of about 10 mm × 10 mm by pre-cracking one edge of the sample with a scriber and propagating the crack by bending the sample with special pliers.

These pieces are introduced in the FIB chamber (QUANTA3DFEG, FEI) and different microbeam geometries are machined using the following general procedure.

The sample is stuck on a holder and introduced in the chamber with the top surface perpendicular to the electron beam. The sample is tilted 52º so the surface is perpendicular to the ion beam and the top geometry is defined (see figure 1a). Positioning marks, which will help the positioning of the tip when testing each beam at the nanoindenter, are also machined in this step.

a)   b)
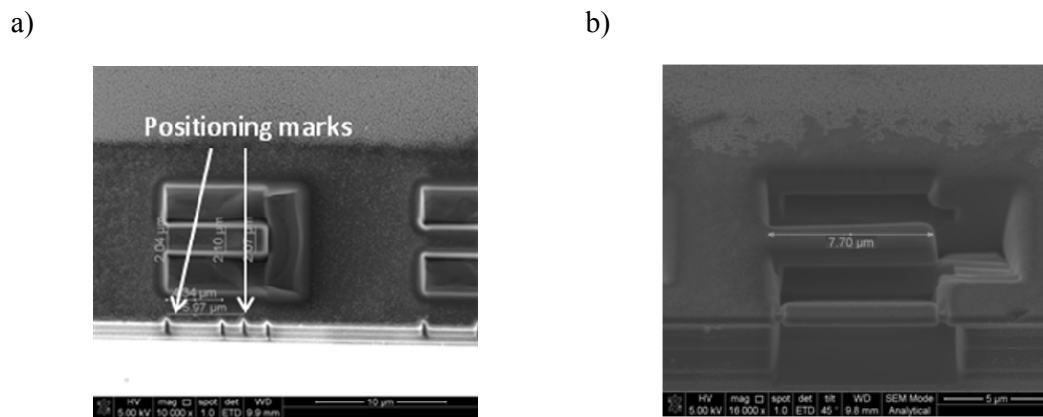
Fig. 1. *SEM images showing a) top view of details of the first step of the machining process for cantilever beams; b) view of the beam tilted 45º showing the typical geometry.*

Then, the sample is taken out of the chamber and is rotated 90º, so the top surface is now parallel to the electron beam. To define the thickness of the beam and allow its deflection a trench is machined in cross section. This trench is milled at a distance h from the top surface, determining the thickness of the beam. Figure 1b shows the typical geometry obtained using the described method.

2.3. Testing conditions

The beams are deflected at the TriboIndenter™ (Hysitron, USA) using a conical tip (tip radius 1.86 μm) until fracture occurs (this point can be detected as a sudden jump in displacement in the load – displacement record).

The testing process is as follows. First, an SPM (Scanning Probe Microscopy) image of the beam is taken with the imaging mode of the TriboIndenter™. In this mode the center of the image is the point where the load is applied, characterized by the distance to the fixed end ($L/2$ for the case of beams fixed at both ends and L for cantilever beams). All the tests are carried out under displacement control. After testing, a fractographic analysis is performed at the FIB and the crack initiation sites and/or propagation paths are analyzed.

3. RESULTS AND DISCUSSION

3.1. Polymer beams

When working with very thin films, if a simple beam is machined (with the thickness limited by the total one of the film) the resulting geometry is often too compliant and the machine is not able to detect the surface, breaking the sample without any possibility of capturing data. This problem was overcome by machining composed beams (2.5 µm of Si supporting the polymeric film) increasing this way the stiffness of the system and making it possible to achieve the fracture point.

This configuration leads to successful tests for this material because a crack starts at the polymer and propagates through all the thickness of the beam. Figure 3a shows an example of a polymer-Si beam after testing and figure 3b illustrates a typical load-displacement record.

With a simple analytical analysis of a cantilever beam, two points in which fracture can start can be identified (figure 4): A (maximum stress in the ILD) and B (maximum stress in the Si).

a)   b)
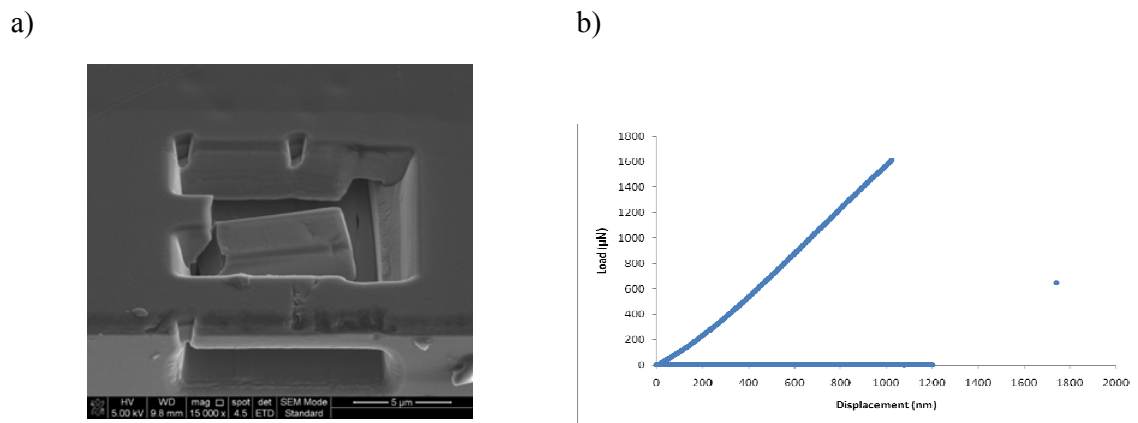

Fig. 3a. SEM image showing a fractured polymer-Si cantilever. 3 b) Typical load–displacement record of a polymer-Si cantilever
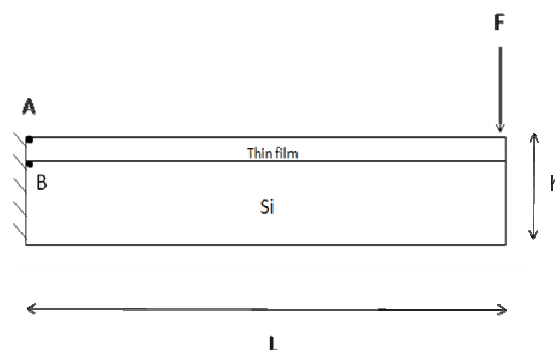

Fig. 4. Sketch of a test in a cantilever beam with the 2 points with maximum stresses identified (A for the ILD and B for the Si).

The stresses in A and B are calculated using the bending theory of beams as

$$\sigma_A = \frac{F \cdot L \cdot z_A}{I_{eq}} \cdot \frac{E_1}{E_2} \qquad (1)$$

$$\sigma_B = \frac{F \cdot L \cdot z_B}{I_{eq}} \qquad (2)$$

where F is the applied load, L the distance between the fixed end and the point at which the load is applied, z is the distance to the neutral axis, I_{eq} is the equivalent moment of inertia with respect to the transversal axis and E_1 and E_2 are the Young's modulus of the thin film and the Si, respectively.

The crack should start in the ILD if the mechanical properties of the ILD are to be evaluated. The condition for this is that the relation between the fracture strength of the thin film and the Si must fulfill:

$$\sigma_{fracture,Si} > \sigma_B$$

when

$$\sigma_A = \sigma_{fracture,ILD} = \frac{F \cdot L \cdot z_A}{I_{eq}} \cdot \frac{E_1}{E_2} \qquad (3)$$

An expression of F as a function of $\sigma_{fracture,ILD}$ can be derived and substituted in (2), which leads to the following ratio between the strength of the Si and the ILD to have fracture starting at the ILD:

$$\frac{\sigma_{fracture,Si}}{\sigma_{fracture,ILD}} > \frac{z_B}{z_A} \cdot \frac{E_2}{E_1} \qquad (4)$$

In the tests performed, $\dfrac{z_B}{z_A} \approx 0.6$ and $\dfrac{E_2}{E_1} \approx 15.5$, so $\sigma_{fracture,ILD} < \dfrac{\sigma_{fracture,Si}}{9.3}$ (5)

Eq 5. gives a theoretical upper bound for the fracture stress of the thin film that can be obtained using the current dimensions. Using these analytical calculations together with the maximum load obtained in the experiments, the dimensions of the beams and assuming a Young's modulus of 10 GPa for the polymer, the following fracture strength of the polymer is obtained:

$\sigma_{fracture, ILD} = 560 \pm 100$ MPa

Assuming a fracture strength of 7000 MPa for the Si, equation (5) is fulfilled. So the crack is starting at the polymer, as desired.

3.2. Cu beams

Following the methodology described above, a first attempt with composed cantilever beams was made in Cu samples. Due to the ductility of the Cu, the crack starts at the Si, making it very difficult to extract any meaningful result out of this kind of test. Figure 5 shows a Cu-Si beam with the crack starting at the Si, illustrating this problem.
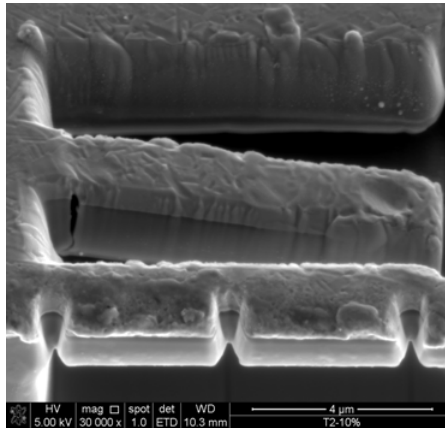
Fig. 5. SEM image showing a cantilever beam of Cu-Si with a crack starting at the Si.

Inducing a stress concentration in the beams (for instance through notching) was envisioned as a possible approach for ductile materials. The pre-notch induces high stresses in the beam and forces the crack to start at this place. In this way repetitivity in the crack initiation site is obtained.

The thickness of the beam is determined by the thin film and the pre-notch further reduces the stiffness of the beam. In order to increase the stiffness of the beams without any Si support at all, the beams have been tested applying the load at the cross-section. The typical test configuration and the load-displacemtne record are shown in figure 6.

a)

b)
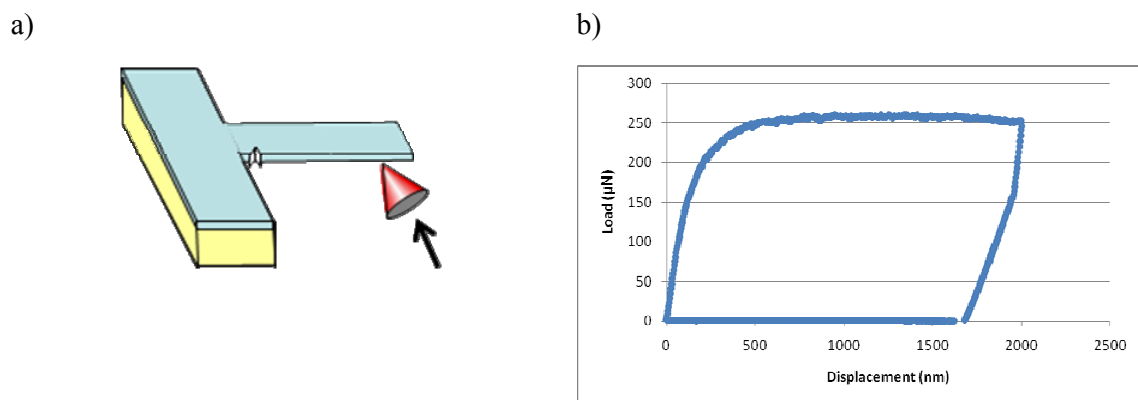
Fig. 6. a) Sketch of a pre-notched cantilever beam with Cu on top and tested from the cross-section; b) Typical load- displacement record obtained with this methodology

Figure 7 shows a pre-notched cantilever of 1 µm Cu, before and after the test. The crack has propagated through the notch, as desired.

As a first attempt to characterize the fracture behavior of ductile thin films, plotting a "resistance curve" is proposed. Figure 8 shows the evolution of the total energy absorbed during the test with the propagated crack area for the cases of 0.5 and 1 µm Cu thick pre-notched cantilevers.

a)   b)
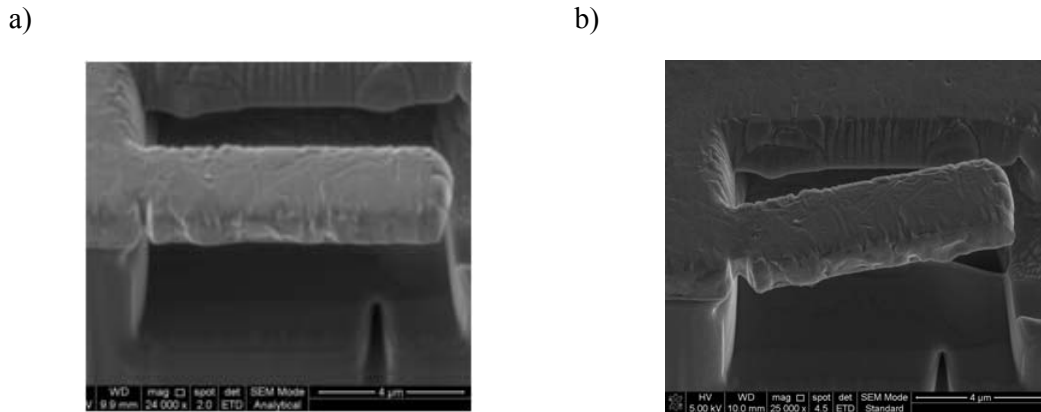
Fig.7. SEM image showing a pre-notched cantilever beam of 1 µm Cu a) before and b) after testing.

In these plots the propagation of the crack was evaluated making several cuts with the ion beam once the test was done. This way, the total cracked area can be measured. On the other hand, the energy introduced during the test was evaluated as the area below the load–displacement curve.

A further effort to rationalize the data obtained for ductile materials can be made taking into account the contribution of the plastic deformation to the total energy in the test (equation (6)),

$$W = W_f \cdot \Delta a \cdot h + W_p \cdot Fa^2 \cdot h + W_b \cdot h \qquad (6)$$

where W is the total energy in the test , $W_f \cdot \Delta a \cdot h$ is the energy spent in the fracture propagation and $W_p \cdot Fa^2 \cdot h + W_b h$ accounts for the plastic energy spent during the crack propagation including the blunting of the crack tip.

a)   b)
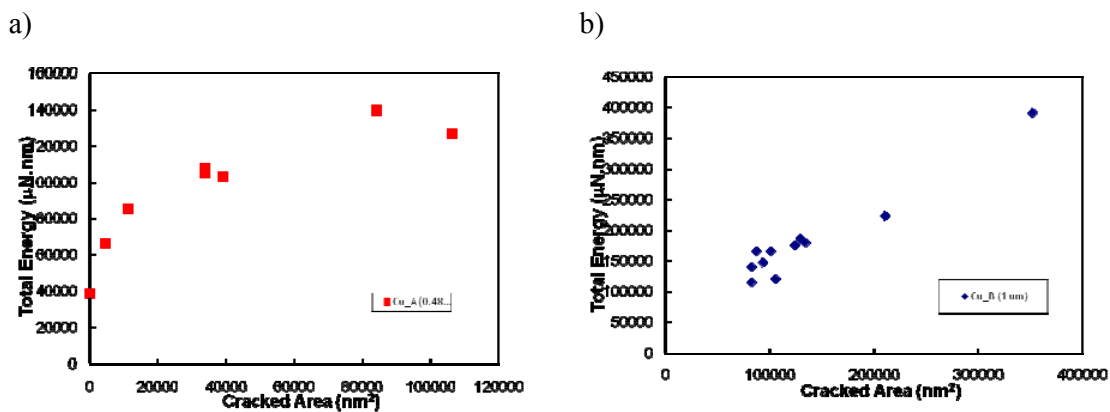
Fig. 8. Total energy vs. cracked area for pre-notched cantilevers with a) 0.5 µm of Cu; and b) 1 µm of Cu.

Taking into account equation (6) from the experimental data the fracture energy of the Cu films studied can be obtained:

$$W_{f\,Cu\,-\,1\mu m} = 1 \text{ kJ/m}^2$$

$$W_{f\,Cu\,-\,0.5\mu m} = 0.7 \text{ kJ/m}^2$$

4. CONCLUSIONS

The ability of microbeam testing to obtain fracture properties in very thin films has been demonstrated. The technique has been developed and tested for polymeric and metallic thin films.

Even though the technique is best suited for brittle films, meaningful results can be obtained for ductile materials (such as metals).

REFERENCES

[1] Dauskardt, R.H., Lane, M., Ma, Q. and Krishna, N., *Adhesion and debonding of multi-layer thin film structures*. Engng. Fracture Mech. 61: 141-162, 1998

[2] Sánchez, J.M., El-Mansy, S., Sun, B., Scherban T., Fang, N., Pantuso, D., Ford, W., Elizalde M.R., Martínez-Esnaola, J.M., Martín-Meizoso, A., Gil-Sevillano, J., Fuentes M. and Maiz, J., *Cross-sectional nanoindentation: a new technique for thin film interfacial adhesion characterization*. Acta mater 47: 4405-4413, 1999

[3] Ocaña I., Molina-Aldareguia, J.M., Gonzalez D., Elizalde M.R., Gil Sevillano, J., Scherban, T., Pantuso, D., Sun, B., Xu, G., Miner, B., He, J. and Maiz, J., *Fracture characterization in patterned thin films by cross-sectional nanoindentation*. Acta Mater 54: 3453–3462, 2006

[4] Huang, R., Prévost, J.H., Huang, Z.Y. and Suo, Z., *Channel-cracking of thin films with the extended finite element method*. Engineering Fracture Mechanics 70: 2513-2526, 2003

[5] Anstis, G.R., Chantikul, P., Lawn, B.R., Marshall, D.B., *A critical evaluation of indentation techniques for measuring fracture-toughness: I, Direct crack measurements*. J Am Ceram Soc 64(9):533–8, 1981

[6] Harding, D.S., Oliver, W.C. and Pharr, G.M., Mater. Res. Soc. Symp. Proc.356 663, 1995

[7] Dylan J., Morris and Robert, F., *Radial fracture during indentation by acute probes: I, description by an indentation wedging model*. Int J Fract 136(1–4):237–64, 2005

[8] Bhattacharya, A.K. and Nix, W.D., *Finite element analysis of cone indentation*. Int J Solids Struct 27(8):1047–58, 1991

[9] Matoy, K., Schönkerr, H., Detzel, T.a nd Dehm, G., *Micron-sized fracture experiments on amorphous SiOx films and SiOx/SiNx multi-layers*. Thin Solid Films 518: 5796-5801, 2010

Microstructure and corrosion properties of laser treated Aluminium-Nickel Bronze alloy

[1]R. Losada, [1]J. Miniño, [1]X. R. Nóvoa, [1]M. C. Pérez*, [2]L. Mera, [2]P. Vázquez
[1]*ENCOMAT group, E. E. I; Universidade de Vigo, 36310 Vigo, Spain (*mcperez@uvigo.es)*
[2]*AIMEN Technological Centre, Relva 27 A, 36410 Porriño, Spain*

Abstract Laser surface melting, LSM, was employed to modify the microstructure and corrosion properties of a nickel-aluminium-bronze alloy. The results were compared with those obtained on "as cast" sample to assess the influence of LSM treatment in corrosion resistance.
After LSM the microstructure becomes finer and more homogenised, which greatly modifies the corrosion resistance. The dealloying corrosion analysis and the electrochemical tests revealed for LSM sample a superior corrosion resistance. On the basis of the reported data some possible reasons to explain such behaviour have been suggested.

1   Introduction

The optimal properties of Nickel-aluminium bronzes are attributed to their composition and microstructure. These alloys are easily fabricated and have been widely used in numerous applications, particularly in marine engineering [1]. Most of the times, corrosion limits the performance of these alloys. Corrosion is a surface phenomenon that can be minimized by appropriate surface treatment [2]. Laser surface melting (LSM) is an interesting method of surface modification for improving corrosion resistance in the field of materials processing. Focussed laser energy is used to melt the near surface region to improve the surface dependent properties. Since melting and solidification occur within a very short interaction time and remain confined only to the top surface, the bulk provides self-quenching without any noticeable change in the microstructure. In addition, short processing time, flexibility in operation, economy in time and material consumption, and precision are the important advantages of laser surface modifications. LSM enhances surface properties via homogenisation and refinement of the structure and is expected to be an effective technique for the homogenisation of complex alloys. In fact, LSM has been used to reduce the dealuminification of aluminium bronze in NaCl solution [3], to improve the erosion corrosion resistance of MAB alloys [4], and to improve the hardness and wear of many ferrous and nonferrous alloys.

In this work the laser surface melting of a nickel-aluminium bronze alloy in "as cast" condition was examined to improve the alloy's corrosion resistance. The goal was to explore the influence of the microstructural changes due to LSM in corrosion properties. For this purpose, characterization techniques as Scanning Electron Microscopy, SEM, and Optical Microscopy, OM, have been combined with potentiodynamic polarization and electrochemical impedance spectroscopy, EIS. Further, dealloying corrosion resistance of these materials was studied according to a standard test for dealloying brasses.

2   Experimental

2.1 Materials and sample preparation

The composition of "as cast" Al-Ni-Fe-Cu alloy in weight percentage is given in Table 1. Those data were obtained with a spark emission spectroscopy using a Spectromax LMF04 (Spectro) and the Spark Analyser Mx and DIA2000SE software. The "as cast" samples were identified as

"B". These samples were laser surface-melted with a Nd:YAG DY044 Laser. The laser beam was transmitted by means of an optical fibre and focused onto the specimen by a glass lens with a focal length of 200 mm. Argon flowing at a rate of 15 l/min was used as shielding gas. A melt surface was achieved by parallel melt tracks with 50% overlap between adjacent tracks. After preliminary studies, the laser processing parameters selected was: Laser Power: 3kW, Scanning speed: 5mm/s. The Laser surface melting samples were designated as "LSM".

Table 1- Chemical composition in wt%

	Cu	Al	Ni	Fe	Mn	Si	Zn	others
wt%	78.86	8.34	4.77	4.79	1.17	0.13	1.89	0.04

Both (B and LSM) type of specimens for microstructural characterization were abraded with SiC paper down to 1500 grit and finally polished using 1 μm diamond paste and 0.04 μm colloidal Si. The samples were degreased with acetone and deionized water and were dried before testing.

2.1 Surface Microstructural Characterization

Prior to microstructural characterization, the "B" and "LSM" samples were etched in a $FeCl_3$-HCl-ethanol solution. The microstructure was examined using optical microscopy (GX-71 OLYMPUS) and Field Emission Gun Scanning Electron Microscopy (HITACHI S4800). The average grain size was obtained using image analysis. The major phases present were analysed by X-ray diffractometry (XRD apparatus from BRUKER).

2.2 Dealloying Resistance

The dealloying resistance of the materials was studied according to the UNE-EN ISO 6509 standard test for dealloying of brasses. The test consists of a microscopical study of the dealloyed layer after exposure to 1% $CuCl_2$ solution. The tested surface area was 2 cm^2. The exposed surface was delimited using a cell in which the ratio volume of solution to metal surface was 100 mL·cm^{-2}. The evolution of corrosion was monitored visually. After extraction, the samples were rinsed and dried, and the exposed surface and cross sections were examined at the optical microscope. The depth of the attacked zones was measured by an image analysis program.

2.3 Electrochemical Characterization

Electrochemical experiments were performed at room temperature in a conventional three electrode all glass cell where the working electrode was the bronze aluminium alloy (0.28 cm^2 exposed area). A Pt mesh was used as large surface counter electrode and a Saturated Calomel Electrode, SCE, as reference electrode. The testing solution was 3.5% NaCl solution, pH= 7.9 adjusted using NaOH solution.

An AUTOLAB PGSTAT 30 with FRA module (from Ecochemie NL) was used for all the electrochemical measurements. Cyclic voltammetry measurements, CV, were performed from 1.5 V to +0.75 V vs SCE at 1mV s^{-1} scan rate. The electrochemical impedance spectra were recorded at the open circuit potential, OCP, after 1h stabilisation in the solution. The evaluated frequency range was from 100 kHz down to 10 mHz. The amplitude of the superimposed AC-signal was 10 mV rms. To test reproducibility each experiment was carried out at least twice.

3   Results and discussion

3.1. Microstructural characterization

To analyse the changes in the microstructure of the material, resulting from laser treatment, metallographic observations were made on both materials. Figure 1 shows the optical micrograph of the "as cast" material for different magnifications.
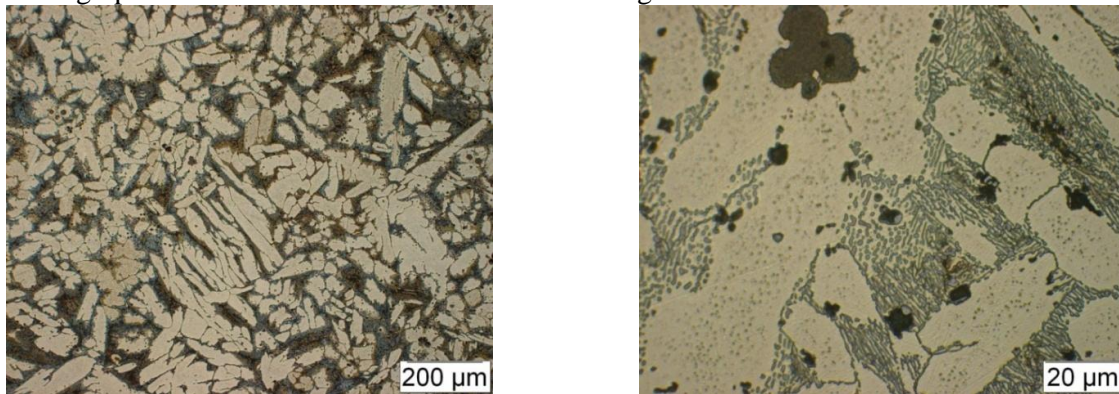
Figure 1 – OM images of "as cast" sample.

The microstructure of non-treated material can be described as follows: under normal casting conditions the Al-Cu alloy presents a microstructure consisting of light etched areas of α-phase about 50-70µm size, which is a FCC Cu-rich solid solution. Several intermetallic phases referred as κ-phase and some retained β-phase (Al rich solution) are also present. The κ-phases appear over a broad range of chemical compositions.

For the laser treated samples, several samples of the parallel tracks with 50% overlapping between adjacent tracks were studied. Cross-sections have been prepared by standard metallographic techniques to make them suitable for optical microscopic examinations, as shown in Figures 2 and 3.

Figure 2 – OM images of overlapped melt tracks from LSM samples.
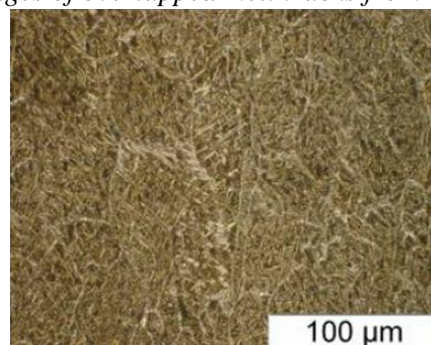
Figure 3 – OM images of LSM sample in the centered zone of laser modified surface, at the top.

Under the laser treatment conditions, a thin surface layer of the sample is melted and then rapidly solidified to form a homogeneous layer fine grained. The area affected by laser results in the breakup and decomposition of the coarse α phase and in a more uniform distribution of all phases and alloying elements. The melted zone of the sample consists of fine light etching Widmanstätten α-phase and dark etching β-phase with κ phases imbibed in α solid solution.

3.2 Dealloying Corrosion Analysis

The dealloying corrosion resistance was studied according to the UNE-EN ISO 6509 standard test for dealloying brasses.

The observation of the development of the dealuminization reaction revealed that dissolution occurs at the interface between the α matrix and the eutectoid structure. After 24 h, all samples exhibit corrosion process. The average values of the measured depths of the corroded zones are shown in Table 2.

Table 2- *Depth of dealloying in standard test for the different analysed samples*

Sample	Average depth (µm)
B	60.5±12.4
LSM	16.9±2.9

The results indicate that the attack is more intense, both in depth and density of pits for the "as cast" samples. The main effect of LSM on the microstructure, as above mentioned, was decomposition of the coarser phases and the homogenization of structure. Those seem to be responsible of the improvement of dealloying corrosion resistance [5]. It is known that refined structures resulted in lower attack which does not allow the formation of a continuous path for the penetration of the selective dissolution. Moreover, a more homogeneous distribution of the phases and the alloying elements reduces the number of sites available for galvanic coupling.

3.3 Electrochemical corrosion tests

3.3.1 Open circuit potential measurements

The evolution of open circuit potential (OCP) in the two different surfaces was monitored over a period of 1 hour in 3.5% NaCl solution. Figure 4 shows the obtained results.
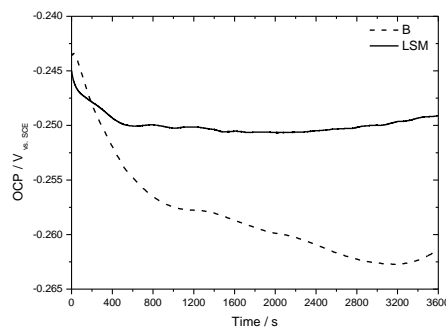
Figure 4-*Evolution of the Open circuit potential (OCP) with time in 3.5% NaCl pH=7.9*

For both samples, the OCP values shifted in the cathodic direction and then stabilized around -0.25V for LSM and -0.26V for "as cast" sample. The stabilisation time was shorter for the LSM samples (about 10 min.) than for for B samples, as can be seen in Figure 4. The role of Al, Ni and Fe in the passivation of copper alloys was assumed to be due to their incorporation to the oxide lattice, reducing the rate of oxygen reduction (cathodic reaction). Thus, the cathodic displacement of OCP values, in both alloys, can be attributed to the progressive development of such protective layer. The fact that LSM samples reached the steady state potential faster seems to indicate that their microstructure allows a faster growing and stabilization of the oxide film generated on surface.

3.3.2 Cyclic Voltammetry (CV)

Cyclic voltammetry (CV) was used to investigate the reactions occurring at the electrode surface. Figure 5 shows the cyclic voltammogram of "as cast" and LSM samples in chloride containing media.
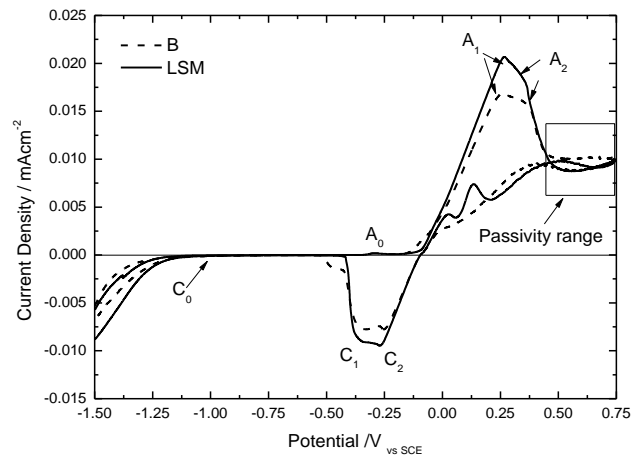
Figure 5- *Cyclic voltammogram (from -1.5 to 0.75 V vs SCE) in 3.5% NaCl solution at 1 mV s^{-1} scan rate for as cast (B) and "LSM" samples.*

The features observed on bronze aluminium alloys are similar to that of copper metal [6]. Thus, the small current peak A_0 may be related with the Cu_2O formation and the anodic peaks A_1 and A_2 represent the formation of $CuCl^-$ and CuO. After those signals, the current density decreased as the potential goes anodic, indicating the formation of a protective film. C_1, C_2 and C_0 are the corresponding reduction peaks of A_0, A_1, and A_2 oxidation peaks.

As can be seen in Figure 5, the shape of the cyclic voltammograms for the B and LSM sample is very similar. Nevertheless, there are several important differences can be noticed. The current density involved in processes of peaks A_1 and A_2 is larger for LSM than for non-treatment samples. This could be explained considering that the grain size was reduced by Laser treatment, therefore the area of grain boundaries was increased. The atoms localized at the grain boundaries bear higher energy thus they can easily take part in the electrochemical reactions, as consequence, the current registered for the electrochemical processes is higher for LSM samples. Another remarkable difference of the potentiodynamic curves, concerns the current values registered in the passivity region. Here, the as-received alloy shows fluctuating and higher current values than the laser treated samples. This indicates that the homogeneous microstructure and finer grain size of the LSM treated sample allow the formation of a more stable and protective film.

It is also interesting to note the displacement of the potential at which peak A_1 starts, as can be observed in Figure 6. For LSM samples, this potential is 0.1 V more anodic than that for the "as cast"condition. This fact could indicate a less conducting oxide formed in the potential corresponding to A_0 peak for LSM samples, due to a major incorporation of Al ions. So, an increase in the film resistivity of the oxide (higher IR drop) will explain the anodic displacement of the oxidation potential.
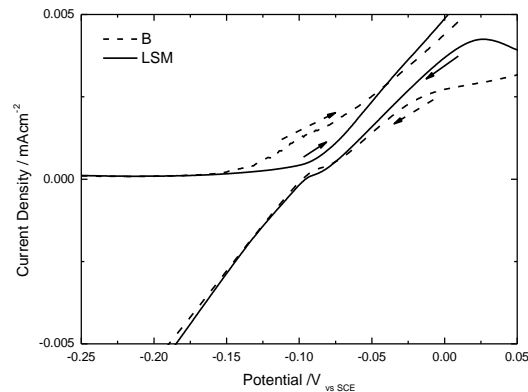
***Figure 6**- Detail of cyclic voltammogram in the potential region where peak A1 starts.*

3.3. SEM Analysis of the Sample Surface

The morphology of the corrosion products covering the "as cast" and LSM samples after cyclic voltammetry were analysed by SEM. The micrographs obtained are shown in Figure 7. The surface of both samples was completely covered with corrosion products. SEM images reveal a more compact structure for the film developed on LSM samples while the one developed on B material was more cracked. These results are consistent with the less protective character determined for B from the cyclic voltammogram analysis.
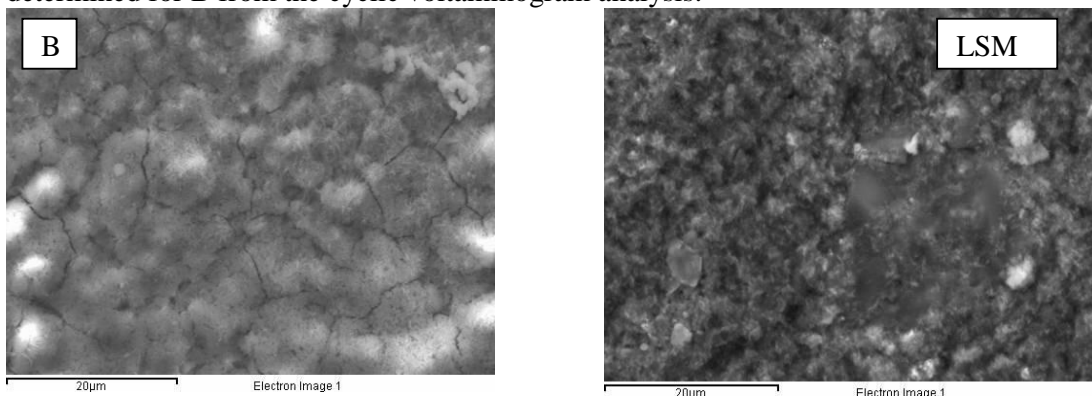
***Figure 7**: SEM images showing the surface morphologies for B and LSM samples after cyclic Voltammetry in chlorinated medium.*

3.4 Electrochemical Impedance Spectroscopy (EIS)

To verify the results obtained from cyclic voltammetry, EIS measurements were carried out. The electrodes were immersed in the testing solution until a stable OCP was reached. The impedance spectra were obtained at that potential. The corresponding Nyquist plots are depicted in Figure 8. The Nyquist diagrams recorded for both samples are similar in shape, presenting a capacitive arc. However, this capacitive arc obtained on LSM surface has a much larger diameter (six times higher) in comparison with the obtained for samples B. That difference indicates that the corrosion resistance of LSM samples is higher, result consistent with cyclic voltammetry and dealloying tests results.
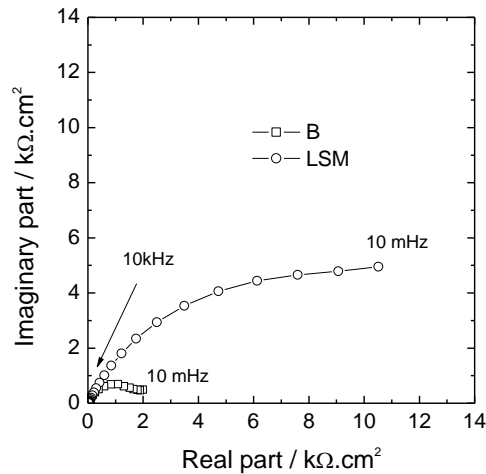
Figure 8*: Nyquist plot for samples ("B" and "LSM") at the corresponding OCP in NaCl sol.*
From the impedance data it follows also that the laser treatment performed on the surface of the Al-Cu alloy promotes the formation of a more homogeneous and protective passive film than the material without treatment. This result is consistent with the bibliography [7] and seems to prove the development of a more protective layer on LSM samples.

4   Conclusions
The corrosion resistance of laser treated aluminium-nickel bronze alloy was studied and compared with that of the "as cast" alloy. The following conclusions can be drawn:
The results obtained from dealloying corrosion, CV and EIS test indicate that the corrosion resistance of LSM samples is better than the as cast samples. The better resistance for LSM is justified in terms of its more homogeneous distribution of the alloying elements, mainly Al, and a minor grain size. Both facts hinder the existence of a continuous path for dealuminization, limiting the number of sites available for galvanic coupling and favouring the formation of a more protective passive film in chloride solution on LSM samples.

5. Acknowledgements

6. References

[1] Tuthill AH,"Guidelines for the use of copper alloys in seawater" Mater. Performance vol. 26, Num.9, pp. 12-22, 1987

[2] Fontana MG (Ed), Corrosion engineering, McGraw-Hill, New York, p.71, 1987

[3] Draper C" The use of LSM to homogenize Fe-Al bronzes" J Mater Sci,vol.16, 2774-2780, 1981

[4] Tang CH, Cheng FT, Man HC, "Effect of LSM on the corrosion and cavitation erosion behaviors of Mn-Ni-Al bronze" Mater Sci Eng A, vol. 373, pp.195-203, 2004

[5] Zhang D, Chen R, Zhang W, Luo Z, "Effect of the microstructure on the mechanical and corrosion behaviors of a hot extruded Ni-Al-bronze", Acta Metall Sin (Engl Lett), Num.23, pp.113-120, 2010

[6] Chun Y-G, Pyun S-I, Kim Ch-H, "Effect of Al content on the anodic behavior of Cu-Al alloys in 3.5% wt% NaCl solution" Mater Lett, vol. 20, pp.265-270, 1994

[7] Klassen RD, Hyatt CV, Roberge PR ,"Passivation of laser treated Ni- Al bronze as measured by EIS" Can Metall Q, vol.39, Num. 2, pp. 235-245, 2000

The effect of different heat treatment on the wear and corrosion behaviour of a Bronze Al-Ni alloy

[1]R. Losada*, [1]X. R. Nóvoa, [1]M. C. Pérez, [2]L. Mera, [2]S. Trillo, [2]P. Vázquez

[1]*ENCOMAT group, E. E. I; Universidade de Vigo, 36310 Vigo, Spain*
(*ricardo.losada@uvigo.es)
[2]*AIMEN Technological Centre, Relva 27 A, 36410 Porriño, Spain*

Abstract. The effect of two different treatments, annealing and deep cryogenic treatment, on the surface properties of a complex bronze Al-Ni alloy was studied in this work. The treatments were compared in terms of microstructures produced, tribological behaviour and corrosion resistance. The results indicate that the deep cryogenic treatment did not promote microstructural changes. Nevertheless, the annealing treatment transforms the initial microstructure in a more homogenised one. These microstructural changes can explain the larger wear and higher friction coefficient observed for the annealed samples. On the other hand, both annealing and deep cryogenic treatments improve the corrosion resistance in all the analysed conditions. The improved corrosion resistance was interpreted, for the annealed samples, in terms of the more homogeneous microstructure that promotes the development of a more protective oxide layer. The better corrosion resistance of the cryogenised samples was ascribed to their lower residual stress and free energy, compared to the parent material.

1 Introduction

The bronze Al-Ni alloys are a class of materials that offer a good combination of mechanical properties and corrosion resistance. That is the reason why they have been widely used in numerous applications, particularly for propulsion and seawater handling systems [1]. These alloys typically contain 9-12 % Al with additions up to 5% of Ni and Fe. They are generally employed in "as-cast" condition, but in the literature there are recommendations to improve their properties by submitting the alloys to different thermal treatments [2]. In this work two different alternatives were considered, deep cryogenic, DC, and annealing treatments. The treatment DC is an extension of cooling process for the standard heat treatment [3]. It is believed that DC could reduce the magnitude of internal stresses mainly by stabilisation of the dislocation structure, which should result in decreasing the atomic free energy of and improved properties [4]. Annealing treatment is commonly used for bronze-aluminium in marine applications. The treatment favours the development of a microstructure that markedly improves the corrosion resistance of the alloy.

The aim of this paper is to evaluate the influence of both annealing and deep cryogenic treatments in the microstructure of a complex bronze Al-Ni alloy, and how that affects surface and interface properties as corrosion resistance and wear behaviour.

2 Experimental

The nominal chemical composition of the alloy employed in this study is presented in Table 1. The "as cast" material was identified as "B". The annealed samples were designated as "BR", the DC samples as "BC". The experimental parameters for annealing were 675ºC (±10ºC) for 2 hours and air cooled, according to ASTM B148. The DC treatment parameters were minimum temperature -180ºC, cooling rate 2.5ºC min^{-1} and return the to the room temperature was also at 2.5ºC min^{-1}.

Table 1 - *Chemical composition of the alloy studied, wt%*

wt%	Cu	Al	Ni	Fe	Mn	Si	Zn	other
	78.86	8.34	4.77	4.79	1.17	0.13	1.89	0.046

Specimens of 2.5 cm × 2.5 cm were cut and prepared for characterization as follows: first abraded with SiC-paper starting from 220 and then sequentially with 500, 1200 and 2400 grades. Finally, the samples were polished with diamond paste from 9 to 3 and 1 μm, and finished to 0.04 μm with colloidal silica.

2.1 Microstructural Characterization:

Prior to microstructural characterization the samples were etched in a $FeCl_3$-HCl-ethanol solution. The microstructure was examined using optical microscopy, OM, using an Olympus GX51 optical microscope equipped with an image analysis program Olympus analysis five and scanning electron microscopy, SEM, using a JEOL 5410 scanning electron microscope equipped with energy dispersive X-ray spectroscopy, EDX, facility.

2.2 Tribological behaviour:

A pin-on-disk wear testing machine, from Microtest, was employed to evaluate the wear resistance of the tested samples. Wear test were conducted at room temperature, humidity of 35-45%, and a velocity of 3.14×10^{-3} ms^{-1}. AISI 304 stainless steel pin balls $\phi = 4$ mm were employed as counter-face. The tests were carried out using 10 N loads. After 11 m, the samples were taken out of the wear machine and characterized.

2.3 Dealloying Resistance:

The dealloying resistance of the materials was studied according to the UNE-EN ISO 6509 standard test for dealloying of brasses. The test consists of a microscopic study of the de-alloyed layer after 24 hours exposure to 1% $CuCl_2$ solution. The exposed surface was of 2 cm^2. After extracting the samples, they were rinsed and dried. The exposed surface and its cross sections were examined with the optical microscope. The depth of the attacked zones was measured by an image analysis program.

2.4 Electrochemical Characterization:

Electrochemical experiments were performed at room temperature in a conventional three electrode cell where the working electrode was the bronze aluminium alloy (0.28 cm^2 exposed area). A Pt mesh was used as a counter-electrode and (saturated calomel electrode) SCE as a reference one. As test solution was used a 3.5 %w NaCl solution and the pH was adjusted at 7.9 adding NaOH solution. All electrochemical measurements were obtained using a potentiostat PGSTAT 30 Autolab (Ecochemie). Polarizations were performed with a scan rate of 1mV s^{-1}. The use of low scan rate was to give more reliable results.

3 Results and discussion

3.1 Microstructural characterization

The microstructure of B, BR and BC samples is shown in Figure 1. The B and BC conditions do not show important differences. Both samples present a similar microstructure consisting of light etched areas of α-phase which is a FCC Cu-rich solid solution, some retained β-phase, and several intermetallic phases referred as κ-phase. κI phase is iron rich solid solution with globular morphology or rosette shaped. κII phase is also iron rich solid solution rosette shaped but smaller than κI phase and distributed at the α boundary. κIII phase appears at α-β boundary forming α+κIII eutectic and it is Ni rich. κIV phase represents an enrichment in Fe and appears forming fine precipitates within the α-phase.
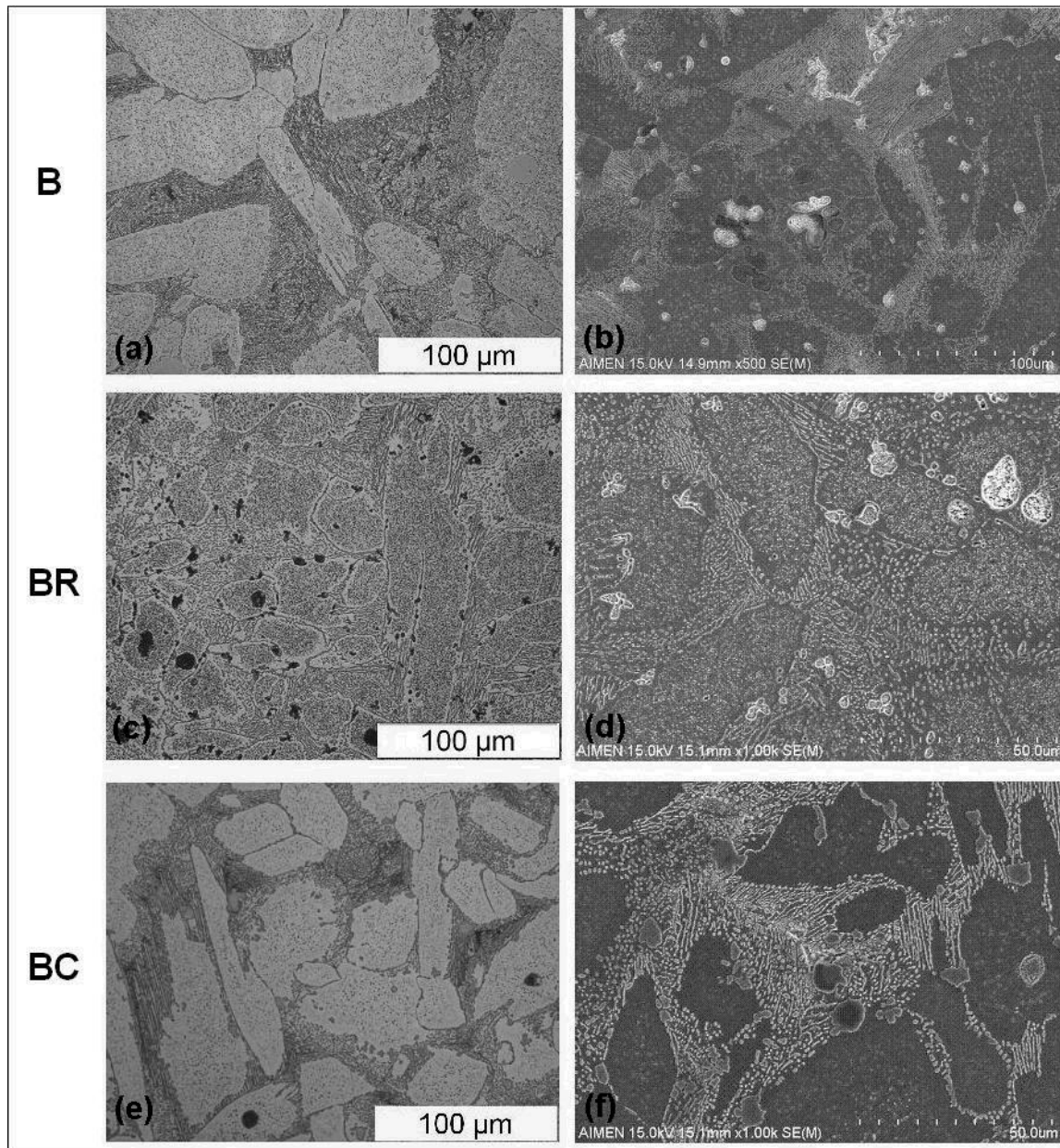
***Figure 1.** Micrographs obtained by optical microscopy (a, c, e) and scanning electron microscopy (b, d, f) for samples in the B, BR and BC states.*

       Annealing, the BR condition, results in elimination of the retained β-phase, spheroidization of κ_{III} and increasing the density of fine κ_{IV}-phase precipitates in the α-phase, and the presence of κ_V-phase precipitates in the α-phase, in the form of fine precipitates, cylindrical shaped and rich in Ni and Al.

3.2 *Friction and wear behaviour*

Friction and wear tests were carried out to assess the effect of the thermal treatments in surface properties. The wear marks for the different samples (B, BR and BC) obtained after wear test are shown in Figure 2.
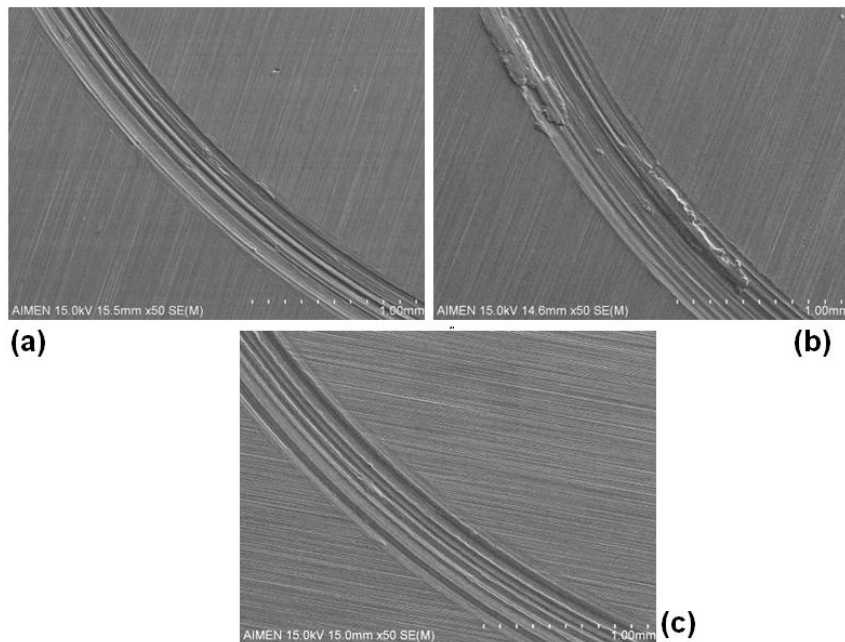
Figure 2. *SEM micrographs of wear tracks on (a) B, (b) BR and (c) BC samples.*

It can be observed in Figure 2 that all the samples show abrasive wear with certain adhesive component in the form of adhered metallic particles. The adhesive component of wear is more evident for the BR samples. The experimental data obtained for wear test are summarized in Table 2.

Table 2 *- Wear losses and friction coefficient of B, BR, and BC samples under loads of 10 N and 3.14 10^{-3} ms^{-1} sliding velocity.*

Sample	Volume loss (mm^3)	Friction coefficient, k (mm^3/N m)
B	0.059	5.26 10^{-4}
BR	0.081	7.20 10^{-4}
BC	0.067	5.92 10^{-4}

Table 2 shows that the friction coefficient, k, and the wear losses are higher for BR samples than for the B and BC, about 30% higher. Studies on the effect of the microstructure on the tribological behaviour of bronze Al alloys [5] show that the structure of the near surface appears to control the wear behaviour. In this sense, it was reported that lower friction coefficients are related to the formation of a Cu_2O coherent layer. However, when the Al oxide distribution at the surface increases, the areal fraction of Cu oxides decreases which causes breakdown of the coherent Cu_2O layer. That results in increased wear rates and higher friction coefficients. Also, the abrasive character of the Al oxides contributes to decreasing the wear resistance [6]. This fact can be related to the effect of the annealing treatment in the distribution of the alloying elements, especially for aluminium.

The results obtained from the EDX analysis (see Table 3) show higher Al concentration on the surface of the BR samples, which is consistent with the previous interpretation on the effect of Al in wear behaviour. Moreover, the EDX analysis showed Al enrichment in the wear debris for BR samples, whereas for B and BC samples Al concentration in the wear debris was lower than the bulk concentration. The larger presence of hard Al oxide in the wear debris of BR samples contributes to abrasion of the sample surface. Further, it is known that the adhesive character of the surface increases as Al content does [7], thus the more adhesive character of wear for BR samples also may be justified in terms of the increased presence of Al oxides.

Table 3*. EDX aluminium concentrations, wt%, on the sample's surfaces and wear debris.*

Sample	Wear debris	Surface
B	6.1	8.5
BR	8.6	8.7
BC	6.9	8.2

When comparing DC and "as cast" samples, one can see that both materials have a similar amount of Al on their surface and in their wear debris, therefore the values of "k" and wear loss are similar, although slightly greater for BC samples. The small difference observed in the amount of Al present in the wear mark for BC samples appears to be related to the adhesive behaviour of Al oxides, increasing both the "k" and volume loss.

It is known that most alloys will not show important changes in tribological behaviour due to cryogenic processing. This treatment will not itself harden the metal as quenching and tempering do. It is not a substitute for heat treatment; it is an addition to heat treating.

3.3 Dealloying corrosion

The major corrosion problem encountered in bronze-aluminium in sea water applications is dealloying corrosion. Dealloying is the selective dissolution of one element or phase in the material. In the case of aluminium bronze alloys, aluminium is the preferentially removed element [8]. The dealloying corrosion resistance of B, BR and BC samples was studied according to the UNE-EN ISO 6509 standard test for dealloying brasses. The discussion focuses on the most representative results obtained in samples that have been exposed to the solution for 24h. The cross section of the tested samples is shown in Figure 3.
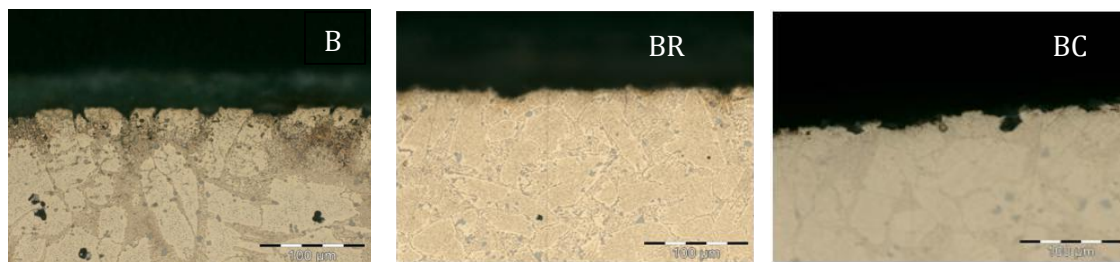
Figure 3. *Cross section of samples B, BR and BC after dealloying test .*

The average corrosion depth of the analysed samples is shown in Table 4.

Table 4 *- Depth of dealloying in standard test for the different analysed samples*

Sample	Average depth (μm)
B	60.5
BC	16.3
BR	21.0

Employing B samples as the material reference, the average corrosion depth for BR decreased by 65% and about 73% for BC. Annealing and DC treatments markedly improve the dealloying corrosion resistance. It is worth noting that no significant differences were found comparing BR and BC. In general, dealloying corrosion of multi-phase copper alloys is reported to be confined to the retained β and α+κ_{III} phases. The galvanic coupling between the anodic α phase, the cathodic Al and Ni rich β and α+κ_{III} phases is the driving force for dealloying. The high difference in chemical composition between the phases facilitates the formation of galvanic cells, and consequently, the corrosion resistance decreases.

From the microstructural analysis, it was observed that annealing treatment promotes a more homogeneous distribution of the alloying elements in the bulk material, and hence the fraction of β' phase decreases. This fact reduces the number of sites available for galvanic coupling9 which turns in a more dealloying resistant microstructure [9].

For BC samples, DC treatment did not change the microstructure (see Figure 1). However, it is known that cryogenic treatment forces the system to equilibrium at -196°C and the material entropy reaches lower values than the "as cast" condition. This lower entropy allows the establishment of long range order which leads to the minimization of galvanic couples improving dealloying resistance [10].

3.3 Characterization of the alloys by cyclic voltammetry

To evaluate the effect of the different treatments in the corrosion behaviour of the material, polarization curves were obtained for B, BR and BC samples. Figure 4 shows the cyclic voltammograms of the alloys in 3.5% NaCl solution, pH 7.9. The potential scan started at -1.5 V to 0.75 V (all potentials are referred to saturated calomel electrode, SCE) and then reversed in the cathodic direction at 1 mV s^{-1} scan rate.
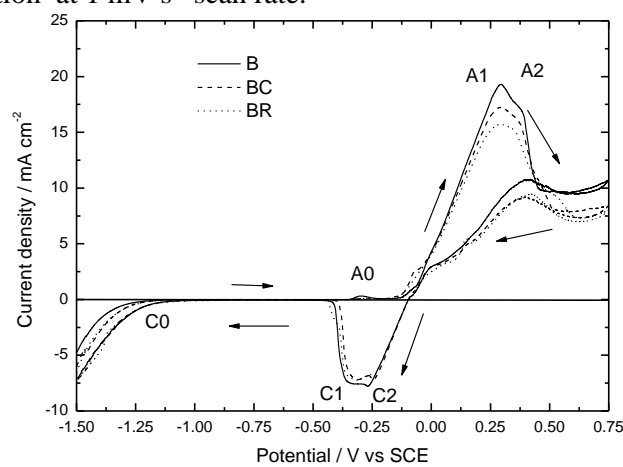
Figure 4- *Cyclic voltamograms (from -1.5 to 0.75 V vs SCE) in NaCl 3.5% solution, pH=7.9, 1 mV s^{-1} for B, BR and BC samples.*

In the anodic sweep, three oxidation peaks were observed and their assignation is as follows

Peak A_0 (at -0.29V) corresponds to the formation of Cu_2O

Peak A_1 (at + 0.29V) it may be assigned to the process indicated in Equation 1.

$$Cu + Cl^- \longrightarrow CuCl + e^-$$

$$CuCl + Cl^- \longrightarrow CuCl_2^- \qquad (1)$$
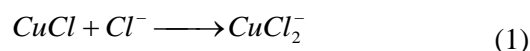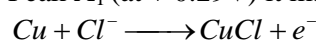
Peak A_2 (at + 0.38V): It may be related to the formation of CuO.

During the backward scan, three reduction peaks were detected and related with the species generated in the anodic sweep. So, the reduction of the Cu_2O, CuCl and CuO are recorded at cathodic peaks C_0, C_1 and C_2. Peak C_2 is related with the reduction of CuO and the following cathodic peak, C_1, can be attributed to the reduction of the CuCl precipitated layer. Finally C_0 peak is attributed to the reduction of Cu_2O formed in A_0.

Current densities involved in all the potential range are smaller for BR and BC than for B. This effect is markedly noted at peaks A_1 and A_2 and can be explained from the enhanced dissolution of the material, which result probably from the dealuminization reaction [11]. The peak current A_2 is followed by a region of limiting current density as can be observed in Figure 5. Here, the higher current values measured for B sample seem to indicate that the layers formed on BR and BC samples have lower solubility than the film formed on B. Moreover, a hysteresis loop is observed for B samples during the backward scan. This is likely due to loose of protective properties of the surface layer. Neither BR nor BC samples present such hysteresis loop which seems to be related with the larger stability and better protective properties of the film formed on those ones [12].
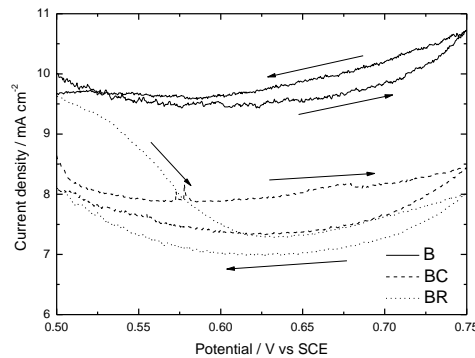
Figure 5- *Detail of the cyclic voltamogram (from -1.5 to 0.75 V vs SCE) in 3.5% NaCl pH=7.9 at a scan rate 1 mV s⁻¹ for B, BR, BC samples.*

4   Conclusion

The purpose of this work was to investigate the effect of annealing and deep cryogenic treatments on microstructure, wear and corrosion resistance of a bronze Ni-Al alloy.

The microstructural characterization did not show any effect of the DC treatment. The microstructures of B and BC samples are equivalent, consisting of α grains, some retained β-phase, and precipitates of κ-phase. Nevertheless, after annealing, the retained β-phase disappears and increases the density of fine κ-phase precipitates in the α-phase which results in a more homogenised microstructure for BR samples. These microstructural changes can explain the higher friction coefficient for BR due to the different nature of the surface oxides formed on this sample. No significant differences on wear behaviour were detected between B and BC samples.

Annealing and DC seem to exert beneficial effects on the corrosion resistance of bronze Ni-Al alloys, improving the corrosion resistance of the alloys in all the studied conditions. In NaCl solution, the current density registered in the cyclic voltammetry for these samples is clearly lower and in dealloying test this improvement is indicated by the lower intensity of the dealloying attack.

5. Acknowledgements

6. References

[1] Tuthill AH, Mater. Performance 26 (9) (1987), 12
[2] Campbell HS "Aluminium bronze corrosion resistance guide", Publication 80, Copper Development Association, U.K., 1-27 (1981)
[3] Popandopulo N, Zhukova Z, Met Sci Heat Treatment 22 (10), (1980) 708
[4] Dong Y, Lin XP, Deep HS, Heat treat Met 25, (1998) 55
[5] Li Y, Ngai TL, Xia W, Wear 197 (1996), 130-136
[6] Wert JJ, Cook WM, Wear 123 (1988), 171-192
[7] Reddy AV, Sundarajan G, Sivakumar R, Rao PR, Acta Metall, 32 (9) (1984), 1305
[8] Han Z, He YF, Lin HC, Journal of Material Science Letters 19 (2000), 393
[9] Ni DR, Xiao BL, Ma ZY, Quiao YX, Zheng YG, Corros Sci 52 (2010), 1610
[10] Sendoornan S, Raja P, I J S T, 3 (2011), 3992-3996
[11] Chun Y-G, Pyun S-I, Kim Ch-H, Material Letters 20 (1994), 265
[12] Kear, G, Barker BD, Stokes KR, Walsh FC, Electrochim Acta 52 (2007), 2343

A Vision-based IEKF Full-Motion Estimation on Long-Deck Suspension Bridges

C. Almeida Santos[1], C. Oliveira Costa[2], J. Pereira Batista[3]

[1]*Laboratório Nacional de Engenharia Civil, Av. do Brasil, 101, Lisboa, Portugal,*
csantos@lnec.pt

[2]*Laboratório Nacional de Engenharia Civil,* [3]*ISR-DEEC-Universidade de Coimbra*

Abstract The communication describes a kinematic model-based solution to estimate the motion of a structure from a sequence of images captured by a set of cameras along the time. Using an arbitrarily number of noisy images and assuming a smooth structure's motion, an Iterated Extended Kalman Filter (IEKF) is used to recursively estimate the 6-D structure's motion (displacement and rotation) over time. The requirements are a minimum of two cameras and a minimum of three non-collinear targets (control points). Results related to the performance evaluation, obtained by numerical simulations and real experiments, are presented. The scenario conditions created for the numerical simulations were inspired in the suspension bridge 25 de Abril over the river Tagus, in Lisbon, whilst for the real experiments we used a reduced structure model to fix the targets and to impose the controlled motion.

1   Introduction

A significant mount of work has been developed in the area of Structural Health Monitoring (SHM), with special emphasis on the last decades. The research growth on SHM is justified by its role in the assessment of structure's health, having in mind its own safety as well as of its users. This activity is essential to detect and to identify any failures that may occur at any component that comprises the structure during the service life of the structure, as well as during the construction and demolition stages. Without an efficient monitoring system, a component failure can cause irreversible damages in the structure and, eventually, a possible loss of human lives. SHM is the key to increase the confidence of structure owners and users and to protect it from serious damages.

The SHM accomplishment requires the measurement of several quantities, some of them related to the external actions that act over the structure (e.g. wind, load) and others related to the respective structure response (e.g. deformation, displacement). In the last group are the displacements and rotations of the structure, where its measurement is very important for the structure safety assessment. However, in general case, the traditional transducers and measurement techniques cannot be applied since the displacements of the structure can, usually, reach high amplitude (more than one meter) and, most of the time there is not a fixed point in the neighbourhood of the part of the structure to be monitored. A common solution is to measure the acceleration, and sometimes the velocity, and estimate the displacement by mathematical integration. Though, this solution has many drawbacks since the degree of accuracy depends on various factors, such as the sampling rate, the data record length, the drift and the offset of the electrical signal, etc [1].

To overcome the aforesaid limitations, we developed a non-contact vision-based measurement system, with dynamic response, accuracy and amplitude range well-suited to the

physical phenomenon, allowing to estimate the 6-D motion of large structures, and in particular, of long-deck bridges. The system setup comprises a set of digital cameras coupled to large focal lenses, fixed at the pier's base – reference point –, tracking the position of a set of active targets fixed in the deck – monitoring zone – as shown on Figure 1. The system aims to measure displacements with amplitude higher than a couple of meters, satisfying a standard accuracy and resolution better than 10 mm and 1 mm, respectively, and a minimum sampling rate of 20 Hz. To accomplish these goals, namely the high accuracy level, it is essential: i) performing the vision system calibration; and ii) modeling the motion of the structure.

The current communication only addresses the second issue – motion estimation – since the first one was already addressed in others publications [2, 3]. Therefore, the communication describes a kinematic model-based solution to estimate the position and the rotation of long deck suspension bridges from a sequence of images captured by a set of cameras. Using an arbitrarily number of images, captured from several cameras (minimum of two), and assuming a smooth deck bridge motion, an Iterated Extended Kalman Filter (IEKF) is implemented to recursively estimate the full-motion of the bridge deck along the time. To fulfil this goal we use a kinematic parameters set to create a state-space model, whereas the displacement of the bridge deck is modelled by a standard rectilinear motion with constant acceleration whilst the rotation, described by quaternions, is modelled assuming a constant precession. Further, we assume that the cameras are modelled by the affine camera projection model, which is a reasonable assumption considering the long distance between the cameras and the zone of the structure to be monitored [2, 3].

2 Recursive Filter Formulation

In this section we will present the formulation of the recursive filter which includes the kinematic motion models that will be embedded into the IEKF. The motion model that will be described was inspired on the work proposed by Young *et al.* [4], where the coordinates of a set of points in the space and time were assumed to be known. In the current case, we will use the information provided by the cameras, namely the coordinates of the points in the images. However, to carry out our algorithm we assume that the projection matrices of the cameras are known, i.e. the vision system calibration was performed in an offline mode [2, 3].

Additionally to the motion statement, we will assume that: i) a minimum of two cameras are available and they view a minimum of three non-collinear points; ii) the zone of the structure to be monitored is assumed to behave as a rigid body; iii) the capture of the images is synchronized at all cameras; and iv) the coordinates of the points in the images are known, as well as their correspondence between images, which means that the images processing is assumed to be accomplished. Further, we will also assume that the motion in one direction is independent from the others (i.e. decoupled) and the noise (disturbance) affecting the coordinates of the points is independent of the image and direction, and may take different variances values.

Coordinates Systems

The motion model assumes several coordinates systems, as shown on Figure 1: i) an inertial reference coordinate system (O_I), settled in the zone of the structure to be monitored (e.g. bridge deck space); ii) an inertial coordinate system settled in each camera (O_C); iii) a mobile coordinate system settled in the object's centroid (O_B); and iv) a mobile coordinate system settled in the centre of rotation of the bridge deck (O_R), fixed with respect to O_B and with the same orientation, behaving as a rigid body with respect to O_B.
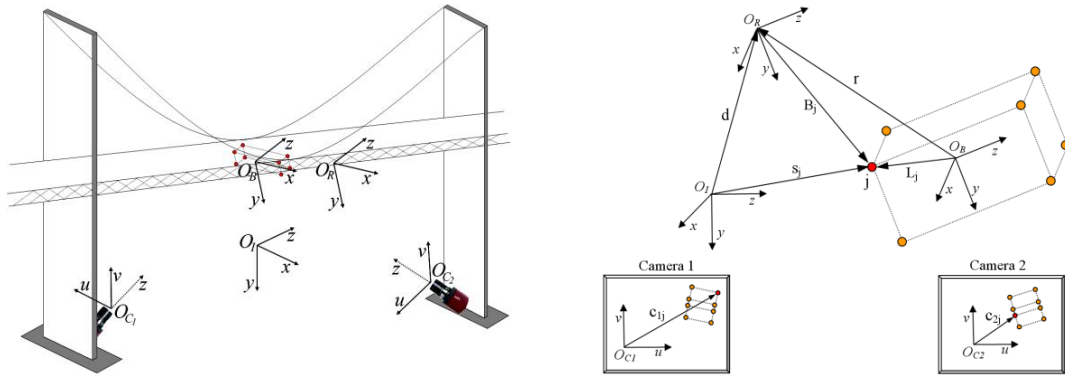
Figure 1 - *coordinates systems used to model the motion of the bridge deck*

Space Model

According to Figure 1, the position of the target **j** in the reference coordinate system O_I, at the instant t_i, is given by the vector $s_j(t_i) = [x_j(t_i), y_j(t_i), z_j(t_i)]^T$. As a matter of fact, since the coordinates of the targets in the images are affected by noise, one must write instead $\tilde{s}_j(t_i) = [\tilde{x}_j(t_i), \tilde{y}_j(t_i), \tilde{z}_j(t_i)]^T$ to reflect this influence in the inaccuracy of the reconstructed target's position. Further, since the coordinate system O_B has the same orientation as O_R, we may express the coordinates of the target **j** in the coordinate system O_B as $\tilde{B}_j = \tilde{L}_j - r$, where the vector $r = [r_x, r_y, r_z]^T$ represents the coordinates of the centre of rotation O_R and L_j the coordinates of the target **j**, both with respect to the object's coordinate system (O_B).

The relationship between the vectors $\tilde{s}_j(t_i)$ and B_j is given as $s_j(t_i) = d(t_i) + R(t_i) \cdot \tilde{B}_j$, where the vector $d(t_i)$ represents the coordinates of O_R with respect to the reference coordinate system O_I and the matrix $R(t_i)$ the rotation of the coordinate system O_B (or O_R) with respect to O_I, at the instant t_i; replacing B_j one obtains Equation (1).

$$\tilde{s}_j(t_i) = d(t_i) + R(t_i) \cdot \left(\tilde{L}_j - r \right) \tag{1}$$

Object Model

With long focal lens it is common to model the camera as an affine camera which is a reduced model of the perspective camera model [5, 6]. In this case, a 3D point in the scene (bridge deck) with the coordinates $L_m = [X_m, Y_m, Z_m]^T$ is projected into the image plane of the camera at the coordinates $l_{nm} = [u_{nj} - \bar{u}_n, v_{nj} - \bar{v}_n]^T$ according to Equation 2, where M_n represents the projection matrix of the camera **n** and $\bar{l}_n = [\bar{u}_n, \bar{v}_n]^T$ the coordinates of the camera coordinate system (O_{Cn}) in the image plane, both determined at the calibration stage.

$$\underbrace{\begin{bmatrix} u_{nm} - \bar{u}_n \\ v_{nm} - \bar{v}_n \end{bmatrix}}_{l_{nm}} = \underbrace{\begin{bmatrix} m_{11} & m_{12} & m_{13} \\ m_{21} & m_{22} & m_{23} \end{bmatrix}}_{M_n} \cdot \underbrace{\begin{bmatrix} X_m \\ Y_m \\ Z_m \end{bmatrix}}_{L_m} \tag{2}$$

Expanding Equation 2 for the case of **n** cameras and **m** targets one obtains Equation 3, used to reconstruct the position of the points in the space, where $[M]^\nabla$ represents the pseudo-inverse of the matrix **M** and the vector $[\hat{u}_n, \hat{v}_n]^T$ the coordinates of the centroid of the points in the image of the camera **n**, determined as $[\hat{u}_1 \quad \hat{v}_1 \quad \cdots \quad \hat{u}_n \quad \hat{v}_n]^T = \frac{1}{m} \cdot \left[\sum_{j=1}^{m} u_{1j} \quad \sum_{j=1}^{m} v_{1j} \quad \cdots \quad \sum_{j=1}^{m} u_{nj} \quad \sum_{j=1}^{m} v_{nj} \right]^T$.

$$[L_1 \quad \cdots \quad L_m] \underbrace{}_{L} = \underbrace{\begin{bmatrix} M_1 \\ \vdots \\ M_n \end{bmatrix}}_{M}^{\nabla} \cdot \begin{bmatrix} u_{11}-\hat{u}_1 & \cdots & u_{1m}-\hat{u}_1 \\ v_{11}-\hat{v}_1 & \cdots & v_{1m}-\hat{v}_1 \\ \vdots & \ddots & \vdots \\ u_{n1}-\hat{u}_n & \cdots & u_{nm}-\hat{u}_n \\ v_{n1}-\hat{v}_n & \cdots & v_{nm}-\hat{v}_n \end{bmatrix} \tag{3}$$

As aforementioned, the shape of the object **L**, defined by the position of the **m** points in O_B, does not change over time. Therefore, considering that the coordinates of the points in the image may be affected by noise one may enhance the accuracy of the coordinates of the points **L** averaging the coordinates recursively, as:

$$\overline{L}(t_i) = \frac{i}{1+i} \cdot \overline{L}(t_{i-1}) + \frac{1}{1+i} \cdot \tilde{L}(t_i), \tag{4}$$

where t_i represents the instant of the capture of the images (see below), **i** the number of frames captured from the beginning and $\tilde{L}(t_i)$ is determined using Equation 5. The second part of Equation 5 is used to determine the unit directional vectors (e_x, e_y, e_z) along the axes of the object, since O_B may be rotated with respect to O_I. After a few iterations the reconstructed 3D position of the points (L_j) tends to converge to the true state.

$$\tilde{L}(t_i) = [L_1(t_i) \quad \cdots \quad L_m(t_i)] \cdot \begin{bmatrix} e_x(t_i) \\ e_y(t_i) \\ e_z(t_i) \end{bmatrix} \quad \text{with} \quad \begin{bmatrix} e_x(t_i) \\ e_y(t_i) \\ e_z(t_i) \end{bmatrix} = \begin{bmatrix} \dfrac{L_2(t_i)-L_1(t_i)}{\|L_2(t_i)-L_1(t_i)\|} \\ e_x(t_i) \times e_y(t_i) \\ \dfrac{e_x(t_i) \times (L_3(t_i)-L_1(t_i))}{\|e_x(t_i) \times (L_3(t_i)-L_1(t_i))\|} \end{bmatrix}. \tag{5}$$

Motion State Model

In general case, the motion of a large structure may be characterized, broadly, as an oscillatory motion with one main component of low frequency and considerable amplitude and several components, of random nature, with higher frequency and lower amplitude. A kinematic state model is defined by setting a certain derivative of the motion to zero which, in the absence of any random inputs, is characterized by a polynomial function in time [7]. The random components of the motion as well as any disturbance affecting the system are modelled as white noise.

Assuming that the motion of the bridge deck is smooth, assuming a constant acceleration over time, the state equation for the translation motion is described by Equation 6a), where the vectors $a = [a_x, a_y, a_z]^T$, $v(t) = [v_x(t), v_y(t), v_z(t)]^T$ and $d(t) = [d_x(t), d_y(t), d_z(t)]^T$ represent, respectively, the acceleration, the velocity and the displacement components of O_R with respect to O_I, at the instant **t**. The integration of Equation 6a) in the time domain gives the closed-form solution described by Equation 6b), where $\tau = t_{i+1} - t_i$ represents the time elapsed between the instants t_{i+1} and t_i and the vectors **a**, **v(t)** and **d(t)** are the state variables describing the translational component of the motion.

$$a) \quad \begin{cases} \dot{d}(t) = v(t) \\ \dot{v}(t) = a(t) \\ \dot{a}(t) = 0 \end{cases} \qquad b) \quad \begin{cases} d(t_{i+1}) = d(t_i) + v(t_i) \cdot \tau + 0.5 \cdot a(t_i) \cdot \tau^2 \\ v(t_{i+1}) = v(t_i) + a(t_i) \cdot \tau \\ a(t_{i+1}) = a(t_i) \end{cases} \tag{6}$$

Likewise, the rotation motion is modelled assuming that the precession is almost constant. Let the vectors $w(t) = [w_x(t), w_y(t), w_z(t)]^T$ and $p = [p_x, p_y, p_z]^T$ be, respectively, the instantaneous

angular velocity of the bridge deck and the precession, both with respect to $\mathbf{O_R}$ and with components in $\mathbf{O_I}$. Further, lets define the matrices $\Omega[\mathbf{w(t)}]$ and $\mathbf{P(p)}$ as

$$\Omega[w(t)] = \frac{1}{2} \cdot \begin{bmatrix} 0 & -w_z(t) & w_y(t) & -w_x(t) \\ w_z(t) & 0 & -w_x(t) & -w_y(t) \\ -w_y(t) & w_x(t) & 0 & -w_z(t) \\ w_x(t) & w_y(t) & w_z(t) & 0 \end{bmatrix} \text{ and } P(p) = \begin{bmatrix} 0 & -p_z & p_y \\ p_z & 0 & -p_x \\ -p_y & p_x & 0 \end{bmatrix}.$$

Using the quaternion vector to describe the orientation of the rigid object, $q(t) = [q_1(t), q_2(t), q_3(t), q_4(t)]^T$, one gets Equation 7a) which represents the state equation of the rotational motion [4, 8]; the closed-form solution is given by Equation 7b), where $\phi_1[\mathbf{p};\, \tau]$ and $\phi_2[\boldsymbol{\lambda};\, \tau]_{\lambda = \mathbf{p};\, \lambda = \mathbf{w(t_i) - p}}$ takes the form described by Equation 8, $c_p = cos(\|p\| \cdot \tau)$, $s_p = sin(\|p\| \cdot \tau)$, $[a_1, a_2, a_3]^T = \left[\dfrac{p_x}{\|p\|}, \dfrac{p_y}{\|p\|}, \dfrac{p_z}{\|p\|} \right]^T$, and $\mathbf{I_3}$ and $\mathbf{I_4}$ represents, respectively, a *3x3* and *4x4* identity matrix. The vectors $\mathbf{p}$, $\mathbf{w(t)}$ and $\mathbf{q(t)}$ represent the state variables describing the rotational component of the motion.

$$a)\quad \begin{cases} \dot{q}(t) = \Omega[w(t)] \cdot q(t) \\ \dot{w}(t) = P(p) \cdot w(t) \\ \dot{p}(t) = 0 \end{cases} \qquad b)\quad \begin{cases} w(t_{i+1}) = \phi_1[p;\, \tau] \cdot w(t_i) \\ q(t_{i+1}) = \underbrace{\left\{ \phi_2[p;\, \tau] \cdot \phi_2[w(t_i) - p;\, \tau] \right\}}_{\phi_2[p;\, w(t_i) - p;\, \tau]} \cdot q(t_i) \\ p(t_{i+1}) = p(t_i) \end{cases} \tag{7}$$

$$\phi_1[p;\, \tau] = \begin{cases} I_3 & if \quad \|p\| = 0; \\[4pt] otherwise: \\ \begin{bmatrix} a_1^2 + (1 - a_1^2) \cdot c_p & a_1 \cdot a_2 \cdot (1 - c_p) - a_3 \cdot s_p & a_1 \cdot a_3 \cdot (1 - c_p) + a_2 \cdot s_p \\ a_1 \cdot a_2 \cdot (1 - c_p) + a_3 \cdot s_p & a_2^2 + (1 - a_2^2) \cdot c & a_2 \cdot a_3 \cdot (1 - c_p) - a_1 \cdot s_p \\ a_1 \cdot a_3 \cdot (1 - c_p) - a_2 \cdot s_p & a_2 \cdot a_3 \cdot (1 - c_p) + a_1 \cdot s_p & a_3^2 + (1 - a_3^2) \cdot c_p \end{bmatrix} \end{cases}$$

$$\phi_2[\lambda;\, \tau] = \begin{cases} I_4 & if \; \|\lambda\| = 0; \\[4pt] otherwise: \\ I_4 \cdot cos\left(\dfrac{\|\lambda\| \cdot \tau}{2} \right) + \dfrac{2}{\|\lambda\|} \cdot sin\left(\dfrac{\|\lambda\| \cdot \tau}{2} \right) \cdot \Omega[\lambda] \end{cases} \tag{8}$$

The relation between the rotation matrix $\mathbf{R(t_i)}$, presented in Equation 1, and the quarternion $\mathbf{q}$ is described by Equation 9 (time dependence was suppressed to simplify the expression).

$$R(t_i) = \begin{bmatrix} q_1^2 - q_2^2 - q_3^2 + q_4^2 & 2 \cdot (q_1 \cdot q_2 + q_3 \cdot q_4) & 2 \cdot (q_1 \cdot q_3 - q_2 \cdot q_4) \\ 2 \cdot (q_1 \cdot q_2 - q_3 \cdot q_4) & -q_1^2 + q_2^2 - q_3^2 + q_4^2 & 2 \cdot (q_2 \cdot q_3 + q_1 \cdot q_4) \\ 2 \cdot (q_1 \cdot q_3 + q_2 \cdot q_4) & 2 \cdot (q_2 \cdot q_3 - q_1 \cdot q_4) & -q_1^2 - q_2^2 + q_3^2 + q_4^2 \end{bmatrix}, \tag{9}$$

State Transition Equation

The so called state transition equation is used to propagate the state vector from the instant $t = t_i$ to the instant $t = t_{i+1}$ (prediction stage), as described by Equation 10, where $\mathbf{O_3}$ and $\mathbf{O}$ represent, respectively, a *3x3* and a *3x4* null matrices. As aforementioned, it is assumed that the vector $\mathbf{r}$ is almost unchangeable over time, which means $r(t_{i+1}) = r(t_i)$.

$$\underbrace{\begin{bmatrix} d(t_{i+1}^-) \\ v(t_{i+1}^-) \\ a(t_{i+1}^-) \\ r(t_{i+1}^-) \\ q(t_{i+1}^-) \\ w(t_{i+1}^-) \\ p(t_{i+1}^-) \end{bmatrix}}_{x(t_{i+1}^-)} = \underbrace{\begin{bmatrix} I_3 & I_3 \cdot \tau & 0.5 \cdot I_3 \cdot \tau^2 & O_3 & O & O_3 & O_3 \\ O_3 & I_3 & I_3 \cdot \tau & O_3 & O & O_3 & O_3 \\ O_3 & O_3 & I_3 & O_3 & O & O_3 & O_3 \\ O_3 & O_3 & O_3 & I_3 & O & O_3 & O_3 \\ O^T & O^T & O^T & O^T & \phi_2[p;\, w(t_i^+) - p;\, \tau] & O^T & O^T \\ O_3 & O_3 & O_3 & O_3 & O & \phi_1[p;\, \tau] & O_3 \\ O_3 & O_3 & O_3 & O_3 & O & O_3 & I_3 \end{bmatrix}}_{\phi_x[x(t_i^+);\, \tau]} \cdot \underbrace{\begin{bmatrix} d(t_i^+) \\ v(t_i^+) \\ a(t_i^+) \\ r(t_i^+) \\ q(t_i^+) \\ w(t_i^+) \\ p(t_i^+) \end{bmatrix}}_{x(t_i^+)} \tag{10}$$

$$\underbrace{}_{f[x(t_i^+);\, t_i]}$$

Measurement Equation

Equation 11 represents the model that allows estimate (predict) the observations at the instant $t = t_i$, based on the current values of the state vector. Indeed, Equation 11 represents the prediction of the coordinates $(\hat{u}_{nm}, \hat{v}_{nm})$ of the **m** points projected in the image of the **n** cameras at the instant $t = t_i$, where **L$_m$(t$_i$)** represents the 3D coordinates of the point **m**, determined at the instant **t$_i$** using Equation 4; the vectors **d(t$_i$)**, **q(t$_i$)** and **r(t$_i$)** are estimated by the filter.

$$
\underbrace{\begin{bmatrix} \hat{u}_{11}(t_i) \\ \hat{v}_{11}(t_i) \\ \vdots \\ \hat{u}_{n1}(t_i) \\ \hat{v}_{n1}(t_i) \\ \vdots \\ \hat{u}_{1m}(t_i) \\ \hat{v}_{1m}(t_i) \\ \vdots \\ \hat{u}_{nm}(t_i) \\ \hat{v}_{nm}(t_i) \end{bmatrix}}_{\hat{z}(t_i)} = \underbrace{\begin{bmatrix} M_1(t_i) \\ \vdots \\ M_n(t_i) \\ \vdots \\ M_1(t_i) \\ \vdots \\ M_n(t_i) \end{bmatrix} \cdot \left\{ \begin{bmatrix} d(t_i) \\ \vdots \\ d(t_i) \\ \vdots \\ d(t_i) \\ \vdots \\ d(t_i) \end{bmatrix} + \begin{bmatrix} R[q(t_i)] \\ \vdots \\ R[q(t_i)] \\ \vdots \\ R[q(t_i)] \\ \vdots \\ R[q(t_i)] \end{bmatrix} \cdot \left(\begin{bmatrix} L_1(t_i) \\ \vdots \\ L_m(t_i) \\ \vdots \\ L_1(t_i) \\ \vdots \\ L_m(t_i) \end{bmatrix} - \begin{bmatrix} r(t_i) \\ \vdots \\ r(t_i) \\ \vdots \\ r(t_i) \\ \vdots \\ r(t_i) \end{bmatrix} \right) \right\}}_{h[x(t_i); t_i]}
\qquad (11)
$$

Iterative Extended Kalman Filter Formulation

Considering that: i) the system state is modelled by Equation 12a), where **f** is a known nonlinear function of **x(t)** and **t**, and **v(t)** is a zero-mean white Gaussian noise process satisfying the conditions expressed on Equation 12b) and entering in the system in a linear additive fashion [7, 8]; and ii) the measurements are modelled by a nonlinear function, as described by Equation 13a), where **h** is a known vector of functions that depends on the state vector **x(t)** and **t**, and **w(t)** is a zero-mean white Gaussian noise sequence and covariance kernel satisfying the condition expressed on Equation 13b):

a) $\quad x(t_{i+1}) = f[x(t_i); t_i] + v(t_i)$ $\qquad$ b) $\quad E[v(t_i)] = 0; \qquad E[v(t_i) \cdot v^T(t_j)] = Q(t_i) \cdot \delta_{ij}$ $\qquad$ (12)

a) $\quad z(t_i) = h[x(t_i); t_i] + w(t_i)$ $\qquad$ b) $\quad E[w(t_i)] = 0; \qquad E[w(t_i) \cdot w^T(t_j)] = R(t_i) \cdot \delta_{ij}$ $\qquad$ (13)

the Jacobian **F** and **H** are determined as the partial derivatives of **f** (Equation 10) and **h** (Equation 11), respectively, with respect to the state vector **x(t)** as $F[\hat{x}(t_i); t_i] = \left. \dfrac{\partial f[x; t_i]}{\partial x} \right|_{x = \hat{x}(t_i)}$ and $H[\hat{x}(t_i); t_i] = \left. \dfrac{\partial h[x; t_i]}{\partial x} \right|_{x = \hat{x}(t_i)}$.

Assuming that the state vector at the instant **t$_0$** is a Gaussian random vector with mean **$\hat{x}_0$** and covariance **P$_0$**, and uncorrelated with the two noise sequences **v(t)** and **w(t)**, which are also assumed to be mutually independent, the propagation of the state vector and of the covariance matrix **P** are carried out to the instant $t = t_{i+1}^-$ according to Equations 14 and 15, respectively.

$$\hat{x}(t_{i+1}^-) = f[\hat{x}(t_i^+); t_i] = \phi[x(t_i^+); \tau] \cdot \hat{x}(t_i^+) \qquad (14)$$

$$P(t_{i+1}^-) = F[\hat{x}(t_i^+); t_i] \cdot P(t_i^+) \cdot F^T[\hat{x}(t_i^+); t_i] + Q(t_i) \qquad (15)$$

After the measurement **z(t$_{i+1}$)** has been carried out, at the instant $t = t_{i+1}$, the iterative part starts, being used to update the estimate of **$\hat{x}(t_{i+1}^+)$**, where $\breve{x}_k = \hat{x}(t_{i+1}^-)$ in the first iteration

($k = 0$). $\hat{\mathbf{z}}(\mathbf{t_{i+1}})$ is evaluated using the current value of $\breve{\mathbf{x}}_\mathbf{k}$ in the measurement model (Equation 11), as well as $\mathbf{H}[\breve{\mathbf{x}}_\mathbf{k}; \mathbf{t_{i+1}}]$. The matrix $\mathbf{H}$ obtained is applied in Equation 16 to determine the filter gain matrix at the instant $\mathbf{t_{i+1}}$, which in turn is used to obtain the estimative of $\breve{\mathbf{x}}_\mathbf{k+1}$, as described in Equation 17.

$$K_k(t_{i+1}) = P(t_{i+1}^-) \cdot H^T[\breve{x}_k; t_{i+1}] \cdot \left\{ H[\breve{x}_k; t_{i+1}] \cdot P(t_{i+1}^-) \cdot H^T[\breve{x}_k; t_{i+1}] + R(t_{i+1}) \right\}^{-1} \tag{16}$$

$$\breve{x}_{k+1} = \hat{x}(t_{i+1}^-) + K_k(t_{i+1}) \cdot \left\{ z(t_{i+1}) - \hat{z}_k - H[\breve{x}_k; t_{i+1}] \cdot [\hat{x}(t_{i+1}^-) - \breve{x}_k] \right\} \tag{17}$$

The cycle (iteration) is repeated until the improvement in $\breve{\mathbf{x}}_\mathbf{k}$ be less than a preselected threshold or a preselected number of iterations (**k**) is reached. At the end of the cycle, the state vector is upgraded as $\hat{x}(t_{i+1}^+) = \breve{x}_k$, and the approximate covariance matrix is updated according to Equation 18.

$$P(t_{i+1}^+) = \left\{ I - K_k(t_{i+1}) \cdot H[\breve{x}_k; t_{i+1}] \right\} \cdot P(t_{i+1}^-) \cdot \left\{ I - K_k(t_{i+1}) \cdot H[\breve{x}_k; t_{i+1}] \right\}^T + K_k(t_{i+1}) \cdot R(t_{i+1}) \cdot K_k^T(t_{i+1}) \tag{18}$$

3   Experimental Results

Bearing in mind the assessment of the algorithm, several tests were carried out by means of numerical simulation and with real imagery. The main characteristics of P25A were used as a model to produce a digital simulated deck bridge trajectory whereas a reduced model was developed and used to carry out the real experiments. The results that will be presented below were obtained considering a configuration with two cameras and four points (targets).

Numerical Simulation

The setup comprises two digital video cameras with the resolution of 1920 x 1080 pixels, coupled to a lens with 600 mm of focal length, as showed in Figure 2. The pixels have square shape with 7.4 µm side's length. The cameras are placed at the pier's base of the bridge (front-to-front) and the targets (control points) in the mid-span of the deck. It was assumed that the mid-span of the bridge deck is 500 m length and the height from the pier's base to the bridge deck is 100 m[1]. Further, it was also assumed that the centre of rotation ($\mathbf{O_R}$) was positioned at the coordinates $r = [0, -5, 0]^T$ (m), in $\mathbf{O_B}$.
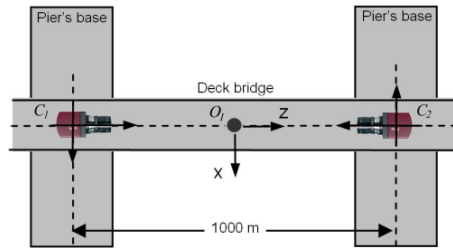
Figure 2 - *vision system layout with two cameras*

The reference coordinate system for the bridge deck is a direct orthonormal basis with origin in $\mathbf{O_I}$ and the z-axis aligned in the longitudinal direction of the deck. In the same way, in each of the cameras a direct orthonormal coordinate system $\mathbf{O_{Ci}}$ is established with the z-axis perpendicular to the image plane and pointing in the direction of the origin of the deck's reference coordinate system. Four targets were used, positioned such as they establish an

---

1 These parameters values are approximated to the real values of the bridge 25 de Abril over the river Tagus.

orthogonal coordinates system with the centroid position matched with $\mathbf{O_I}$. The distance between the targets in the *x*-direction (transversal) is 5 m, in the *y*-direction (vertical) is 0.8 m and in the *z*-direction (longitudinal) is 1 m.

A simulated deck trajectory (translation and rotation) comprising 36000 points[2] was created, where each motion component is a combination of a couple of signals with different frequencies and amplitudes. Figure 3 represents the first sixty seconds of the translation and rotation components and of the respective position of the deck in the space. To simulate the sources of disturbance, for each image captured, independent Gaussian noise with zero mean and a standard deviation of two pixels was added to the coordinates of the points in the image. Further, as aforesaid, in the current case it was assumed that the projection matrices of the cameras were known.
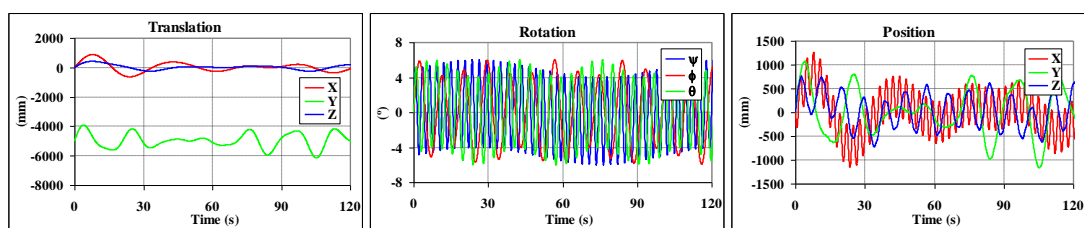
Figure 3 - *detail of the simulated bridge deck trajectory (first two minutes)*

Figure 4 shows the deviation on the estimation of the main motion parameters (position and rotation of the deck) related with the first seconds of the time series. Likewise, Table 1 presents the results obtained with two pixels of noise and they represent the mean deviation (standard deviation in parentheses) of the distance between the ground-truth and the estimated value of the time series, measured in the plane *XY* (transversal/vertical) and in the space *XYZ*[3]. Related with the angles of rotation, the results represent the root mean square deviation of the respective time series. As shown, the convergence stage occurs very quickly, within the first set of frames, with the position of the deck being estimated within a margin of error significantly lower than 10 mm on the plane *XY* and lower than 20 mm on *XYZ*. As shown, the deviation of the longitudinal component is slightly higher than the others two components since this component is more difficult to estimate with affine cameras (high distance between the cameras and the monitoring zone).

Experiments with real imagery

The experimental tests were performed using a set of four targets and two cameras, with a resolution of 1920 x 1080 pixels, coupled to a 565 mm focal length lens (Figure 5). In the indoor test, the distance between the cameras and the targets was about 50 m and the height difference was about 2 m, whereas in the outdoor test the distance between the cameras and the targets was about 85 m and the height difference was about 10 m. The distance between the targets was about 300 mm in the transversal direction (*x*-direction), 125 mm in the vertical (*y*-direction) and 140 mm in the longitudinal (*z*-direction). Each target was made up by one near infrared LED, which radiates a high power concentrated beam (875 nm). Further, to reduce the daylight effect on the optical system, a near infrared pass-band optical filter was coupled to the camera's lenses. The targets were fixed in a grid, supported on a mobile mechanism built with gears, guide bars and worm gears (Figure 5), that allows two degrees of freedom (horizontal and vertical movement) – rotationless motion. The ground-truth data of

---

2 Assuming a sampling frequency of 20 Hz, this is equivalent to 30 minutes of motion.

3 Since the algorithm requires a set of frames to reach the state of convergence, the first 60 seconds were not considered in the deviation.

the structure's displacement was obtained by two displacement transducers (DT) with 200 mm range[4], installed nearby to the motion axes of the structure.

Table 1 – *deviation of the main motion parameters (standard deviation in parentheses)*

	translation	position of centre of rotation	position of bridge deck		rotation components
XY (mm)	7.3 (4.0)	2.0 (1.1)	6.5 (3.6)	ϕ (°)	0.30
XYZ (mm)	18.4 (10.9)	5.8 (5.3)	18.7 (11.6)	θ (°)	0.41
				ψ (°)	0.07
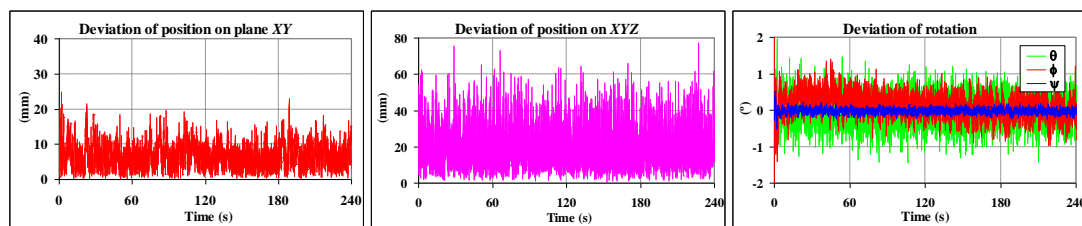
Figure 4 - *deviation of the main motion parameters as function of the time (number of frames) obtained considering a disturbance of 2 pixels (shown only the first minutes)*

Considering the cameras layout chosen for the tests, each target must radiate in the two opposite directions. To satisfy this requirement, we developed a solution with two LEDs, fixed to the structure using a support device, each one radiating in the direction of each camera, as shown on Figure 5; the distance between each LEDs pair was about 30 mm. The 3D position of all LED was measured at the LCAM (*Laboratório Central de Apoio Metrológico)* of the LNEC, using a 3D measurement device (DEA/Gamma 22.03). This operation allowed us to assess the out of parallelism and the orthogonality between the planes made up by the respective targets. The results obtained shown that, in the worst case, the out of parallelism was 2.41º and the orthogonality between the planes was 89.24º.

Figure 5 - *experimental test: (left) the camera C_1 mounted in the tripe; (centre) the targets structure and displacement transducers mounted in the platform; (right) detail of the LED support, where the target is represented by a pair of LEDs.*

Among others, the set of motions evaluated comprised the following type of motions: i) stationary; ii) transversal (*x*-direction); iii) vertical (*y*-direction); iv) transversal and vertical (diagonal); and v) transversal and vertical by steps. Considering that the bearings of the mobile mechanism has small gaps, particularly when the motion is inverted, to reduce a probable mismatch between the data provided by the DT and those estimated by the vision

---

4 The calibration of the transducers (including all measurement system) showed a non-linearity error smaller than 0.25 mm for the horizontal transducer and 0.1 mm for the vertical transducer.

system, it was decided to process each motion individually. Figures 6 and 7 show the results obtained on the indoor and on outdoor tests, respectively, for three types of motions. Likewise, Table 2 presents the mean deviation of the displacement estimated by the vision system, measured on the plane *XY* and on *XYZ*, for the several types of motions. The vision system calibration was carried out according the methodology described in [2, 3].
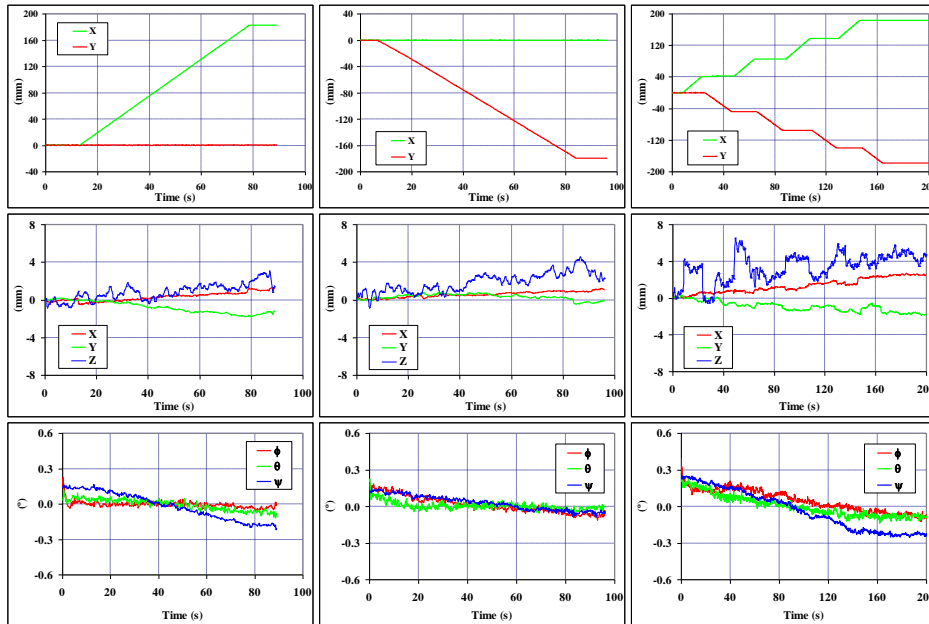
Figure 6 - *horizontal (**X**) and vertical (**Y**) reference displacements (top), measured with the displacement transducers, the respective displacement deviation (centre) and the rotation estimated by the vision system in the indoor environment*
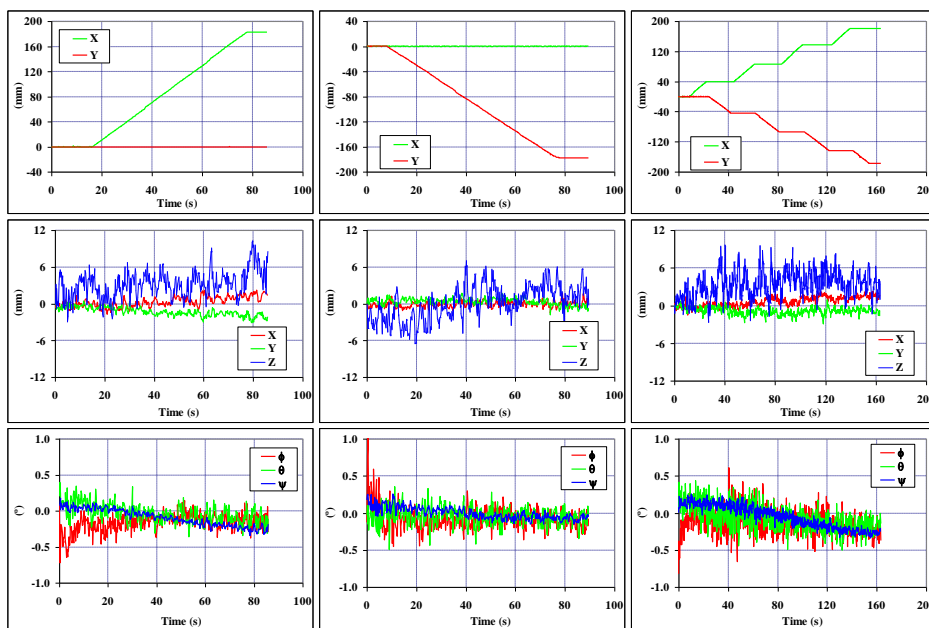
Figure 7 - *horizontal (**X**) and vertical (**Y**) reference displacements (top), measured with the displacement transducers, the respective displacement deviation (centre) and the rotation estimated by the vision system in the outdoor environment*

Table 2 - *mean deviation of position, measured on the plane **XY** and on **XYZ**, obtained in the indoor and in outdoor experimental tests*

	Indoor		Outdoor	
Method	XY (mm)	XYZ (mm)	XY (mm)	XYZ (mm)
still	0.45	0.80	1.11	3.03
transversal	0.94	1.42	1.54	3.77
vertical	0.71	2.05	0.72	2.49
diagonal	1.21	2.84	1.40	3.77
steps	1.66	3.82	1.28	3.81

The displacement measured by the vision system follows very closely the reference provided by the DT. Despite of that, as the structure moves from one side to the opposite side, a slightly drift comes out in the estimation of the displacement as well as of the rotation components. The explanation may be due to a misalignment between the coordinates system established by the DT and the coordinates system established by the vision system. The friction between the parts of the mobile mechanism may also cause a rotation of the structure, which was assumed to be null and, as a result, was not measured.

In general, the results obtained in outdoor are very similar with those obtained in indoor, showing, however, a high frequency disturbance as result of the wind effect and of the high sunshine focused in the direction of the cameras (the cameras as well as the targets were not protected). As a matter of fact, in the outdoor test the exposition time was largely reduced to avoid the saturation of the camera's sensor[5]. As a result, in this case, the disturbance effect becomes much stronger than in the indoor test. These sources of disturbance and an occasional air turbulence effect may also explain some of the ledges that appear in the signal.

4   Conclusions

The communication describes a recursive algorithm to estimate the full motion tracking of large structures, and in particular of long deck suspension bridges, having in mind its health monitoring. To fulfil this goal, a minimum of two cameras and three non-collinear points (targets) are required.

The assessment of the algorithm was performed through several tests carried out either by numerical simulation or with real imagery, using the aforementioned minimal requirements. At more than 500 m of distance between each camera and the targets, under two pixels of noise and a trajectory with high displacement and rotation amplitudes, the results obtained from the simulation shown, in the worst case, a deviation lower than 6.5 mm in the plane *XY* and lower than 18.7 mm in *XYZ*. Regarding the real experiments, performed in indoor and outdoor environment, with a distance between the camera and the targets of about 50 m and 85 m, respectively, the results shown a high accuracy with a global mean deviation lower than 1.7 mm in the plane *XY* and lower than 3.8 mm in *XYZ*. The results obtained in all tests shown a high accordance with the ground-truth values, which confirms the reliability and the robustness of the proposed algorithm. As a final conclusion, we may say that the algorithm is adequate to perform the motion tracking of large structures such as the long deck suspension bridges.

---

5 The outdoor test was performed after mid day, in a summer sunshine day, and under the influence of occasional wind.

As a final conclusion, one may say that the algorithm proposed is adequate to estimate the full motion tracking of large structures such as the long deck suspension bridges.

5 References

[1] A. Wahbeh, P. Caffrey and S. Masri, "*A Vision-based approach for the direct measurement of displacements in vibrating systems*", Smart Materials and Structures, Vol. 12, pp.785-794, 2003

[2] C. Santos, C. Costa and J. Batista, "*Calibration methodology of a vision system for measuring the displacements of long-deck suspension bridges*", Structural Control and Health Monitoring, Vol. 19, Num. 3, pp. 385-404, DOI: 10.1002/stc.438, 2011

[3] C. Santos, C. Costa and J. Batista, "*Long deck suspension bridge monitoring: the vision system calibration problem*", Strain, Vol. 48, Num. 2, pp. 108-123, DOI: 10.1111/j.1475-1305.2011.00803.x2011, 2011

[4] G. Young and R. Chellappa, "*3-D Motion estimation using a sequence of noisy stereo images: models, estimation, and uniqueness results*", IEEE Transactions on Pattern Analysis and Machine Intelligence, Vol. 12, Num. 8, pp. 735-759, 1990

[5] C. Tomasi and T. Kanade, "*Shape and motion from image streams under orthography: a factorization method*," International Journal of Computer Vision, Vol. 9, Num. 2, pp. 137-154, 1992

[6] R. Hartley and A. Zisserman, "*Multiple view geometry in computer vision*", Cambridge, University Press, 2nd Edition

[7] Y. Bar-Shalom and X. Li, "*Estimation and tracking: principles, techniques, and software*", Artech House, Inc. MA: Norwood, 1993

[8] T. Broida, S. Chandrashekhar and R. Chellappa, "*Recursive 3-D motion estimation from a monocular image sequence*", IEEE Transactions on Aerospace and Electronic Systems, Vol. 26, Num. 4, pp. 639-656, 1990

[9] P. Maybeck, "*Stochastic models, estimation and control*", Navtech Book & Software Store, VA: Arlington, 1994, Vol. 2, pp. 23-59

Fatigue crack propagation behaviour of a puddle iron under constant and variable amplitude loading

J.M.C. Maeiro[1], A.M.P. de Jesus[2], A.S. Ribeiro[2], A.L.L. Silva[3]

[1] ECT, University of Trás-os-Montes e Alto Douro, jmaeiro@gmail.com

[2] IDMEC/ECT, University of Trás-os-Montes e Alto Douro, ajesus@utad.pt;
aribeiro@utad.pt

[3] UCVE-IDMEC, Rua Roberto Frias, 4200-465Porto, Portugal; a.luis.l.silva@gmail.com

Abstract The main goal of this paper is to assess the fatigue crack propagation behavior of a material from an old riveted steel bridge, based on an experimental program of constant and variable amplitude fatigue tests. The material under consideration is a centenary puddle iron, for which information on fatigue crack propagation, under variable amplitude loads, is not available in literature. An experimental program was performed to characterize the fatigue crack propagation behavior of the material, using Compact Tension (CT) specimens under: i) constant amplitude loading, ii) constant amplitude loading with single overloads and iii) variable amplitude block loading. The derived constant amplitude data is compared with data available in literature for other bridge materials. Furthermore, a crack closure analysis was performed using strain gauges applied on the back face of CT specimens. Finally, the experimental results were used to assess the performance of several crack propagation models. The Paris model, with linear damage rule by Miner was considered. More advanced crack propagation models, proposed to model retardation effects of overloads were considered, such as the Wheeler and the modified Wheeler models. The Hudson and the modified Miner models were also assessed using variable amplitude data.

1 Introduction

The fatigue phenomenon has been assumed one of the most important causes of failure of machine parts, bridge members, aircraft components, among other structural details. Therefore, the undestanding of the fatigue phenomenon is of primordial importance to allow safe structural design. According to the American Society of Civil Engineers, fatigue is responsible for 80 to 90% of failures observed in metallic structures [1], leading to significant industrial production reductions, finantial losses and occasionally human injuries and fatalities. For this reason, fatigue and fracture should be conveniently accounted in the definition of appropriate reliability levels of structures.

The particular, the operational conditions of old metallic bridges makes the integrity assessment of these stuctures an imperative task. There is a special concern with respect to the riveted metallic bridges since the majority of these bridges were designed and placed into service at the end of XIX century/ begining of XX century. Due to economic restrictions, many of these bridges are still in operation. These bridges are very likely subjected to significant damage levels, mainly due to important increases in traffic intensity over the

operational years (gross vehicle weights and crossing frequencies), which may reduce significantly the safety levels of these bridges.

Onsite inspection programs have revealed significant fatigue cracking in the old riveted metallic bridges. Therefore, residual life studies may be supported on Fracture Mechanics principles. In the practice, there is a lack of experimental data concerning the fatigue behaviour of the materials from old riveted bridges. The available crack propagation data is very often limited to constant amplitude loading [2], which does not account for sequential effects that may occur due to varible amplitude loading. On effect, the available experimental crack propagation data concerning the old metallic materials is limited to the identification of the Paris's constants [3], which has been evaluated based on ASTM E647 procedures [4]. This data may, eventually, be considered limited taking into account the actual variable amplitude loading experienced by bridges.

The Paris's relation has been recognised the first fatigue one to adopt the stress intensity factor concept to correlate the fatigue crack growth rates. This relation was originally proposed for propagation regimes II and is assumed a constant amplitude fatigue crack propagation model. After the Paris proposition, many other researchers have proposed alternative crack propagation models, for both constant and variable amplitude loading. These models resulted from a better understanding of the physical phenomena related to the fatigue crack propagation both under constant and variable amplitude loading. Sequential effects may occur for specific loading histories, under variable amplitude loading, [5][6]. It is recognised that the application of an overload induces retardation effects on fatigue crack propagation due to crack closure phenomena [7][8]. There are several literature reviews available about fatigue crack propagation models. Skorupa [9][10] carried out a literature review about fatigue crack propagation behaviour of materials under variable amplitude loading. Latter on, Xiaoping *et al.* [11], Molent *et al.* [12] Haman *et al.* [13], Wang *et al.* [14], among others, have performed similair works, publishing review papers, including new models and validation studies.

This paper presents the results of an experimental program concerning the fatigue crack growth characterization of a puddle iron from an old Portuguese riveted metallic bridge - the Fão bridge. Fatigue crack growth experiments were performed on original material from the bridge for constant and variable amplitude loading. Fatigue crack growth rates were evaluated along the longitudinal and transverse directions of bridge members removed from the bridge, under constant load amplitude. In addition, variable amplitude loading tests were performed. Two types of fatigue spectra were appplied: i) contant amplitude loading with single overloads; ii) spectrum block loading. The generated data was used to assess constant and variable amplitude crack propagation models.

2   The Fão bridge

The Fão bridge is a riveted metallic road bridge that crosses the Cávado river at Esposende, in the northwest region of Portugal. This bridge was inaugurated on 7th August 1892. This bridge has a total length of 267 meters, composed of 8 spans of 33.5 meters each, supported on 7 masonry piers. The material used to build the bridge was puddle iron. Figure 1a gives a global overview of the bridge.

In 2007, the bridge was rehabilitated and some original side diagonals from the bridge (see Figure 1b were replaced. Specimens required for the experimental work proposed in this paper were extracted from the referred diagonals.
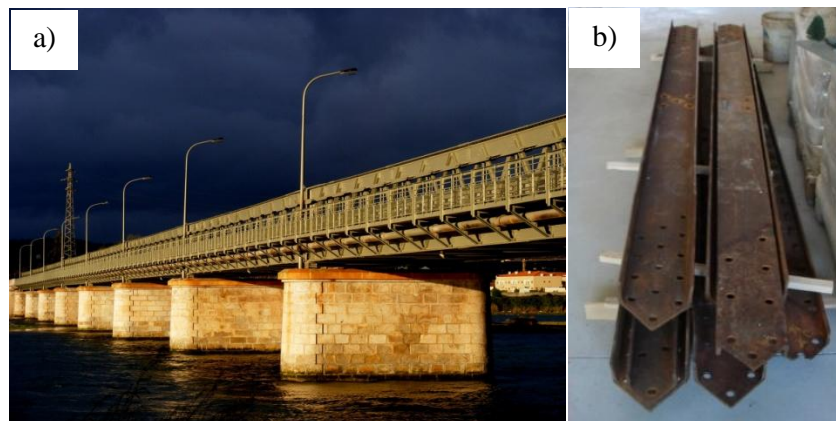
Figure 1 *– Riveted metallic Fão bridge: a) global overview of the Fão Bridge; b) original side diagonals removed from the bridge.*

3   Fatigue crack growth under constant amplitude loading

Fatigue crack growth tests were conducted according to the ASTM 647 standard [4] using the compact tension (CT) specimens (t=8 mm, W=50 mm) that were extracted from the original diagonals replaced in the Fão bridge. All tests were performed in air, at room temperature, under a sinusoidal waveform at a maximum frequency of 20 Hz. A total of 20 CT specimens were tested, namely 8 specimens along the transverse direction and 12 specimens along the longitudinal direction, covering the following stress R-Ratios: R_σ=0, R_σ=0.25, R_σ=0.50 and R_σ=0.75. Fatigue crack growth rates were measured using direct optical observations, through a travelling microscope. Crack growth was measured on both faces of the specimens and average crack size values were adopted in the fatigue crack growth computations. Figure 2 compares the fatigue crack growth rates between the longitudinal and transverse directions, for each stress R-Ratio. It is clear that the material from the Fão bridge shows significantly higher fatigue crack growth rates along the longitudinal direction than in transverse direction. This means an anisotropic crack propagation behaviour, the longitudinal direction showing the lowest fatigue crack propagation resistance. The experimental results were correlated using a power relation between the crack growth rate (da/dN) and the stress intensity factor range (ΔK), as proposed by Paris [30]:

$$\frac{da}{dN} = C\Delta K^m \tag{1}$$

where da/dN is the fatigue crack growth rate, ΔK represents the stress intensity factor range, C and m are material constants. Figure 2 also represents the Paris's law, resulted from linear regression analysis of $log(da/dN)$ vs. $log(\Delta K)$ data. The respective determination coefficient, R^2, is also shown. For some test series, a significant scatter is observed, which is justified by a high level of heterogeneities in the material. It is interesting to note that the slopes of the crack propagation curves are aproximately the same for each propagation direction. Figure 3 presents a comparison of the fatigue crack propagation rates given by the Paris's relation. It is clear an increase in the fatigue crack growth rates with the increase of the stress R-Ratio, R_σ, for each crack propagation direction. The effect of the stress ratio is slightly higher for cracks propagating along the longitudinal direction.

Figure 4a compares all longitudinal and transverse fatigue crack propagation data obtained for the Fão material. The higher fatigue crack propagation rates along the longitudinal direction is

again verified. The figure also includes the Paris correlations for all stress R-ratios combined together.
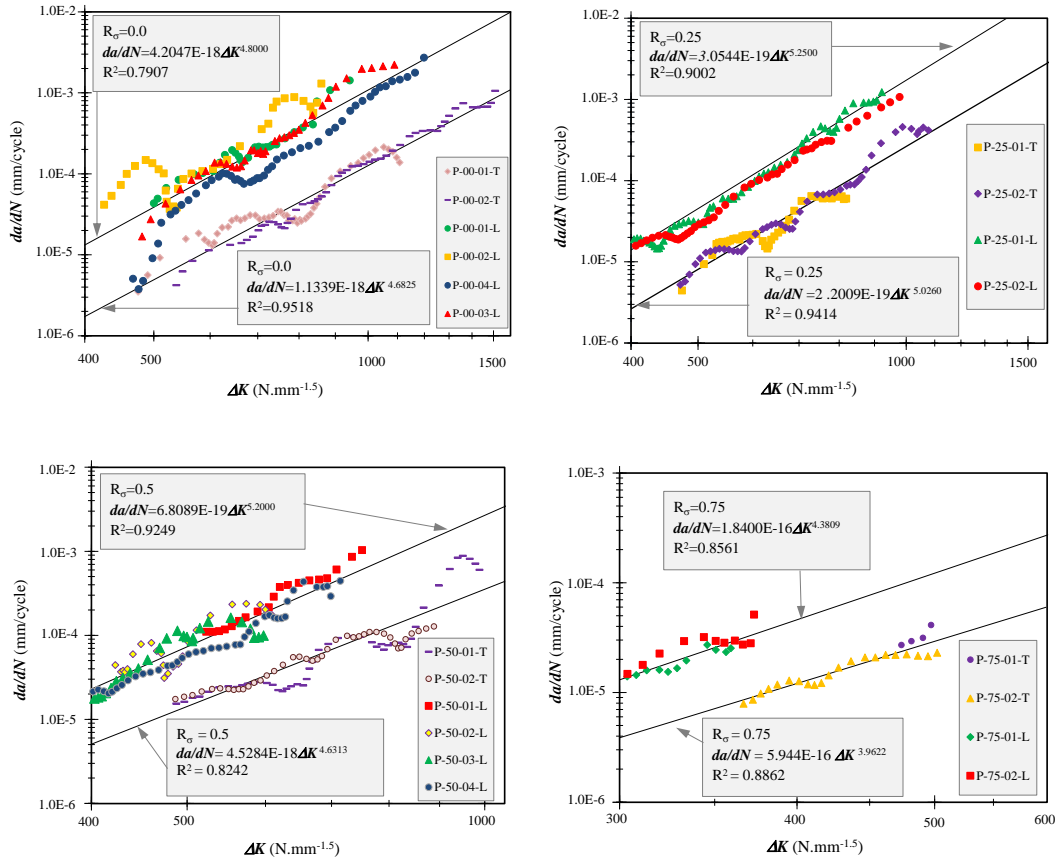

Figure 2 – *Comparison of fatigue crack growth rates for the material from Fão bridge between the transverse and longitudinal directions.*
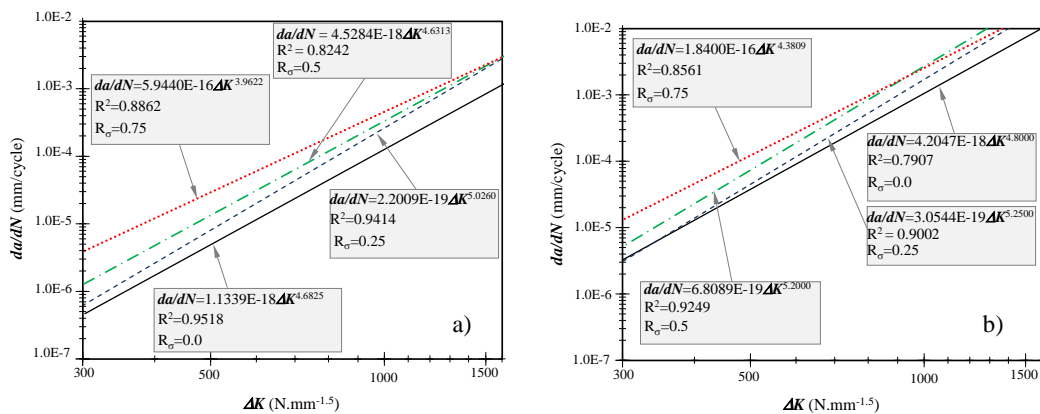
Figure 3 – *Paris correlations of the material from the Fão bridge: a) transverse direction; b) longitudinal direction.*
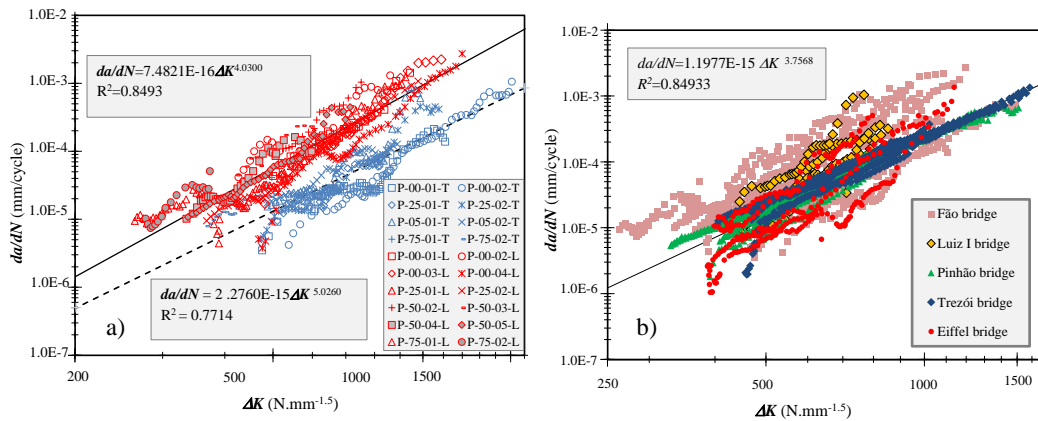
Figure 4 – *Comparison of fatigue crack propagation data: a) transverse vs. longitudinal directions; b) Fão material vs. other bridge materials.*
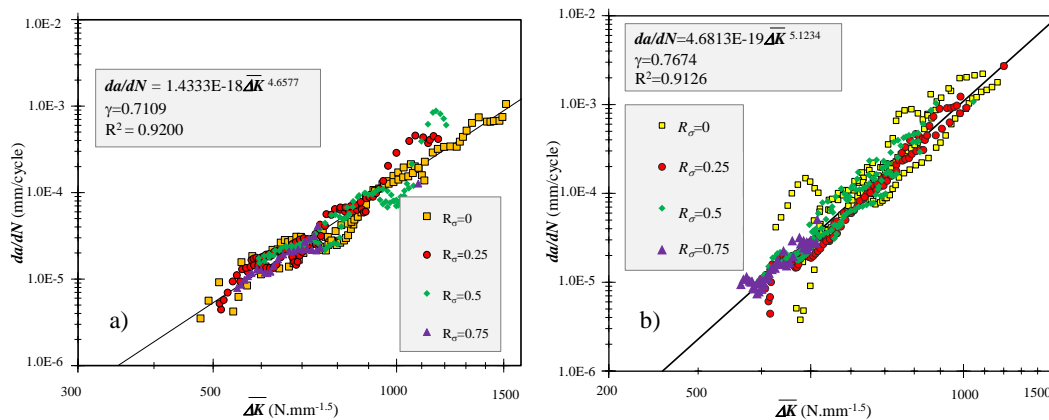
Figure 5 – *Walker correlations for fatigue crack propagation: a) transverse direction; b) longitudinal direction.*

Figure 4b compares the crack propagation data obtained for the Fão bridge with similar data obtained for other Portuguese ancient metallic bridges, namely the Trezói [2], Eiffel [15], Luiz I [16], and Pinhão bridges [17]. The data from the Fão bridge shows higher scatter than other bridge materials. This may be justified by the fact that data from the Fão bridge resulted from two distinct propagation directions – transverse and longitudinal directions, while data from other bridges corresponded to a single direction. Fatigue crack propagation rates obtained for the material from the Fão bridge show the highest values. Only materials from Luiz I brige approached these crack propagation rates. The material from Trezói and Pinhão bridges showed the lowest scatter. The slope of the proposed global Paris relation, m=3.76, is higher than the underlying value of modern design codes (m=3).

Since the Paris's law does not account for stress ratio efects, alternative models have been proposed in literature to overcome this limitation. The Walker proposition is one of the most simpler alternatives to the Paris's law to model stress ratio effects. The Walker's model consists on replacing in the Paris's model, the stress intensity range by an effective stress range, given by [5]:

$$\frac{da}{dN} = C\left[\frac{\Delta K}{(1-R_\sigma)^{1-\gamma}}\right]^m = C\overline{\Delta K}^m \tag{2}$$

where C, m and γ are constants. Figure 5 presents the fatigue crack propagation data correlated with the Walker's equation for the material from the Fão bridge with cracks propagating along the transverse (Figure 5a) and longitudinal (Figure 5b) directions. A significant increase in the determination coefficients, R^2, is verified by a direct comparison of Figures 5 and 4a.

Four extra CT specimens were instrumented with electrical strain gauges (CEA-06-250UW-350/ Micro-Measurements) glued at the back face of the specimens in order to allow a crack closure assessment [4]. The crack closure may be induced by compressive residual stresses [18], surface roughness or plasticity induced closure. Each specimen was tested under constant amplitude loading, along the transverse direction, for distinct stress R-ratios (R_σ=0.0, 0.25, 0.50 and 0.75). The crack opening loads were evaluated for distinct crack sizes. The opening loads were evaluated through the analysis of the load-strain graphs. These loads corresponded to the inflection points verified in the load-strain data. An approximately linear correlation between the opening load and the crack size was verified. The effective stress intensity factor range was computed excluding the load incursions bellow the opening loads. Figures 6a and 6b present the correlation of the fatigue crack propagation data with the Paris law, using the applied stress intensity factor range and the effective stress intensity factor range, respectively. A very significant scatter is observed in the experimental data. The correlation of the experimental data using the effective stress intensity factor range results in a higher determination coefficient. However, the increase of the determination coefficient is not very significant.
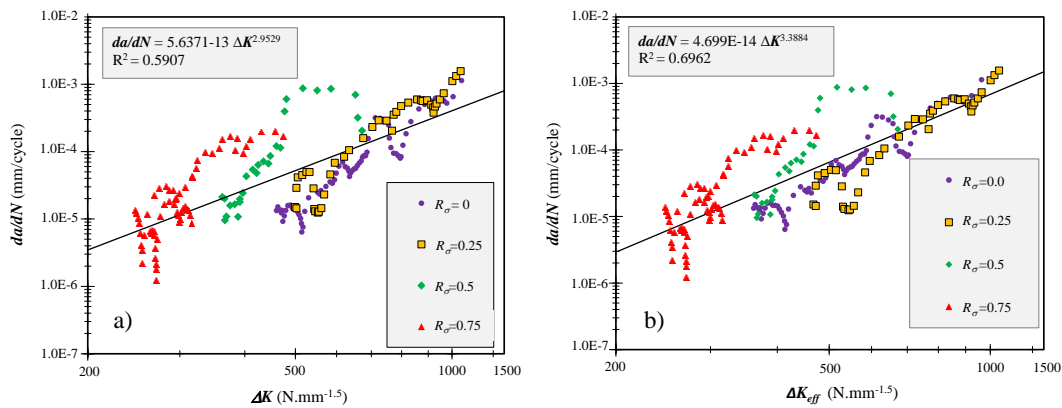
Figure 6 – *Constant amplitude crack propagation data for the transverse direction: a) correlated with applied stress intensity factor range; b) correlated with the effective stress intensity factor range.*

4   Fatigue crack growth under constant amplitude loading with single overload

4.1   Theoretical models

The Paris's law is primarily concerned with fatigue crack propagation under constant amplitude loading. However, actual loading acting on bridges is essentially of variable amplitude nature. The Paris's law is often used to assess variable amplitude loading supported by a damage rule, such as the Miner's linear rule [19]. This approach may produce

satisfactory results for random loading. However, it does not account the fatigue crack growth behavior for some specific loading conditions, such as overloads. Several models have been proposed to consider overload effects on crack growth. Wheeler [20] proposed a model that account for the retardation effects after an overload through the following equation:

$$\frac{da}{dN} = \phi_R . C(\Delta K)^m \qquad (3)$$

where ϕ_R is a retardation parameter. However, more recent studies have proved that crack growth acceleration may occur right after the overload application. Yuen and Taheri [21] added one more correction to the Wheeler model, resulting the following equation:

$$\frac{da}{dN} = \phi_R . \phi_D . C(\Delta K_{acc})^m \qquad (4)$$

where ϕ_R and ϕ_D are two parameters introduced to model the retardation and delayed-retardation growth, respectively; C and m are identical to the parameters used in the Paris's law (Eq. (1)); ΔK_{acc} is the so-called accelerated stress intensity factor range that will be defined. For stable crack growth, $\phi_R=1$, $\phi_D=1$, and $\Delta K_{acc} =\Delta K$. The retardation correction factor ϕ_R is defined by:

$$\begin{cases} \phi_R = \left[\dfrac{r_{p,k}}{a_{OL} + r_{p,OL} - a_k}\right]^n \\ if \quad a_k + r_{p,k} < a_{OL} + r_{p,OL} \end{cases} \quad or \quad \begin{cases} \phi_R = 1 \\ if \quad a_{OL} + r_{p,OL} \le a_k + r_{p,k} \end{cases} \qquad (5)$$

where a_k is the current crack length; $r_{p,k}$ is the size of plastic zone created by the post overload constant amplitude loading at a crack length of a_k; n is an adjustable experiment-based shaping exponent; a_{OL} denotes the crack length at which a single tensile overload is applied or a higher loading amplitude is switched to a lower amplitude; $r_{p,OL}$ denotes the size of the plastic zone created by the single tensile overload or the higher loading amplitude in step loading at the crack length of a_{OL} [14]. The size of the plastic zones may be estimated using the following approach:

$$r_{p,k} = \alpha . \left(\frac{\Delta K_k}{2\sigma_y}\right)^2 \quad or \quad r_{p,OL} = \alpha . \left(\frac{K_{OL}}{\sigma_y}\right)^2 \qquad (6)$$

where σ_y is the yield stress of the material, ΔK_k is the stress intensity factor range at the current crack length a_k and α is the effective plastic zone size constant. If the plane stress condition is postulated, Irwin [22] states that $\alpha=1/\pi\cong0.32$. For plane strain conditions r_p may be 1/3 of the corresponding value for plane stress conditions ($\alpha=1/3\pi\cong0.11$). This constant may be experimentally established in order to correlate the total retardation crack length, which is the distance over which the retarded crack propagates before the constant amplitude crack growth rate resumes. The K_{OL} parameter in Eq. (6) is defined as follows: for the constant amplitude loading with a single tensile overload, it corresponds to the maximum value of the overload stress intensity factor, while for the two step high-low loading sequence, K_{OL} is the maximum stress intensity factor of the preceding higher loading step.

The delayed-retardation parameter ϕ_D is defined as:

$$\begin{cases} \phi_D = \left[\dfrac{a_{OL} + r_{D,OL} - a_k}{r_{D,k}} \right]^q \\ if \quad a_k + r_{D,k} < a_{OL} + r_{D,OL} \end{cases} \quad or \quad \begin{cases} \phi_D = 1 \\ if \quad a_{OL} + r_{D,OL} \le a_k + r_{D,k} \end{cases} \tag{7}$$

where q is an additional shaping parameter; $r_{D,k}$ is the current effective delayed zone size determined by the first formula in Eq. (6), replacing $r_{p,k}$ by $r_{D,k}$; $r_{D,OL}$ denotes the size of the effective delayed zone size, which is related to $r_{p,OL}$ by:

$$r_{D,OL} = \xi \cdot r_{p,OL} \tag{8}$$

where ξ is an experimentally based fitting constant. The accelerated stress intensity factor range ΔK_{acc} is defined as:

$$\begin{cases} \Delta K_{acc} = \Delta K_k + \\ (\Delta K_{OL} - \Delta K_k) \cdot \left(1 - \dfrac{r_{D,k}}{a_{OL} + r_{D,OL} - a_k} \right)^q \\ if \quad a_k + r_{D,k} < a_{OL} + r_{D,OL} \end{cases} \quad or \quad \begin{cases} \Delta K_{acc} = \Delta K_k \\ if \quad a_{OL} + r_{D,OL} \le a_k + r_{D,k} \end{cases} \tag{9}$$

The stress intensity factor range ΔK_{OL} is set to be $K_{OL} - K_{min}$ for the overloading condition where K_{min} corresponds to the minimum load of the constant amplitude loading. For a high-low block loading sequence, ΔK_{OL} is set to be the stress intensity factor range ΔK_H of the preceding higher loading step.

Comparing with the Paris's model, the modified Wheeler model defined in Eq. (4) proposes three additional constants, namely n, q and ξ. These constants must be determined from overloading crack growth experiments. The value of n may be estimated by best fitting experimental data in the gradual return to steady state rate behaviour. The value of ξ may be determined by fitting the size of delayed zone; q may be estimated by best fitting the crack growth rate in the delayed zone. The extension of the return to steady state regime is also used to assess the α constant in Eq. (6). Constants C and m were adjusted considering the steady state fatigue crack propagation for each specimen.

4.2 Experimental results

CT specimens were subjected to simple overloads to allow the identification of the constants of the Wheeler model and modified Wheeler model. A total of three specimens were tested under null stress R-Ratio, with cracks propagating along the longitudinal direction. The test load was adjusted to result an initial stress intensity factor range, $\Delta K_i = 14$ MPa.m$^{0.5}$. The single overload was applied when crack propagates 5 mm from the CT notch root, which means $a_{OL} = 5 + 10 = 15$ mm. The ΔK_{OL} was set equal to $1.5 \Delta K_i$.

Figure 7 illustrates the experimental fatigue crack growth data obtained for three specimens. It is possible to verify some irregularity (instability) in the material response, but the effects of the overloads are clearly visible in the graph. The irregularity in the experimental response is due to the heterogeneities in the material, such as slag inclusions. Those heterogeneities may function as obstacles to the crack propagation, producing instabilities in fatigue crack propagation. The crack propagation acceleration right after the overload is not visible in the material response. Only the delay retardation and the gradual return to steady state rate behavior is observed. Using a trial and error procedure, constants of

the Wheeler and modified Wheeler models were identified for each specimen. Figure 7 compares the response of the modified Wheeler model with the experimental fatigue crack propagation data. Satisfactory agreement between the experimental data and the modified Wheeler's model prediction is observed. For the metallic material of the Fão Bridge under consideration, the yield stress adopted was the monotonic yield stress of the material, $\sigma_y = 220$ MPa [23]. Table 1 summarizes the constants of the modified Wheeler model. The original Wheeler model was also used to correlate the fatigue propagation data and was verified that this model is able to produce similar satisfactory correlation of the experimental data as obtained with the modified Wheeler model. Table 1 also includes the constants of the Wheeler model. Figure 7 also shows the superposition of the fatigue crack propagation data from the three specimens. A significant scatter was observed in the experimental data, which difficult the calibration of the Wheeler and modified Wheeler models. Nevertheless, an attempt was made, leading to the prediction also included in Figure 7. Both original and modified Wheeler models produced very similar results. The use of a more advanced crack propagation model did not result in noticeable improvements in the predictions. On effect, the modified Wheeler model allows the prediction of the immediate crack acceleration and a better control of the delay retardation after the overload. However, the puddle iron did not exhibit the crack acceleration rate after the overload and a very high scatter masked the delay retardation phenomena. Therefore, the use of the modified Wheeler model is not justifiable for this puddle iron.
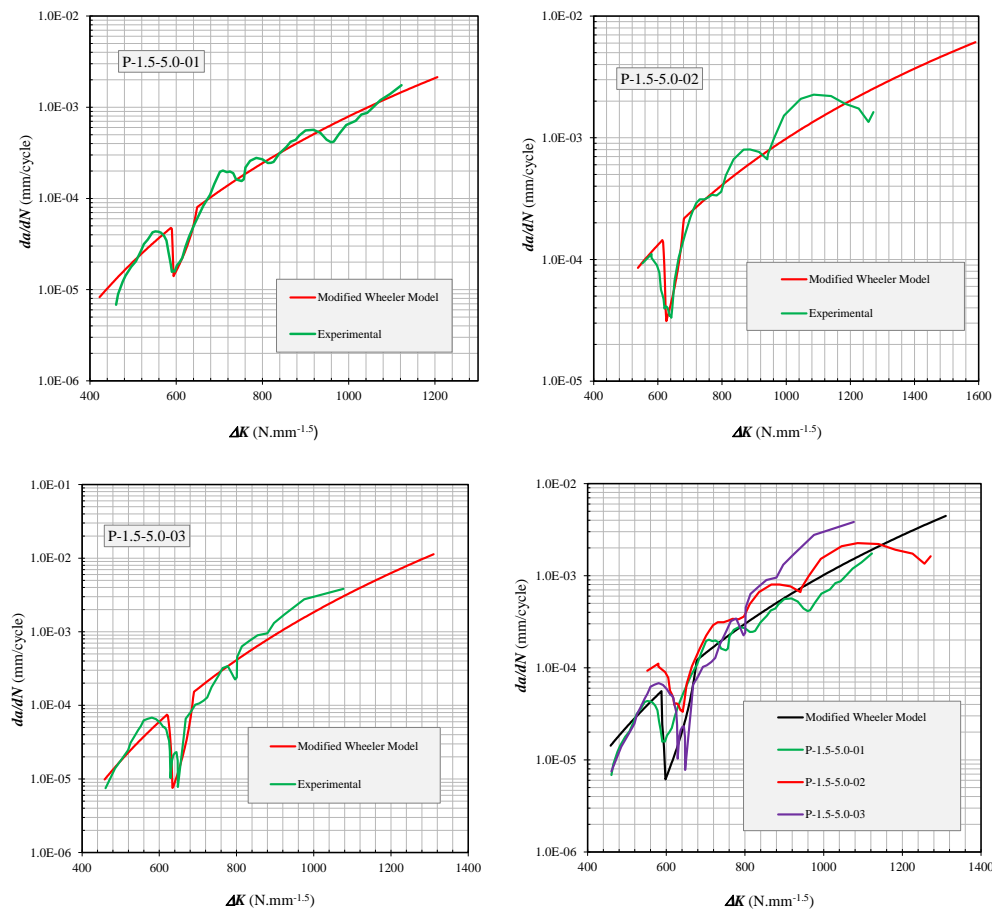
Figure 7 – *Correlation of overloading fatigue crack propagation data with the modified Wheeler model.*

Table 1 – Wheeler and modified Wheeler model constants.

Specimens	Model	n	α	q	ξ	C*	m
P-1.5-5.0-01	Wheeler	0.60	0.10	-	-	1.02E-19	5.30
P-1.5-5.0-02		0.70	0.10	-	-	1.58E-15	3.94
P-1.5-5.0-03		1.1	0.10	-	-	1.37E-23	6.71
All data		1.00	0.16	-	-	6.07E-20	5.41
P-1.5-5.0-01	Modified Wheeler	0.60	0.10	1.00	0.17	1.02E-19	5.30
P-1.5-5.0-02		0.80	0.10	1.00	0.24	1.58E-15	3.94
P-1.5-5.0-03		1.25	0.10	1.00	0.28	1.37E-23	6.71
All data		1.00	0.15	1.00	0.19	3.98E-15	5.47

da/dN in mm/cycle and ΔK in N.mm$^{-1.5}$

5   Fatigue crack growth under constant variable amplitude loading

The experimental program also included fatigue crack propagation tests of CT specimens under variable amplitude loading. Two types of loading spectra were considered in this study. One load spectrum consisted on a random spectrum defined by the repetition of a block of variable amplitude loading. The block is composed by 100 individual load cycles with null stress ratio and the maximum load of the cycle defined in a random manner, but limited to 7.044 KN, which corresponds to K=17 MPa.m$^{0.5}$ for a=10 mm (start of crack propagation in the CT specimens). Figure 8 represents the block loading, by load-time history graphs and load histograms. Another variable amplitude loading was defined based on an assumed load histogram considered typical for bridges, as illustrated in Figure 9a, with a shape factor, ν=4.0 [24]. The block was defined assuming a total of 250 individual cycles with null stress ratio and a maximum load limited to 17 MPa.m$^{0.5}$, for a=10 mm (see Figure 9b) .

Two CT specimens were tested with the random block loading (P-R-01 and P-R-02); three specimens were tested with the block spectrum typical of bridges (CT-H-P-01; CT-H-P-02; CT-H-P-03). Figure 10 presents the experimental fatigue crack propagation data. This data was evaluated for cracks propagating along the longitudinal direction. Figure 10a shows the results of the two specimens tested under random block loading; Figure 10b shows the results of the three specimens tested under spectrum block typical of bridges.
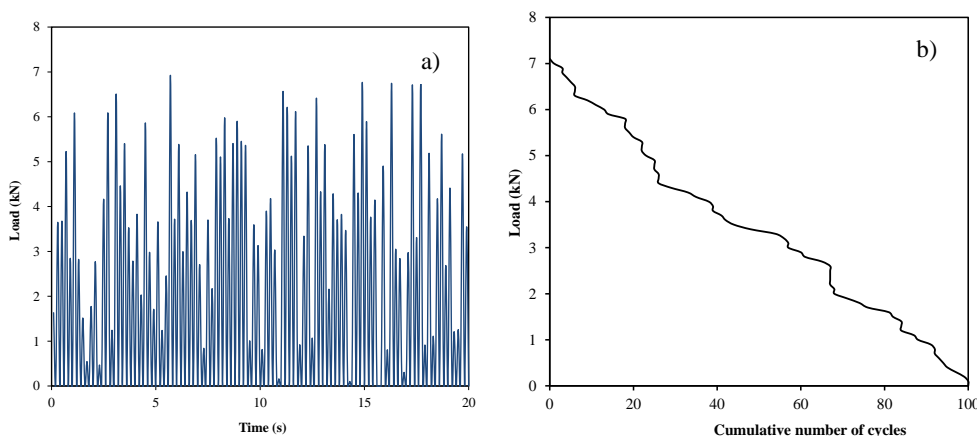
Figure 8 – Definition of the random block loading: a) load-time history definition; b) load histogram.
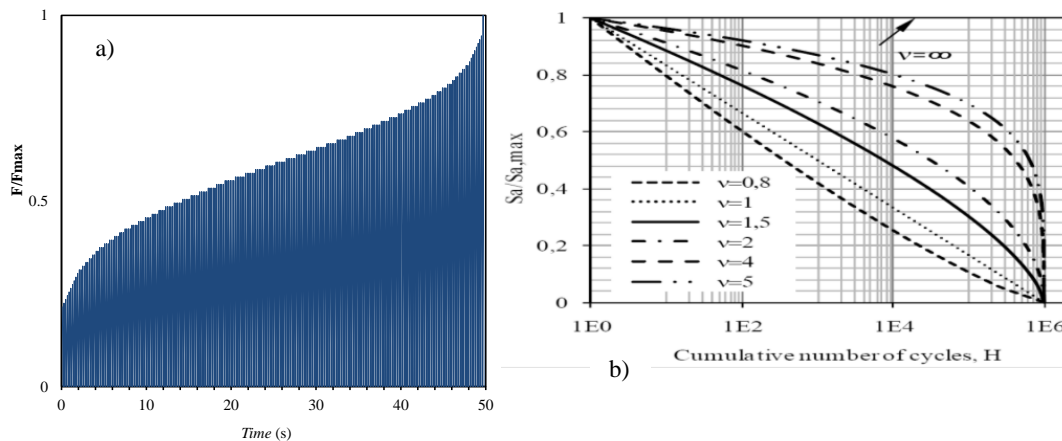
***Figure 9** – Definition of variable amplitude block loading typical of bridge loading: a) load-time history definition; b) load histogram.*
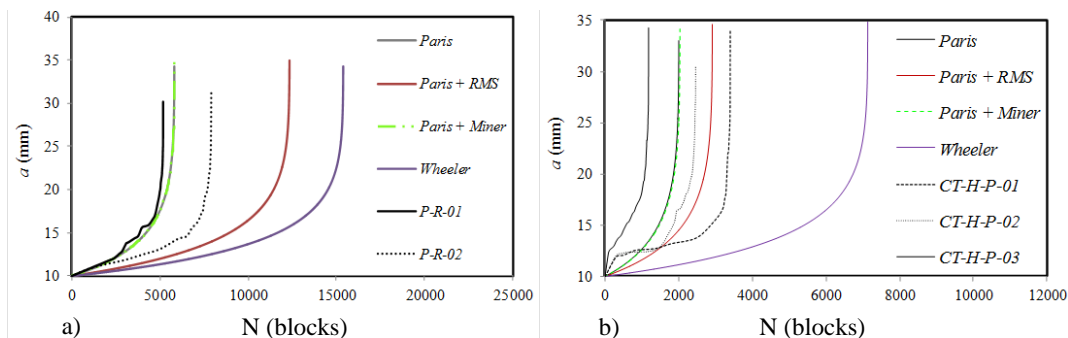
***Figure 10**– Fatigue crack propagation predictions: a) random loading; b) typical bridge histogram.*

Models for fatigue crack propagation prediction were used to estimate the propagation curves for the variable amplitude loading. The Paris's model was used to simulate the fatigue crack propagation, using a cycle-by-cycle integration. Also, the Paris model with the root mean square values of the stress intensity factor ranges, ΔK_{RMS}, was used, as proposed by Hudson [25]. The Paris model was also applied using an equilavent stress intensity factor range defined using the Miner relation. Finnaly, the original Wheeler model was used to simulate the crack propagation, using a cycle-by-cycle integration procedure (see reference [26] for details). The modified Wheeler model was not used for this purpose, since this model produces results similar to the original Wheeler model. Figure 10 presents the predictions to allow a direct comparison with the experimental data. The analysis of the results allows the following observations: i) the Paris model and the Paris model with equivalent stress intensity factor ranges produced always the same predictions; ii) the Paris model produced satisfatory results for both types of variable amplitude loading – the predictions are within the experimental data variation range; iii) the Wheeler model always overstimated the fatigue lives; iv) the Paris model with the RSM ΔK values produced also satisfatory predictions for variable amplitude block loading based on bridge load spectrum.

6   Conclusions

Experimental fatigue crack growth data was derived for the puddle iron from the road Fão bridge under constant amplitude loading covering several stress R-Ratios. The Paris's equation was used to correlate the experimental data. Furthermore, the Walker's equation was used to improve the description of the stress R-ratio effects.

The constant amplitude fatigue crack growth rates of the material from the Fão bridge was compared with similar data of other bridge materials. Higher fatigue crack growth rates were observed for the material from this study.

The fatigue crack growth behaviour was also characterized for single overloads. A crack growth retardation was verified right after the overload followed by gradual return to steady state. A modified version of the Wheeler model proposed by Yuen and Taheri was used to fit the experimental data. A good adjustment was verified for each individual test data. The modified Wheeler model did not resulted in improved description of the material behaviou since the puddle iron did not showed crack growth acceleration after the overload. Also the signicant experimental scatter makes the use of the modified Wheeler model not justifiable with respect to the original Wheeler model.

The scatter is a markedly characteristic of the puddle iron investigated in this study, which is justified by the high level of heterogeneities. This characteristic difficult the assessment of the crack propagation behaviour under variable amplitude loading, since the effects of materials heterogeneities may mask the load sequential effects.

Variable amplitude block loading was tested. The resulting crack growth rates were used to assess alternative models, such the Paris model with the Miners rule and the Wheeler model. It was verified a superior performance of the Paris model. The Wheeler model resulted always in crack growth overpredictions.

References

[1] M.S. Cheung, W.C. Li, *"Probabilistic fatigue and fracture analyses of steel bridges"*, Structural Safety, Vol. 23, pp. 245–262, 2003.

[2] J.A.F.O. Correia, A.M.P. Jesus, M.A.V. Figueiredo, A.S. Ribeiro, A.A. Fernandes, *"Variability analysis of fatigue crack growth rates of materials from ancient Portuguese steel bridges"*, Proceedings of the Fourth International Conference on Bridge Maintenance, Safety and Management, Seoul, Korea, pp. 1249-1301, 2008.

[3] P.C. Paris, F. Erdogan, *"A critical analysis of crack propagation laws"*, Transactions of The ASME. Series E: Journal of Basic Engineering, Vol. 85, pp. 528-534, 1963.

[4] ASTM E647, "Standard Test Method for Measurement of Fatigue Crack Growth Rates", ASTM Standard, American Society for Testing and Materials, 1999.

[5] N.E. Dowling, *"Mechanical Behaviour of Materials – Engineering Methods for Deformation, Fracture and Fatigue"*, Second Edition, Prentice Hall, New Jersey, USA, 1998.

[6] L. Borrego, *"Propagação de fendas de fadiga a amplitude de carga variável em Ligas de Alumínio AlMgSi"*, Tese de Doutoramento, FCTUC, Portugal, 2001.

[7] W. Elber, "*Fatigue crack closure under cyclic tension*", Engineering Fracture Mechanics, Vol. 2, pp. 37-45, 1970.

[8] W. Elber, "*The significance of fatigue crack closure*", In: Damage Tolerance in Aircraft Structures, ASTM STP 486, American Society for Testing and Materials, pp. 230-242, 1971.

[9] M. Skorupa, "*Load interaction effects during fatigue crack growth under variable amplitude loading – a literature review. Part I: empirical trends*", Fatigue & Fracture of Engineering Materials & Structures, Vol. 21, pp. 987-1006, 1998.

[10] M. Skorupa, "*Load interaction effects during fatigue crack growth under variable amplitude loading – a literature review. Part II: qualitative interpretation*", Fatigue & Fracture of Engineering Materials & Structures, Vol. 22, pp. 905-926, 1999.

[11] H. Xiaoping, T. Moan, C. Weicheng, "*An engineering model of fatigue crack growth under variable amplitude loading*", International Journal of Fatigue, Vol. 30, pp. 2–10, 2008.

[12] L. Molent, M. McDonald, S. Barter, R. Jones, "*Evaluation of spectrum fatigue crack growth using variable amplitude data*", International Journal of Fatigue, Vol. 30, pp. 119–137, 2008.

[13] R. Haman, S. Pommier, F. Bumbieler, "Variable amplitude fatigue crack growth, experimental results and modeling", International Journal of Fatigue, Vol. 29, Num. 9-11, pp. 1634–1646, 2007.

[14] X. Wang, Z. Gao, T. Zhao, Y. Jiang, "*An experimental study of the crack growth behaviour of 16MnR pressure vessel steel*", Journal of Pressure Vessel Technology, Vol. 131, pp. 021402-9, 2009.

[15] J.A.F.O. Correia, A.M.P. de Jesus, M.A.V. Figueiredo, A.S. Ribeiro, A.A. Fernandes, "Fatigue assessment of riveted ralway bridges connections. Part 1: Experimental investigations", Steel Bridges Advanced Solution & Technologies, 7th International Conference on Steel Bridges, vol. II, pp. 329-338, 2006.

[16] A.A. Fernandes, P.T. Castro, M. Figueiredo, F. Oliveira, "*Structural integrity evaluation of highway riveted bridges*", Proceedings of the 2nd International Conference on Bridge Maintenance, Safety and Management, Kyoto, Japan, 2004.

[17] A.M.P. de Jesus, M.A.V. Figueiredo, A.S. Ribeiro, P.M.S.T. de Castro, A.A. Fernandes, "*Residual Lifetime Assessment of an Ancient Riveted Steel Road Bridge*", Strain, Vol. 47, pp. e402–e415, 2011.

[18] M. Beghini, L. Bertini, "*Fatigue crack propagation through residual stress fields with closure phenomena*", Engineering Fracture Mechanics, Vol.36, Num. 3, pp.379-387, 1990.

[19] M.A. Miner, "*Cumulative Damage in Fatigue*", ASME Journal of Applied Mechanics, Vol. 67, pp. A159–A164, 1945.

[20] O.E. Wheeler, "*Spectrum Loading and Crack Growth*", ASME Journal of Basic Engineering, Vol. 94, pp. 181–186, 1972.

[21] B.K.C. Yuen, F. Taheri, "*Proposed modifications to the Wheeler retardation model for multiple overloading fatigue life prediction*", International Journal of Fatigue, Vol. 28, pp. 1803–1819, 2006.

[22] G.R. Irwin, "*Analysis of Stresses and Strains Near the End of a Crack Tip Traversing a Plate*", ASME Journal of Applied Mechanics, Vol. E24, pp. 361–364, 1957.

[23] A.M.P. de Jesus, A.L. Silva, J.F. Silva, J.M. Maeiro, P.L.B. Silva, "*Caracterização à fadiga do material da ponte metálica rodoviária de Fão*", P.J.S. Cruz, T. Mendonça, L.C. Neves and L.O. Santos (eds.), Proceedings of 1st Portuguese Conference on Safety and Rehabilitation of Bridges, Lisboa, Portugal, pp. (III)175-182, 2009.

[24] J.D. Costa, J.A.M. Ferreira, L.P. Borrego, "*Influence of spectrum loading on fatigue resistance of AA6082 friction stir welds*", International Journal of Structural Integrity, Vol. 2, Num. 2, pp.122 – 134, 2011.

[25] S.M. Beden, S. Abdullah, A.K. Ariffin, "*Review of Fatigue Crack Propagation Models for Metallic Components*", European Journal of Scientific Research, Vol. 28, pp. 364-397, 2009.

[26] J.M.C. Maeiro, "Caracterização das Taxas de Propagação de Fendas de Fadiga do Material da Ponte Metálica Rebitada de Fão Sob Acção de Solicitações de Amplitude Constante e Variáveis", MSc. Thesis, University of Trás-os-Montes and Alto Douro, Vila Real, 2011.

A contribution to the characterization of the mechanical behavior of S355NL structural steel

C. Thies[1,3], C. Albuquerque[2], S. M. O. Tavares[2], V. Richter-Trummer[1], M. A. V. Figueiredo[1], P. M. S. T. de Castro[1]

[1] *Bauhaus-Universität Weimar, Germany; ERASMUS exchange student at 3*

[2] *Depart. of Civil Engineering, Faculdade de Engenharia da Univ. do Porto, Portugal*

[3] *Department of Mech. Engineering, Faculdade de Engenharia da Univ. do Porto, Portugal*

Abstract The present work is a contribution to the characterization of the mechanical behavior of a commonly used structural steel, S355NL, through fatigue crack growth rate and toughness measurements performed on 32mm thick C(T) specimens.

Further to a full characterization of the Paris law regime, the near threshold stress intensity factor range was experimentally measured for the load ratios R = 0.1 and R = 0.7, and crack closure measurements were made in order to explain the different values found for both load ratios. Flat surface and side grooved C(T) specimens were used for fracture toughness determination. Substantial stable ductile crack growth was observed, particularly in the non-grooved specimen as expected. The maximum load J_0 value was taken as elasto-plastic toughness measurement, and a very substantial drop in fracture toughness was observed for the grooved specimens. In order to explain the fracture toughness differences between flat surface and grooved specimens, a 3D finite element analysis of both types of specimens was performed using the software ABAQUS and the modified virtual crack closure technique (mVCCT). The finite element analyses indicate a strong increase in degree of plane strain for the grooved specimens.

1 Introduction

This paper extends the mechanical characterization of the S355NL steel used for the composite railway bridge in Álcacer do Sal, Portugal, presented in [1]. The new data presented includes near threshold fatigue crack growth rates for two different R ratios, and fracture toughness measurements carried out on specimens with and without side grooves. Finite element analyses of those specimens are presented, in order to discuss the fracture toughness behavior found.

Although SN approaches are commonly used for the design of welded steel structures, *e.g.*, Eurocode 3, [2], Fracture Mechanics methodologies taking into account the behaviour of existing or assumed cracks may be used for finer fatigue analyses particularly for fitness for purpose assessment. These are based on the concept of stress intensity factor K, and typically relate fatigue crack growth (FCG) rate da/dN with stress intensity factor range ΔK, [3,4]. One input for those analyses is the characterization of the material's FCG according to the ASTM standard E647, [5].

The threshold stress intensity factor range (ΔK_{th}) indicates the cyclic loading under which the crack will not grow. The threshold value ΔK_{th} is the asymptotic ΔK at which da/dN approaches zero. Published fitness for purpose criteria for steel structures, as BS 7910:2005,

[6], give suggested values of ΔK_{th}; however, these represent conservative lower bounds for a variety of structural steels, and it is desirable to know through testing the actual performance of a steel of interest.

At the service temperatures of bridges in Portugal, S355NL steel is very ductile, and the measurement of its fracture toughness requires elastic plastic criteria and tests. Flat surface fracture toughness specimens such as the compact tension (C(T)) are expected to lead to very high toughness values. However, toughness decreases with increasing degree of plane strain, implying that effects of constraint should be analyzed, since flat surface specimens may be unrepresentative of the real constraint conditions found in particular structural details. It is therefore of interest to study the influence of side grooves, since they represent a ready method to vary crack tip constraint. A variety of procedures are available for performing these tests, including ASTM E1820, [7], BS 7448, [8], and the EFAM procedure described in [9].

The finite element method provides a means to model the behavior of the fracture specimen, and among many different modeling approaches available the modified virtual crack closure technique (mVCCT), [10], gives quick and accurate evaluations of stress intensity factor and of the near crack tip stress field so that the degree of plane strain can be obtained as a function of side grooves' depth.

2 Fatigue crack growth tests

A servo-hydraulic MTS machine of 100kN capacity was used for the initial stage of the preparation of fracture mechanics specimen (pre-cracking), and for fatigue crack growth testing. For toughness tests, given the higher loads expected, a servo-hydraulic MTS machine of 250kN capacity was used. The measurement of crack length was made using travelling microscopes, one on each side of the specimen, mounted on rail-slides including digital linear rulers.

The C(T) specimen is one of several specimens which are used for analyzing crack propagation, both for fatigue crack growth studies, [5], as well as for fracture toughness, [6-8]. The geometry of the C(T) specimens used is shown in Figure 1. For toughness measurements grooved and non-grooved specimens were used. 90° grooves on the cracking plane were obtained using a milling machine, Figure 2. The basic properties of S355NL are listed in [11].

Pre-cracking provides a sharpened fatigue crack of adequate size and straightness which ensures that the effect of the machined starter notch is removed from the specimen K calibration, and the effects on subsequent crack growth rate data caused by changing crack front shape or pre-crack load history are eliminated. Several recommendations are listed to calculate the maximum load for creating pre-cracks. ASTM E647 [5] indicates that precrack shall not be less than 0.1B (thickness), the final K_{max} during pre-cracking shall not exceed the initial K_{max} of the actual test, and the reduction in P_{max} for any step should be not greater than 20 %.

The EFAM GTP 02 guidelines for creating pre-cracks in compact specimens intended for fracture toughness measurement state that $0.45 < a/W < 0.65$ [8], and specifies the loading to achieve the pre-crack and its minimum dimensions.

The initial load regimes of precracking influence the determination of threshold values. Due to this fact it is advisable to reach the lowest load level as possible during precracking.
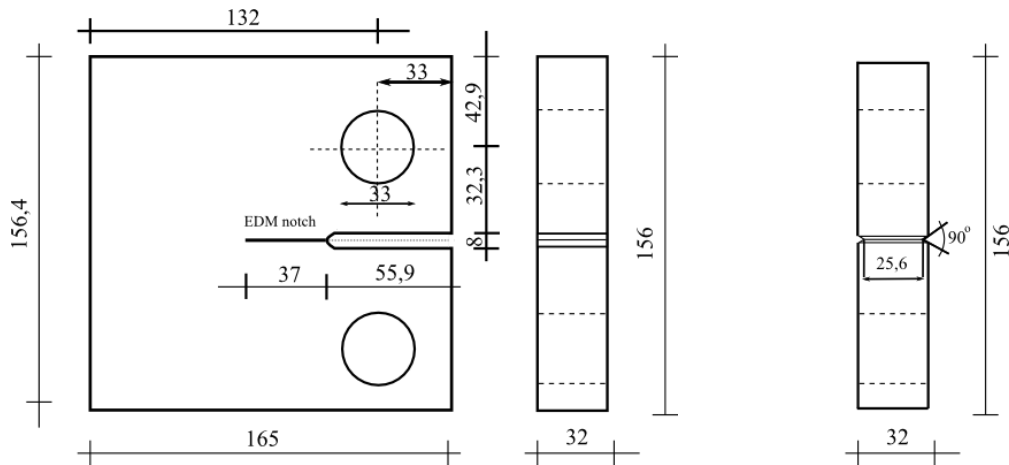
Figure 1, a - *geometry of CT specimen.* **b** - *grooves.*

According to ASTM E647 [5] the determinatiomn of the fatigue crack growth threshold ΔK_{th} (that asymptotic value of ΔK at which da/dN approaches zero) should involve at least five da/dN, ΔK data points of approximately equal spacing in the range of growth rates between 10^{-9} m/cycle and 10^{-10} m/cycle. The K-decreasing procedure is started by load cycling at ΔK and K_{max} levels equal or greater than the terminal pre-cracking values. Subsequently, forces are decreased (shed) as the crack grows until the lowest ΔK or crack growth rate of interest is achieved. The parameter C (normalized K-gradient) must be greater than -0.08mm^{-1};

$$C = \left(\frac{1}{K}\right)\left(\frac{dK}{da}\right) > 0.08mm^{-1}$$

For each load step, da/dN values are recorded only after a crack extension of 0.5mm, to enable the growth rate to establish a steady state value. The load is decreased by 10 percent steps, aiming at C>-0.08mm^{-1}, and the threshold is determined when crack propagation stops or the growth rate of 10^{-10} m/cycle is reached. In threshold testing, it is good practice to initiate fatigue cracks at the lowest possible stress intensity factor range ΔK. Figure 2 shows schematically the a *vs.* time (or number of cycles) for such a test, whereas Figure 3 shows schematically the time (or number of cycles) dependency of ΔP and of ΔK.
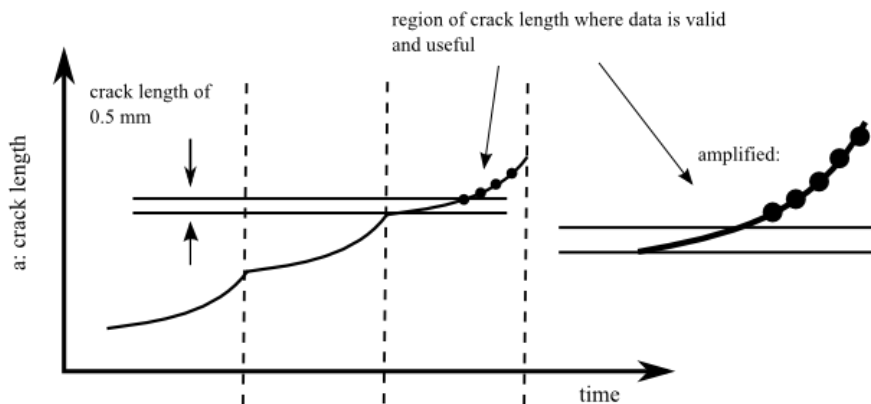

Figure 2 - *schematic representation of the a vs. time (or number of cycles) data.*
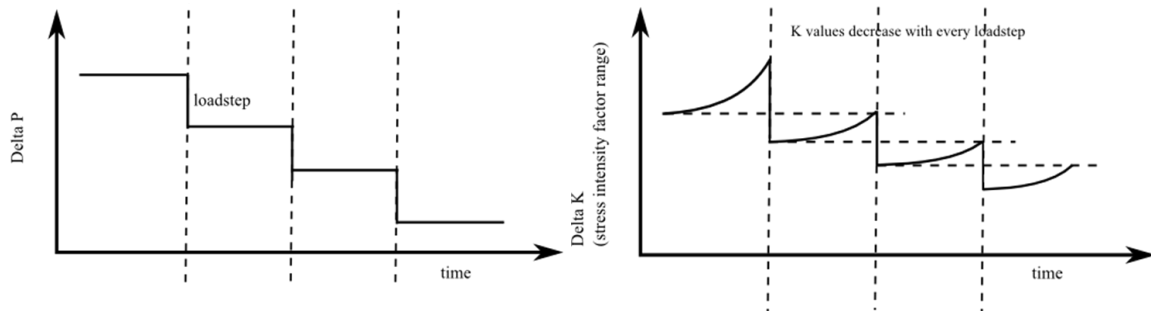
Figure 3 - *schematic representation of the ΔP and ΔK vs. time (or number of cycles) data.*

Examples of measurements are given in Figure 4, concerning R=0.1 and 0.7. It is apparent that the hollow squares, corresponding to the near threshold determination, present greater scatter than the hollow diamonds, pertaining to the Paris law regime. This is due to different data reduction techniques used: secant method for the near threshold regime, and incremental polynomial method for the Paris law regime.
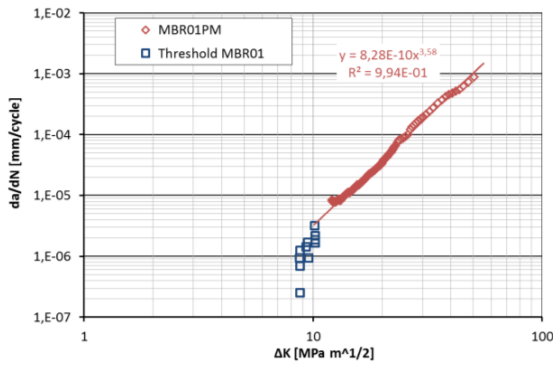
Figure 4a *– test at R=P_{min}/P_{max} = 0.1.*
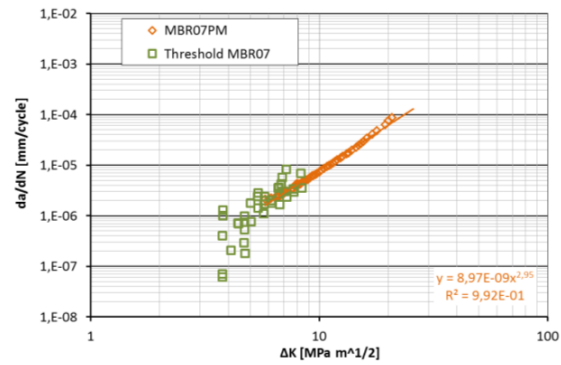
Figure 4b *– test at R=P_{min}/P_{max} = 0.7*

As an example of actual testing data, Figure 5 presents the load shedding data (expressed as the variation of ΔK) for the R=0.7 specimen.
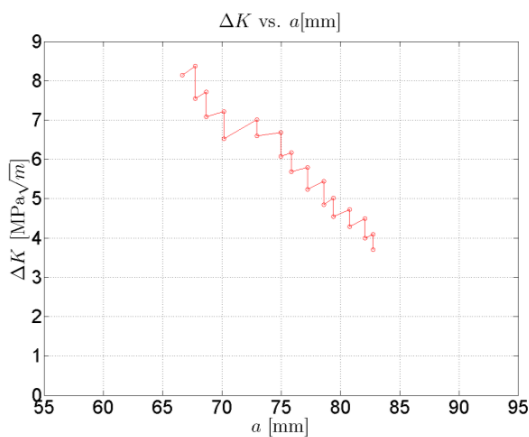
Figure 5 *– force shedding steps for R=0.7 test*
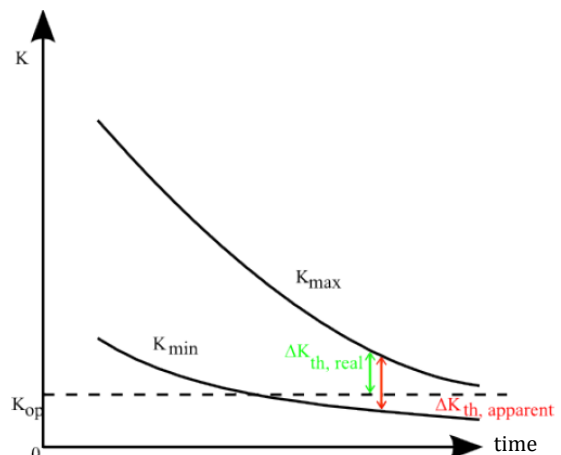
Figure 6 - *schematic explanation of the R effect upon threshold FCG behavior*

The present values of near threshold stress intensity factor range were compared with data taken from BS7910:2005, [6]. That document indicates the values, in $Nmm^{-3/2}$, ΔK_{th}=63 for

R>0.5 and ΔK_{th}=170-214R, for R<0.5, *i.e.* 2MNm$^{-3/2}$ for R=0.7, and 4.7MNm$^{-3/2}$ for R=0.1, both lower than the values obtained in the present work, as it should be expected given the conservative nature of this type of standards.

The substantial variation in ΔK_{th} found in the present work, approximately 9 MNm$^{-3/2}$ for R=0.1 and approximately 4 MNm$^{-3/2}$ for R=0.7, may be explained by the closure effects. Testing with the back face strain gauge revealed that the opening load is rather small, between approximately 3 and 1.3kN, decreasing with increasing a/W ratio. These values are above minimum loads for the R=0.1 tests, but lower than minimum load for the R=0.7 test. This may influence near threshold FCG experiments, as suggested in the schematic Figure 6 adapted from Smith and Piascick [12]. This Figure shows, schematically, K_{max} and K_{min} for a decreasing load range test, under constant R. For a low R value, when the crack tip region is subjected to the real ΔK_{th} (which takes into account opening load effects), the nominal or apparent ΔK_{th} is higher. Clearly, for higher R values, this effect will no longer be felt, since real and nominal ΔK_{th} will coincide. These facts justify that the measured near threshold stress intensity factor range for R=0.1 should be greater than for R=0.7.

3   Toughness tests and FEM modeling of grooved specimens

The first standards for fracture toughness measurement concerned situations where LEFM could be applied, particularly the plane strain fracture toughness standard ASTM E399 [13]. Later, standards for elastic-plastic fracture were developed, as ASTM E813, [14]. More recently, integrated standards covering a wide range of situations appeared, as ASTM E1820, [7] or BS7448, [8]. Basically the test consists in the monotonically loading of a precracked specimen, characterizing the crack unstable or stable crack propagation through a variety of concepts, including critical stress intensity factor or J integral and, in the case of stable crack propagation, resistance curves. In this context reference should be made to the GKSS document, [9] 'EFAM GTP 02 - the GKSS test procedure for determining the fracture behavior of materials', that discusses in detail the several possible situations and alternatives, providing useful testing guidelines.

One 20% deep 90° sidegrooved specimen and one flat surface specimen, both with 32mm overall thickness, were tested for fracture toughness determination. Testing consisted on monotonic loading, recording actuator displacement, loadline displacement measured using a clip gauge, and load. The loadline displacement is intended for evaluation of ductile tearing using compliance measurements during partial unloadings. In this presentation, however, actuator displacement records were used and the point of interest in the tests was considered to be maximum load. The criteria of [9] (section 6.3.1.1, page 43), was used for the evaluation of $J_{0,max}$ and those values are taken as toughness of the present specimens.

$$J_0 = \frac{K^2(1 - v^2)}{E} + J_{pl}$$

where K is calculated for the point of interest (P_{max} in this work), and J_{pl} is the plastic component of J, as presented for example in ASTM E1820, [7]. The results obtained are $J_{0,max}$= 0.38 kN/mm in the case of the grooved specimen and 2.04 kN/mm in the case of the flat surface specimen. These are likely to be overestimates given use of actuator displacement in the calculations.

The numerical modeling performed aims at contributing to the explanation of the above results. Grooving increases the degree of plane strain, and therefore implies a reduction of toughness, as verified in the present experimental work. Figure 7 shows the grooved specimen

after testing. Figure 8 shows the characteristic plane stress behavior displayed by the flat surface specimen.
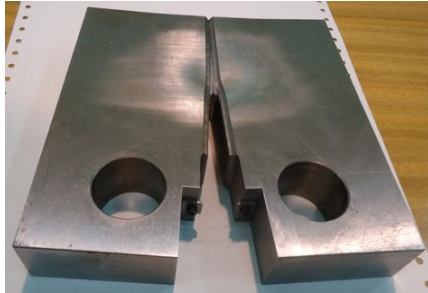
Figure 7 – *grooved specimen after testing*
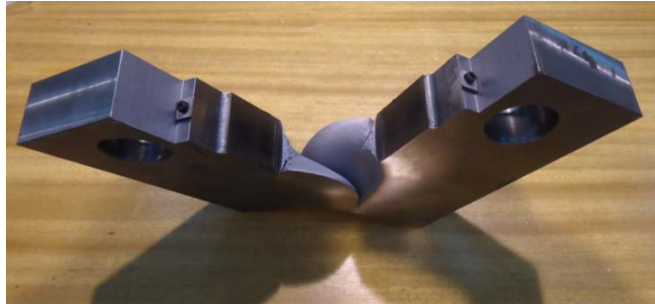
Figure 8 – *flat surface specimen after testing, revealing typical plane stress behavior*

4   Finite elements modeling of the grooved specimen

A 3D analysis of the specimen was made using ABAQUS. The mesh was designed using a tridimensional hexagonal elements (C3D20R) with 20 integration points. The numerical solution is solved by Newton's method using reduced integration. The number of elements changes in every stage of crack length but every model is at least made of 10000 elements.
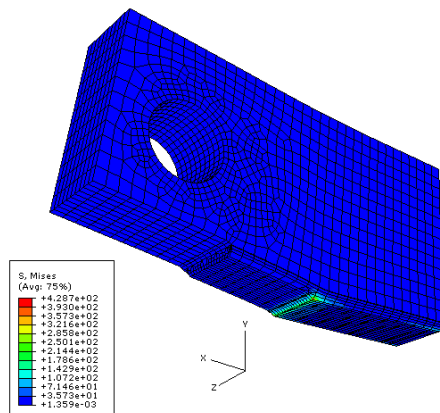
Figure 9 - *FEM-model of one of the C(T) specimen geometries studied*
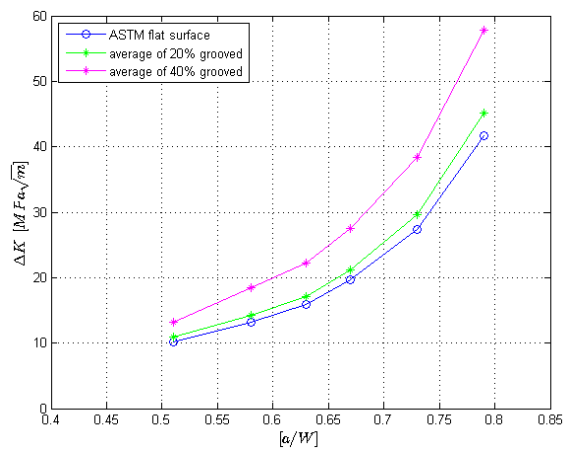
Figure 10 – *Stress intensity factor VCCT results for flat surface, and 20% and 40% grooved specimen*

Figure 9 presents the mesh used for one of the cases analysed, whereas Figure 10 presents the influence of the grooves upon the K value. The FEM calibration of the flat surface specimen almost coincides with the ASTM calibration, and is not shown in the picture. Increasing grooves' depth increases the K value. The effect of side-grooves on constraint was quantified by using the ratio of σ_z to $\nu(\sigma_x + \sigma_y)$, which is equal to one for plane strain. The through thickness variation of crack front constraint is shown for a flat surface specimen, for a 20 percent grooved specimen and for a 40 percent grooved specimen in Figure 11, where the horizontal axis indicates the specimen half thickness: 16mm for the flat surface specimen, and half distance between tips of the grooves for the other two cases.
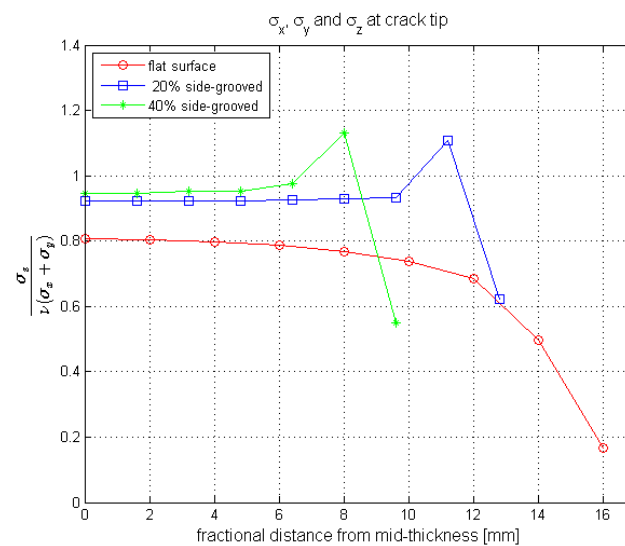
Figure 11 - *Crack tip constraint for C(T) specimen with and without sidegrooves*

Although, in Figure 10, 20% sidegrooves were shown to have little influence on K, they have a more marked influence on the degree of plane strain, as shown in Figure 11, where degree of plane strain for 20% and 40% is similar.

5   Conclusions

Tests aiming at the determination of near-threshold FCG data for S355NL steel were performed using 32mm thick flat surface C(T) specimens and the load shedding procedure, for load ratios R=0.1 and 0.7. Values of approximately 9 MNm$^{-3/2}$ and 4MNm$^{-3/2}$ were obtained for R=0.1 and 0.7 respectively. The different near-threshold values for R=0.1 and 0.7 were explained on the basis of crack closure effects.

Near threshold stress intensity factor range values for R=0.1 and R=0.7 were compared with generic values indicated in the British Standards Institution standard BS 7910:2005, which gives methodologies for assessing the acceptability of flaws in metallic structures. The present values are higher than those indicated in BS 7910:2005, as it should be expected since the standard procedures are conservative.

Fracture toughness tests were carried out on 32mm thick C(T) specimens one with flat side surfaces, and the other with 20% deep 90° side grooves, respectively. It was found that the flat surface specimen displayed a plane stress type of behavior, with the initial fatigue pre-crack growing at approximately 45° to the middle plane of the specimen. The grooved specimen, due to its higher degree of plane strain, presented ductile tearing along the middle plane of the specimen. A substantially higher toughness value was measured for the flat surface specimen.

Numerical modeling of the CT specimens used in the experimental program was performed using ABAQUS and the modified 3D VCCT technique for evaluating SIF. Further to flat surface and 20% deep 90° side grooves, the case of 40% deep 90° side grooves was also studied, in order to evaluate more thoroughly the effect of side groove depth on this type of specimen. SIF calibration for flat surface C(T) specimens is given in standards; the calibration for side grooved specimens relies upon generic formula for effective thickness (B$_{eff}$). The present results for flat surface specimens agrees very well with the ASTM calibration, validating the FEM and VCCT methodology used in the present work. The effect

of side-grooves on constraint was quantified by using the ratio $\sigma_z/\nu(\sigma_x+\sigma_y)$. The increase in degree of plane strain was correlated with the decrease in fracture toughness assessment caused by side-grooving.

Acknowledgments

References

[1] C.M.C. Albuquerque, R. Miranda, V. Richter-Trummer, M.A.V. de Figueiredo, R. Calçada, P.M.S.T. de Castro, 'Fatigue crack propagation behaviour in thick steel weldments', International Journal of Structural Integrity, in press, 2012

[2] Eurocode 3: Design of steel structures. Part 1-9: Fatigue, EN 1993–1–9. 2005

[3] J.M. Barsom, S.T. Rolfe, Fracture and Fatigue Control in Structures, 3rd ed., 1999

[4] B. Kühn, M. Lukić, A. Nussbaumer, H.-P. Günther, R. Helmerich, S. Herion, M.H. Kolstein, S. Walbridge, B. Androic, O. Dijkstra, Ö. Bucak, Assessment of Existing Steel Structures: Recommendations for Estimation of Remaining Fatigue Life, in: G. Sedlacek *et al* eds., JRC Scientific and Technical Reports, European Commission, Joint Research Centre, 2008

[5] ASTM E647-08, Standard test method for measurement of fatigue crack growth rates, American Society for Testing and Materials, 2008

[6] BS 7910:2005, Guide to methods for assessing the acceptability of flaws in metallic structures, British Standards Institution, 2005

[7] ASTM E 1820-08a, Standard test method for measurement of fracture toughness, American Society for Testing and Materials, 2008

[8] BS 7448, Fracture mechanics toughness tests, British Standards Institution, 4 parts, various dates

[9] K. H. Schwalbe, J. Heerens, U. Zerbst, H. Pisarski, M. Koçak, EFAM GTP 02: the GKSS test procedure for determining the fracture behaviour of materials. GKSS-Forschungszentrum (Geesthacht), 2003

[10] R. Krueger, The virtual crack closure technique: History, approach, and applications. Technical report, NASA/CR-2002-211628 ICASE Report No. 2002-10, 2002

[11] R. Miranda, Study of fatigue crack propagation in metallic structures, Masters thesis, Faculdade de Engenharia da Universidade do Porto, Portugal, 2010

[12] S. W. Smith and R. S. Piascik, 'An indirect technique for determining closure-free fatigue crack growth behavior', in: ASTM STP 1372, 2000, pp.109-122

[13] ASTM E399-08, Standard test method for Linear-Elastic Plane-Strain fracture toughness K_{Ic} of metallic materials, American Society for Testing and Materials, 2008

[14] ASTM E813, Test method for J_{IC}, a measure of fracture toughness (withdrawn 1997)

Wheel/rail contact fatigue: theoretical and experimental analysis

L. Reis, P. Santos, B. Li and M. de Freitas

ICEMS & Departamento de Engenharia Mecânica

Instituto Superior Técnico

Av. Rovisco Pais, 1, 1049-001 Lisboa, Portugal.

E-mail: luis.g.reis@ist.utl.pt

E-mail: mfreitas@dem.ist.utl.pt

Abstract   Rolling Contact Fatigue is a severe and growing problem for many railways in the world. The goal of this study is to evaluate the wheel/rail contact fatigue, both theoretical and experimental analyses of the mechanical behavior between the wheel and the rail under cyclic loading conditions were performed. Experimental work was carried out by a biaxial fatigue testing machine, where different loading paths, i.e., typical combined compression stress and shear stress conditions simulating the wheel/rail contact were applied. Cyclic elastic-plastic behavior of the materials used in this study was also obtained. Numerical and theoretical models were implemented. The numerical study enabled us to characterize the nature of stresses that are present in the wheel/rail, regarding the rolling direction. Other approaches were more focused on the material's mechanical behavior and also used to compute the crack initiation plane angle – critical plane models. To characterize fracture surfaces under these typical loading paths some fractographic analyses were also carried out. The paper concludes with some remarks: the loading trajectories severely affect the fatigue life, the initial crack plane and consequently the fracture surface.

1.   INTRODUCTION

Railway sector places an important role in the means of transportation for many countries. Rolling Contact Fatigue (RCF) is a severe and growing problem for many railways in the world, e.g. each year in Europe, there are several hundred broken rails due to cracks caused by RCF. It is estimated that the annual cost of reprofiling rail and repairing rail damage within the EU is some hundred million Euros [1].

Important factors to consider in RCF of railway rails are the axle loads, wheel and rail profiles and the friction coefficients, whose magnitudes largely determine the contact stresses, the material's response and therefore fatigue crack initiation. Lubricants affect the friction condition and therefore the contact stresses and rate and type of wear, and therefore affect both crack initiation and crack propagation. The fatigue life regime of interest for railway rails is dependent on the combination of the above described factors. For instance, a high axle load or friction coefficient leads to crack initiation due to low cycle fatigue, whereas a low axle load and friction coefficient may result in crack initiation due to high-cycle fatigue. In-field observations and laboratory investigations of cracks initiated in railway rails, e.g. head checks, confirm that low-cycle fatigue is the dominating fatigue life regime for railway wheels [2, 3].

In service, the wheels are subjected to multiaxial loading conditions. The main load is associated with the weight of the carriage and can be defined as a vertical load. The second load is due to the existence of friction between the wheel and the rail, with a longitudinal orientation. The third load is only present when the train is describing a curve, and represents the centrifugal load, having a lateral direction.

The goal of this study is to evaluate the fatigue behaviour of the wheel material of an AVE S-101 train under rolling contact conditions. Finite element method is applied to study the stress/strain distributions at the interface in the rail/wheel contact, the multi-axial fatigue models are applied to estimate the fatigue strength and the service life. Experimental studies are carried out by a biaxial fatigue testing machine to achieve the material behaviour under the typical combined compression stress and shear stress conditions due to the rail/wheel contact. Fractographic analysis was also performed to identify the crack initiation and early crack growth orientations.

2. THEORETICAL ANALYSIS

2.1. Stress analysis under rolling contact conditions

Under rolling contact conditions, such as rail/wheel and so on, the material element under the surface of contact is subjected to non-proportional (out-of-phase) normal and shear stresses. Considering the situations as shown in the following Figure 1, one wheel rolling from left side to right side [4]. At the *Time 1*, the material element A under the wheel is only subjected to compressive stress without shear stress, but the neighbour element B is subjected to shear stress, and element C is also subjected to shear stress, but a very small value because it is far away from the contact point. When the wheel run to the next position, *Time 2*, the element B is subjected to only compressive stress, but the neighbour elements A and C are subjected to shear stress. When the wheel run to the position *Time 3*, the element C is subjected to only compressive stress, but the neighbour element B is subjected to shear stress, element A is also subjected to a very small shear stress, because it is far away from the contact point. Therefore, one material element (for example element A) is subjected to the maximum compressive stress at *Time 1* and the maximum shear stress at *Time 2*, which are non-proportional normal and shear stresses as shown in Figure 2. The value of the maximum shear stress is about 25% of the maximum compressive stress. Similar to the above discussions about the stress distributions in the rail, the stress distributions in the sub-surface of the wheel are also subjected to non-proportional stresses as shown in the Figure 2, but there are differences of the maximum stress values between the wheel and rail, due to the effect of the radius R (R is considered as infinite for the rail). Within the scope of this work, the finite element code ABAQUS was used to evaluate the local values of the normal and shear stresses that are present in the wheel and the rail under rolling contact conditions.

| Time 1 | Time 2 | Time 3 |
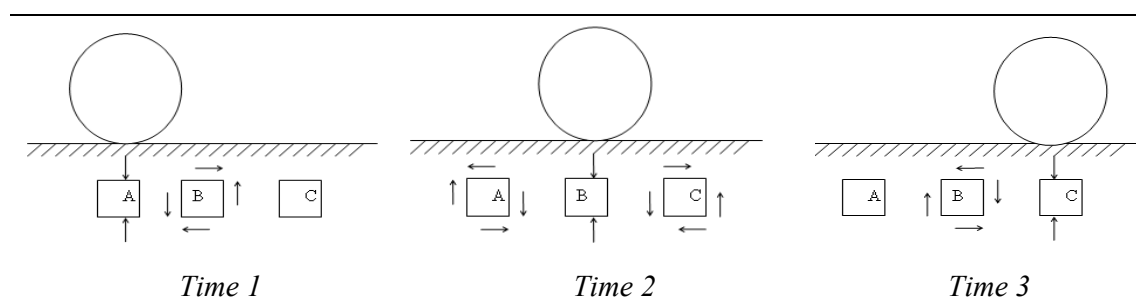
Figure 1 - *Stresses caused by rolling contact.*

Figure 3 a) shows the normal stress distributions in the rail and wheel under rolling contact fatigue (RCF) conditions. The results show that compressive normal stresses are mainly concentrated in the zone just under the contact point as discussed formerly in the theoretical analysis. Figure 3 b) shows the shear stress distributions, where it is shown that the shear stresses are concentrated in the zone next to the contact point. According to the conventions of defining the signs of the shear stress, the shear stress is positive in the left side to the contact point, since the shear stress causes the element rotating in the clockwise direction. Correspondingly, the shear stress is negative in the right side to the contact point, since the shear stress causes the element rotating in the anti clockwise direction.
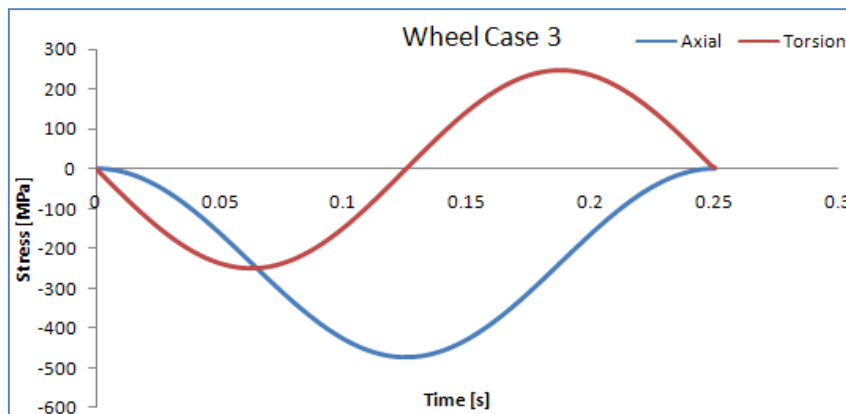
Figure 2 - *Non-proportional loading caused by rolling contact.*

| a) | b) |
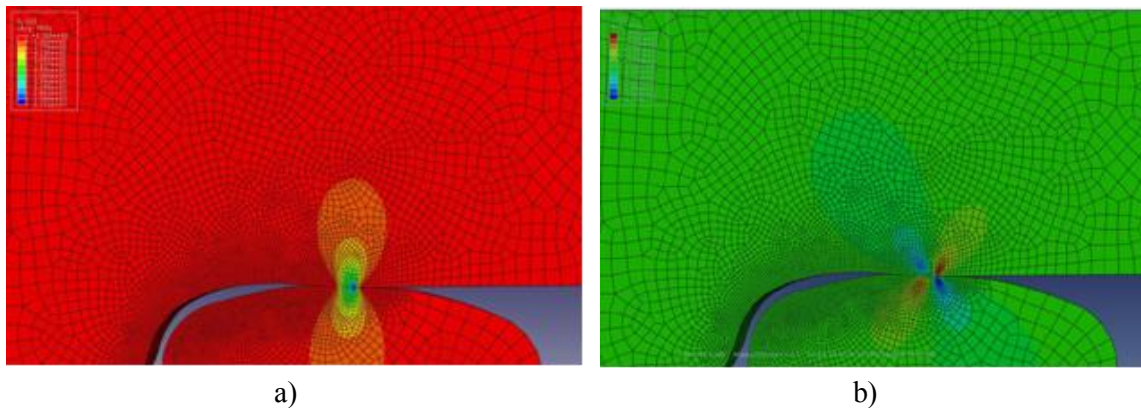
Figure 3 – *Under RCF: a) normal stress distribution and b) shear stress distribution.*

2.2. Multiaxial fatigue models

The analysis of rolling contact fatigue differs from the 'classic' fatigue analysis in several aspects: a) The rolling contact loading causes a multiaxial state of stress with out-of-phase stress components and consequently rotating principal stress directions as discussed in section 2. b) In a predominantly compressive loading, the validity of traditional fatigue models may be questioned. In the present study *Findley, Brown-Miller, Fatemi-Socie, and Smith, Watson and Topper* critical plane models were applied and evaluated [5].

3.   EXPERIMENTAL PROCEDURE

The material used in this study was provided by Alstom Spain. The used specimens were manufactured from an Alta Velocidad Española (AVE) train wheel and its chemical composition is available in Table 1 and Table 2 shows the mechanical properties of the same material. Figure 4 a) shows the geometry and dimensions of the specimens used in this study. Tests were carried out in a biaxial servo-hydraulic test machine as shown in Figure 4 b).
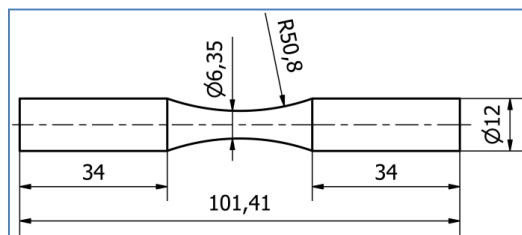
a)	b)

Figure 4 – a) *Specimen geometry and dimensions (mm), b) Experimental setup*

Table 1 - *Material chemical compositions.*

	Chemical Composition (%)									
	C	Si	Mn	P	S	Cr	Mo	Ni	Al	Cu
AVE Wheel	0.49	0.25	0.74	0.01	<0.005	0.26	0.06	0.18	0.03	0.12
	W	Pb	Sn	As	Zr	Ca	Sb	B	Zn	Fe
	<0.01	<0.03	<0.01	<0.01	<0.002	<0.003	<0.002	<0.0001	<0.003	97.8

Table 2 - *Material mechanical properties.*

Tensile strength	S_u (MPa)	810
Yield strength	S_y (MPa)	460
Young´s modulud	E (GPa)	210
Elongation	A (%)	20
Poisson´s ratio	ν	0.3

In order to study the fatigue behavior of this type of material, uniaxial and multiaxial fatigue tests were carried out. Three different types of loading paths were performed to simulate biaxial loading conditions. Case I and case II loading paths were only carried out so that they can be stated as a reference, Case I as a proportional loading case, Case II as a non-proportional loading case 90º out of phase, and the third case it is intended to simulate the loads that the wheel is subjected when interacting with the rail. Figure 5 presents all the loading cases carried out. The loading path WheelCase 3 corresponds to the non-proportional stress-time history as represented in Figure 2 [6].

After testing the specimens in the biaxial machine, a fractographic analysis was performed in order to measure the angle of crack initiation plane and also to observe the fracture surfaces.

| Case I | Case II | WheelCase 3 |
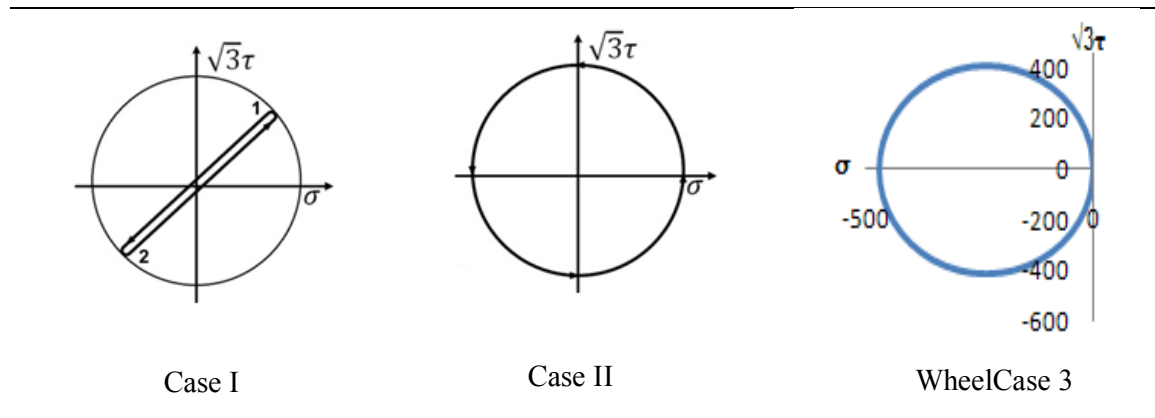
Figure 5 - Multiaxial loading paths carried out in experimental tests

4.   RESULTS AND DISCUSSIONS

Fatigue lives obtained from experimental tests are shown in Table 3. The loading Case II causes more damage than the other two loading cases. A difference of less than 100 MPa in the Axial Stress results in a reduction of the material's life in more than one quarter. The Wheel Case 3 specimens have the longest lives when compared to the other types of loading.

Table 3 - Fatigue life results.

Type of Loading	Specimen	Axial Stress [MPa]	Shear Stress [MPa]	Life (Number of Cycles)
Case I	D	289.5	167.1	139450
Case II	F	434.3	250.7	11800
	B	372.4	215	51878
Wheel Case 3	A	524.2	277.5	111000
	E	473.9	250.7	442000
	C	384.9	208.9	1150000

After performing the experimental fatigue tests, the fractured specimens were subjected to fractographic analysis to measure the crack initiation plane angle. The crack initiation plane angle is defined as the angle where the damage parameter has its maximum value [7, 8]. Table 4 presents the theoretically predicted critical plane angles versus the measured ones.

Case I loading path has similar results for the measured angles and every model with the exception of the SWT model. Case II loading path is the only one where all the angle values are in agreement with the predicted ones. The WheelCase 3 loading shows different results for every model when compared with the measured values.

***Table 4** – Critical plane angles.*

Angle Value	Type of Loading		
	Case I	Case II	Wheel Case 3
Experimental	-15°	0°	-18°/-20°
Findley	-12° / 61°	0°	-81° / 81°
Brown Miller	-15° / 64°	0°	-84° / 84°
Fatemi Socie	-9° / 59°	0°	-78° / 78°
SWT	25°	0°	-48° / 48°

5.   CONCLUDING REMARKS

- Normal and shear stress distributions in the sub-surface under rolling contact condition are analyzed both theoretically and numerically, main and secondary stresses are identified and the non-proportional stress state is also identified;

- Experimental fatigue tests were carried out under the real non-proportional stress state, both fatigue lives and early crack growth angles were analyzed and measured;

- Critical plane models allow to predict the fatigue life and critical plane orientations; results obtained for loading cases I and II agree with the predicted ones. Values obtained for loading Wheelcase 3 do not match with predicted ones.

Further research work is ongoing to improve the models for the predominantly compressive stress states such as those of RCF.

References

[1] Cannon DF, Pradier H. Rail rolling contact fatigue —Research by the European Rail Research Institute. *Wear* 1996;191: 1–13.

[2] Ringsberg JW, Loo-Morrey M, Josefson BL, Kapoor A, Beynon JH. Prediction of fatigue crack initiation for rolling contact fatigue. *Int. journal of Fatigue*, 22 (2000) 205–215.

[3] D.F.C. Peixoto, P.M.S.T. de Castro and L.A.A. Ferreira, "*Fatigue Crack Growth in Railway Steel",* Proceedings of the First International Conference on Railway Technology: Research, Development and Maintenance, 2012.

[4] Johnson, K.L. (1985). "Contact Mechanics". *Cambridge University Press*.

[5] Socie, D.F. and Marquis, G.B. (2000). "*Multiaxial Fatigue*". Society of Automotive Engineers, Warrendale, PA 15096-0001.

[6] M.G. Tarantino, S. Beretta, S. Foletti, J. Lai, "A comparison of Mode III threshold under simple shear and RCF conditions", *Engineering Fracture Mechanics*, Volume 78, Issue 8, May 2011, Pages 1742-1755, 2011.

[7] B. Li, L. Reis and M. De Freitas, "Simulation of cyclic stress/strain evolutions for multiaxial fatigue life prediction," *Int. journal of fatigue*, vol. 28, pp. 451–458, 2006.

[8] L. Reis, B. Li, and M. De Freitas, "Analytical and experimental studies on fatigue crack path under complex multi-axial loading," *Fatigue & Fracture of Engineering Materials & Structures*, vol. 29, pp. 281–289, 2006.

Wheel/rail contact: fatigue behavior

Daniel Peixoto[1]*, Luís A. Ferreira[1], Paulo M. S. T. de Castro[1]

[1]1Mechanical Engineering Department
Faculdade de Engenharia da Universidade do Porto
Rua Dr. Roberto Frias, 4200-465 Porto, Portugal
*dpeixoto@fe.up.pt

Abstract The work presented is part of a project where it is intended to develop a methodology to anticipate the need for repair or replacement of wheels or rails, and in particular to establish time limits for intervention on wheels or rails where one or more defects were detected.

Fatigue crack growth rate measurements, including low values of stress intensity factor range, and twin disc tribological tests, are being performed in order to characterize the fatigue crack initiation and propagation behavior of wheel and rail materials, as this is essential for the objectives mentioned above.

Further to initiation of defects in the contact region, tribological twin disc tests also provide wear rate characterization. Some related issues as chemical compositions, microstructure analyses, wheel hardness profile and striation spacing counting in the wheel and rail were also assessed and will be discussed in this paper.

1 Introduction

Rolling contact fatigue appears in components subjected to variable contact stress.

In this kind of fatigue loading, rupture is caused by cracks that appear not only on the surface but also in the interior of the bodies in contact. It is clear that the analysis of rolling contact fatigue defects on rails is more complicated than on wheels because of greater randomness and deviations in acting loads, contact geometries and fatigue strengths. The rolling contact fatigue problem in railway components is dealt in, *e.g.*, refs. [1]-[5].

Some aspects such as wear, corrosion, and surface corrugation, affect components fatigue life and must be considered in this type of fatigue behaviour.

It has been shown by G. Donzella *et al* in [6] that there is a competition between fatigue crack propagation and wear. Improving material wear resistance implies a reduction of the maintenance costs, increasing grinding intervals and extending the rail life but it also increases the risk that small cracks are not worn away and can grow to a critical size causing rail failure.

The stresses and strains in the contact zone between the mechanical elements must be known to properly design the mechanisms and prevent fatigue phenomena or other damage.

The behaviour of solids in contact may be analysed by the theories of contact between elastic bodies. These theories, firstly developed by Boussinesq, Cerutti and Hertz, e.g. [7], are concerned with the quantification of displacements, deformations and stresses resulting from an applied load.

Nowadays, surface and sub-surface contact fatigue damage is the most common failure mechanism in rolling bearings, gears and in wheels and rails.

Such failures are strongly dependent on the operating conditions, such as load, speed, sliding, presence of lubricant and surface quality.

The fatigue analysis of contact problems is a very complex problem since it implies the analysis of a multiaxial stress state and in general, a complete RCF load cycle involves changes in the principal stresses' orientation. In order to solve this issue several multiaxial fatigue criteria were developed, e.g. Findley [8], Matake [9], Crossland [10], Sines [11], Dang Van [12]. These criteria aim to establish an equivalent stress which can be comparable with material parameters obtained by uniaxial tests. In [13] the Dang Van fatigue criterion is applied to the wheel\rail contact problem.

2 Material characterization

Fatigue crack growth rate measurements and twin disc tests, are being performed in order to characterize the fatigue crack initiation and propagation behaviour of railway wheel and rail material, as this is essential to develop a methodology to anticipate the need for repair or replacement of wheels or rails, and in particular to establish time limits for intervention on wheels or rails where one or more defects were detected.

Before starting with these complex tests some tests were performed in samples taken from an AVE train wheel and from a UIC60 rail in order to characterize their chemical composition, mechanical properties, microstructure and hardness.

The chemical composition of these two material are presented in Table 1. Table 2 presents the mechanical properties of the wheel and rail materials.

Table 1 - Wheel and railmaterial chemical composition in %.

	C	Mn	Si	P	S	Ni	Mo	Al	Cr	Cu
Wheel	0.49	0.74	0.25	0.01	<0.005	0.18	0.06	0.03	0.26	0.12
rail	0.72	1.1	0.35	0.02	0.01	0.02	<0.001	<0.005	0.02	<0.02

Table 2 - Mechanical properties of wheel and rail materials.

Material	Young modulus [GPa]	Yield strength [MPa]	Tensile strength [MPa]	Elongation [%]	Reduction in area [%]
wheel	197	503	859	18	51
rail	191	504	950	13	19

The microstructures of the wheel and rail materials and their correspondent hardness are shown in Figure 1.
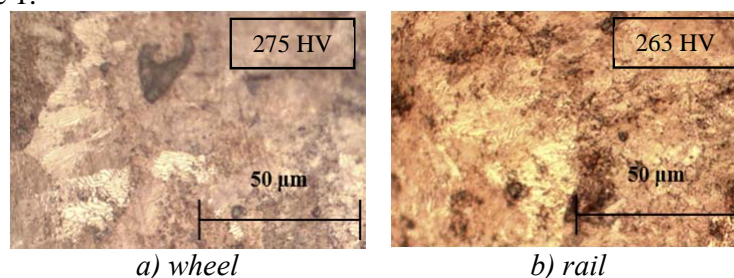
a) wheel   b) rail
Figure 1 - Studied materials microstructure.

From these analyses it can be concluded that the studied materials present a pearlitic microstructure.

It was expected that the rail material hardness was higher than the wheel material, wich was not verified. In order to understand this results it was decided to perform several hardness measurements in a wheel cross-section sample to obtain the hardness distribution in the wheel cross-section. Analysing the obtained results, shown in Figure 2, it can be concluded that the

higher hardness values appears in the center of the wheel tread, the wheel/rail contact zone, since the used sample was taken from a used wheel.
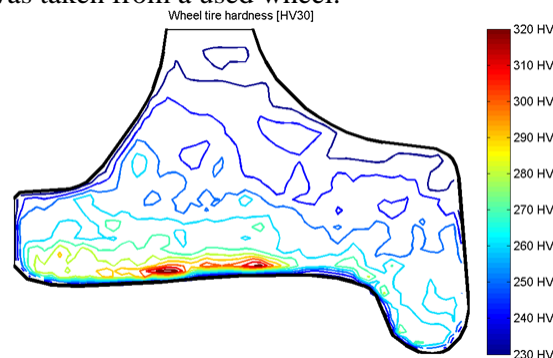
Figure 2 - Wheel hardness distribution.

3 Fatigue crack growth rates

Fatigue crack growth (FCG) rate measurements were made according to the ASTM E647-08 standard [14] in order to characterize wheels' and rails' steels resistance to stable crack propagation under cyclic loading.

During these tests the crack length (*a*) is recorded as a function of the number of cycles (*N*), together with the maximum and minimum values of the applied load (*P*). Typically the load range (*ΔP=Pmax-Pmin*) and load ratio (*R= Pmin / Pmax*) are kept constant during tests.

Using these data and its treatment, e.g. according to the algorithm given in the standard, it is possible to obtain the fatigue crack growth rates (*da/dN*) and the corresponding values of the crack-tip stress-intensity factor range (*ΔK*).

Expressing *da/dN* as a function of *ΔK* provides results that are not dependent on the specimen type or geometry, which enables comparison of results obtained from a variety of specimen configurations and loading conditions.

In this work single edge-notch specimen called compact specimens, C(T), were used because this type of specimen has the advantage of requiring a smaller amount of material and only tension-tension loads (R>0) were used.

Since one main goal of the project, where the present study is included, is to characterize the behaviour of the wheel and rail steels in the presence of defects near the contact surfaces, the wheel specimens were extracted from the wheel tread, and the rail specimens from the rail head, as shown in Figure 3.
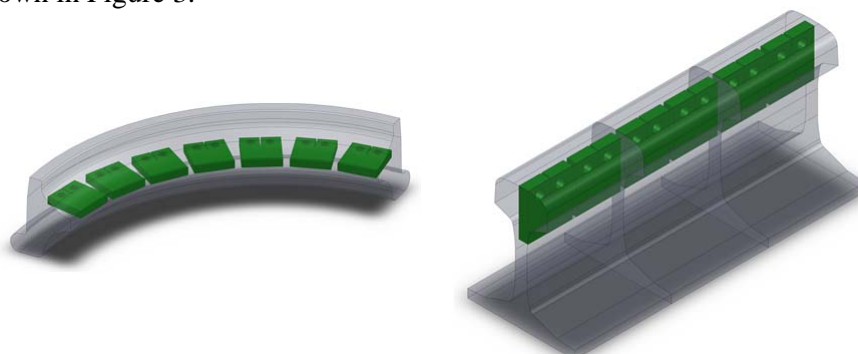
a) loaction of wheel C(T) specimens.   b) loaction of rail C(T) specimens.
Figure 3 - Location for C(T) specimens extractionon.

Figure 4 shows the dimensions adopted for the C(T) specimens, according to the standard ASTM E647-08.

All fatigue crack growth tests were made at room temperature on a MTS® servo-hydraulic machine equipped with a 250kN load cell. This machine was also equipped with two traveling microscopes to measure the crack length.
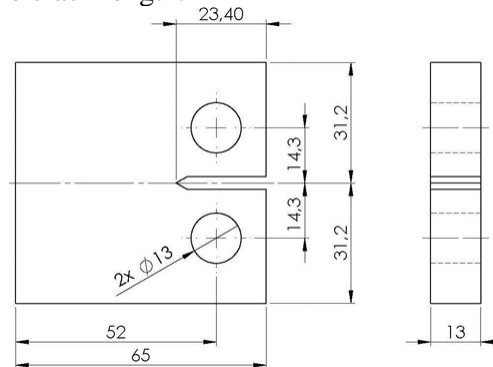

Figure 4 - *C(T) specimens dimensions.*

These specimens were loaded in constant amplitude load with a sinusoidal waveform, and three different load ratios, *R*=0.1, *R*=0.4 and *R*=0.7, were tested.

The seven point incremental polynomial method, presented in the ASTM E647 standard, was used to calculate the fatigue crack growth rates from the experimental results (*a vs. N*). The obtained results are shown in Figure 5.
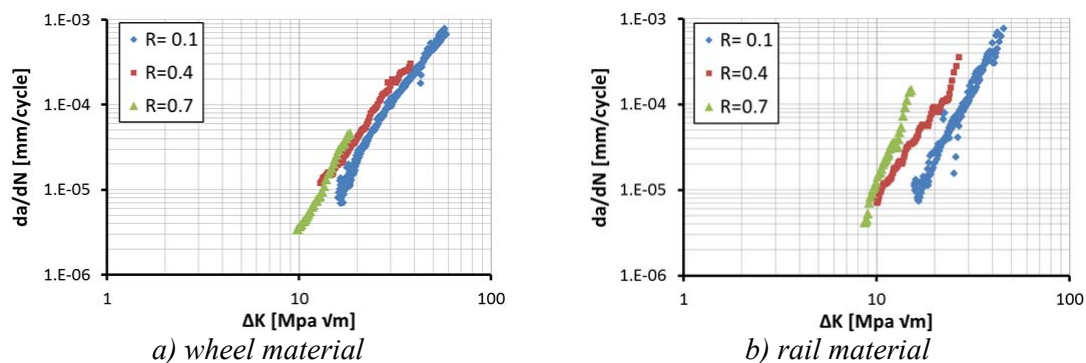
a) wheel material   *b) rail material*
Figure 5 - *Fatigue crack growth rates for wheel and rail materials.*

It is observed that for the wheel material *R-ratio* has a small influence, with greater *R* implying higher fatigue crack growth rates. For the rail the *R-ratio* influence is more considerable. The literature suggests that in the Paris law regime little influence of *R-ratio* is expected, [15], as observed *e.g.* in [16].

Some C(T) fatigue surfaces were observed on a high resolution Scanning Electron Microscope (SEM) in order to identify the presence of striations and if their spacing can be correlated with fatigue crack growth rates.

The analysis of the obtained results, presented in Figure 6 a), suggests that striation spacing (*S*) for the rail material is higher than for wheel material.

Furthermore, in the case of rail material striation spacing increases with *R*, an effect not found in the wheel steel.

No striation spacing vs. *da/dN* correlation was found, as in other studies, *e.g.* [16], since striation spacing was found to be approximately constant for values of *da/dN* between approximately 10^{-5} and 10^{-4} mm/cycle.

It was also observed a random behaviour in the striation orientation, has sugested in Figure 6 b).
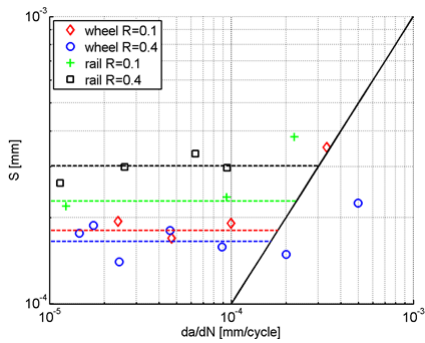
| a) Striation spacing vs. fatigue crack growth rate. | b. rail R=0.1 specimen fatigue surface striations photography. |

Figure 6 - *Striation spacing observations and results.*

4 Twin disc tests

Twin disc test machines are commonly used to simulate heavy loaded contacts like the wheel/rail contact and to predict materials behaviour in rolling contact fatigue.

The twin disc test consists of two rotating discs in contact subjected to a constant applied load. In this type of tests the most important parameters are the discs' geometry, their rotating speed, the normal loading contact force, the presence of a lubricant and its flow rate and temperature. The main results obtained with twin disc tests are the specimens' contact surface wear, the surface fatigue cracking analysis and surface scuffing, depending on the test conditions.

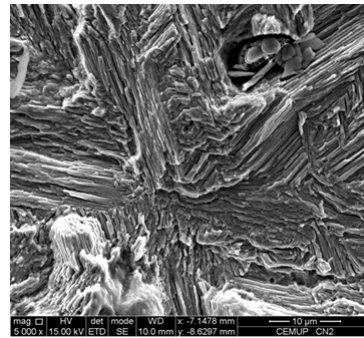Wear is the principal consequence of friction and is defined as the progressive material loss of the active surface of a body in contact with other in relative movement. This phenomenon is expressed as wear rate (wear per cycle or distance rolled) and is subsequently related to the contact parameters.

Two types of discs are being used in twin discs tests, one cylindrical and another with a 'spherical' contact surface with 35 mm radius; both discs have 70 mm diameter and 7 mm thickness, as shown in Figure 8. These types of discs were joined in pairs composed of one cylindrical disc and one 'spherical' disc. The cylindrical discs were taken from a UIC60 rail sample and the 'spherical' ones from a Spanish AVE wheel.
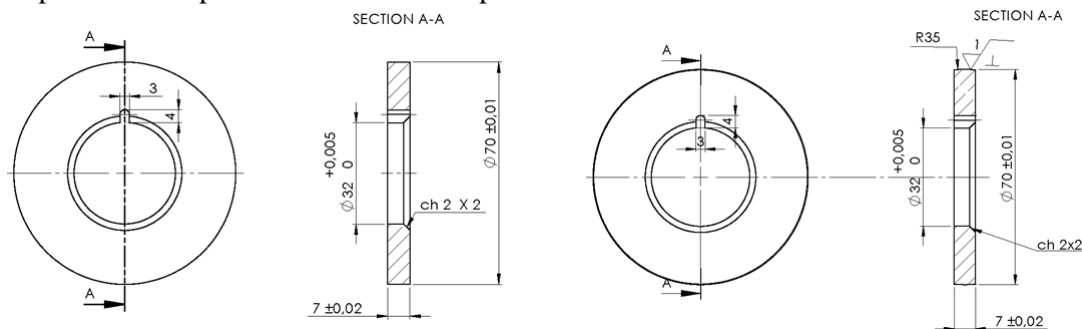
| a) 'cylindrical' disc | b) 'spherical' disc |

Figure 7 - *Disc dimensions.*

Since the specimens were extracted from the real wheel and rail profiles it was decided to verify if the specimens' orientation and location has any influence in the RCF behaviour. As shown in Figure 8, these specimens were taken in different orientations and locations on these two profiles.

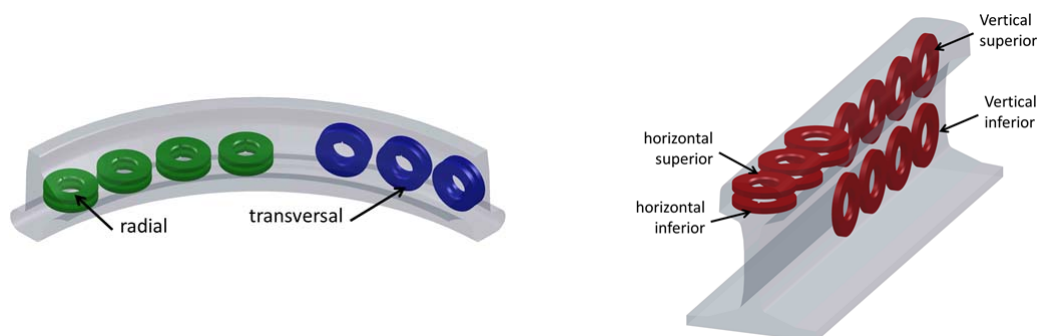*a) wheel discs' location*   *b) rail discs' location*
Figure 8 - *Location of disc specimens extraction on the wheel and on the rail.*

These specimens where tested in a twin disc machine available at CETRIB-INEGI that was recently up-graded, see [17].

The applied load was F=2200 N in order to achieve a contact pressure of $p0$=2.1 GPa. Due to the discs' geometry, load and according to Hertz theory, the contact area assumes an elliptical shape with minimum and maximum radii a=0.56 mm and b=0.88 mm respectively. The discs rolled under pure rolling conditions at a speed of 3000 rpm. In these tests, Galp TM100 oil was used as a lubricant, with no special additives. Lubricant properties are shown in Table 3.

Table 3 - *Lubricant properties.*

Viscosity at 40°C [cSt]	Viscosity at 100°C [cSt]	Density [kg/m3]	Viscosity index
100	11.1	891	95

Because the behaviour in rolling contact of these two materials was unknown and the quantity of material available to extract specimens is too small, it was decided to perform preliminary twin disc tests in two disc pairs.

These two disc pairs were composed by discs taken in different positions of the wheel and rail as indicated in Table 4.

Table 4 - *Disc pairs composition.*

# disc pair	material	position	reference
I	Wheel	transversal	TRV6
	Rail	horizontal superior	DHS2
II	Wheel	radial	RAD8
	Rail	horizontal inferior	DHI2

Along the twin disc tests mass measurements were made to evaluate mass loss due to wear. The obtained results are presented in Figure 9 and Figure 10.
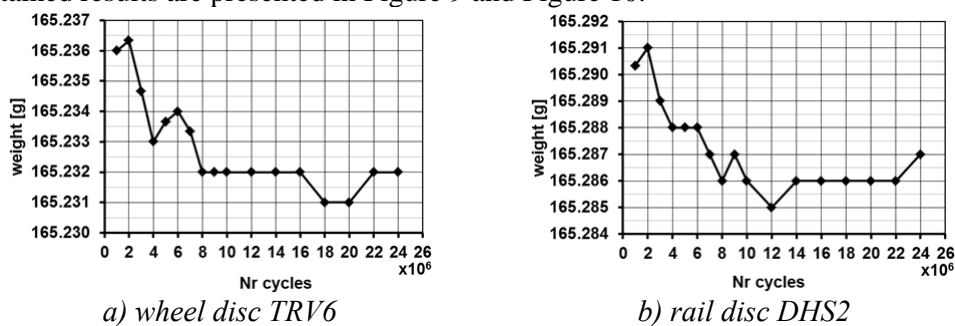
a) wheel disc TRV6   *b) rail disc DHS2*
Figure 9 - *Disc pair I weight variation.*

a) wheel disc RAD8   *b) rail disc DHI2*
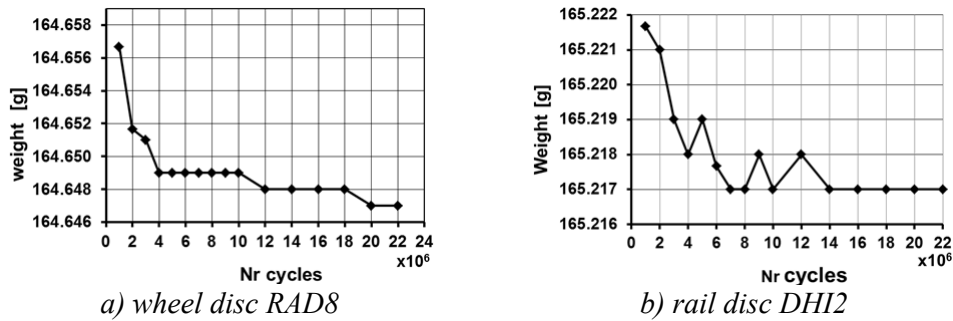
Figure 10 - *Disc pair II weight variation.*

Roughness and topography measurements were made during twin disc tests interruptions with the objective to follow their evolution during the rolling contact fatigue process. Figure 11 and Figure 12 shows the evolution of some roughness parameters such the roughness average (Ra) and the RMS roughness average (Rq) along these tests. The recorded topography roughness average (Sa) and the RMS roughness average (Sq) are also shown.

a) wheel disc TRV6   *b) rail disc DHS2*
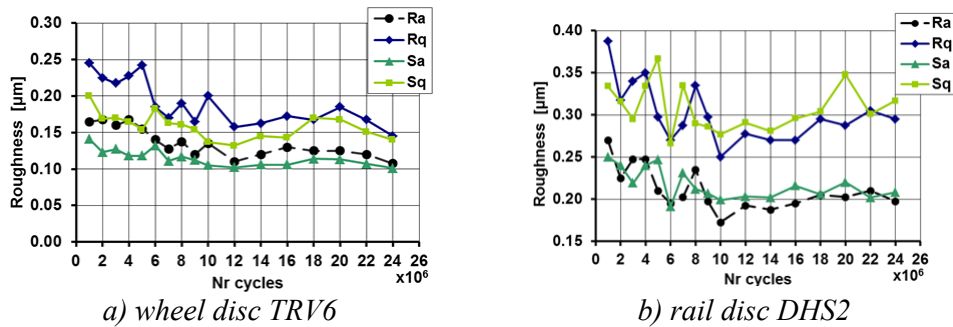
Figure 11 - *Disc pair I roughness variation.*

a) wheel disc RAD8   *b) rail disc DHI2*
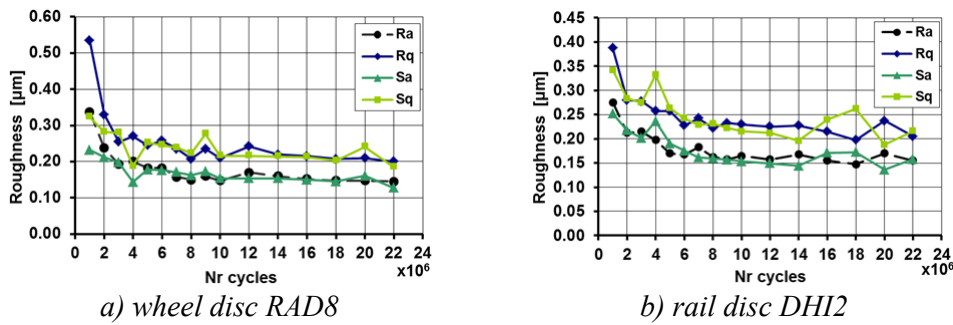
Figure 12 - *Disc pair II roughness variation.*

The 3D roughness of the disc pair II after rolling 10 million cycles is shown in Figure 13. These measurements were performed on a HOMMELWERKE T8000 measuring station equipped with a drive unit LV-50/50 E and a TKL 300 measuring probe.

a) wheel disc RAD8   *b) rail disc DHI2*
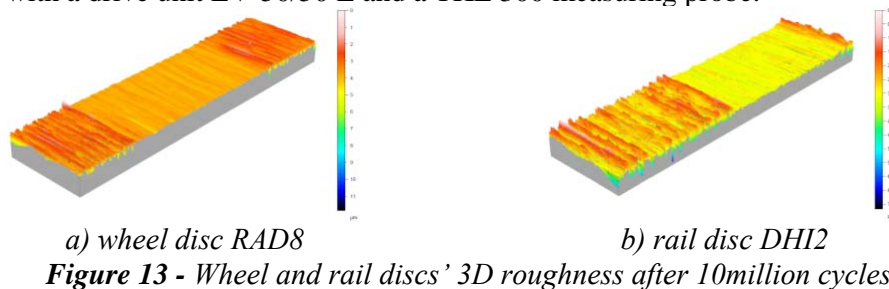
Figure 13 - *Wheel and rail discs' 3D roughness after 10million cycles.*

Some microscopic observations of the contact surfaces were made and some defects, *e.g.* pits and surface cracks, were identified, as shown in Figure 14.

a) pit	*b) crack*	*c) crack*
(RAD8 24x10^6 cycles)	*(TRV6 24x10^6 cycles)*	*(DHI2 24x10^6 cycles)*
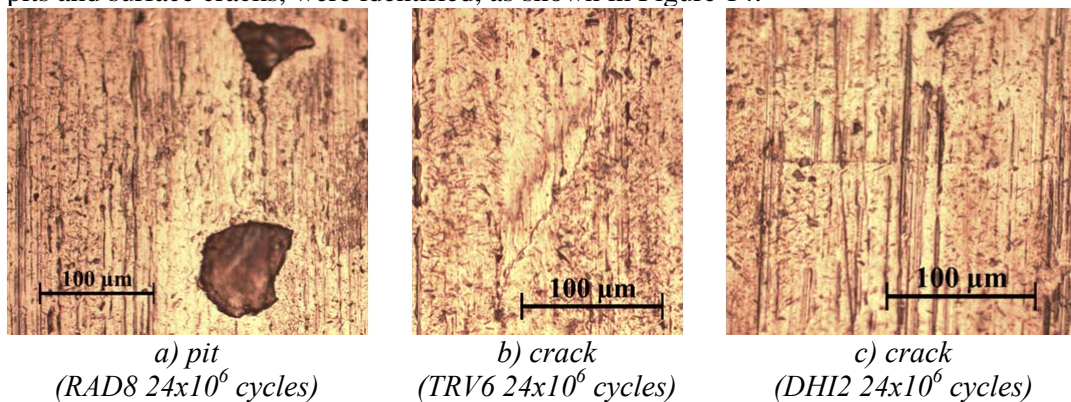
Figure 14 - *Some fatigue surface defects detected.*

5 Cocluding remarks

Mode I fatigue crack growth tests were performed according to the ASTM E647-08 standard on C(T) specimens taken from a Spanish AVE train wheel and a UIC60 rail, tested with 0.1, 0.4 and 0.7 load ratios.

The rail material presents higher fatigue crack growth rates than the wheel material.

No substantial effect of *R-ratio* was found in the Paris law regime of fatigue crack propagation.

Preliminary twin disc tests performed in wheel and rail materials allowed to conclude that:
- rolling contact fatigue cracks appear at the contact surface between 22 and 24 million cycles;
- the running-in phase of these materials ends after approximately 5 million rotations;
- the wheel material has a higher wear rate than the rail material and is more sensitive to defects initiation, since the a larger number of defects is observed at the wheel disc specimens.

References

[1]   Ekberg A., Kabo E., *"Fatigue of railway wheels and rails under rolling contact and thermal loading—an overview"*, Wear, Vol. 258, pp. 1288-1300, 2005

[2]   Cannon D., Pradier H., *"Rail rolling contact fatigue research by the European rail research institute"*, Wear, Vol. 191, pp. 1–13, 1996

[3]   Clayton P., *"Tribological aspects of wheel–rail contact: a review of recent experimental research"*, Wear, Vol. 191, pp. 170–183, 1996

[4]   Kabo E., Ekberg A., *"Fatigue initiation in railway wheels—on the influence of defects"*, Wear, Vol. 253, pp. 26–34, 2002

[5]   Zerbst U., Beretta S., *"Failure and damage tolerance aspects of railway components"*, Engineering Failure Analysis, Vol. 18, pp. 534–542, 2011

[6]   Donzella G., Faccoli M., Ghidini A., Mazzu A., Roberti R., *"The competitive role of wear and RCF in a rail steel"*, Engineering Fracture Mechanics, Vol. 72, pp. 287–308, 2005

[7]   Johnson K., *Contact Mechanics*, Cambridge University, 1985

[8]   Findley W., *"A theory for the effect of mean stress on fatigue of metals under combined torsion and axial load or bending"*, Journal of Engineering Industry, Trans ASME Vol. 81, pp.301-306, 1959

[9]   Matake T., *"An explanation on fatigue limit under combined stress"*, Bull JSME, Vol. 20, pp.257-263, 1977

[10]   Crossland B., *"Effect of large hydrostatic pressures on the torsional fatigue strength of an alloy steel"*, Proc. Int. Conf. on Fatigue of Metals, Institute of Mechanical Engineering, London, pp.138-149, 1956

[11]   Sines G., *"Metal Fatigue"*, (edited by G. Sines and J. Waisman), McGraw Hill, N.Y, pp.145-169, 1959

[12]   Dang Van K., *"Macro-micro approach in high-cycle multiaxial fatigue. Advances in Multiaxial Fatigue"*, ASTM STP 1191, D.L. McDowell and R. Ellis, Eds., American Society for Testing and Materials, Philadelphia, pp.120-130, 1993

[13]   Peixoto D.F.C., Ferreira L.A.A., de Castro P.M.S.T., *"Application of the Dang Van fatigue criterion to the rail/wheel contact problem"*, World Tribology Congress 2009, Kyoto, Japan, September 6-11, 2009

[14]   Standard ASTM E647-08, *"Standard Test Method for Measurement of Fatigue Crack Growth Rates"*, American Society for Testing and Materials.

[15]   Albuquerque C., Miranda R., Richter-Trummer V., de Figueiredo M., Calçada R., de Castro P. M. S. T., *"Fatigue crack propagation behaviour in thick weldments"*, International Journal of Structural Integrity, Vol. 3, 2, pp. 184-203, 2012

[16]   Roven H.J., Nes E, "Cyclic deformation of ferritic steel-II. Stage II crack propagation", Acta Metallurgica et Materialia, Vol. 39, 8, pp. 1735–1754, 1991

[17]   Rego A.A.L., Peixoto D.F.C.; Ferreira L.A.A., *"Rolling contact fatigue tests in a twin disc machine"*, IBERTRIB 2011- VI Iberian Congress on Tribology, Madrid, Spain, June 16-17, 2011.

FSW – Most influent welding parameters and their interactions on joints mechanical properties

E. R. Libanio[1], R. R. Rodriguez[1], A. Silva[1], M. A. V. de Figueiredo[1], P. M. G. P. Moreira[1]

[1]*Institute of Mechanical Engineering and Industrial Management, University of Porto, Porto, Portugal*

Abstract

Previous studies that can be found in literature about Friction Stir Welding are not based on optimized parameters. Trying to fill that blank, this project is focused on the optimization and prediction of the joint strength using the Taguchi technique to determine the interactions between parameters in order to achieve improved welding solutions. This paper presents the first mechanical results obtained for that frame.

A Taguchi array was chosen to define the best combinations of parameters to perform the FSW experiments. The selected parameters were: the rotational speed (A), welding speed (B), tilt angle (C), probe distance from the root surface (D), and shoulder/probe diameters ratio(E), each one with three levels. Butt joints of AA6082-T6 aluminium were performed and the mechanical properties possible to obtain from tensile tests were analyzed, tensile and yield strengths and elongation. After the welding trials, and respective analysis it was observed that the interaction between tool rotational speed and welding speed and as individual parameter the probe/shoulder diameter ratio are the most influent for the mechanical properties response, Figure 1.
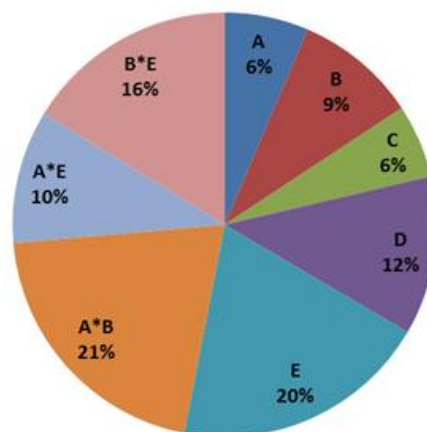
Figure 1 – Parameters influence for mechanical properties

Acknowledgments

Local Property Characterization of Friction Stir Welded Titanium- 5111

Sal Nimer[1], Jenn Wolk[2], Marc Zupan[1,3]

[1]*UMBC- University of Maryland, Baltimore County, Department of Mechanical Engineering, 1000 Hilltop Circle, Baltimore MD 21250, United States of America*

[2]*NSWCCD- Naval Surface Warfare Center, Carderock Division, 9500 MacArthur Boulevard, Bethesda MD 20817, United States of America*

[3]*FEUP- Faculdade de Engenharia da Universidade do Porto, Departamento de Engenharia Mecânica, Rua Dr. Roberto Frias, 4200-465 Porto, Portugal*

Abstract

Friction stir welding (FSW) provides many advantages over traditional joining techniques, most significantly, lower cost of fabrication. Titanium alloys provide a high specific strength and increased corrosion resistance, which makes them an attractive material for use in harsh sea environments such as those experienced by Naval marine vessels. This research is focused on understanding the mechanical properties of a FSW of a 12.7 mm thick plate of Ti-5111 in the two plate loading directions. The weld showed significant strength and ductility increases in the stir zone in both directions. The retreating side of the weld showed reduced strength and ductility below the base property. This result, however, was found to be limited to the micro-scale. The longitudinal direction showed slightly higher strengths, and lower ductility than the transverse direction. The understanding from this research will lead to future process optimizations of FSW.
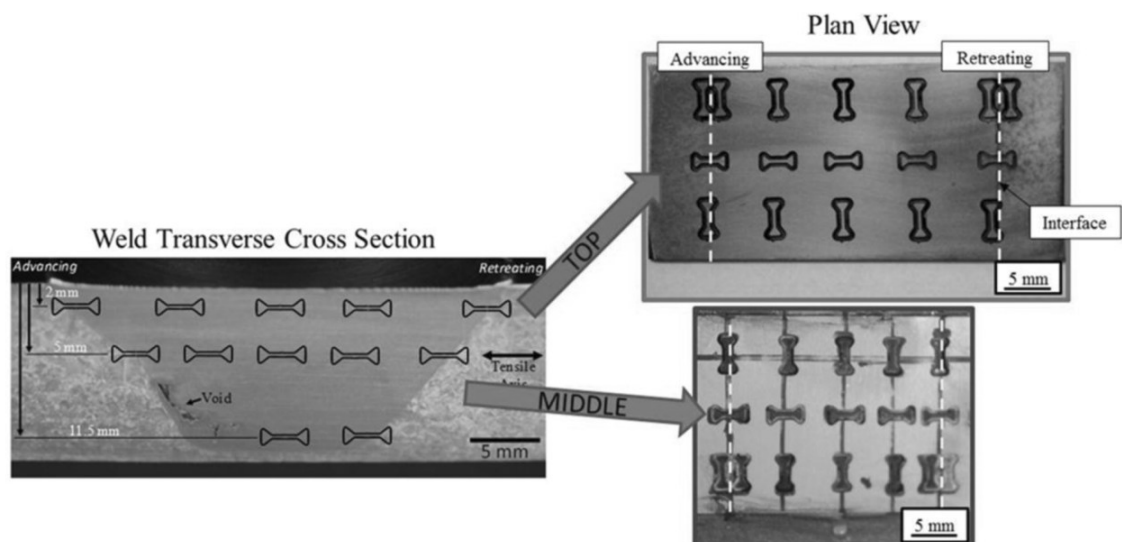
Figure 1 - Microsamples harvested from within the different regions of a Ti-5111 Friction Stir weld. The samples enable the direct measurement of local weld mechanical properties.

Defects Detection in Aeronautical Structures Joined by Friction Stir Welding

Sérgio M. O. Tavares[1], Telmo G. Santos[2],

[1]*Faculdade de Engenharia da Universidade do Porto, Portugal*

[2] *UNIDEMI, Departamento de Engenharia Mecânica e Industrial, Faculdade de Ciências e Tecnologia, Universidade Nova de Lisboa, 2829-516 Caparica, Portugal*

Abstract Damage tolerant design philosophies have a considerable impact in the weight reduction in aeronautical structures and at the same time in increasing the life cycle extensively without compromising the structural integrity, due to crack nucleation prediction and estimations of fatigue crack growth. The understanding of these phenomena allows the definition of maintenance tasks to check structural defects and their severity. The application of Non-Destructive Testing (NDT) techniques has been essential for these maintenance check-ups, since the minimum defect size to be considered in the life cycle estimations of the structure needs to be detectable by the available techniques. NDT techniques are taken into account in early phases of the structural design, given the close interplay of actual defects measurement, the probability of detection and damage propagation modeling for damage tolerant assessments and structural optimizations. In this work, the application of different state-of-the-art NDT techniques is presented, focused in structures where the riveting process can be replaced by friction stir welding. This joining technique presents several advantages over the riveting processes, although it implies the need for structural integrity of the welded joint. The NDT techniques considered are based on different physical phenomena, giving indications about the best approach for the detection of the most demanding defect in friction stir welds, root flaws. It was concluded that techniques based on eddy currents will have an important role in future NDT for new manufacturing processes as friction stir welding, since these processes have good capabilities to detect near surface defects and good resolution for the small defects detection.

1   Introduction

Friction stir welding (FSW) is a breakthrough welding process, invented in The Welding Institute, UK, by W. Thomas, [1]. It is a quasi-solid-state welding process that joins materials without fusion. The main principle of this process is a non-consumable rotating tool composed by a pin and a shoulder that is inserted into the abutting edges of sheets or plates to be joined and traversed along the line of joint, generating friction heat at the interfaces of the shoulder and pin with the base materials. This heat should be sufficient to plasticize the material creating an effect of forging and extrusion that mixes the material of the welding parts, Figure 1 a). Currently, friction stir welding is successfully applied as welding process in different applications and capable to replace older joining process, [2] due to its advantages including leaner joints with less defect susceptibility.

Despite the fact that FSW leads to low defect rates, the process needs to be controlled and the weld inspected to ensure that no defect is present that could compromise the structural integrity. FSW defects have several sources as too cold or too hot welds, tool geometry, tool positioning control, excess of impurities or oxides along the welding line and large gaps along the welding line. These sources can induce several defects as lines of oxides, tunnel defects

due to the insufficiency of heat generation, "kissing-bond" defects due to low frictional force and low heat in the nugget zone, and welding root flaws due to the lack of penetration of the pin instigated by the positioning control instabilities or fluctuations in the plate's flatness, [3] and [4].

a) Friction stir welding process.   *b) Root flaw due to the lack of pin penetration.*
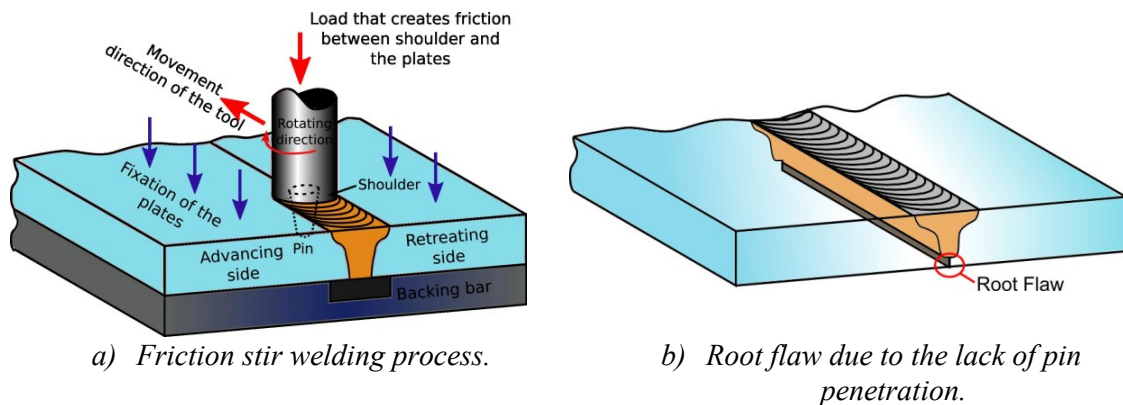
Figure 1 *- Friction stir welding process.*

After an adequate determination of the welding parameters, most of these defects are 100% avoidable, with exception of the root flaws. It is not possible to ensure a constant thickness of the workpieces and constant tool penetration, therefore the distance between the pin tip and the backing bar is not constant, resulting in root flaws when this distance is too high. In addition, the positioning control of the tool can experience perturbations creating occasional root flaws. Figure 1 b) shows schematically a weld with a root flaw. This type of defect has a high stress concentration factor that reduces considerably the fatigue life and the structural integrity, [5].

NDT techniques are routinely used to inspect aeronautical structures and are taken into account in early phases of the structure design given the close interplay of actual defects measurement, and damage propagation modeling used in damage tolerant design. Several types of NDT techniques are available to inspect different types of properties. These techniques can be categorized into six main groups: visual, penetrating radiation, magnetic-electrical, mechanical vibration, thermal and chemical-electrochemical.

Most of these techniques are based on the measurement of the structure reaction to a wave beam; thus these techniques can as well be grouped based on the operation frequency, giving some guidance about their maximum resolution. However, the major limitation usually lies in the sensor sensitivity in the measurement of the structure reaction to the beam. NDT is classified as active or passive, [6]. In the active techniques, energy stimulus is fed onto the structure and its response is measured, with variations to the normal behavior usually indicating that an anomaly is present. Examples of the active techniques are ultrasonics inspection, eddy currents and X-rays. The passive techniques analyze the structure under its load environment or with a visual inspection of the surface, as example: visual inspection, liquid penetrant and acoustic emission, [7]. NDT technologies based on the electromagnetic phenomena and in the acoustic phenomena are the most interesting for friction stir welds, since they can penetrate through the structure and give an indication of the defect depth. On this work, three different innovative active techniques were tested to detect defects in friction stir welded samples. The applied techniques have three different energy sources: ultrasounds,

eddy currents and X-rays. All of them allow looking through the material thickness, enabling the detection of porosities and tunnel defects along the welding line.

2   State of the art of NDT for FSW

Prospective NDT techniques for LOP defects on friction stir welds are based in multiple physical phenomena as X-rays, ultra-sounds (US) and the eddy currents (EC) techniques. The X-Rays mainly detect variations of density, using the radiation absorption effect. However, root flaws do not present significant volumetric discontinuities or density variations, inhibiting the application of this technique. The application of higher resolution sensors and dedicated to this type of defects may be able to deal with this discontinuity; however these sensors are not fully developed.

The ultrasound, in conventional mode or in time of flight diffraction (ToFD) or in phased arrays present advantages compared with other NDT, depending on the materials and defect type, however they have limitations inherent to their physics, namely, the high sensibility to the interfaces including the sensor, the work piece and the transducer, the acoustic attenuations and the limit of defect size (detectability).

The application of the eddy current to aluminum welds may be a prospective technique for root flaws' detection, mainly due to its physical effect, which concentrates the energy density at the surface of the component increasing its sensibility to surface discontinuities.

Several techniques were investigated in order to improve the feasibility of the detection of root flaws. For instance, with eddy currents techniques, Mandache et. al. [8], proposed the application of data image software analysis using the Sobel operator to process the results acquired by pulsed eddy currents in order to distinguish the characteristics of the signal in the presence of a defect. However, this post processing technique proves ineffective in the improvement of the root flaws detection, since from the measured data it was not possible to identify eventual information or variation related to a root flaw for small depths. Lamarre et. al. [9], explored the application of Phased Array US in volumetric defects in the root of friction stir welds. They proposed the application of different NDT techniques combined with data fusion algorithms, in order to increase the feasibility of detection. However the results accomplished didn't show high reliability and repeatability in the detection of root flaws. Similar results were reached by R. Smith [10], applying pulsed eddy currents in order to evaluate the interferences caused by root flaws.

3   Testing Samples

Four AA2024-T3 friction stir welding samples were scanned with three NDT techniques in order to determine their feasibility in the detection of root flaws in friction stir welds without special preparations or changes in the inspection equipment. Three of these samples have root defects, one 200 μm deep, other 60 μm deep and another with oxides alignment along the weld line ("kissing-bond"). The fourth specimen is a regular weldment without any defect. These samples were produced in the scope of the doctoral thesis of dos Santos, [11], where new eddy current probes were developed to detect root flaws in welded specimens in a more efficient way. During the tests, the scanned specimens did not have any indication about the type of defect or defect size, in order to not influence the final conclusions. Figure 2 shows the four samples examined and respective references.

Sample A

Sample B

Sample C

Sample D
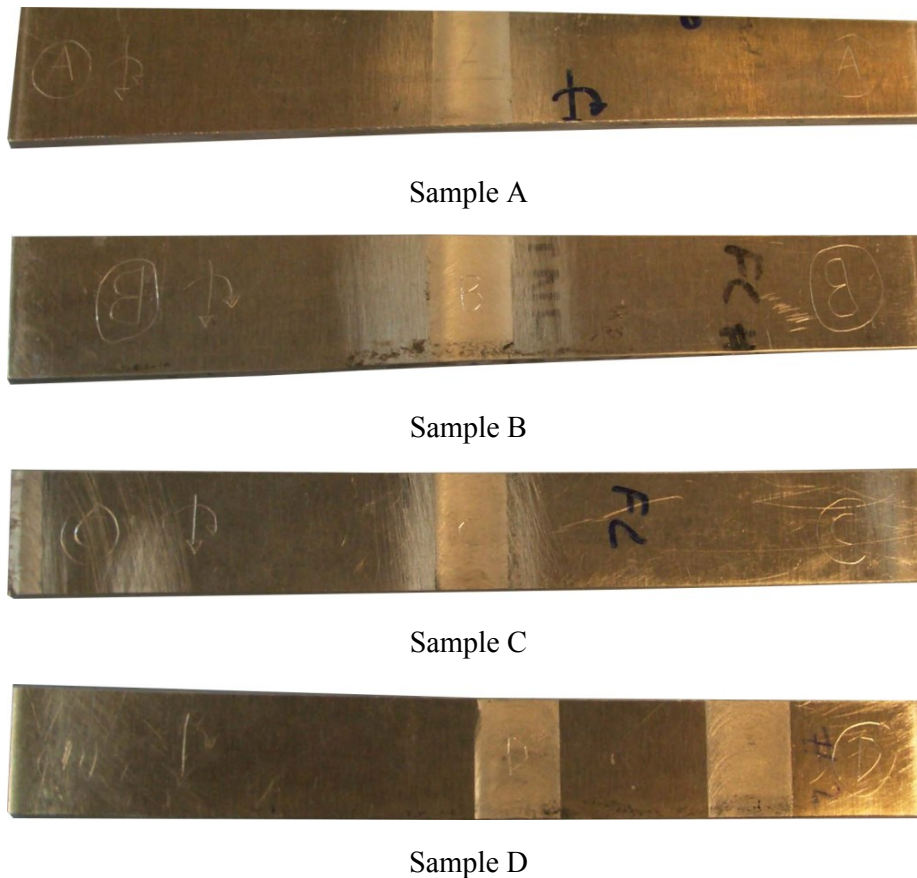
Figure 2 - *Friction stir welds tested.*

4   Results

4.1   Scanning Acoustic Microscope

The acoustical microscopy technique, also known as Acoustic Micro Imaging (AMI), was applied to detect root flaws in the FSW specimens. This type of microscope takes advantage of high frequency ultrasounds, typically from 10 to 500 MHz, to generate images through the thickness. This technique is based on the pulse-echo effect, where short bursts of ultrasonic energy are introduced in the structure. These bursts cross through the structure thickness until they encounter reflecting surface; at this point an echo is reflected will be measured by a transducer, [12]. Through the application of ultra-high frequency ultrasounds, AMI enables to find and characterize physical defects as cracks, voids and porosity that occur during manufacturing or under normal component operation.

The FSW were scanned using the last generation of acoustic micro imaging microscope, Sonoscan Gen5 C-Mode Scanning Acoustic Microscope, shown in Figure 3.

Two different piezoelectric sensor transducers with different operating frequencies were used to measure these specimens: one with 50 MHz, with the capability to measure through the thickness, but with less resolution than higher frequency transducers and other transducer, with a work frequency of 230 MHz, was focusing just below the back surface of the weld area and gating just past the echo from the top surface to collect information about the bulk material below this surface. A focal length of 0.375 in (9.5 mm) was used for all 4 specimens.

Figure 3 *- Sonoscan scanning acoustic microscope.*

Figure 4 shows an example of the scans obtained. This scan was done for the sample B, with the 230 MHz probe and with a focus near to the upper surface (about 60 μm from the surface). In this Figure, aligned discrete dots along the weld line are visible. It is assumed that these aligned discontinuities correspond to a root flaw caused by an incomplete penetration of the pin during the welding. With the spectrum analysis presented in Figure 4 it is not possible to identify porosity depth, since the scale of 200 ns/div corresponds to about 1.2 mm/div (assuming the sound speed in aluminum of 6300 m/sec). However, it is expected that with some modifications of this Scanning Acoustic Microscope it will be feasible to identify these defects in a more effective way.
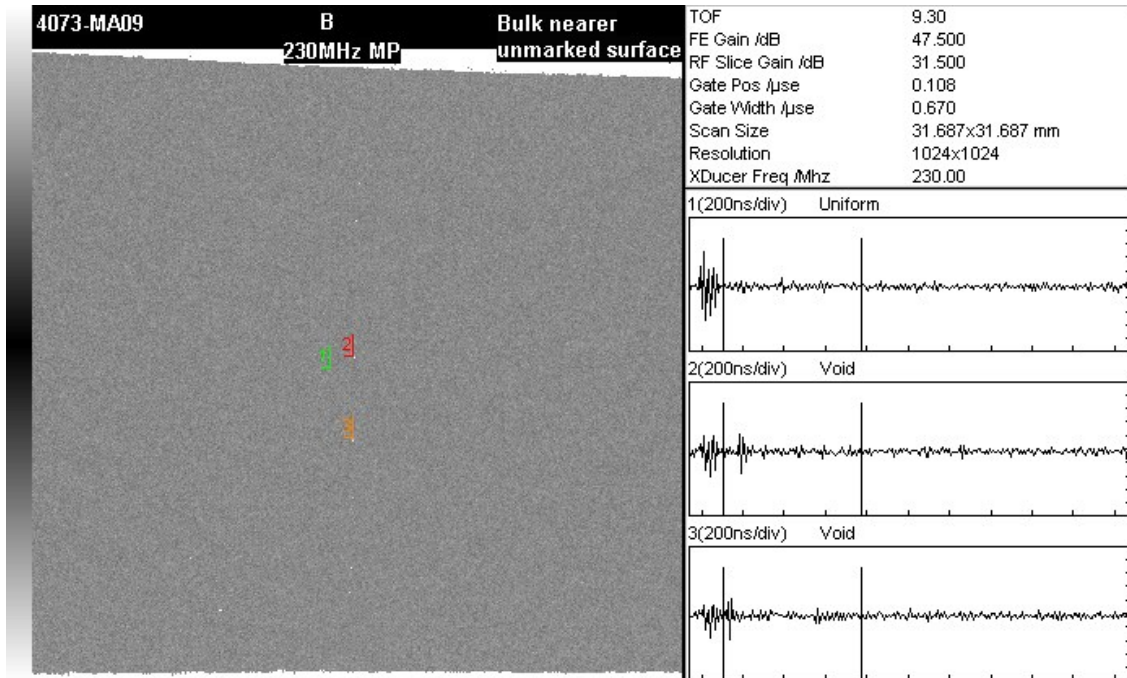
Figure 4 *- Sample B scanned with 230 MHz probe and spectrum analysis.*

4.2 X-ray Computed Microtomography

X-ray Computed Microtomography (XMT) or computed tomography is a nondestructive technique that has been developed using digital panels with high resolution when compared the first digital panels or films. This technique was applied in this work in order to understand if it can offer better resolution for root flaws and kissing bond detection or give more information about the weld region. The measurements were done at Center for Nanoscale Systems in Harvard University (Cambridge, MA, USA), with an X-TEK HMXST225 equipment. This equipment is presented in Figure 5 and was mainly composed by an open source X-ray tube with a maximum resolution of 3-5 μm in reflection mode and 2 μm in transmission mode.

Figure 5 - XTEK tomography equipment with X-Ray source.

Due to the time required to perform each measurement, the procedure was tested just in the sample A. The area of the inspection was confined to the welded region of the specimen. The results are composed by 1800 tomograms, which were used to reconstruct a 3D model of the scanned area. Figure 6 shows two views of this reconstruction, with some degree of transparency to allow the visualization of the internal appearance. The software allows the application of different filters and refinement in the model, however major imperfections were not detected with this technique, even porosities that were detected with AMI. The increase of resolution in this technique might be possible using other sensor closer to the specimen.

a) *Bottom side (Filter A)*   b) *Root side (Filter B)*
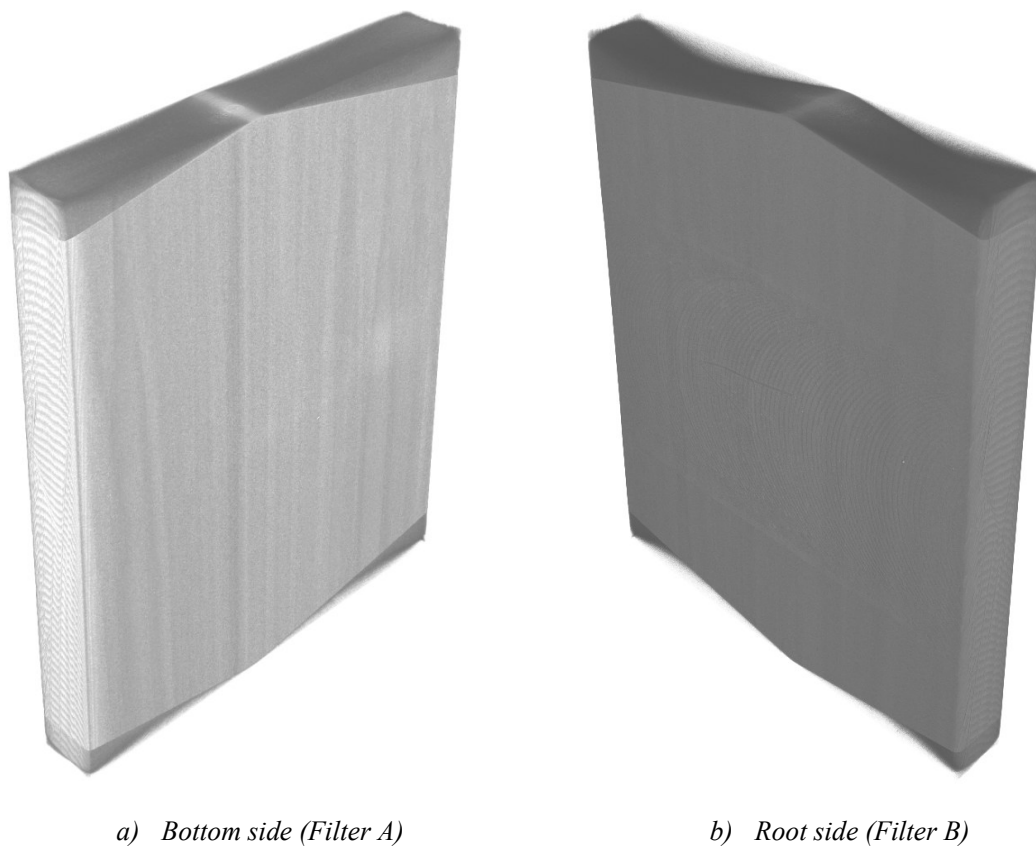
Figure 6 - Computed tomography of the sample A.

4.3   Eddy Currents: Planar Spiral Probes

The FSW samples were also tested using conventional planar circular spiral eddy current probe with 20 coils, Figure 7. The spiral probe has an outside diameter of 9 mm and the coils have 50 μm width, separated by 100 μm.
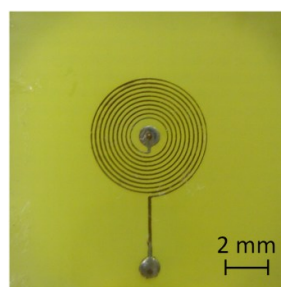
Figure 7 - *Planar circular spiral probe composed by 10 coils and an outside diameter of 9 mm.*

The impedance data (Re{Z} and Im{Z}) was acquired from the root side, along a sweep on the transversal direction to the weld joint. The starting point of the tests was set to 25 mm in the retreating side of the weld bead, and 50 mm long, the segments were characterized in direction to the advancing side, with 250 μm space within each acquisition. The real and imaginary part was measured at different frequencies from 10 kHz to 2 MHz.

Figure 8 presents the acquired results Re{Z} for a frequency of f = 250 kHz. The three curves concerning to the different defects conditions present a very similar trend between

them. In fact, no distinctive signal feature that can allow to differentiate each defect condition was found. As FSW process promotes material conductivity fluctuations, even without imperfections, the weld bead is responsible for the increase of the signal in all defect conditions.

Indeed, the absolute planar spiral probe can only reproduce the global spread increase of conductivity field due to the FSW bead. Such probes are not able to differentiate small suddenly variations of conductivity, caused by a local root defect with small size as those tested. These results exemplify the difficulties that can be found using NDT tecniques based in conventional eddy current techniques to detect root flaws in friction stir welds.
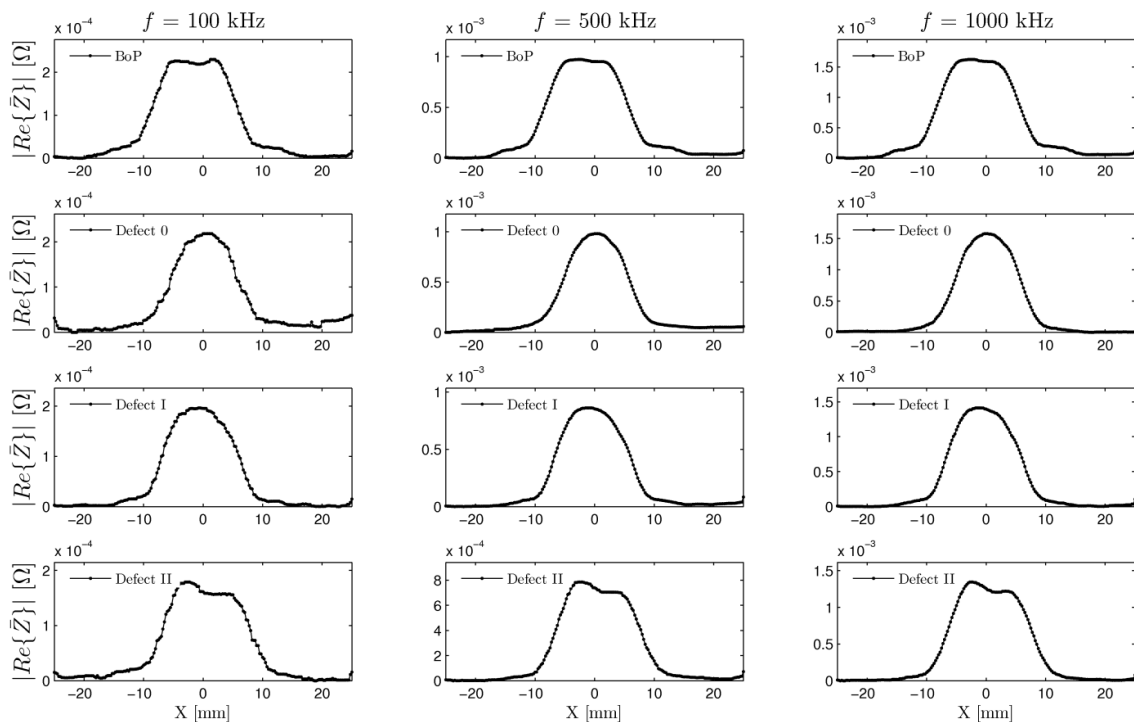
Figure 5 - *Eddy current results using a planar spiral probe for a bead on plate FSW and for defects Type 0, I and II for 100 kHz (left), 500 kHz (middle) and 1000 kHz (right) frequencies*

5   Conclusions

Root flaws in friction stir welds, as the lack of penetration or kissing bond, are defects promoted by inadequate selection of process parameters that can occur in industrial applications. These defects weaken the structural fatigue strength, a fact not tolerated in critical structures. In this way, effective and reliable nondestructive techniques are required for the detection of these flaws.

A benchmark with eddy current technique using conventional and spiral planar probes, ultrasound acoustic micro imaging and X-rays in micro tomography mode, was done evaluating their feasibility to detect lack of penetrations in the friction stir welds.

The results achieved show difficulties in the detection of these types of defects and the defects couldn't be detected with high efficiency, mainly due to lack of special discontinuity. Nevertheless, promising results were obtained with the acoustic micro imaging and with eddy

currents. Furthers developments in these two techniques will allow the detection of root flaws with less than 60 μm with high reliability in order to improve the structural integrity of FSW joints.

6   Acknowledgments

7   References

[1] W. M. Thomas, E. D. Nicholas, J. C. Needham, M. G. Murch, P. Templesmith and C. J. Dawes, 'Improvements relating to friction welding', WO/1993/010935, International patent no. PCT/GB92/ 02203, 1992.

[2] Lohwasser, D. and Chen, Z., 'Friction Stir Welding: From Basics to Applications', CRC Press, 2010.

[3] R. Leal and A. Loureiro, "Defects Formation in Friction Stir Welding of Aluminium Alloys", Materials Science Forum, vol. 455, pp. 299-302, 2004.

[4] H. Chen, K. Yan, T. Lin, S. Chen, C. Jiang, and Y. Zhao, "The Investigation of Typical Welding Defects for 5456 Aluminum Alloy Friction Stir Welds", Materials Science and Engineering: A, vol. 433, no. 1-2, pp. 64-69, 2006.

[5] C. Zhou, X. Yang, and G. Luan, "Effect of Root Flaws on the Fatigue Property of Friction Stir Welds in 2024-T3 Aluminum Alloys", Materials Science and Engineering: A, vol. 418, no. 1-2, pp. 155-160, 2006.

[6] C. Hellier, "Handbook of Nondestructive Evaluation", McGraw-Hill Professional, 2001.

[7] D. E. Bray and R. K. Stanley, "Nondestructive Evaluation: A Tool in Design, Manufacturing, and Service", Boca Raton: CRC Press, rev. ed., 1997.

[8] C. Mandache, L. Dubourg, A. Merati, M. Jahazi, "Pulsed eddy current testing of friction stir welds", Materials Evaluation, ASNT, Nº. 4, Vol. 66; pp. 382-386, 2008.

[9] A. Lamarre, "Eddy current array and ultrasonic phased-array technologies as reliable tools for FSW inspection", Proceedings of the 6th International FSW Symposium, Canada, October 2006.

[10] R. Smith, "The potential for friction stir weld inspection using transient eddy currents" Insight – Non-destructive Testing and Condition Monitoring N.47, Vol. 3, pp.133–143, 2005.

[11] T. Santos, "Ensaios Não Destrutivos por Correntes Induzidas: Desenvolvimento e Aplicação: a Soldadura por Fricção Linear", PhD thesis, Universidade Técnica de Lisboa - Instituto Superior Técnico, Lisbon, Portugal, July 2009.

[12] ASM International Handbook Committee, ASM Handbook, Volume 17 - Nondestructive Evaluation and Quality Control. ASM International, 1989.

Study of Sandwich Panels with Metal Foam Core for Forming Process

H. Mata[1], R. Natal Jorge[1], A. D. Santos[2], M.P.L. Parente[1], R. A. F. Valente[3], A.A. Fernandes[1]

[1]*DMEC - Faculty of Engineering, University of Porto, Rua Dr. Roberto Frias, 4200-465 Porto, Portugal, {dem09005, rnatal, mparente, aaf}@fe.up.pt*

[2]*INEGI - Faculty of Engineering, University of Porto, Rua Dr. Roberto Frias, 4200-465 Porto, Portugal, abel@fe.up.pt*

[3]*Department of Mechanical Engineering University of Aveiro, 3810-193 Aveiro, Portugal, robertt@ua.pt*

Abstract On this work, the authors present the development and evaluation of an innovative system able to perform reliable panels of sandwich sheets with metallic foam cores in order to assist in the design process of forming of composite blanks. This suitable combination of materials provides, on one side, a higher level of strength and stiffness ratios to its mass or weight. As a result of these specific properties this kind of composite turns out to be a highly attractive material, particularly for "ultra-light" structural applications. The present work aims to study the behavior of sandwich structures, composed by a foam core with two outer layers of metal sheet (all structure being aluminum). The study of the composite structure behavior, its mechanical characterization and numerical modeling is essential to analyze the mechanical performance of structures based on this type of materials. This step is fundamental in preliminary design, since the different materials of the composite structure show different mechanical responses [1]. The differences in mechanical behavior are demonstrated by the axisymmetric compressive stress states tests and also by the influence of hydrostatic pressure in the yield of the aluminum foam porous material, while the yield of the homogeneous solid material (aluminum sheet) can be considered as pressure insensitive [2]. In order to correctly characterize separately these two materials of the composite (outer layers and core), a set of tests were performed. The characterization of the aluminum sheet was performed in a series of tensile tests, using three different rolling directions. For the metal foam core characterization a series of uniaxial compression tests were performed. The experimentally obtained results were applied in the development of numerical models for this kind of sandwich structure. The models include elastoplastic constitutive relation, where a distinct plastic domain for different materials is accounted for, as well as, the influence of hydrostatic pressure in the yield of the porous material. Also, the validation of the elastoplastic models is performed by comparing results obtained by numerical simulations with those obtained experimentally.

1 Introduction

The design of passive safety systems in transportations still have a great potential for development as a way to reduce deaths and injuries, which is also associated to the economic costs and social impacts associated with this problem. On the other hand, from an environmental standpoint, the use of advanced composite materials to this end can also represent an optimized level of energy efficiency. The impact energy absorption, with the use of a well-designed light-weight protection system, is directly related to the thermal efficiency

and consumption of the engines, thus leading to a lower level of greenhouse gases sent to the atmosphere.

It is within this framework that fits and makes sense the study and development of composite material systems, composed by a core of aluminium foam, which separates two skins of aluminium sheets (Figure 1). The outer layers of the composite are in aluminum sheet with 1 mm thickness and the core in aluminum metal foam has 8 mm thickness.
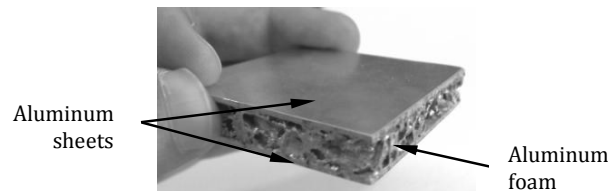
Figure 1 - *Composite structure investigated.*

From the viewpoint of the structural capabilities of the composite structure, the metal foam core is responsible for absorbing energy when plastically deformed, as well as to provide good insulation of vibrations, reduction of weight of the structure. On the other hand, the aluminium plates are responsible for the mechanical resistance factor for the global structure, as well as for granting its structural integrity. This suitable combination of materials provides, on one side, a higher level of strength and stiffness ratios to its mass or weight. As a result of these specific properties this kind of composite turns out to be a highly attractive material, particularly from the viewpoint of "ultra-light" structural applications.

In this work it was investigated experimental and numerical this sandwich panels in order to assist in the design process of forming using a Hydroforming process. This study was dividing in two parts, an experimental component to evaluate the behaviour of the composite and the materials separately. It was also using this first part to obtain the parameters to be using in another second part of numerical work. The numerical work can be described as a set of numerical simulations developing using the finite element method, incorporated on abaqus software and using the parameters obtained previously. The results of the two parts are compared at the end and conclusions are taken.

1.1   Aluminium sheets

Material of the outer skins of the composite is an aluminum alloy (AlMg$_3$) EN AW 5754 (Figure 2), non-heat treatable, 1 mm thickness, with a typical modulus of elasticity of 70GPa, Poisson ratio 0.33 and 80 MPa yield stress [3].

Figure 1 - *Aluminum sheets of the outer skin of the composite.*

1.2   Aluminium metal foam

Metal foams usually retain some of the physical properties of the base material, i.e., they are non-flammable and remain non-flammable, they are usually recyclable and usually they have the ability to float in water. The coefficient of thermal expansion is also similar to the

base material, however the thermal conductivity is lower [4 - 5]. The current study uses the closed cell foam, Alporas (Figure 3), developed in Japan by the Shinko Wire Company in the 90's. It is an aluminium alloy AlCa1,5Ti1,5 with a density of 0.25 g/cm3, and a relative density ($\bar{\rho}$) of about 9%, being the porous size of 4-6 mm (Alporas foam $\bar{\rho} = 9\%$) [3].
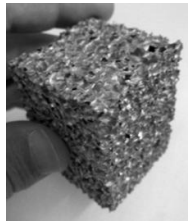
Figure 3 - *Aluminium metal foam (Alporas foam $\bar{\rho} = 9\%$).*

2   Sandwich material characterization and numerical simulations

2.1   Aluminium sheets

The characterization of the aluminum sheets are done by performing tensile test. To these characterization three different directions of rolling 0º, 45º and 90º were being considering. To this end specimens were cut from the panel with the dimension shown in Figure 4.
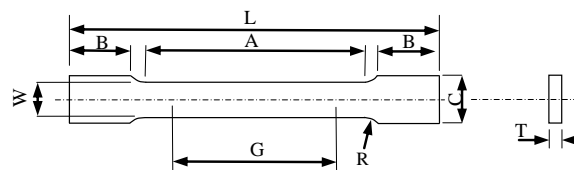
G=50, W=12.5, R=20, L=200, A=75, B=50, C≈20,
T- Thickness [mm]

Figure 4 - *Specimens used on the tensile test.*

Typically the aluminum alloys present a relative degree of anisotropy, and considering these three directions of rolling we can identify and measure the difference between those three directions.

In these work two methods to obtain the characterization were used:
•   A standard mechanical system, with load cell and displacement transducer – global measurement;
•   A Digital Image Correlation method (ARAMIS system), providing local state of deformation on selected surface of sample, Figure 5.
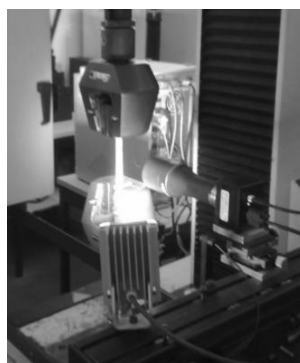
Figure 5 - *Tensile test.*

These tests were performed; one for each direction and results are presented on the graph of Figure 6.

Table 1 - *Number of specimens tested by direction.*

0º	45º	90º	Total
1	1	1	3
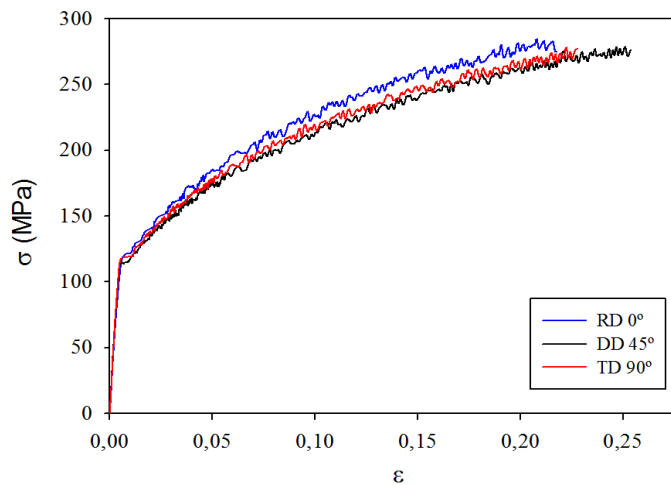
Figure 6 - *True stress – strain curve of the 3 specimens.*

Observing the graph, the curves are similar in progress, but with slightly different depending on each direction, obtained using the traditional method of measure. Higher hardening for 0º when compared to 45º and for 90º the curve presents a serrated be-havior typically of Al/Mg aluminum alloys at select-ed strain rate. The curves of the graph on Figure 6 define the properties of the aluminum sheets. The elastic parameters of the elastoplastic model of the sheet are shown in the Table 2

Table 2 - *Elastic constants - Aluminum sheet.*

	AW 5754
Young Modulus E [GPa]	70
Poisson's Ratio	0.3

It was also obtained for any direction and for any test the respective r-values as are shown in the Table 3.

Table 3 - *Lankford's r-value. - Aluminum sheet.*

	Initial yield stress [MPa]	r-value
r_0	116.45	0,61
r_{45}	108.57	0,84
r_{90}	116.45	0,82

2.2 Aluminium foam

The characterization of the aluminum foam (Alporas foam $\bar{\rho} = 9\%$) has been done by performing uniaxial compression test. To establish this characterization the dimension of the specimen was defined as having to be at least seven times the size of the cells to dissipate the effects of size. The three specimens used in these tests have a size 40x40x50 mm (Figure 7).
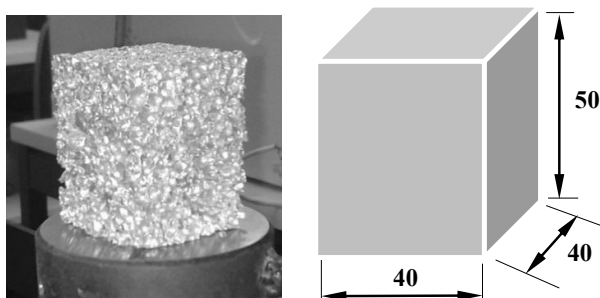
Figure 7 - *Specimen of compression test (Alporas foam $\bar{\rho} = 9\%$).*

From the modelling point of view, as it was considered before with the aluminium sheet, three planes of symmetry with their boundary conditions were considered, i.e., only 1/8 of the real specimen was modelled (Figure 8). The axial compression simulations were also developed in ABAQUS Standard, using 27000 elements of type C3D8RH. In this model was also used a hard surface, where is applying the displacement.
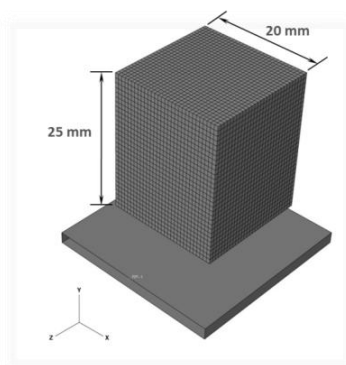
Figure 8 - *Numerical modelling – Uniaxial compression test.*

The elastic parameters Young Modulus, Poisson's Ratio are presented in Table 4.

Table 4 - *Elastic constants - Aluminum foam.*

	Alporas foam $\bar{\rho} = 9\%$
Young Modulus E [GPa]	0.35
Poisson's Ratio	0.33

The plastic parameters used for defined de numerical model are the Compression Yield Stress Ratio k and Plastic Poisson's Ratio υ_p. These two constants can be calculated using the following expressions resulting by geometric definitions of the model [6]:

$$\alpha = \frac{3k}{\sqrt{9-k^2}} \tag{1}$$

$$k = \sqrt{3\left(1-2\nu_p\right)} \tag{2}$$

According to the Deshpande constitutive model for foams, with closed cell structure, the parameter which defines the shape of the yield surface (α) is approximately 2.08 [1] and the related plastic constants can be calculated as:

$$2.08 = \frac{3k}{\sqrt{9-k^2}} \Leftrightarrow k = 1.71$$

$$k = \sqrt{3\left(1-2\nu_p\right)} \Leftrightarrow 1.71 = \sqrt{3\left(1-2\nu_p\right)} \Leftrightarrow \nu_p = 0.013$$

As a result of this test we have the three curves represented in the graph of the Figure 9 a). The three curves are in a good agreement with traditional curves, which describe the typical behaviour of porous material. Comparing the curves among themselves, we can see that the three are very similar, and this allows defining the characteristic curve of the foam (Alporas foam $\bar{\rho} = 9\%$) of the core of this composite. Another relevant aspect and characteristic of the porous material are the large capacity of compaction for a small lateral expansion material and this is visible on the Figure 9 b). A compaction of 30mm, in a specimen with 50mm which is a large compaction, and the lateral expansion it is only approximately 3mm for the three specimens in each transversal direction.
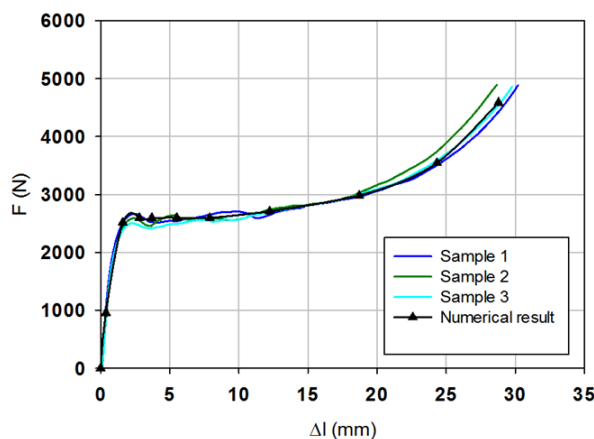
a) Results Tests/Numerical   b) Specimen compression
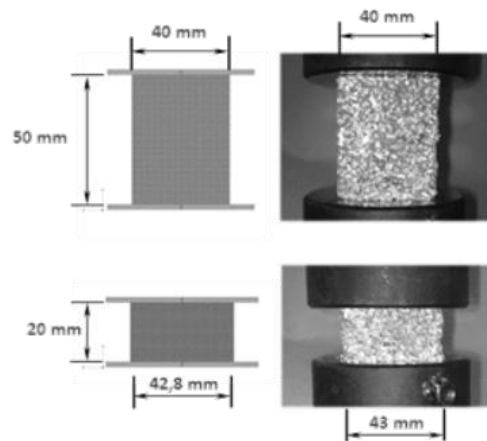
Figure 9 - *Comparison of results - Uniaxial compression tests.*

3   Conclusions

In this work a set of computational models based on the finite element method were developed, which are able to correctly characterize the stress-strain (force-displacement) relations of aluminium composite that are involved in tensile and compressive tests of the

skin metallic sheet and metallic core, respectively. Therefore, it is possible to apply those models to the numerical simulation of complex loading cases, and try to numerically reproduce the real behaviours of this material in demanding applications. Another relevant aspect from the present work is the conclusion that anisotropic effects must also be taken into account in future evolutions of this characterization.

For the foam, we showed the typical stress – strain curve in compression. With this behaviour we could also apply an elastoplastic model valid for this type of material and it was possible to obtain the behaviour similar to the experimental characteristic curve. This shows that the numerical study developed in this work can be used for the numerical modelling of this composite structure for other studies.

Acknowledgement

4   References

[1]   Deshpande, V.S., and N. A. Fleck, Isotropic Constitutive Model for Metallic Foams; Journal of the Mechanics and Physics of Solids, pp. 1253–1276, 2000.

[2]   Ashby, M.F. et al., Metal foams: a design guide, Oxford, Butterworth-Heinemann, 2000.

[3]   http://www.gleich.de

[4]   Duarte, I. M. A., Espumas metálicas Processo de fabrico, caracterização e simulação numérica, Ph.D. Thesis, FEUP, Porto, 2005.

[5]   Mata H. et al, FEM analysis of Sandwich Shells with Metallic Foam Cores, Key Engineering Materials Vol. 473 pp. 659-666, 2011.

[6]   Abaqus, Inc. Abaqus Analysis User's Manual Version 6.4.

Assessment of the interlaminar fracture toughness on nano-filled epoxy/glass fibre composites

H. Silva[1], C. Capela[2], J.A.M. Ferreira[3], J.D.M. Costa[3]

[1]*CEMUC, Mechanical Engineering Department, ESTG, Polytechnic Institute of Viseu,*
heni@demgi.estv.ipv.pt

[2]*CEMUC, Mechanical Engineering Department, ESTG, Polytechnic Institute of Leiria*

[3]*CEMUC, Mechanical Engineering Department, University of Coimbra*

Abstract The improvement of the interlaminar fracture toughness (IFT) has long been an important goal in the fiber reinforced composites field in order to enhance mechanical properties performance. For that purpose some research has recently explored the use of nanoparticle reinforced matrices to improve its interlaminar strength. In present paper it was used a small quantity of nanoclays and carbon nanotubes in order to enhance IFT of glass/epoxy composites. The paper studied mode I and mode II interlaminar fracture toughness improvements obtained by the use of nanofillers in epoxy matrices. The composites sheets were produced by a moulding in vacuum process with the flow directed to get particles preferentially orientated. Mode I interlaminar fracture toughness was significantly improved by the incorporation of nanoclays and carbon nanotubes into the resin, reaching 17% for 1% of nanotubes and 31% for 3% of nanoclays. Mode II IFT exhibits significant dispersion, but on average was obtained a significant increase for composites incorporating nanoparticles, reaching about 30% for 1% of nanotubes and 50% for 3% of nanoclays.

Introdution

Polymer fiber reinforced laminate composites have been widely used in aerospace, automobile and marine industries, despite their low interlaminar fracture toughness (IFT) caused by conventional manufacturing techniques do not provide orientation of the fibers in the thickness direction to sustain transverse load [1]. The improvement of interlaminar strength depends not only on the fiber and matrix properties but also on the interfacial properties between the fibers and the matrix [2]. The enhancement of IFT can be done by modifying the interfacial properties.

Many researchers have explored the matrix modification through the addition of nanofillers, such as nanoclay or nanotubes, in order to improve fracture toughness, but the results reported in the literature showed no apparent consensus. For example, Weiping et al. [3] studied the performance of epoxy nanocomposite reporting an increase by 80% and 152% in K_{1C} e G_{1C} respectively, at 12 phr clay loading, while, in contrast, Kornmann et al. [4] and Kinloch et al. [5] concluded that the fracture toughness of the epoxy/clay nanocomposites is lower than that of microcomposite. The outcomes obtained when using multiwalled carbon nanotubes (MWNT) in epoxy resin have also produced mixed results. Allaoui et al. [6] doubled the Young's modulus and yield strength of epoxy matrix by adding 1 wt% of MWNT. However, Lau [7] obtained a negative effect on the mechanical properties using MWNT filler in epoxy resin.

The improvement of the IFT of hybrid laminate composites by using nanofilled matrices was recently studied with positive results. For example, Zhou et al. [8] and Goinv et al. [9]

obtained an increase of above 20% on IFT adding 2 wt% carbon nanofibers and 0.3 wt% double-walled carbon nanotube, respectively, into glass fiber reinforced epoxy.

The orientation of the particles on the interface layer can play a significant role on mechanical properties and particularly on IFS. Literature results suggest that distributing the nanoparticles preferentially orientated into the resin between layers, may improve the IFT of fiber reinforced laminated composites. An example of an improvement of IFT was obtained by Fan et al [10] in glass/epoxy composites filled with a small quantity of preferentially orientated oxidized multi-walled carbon nanotubes manufactured by double vacuum assisted resin transfer molding method.

Materials and testing

Present work studied both mode I and mode II interlaminar fracture toughness (IFT) using double cantilever beam (DCB) and end-notched flexure (ENF) tests specimens, respectively. The materials were glass fiber reinforced composites of filled epoxy matrix resin. The matrix was the epoxy resin Biresin® CR120, combined with the hardener CH120-3, both supplied by Sika. The reinforcement was fiber glass triaxial mats ETXT 450, supplied by Saapi, with fiber orientation 0/±45º. The nanoclay was the commercially available, Nanomer I30 E, provided by Nanocor Inc. The nanotubes used in current study were multiwalled carbon nanotubes (MWNT) with 98% in carbon supplied by Sigma-Aldrich.

The mixture of resin with the desired amount of clay was done using high rotation during 1 h. Then, it was degassed under vacuum for 15 minutes and afterwards, the hardener agent was added. The MWNT were dispersed into the epoxy resin using also a direct mixing method. The mixture of resin and desired amount of nanotubes was done using high rotation during 15 minutes, followed by 15 minutes of degassed under vacuum before add the hardener agent.

Table 1 indicates the five material batches manufactured with different matrix formulation.

Table 1- Formulation of composite matrix

Reference	Epoxy (wt %)	Nanoclay (wt %)	MWNT (wt %)
GF/E	100	-	-
GF/ENC1	99	1	-
GF/ENC3	97	3	-
GF/ENT0.5	99.5	-	0.5
GF/ENT1	99	-	1

Fibres and resin were hand placed in a mould with all the fibers layers oriented in the same direction and subjected to a low compression. The plates were processed in vacuum bag with 10 fiberglass layers. In the manufacture of the plates was applied alternately woven fiberglass layer and resin, while ensuring the complete impregnation of the fibers. The composite was cured at room temperature for 8 hours. Post cure process was carried out as follows: 55 ºC during 16 hours, 75 ºC during 3 hours and finally 120 ºC during 12 hours. The delamination was simulated with a 0.004 mm thickness Teflon layer placed at half thickness of the sample. The specimens were machined from plates, nominally 300 mm long, 100 mm wide and 4 mm thick. The dimensions of the specimens are indicated in Fig. 1a) for double cantilever beam (DCB) tests (according ASTM D 5528 standard) and in Fig. 1b) for ENF tests.

The tests were performed using a Shimadzu SLBL-5kN testing machine. Load, axial displacement and crack length were monitored during the tests. An auxiliary video image camera was used to measure the crack length.
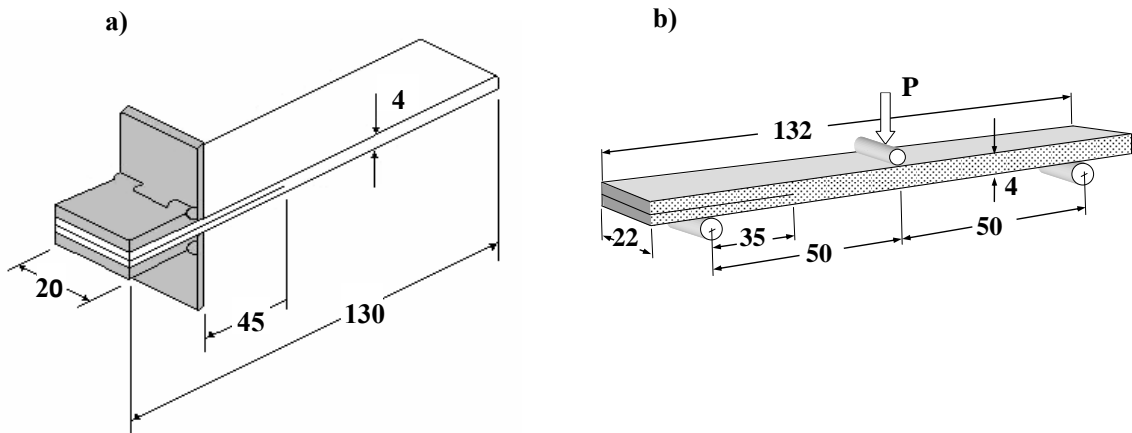
***Figure 1**– Specimens geometry: a) DCB; b) ENF.*

Mode I strain energy release rate, G_I, was calculated according ASTM D 5528 standard by means the modified beam theory (MBT) method, the compliance calibration (CC) method and the modified compliance calibration (MCC) method, using equations (1), (2) and (3), respectively:

$$G_I = \frac{3P\delta}{2b(a+\Delta)}$$ (1)

$$G_I = \frac{nP\delta}{2ba}$$ (2)

$$G_I = \frac{3P^2 C^{2/3}}{2A_I bh}$$ (3)

where: P is the load, δ is the load point displacement, b is the specimen width, h is the thickness, a is the delamination length, C is the compliance, Δ is the modulus of a correction factor obtained experimentally by generating a least squares plot of the cube root of the compliance C against the delamination length a (Δ is the a value for $C^{1/3}$ equal to zero), n is a correction factor given by the slope of the straight line generated by a least squares plot of the log of the compliance C against the log of the delamination length a and A_I is a correction factor given by the slope of the straight line generated by a least squares plot of a/h against $C^{1/3}$.

Mode II strain energy release rate, G_{II}, was calculated, according the direct beam theory (DBT) and the compliance calibration method (CCM) using the equations (4) and (5), respectively:

$$G_{II} = \frac{9P\delta a^2}{2b(2L^3 + 3a^3)}$$ (4)

$$G_{II} = \frac{3mP^2 a^2}{2b}$$ (5)

where: L is half span of the ENF specimen, m is a correction factor given by the slope of the straight line generated by a least squares plot of the compliance C against the cube of the delamination length, a^3.

Results and discussion

Mode I tests

DCB tests showed that nanofilled matrix composites exhibit higher interlaminar failure loads which indicate possible benefices in terms of the toughness. The interlaminar fractute toughness, G_I, was calculated using equations (1) to (3) and plotted against the crack length for the five material compositions. Fig. 2 shows an exemplary plot for the case of 3% nanoclyed resin. The values of the IFT obtained using the three different calculation methods are closed for the five materials. As expected the IFT tends to a stabilized value for long crack size. The average value of G_I in the stabilized region was assumed as G_{IC}. Fig. 3 shows the average G_{IC} (from at least four tests) against the percentage of nanoparticles. Significant IFT improvements are obtained for the composites incorporating nanoparticles fillers, reaching 17% for 1% of nanotubes and 31% for 3% of nanoclays.
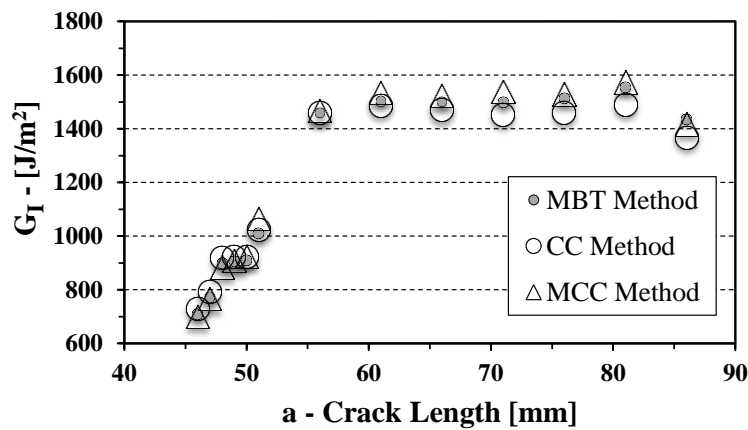
Figure 2 - *IFT versus crack length for GF/ENC3 material under mode I.*
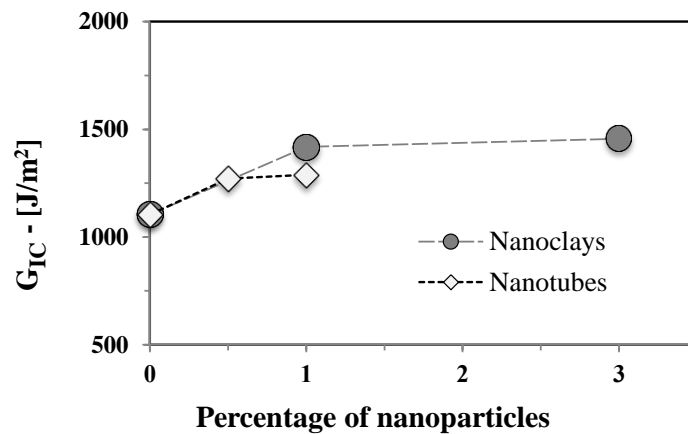
Figure 3 *- Mode II IFT versus filler content.*

Mode II tests

G_{II} was calculated using equations (4) and (5). Figure 4 shows an exemplary plot for the case of unfilled matrix. IFT values obtained using the two calculation methods are very close for all crack size in most of the tests.
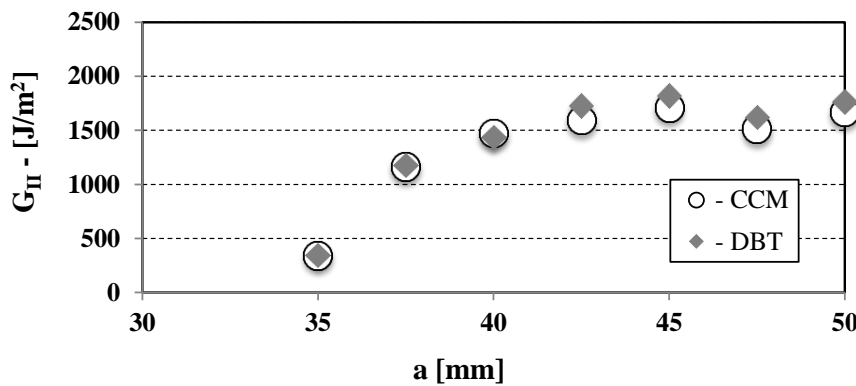
Figure 4 *- IFT versus crack length for GF/E composite under mode II.*

Figure 5 shows Mode II strain energy release rate, G_{II}, calculated using the compliance calibration method (CCM) against the crack length for the five materials. Strain energy release rate tends toward a stabilized value for crack length above 40 mm. The average value of G_{II} in this region was assumed as G_{IIC}. Some material configurations exhibits significant dispersion in the results obtained from different samples. Fig. 6 shows the average G_{IIC} against the percentage of nanoparticles. Despite the above-mentioned dispersion, figure 6 shows a significant increase of IFT for composites incorporating nanoparticles reaching about 30% for 1% of nanotubes and 50% for 3% of nanoclays.
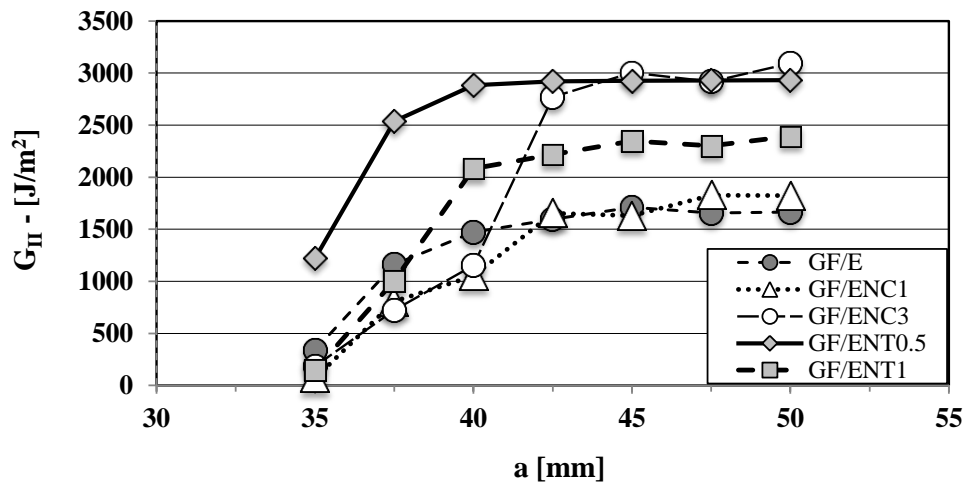
Figure 5 *– Comparison of IFT under mode II versus crack length for the five materials*
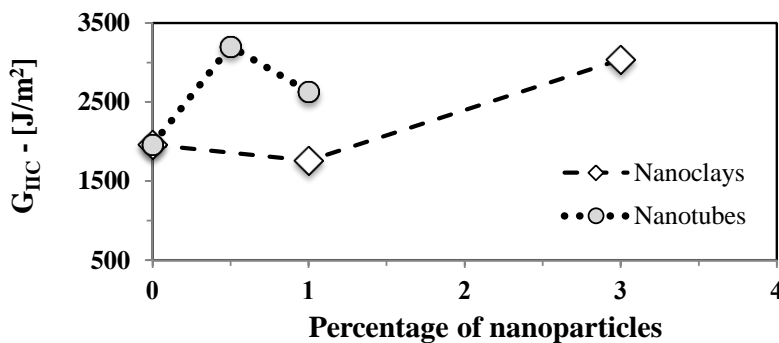
Figure 6 *– IFT versus resin filler content for mode II*

Conclusions

Mode I interlaminar fracture toughness was significant improved by the incorporation of nanoparticles fillers, reaching 17% for 1% of nanotubes and 31% for 3% of nanoclays.

Mode II interlaminar fracture toughness exhibits significant dispersion. Despite the scatter, it was observed a significant increase of mode II interlaminar fracture toughness in composites incorporating nanoparticles reaching about 30% for 1% of nanotubes carbone and 50% for 3% of nanoclays.

Acknowledgements

References

[1] Rosselli F, Santare MH,*Comparison of the short beam shear (SBS) and interlaminar shear device (ISD) tests*, Compos Pt A: ApplSciManuf, Vol. 28, Num. 6, pp.587–594, 1997.

[2] Zhang S.,*A simple approach to the evaluation of fiber/matrix interfacial shear strength and fracture toughness*, Compos SciTechnol, Vol. 60, pp.145–158, 2000.

[3]WeipingLui, Suong V. Hoa, Martin Pugh, *Organoclay-modified high performance epoxy nanocomposites*, Composites Science and Technology, Vol. 65, pp.307–316, 2005.

[4] Kornmann, X., Thomann, R., Mulhaupt, R., Finter, J., Berlund, L., *Synthesis of Amine-cured, epoxy-layered silicate nanocomposites: The influence of the silicate surface modification on the properties,* J. Appl. Polym. Sci., Vol. 86, pp.2643-2652, 2002.

[5] Kinloch, A. J.; Taylor, A. C., *Mechanical and fracture properties of epoxy/inorganic micro- and nano-composites*, J MATER SCI LETT, Vol. 22, pp.1439-1441, 2003.

[6] Allaoui A, Bai S, Cheng HM, Bai JB., *Mechanical and electrical properties of a MWNT/epoxy composite,* Matrix, Vol. 62, pp.1993–1998, 2002.

[7] Lau K-tak, Hui D., *Effectiveness of using carbon nanotubes as nanoreinforcements for advanced composite structures*, MechEng, Vol. 40, pp.1605–6, 2002.

[8] Zhou Y, Pervin F, Rangari VK, Jeelani S., *Fabrication and evaluation of carbon nanofiber filled carbon/epoxy composite*, Mater SciEng A, Vol. 426, pp.221–228, 2006.

[9] Gojny FH, Wichmann MHG, Fiedler B, BauhoferW, Schulte K., *Influence of nano-modification on the mechanical and electrical properties of conventional fibre-reinforced composites*, Compos Pt A: ApplSciManuf, Vol. 36, pp.1525–1535, 2005.

[10] Fan Z, Santari MH, Advani SG., *Interlaminar shear strength of glass fiber reinforced epoxy composites enhanced with multi-walled carbon nanotubes*, Compos Pt A: ApplSciManuf, Vol. 39, pp.540–554, 2008.

Mechanical behavior of composite materials with enhanced energy absorption properties

José M. Silva[1], Paulo Fael[2], João Morgado[1], Alexandre Menezes[1],

1Department of Aerospace Sciences, University of Beira Interior, 6201-001 Covilhã – Portugal, jmas@ubi.pt

2Department of Electromechanical Engineering, University of Beira Interior, 6201-001 Covilhã – Portugal

Abstract The objective of this paper is to present a set of experimental results regarding the mechanical characterization of composites with enhanced energy absorption properties. The improvement of the resilient properties of high performance CFRPs was attained through the use of cork derivatives combined with carbon-epoxy composite material considering two types of configurations: 1) a cork based core in a sandwich component; 2) a conventional laminate with embedded cork granulates. Static properties were obtained from 3-point flexural testing whereas the energy absorption capability was characterized through low velocity impact testing. Experimental results were supported by an analysis of the damage extension based either in microscopic observations or residual strength testing. Regardless the type of specimens, results are encouraging about the positive effect of viscoelastic materials in the improvement of the energy absorption properties of high performance composites with a minor impact in their original mechanical properties, which is a major benefit for the structural integrity of aerospace structures under severe operational conditions, such as foreign object damages and aeroelastic problems.

1   Introduction

Composite materials are being increasingly used in aerospace structures and components due to their improved mechanical properties and low specific weight. In addition, the continuous demand for lighter and more efficient aircraft led to an increased use of sandwich composite technology. Composite sandwich construction consists of a light core material sandwiched between to facings of a high strength material, normally in the form of laminated fiber reinforced plastics (FRPs). Honeycombs, foams and balsa wood are the most common materials used as sandwich core, but recently new types of cellular core structures are being considered as viable alternatives [1]. According to Vinson [1] and Zenkert [2] the most important properties of core materials are: high shear modulus, low density, elevated stiffness perpendicular to the faces, high shear strength and good thermal/acoustic insulation characteristics. There are many synthetic materials that address to these requirements (especially in the form of polymeric foams), but the present global concerns about the importance of developing engineering solutions with an increased amount of "green" materials have been shifting the research efforts towards the application of natural materials in sandwich components.

Cork is a natural material with an alveolar cellular structure which provides most of the required properties when used as a core material in a sandwich component, i.e., a high damage tolerance to impact loads, good thermal and acoustic insulation capacities and

excellent damping characteristics for the suppression of vibrations [3]. This intrinsic cellular morphology has a strong influence on the overall mechanical properties of cork-based materials, which may reveal a specific strength comparable to some rigid synthetic foams. Silva et al. [3] present an extended review focused on the physical and mechanical properties of natural cork, indicating some high-valued potential applications due to its unique characteristics. In addition to the excellent mechanical and thermal properties, cork is a natural, sustainable and biodegradable material, whereas foam and honeycomb core materials are usually non-recyclable and non-biodegradable. All together, these facts are in the base of the increasing use of cork based composites in engineering applications, having attesting their superior performance in thermal/acoustic insulating sandwich panels [4] or even in sandwich components designed for load carrying structural applications [5, 6].

.Even with notable mechanical properties, composite sandwich components have some drawbacks that can limit its usage under certain types of operational conditions, particularly their limited damage tolerance under impact loading [5, 7]. Sandwich structures are often susceptible to foreign object damages resulting from impacts. These impact events may have a significant influence on the strength, stability and durability of the structure, even when low energy impact levels are involved. Therefore, the structural integrity of impacted components has been undergoing a continuous research considering different sandwich core and face sheet materials [8–15]. The proper design and application of sandwich components depends on a throughout characterization and understanding of the distinct sandwich constituent materials (face sheets, core and adhesive), and also of the whole structure under quasi-static and dynamic loading scenarios. Therefore, since the composite sandwich technology is complex, the analysis of impact events, with a particular emphasis in low velocity impact, remains an active research topic with ongoing developments as new types of materials have to be adequately characterized.

This paper aims at characterizing the mechanical behavior of two types of cork based composites: a sandwich formed by carbon-epoxy facesheets with a cork based core and a carbon-epoxy laminate with embedded cork granulates. A particular attention has been put in the energy absorption capability of these materials under low velocity impact loading. Damage tolerance was assessed from subsequent residual strength testing of impacted specimens. Results were compared with data extracted for similar sandwich components using low-density polymeric foam which is a benchmark material in aeronautical applications. The conclusions of this paper were oriented in view of confirming the use of cork-based composites as a mechanically viable, natural and cost-effective solution in sandwich components for high performance engineering applications.

2   Description of experimental testing

The two types of materials considered for experimental purposes are representative of the usual configurations of composite structures used in most aircrafts, namely, high strength/stiffness laminates and sandwich components with lightweight core materials. More specifically, static and dynamic tests aimed at determining the overall mechanical properties of carbon-epoxy specimens combined with cork derivatives in two distinct configurations: 1) a sandwich component made of a cork-based core and CFRP facesheets; 2) a carbon-epoxy laminate with embedded cork granulates.

In the first case, each facesheet of the sandwich was made through a hand layup process placing three plies of a 196g/m2 carbon fiber fabric with a [0°/90°/0°] orientation. Regarding the core material, the behavior of a new type of cork-epoxy agglomerate which was

177

developed in the course of a previous work [5] was compared with other materials, namely, a polymethacrylimide (PMI) foam, which is a reference material commonly used in sandwich construction of aeronautical components due to its very low density and an agglomerate of expanded cork (frequently know as insulation cork board, or ICB). The major driver in the base of the development of the cork-epoxy core was the need for a superior mechanical performance of cork based materials suitable for structural applications, while keeping unaffected the excellent vibration, thermal and acoustic insulating properties typical of this viscoelastic material. This specific agglomerate was obtained using an optimized molding process considering different fabrication variables, namely compacting pressure level, granulate sizes and resin weight fractions envisaging the best mechanical strength with a minimum weight; more details can be found in reference [5]. Two core thicknesses were obtained from this process: 20mm and 30mm. In each case, the cork-resin proportion was adjusted to get the same density of the agglomerate ($260kg/m^3$), which is comparably higher than the corresponding values for the other two core materials, respectively $75kg/m^3$ for PMI foam and $100kg/m^3$ for ICB cork agglomerate.

The dimensions of sandwich specimens were chosen taking into account the requirements of the impact and residual strength tests, which were performed in accordance to the recommendations of ASTM C393/C393M [16] and ASTM D7136/D7136M [17]. The guidelines of these standards had to be slightly adjusted to the particular sandwich configuration of the specimens under testing, which had a rectangular shape with the dimensions shown in Figure 1. The dashed region visible in this figure is representative of a metallic frame which constitutes the impact window. The impact zone is located on the lateral side of the specimen due to the need for the subsequent residual strength flexural tests, which in turn will imply a loading region located in the central position.
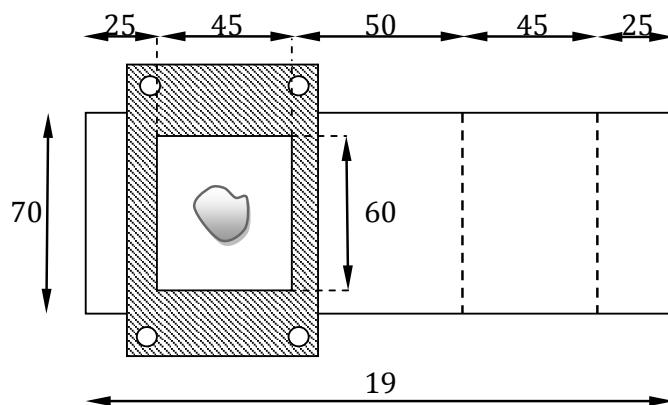
Figure 1 – Schematic representation of the dimensions of specimens used in the low velocity impact tests (the dashed frame corresponds to the impact window).

Carbon-epoxy laminates with embedded cork granulates were fabricated using an autoclave process. The geometry of these specimens was chosen in accordance to ASTM D7136/D [14], having a 150mm x 100mm rectangular shape. A 5mm thickness was obtained through manual stacking of 28 plies of Texipreg HS 160 REM prepreg. All the plies were oriented parallel to the longitudinal axis of the specimens considering two distinct locations of the cork granulate layer (between the 4th-5th or 23rd-24th plies). Two cork granulate sizes were considered: small (0.5mm) and medium (0.9mm).

The above mentioned impact tests were performed using a drop tower apparatus with a free-falling mass connected to a 20mm hemispherical impactor. The variation of the energy of impact was achieved through the choice of different departure heights of the falling mass. Impact loads were acquired with a piezoelectric force transducer located between the impactor and the load carriage. Specimens were constrained in each lateral side of a fixed support on the impact apparatus. The damage tolerance capability of sandwich specimens was assessed from residual strength characterization after impact based on four-point flexural tests, since these allow characterizing various types of damage mechanisms, in particular shear loads in the core material and tension/compression loads in the facesheets with or without impact damage. A digitally controlled servo-hydraulic machine has been used for this purpose.

3 Results and discussion

The first stage of the experimental testing program intended to characterize the mechanical behavior of the different materials under static loading. In all cases, three-point flexural tests were used but aiming at obtaining distinct information regarding each type of material. In fact, in regards to sandwich specimens, the results were oriented to the quantification of the stress limits of the sandwich core material, as well as to characterize the failure modes of each type of material. On the other hand, static tests were a crucial step for the evaluation of the likely detrimental effect of embedded cork granulates in the strength limit of carbon-epoxy laminate specimens.

Figure 2(a) presents the *Force-Displacement* curves for the three types of core materials used in the sandwich configuration (ICB, PMI and cork-epoxy). One immediate conclusion from these results is that specimens with PMI foam have a predominantly linear-elastic behavior in contrast with the occurrence of a yielding condition in the other two materials, particularly for the ICB core, where large displacements were obtained even for relatively small values of loading. These distinct behaviors are a direct consequence of the viscoelastic nature of the cork based materials, which withstand large strain levels until the final rupture of the component is achieved. The viscoelastic properties of cork are also in the base of a reversibility capability of the material even for high deformation levels (i.e., upon yielding), which means that the deformed specimen tends to recover its original shape. It was also found that cork based sandwich specimens present a less sudden total fracture after the yielding limit has been reached, having a shear-dominated failure mechanism characterized by a 45° shear crack which propagates from the middle plane towards the facesheets of the specimen, as visible in Figure 2(b). This behavior is a good indicator of the high damage tolerance of cork composites comparatively with other core materials, which is an important issue when electing the proper materials for damage tolerant structures. Additionally, static flexural tests allowed confirming the superior shear strength limit of cork-epoxy agglomerates when compared with the other two types of materials (0.94MPa, against 0.6MPa for PMI foam and 0.23MPa for ICB cork core).

The damage tolerant capabilities of cork based composites were confirmed from impact tests followed by residual strength flexural tests. Figure 3(a) shows the energy-time curves obtained for the sandwich type specimens considering the lowest and highest energy levels used in impact testing (5 Joule and 20 Joule). As we can see, there is a visible difference between the behavior of specimens with cork-epoxy core and the other two core materials (including the cork based ICB core), since in the first case there is a significant energy release after the energy peak (coincident with the impact event) has been reached. This effect is more pronounced for the lowest value of energy of impact (5J), whereas for the higher energy level (20J) there is an almost total absorption of energy by the PMI and ICB core materials. This

absorbed energy will be transformed in some form of damage of either the facesheets or the core material of the sandwich, which proves that cork-epoxy cores provide better damage tolerant characteristics than the other materials under analysis.

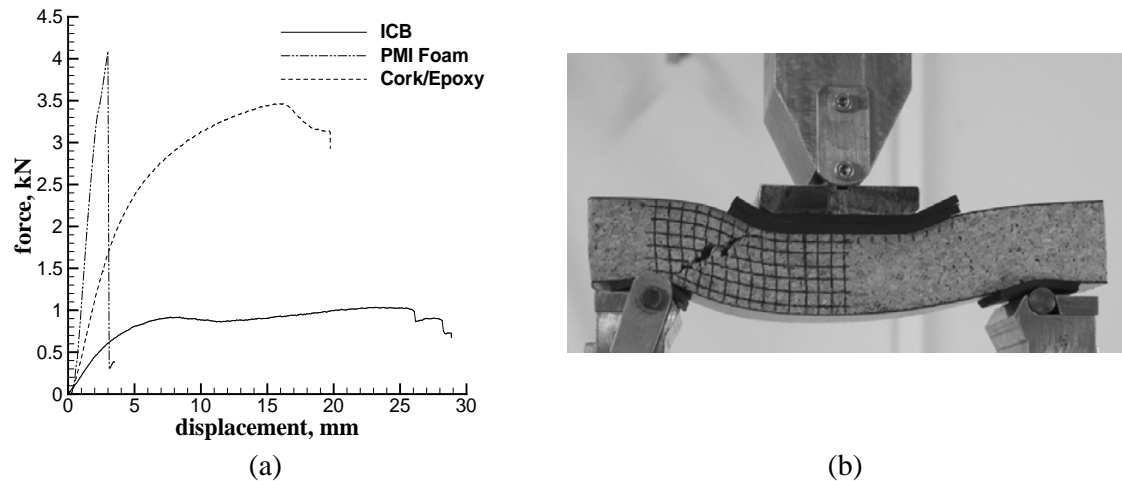|	
(a)	(b)

Figure 2 – (a): Force-Displacement curves obtained from flexural testing for the three types of core materials (cork-epoxy, PMI foam and ICB); (b): image of a cork-epoxy specimen under flexural testing.

Flexural testing after impact allows assessing the effect of damage as a function of the energy level of impact depending on the type of core material. Table 4 presents the ultimate loads as obtained for both impacted and non-impacted specimens. These results are clear about a noticeable strength reduction after impact in the PMI sandwiches, which can reach about 19% in the case of the 20J impact event. Considering this level of impact energy, the strength reduction concerning the ICB cork core is around 5.4%, whereas specimens with cork-epoxy core had an unexpectedly higher residual strength than that for non-impacted specimens (14.2%), which is a rather interesting result without any apparent solid explanation. Nevertheless, this behavior is definitely an additional confirmation of the high energy recovery capacity of cork-epoxy cores yielding a protective effect of the facesheet materials with a consequent reduction in the area of damage.

The impact behavior of cork based laminates can be observed from Figure 3(b), which refers to the highest level of energy considered for this type of specimens (i.e., 15 Joule). It is clear that cork based laminates evince a higher level of absorbed energy, which seems to be unaffected by the granulate size. The improvements regarding energy absorption are a consequence of an arresting effect caused by the inclusion of cork layers in the interior of the laminate in terms of the propagation of the energy waves resulting from the impact event. This means that the use of very thin viscoelastic layers can have a positive effect in the minimization of the extension of impact damage, as visible in Figure 4. These images were obtained from the observation of the cross-section of laminate specimens with and without cork granulates after being impacted with an identical energy level (15J). Visible damage refers to the same cross-section distance from the point of contact of the impactor, i.e., 10mm. The better energy absorption properties of cork based laminates result into a lesser extension of damage when compared with plain CFRP laminates, both in the thickness and in the laminate plane directions. This effect is more perceptible in the case of those laminates having medium size cork granulates

(a)   (b)
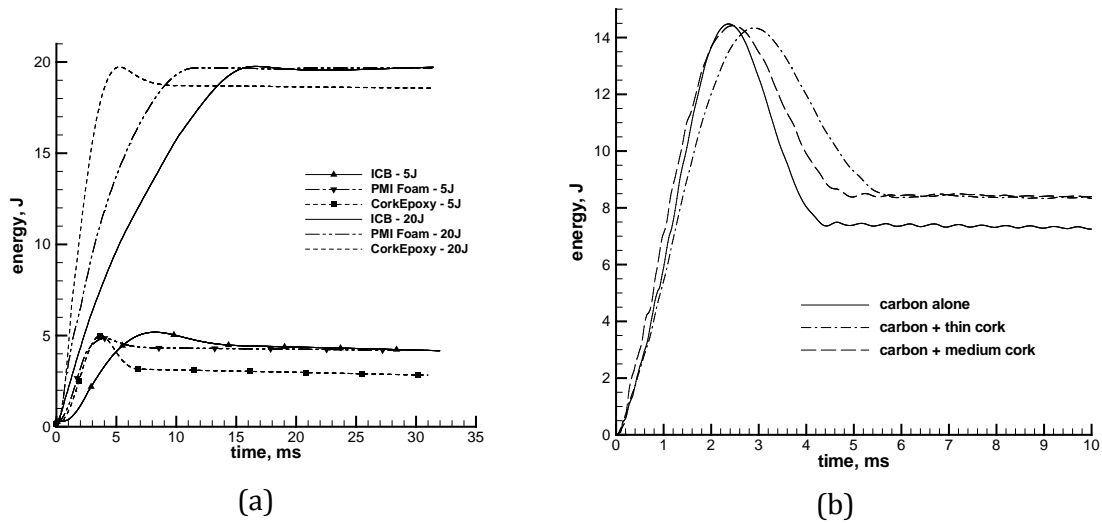
Figure 3 – Energy-Time curves for the two configurations of specimens: (a) - sandwich specimen with different core materials (cork-epoxy, PMI foam and ICB) considering two levels of energy of impact (5J and 20J); (b) - CFRP laminates with and without embedded cork granulates (15J impact energy)

Table 4. Load limit obtained for the different core materials from the post-impact residual strength bending tests (t = 30mm thickness).

Material	without impact, kN	5J impact, kN	Force variation (5J vs no-impact)	20J impact, kN	Force variation (20J vs no-impact)
Cork-epoxy	3.24	3.53	+8.9%	3.70	+14.2%
PMI foam	4.58	3.22	-29.7%	3.72	-18.8%
ICB	0.95	0.84	-10.9%	0.89	-5.4%

(a)   (b)
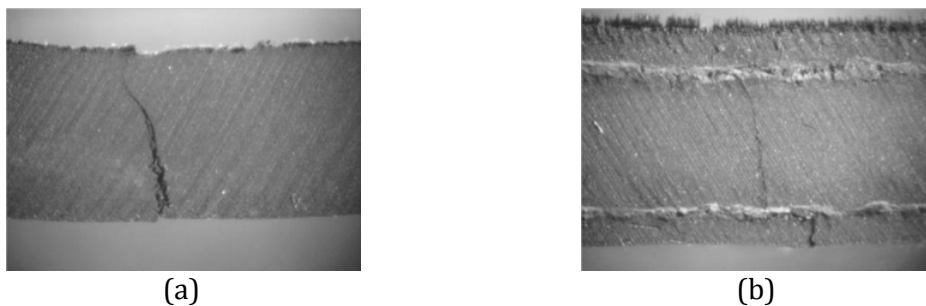
Figure 5 - Images of the cross-sections of laminate specimens showing the internal damage extension caused by impact (considering a 10mm distance from the point of contact of the impactor); (a) – plain CFRP laminate; (b) laminate with two cork layers. Magnification 64x.

4   Conclusions

Experimental results are conclusive about the superior energy absorption properties of cork based composites, either in the form of a core material in a sandwich component or as a very thin viscoelastic layer embedded in a fibre reinforced laminate. Impact tests showed that the use of cork based materials provide a shielding effect, resulting in a lesser extension of damage of both the core and facesheets when compared with other reference core materials (like PMI foams). Residual strength flexural tests after impact are in line with this evidence, as the cork based components withstand higher values of ultimate load for the same level of energy of impact. The confirmation of the enhanced energy absorption properties of cork based materials encourages their use as a viable and cost effective mean of improving the resilience of high performance composites with a minor impact in their original mechanical properties, which promotes structural integrity under particular operational conditions with an high probability of occurrence of impact events, such as foreign object damages in aeronautical components.

5   References

[1]   J. Vinson, *The behaviour of sandwich structures of isotropic and composite materials*. Lancaster: Technomic Publishing Co. Inc., 1999.

[2]   D. Zenkert, "The handbook of sandwich construction," in *North European engineering and science conference series*, 1997.

[3]   S. P. Silva, M. a. Sabino, E. M. Fernandes, V. M. Correlo, L. F. Boesel, and R. L. Reis, "Cork: properties, capabilities and applications," *International Materials Reviews*, vol. 50, no. 6, pp. 345-365, Dec. 2005.

[4]   Sargianis, J., Kim, H., Suhr, J.; "Natural Cork Agglomerate Employed as an Environmentally Friendly Solution for Quiet Sandwich Composites"; Scientific Reports, 2, Art. Nr. 403; 2012.

[5]   O. Castro, J. M. Silva, T. Devezas, A. Silva, and L. Gil, "Cork agglomerates as an ideal core material in lightweight structures," *Materials & Design*, vol. 31, no. 1, pp. 425-432, Jan. 2010.

[6]   J.M. Silva, C.Z. Nunes, N. Franco, P.V. Gamboa; "Damage tolerant cork based composites for aerospace applications"; The Aeronautical Journal, Vol. 115, No 1171; 2011; 567-575;

[7]   L. Aktay, A. F. Johnson, and M. Holzapfel, "Prediction of impact damage on sandwich composite panels," *Computational Materials Science*, vol. 32, no. 3–4, pp. 252-260, Mar. 2005.

[8]   P. M. Schubel, J.-J. Luo, and I. M. Daniel, "Impact and post impact behavior of composite sandwich panels," *Composites Part A: Applied Science and Manufacturing*, vol. 38, no. 3, pp. 1051-1057, Mar. 2007.

[9]   P. M. Schubel, J.-J. Luo, and I. M. Daniel, "Low velocity impact behavior of composite sandwich panels," *Composites Part A: Applied Science and Manufacturing*, vol. 36, no. 10, pp. 1389-1396, Oct. 2005.

[10]   J. Yu, E. Wang, J. Li, and Z. Zheng, "Static and low-velocity impact behavior of sandwich beams with closed-cell aluminum-foam core in three-point bending," *International Journal of Impact Engineering*, vol. 35, no. 8, pp. 885-894, Aug. 2008.

[11]   N. a. Apetre, B. V. Sankar, and D. R. Ambur, "Low-velocity impact response of sandwich beams with functionally graded core," *International Journal of Solids and Structures*, vol. 43, no. 9, pp. 2479-2496, May 2006.

[12]   P. Rahmé, C. Bouvet, S. Rivallant, V. Fascio, and G. Valembois, "Experimental investigation of impact on composite laminates with protective layers," *Composites Science and Technology*, vol. 72, no. 2, pp. 182-189, Jan. 2012.

[13]   J. Christopherson, M. Mahinfalah, G. N. Jazar, and M. R. Aagaah, "An investigation on the effect of a small mass impact on sandwich composite plates," *Composite Structures*, vol. 67, no. 3, pp. 299-306, Mar. 2005.

[14]   C. Atas and C. Sevim, "On the impact response of sandwich composites with cores of balsa wood and PVC foam," *Composite Structures*, vol. 93, no. 1, pp. 40-48, Dec. 2010.

[15]   C. a. Ulven and U. K. Vaidya, "Post-fire low velocity impact response of marine grade sandwich composites," *Composites Part A: Applied Science and Manufacturing*, vol. 37, no. 7, pp. 997-1004, Jul. 2006.

[16]   ASTM C393/C393M–06 - "Standard Test Method for Core Shear Properties of Sandwich Constructions by Beam Flexure"; ASTM, 2006.

[17]   ASTM D7136/D 7136M-05: Standard Test Method for Measuring the Damage Resistance of a Fiber-Reinforced Polymer Matrix Composite to a Drop-Weight Impact Event; ASTM; 2005.

Effect of composite patch in repaired plate on FCG under different tempered situation

M. Benachour[1], F.Z. Seriari[1], M. Benguediab[2], N. Benachour[1,3]

[1]*IS2M Laboratory, Mechanical Engineering Department, University of Tlemcen, BP230, Tlemcen – 13000, Algeria. mbenachour_99@yahoo.fr*

[2]*Mechanical Engineering Department, University ofSidi Bel Abbes,*
[3]*Physical Department,Faculty of Sciences, University of Tlemcen,*

Abstract   In this paper an investigation on the effect of composite material patch repairing were conducted to characterize the fatigue crack growth behavior in 6061-T6 and 6060-T651 Aluminum alloys (3 mm) plate with a single sided fiber reinforced composite patch. Using empirical analysis, the stress intensity factors were calculated when critical stress intensity factor are based on patched structure, from which the fatigue crack growth rates were evaluated using Nasgro model based on experimentally data. For the patched and un-patched plate, effect of different stress ratio on fatigue crack growth was investigated. The results show that fatigue life was affected by tempered materials and stress ratio and retardation of crack growth is found in the bonded repair. Effect in increasing of stress ratio is characterised by an increasing in fatigue life and fatigue crack growth rates (FCGRs) when maximum cyclic loading is maintained constant.

Key Words: fatigue crack, repair composite patch, retardation, Al-Alloy

Damage tolerance verification of composite spacecraft structures

P.P. Camanho[1], A. Turon[2], P. Portela[3], G. Sinnema[4]

[1]*DEMec, Rua Dr. Roberto Frias, 4200-465 Porto, Portugal, pcamanho@fe.up.pt*

[2]*AMADE, Universitat de Girona, Av. Montilivi, 17071 Girona, Spain, albert.turon@udg.es*

[3]*HPS Lda., Rua Dr. Roberto Frias, 4200-465 Porto, Portugal, portela@hps-lda.pt*

[4]*ESA-ESTEC, European Space Agency, Keplerlaan 1, NL-2200 AG Noordwijk, The Netherlands, Gerben.Sinnema@esa.int*

Abstract This works describes the analysis models required for the certification procedure of composite spacecraft structures. The main failure mechanism addressed is delamination and three levels of analysis with increased complexity and accuracy are proposed (Figure 1). Level 1 corresponds to the crack tip element and it enables fast predictions of delamination propagation that are suitable for preliminary design. Level 2 corresponds to the use of the virtual crack closure technique to predict the onset and the stability of delamination propagation. Finally, level 3 corresponds to the use of cohesive finite elements implemented in non-linear finite element codes. The range of applicability of each analysis methods and the associated best practice guidelines will be presented.
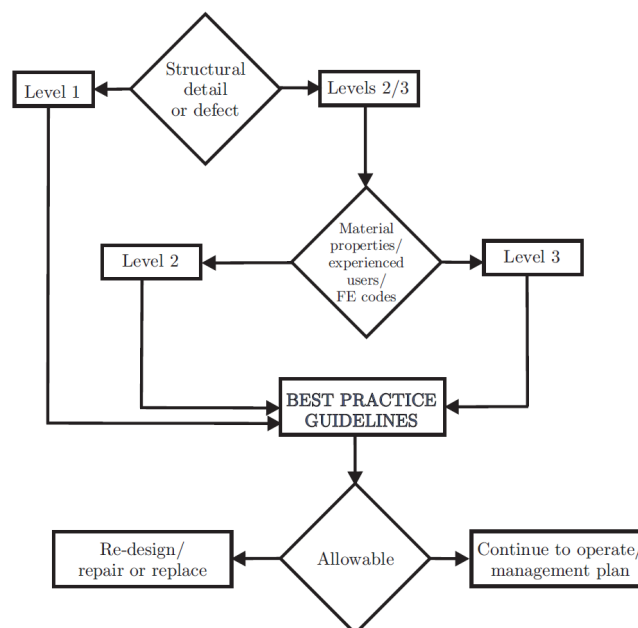
Figure 1 - *Proposed method for the selection of the level of analysis.*

Buckling Response of Hygro-Thermally Curvature-Stable Laminate with Extension-Twisting Coupling

M.H. Shamsudin[1,3], J. Chen[2] and C.B. York[3]

[1]*Universiti Kuala Lumpur, Malaysia Institute of Aviation Technology, Dengkil, Malaysia*

[2]*College of Aerospace and Material Engineering, National University of Defence Technology, Changsha, China.*

[3]*School of Engineering, University of Glasgow, Scotland*

(Corresponding author: Christopher.York@Glasgow.ac.uk)

The bounds on buckling strength of simply supported laminated plates with extension-twisting coupling are investigated. A closed form buckling solution is shown to be applicable to this class of coupled laminate for which the stacking sequences can be derived using standard ply-angle orientations (±45, 0 and 90°) of constant ply thickness. These results are also validated using a commercial finite element code. Attention is focused on a special sub-class of extension-twisting coupled laminate that is free from the thermal distortion that generally arise from the high temperature curing process; these special laminates are generally referred to as hygro-thermally curvature-stable. Bounds on the buckling solutions are presented for all hygro-thermally curvature-stable laminates, possessing extension-twisting (and shearing-bending) coupling and consisting of 8-, 12-, 16- and 20-ply laminates within the range of thin laminates investigated, i.e. up to 21 plies. Improvements in the buckling strength have been observed for laminates with standard ply orientations, compared to those optimized for maximum twist using free-form ply orientations.

1 INTRODUCTION

Coupled composite laminates are known to inherit complicating thermal distortion as a result of the high temperature curing process, which partly explains the continuing reluctance to move away from symmetric laminate designs. However, a recent study [1] has identified 9 classes of coupled laminate with immunity to these complicating thermal warping distortions. These forms of laminate are generally referred to as hygro-thermally curvature-stable (HTCS) laminates. An increasing interest in mechanical coupling behaviour is now evident from the literature, particularly with respect to extension-twisting coupling behaviour, as a result of an original discovery by Winckler [2]. This discovery has led to exploitation of extension-twisting coupling in tilt rotor blade design [3] and to subsequent research, including: maximizing the twist magnitude in HTCS laminate designs [4, 5] and; the integration of bending-twisting coupling, in addition to extension-twisting (and shearing-bending) coupling, at the laminate level [6]. These studies have been performed on thin laminates, but the compression buckling strength of such designs, which represents an important static design constraint, has not previously been considered. The aim of this paper is therefore to investigate the buckling strength performance of HTCS laminates with extension-twisting coupling, by employing a closed-form buckling solution [7] and validating specific results using a commercial finite element code.

Following a summary of the number of stacking sequence solutions found for HTCS laminates with extension-twisting coupling, and containing standard ply orientations, an assessment of the bounds on the buckling load will be presented for the entire range of the solutions found.

2 HTCS LAMINATE WITH EXTENSION-TWISTING COUPLING.

Coupled composite laminates are generally characterized through the form of the extensional (**A**), coupling (**B**), and bending (**D**) stiffness matrices, Eq. (1):

$$
\begin{Bmatrix} N_x+N_x^{Thermal} \\ N_y+N_y^{Thermal} \\ N_{xy}+N_{xy}^{Thermal} \end{Bmatrix} = \begin{bmatrix} A_{11} & A_{12} & A_{16} \\ A_{12} & A_{22} & A_{26} \\ A_{16} & A_{26} & A_{66} \end{bmatrix} \begin{pmatrix} \varepsilon_x \\ \varepsilon_y \\ \varepsilon_{xy} \end{pmatrix} + \begin{bmatrix} B_{11} & B_{12} & B_{16} \\ B_{12} & B_{22} & B_{26} \\ B_{16} & B_{26} & B_{66} \end{bmatrix} \begin{pmatrix} \kappa_x \\ \kappa_y \\ \kappa_{xy} \end{pmatrix}
$$

$$
\begin{Bmatrix} M_x+M_x^{Thermal} \\ M_y+M_y^{Thermal} \\ M_{xy}+M_{xy}^{Thermal} \end{Bmatrix} = \begin{bmatrix} B_{11} & B_{12} & B_{16} \\ B_{12} & B_{22} & B_{26} \\ B_{16} & B_{26} & B_{66} \end{bmatrix} \begin{pmatrix} \varepsilon_x \\ \varepsilon_y \\ \varepsilon_{xy} \end{pmatrix} + \begin{bmatrix} D_{11} & D_{12} & D_{16} \\ D_{12} & D_{22} & D_{26} \\ D_{16} & D_{26} & D_{66} \end{bmatrix} \begin{pmatrix} \kappa_x \\ \kappa_y \\ \kappa_{xy} \end{pmatrix}
$$

(1)

Elements of the ABD stiffness matrix and the thermal force and moment vectors can be calculated from the laminate invariants [8] and lamination parameters, given by Eq. (2) - (3).

$$
\begin{aligned}
&A_{11}=\{U_1+\xi_1 U_2+\xi_2 U_3\}H && B_{11}=\{\xi_5 U_2+\xi_6 U_3\}H^2/4 && D_{11}=\{U_1+\xi_9 U_2+\xi_{10} U_3\}H^3/12 \\
&A_{12}=A_{21}=\{-\xi_2 U_3+U_4\}H && B_{12}=B_{21}=\{-\xi_6 U_3\}H^2/4 && D_{12}=D_{21}=\{U_4-\xi_{10} U_3\}H^3/12 \\
&A_{16}=A_{61}=\{\xi_3 U_2/2+\xi_4 U_3\}H && B_{16}=B_{61}=\{\xi_7 U_2/2+\xi_8 U_3\}H^2/4 && D_{16}=D_{61}=\{\xi_{11} U_2/2+\xi_{12} U_3\}H^3/12 \\
&A_{22}=\{U_1-\xi_1 U_2+\xi_2 U_3\}H && B_{22}=\{-\xi_5 U_2+\xi_6 U_3\}H^2/4 && D_{22}=\{U_1-\xi_9 U_2+\xi_{10} U_3\}H^3/12 \\
&A_{26}=A_{62}=\{\xi_3 U_2/2-\xi_4 U_3\}H && B_{26}=B_{62}=\{\xi_7 U_2/2-\xi_8 U_3\}H^2/4 && D_{26}=D_{62}=\{\xi_{11} U_2/2-\xi_{12} U_3\}H^3/12 \\
&A_{66}=\{-\xi_2 U_3+U_5\}H && B_{66}=\{-\xi_6 U_3\}H^2/4 && D_{66}=\{-\xi_{10} U_3+U_5\}H^3/12
\end{aligned}
$$

(2)

$$
\begin{Bmatrix} N_x^{Thermal} \\ N_y^{Thermal} \\ N_{xy}^{Thermal} \end{Bmatrix} = \frac{H}{2} \begin{Bmatrix} (U_1+U_4)(\alpha_1+\alpha_2)+U_2(\alpha_1-\alpha_2)+\xi_1[U_2(\alpha_1+\alpha_2)+(U_1+2U_3-U_4)(\alpha_1-\alpha_2)] \\ (U_1+U_4)(\alpha_1+\alpha_2)+U_2(\alpha_1-\alpha_2)-\xi_1[U_2(\alpha_1+\alpha_2)+(U_1+2U_3-U_4)(\alpha_1-\alpha_2)] \\ \xi_3[U_2(\alpha_1+\alpha_2)+(U_1+2U_3-U_4)(\alpha_1-\alpha_2)] \end{Bmatrix} \Delta T
$$

$$
\begin{Bmatrix} M_x^{Thermal} \\ M_y^{Thermal} \\ M_{xy}^{Thermal} \end{Bmatrix} = \frac{H^2}{8} \begin{Bmatrix} \xi_5[U_2(\alpha_1+\alpha_2)+(U_1+2U_2-U_4)(\alpha_1-\alpha_2)] \\ -\xi_5[U_2(\alpha_1+\alpha_2)+(U_1+2U_3-U_4)(\alpha_1-\alpha_2)] \\ \xi_7[U_2(\alpha_1+\alpha_2)+(U_1+2U_2-U_4)(\alpha_1-\alpha_2)] \end{Bmatrix} \Delta T
$$

(3)

Where the laminate invariants, U_i, and lamination parameters, ξ_i, are given by Eq. (4) and (5) respectively.

$$
U_1=\frac{\{3Q_{11}+3Q_{22}+2Q_{12}+4Q_{66}\}}{8} \qquad U_2=\frac{\{Q_{11}-Q_{22}\}}{2} \qquad U_3=\frac{\{Q_{11}+Q_{22}-2Q_{12}-4Q_{66}\}}{8}
$$

$$
U_4=\frac{\{Q_{11}+Q_{22}+6Q_{12}-4Q_{66}\}}{8} \qquad U_5=\frac{\{Q_{11}+Q_{22}-2Q_{12}+4Q_{66}\}}{8}
$$

(4)

$$
\begin{aligned}
&\xi_1=\sum_{k=1}^{n} \cos 2\theta_k(z_k-z_{k-1}) && \xi_5=\sum_{k=1}^{n} \cos 2\theta_k(z_k^2-z_{k-1}^2)/2 && \xi_9=\sum_{k=1}^{n} \cos 2\theta_k(z_k^3-z_{k-1}^3)/3 \\
&\xi_2=\sum_{k=1}^{n} \cos 4\theta_k(z_k-z_{k-1}) && \xi_6=\sum_{k=1}^{n} \cos 4\theta_k(z_k^2-z_{k-1}^2)/2 && \xi_{10}=\sum_{k=1}^{n} \cos 4\theta_k(z_k^3-z_{k-1}^3)/3 \\
&\xi_3=\sum_{k=1}^{n} \sin 2\theta_k(z_k-z_{k-1}) && \xi_7=\sum_{k=1}^{n} \sin 2\theta_k(z_k^2-z_{k-1}^2)/2 && \xi_{11}=\sum_{k=1}^{n} \sin 2\theta_k(z_k^3-z_{k-1}^3)/3 \\
&\xi_4=\sum_{k=1}^{n} \sin 4\theta_k(z_k-z_{k-1}) && \xi_8=\sum_{k=1}^{n} \sin 4\theta_k(z_k^2-z_{k-1}^2)/2 && \xi_{12}=\sum_{k=1}^{n} \sin 4\theta_k(z_k^3-z_{k-1}^3)/3
\end{aligned}
$$

(5)

Laminates posses extensional and bending anisotropy when A_{16}, $A_{26} \neq 0$ and D_{16}, $D_{26} \neq 0$, respectively, in Eq. (1). By contrast, the coupling (**B**) matrix, has several complex forms, and classification of each coupling response has been the subject of recent study [1]. This paper focuses a particular class of coupled laminate in which the B_{16}, $B_{26} \neq 0$, giving rise to extension-twisting and shearing-bending coupling in the laminate. A solution for this class of coupled laminate has previously been discovered [2] with immunity to thermal warping distortions, i.e. a HTCS laminate. An eight-ply configuration was developed using the concept of bonding two (or more) symmetric cross-ply [0/90/90/0] sub-laminates, where each sub-laminate is counter-rotated by $\pi /8$, giving rise to the laminate: [22.5/-67.5$_2$/22.5/-22.5/67.5$_2$/-22.5]$_T$, which possesses extension-twisting and shearing-bending coupling. The symmetric cross-ply sub-laminate represents a HTCS configuration, which remains so after rotation and/or combining with additional sub-laminates through stacking or interlacing. A long held misconception is that extension-twisting coupling arises only in anti-symmetric angle-ply laminates. However, angle-ply laminates represent only a very small subset of coupled (and uncoupled) laminate classes and the vast majority in fact contain cross-ply and angle-ply combinations. Furthermore, there are no angle-ply laminate configurations with HTCS behaviour.

The necessary conditions for HTCS behaviour have been shown [1] to be square symmetry in **A**, **B** and **N**$^{\text{Thermal}}$, with **M**$^{\text{Thermal}}$ = **0**; where square symmetry is defined elsewhere [8] as equal stiffness on principal axes, as would be the case in a cross-ply laminate or a fabric with balanced weave. Note that the bending stiffness properties have no influence on the HTCS properties. To prove this, an example is given for one of the 8-ply solutions derived from standard ply orientations: [-45/45/45/-45/0/90/90/0]$_T$. Note that the lamination parameters, ξ_i, are independent of the material properties but are ply orientation dependent. This material independence extends to the form of the ABD matrix for identifying square symmetry, i.e. the HTCS condition. The lamination parameters for this laminate configuration can be calculated using Eq. (5), which gives $\xi_6 = -1.0$, and $\xi_9 = \xi_{11} = 0.09$; all other $\xi_i = 0$. The ABD stiffness matrix can readily be calculated from Eq. (2) using a typical graphite/epoxy material with Young's moduli $E_1 = 155$GPa and $E_2 = 12.1$GPa, shear modulus $G_{12} = 4.4$GPa, Poisson's ratio $\nu_{12} = 0.248$, lamina thickness, $t = 0.15$mm, coefficient of thermal expansion, $\alpha_1 = -0.01800 \ 10^{-6}/°C$, $\alpha_2 = 24.3 10^{-6}/°C$:

$$A = \begin{bmatrix} 79102 & 25260 & 0 \\ 25260 & 79102 & 0 \\ 0 & 0 & 26921 \end{bmatrix} \quad B = \begin{bmatrix} 6492 & -6492 & 0 \\ -6492 & 6492 & 0 \\ 0 & 0 & -6492 \end{bmatrix} \quad D = \begin{bmatrix} 10462 & 3031 & -485 \\ 3031 & 8523 & -485 \\ -485 & -485 & 3231 \end{bmatrix}$$

$$N^{\text{Thermal}} = \begin{Bmatrix} N_x^{\text{Thermal}} \\ N_y^{\text{Thermal}} \\ N_{xy}^{\text{Thermal}} \end{Bmatrix} = \begin{Bmatrix} 1.266 \\ 1.266 \\ 0 \end{Bmatrix} \Delta T \qquad M^{\text{Thermal}} = \begin{Bmatrix} M_x^{\text{Thermal}} \\ M_y^{\text{Thermal}} \\ M_{xy}^{\text{Thermal}} \end{Bmatrix} = \begin{Bmatrix} 0 \\ 0 \\ 0 \end{Bmatrix} \qquad (6)$$

revealing square symmetry in the extensional (**A**) and coupling (**B**) matrices. The thermal load vector is also square symmetric, which equates to thermally isotropic behaviour [9], and that the thermal moment vector is null.

The form of square symmetry in the coupling (**B**) stiffness matrix varies with off-axis material alignment, β, which is summarized in Table 1. In this case the extensional (**A**) stiffness matrix is isotropic, hence the properties are invariant for all off-axis alignments.

Table 1 *– Conditions for HTCS behavior in coupled laminates with standard ply orientations.*

Lamination parameters and stiffness relationships with respect to material axis alignment, β.		
β = mπ/2	β = π/8 + mπ/2 (m = 0, 1, 2, 3)	β ≠ mπ/2, π/8 + mπ/2
$\begin{bmatrix} B_{11} & -B_{11} & 0 \\ -B_{11} & B_{11} & 0 \\ 0 & 0 & -B_{11} \end{bmatrix}$	$\begin{bmatrix} 0 & 0 & B_{16} \\ 0 & 0 & -B_{16} \\ B_{16} & -B_{16} & 0 \end{bmatrix}$	$\begin{bmatrix} B_{11} & -B_{11} & B_{16} \\ -B_{11} & B_{11} & -B_{16} \\ B_{16} & -B_{16} & -B_{11} \end{bmatrix}$
$\xi_5 = \xi_7 = \xi_8 = 0$	$\xi_5 = \xi_6 = \xi_7 = 0$	$\xi_5 = \xi_7 = 0$

The form of the ABD matrix of primary interest corresponds to the off-axis alignment, β = π/8, or 22.5°, since this gives rise to coupling between extension-twisting (and shearing-bending). Applying this design criteria reveals 6, 20, 252, and 3076 solutions for 8-, 12-, 16- and 20-ply HTCS laminates; all containing equal combinations of cross-ply and angle-ply laminates.

3 ASSESSMENT ON BUCKLING PERFORMANCE

Closed form solutions for compression buckling and natural frequency prediction of simply supported rectangular panels are well known and well documented in the literature for both isotropic materials and orthotropic laminated composite materials. Less well known are closed form solutions for coupled laminates, derived previously for cross-ply laminates [10], possessing extension-bending coupling, and for angle-ply laminates [7], with extension-twisting (and shearing-bending) coupling. This is perhaps due to the widespread misunderstanding of coupled laminate buckling behaviour to which these closed form equations have been applied. For instance, many results have been presented for the buckling problem on the false assumption that bifurcation buckling occurs: simply supported rectangular plates consisting of cross-ply laminates with extension-bending coupling will in fact bend, and not buckle, under in-plane compressive load.

Early work investigating the effect of coupling on the buckling strength for simply supported rectangular anti-symmetric angle-ply laminated plates [11] concluded that a decrease in the plate buckling strength, with respect to the fully uncoupled laminate solution, occurs at all plate aspect ratios. This work however precluded the possibility that extension-twisting coupling can be achieved by other forms of laminate stacking sequence [12].

Bounds on the critical buckling load for the 8-, 12-, 16- and 20-ply HTCS extension-twisting coupled laminates are therefore investigated, using the closed-form buckling solution of Eq. (8), derived elsewhere [7, 13]. Here the value of *m* and *n* are the number of buckle half wavelengths in the x and y directions, respectively. The bounds for the critical buckling load are presented in non-dimensional form,

$$k_x = (N_x b^2)/(\pi^2 D_{iso}) \tag{7}$$

across a range of plate aspect ratios, where:

$$N_x = (a/m\pi)^2 \{T_{33} + (2T_{12}T_{23}T_{13} - T_{22}T_{13}^2 - T_{11}T_{23}^2)/(T_{11}T_{22} - T_{12}^2)\}$$

where

$T_{11} = A_{11}(m\pi/a)^2 + A_{66}(n\pi/b)^2$

$T_{12} = (A_{12} + A_{66})(m\pi/a)(n\pi/b)$

$T_{13} = -(3B_{16}(m\pi/a)^2 + B_{26}(n\pi/b)^2)(n\pi/b)$ (8)

$T_{22} = A_{22}(n\pi/b)^2 + A_{66}(m\pi/a)^2$

$T_{23} = -(B_{16}(m\pi/a)^2 + 3B_{26}(n\pi/b)^2)(m\pi/a)$

$T_{33} = D_{11}(m\pi/a)^4 + 2(D_{12} + 2D_{66})(m\pi/a)^2(n\pi/b)^2 + D_{22}(n\pi/b)^4$

and

$$D_{Iso} = E_{Iso}H^3/12(1 - \nu_{Iso}^2) = U_1H^3/12 \qquad (9)$$

Figures 1(a) - (d) illustrate the bounds of the critical buckling load for the 8-, 12-, 16- and 20-ply HTCS laminate solutions with extension-twisting coupling behaviour. The buckling envelope for an equivalent fully isotropic laminate (FIL) is also plotted on each figure for comparison. The bending stiffness, D_{Iso}, of the equivalent FIL, is used to normalise the buckling results.

The bounds in Fig. 1 reveal that HTCS extension-twisting coupled laminate configurations all fall on or below the buckling strength of the equivalent fully isotropic laminates (FIL). The 8-ply laminate example given earlier has the highest extension-twisting coupling magnitude in its ply number grouping, but this results in up to a 16% reduction in buckling strength compared to the equivalent fully isotropic laminate; it represents the lower bound curve shown in Fig. 1(a).

Also presented in Fig. 1(a) are two competing laminate designs from the literature. The buckling envelope corresponding to Ref. [5] represents a configuration that has been optimised for maximum extension-twisting coupling, resulting in a configuration with free-form angle orientations: [-21.5/72.1/57.9/-29.6/29.6/-57.9/-72.1/21.5]$_T$. However, the effect of increased extension-twisting coupling can be seen to have a negative influence on the laminate buckling strength, and the buckling envelope falls below the lower bound for laminates with standard ply orientations in Fig. 1(a). The buckling envelope corresponding to Ref. [3], represents an extension-shear coupled laminate, which has been used in tilt-rotor blade designs to produce extension-twisting coupling behaviour at the structural level. Here, an 8-ply balanced and symmetric stacking sequence, [(0/90)$_2$]$_S$, with off-axis material alignment of 20°, gives rise to the extension-shearing coupling behaviour at the laminate level. However, the off-axis alignment also introduces bending-twisting coupling, which has a significant impact on the compression buckling strength [14]. Given that no exact closed form solution exists for laminates with extension-shearing and bending-twisting coupling, this buckling envelope was developed using a commercial finite element code [15]. The buckling strength for this class of coupled laminate is shown to be up to 11% lower than the equivalent fully isotropic laminate.
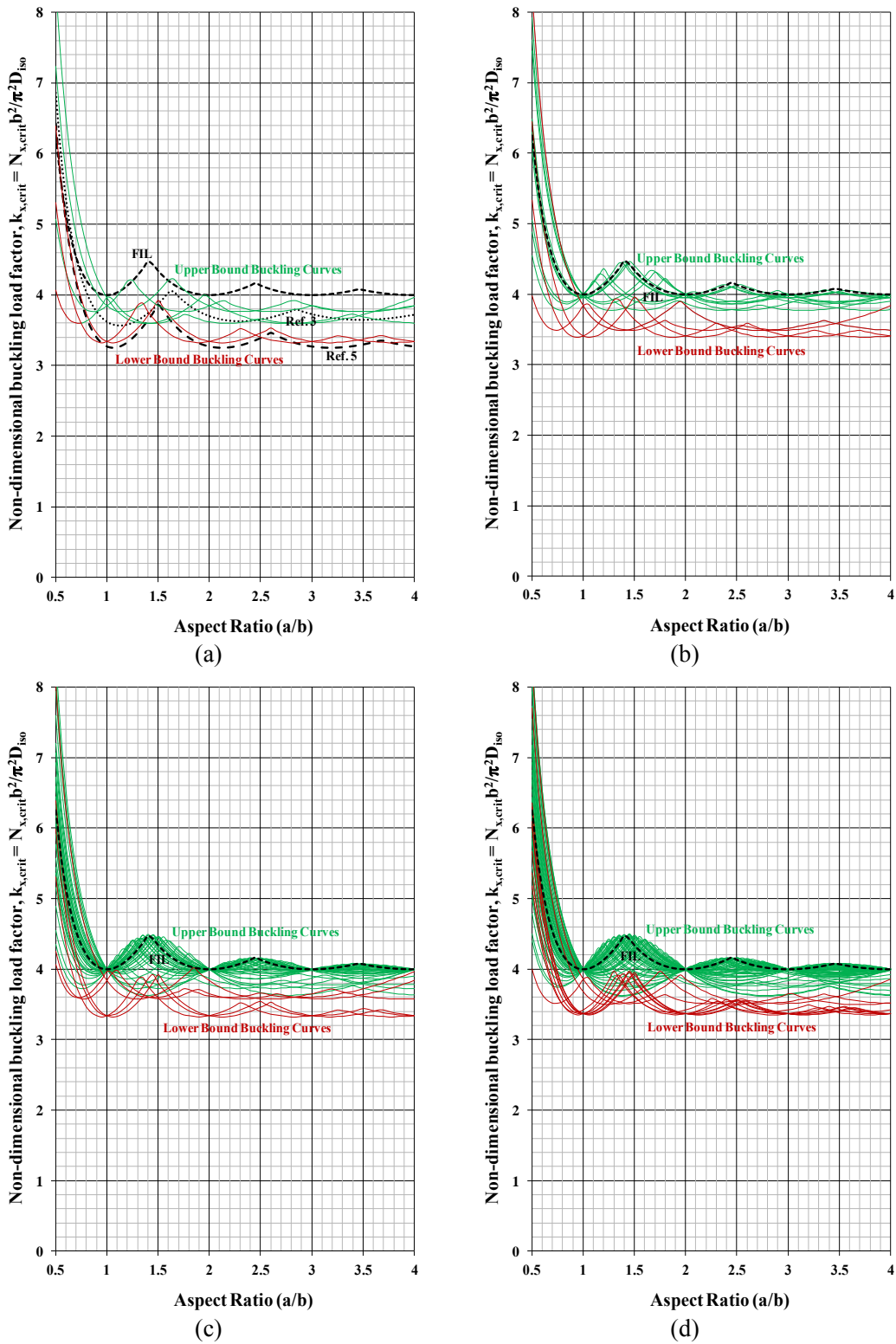
Figure 1 *– Bounds on the compression buckling of extension-twisting (and shearing-bending) coupled HTCS: (a) 8-ply; (b) 12-ply; (c) 16-ply and; (d) 20-ply laminates.*

4   EXTENSION-TWISTING INVESTIGATION

Recent work [16], investigating the twisting magnitude of other classes of extension-twisting coupled laminate, has shown good agreement between experimental results and non-linear finite element model predictions [15]. These validated finite element model simulations, illustrated in Fig. 2, are employed again here to assess the response of these new laminate designs and in particular those laminates identified as possessing maximum extension-twisting coupling behaviour in each ply number grouping. The twisting magnitude of the specimen is assessed up to an axial load corresponding to the predicted failure load; calculated from the Tsai-Wu failure criterion of Eq. (10) for standard carbon/epoxy material properties from which the parameters in Table 2 have been derived. Note that the Tsai-Wu failure stresses in tension are presented in terms of the non-dimensional load factor, k_x. Results are presented in Fig. 3 for the six 8-ply HTCS laminate solutions, possessing extension-twisting (and shearing-bending) coupling.

24mm

180mm

(a)   (b)
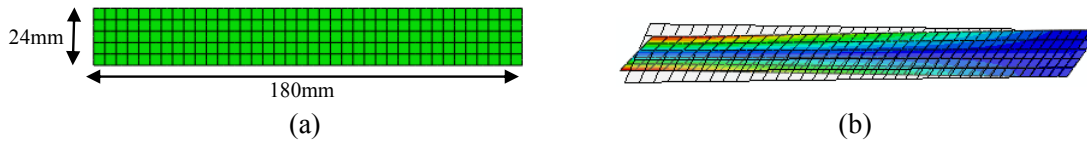
Figure 2 – *Finite Element Model illustrating: (a) Element mesh; (b) Twisting deformation.*

$$F_1\sigma_1 + F_2\sigma_2 + F_{11}\sigma_1^2 + F_{22}\sigma_2^2 + F_{66}\tau_{12}^2 - \sqrt{F_{11}F_{22}}\,\sigma_1\sigma_2 = 1$$

where,   (10)

$$F_1 = \frac{1}{\sigma_1^T} + \frac{1}{\sigma_1^C} \qquad F_2 = \frac{1}{\sigma_2^T} + \frac{1}{\sigma_2^C} \qquad F_{11} = -\frac{1}{\sigma_1^T\sigma_1^C} \qquad F_{22} = -\frac{1}{\sigma_2^T\sigma_2^C} \qquad F_{66} = \left(\frac{1}{\tau_{12}^F}\right)^2$$

Table 2 – *Tsai-Wu failure parameters for graphite/epoxy material*

$\sigma_1^T = 1500$MPa	$F_1 = -0.1333$ 1/GPa
$\sigma_1^C = -1250$MPa	$F_2 = 15.00$ 1/GPa
$\sigma_2^T = 50$MPa	$F_{11} = 0.533$ (1/GPa)^2
$\sigma_2^C = -200$MPa	$F_{22} = 100$ (1/GPa)^2
$\tau_{12}^F = 100$MPa	$F_{66} = 100$ (1/GPa)^2

Figure 3(a) demonstrates that the strength of the laminate decreases as the extension-twisting coupling magnitude increases. Laminates with highest coupling magnitude, i.e. L1 and L6 are capable of generating a twist rate as high as 160 Deg./m while L3 and L4 laminates, with weaker coupling, result in a twist rate of 36 Deg./m. Figure 3(b) provides a comparison between the maximum twist rates achievable for 8-, 12-, 16-, and 20-ply solutions; corresponding to stacking sequences: $[(-22.5/67.5)_S/(22.5/112.5)_S]$, $[(-22.5/67.5)_2/67.5/\pm22.5/112.5_2/22.5/112.5/22.5]$, $[(-22.5/67.5)_{S2}/(22.5/112.5)_{S2}]$, and $[-22.5_2/67.5_2/-22.5/67.5_3/(-22.5/22.5)_2/112.5_3/(22.5/112.5)_S/22.5]$, respectively.
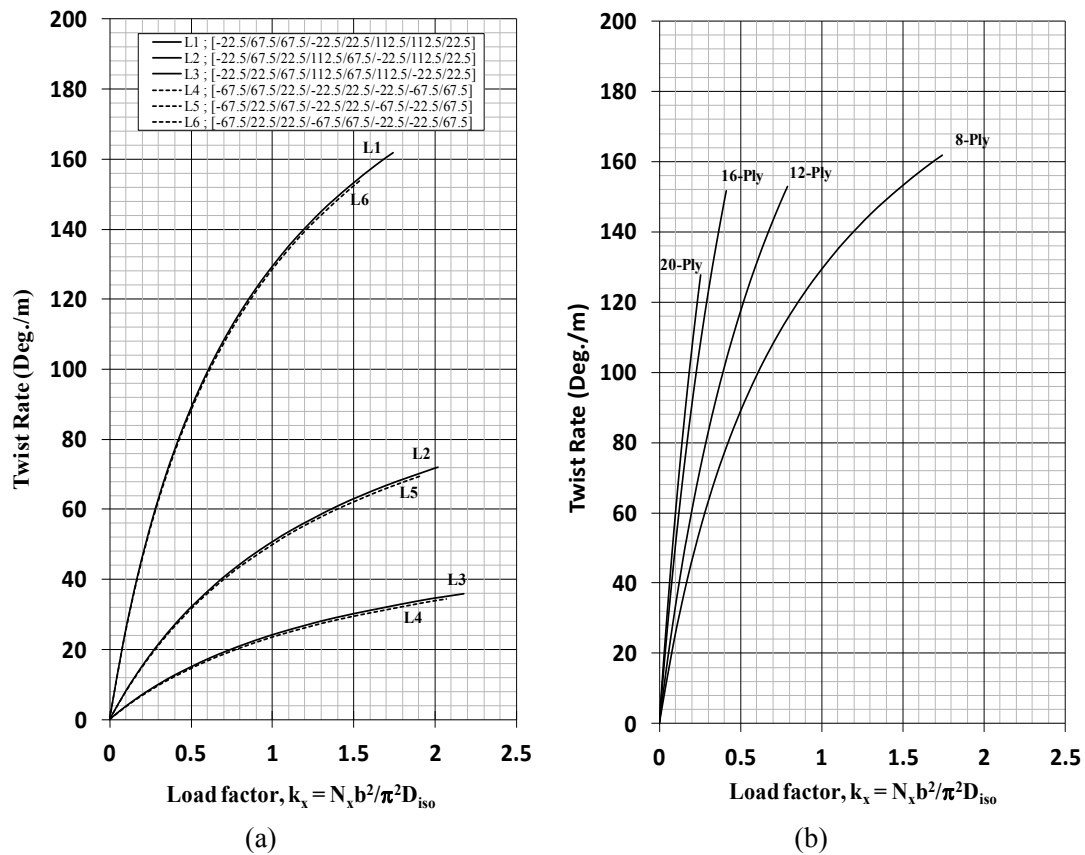
Figure 3 *– Twist rate vs. Load factor for: (a) the six 8-ply HTCS extension-twisting solutions and (b) the maximum extension-twisting solution for each ply number grouping.*

5   CONCLUSION

Bounds on the buckling curves have been presented for the hygro-thermally curvature-stable laminates with extension-twisting (and shearing-bending) coupling for the 8-, 12-, 16-, and 20-ply laminate solutions. All laminates are based on standard ply orientations to which an off-axis orientation is then applied. The upper-bound buckling envelopes are all shown to fall on or below the buckling curve representing the equivalent fully isotropic laminate, used here as a datum configuration against which all comparisons have been made.

Laminates derived from free form angle orientations, which have been optimised for maximum extension-twisting coupling, have been shown to fall below the lower-bound buckling envelope of laminates with standard ply orientations.

Extension-twisting coupling behaviour has been shown to reduce the buckling strength. The material failure strength has also been shown to reduce with increasing extension-twisting coupling magnitude; a trend which extends across all ply number groupings.

6   REFERENCES

[1]   C. York, "Unified approach to the characterization of coupled composite laminates Hygro-thermally curvature-stable configurations," *International Journal of Structural Integrity,* vol. 2, pp. 406-436, 2011.

[2]   S. J. Winckler, "Hygrothermally Curvature Stable Laminates with Tension-Torsion Coupling," *Journal of the American Helicopter Society,* vol. 30, pp. 56-58, 1985.

[3]   M. W. Nixon, "Extension-twist coupling of composite circular tubes with application to tilt rotor blade design," in *Proc. 28th AIAA/ASME/ASCE/AHS/ASC Structures, Structural Dynamics, and Materials*, Monterey, USA, 1987.

[4]   H. P. Chen, "Study of hygrothermal isotropic layup and hygrothermal curvature-stable coupling composite laminates," in *44th AIAA/ASME/ASCE/AHS/ASC Structures, Structural Dynamics, and Materials Conference, April 7, 2003 - April 10, 2003*, Norfolk, VA, United states, 2003, pp. 958-967.

[5]   R. A. Haynes, M. Hyer, E. Armanios, "New families of hygrothermally stable composite laminates with optimal extension-twist coupling," 1801 Alexander Bell Drive, Suite 500, Reston, VA 20191-4344, United States, 2010, pp. 2954-2961.

[6]   R. Haynes and E. Armanios, "Hygrothermally stable extension-twist and bend-twist coupled laminates," in *67th American Helicopter Society International Annual Forum 2011, May 3, 2011 - May 5, 2011*, Virginia Beach, VA, United states, 2011, pp. 2660-2665.

[7]   J. M. Whitney and A. W. Leissa, "Analysis of Heterogenous Anisotropic Plates," *Journal of Applied Mechanics,* vol. 36, p. 261, 1969.

[8]   S. W. Tsai and H. T. Hahn, *Introduction To Composite Materials*: Technomic Publishing Company, Inc., 1980.

[9]   G. Verchery, "Design Rules for the Laminate Stiffness," *Mechanics of Composite Materials,* vol. 47, pp. 47-58, 2011.

[10]   R. M. Jones, "Buckling and Vibration of Unsymmetrically Laminated Cross-Ply Rectangular Plates", *AIAA journal*, vol. 11, pp. 1626-1632, 1973.

[11]   J. M. Whitney and A. W. Leissa, "Analaysis of simply supported laminated anisotropic rectangular plate," *AIAA journal,* vol. 1, pp. pp. 28 - 33, 1970.

[12]   C. B. York, "Extension-Twisting coupled laminates for aero-elastic compliant blade design," *Proc. 53rd AIAA/ASME/ASCE/AHS/ASC Structures, Structural Dynamics and Materials Conference*, 2012, Paper No. AIAA-2012-1457, Honolulu, Hawaii.

[13]   R. M. Jones, *Mechanics of Composite Materials*, 2nd Edition ed. Blacksburg, Virginia: Taylor & Francis, Inc., 1999.

[14]   C. B. York and P. M. Weaver, "Balanced and symmetric laminates – New perspectives on an old design rule," *Proc. 51st AIAA/ASME/ASCE/AHS/ASC Structures, Structural Dynamics, and Materials Conference*, 2010, Paper No. AIAA-2010-2775, Orlando, Florida.

[15]   ABAQUS/Standard v6.10 User's Manual

[16]   M. H. Shamsudin, J. Roussea, J. Verchery, C. B. York, "Experimental Validation of the Mechanical Coupling Response for Hygro-Thermally Curvature-Stable Laminated Composite Materials," in *Proc. 6ᵗʰ International Conference on Supply on the Wings*, Frankfurt, Germany, 2010.

Mixed Mode Behavior for Composite Bonded Joints

M.V. C. Fernández[1], M. F. S. F. de Moura[1], L. F. M. da Silva[1], A.T. Marques[1]

[1]Faculty of Engineering, University of Porto, R. Dr. Roberto Frias, 4200-465 Porto, Portugal

Abstract Nowadays the requirements in increased strength to weight ratio, cost production and other high end parameters steer the industry to the application of composite materials. These materials demand composite bonded joints to take advantage of their full potential as a structural element. Despite the advances in recent years and the exponential growth in which these applications occur, a complete knowledge of the behaviour under fatigue loading is still missing. Adhesive joints are often loaded in mixed mode conditions. For this reason, an analysis of the behaviour of the joints and the contribution of each mode becomes important to predict and simulate accurately. To define this contribution, a relation of the Paris-law has been established, where the parameter C_1 and m represent the Paris-law constants obtained for each one of the modes.

1   Introduction

Many practical adhesives applications involve the use of single lap joints, which leads to a combination of in-plane tension and shear (Modes I and II, respectively) [1]. Therefore, fatigue/fracture characterization under mixed-mode I+II loading is an essential task in order to understand how structures behave in real scenarios. For this reason, an analysis about the appropriateness and applicability of suitable mixed-mode fatigue/fracture characterization tests is becoming very important. There are several types of tests used for fracture characterization under mixed-mode I+II loading. The *S*ingle *L*eg *B*ending (SLB) presents an excellent compromise between its simplicity and equilibrium between the energies dissipated in the two modes. Yoon et al. [2] showed that for a specimen with equal arms thickness, the mode I energy release rate is approximately 57.5% of the total energy, i.e., a mode mixity phase angle φ of 41° [2].

$$\varphi = \tan^{-1} \sqrt{\left(\frac{G_{II}}{G_I} \right)} \qquad (1)$$

The drawback of the SLB is related to the aspect that it provides a fixed mode mixity or a small range of its variation considering arms with different thickness [3]. However, since the pure mode fatigue/fracture studies have been already performed, the mixed-mode results propitiated by the SLB test will allow to assess the influence of the mode mixity on the fatigue behavior of composite bonded joints, namely when compared to the pure mode values. Consequently, the objective of this work is understand how the mixity affects the crack propagation rate.

One of the most common methods to evaluate the crack propagation in fatigue is related with fracture mechanics where the crack propagation rate can be associate to the energy release rate (G) [4]. The plot of this relation allows definition of the specimens life in 3 stages (Figure 1), considering a logarithmic scale. The 1ˢᵗ corresponds to the initiation where the crack is not visible, the 3ʳᵈ is characterized by a rapid and catastrophic crack growth and the 2ⁿᵈ is where the Paris law is applicable (Equation **(2)**).

$$\frac{da}{dN} = C_1 (G_{max})^m \tag{2}$$

The C_1 and m of the Paris law are considered constants of the fatigue crack propagation rate and they represent the characteristics of the specimens and of the experimental conditions (dimensions and materials tested) [5].
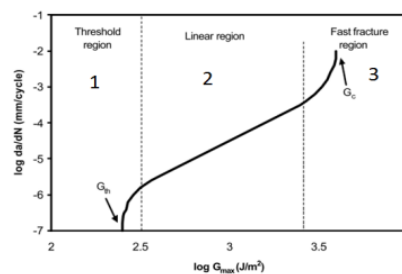

Figure 1 – *Schematic representation of the propagation rate during fatigue tests*

2   Materials and Methods

Materials and Specimens

The SLB specimen consists of two beams bonded with a 0.2 mm thick adhesive layer. Each beam was prepared with 18 plies of unidirectional prepreg (CFRP – Carbon Fiber Reinforced Plastic) leading to an arm thickness of 2.7 mm. A ductile epoxy adhesive, Araldite 2015, was used. The properties of the bulk adhesive and the CFRP adherends were already defined by Campilho et al.[6]. The CFRP properties are shown in Table 1**Error! Reference source not found.**.

Table 1 – *CFRP elastic orthotropic properties for a unidirectional ply aligned in the 0ᵒ direction* [6]

Young's Modulus	Poisson's Ratio	Shear Modulus
$E_1 = 1.09E+05$ MPa	$v_{12} = 0.34$	$G_{12} = 4315$ MPa
$E_2 = 8819$ MPa	$v_{13} = 0.34$	$G_{13} = 4315$ MPa
$E_3 = 8819$ MPa	$v_{23} = 0.38$	$G_{23} = 3200$ MPa

The specimen dimensions were defined in accordance with specimens made for mode I and mode II ($L = 90$ mm, $a_0 = 45$ mm, $B = 25$ mm). The bonded surfaces were polished with sandpaper and cleaned with acetone. After, a 0.2 mm calibrated steel strip was inserted between the two specimen arms to guarantee the adhesive thickness. The next stage was pouring the adhesive, assembling and holding it with pressure. The cure of the adhesive was

performed at room temperature for five days. The initial pre-crack was created with a metal strip during the manufacturing of the specimens.

Testing procedure

The SLB test requires simple experimental equipment [7]. In these tests, the load is applied in the center of the specimen like the End-Notched Flexure tests [8]. Figure 2 shows a schematic representation of this test. Considering that the purpose of this work was to analyze the applicability of the SLB tests to fatigue/fracture characterization under mixed-mode I+II, the load applied was 50% of the static failure load to keep the same conditions already made in previous works. The cyclic fatigue loading of the specimens was carried out on a MTS servohydraulic machine, with a frequency of 4Hz, load ratio (R) of 0.1 and with constant load amplitude. Figure 2 shows the used setup.
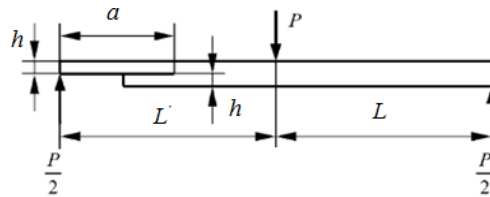
Figure 2 – Schematic representation of the SLB test and geometry of the specimens (width B).

3 Data Reduction Scheme

Calculation of the energy release rate (G_{TSLB}) [9]

The method is based on specimen compliance and beam theory and crack equivalent concept is named Compliance Based Beam Method (CBBM) [9]. This method was already validated for fatigue under Mode I using the DCB test by Fernandez et al. [10].

Using the Timonshenko beam theory, the equation of compliance at the loading point for a crack length a is [9]

$$C = \frac{7a^3 + 2L^3}{8E_1 Bh^3} + \frac{3(a + 2L)}{20G_{13}Bh} \tag{3}$$

The variables are defined in Figure 1 and Table 2. The initial crack length and the initial compliance can be used in Equation (3) to estimate the flexural modulus.

$$E_f = \left(C_0 - \frac{3(a_0 + 2L)}{20G_{13}Bh} \right) \frac{7a_0^3 + 2L^3}{8Bh^3} \tag{4}$$

This procedure allows accounting indirectly for several specificities that are not included in the beam theory, as is the case of stress concentration in the vicinity of the crack tip, the presence of the adhesive and material variability between different specimens. Equation (3) can also be solved in order to get the equivalent crack length during propagation as a function of the current compliance C, i.e., $a_e = f(C)$. This requires the resolution of a cubic equation which can be easily performed using the Matlab software [9]. By applying the Irwin-Kies equation

$$G_T = \frac{P^2}{2B} \frac{dC}{da}$$

(5)

the fracture toughness in mixed-mode can be obtained

$$G_T^{SLB} = \frac{21P^2 a_e^2}{16E_f B^2 h^3} + \frac{3P^2}{10G_{13}B^2 h}$$

(6)

With this procedure the total energy and its components do not depend on crack length measurement during propagation. They depend on the specimen compliance which is used to estimate an equivalent crack length (a_e), hence accounting for the fracture process zone effects, thus constituting an important advantage of this method.

Determination of the fatigue crack growth rate, da_e/dN

The da_e/dN was calculated with the secant method (Equation 8) recommended in the standard ASTM E647 [15]. This method consists on analyzing the variation of equivalent crack length as a function of the number of cycles considering a discrete number of measurements (n) during the fatigue test

$$\left(\frac{da_e}{dN}\right)_{\bar{a}e} = \frac{\left(a_{e_{i+1}} - a_{e_i}\right)}{\left(N_{i+1} - N_i\right)}$$

(8)

$$\overline{a_e} = \frac{\left(a_{e_{i+1}} + a_{e_i}\right)}{2}$$

(9)

where i represents the ith measurement performed during the test ($0 \leq i \leq n$). This gives an average value of the rate in an increment. The corresponding equivalent crack length, for each G_T^{SLB}, is also the average value of the limits of the increments (Equation (9)).

The equivalent crack growth rate was evaluated as a function of the compliance along the fracture test. This variation was registered every 1000 cycles for the test with 50% of the maximum strength. The difference in the acquisition rate is related to the duration of each test.
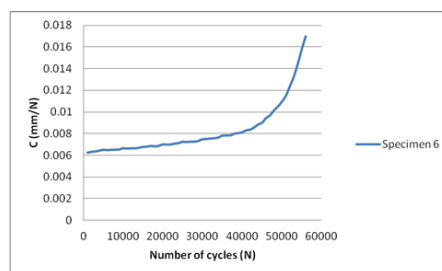
4   Experimental results

Failure characterization and fracture surfaces

In all the specimens tested the crack grew towards the interface. Nine specimens were tested: one failed in the interface (adhesive failure), six failed cohesively and two were by delamination. In this case, the cohesive failure was characterized by an initiation zone where the failure look similar to the fracture zones obtained for Mode II followed by a propagation zone where the surfaces are similar to Mode I fatigue failure (Figure 3). This comparison was made with previous works [10], [11] focused on pure modes fatigue/fracture characterization. In general the damage and crack propagation is stable and smooth variation of the compliance is visible (Figure 4).
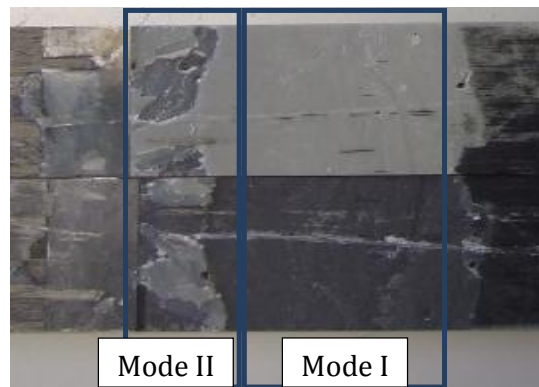
Figure 3 – *Fracture surfaces of the specimens tested with 50% of the load.*

Figure 4 – *Typical compliance (C) versus number of cycles (N).*

Paris Law

All of them presented good results (Figure 5). The experimental coefficients C_1 and m are shown in Table 2; C_1 varies roughly from 0.03 to 0.04 mm/cycle and m from 2.9 to 3.1, which leads to a CoV of 14% and 2%, respectively. The higher scatter of C_1 can be explained by the fact that this parameter depends on the damage initiation instant, which is influenced by the pre-crack fabrication. The correlation coefficient is bigger than 0.9 (***Figure 6***) for the linear region where the Paris law was applied. A general law was defined by using the average values of the specimens (Table 2 and Figure 5) and a correlation between it and the experimental curves shows good agreement (Figure 5), i.e., the average law lies in between the specimen's laws. Also, ***Figure 6*** shows how coincident this law is when compared with the da_e/dN of each specimen.
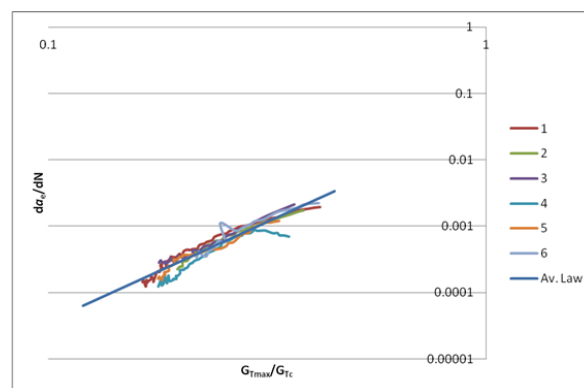
Figure 5 – *Stable crack growth (linear region) of the specimens tested at 50% of the maximum static load.*
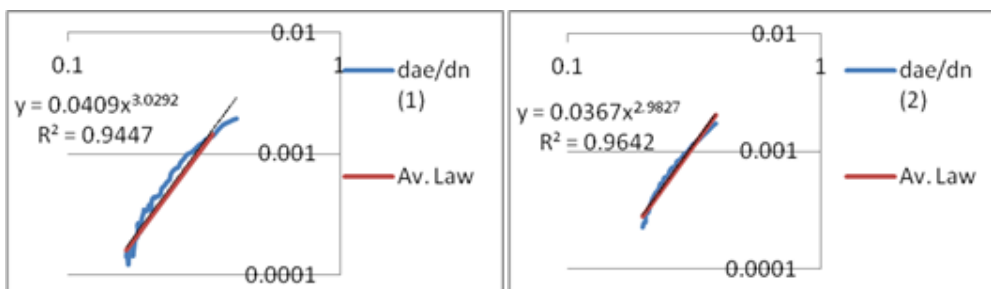
Figure 6 – *Paris law and verification of the general law for each specimen.*

Table 2 – *Paris law constants of the validated specimens.*

Spec. Num.	C_1	m
1	0.0409	3.0292
2	0.0367	2.9827
3	0.0381	2.9097
4	0.0293	3.0597
5	0.0354	3.0136
6	0.0441	3.0833
Av.	*0.037*	*3.013*
Std. Dev	*0.005*	*0.062*
CoV	*14%*	*2%*

Mixed-mode correlation for the Paris Law

Finally, an evaluation of the Paris law parameters as a function of the mixed mode variation was performed. It was found that the propagation rate changes with the type of load (Figure 7). The crack propagation rate for mode I specimen is much higher than for mode II and mixed mode I+II, which present both similar values. It can be concluded that the presence of mode II loading is beneficial concerning this aspect, since it contributes to delay the final collapse under fatigue loading.
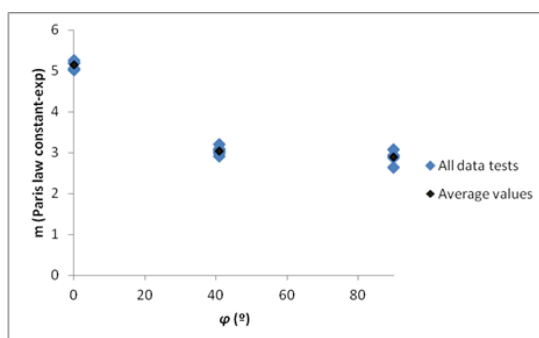

Figure 7 – *Paris-law m parameter as a function of the mixity.*

5 Conclusions

In general, very consistent results with low scatter concerning the parameter of the Paris law that defines the crack propagation rate were obtained. It was also observed that the linear crack propagation rate has an excellent behavior, since the linear correlation was higher than 0.9 for all specimens.

On the other hand the *m* parameter is similar relative to pure mode II case and lower to the pure mode I case. Thus, it was concluded that the presence of a mode II component has a beneficial effect on bonded joints life.

6 References

[1] X. X. Xu, A. D. Crocombe, and P. A. Smith, "Mixed-Mode fatigue and fracture behaviour of joints bonded with either filled of filled and toughened adhesive," *Int. J. Fatigue*, vol. 17, no. 4, pp. 279–286, 1995.

[2] S. H. Yoon and C. S. Hong, "Modified end notched flexure specimen for mixed mode interlaminar fracture in laminated composites," *International Journal of Fracture*, vol. 43, no. 1, pp. R3–R9, May 1990.

[3] J. Hutchinson and Z. Suo, "Mixed Mode Cracking in Layered Materials," *Advances In Applied Mechanics*, vol. 29, 1992.

[4] I. Ashcroft and S. Shaw, "Mode I fracture of epoxy bonded composite joints 2. Fatigue loading," *Int. J. Adhes Adhes*, vol. 22, no. 2, pp. 151–167, 2001.

[5] D. L. Erdman and J. M. Starbuck, "Fatigue Crack Growth in Adhesive Joints," in *SAMPE-ACCE-DOE-SPE Midwest Advanced Materials and Processing Conferences*, Dearborn MI, 2000.

[6] R. Campilho, M. Moura, and J. Domingues, "Stress and Failure Analyses of Scarf Repaired CFRP Laminates using a Cohesive Damage Model," *J of Ad Sci and Tech*, vol. 21, no. 9, pp. 855–870, 2007.

[7] A. Szekrenyes and J. Uj, "Beam and finite element analysis of quasi-unidirectional composite SLB and ELS specimens," *Comp. Sci. and Tech*, no. 64, pp. 2393–2406, 2004.

[8] R. Krueger and T. K. O'Brien, "A shell/3D modeling technique for the analysis of delaminated composite laminates," *Composites Part A: Applied Science and Manufacturing*, vol. 32, no. 1, pp. 25–44, Jan. 2001.

[9] J. M. Q. Oliveira, M. F. S. F. de Moura, and J. J. L. Morais, "Application of the end loaded split and single-leg bending tests to the mixed-mode fracture characterization of wood," *Holzforschung*, vol. 63, no. 5, pp. 597–602, 2009.

[10]   M. V. Fernández, M. F. S. F. de Moura, L. F. M. da Silva, and A. T. Marques, "Composite bonded joints under mode I fatigue loading," *International Journal of Adhesion and Adhesives*, vol. 31, no. 5, pp. 280–285, Jul. 2011.

[11]   M. V. Fernández, M. F. S. F. de Moura, L. F. M. da Silva, and A. T. Marques, "Characterization Of Composite Bonded Joints Under Pure Mode II Fatigue Loading."

Experimental Investigation of Initial Flaws in Aircraft 2024-T3 Thin Sheet

Wyman Zhuang[1], Qianchu Liu and Cathy Smith

Air Vehicles Division, Defence Science and Technology Organisation

Melbourne, VIC3207, Australia

[1]*wyman.zhuang@dsto.defence.gov.au*

Abstract The fuselage of a common pilot training aircraft is a semi-monocoque structure, with thin skin, conventional bulkheads and stringers. Most of this aircraft components are made of aluminium alloy 2024-T3 thin sheet. Maintaining aircraft structural integrity to ensure safe operation of the fleet is critically dependent on accurate analysis and reliable prediction of fatigue crack growth in such a thin-walled airframe subjected to flight spectrum loading. One of the challenging topics in the prediction of fatigue crack growth is to identify representative initial flaws and defects that can cause fatigue crack initiation and subsequent crack growth. This paper, therefore, addresses this challenge with a critical literature review and experimental assessment of initial flaw types that may cause fatigue crack initiation. With a focus on aluminium alloy 2024-T3 thin sheet, the results cover various discontinuities from microstructural constituent particles inherent from the material process to macrostructural defects and surface discontinuities (such as burrs and machining marks) introduced during the production of airframes. Considering that not all discontinuities in aluminium alloy 2024-T3 thin sheet will be definite sources of fatigue crack initiation, the material flaws and machining defects that dominate fatigue initiation were investigated experimentally. The paper concludes with a summary of flaws and defects dominated fatigue initiation, and based on the findings, recommendations on future research were made for fatigue crack growth prediction for thin-walled aluminium alloy 2024-T3 airframes.

1   Introduction

The Royal Australian Air Force (RAAF) PC-9/A is a conventional configuration, low wing trainer aircraft for pilot training from basic to advanced courses. Defence Science and Technology Organisation is currently supporting the RAAF PC-9/A empennage and aft-fuselage recertification and life assessment program. The ultimate goals of this program are twofold: first to manage the risk level of the fleet operations in accordance with aircraft airworthiness standards; and secondly to optimise the fleet management strategy to minimise cost and downtime. The PC-9/A aircraft fuselage is a conventional semi-monocoque structure, with thin skin, thin-walled bulkheads and stringers, and most of its fatigue critical structures are made of Aluminium Alloy (AA) 2024-T3 thin sheet because of the high strength and relatively high fracture toughness of the material. Maintaining aircraft structural integrity to ensure the safe operation of the fleet is critically dependent on accurate modeling and reliable prediction of fatigue crack growth in thin-walled airframes subjected to flight spectrum loading. One of the challenging topics in the prediction of fatigue crack growth is to identify initial flaw types that dominate fatigue crack initiation and subsequent crack propagation.

Various initial flaws and defects that may cause fatigue crack initiation can be introduced into aircraft structures as a result of material processing, airframe manufacturing and fleet maintenance [1]. For unclad AA2024-T3 thin sheet, DeBartolo and Hillberry in early 2000

found that some of the constituent particles, particularly the larger ones, can get broken and cracked or debonded from the surrounding matrix by the rolling process used to produce sheet material [2,3]. After fatigue testing, the examination of fatigue nucleation site discovered that the typical nucleation sites in the unclad thin sheet were those constituent particles that had been damaged during material processing. According to the engineering drawing data of the Original Equipment Manufacturer (OEM), most of PC-9/A airframe components and parts were made of unclad AA2024-T3 thin sheet. *Figure 1* shows a cracked constituent particle in an unclad AA2024-T3 thin sheet sourced from a PC-9/A vertical stabiliser from this study.
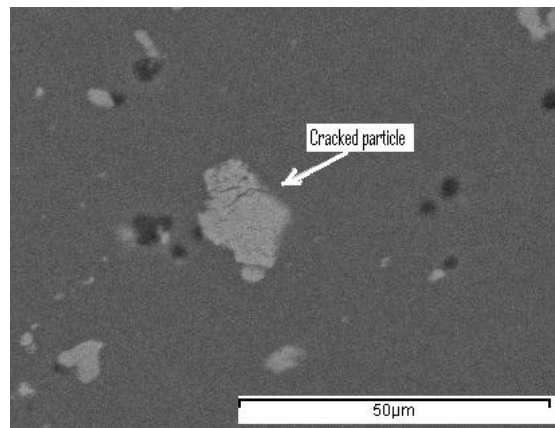
Figure 1 - Cracked constituent particle in PC-9/A AA2024-T3 thin sheet

In contrast to unclad AA 2024-T3, Merati in 2005 [4] and Okoro et al in 2010 [5] conducted fractography analysis using Scanning Electron Microscopy (SEM) and found that fatigue damage in the clad AA2024-T3 initiated mainly from the multiple nucleation sites along the exterior clad layer and the interior clad layer which were quite rough due to corrosion and surface preparation before painting, and their studies found no constituent particle involvement at the fatigue nucleation sites.

Initial flaws and defects can also be introduced into aircraft structures from component manufacturing, from poorly finished holes [6], machining marks, surface treatments [7,8,9], corrosion pits [10,11] and surface rumpling and microcracks due to fastener joint fretting and deformation [12,13].

Considering most of the PC-9/A fuselage skin panels and frames are fastened together with various rivets, rivet hole quality is likely to be the predominant factor affecting fatigue life. Ralph et al in 2009 [6] examined the interrelated effects of the beneficial compressive residual hoop stress induced by riveting process and the deleterious surface machining marks produced by drilling the pilot hole. In the drilling process, gouge marks from the drill bit, scoring marks from the bit withdrawal, rifling marks from chip removal and burrs due to the bit penetration of the exit surface can all have an impact on the final hole quality. Limited by productivity requirements during aircraft assembly, the burrs at the exit faces of thousands of rivet holes in the structures were typically not deburred before riveting [6]. It is believed that the burrs are likely crushed or plastically deformed by riveting or fastening. The hole surface-quality effects, particularly the straight marks left by a bit withdrawal after the bit was fully stopped, were assessed. Such a straight machining mark is oriented in an ideal direction to initiate a fatigue crack; possibly having a much more significant influence on fatigue life than the subsurface residual stresses.

It is worth noting that Equivalent Initial Flaw Size (EIFS) [14] is different from microstructural flaws inherent from the material process and macrostructural defects introduced during the production of the airframes. EIFS is dependent on the parameters used in fatigue crack growth models, such as specimen geometry and the load conditions that were used to calculate EIFS. Therefore, the EIFS will not be considered and discussed in this paper. The following sections, however, will be concentrated on the experimental assessment of material flaws and machining defects that may dominate fatigue crack initiation.

2 Microstructural Characterisation of AA2024-T3 Thin Sheet

The sample material used in this metallographic examination was taken from a skin panel of PC-9/A vertical stabiliser. Semi-quantitative chemical analysis of the samples was carried out using the Energy Dispersive (X-Ray) Spectrometer (EDS) attachment to a SEM. Approximate weight percentages of each material element were measured. *Table 1* shows the measured sample results compared with the specification for AA2024-T3 documented in Reference [15].

Table 1 – Assessment of material compositions measured from the Semi-quantitative EDS

Material	Al	Cu	Mg	Mn	Fe	Si
PC-9/A	Balance	4.0	1.5	0.34	-	-
AA2024 [15]	Balance	3.8-4.9	1.2-1.8	0.3-0.9	0.5 max	0.5 max

Cross-sections of the sample material were prepared for microhardness testing and microstructural examination. Optical microscopy was utilised to assess the microstructure of the section samples. *Figure 2* presents the micrograph of the etched sample (Keller's reagent) in the three plane orientations and it shows that the microstructures consist of elongated aluminium grains with the grain size ranging from 32 μm to 47 μm. The intermetallic particles can be clearly observed. The microstructure appeared to be typical of AA2024-T3 in terms of grain size and shape. Vickers microhardness testing was also undertaken (50g load), and the average of 10 measurements was 139 HV, which is consistent with the requirement in the specification. Optical microscope assessment and SEM analysis were performed on the failed coupons. As can be seen in *Table 1*, except the manganese (Mn) content of the PC-9/A sample was at the low end of the referenced AA2024-T3, the rest element contents of the sample were close to the specification. The results from this examination and the OEM engineering drawing data confirmed that the material examined was AA2024-T3.

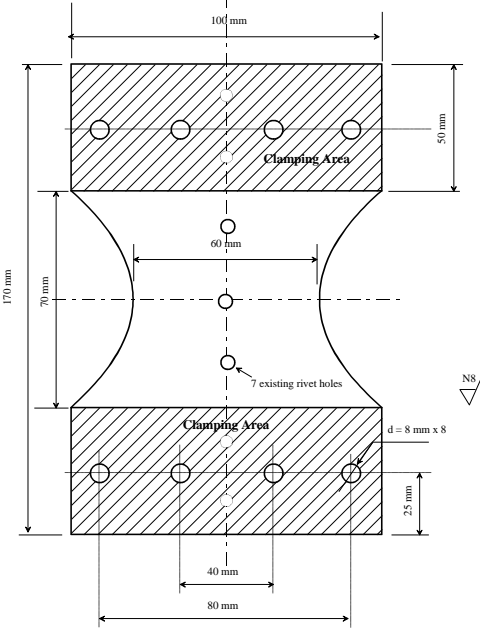## 3 Fatigue Testing of Initial Flaws and Defects

A total of 25 coupons used in fatigue testing of initial flaws and defects were manufactured from AA2024-T3, sourced from the vertical stabiliser skin panels of two different PC-9/A aircraft [16]. The stabilisers had been retired from RAAF service after they had accrued approximately 6,500 airframe hours. The configuration and dimensions of fatigue test coupons are illustrated in *Figure 3*. As can be seen, the holes along the centre line of the coupon are the existing rivet holes in the vertical stabiliser skin panels. The vertical stabilisers were carefully dissassembled so that the initial build quality was preserved.
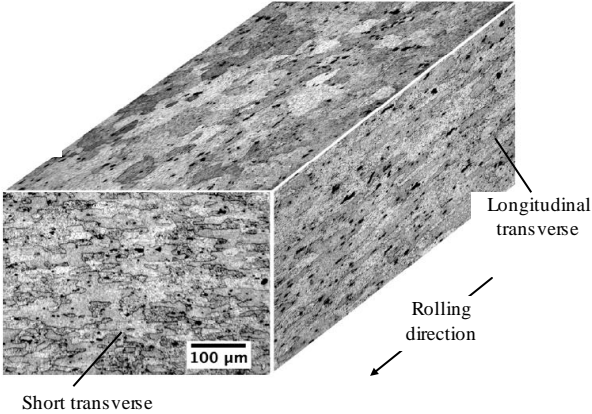
Figure 2 *- Micrographs of PC-9/A 2024-T3 in the etched conditions showing the distribution of constituent particles*

All coupons were fatigue cycled in a MTS 15kN servo-hydraulic testing machine under constant amplitude load with 1 percent load accuracy, until failure in laboratory air. The maximum applied stress was 130 MPa with the stress ratio (R) of 0.1 and the loading frequency was 10 Hz [16]. The coupons were tested without any additional surface treatment, the surface paint was not removed before the testing. No anti-buckling guide plates was used in the tests because the R ratio was positive.


Figure 3 *- Configuration and dimensions of fatigue test coupon (thickness t=0.6 mm)*

## 4   Initial Flaws and Defects in PC-9 AA2024-T3 Coupons

All coupons failed from a crack initiated at a rivet hole. A typical example is shown in *Figure 4*. The SEM image clearly showed that the fatigue crack initiated from a burr at the corner of a poor quality hole (*Figure 5*). This large deformed burr at the corner of a rivet hole was clearly observed (arrowed). Generally speaking, burrs or other types of surface discontinuities increase stress concentration, resulting in early crack initiation under a cyclic fatigue loading. An examination of the other coupons revealed that similar poor hole quality existed in all of the coupons. *Figure 6* shows typical examples of surface defects/or discontinuities. As can be seen, in the coupon from aircraft #1, machining marks were clearly observed to be present in the interior bore surface of the rivet hole. However, such poor hole finish was not obvious in the coupon from aircraft #2 and the corresponding quality was relatively good; these holes had a larger diameter (*Figure 6 (b)*). In addition, the investigation has found that there were burrs or drill scratches in the bores of rivet holes of all test coupons, as shown in *Figure 7*. It is believed that these surface discontinuities were caused by drilling or were deformed burrs resulting from the installation of the rivet.
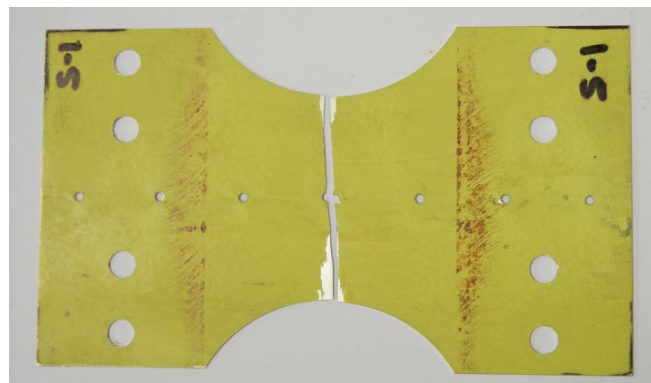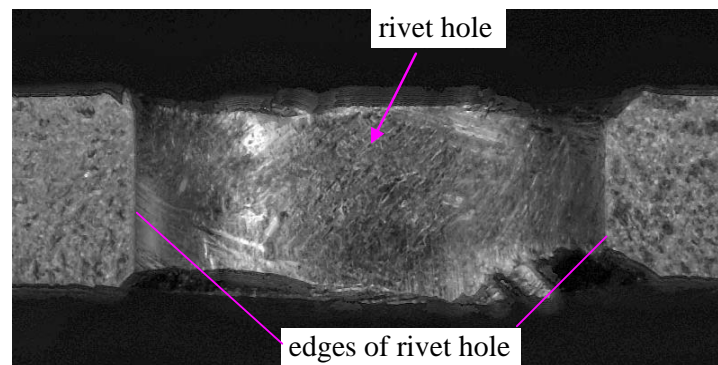

Figure 4 - *Fatigue cracking from a rivet hole in a coupon*
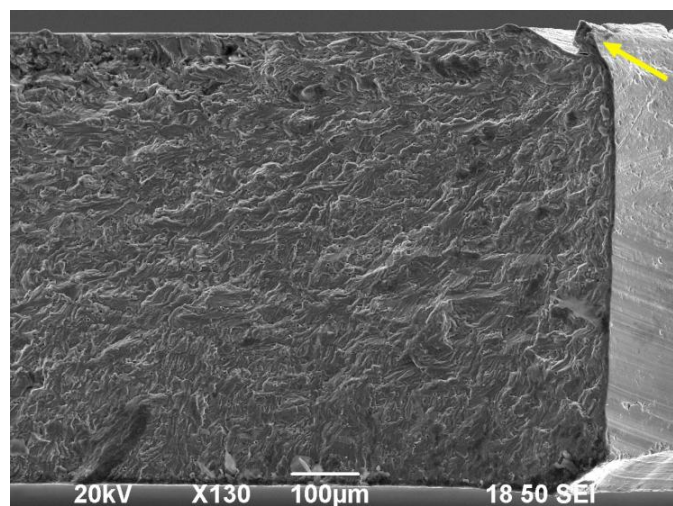
Figure 5 – *SEM image showing a deformed burr (arrowed) at the hole corner from which the fatigue crack initiated.*

(a)   **(b)**
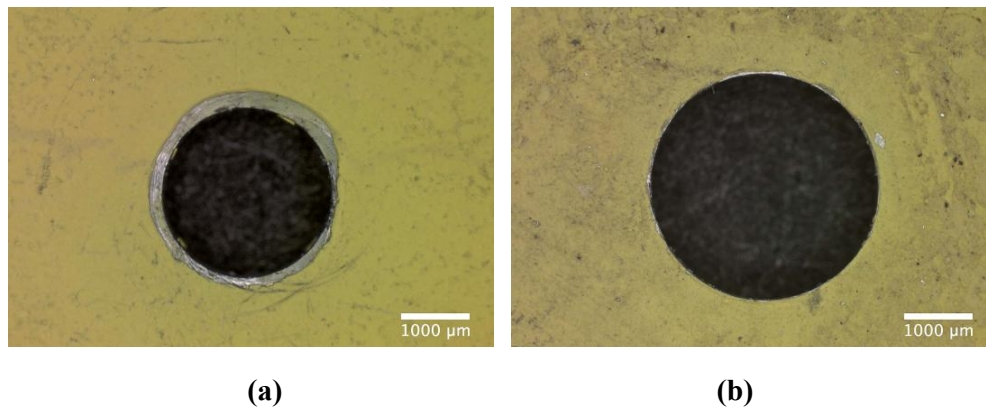
Figure 6 - *Poor quality of the rivet holes: (a) from the coupon from aircraft #1 and (b) from the coupon from aircraft #2*

Figure 7 – *Top view of the composite optical image using the deep focus technique, showing various surface discontinuities in the bore of a rivet hole, which resulted in fatigue crack initiation*

5   Conclusions

Fatigue testing using coupons manufactured from AA2024-T3 thin skin panels from two different PC-9/A aircraft were conducted to determine the effect of initial flaws and defects. The post-test failure analysis using optical microscope and scanning electron microscopy found that machining defects dominate fatigue crack initiation and subsequent crack propagation. The following conclusions and recommendations can be drawn:

1) Fatigue cracks originated from the bore surface discontinuities of rivet holes in the PC-9 test coupons rather than microstructural material defects of AA2024-T3 inherent from the material process;

2) The crack origins typically consisted of surface defects such as deformed burrs, scratches or machining marks;

3) The hole quality is a dominant factor affecting the fatigue crack initiation and subsequent propagation in riveted joints of PC-9/A aft fuselage structure.

4) The investigation has found that quantifying fatigue initial flaws which resulted from poorly finished fastener holes with arbitrary discontinuities at the surface is a challenging topic. This topic is currently under investigation using a statistics based analysis of initial flaws in the prediction of fatigue crack growth.

6   References

[1]   S. Barter, L. Molent and R. Wanhill, "*Typical fatigue-initiating discontinuities in metallic aircraft structures*", International Journal of Fatigue, Vol. 41, pp. 11-22, 2012.

[2]   E. DeBartolo and B. Hillberry, "Predicting fatigue life under spectrum loading in 2024-T3 aluminum using a measured initial flaw size distribution", Journal of ASTM International, Vol. 1, No. 2, pp. 75-86, 2004.

[3]   E. DeBartolo and B. Hillberry, *"A model of initial flaw sizes in aluminum alloys"*, International Journal of Fatigue, Vol. 23, 2001, pp. S79-S86, 2001.

[4]   A. Merati, *"A study of nucleation and fatigue behavior of an aerospace aluminum alloy 2024-T3"*, International Journal of Fatigue, Vol. 27, pp. 33–44, 2005.

[5]   E. Okoro and M. Cavalli, *"Simulated corrosion-fatigue via ocean waves on 2024-Aluminium"*, Proceedings of the DEM Annual Conference, Indiana USA 2010.

[6]   W. Ralph, W. Johnson, P. Toivonen, A. Makeev and J. Newman, *"Assessment of residual stresses and hole quality on the fatigue behaviour of aircraft structural joints",* DOT/FAA/AR-07/56, V2, 2009.

[7]   R. Everett, *"The effect of hole quality on the fatigue life of 2024-T3 aluminum alloy sheet",* NASA/TM-2004-212658, NASA, 2004.

[8]   C. Rodopoulos, S. Cutis, E. de los Rios and J. SolisRomoero, *"Optimisation of the fatigue resistance of 2024-T351 aluminium alloys by controlled shot peening – methodology, results and analysis",* International Journal of Fatigue, Vol. 26, pp. 849-856, 2004.

[9]   C. Brown, F. Dupont and B. Snior, *"Machined surface flaws on the high strength aluminium alloys 7075 and 2024",* Materials Science and Engineering: A, Vol. 118, pp. 53-58, 1989.

[10]   V. Chandrasekaran, A. Taylor, Y. Yoon and D. Hoeppner, *"Quantification and correlation of pit parameters to small fatigue crack"*, ICAF99, online, 1999

[11]   King William, *"Critical corrosion pit depth for fatigue crack initiation in 2024-T3, 6061-T6 and 7075-T6 aluminium alloys",* UMI Thesis online, 2007.

[12]   Z. Connor, M. Fine and B. Moran, *"A study of fatigue crack generation and growth in riveted alclad 2024-T3 specimens",* Proceedings of the FAA-NASA Symposium on the Continued Airworthiness of Aircraft Structures, Georgia USA, August 28-30, 1997.

[13]. J. Mann, G. Revill and R. Pell, *"Influence of hole surface finish, cyclic frequency and spectrum severity on the fatigue behaviour of thick section aluminium alloy pin joints",* ARL-AR-004-570, DSTO Melbourne, 1987.

[14]. S. Fawaz, *"Equivalent initial flaw size testing and analysis of transport aircraft skin splices",* Fatigue and Fracture of Engineering Materials and Structures, Vol. 26, pp. 279-290, 2003.

[15] ASM Handbooks, *"Nonferrous alloys and special-purpose materials",* ASM Handbook, Vol 2, ASM International, 1990.

[16]. Q. Liu, *"PC-9/A fatigue initial flaw testing plan",* DSTO AVD FFL-2011/1071139/1, DSTO Melbourne, 2012.

Finite element crack propagation analysis of shear loaded buckling panels

Julia Bierbaum[1], Peter Horst[2]

[1, 2]*Institute of Aircraft Design and Lightweight Structures, Technische Universität Braunschweig, Hermann-Blenk-Straße 35, 38108 Braunschweig, Germany*
[1]*j.bierbaum@tu-braunschweig.de*
[2]*p.horst@tu-braunschweig.de*

Abstract: Test results of crack propagation in aluminum panels due to cyclic shear loading show that the maximum principle stress is the main factor influencing the crack growth rate. For larger cracks it is accelerated by the increasing out-of-plane deformation. To analyze these influences, a finite element model is presented, which respects the boundary conditions of the test-set-up. Results of the stress intensity factors K_I calculated by the FE model provide a function which is used to run a crack propagation analysis based on Forman law. The results are in good agreement with test results and improve the prediction of a simplified approach. Limitations of the application are discussed.

1   Introduction and motivation

In aeronautics, damage tolerance behavior and buckling stability failure are two of the main drivers for the design. For metallic structures, these two are treated separately due to their different critical loading conditions. While tension is the critical load case for accidental damages or fatigue growth, torsion, shear forces or compression lead mainly to stability problems. Both subjects have been presented separately in many papers. But considering accidental damages, for example in fuselage side shells, a combined occurrence of buckling and cracks is possible, at least under shear loading. This system has been investigated by shear tests on aluminum panels containing a crack as well as numerical analyses have been performed at the Institute of Aircraft Design and Lightweight Structures.

Some work dealing with cracks and buckling focus on the influence of cracks on the critical buckling load. This has been analyzed for different boundary and loading conditions mainly with the help of finite element method (FEM). To give some examples, Brighenti [6, 7, 8] says that the critical buckling load for plates loaded with compression or tension decreases with increasing crack length. Varizi et al [11] compare pressurized fuselage shells containing a crack in combination with axial loading. Alinia et al [2, 3] analyzed cracked shear loaded shells with FEM again focusing on the critical buckling load. It is shown that a crack lying along the compression field in the center of the panel is the most critical case. All these studies confirm that the critical buckling load decreases with increasing crack length.

Less information has been published concerning the influence of buckling on crack propagation parameters. Regarding the curvature of a panel on the crack propagation behavior Obodan et al [9] present numerical and experimental results saying that an increasing curvature leads to increasing J-integral values. This is confirmed by Young et al [12] regarding stiffed fuselage panels under compression load: Skin buckling can have a significant effect on the circumferential stress and may, therefore, influence the residual strength and crack propagation rate.

In [5] a simplified approach has been introduced, which was able to predict crack growth in a shear buckling plate up to a crack length, which had approximately half the size of the width of the main buckle. This paper investigates the crack growth for larger cracks by means of the FEM in order to take into account the mutual interaction of cracks and buckling.

2   Test results and a simplified approach

Tests were performed on cracked, shear loaded aluminum panels. The crack propagated because of the buckling deformation and crack propagation direction was always perpendicular to the maximum principle stress $\sigma_{princ,\ max}$ (diagonal in the panel), no matter of the initial condition. An influence of the bending moment perpendicular to the crack was obviously not essential. This led to the assumption that $\sigma_{princ,\ max}$ in the midplane and its direction have the main influence on the crack propagation. Detailed information concerning the experiments are presented in [4].

The simplified approach of [5] was based on a buckling analysis of the un-cracked specimen by finite elements. It turned out that it was sufficient to use $\sigma_{princ,\ max}$ distribution of the elements' mid-plane along the cross-section where the crack was supposed to grow, and to use this distribution to derive the stress intensity factors under mode I (see figure 1). In a way this is a simplified application of Bueckner's principle to cracks in buckling structures. These stress intensity factors were used to calculate crack propagation by Forman law to predict the crack growth rate.
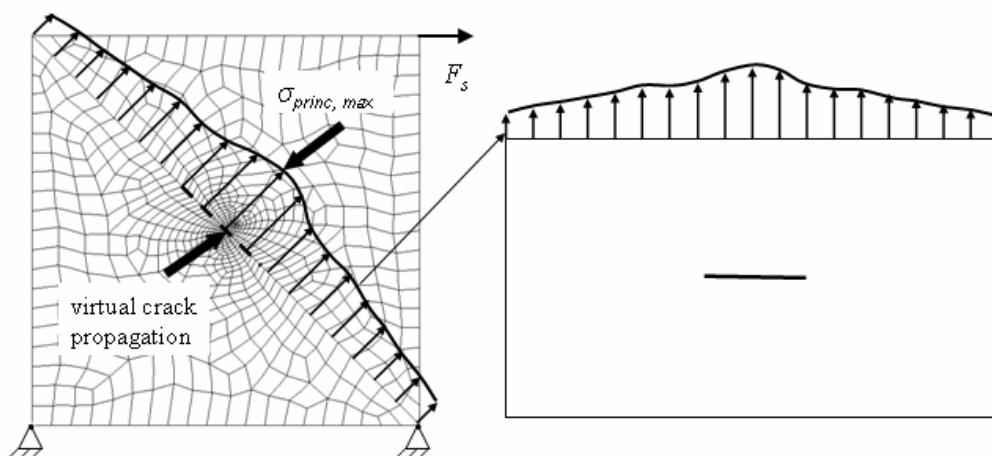

Figure 1 – Principal idea of simplified approach

As shown in [5] and mentioned in the introduction, it turned out that this method yielded good results compared with tests performed by the authors up to a crack length which was in the order of *2a = 100* mm, which is in turn approximately half the width of the major buckle in these cases. Beyond this crack length, the simplified approach predicted a slower crack growth than actually measured. For further information, please refer to [5].

Starting from these results, it was concluded that the mutual interaction of buckling and existing cracks had a growing influence so that the simplified approach was not enough to predict the crack growth beyond this point. One hint which supports this assumption is the fact that the out-of-plane deformation of the major buckle increases considerably with growing crack length. It was the logical next step to use a finite element approach which takes into account both, cracks and buckling to predict the crack propagation for longer cracks. The results of this investigation are given in the next sections.

### 3   Buckling analysis of the cracked plate

3.1   Finite element model

The finite element model of the quadratic test specimen including the area of a certain crack is shown in figure 2. Dimensions are 500 x 500 mm² with thicknesses $t_1 = 2$ mm or $t_2 = 3.2$ mm, respectively. Cracks of length $2a$ are introduced under 45° at a position x, y. The specimens are made of aluminium 6056 T4. A Young's modulus of $E = 72$ GPa and a Poisson ratio of $v = 0.33$ have been assumed. The Forman parameters $c_f = 2.95 \cdot 10^{-7}$, $Kc_f = 2800\,\text{MPa}\sqrt{\text{mm}}$ and $m_f = 2.39$ have been used to calculate the crack growth rate. The stress-ratio is $R = \dfrac{\sigma_{\min}}{\sigma_{\max}} = 0$.
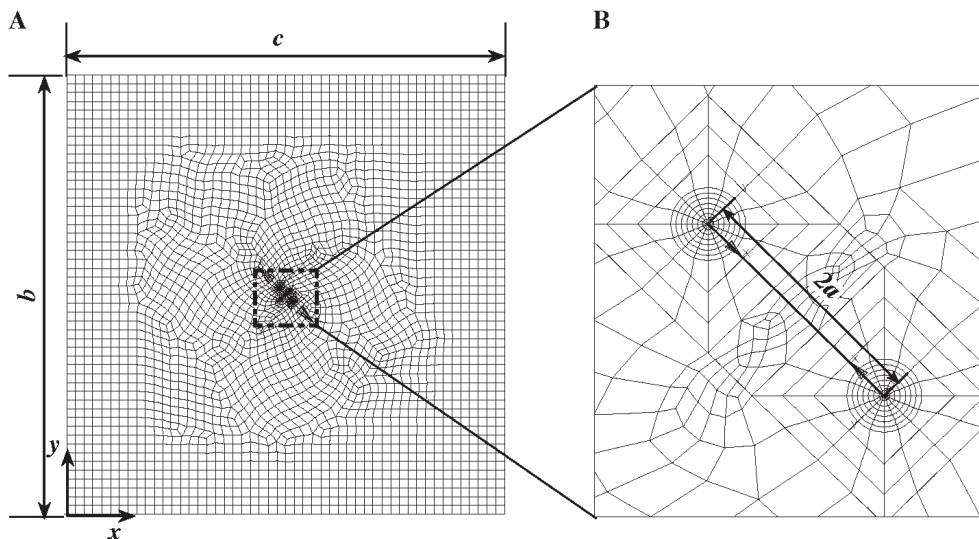
Figure 2 – Finite element model of (A) the test specimen and (B) the crack tip elements

Specimen is under clamped conditions at all boundaries, because the test frame is built of massive steel girders. Shear force is introduced at one single node and distributed by multiple point constraints (MPCs) along the boundaries, as indicated in figure 3.
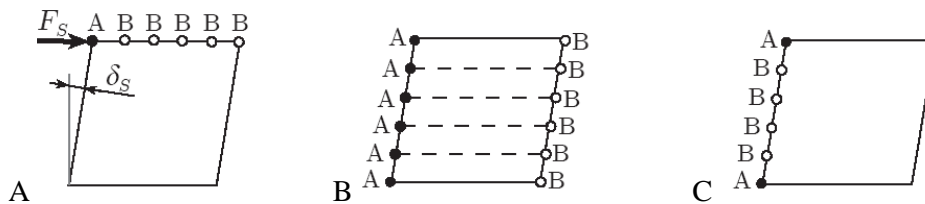
Figure 3 – MPCs realize the boundary conditions of the test frame

The panel is modeled with ABAQUS®' second order shell elements (S8R5). The lack of bending influence on the crack allows to reduce the model to two dimensions and focus on the mid-plane. The elements are degenerated to quarter point elements at the crack tips. The mesh surrounding the crack tip is adapted to be able to calculate the stress intensity factors with ABAQUS® (see figure 2B). For all crack lengths the mesh refinement around the crack tip and in the plate remains the same.

3.2 Finite element results

The model is approved by several results of the tests and classical, theoretical approaches presented in Table 1 (only in extracts due to limited space): First, the critical buckling load calculated on the one hand by ABAQUS® and on the other with the help of a classical approach [10] is equivalent for different thicknesses. Second, the principle stresses ($\sigma_{princ,\ max}$, $\sigma_{princ,\ min}$), measured with strain gauges at different positions and both sides of the panels, are in very good agreement to the FE results. Third, the general out-of-plane deformation is identical to the one found in the experiment, even if the maximum out-of-plane deformation u_3 is overestimated by the results of FE model. Reasons for this deviation could be imperfections of the test panels or plastic deformation for larger cracks, which are not taken into account in the experiments by the optical measurement system. Therefore it is assumed that the real $u_{3,\ max}$ tends to be larger than measured, which corresponds to the FE-results.

Table 1 – Comparison of test and FE-results of extracted, un-cracked panels

	Panel 01 (t=2 mm, F_s = 40 kN)		Panel 04 (t=2 mm, F_s = 50 kN)		Panel 12 (t=3.2 mm, F_s = 83 kN)	
	Test	FE	Test	FE	Test	FE
Critical buckling shear stress / kN	15.95 *	15.56	15.95 *	15.56	65.33 *	63.97
$\sigma_{princ,\ max}$ / MPa	115.75	110.49	112.96	150.0	113.24	109.8
$u_{3,\ max}$ / mm	4.37	5.087	4.89	5.901	3.57	3.751

* results of theoretical critical buckling shear stress based on [10]

The crack propagation analysis is not realized by automatic crack growth and remeshing, but by 17 single-analyses with different predefined crack-lengths for each panel. So the FE analyses do not give any information about the crack growth rate but about the stress field at the crack tips including the increasing out-of-plane deformation based on crack growth. Due to the crack-tip modelling, ABAQUS® calculates the stress-intensity factor K_I using an interaction integral method based on the J-integral method [1]. The results of K_I for different crack lengths and panels are shown in figure 4.
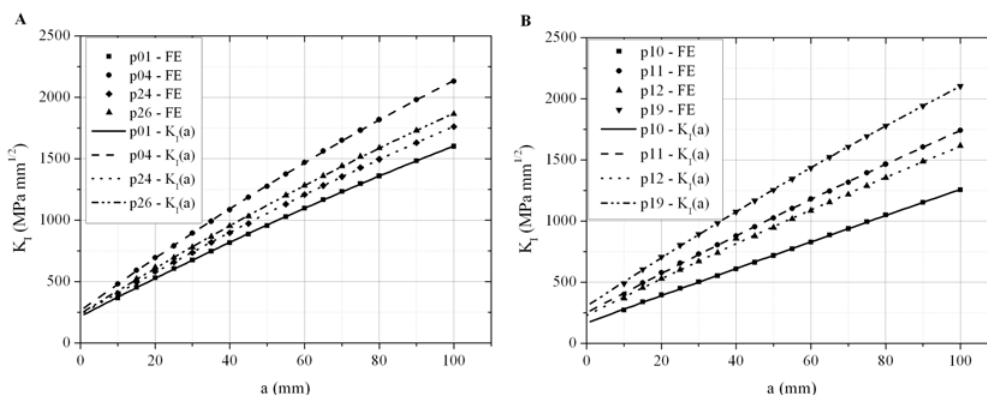

Figure 4 – Stress intensity factor K_I of FE-analysis and its best-fit-function for panels with (A) t_1 = 2 mm or (B) t_2 = 3.2 mm and different F_s

4   Crack propagation analysis by cracked-FEM solution based

The K_I -values of the FE analysis provide a stress-intensity-factor function $K_I(a)$, which is e.g. given for panel 01 as:

$$p01: K_I(a) = 216.28 + 15.881 \cdot a - 0.0201 \cdot a^2 \qquad (1)$$

A crack propagation analysis based on (1) includes the bending crack edges and the increasing out-of-plane deformation. The crack propagation results of different tests with the simplified approach (smpl a) and the cracked-FEM solution (FE) are shown in figure 5. For all presented cases the cracked-FEM solution follows the curve progression of the test results even for longer cracks. It underestimates the total number of cycles observed during the test but the difference is less than 10%. The unstable crack growth rate before collapse is very well represented, but is completely missing in the simplified approach. So the crack propagation prediction is in good agreement to the test results for central cracks in a shear loaded buckling panel.
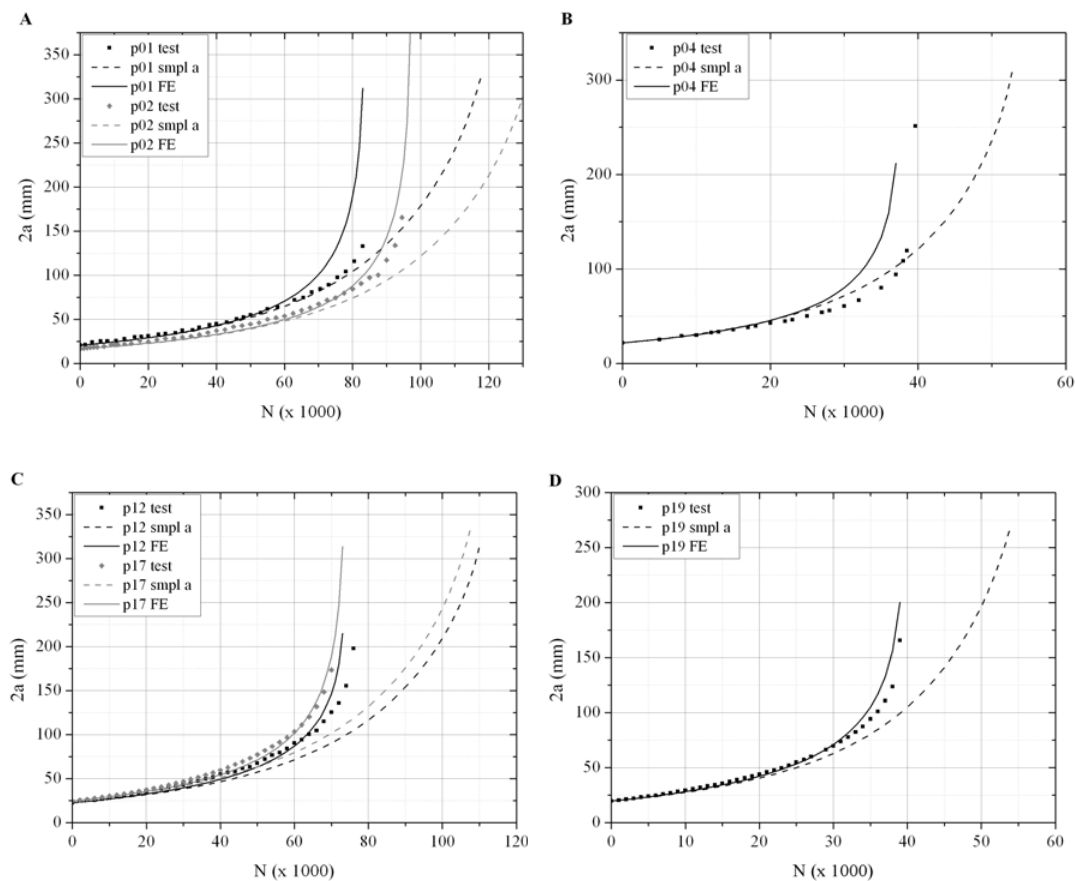
Figure 5 – Comparison of crack propagation results from test, simplified approach (smpl a) and cracked-FEM solution for (A) p01 and p02: $t_1 = 2$ mm and $F_s = 40$ kN but different initial crack conditions, (B) p04: $t_1 = 2$ mm and $F_s = 50$ kN, (C) p12 and p17: $t_2 = 3.2$ mm and $F_s = 83$ kN and identical initial crack conditions, (D) p19: $t_2 = 3.2$ mm and $F_s = 100$ kN

Further analyses show limitations, too, which sould be true without further details. As it is known for other crack propagation calculation methods, the cracked-FEM solution is very

sensitive to the initial crack length. Variations of 1 mm can lead to remarkable differences in the life time prediction (see for example figure 5C). This becomes more obvious if both crack tips are analyzed separately.

Futhermore, it seems that the cracked-FEM solution gives better results for panels with $t_2 = 3.2$ mm. Regarding the FE-results, the out-of-plane deformation and principle stresses are in better agreement to the test results compared to $t_1 = 2$ mm, too. This shows that once $\sigma_{princ, max}$ in the tests deviates from the ideal model (for example due to imperfections, pre-loadings, internal stresses…, which are not taken into account by the FE-model), the analysis of the test specimen can lead to greater deviations.

5   Conclusion

An ABAQUS® FE model of a cracked shear loaded panel with buckling deformation is presented. The results are in good agreement with the test results. The crack propagation observed in the experiments is very well represented. This improves the results of a simplified approach published earlier for larger cracks.

Acknowledgement

References

[1]   ABAQUS Theory Manual (version 6.9 html-documentation), Dassault Systèmes Simulia Corp, Providence, RI, USA, 2009

[2]   M.M. Alinia, S.A.A. Hosseinzadeh, H.R. Habashi, *"Influence of central cracks on buckling and post-buckling behaviour of shear panels"*, Thin-Walled Structures, Vol. 45, pp. 422-431, 2007

[3]   M.M. Alinia and S.A.A. Hosseinzadeh and H.R. Habashi, *"Numerical modelling for buckling analysis of cracked shear panels"*, Thin-Walled Structures, Vol. 45, pp. 1058-1067, 2007

[4]   J. Bierbaum, P. Horst, *"Crack propagation in aluminium panels due to shear forced buckling",* Proceedings of 18ᵗʰ European Conference on Fracture, Dresden, 2010

[5]   J. Bierbaum, P. Horst, *"Crack propagation in buckling plates: test results and a simplified numerical approach"*, International Journal of Structural Integrity, Vol. 2, Num. 4. pp. 373-382, 2011

[6]   R. Brighenti, *"Buckling sensitivity analysis of cracked thin plates under membrane tension or compression loading"*, Nuclear Engineering and Design, Vol. 239, pp. 965-980, 2009

[7]   R. Brighenti, *"Buckling of cracked thin-plates under tension or compression"*, Thin-Walled Structures, Vol. 43, pp. 209-224, 2005

[8]   R. Brighenti, *"Numerical buckling analysis of compressed or tensioned cracked thin plates"*, Engineering Structures, Vol. 27, pp. 265-276, 2005

[9]   N. Obodan, V. Adlutskii, A. Patsyuk, G. Sherstyuk, *"Influence of the curvature of thin-walled elements with cracks on the parameters of fracture (Theoretical and experimental investigation)"*, Strength of Materials, Vol 38, pp. 271-277, 2006

[10]   A. Pflüger, *"Stabilitätsprobleme der Elastostatik"*, Springer-Verlag, 3. Auflage, 1975

[11]   A. Vaziri, H.E. Estekanchi, *"Buckling of cracked cylindrical thin shells under combined internal pressure and axial compression"*, Thin-Walled Structures, Vol 44, pp. 141-151, 2006

[12]   R.D. Young, C.A. Rose, J.H.Jr. Starnes, *"Skin, Stringer, and Fastener Loads in Buckled Fuselage Panels"*, NASA Langley Technical Report Server (AIAA-2001-1326), 2001

Investigation of Fatigue Scatter
in Laser Peened Aluminum Test Coupons

Kristina Langer[1], Thomas J. Spradlin[2]

[1]*Air Force Research Laboratory, AFRL/RBSM, 2790 D Street, Wright-Patterson Air Force Base, OH, 45433, United States, kristina.langer@wpafb.af.mil*

[2]*Universal Technology Corporation, AFRL/RBSM, 2790 D Street, Wright-Patterson Air Force Base, OH, 45433, United States, Thomas.spradlin@ctr.wpafb.af.mil*

Abstract The military aircraft that comprise the current fleet of the United States Air Force (USAF) have been flying, on average, for more than 20 years [1]. As these planes continue to age, service life extension and maintenance reduction can become costly concerns. Recently, the Air Force Research Laboratory (AFRL) has been investigating the application and transition of laser peening (LP) as a surface treatment for enhancing the fatigue life of airframe structural components. With the LP process, compressive residual stresses are induced mechanically into select near surface regions, the intent being to counter the fatigue-inducing tensile stresses resulting from service loads.

While the focus of this research program has been on the development and validation of physics-based, predictive modeling tools for evaluating the induced residual stresses and subsequent fatigue response, recent laboratory testing in Al2024 fatigue coupons has suggested that, in some cases, the fatigue scatter after LP is applied can be significantly greater than that in the un-peened specimens [2]. From an aircraft reliability perspective, this increased scatter can offset the beneficial effects of LP, and can even negate the potential benefits completely. In these cases, although increases in average coupon life (cycles to failure under constant amplitude, uniaxial fatigue loading) were observed, the range of individual test responses after peening was 2-20 times the range of the un-peened specimen responses.

In this paper, we investigate scatter effects in laser peened Al2024 test coupons using finite element (FE) based sensitivity analysis techniques. Two- and three-dimensional parametric FE models are used in a multi-tier design of experiments (DOE) evaluation, with a simple stress-life algorithm used to estimate the cycles to failure under constant amplitude cyclic loading. Scatter effects are investigated by creating small variations in the LP parameters and assessing their relative contributions within the prescribed DOE framework with respect to the predicted fatigue response. Variations in coupon parameters and applied loading are also studied to evaluate the degree to which small geometric disparities and deviations in service use are affected by the LP application.

References:

1. T. Mehuron, *The Graybeard Fleet*, AIR FORCE Magazine, February 2004, p. 12.

2. K. Langer, S. VanHoogen, and J. Hoover II, *Fatigue Response of Aluminum Aircraft Structure under Engineered Residual Stress Processing*, Fatigue and Fracture Mechanics, Vol. 36, ASTM Special Technical Publication STP 1508, 2009, p. 122.

AA2024-T3 FSW tailor welded blanks: fatigue crack growth behavior

P M G P Moreira[1], P. M. S. T. de Castro[2]

[1] *INEGI, Instituto de Engenharia Mecânica e Gestão Industrial, Rua Dr. Roberto Frias 400, Porto, Portugal, email: pmgpm@fe.up.pt (corresponding author)*

[2] *Department of Mech. Engineering, Faculdade de Engenharia da Univ. do Porto, Portugal*

Abstract A 'tailor welded blank' is a part made up of different strengths or thicknesses of an alloy, typically manufactured by laser welding. Although frequent in automotive engineering applications of high strength steel, other applications are of interest, including aeronautical applications with aluminum alloys and using FSW instead of laser. This paper presents a study of fatigue crack growth behaviour of friction stir welded butt joints of plates of different thickness of AA2024-T3, an alloy commonly used in fuselage structures.

Friction stir welding (FSW) is a solid-state joining process which emerged as an alternative technology to join high strength alloys that were difficult to weld with conventional techniques, *e.g.* [1]. An advantage of this joining technique is its low heat input when compared with arc welding processes, allowing the achievement of high mechanical properties, low distortion and low residual stresses. Also, hydrogen cracking or heat affected zone (HAZ) softening phenomena are limited. Crack growth studies are usually carried out using uniform thickness joints, ASTM E647. Nevertheless, for applications such as tailor welded blanks, there is a need to test specimens with defects growing in the thickness transition region. Fatigue crack growth tests on such welded connections are not standard. The present study concerns butt joints made using two AA2024-T3 plates 3.8mm and 4.0mm thick.

The mechanical behaviour of the joint was studied performing tensile and fatigue crack growth tests. The fatigue crack growth rate of cracks growing in different zones of the welded joint (nugget, HAZ) and in base material was analyzed. The influence of the welding process in each weld zone was evaluated using microhardness profiles. Further to higher static properties, welded joints present lower crack growth rates when compared with its base material.

Figure – example of specimens tested, with crack in the nugget (left) and in the HAZ (right)

References

[1]	Pedro Vilaça and Wayne Thomas, 'Friction Stir Welding Technology', in: Moreira, Pedro M.G.P.; da Silva Lucas F. M.; de Castro, Paulo M.S.T., eds., 'Structural Connections for Lightweight Metallic Structures', (Advanced Structured Materials, vol. 8), Springer, 2012, ISBN 978-3-642-18186-3, pp.85-124

Evaluation of multiaxial fatigue loading paths in different shear stress spaces

L. Reis[1,2], V. Anes[1,2], B. Li[1,2], M. de Freitas[1,2]

[1]Instituto de Ciência e Engenharia de Materiais e Superfícies, Instituto Superior Técnico, T.U.Lisbon, Av. Rovisco Pais, Lisbon, Portugal

[2]Departamento de Engenharia Mecânica, Instituto Superior Técnico, Av. Rovisco Pais, Lisbon, Portugal.

Email: luis.g.reis@ist.utl.pt

Abstract In the multiaxial high cycle fatigue regime, crack nucleation generally dominates most of the fatigue life. Since the shear mode is the main mechanism for crack nucleation, it is of prime importance to determine the correct shear stress amplitude under multiaxial loading conditions. In this context determining the right shear stress amplitude is of prime importance. Conventionally the evaluation of the shear stress amplitude carried out on invariant models is determined by considering the Tresca or von Mises shear stress spaces where the theoretical relation between the shear stress and axial stress components is 0.5 for Tresca or 0.577 for von Mises criterion. However, from experimental data, it was found that relation varies from 0.5 to 1 depending on the material. In this study is determined the appropriate shear stress space for the structural steel 42CrMo4 and used the Minimum Circumscribed Ellipse (MCE) approach to determine the shear stress amplitude for a series of experimental loading paths carried out. The results show a significant improvement on the multiaxial fatigue characterization using the MCE approach and the experimentally determined shear stress space.

1 Introduction

The mechanical design against fatigue failure under multiaxial loadings can be performed by two ways: One is considering the fracture mechanics methodologies where an existing flaw/crack will propagate with a specific material velocity, another one is to estimate the fatigue life limit where that flaw begins to appear. At HCF regime, the time spent on the crack initiation is much bigger than the one spent on the crack propagation, for the most materials. It is usual considered that the time spent on the fatigue crack propagation is around 20 % of total fatigue life. In this sense fatigue design based only on the fracture mechanics can lead to inaccurate results in HCF regime. The fatigue design considering the threshold limit, where the flaw initiates to appear, can lead to more accurate results on multiaxial fatigue life estimations. The scientific community research in the multiaxial fatigue field remains to pursuit for the optimal criteria to estimate fatigue life under multiaxial loading conditions.

Several criteria have been developed and proposed in the literature, [1], however, some of them are difficult to implement and have many constraints. The verification and validation of those criteria discouraged the use of those methods. Moreover, many of the models proposed in the literature are validated by the own author data and usually are not corroborated with other author's lab work. In this context, a simple multiaxial fatigue method is of prime importance to create a more general methodology to be validated and used by other

researchers and engineers in an easy way. There are about three main categories on the multiaxial fatigue characterization, i.e. critical plane, stress invariants and integral approaches [2]. The critical plane approach has been gained great popularity in the last years due to the simple physical concept involved around the methodology; it is common to find in the literature multiaxial energy models based on the critical plane formulations [3], [4] or even integral ones [2].

The main methodology in this type of approach is to find the critical plane where the shear stress or strain amplitude is greater, once the critical plane is identified the shear contribution can be adjusted with the normal stresses or strains in that plane, which is exemplified by the cases of Findley [5], Fatemi-Socie [6] models, respectively. Despite the popularity achieved by this approach, critical plane criteria have some shortcomings, such as, in some cases, the same stress amplitude is obtained for different planes, indicating several critical planes however the fractographic examination generally indicates only one initiation spot. The integral approaches are based on the stresses average within a elementary volume [2], where the damage is accounted in all possible material planes [7].

The invariant methods are based on the premise that a generic stress tensor can be divided into two other stress tensors, the deviatory and the hydrostatic one. Another premise is that at HCF regime, the crack nucleation process occurs, mainly from the shear stress/strain contribution. Moreover, the hydrostatic stress had a secondary role during the fatigue degradation process. Under this paradigm, the shear stress amplitude determination is of prime importance and can be determined from the deviatory stress tensor. The invariant approaches are based on the shear stress amplitude determination on the π plane which can be adjusted with the hydrostatic stress according to some author's methodology such as Sines [8], Crossland [9], Dang Van [10] or even von Mises, which doesn't consider the effect of hydrostatic stress.

Conventionally, the shear stress amplitude is usually evaluated by the Longest Projection (LP) or the Minimum Circunscribed Circle (MCC) approach in the shear stress space based on the von Mises equivalence ($\tau=\sigma/sqrt(3)$) or the Tresca equivalence ($\tau=\sigma/2$) for the multiaxial loading conditions. However, the relationship of the equivalent shear stress component related to the axial stress component may vary significantly depending on the type of the material. For example, the ratio of the torsion fatigue limit over the bending fatigue limit τ_{-1}/σ_{-1} varies from 0.5 for mild metals to 1 for brittle metals, [1].

In this study systematic fatigue experiments are presented for a structural steel, 42CrMo4, under typical axial-torsional multiaxial loading paths. Eight different loading paths are used to simulate the same equivalent shear stress amplitude according to the Minimum Circunscribed Ellipse (MCE) approach [11, 12]. A series of experimental fatigue tests were carried out in HCF regime, where multiaxial fatigue parameters are used: the phase angle between the axial stress component and the shear stress component and the stress amplitude proportional ratio.

For the 42CrMo4 steel studied, two kinds of shear stress space for evaluating the shear stress amplitude were used: one is the shear stress space with the equivalence of $\tau=\sigma/sqrt(3)$ and another one is the shear stress space with the equivalence of $\tau=\sigma*\beta$, where $\beta=(\tau_{-1}/\sigma_{-1})$ is determined experimentally from fatigue tests.

The experimental fatigue life results obtained under the loading paths carried out are analyzed and compared with estimations by the MCE approach.

2   Materials and Methods

The 42CrMo4 quenched and tempered high strength steel is the material used in this work. Specimens used in the tests series had been produced from rods of 25 mm of diameter, its geometry and dimensions are presented in Figure 1.
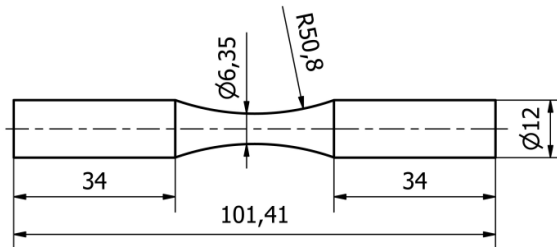
***Figure 1**. Specimen dimensions used on multiaxial fatigue tests [mm].*

The specimens had been inspected and manually polishing through sandpapers of decreasing grain since the 200 until a 1200. The monotonic and cyclical properties of 42CrMo4 [13] are presented in Table 1.

***Table 1**. Monotonic and cyclic mechanical properties of the studied material, 42CrMo4.*

Tensile strength (MPa)	1100	Cyclic strength coefficient (MPa)	1420
Yield strength (MPa)	980	Cyclic strength exponent	0.12
Elongation (%)	16	Fatigue strength coefficient (MPa)	1154
Young´s modulus (GPa)	206	Fatigue strength exponent	-0.061
Hardness (HV)	362	Fatigue ductility coefficient	0.18
Cyclic yield strength (MPa)	640	Fatigue ductility exponent	-0.53

Fatigue tests were carried out through a servo-hydraulic machine of Instron 8874, as shown in Figure 2. In order to study the different loading paths effects on material fatigue strength, specimens were tested using eight different loading paths under the combined loads, axial and torsion.

***Figure 2-** Experimental setup.*

In Figure 3 it is shown the loading paths used in this study represented in the von Mises shear stress space.
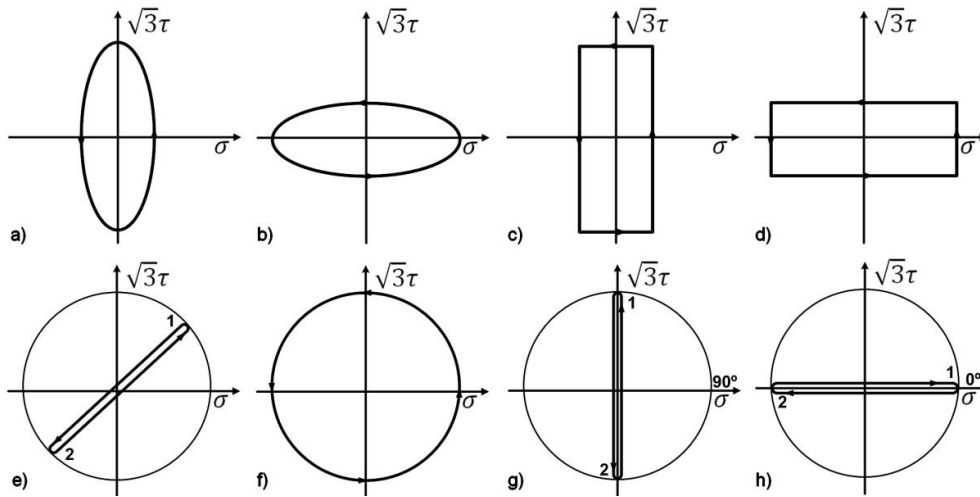

Figure 3 – *Loading paths in the von Mises shear stress space, a) Ellipse up, b) Ellipse down, c) Box up, d) Box down, e) Proportional at 45°, f) Out of phase 90° as shift phase, g) Pure shear and h) Pure tension*

3 Results and Discussion

Experimental fatigue life data obtained for each loading path presented in Figure 3 is represented in Figure 4. Results for von Mises criterion (Fig. 4a) and for MCE approach are exhibited versus experimental fatigue life as a multiaxial fatigue equivalent stress.

One of the main goals of this study is to correlate fatigue experimental data with a theoretical model in such a way that the fatigue life estimations can be performed using a uniaxial fatigue trend equation in tension or shear mode.
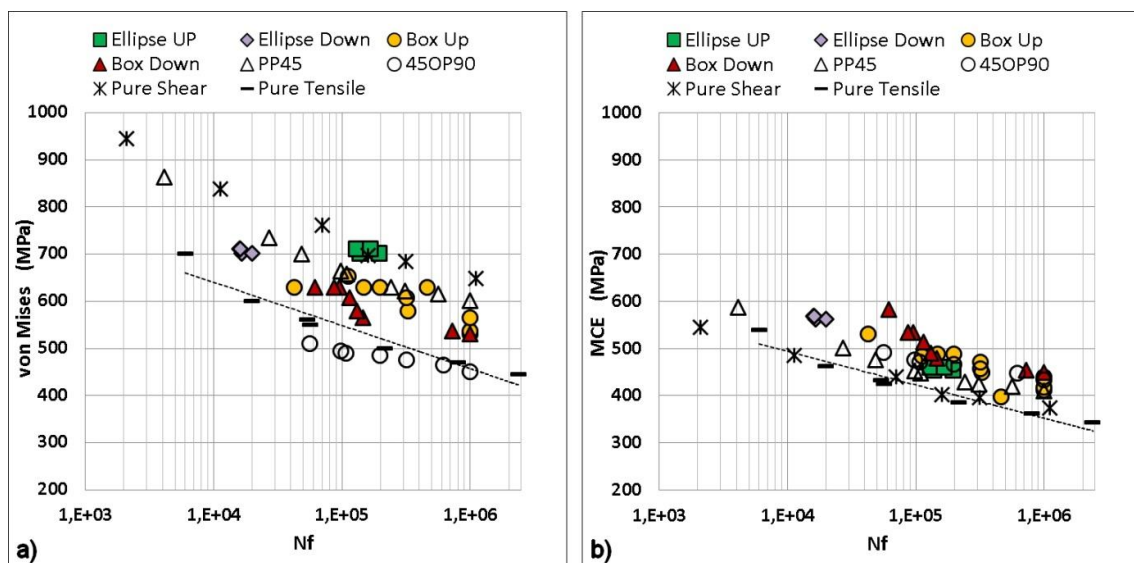

Figure 4 – *SN curves using: a) von Mises criterion and b) MCE approach.*

In Figure 4 a) von Mises criterion shows a greater scatter comparing with MCE equivalent stress approach, failing on the attempt to estimate fatigue life through the uniaxial tension trend curve represented with the dash line on Figure 4 a). MCE criterion using the proper material shear stress space can reach better results than the ones obtained by the von Mises shear stress space.

A fixed ratio (sqrt(3)) between the shear stress component and the axial stress component as used in von Mises criterion for all kind of materials does not allow to take into account the physical relation between the shear stress and tension stress components in multiaxial fatigue conditions. However, determining the uniaxial material fatigue limit in tension σ_{-1} and the shear fatigue limit τ_{-1} permits to determine the appropriate relation between the shear stress and tension stress components. In Figure 4 b) can be seen the match between the uniaxial fatigue results achieved by considering the material shear stress space where the relation between shear and tension is given by $\beta = \tau_{-1}/\sigma_{-1} = 0.7$ experimentally determined.

Figure 5 presents the obtained fatigue results for the Box up loading path where the influence of the shear stress component versus axial stress component can be easily understood. For a similar value of the equivalent von Mises stress around 600 MPa an increase in experimental number of cycles was achieved. This factor is of prime importance and demonstrates in a clear way how the changing of the shear stress component versus the axial stress component influences the fatigue strength of the material.
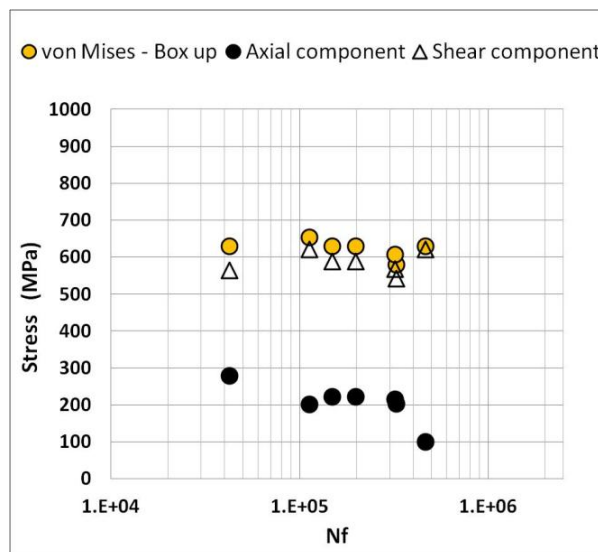
Figure 5 – *Results of the axial stress vs torsion stress component in Box up loading path.*

4   Conclusions

In this paper eight multiaxial fatigue loading paths with different non-proportionality and stress amplitude ratios were analysed in the structural steel 42CrMo4 considering the von Mises criterion and MCE approach. For the von Mises criterion the relation between the tension stress component and the shear stress component was the one resulted from the theoretical formulation on the octahedral plane; alternatively the one considered on the MCE criterion is the one obtained from the experimental fatigue tests.

With MCE criterion using the proper material shear stress space, i.e. taking into account the experimentally determined relation between shear stress and tension stress components, given by $\beta = 0.7$, better results were obtained. Moreover, with the loading paths carried out it was clearly demonstrated the great influence of this ratio on the fatigue life of materials subjected to multiaxial loading conditions. This work also proves that MCE approach can deal with complex multiaxial loading paths in a simple and efficient way.

Acknowledgements

5   References

[1]   D. Socie and G. Marquis. *Multiaxial Fatigue*, Society of Automotive Engineers, Warrendale, 2000; PA 15096-0001.

[2]   H. Zenner, A. Simbürger, and J. Liu, "On the fatigue limit of ductile metals under complex multiaxial loading," *Int. journal of fatigue*, vol. 22, no. 2, pp. 137–145, 2000.

[3]   T. Lagoda, E. Macha, and W. Bedkowski, "A critical plane approach based on energy concepts: application to biaxial random tension-compression high-cycle fatigue regime," *International journal of fatigue*, vol. 21, no. 5, pp. 431–443, 1999.

[4]   K. Walat, M. Kurek, P. Ogonowski, and T. Łagoda, "The multiaxial random fatigue criteria based on strain and energy damage parameters on the critical plane for the low-cycle range," *International Journal of Fatigue*, 2011.

[5]   W. N. Findley, *A theory for the effect of mean stress on fatigue of metals under combined torsion and axial load or bending*. Engineering Materials Research Laboratory, Division of Engineering, Brown University, 1958.

[6]   D. Socie, "Critical plane approaches for multiaxial fatigue damage assessment.," *ASTM Special Technical Publication*, vol. 1191, pp. 7–7, 1993.

[7]   I. V. Papadopoulos, "A High-cycle fatigue criterion applied in biaxial and triaxial out-of-phase stress conditions.," *Fatigue & Fracture of Engineering Materials & Structures*, vol. 18, no. 1, pp. 79–91, 1995.

[8]   G. Sines, "Behavior of metals under complex static and alternating stresses," *Metal fatigue*, vol. 1, pp. 145–169, 1959.

[9]   B. Crossland, "Effect of large hydrostatic pressures on the torsional fatigue strength of an alloy steel," in *Proceedings of the int. conf. on fatigue of metals*, 1956, pp. 138–149.

[10] K. Dang-Van, "Macro-micro approach in high-cycle multiaxial fatigue," *ASTM SPECIAL TECHNICAL PUBLICATION*, vol. 1191, pp. 120–120, 1993.

[11] M. De Freitas, B. Li, and J. L. T. Santos, "Multiaxial Fatigue and Deformation: Testing and Prediction, ASTM STP 1387, S," *American Society for Testing and Materials, West Conshohocken, PA*, pp. 139–156, 2000.

[12] B. Li, L. Reis and M. De Freitas, "Simulation of cyclic stress/strain evolutions for multiaxial fatigue life prediction," *Int. journal of fatigue*, vol. 28, pp. 451–458, 2006.

[13] L. Reis, B. Li, and M. De Freitas, "Analytical and experimental studies on fatigue crack path under complex multi-axial loading," *Fatigue & Fracture of Engineering Materials & Structures*, vol. 29, pp. 281–289, 2006.

Modelling Fatigue Crack Growth in Aluminium Plates Reinforced by Bonded Fibre-Metal Laminates GLARE

J. Doucet[1*], X. Zhang[2], P.E. Irving[1]

[1]*School of Applied Science, Cranfield University, Cranfield, Bedford, UK, j.doucet@cranfield.ac.uk*

[2]*School of Engineering, Cranfield University, Cranfield, Bedford, UK*

Abstract:

In order to exploit high strength aluminium alloys and extend design service life in damage tolerant designs of aircraft, the benefits of bonded crack retarders have been explored. These are straps of fatigue crack resistant material such as GLARE bonded to the aircraft structure to reduce substrate crack propagation rates. In this work a 3 D finite element model with three layer shell elements has been developed to calculate changes in substrate stress intensity and in fatigue crack growth rate produced by bonded strap reinforcement. Both circular and elliptical strap delamination geometries were incorporated into the model. Calculated stress intensity factors were used together with measured fatigue crack growth data for substrate material to predict fatigue crack growth rates for the strapped condition. The model predicted a decrease in the stress intensity factor and a retardation of fatigue crack growth rates. The stress intensity factor was predicted to vary through the thickness of the substrate due to the phenomenon of secondary bending and also the bridging effect caused by the presence of the strap. The influence of delamination shape and size on substrate crack stress intensity and delamination strain energy release rate has been calculated.

Keywords: Bonded crack retarder, strap, integral metallic structure

1   Introduction

Current trends in the aircraft industry are to produce lighter aircraft having extended life with reduced manufacturing cost and less frequent maintenance. For metallic airframe parts, integral structures are one option. To overcome the inherent lack of fail safety and to satisfy the damage tolerance requirements, reinforcement technologies have been developed, e.g. the selective reinforcement [1], bonded crack retarders (BCR) [2-3], and crenulations [4].

Numerical models based on the finite element method (FEM) have been developed to assist the design process; for this application there are some similarities to models for bonded patch repairs developed earlier. One example is the way the substrate, strap/patch, and adhesive interface are modelled using fracture mechanics theory to predict debonding or delamination failure. For example, Hosseini-Toudeshky et al. [5] developed a model taking into account the mixed mode fracture condition of the substrate crack tip. They calculated the substrate crack growth life and the crack front shape using the modified virtual crack closure technique MVCCT [6] and the failure criterion in [7]. The prediction is in good agreement with the experimental test that they performed [8]. Gu et al. [9] studied the crack behaviour of a single edge notched plate made of aluminium alloy 7075-T6 reinforced with a composite patch using a 3D FE model. They calculated the influence of the repair on the crack tip stress intensity factor and the crack opening displacement dependency on the patch material, patch thickness and adhesive thickness. They show that boron/epoxy patch was more efficient than carbon/epoxy patch and that a thinner adhesive layer provided more reduction in stress intensity factor. Umamaheswar et al. [10] performed 3D FE analysis of a thin cracked aluminium sheet reinforced by a composite patch. The model demonstrated the feasibility of

modelling a repair patch using 3D non-linear FEA with a single element through the thickness. However, none of these models takes into account of the delamination/debonding failure that is commonly observed between the cracked panel and the patch.

Although there are similarities between bonded patch repairs and bonded straps, the function of bonded straps is different in the two situations. First, in BCR design, once a crack has initiated in the substrate it will approach and then pass the nearby strap. Consequently, stresses in the cracked substrate will be transferred by the adhesive bond to the nearby straps reducing the crack tip stress intensity factor and consequently the crack growth rate. In contrast, a repair patch is used to cover the entire substrate crack to stop it from propagating. Delamination/debonding failure is desirable in the bonded strap design to prevent the strap from being broken and hence to bridge the crack opening displacement resulting in crack growth retardation. Crack bridging models for BCR design have been developed. For example, a multiple layer model has been developed to model the key mechanisms of debonding and crack bridging [11-12]. There was also an earlier and similar model developed by Xie and Bigger [13-14] . Both models incorporate the action of delamination in a quasi-static load analysis. However, interaction of debonding/delamination with substrate crack propagation and the influence of fatigue loading on damage growth rates were not considered in these models.

Recently, cohesive interface elements have been used for modelling fatigue delamination. These cohesive elements are governed by a specific constitutive law so that they can mimic fatigue delamination growth rates [15-16].

This paper presents the development of a 3D FE model created to explore the interaction of two types of damage found in bonded crack retarder structures, i.e. debonding/delamination and substrate crack.

## 2   Modelling approach

2.1 Geometry and dimensions

The model is of a reinforced middle crack tension, M(T) sample 400 mm long, 140 mm wide and 5 mm thick (Fig. 1a). The substrate is of aluminium alloy 2624-T351, It is reinforced by two bonded straps 180 mm long, 25.83 mm wide and 3.7 mm thick of Glare-2 6/5 (0.4) fibre-metal laminate . The straps were located 13.5 mm equidistant from the sample centre line, and the central crack was of 20 mm total length. Straps were bonded using FM94 adhesive.

 Glare is made of alternating layers of aluminium 2024-T3 and two layers of unidirectional glass fibre reinforced FM94 epoxy adhesive designated as FM94/S2 prepreg. In Glare-2 6/5 (0.4) configuration, it consists of 6 layers of aluminium and 5 double-layers of unidirectional FM94/S2 prepreg (Fig. 1b). Among the different material choices available for the straps, Glare is preferred to aluminium, titanium and GFRP because previous studies [2-3] showed that it has lower density and provides the best retardation for the case of variable amplitude loading. The strap-specimen combination develops residual stresses on bonding due to the elevated temperature curing process used with FM94. On loading the substrate out-of-plane bending develops due to the asymmetric one-sided reinforcement (Fig. 2). It was observed in previous work that as the substrate crack propagates underneath the strap, debonding at the adhesive interface and delamination in the composite material strap develop [2-3].

Mechanical properties for 2624-T351 are E = 71 GPa, v = 0.33, yield strength = 330 MPa, ultimate tensile strength = 434 MPa and density = 2770 kg/m^3. Glare properties are given in Table 1.

(a)   (b)
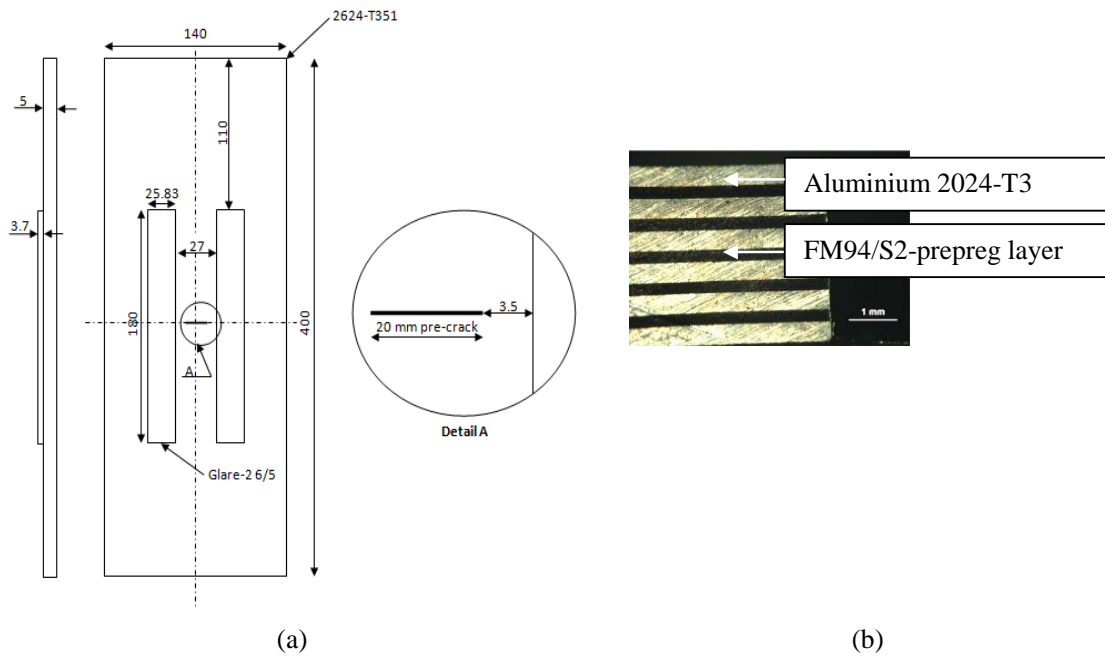
Figure 1 (a) M(T) Specimen dimensions and geometry; (b) Glare-2 6/5 (0.4) cross section
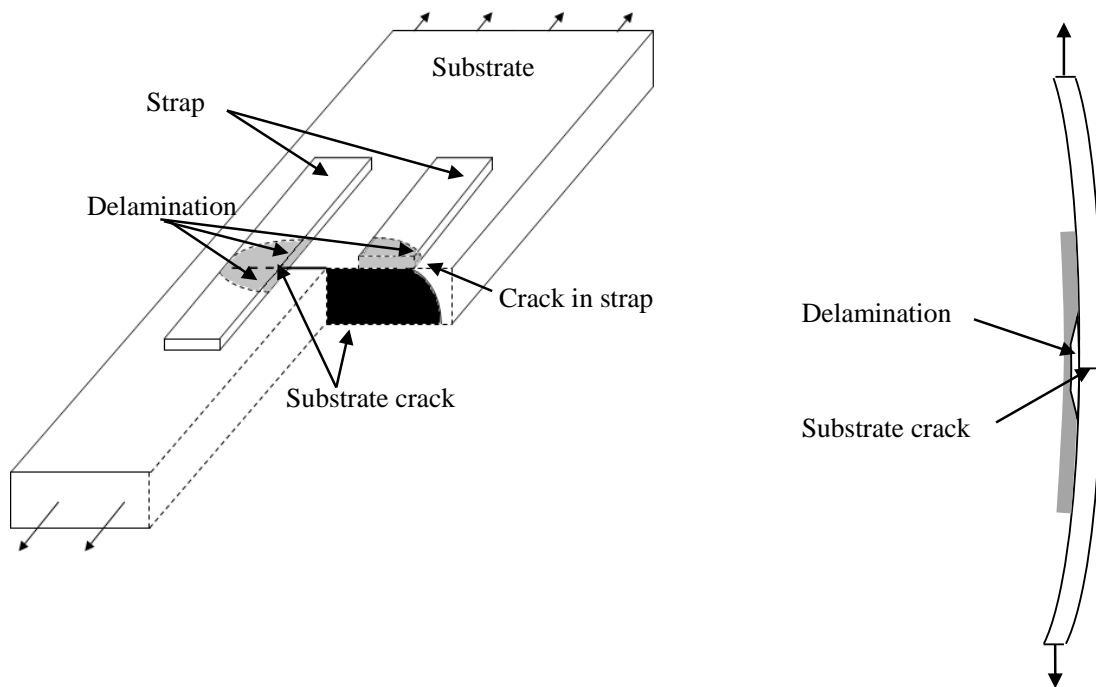
Figure 2 Location of failure modes observed on M(T) samples with bonded straps

Table 1 : Mechanical property of Glare constituents

	Al 2024-T3	FM94/S2-prepreg
E_1 (GPa)	72	50.3
E_2, E_3 (GPa)	72	5.5
$v_{12} = v_{23}$	0.30	0.310
v_{21}	0.30	0.034
G_{12} (GPa)	28	1.995
G_{23} (GPa)	28	2.099
α_1 (/°C)	2.32e-5	2.88e-6
α_2 (/°C)	2.32e-5	4.03e-5
Density (kg/m³)	2,770	1,972

One important parameter defining the sample is the stiffness ratio of the straps and the overall assembly, μ, as defined by eq. (1):

$$\mu = \frac{\sum E_{Strap} A_{Strap}}{E_{Sub} A_{Sub} + \sum E_{Strap} A_{Strap}} \qquad (1)$$

where A_{Strap} and A_{Sub} are cross-sectional areas of the strap and substrate respectively.

The stiffness ratio in [2-3] was 0.17. It was shown experimentally that higher stiffness ratios provide more retardation in crack growth rate [2-3]. The stiffness ratio in this model was 0.2.

2.2 FE model

Previous tests [2, 17] showed that when a middle crack tension M(T) specimen was reinforced with Glare straps bonded with FM 94, under fatigue loading the substrate crack extended to the first layer of aluminium in the Glare strap, cutting through the layer of FM94 adhesive (Fig. 3 and 4). In addition, fatigue delamination was also observed between the first layer of aluminium and the first layer of S2-prepreg present in the Glare strap. All these considerations should be taken into account when modelling the M(T) specimen.

The commercial finite element software package Abaqus was used to model the specimen. Due to the double-symmetry configuration, only one quarter of the specimen is modelled (Fig. 5). In order to take into account the fatigue delamination, the strap is divided into two separate layers in the model. One represents the first layer of aluminium made of 8-node continuum shell elements with one element through the thickness that is subjected to fatigue crack growth and delaminates from the rest of the Glare strap. The second layer models the rest of the Glare strap using also the 8-node continuum shell elements with one element through the thickness. Because Glare is elastically orthotropic the Abaqus composite layup property tool was employed. The substrate was modelled by 8-node continuum shell elements with one element through the thickness. Tie constraint was used between the first layer of Glare aluminium and the substrate to simulate the adhesive that bonds these two components (Fig. 5).
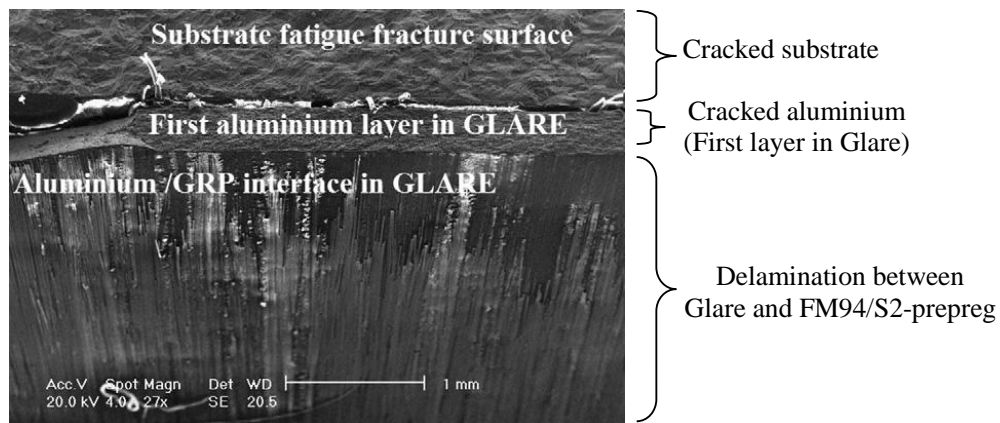
Figure 3 SEM picture demonstrating the delamination path [17]
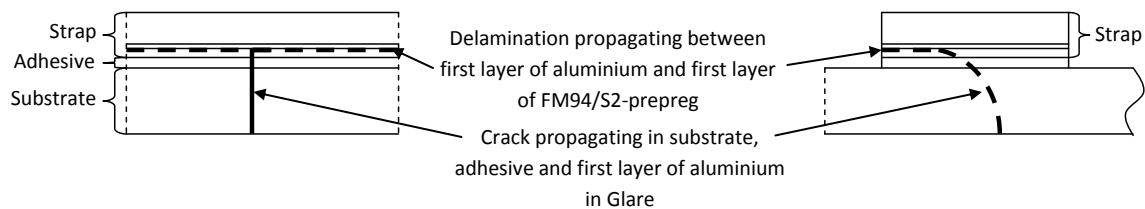
Figure 4 Schematic representation of substrate crack and disbond location.

Delamination growth was modelled using the DEBOND option in Abaqus [18] by disconnecting the tied nodes. As the substrate crack front advanced, (assumed equal increments on each surface) nodes were disconnected at the delamination front to model the delamination growth. For all the cases presented here, it was assumed that delamination front grew so as to be one element ahead of the substrate crack tip in the direction of crack growth. Perpendicular to the crack plane the delamination was grown so as to maintain the same circular or elliptical profile as at the start of the simulation. This assumed growth pattern was based on previous experimental observation [2].

Three cases were studied; without delamination, with circular and with elliptical (aspect ratio of ½) delaminations (Fig. 6). For each case, 14 crack increments were modelled corresponding to substrate crack growth from 10 to 60 mm. For every crack increment, it was assumed that the crack front was uniform through the thickness. The applied stress was 60 MPa. Figure 7 shows the calculation procedure for stress intensity and for fatigue crack growth rate prediction.

The Mode I stress intensity factor at the substrate crack front was calculated using the MVCCT technique [6].

$$G_I = \frac{1}{2\Delta A} F_y \delta_y \ \text{ and } \ K_I = \sqrt{G_I E} \qquad (2)$$

where G_I and K_I are the calculated mode I strain energy release rate and stress intensity factor, ΔA the crack extension area. F_y the nodal force at crack tip, δ_y the nodal displacement one element behind the crack tip and E the Young's modulus of 2624-T351.

The stress intensity factor range ΔK was then used to evaluate the fatigue crack growth rate of the substrate using fatigue crack growth rate data of aluminium 2624-T351. Measured crack growth rate data were linearly interpolated from experimental data points [19].
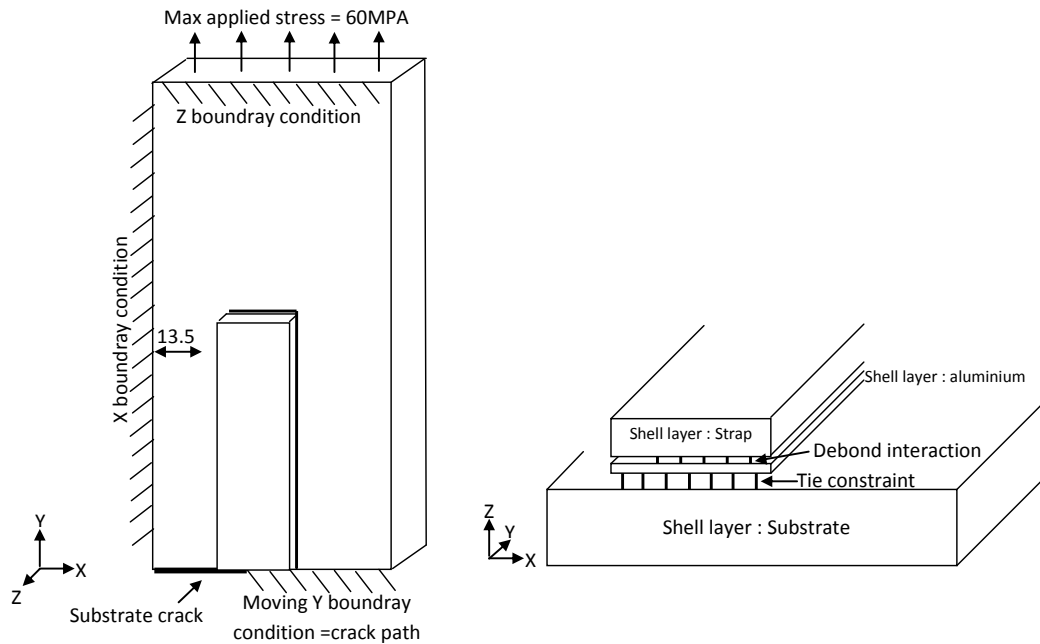
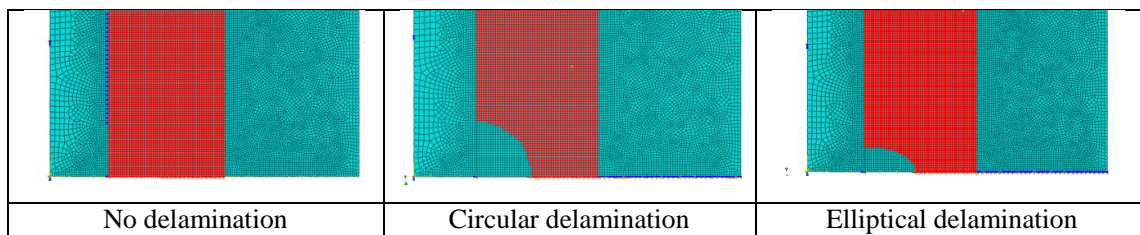**Figure 5** Boundary constraints and loadings in the –FE Model

| No delamination | Circular delamination | Elliptical delamination |

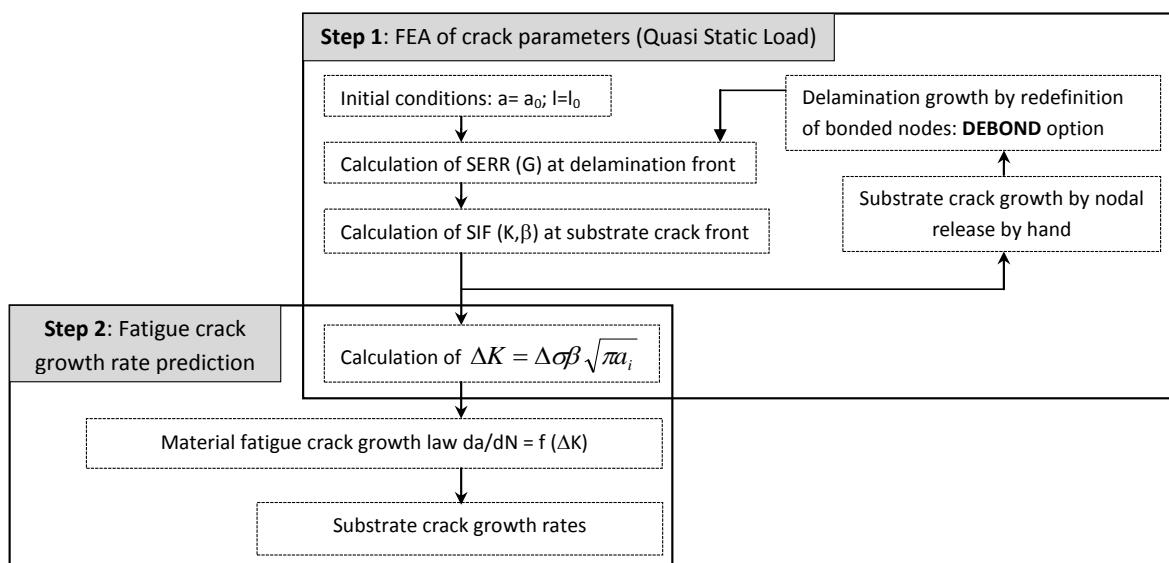**Figure 6** FE model of delamination (substrate half crack length $a = 25$ mm)

Figure 7 Flow chart for calculation of stress intensity and fatigue crack growth rates

3 Results

3.1 SIF of substrate crack

The Stress Intensity Factor Coefficient (SIFC or *β*) could be found by eq. (3). In its traditional formulation it can be used to represent the difference between stress intensities of cracks in infinite plates (β=1 at all crack lengths) and real items of finite width (β =*f(geometry, crack length.)* In this case as well as sample geometry and crack length the value of β will include the effects of the strap in modifying stress intensity. It is a useful parameter for comparing the various straps and delaminations and of course is essential for crack growth life prediction calculations.

$$\beta = \frac{K}{\sigma\sqrt{\pi a}} \qquad\qquad (3)$$

Calculated *β* values for strap reinforced M(T) specimens are compared to the analytical solution of an un-reinforced M(T) [20] in figure 8.

Figure 8 shows the variation of *β* for different crack lengths on both the strap side (bond face) and back face of the specimen for the different delamination cases. For the bond face, it is observed that initially all stress intensity factor coefficients are smaller than the un-reinforced case (analytical solution) with *β* approximately 0.75 compared to 1. As the crack tip passes underneath the strap, the difference between the reinforced and un-reinforced stress intensity factors increases. The elliptical delamination shows more effect in reducing SIFC than the circular one. This difference is explained by the fact that the delamination area is bigger for the circular delamination shape compared to the elliptical case, hence less loads is transferred from cracked substrate to the strap through the adhesive bond. On the other hand, for the "no-delamination" case, more load is transferred over the whole bond area, hence the SIFC is the lowest. As the crack tip passes the edge of the strap, SIFC starts to increase again. Nevertheless, the presence of the strap is still very effective in reducing SIF due to the strap crack bridging effect producing a decrease in β at all crack lengths on the bond face of between 25% and 75% depending on the crack length and the delamination geometry.

Figure 8 also shows β values for crack tip emerging on the specimen back face. Before the substrate crack tip reaches the strap and also underneath the strap, β is about the same as for the un-reinforced case. After the crack tip has passed the strap, β values for the two delamination cases are about 5% greater than that of the un-reinforced specimen. This is due to the secondary bending effect caused by one-side strap as identified in our previous work [11-12].

For Glare straps, the curing process induced residual stresses. In the substrate these are in tension and about 15 MPa on the strap bond face [21]. This stress was not modeled in the first stage work reported in this paper.
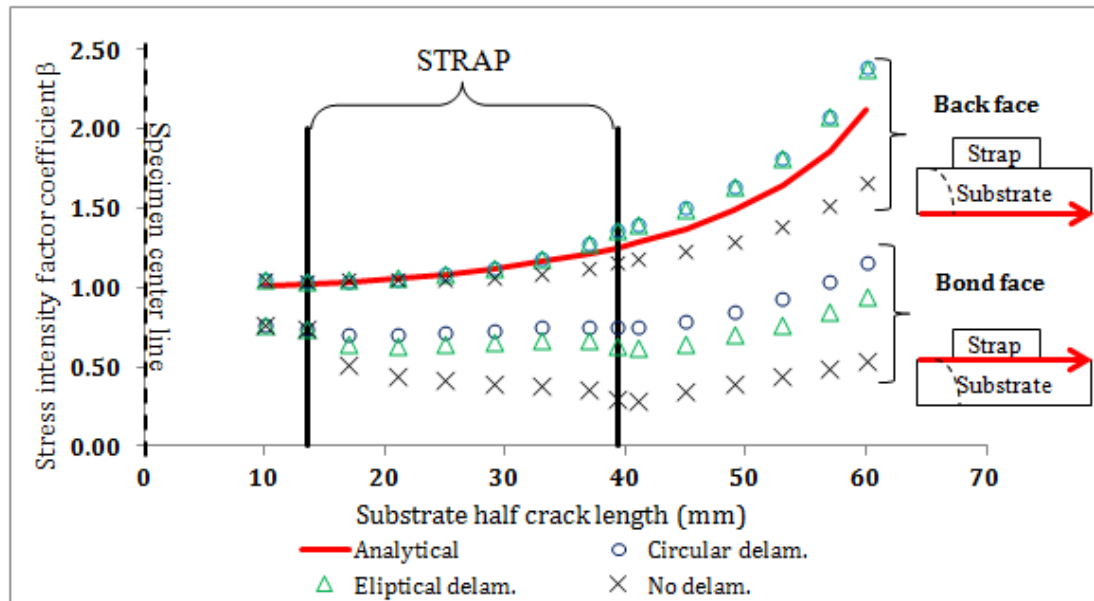
Figure 8 Stress intensity factor coefficient vs crack length for substrate bond face and back face.
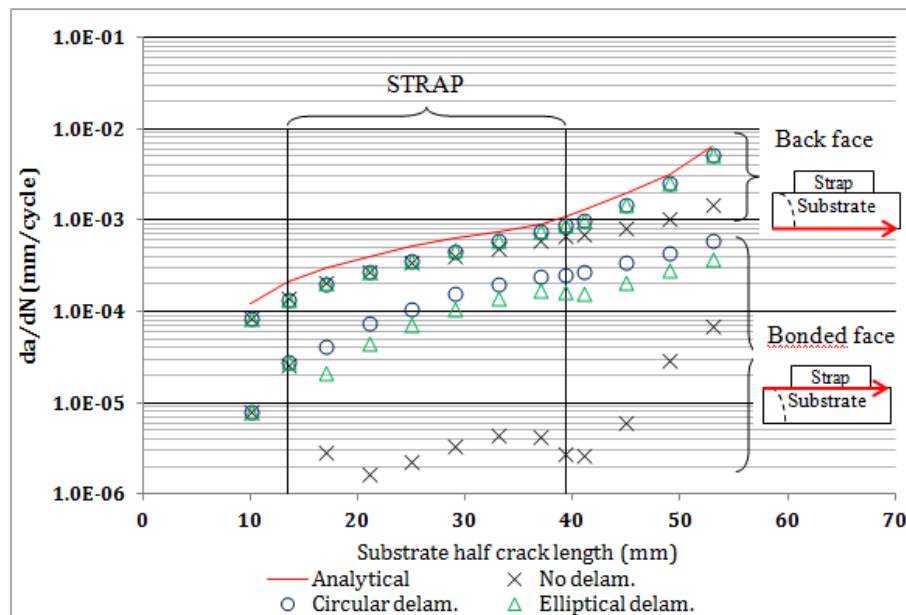

Figure 9 Calculated Fatigue crack growth rate for substrate bond face and back face showing the influence of delamination on crack growth rates

3.2 FCG rate predictions

Fatigue crack growth (FCG) rates on the strapped sample were derived using the calculated SIF range and the measured FCG rate for the substrate material [19]. The calculation procedure is shown in figure 7.

Figure 9 shows predicted FCG rates on the bond side and back face. On the bond side, bonded straps decrease the FCG rates by a factor of 10 for half crack lengths up to 25 mm. Crack growth rates increased as the crack tip approached the edge of the strap, but as the crack emerged from the strap, retardation increased again to a factor of 10. The circular delamination provided less retardation than the elliptical delamination for reasons explained in Section 3.1. It should be noted that these predictions do not take into account the tensile residual stresses in the substrate, of the order of 15 MPa, which will make the crack grow slightly faster.

Figure 9 also shows the FCG rates on the back-face. The FCG rates are only slightly decreased compared to the benchmark un-reinforced specimen. When the crack tip has passed the strap the FCG rate almost reaches the same value of the un-reinforced specimen. This implies that the bonded strap does not have much influence on the FCG rate on the non-reinforced surface. However, the much retarded crack growth rate on the bonded face will significantly reduce the average FCG rate for each crack front profile. In this model substrate crack lengths were assumed equal when the stress intensity was calculated. The conclusion that the stress intensities on the two faces are very different indicates that the crack growth rates will be unequal and the crack lengths should be unequal when the stress intensity is calculated. This will further change the calculated stress intensity on each surface. An iterative procedure is required to accurately calculate stress intensities, crack profiles and crack growth rates. This is discussed later in the paper.

One phenomenon that clearly appears in these results is the out-of-plane bending due to the single-side strap. When subjected to applied in-plane tensile loads, the specimen bends towards the strap (Fig. 2). Hence, the back face is under a larger tensile stress, whereas the bonded face will have a reduced tensile stress and the bonding induced tensile residual stress will partially offset this effect on the bonded side. This explains why the effect of the reinforcement is more significant on the bonded side compared to the unbonded one (Fig. 8 and 9). Figures 8 and 9 also suggest that substrate crack will grow faster on the unbonded side, leading to a non-symmetrical crack front. This phenomenon was also observed by Hosseini-Toudeshky et al. [6] and Irving et al. [21] where crack was growing non-uniformly through the substrate thickness due to out-of-plane bending, residual stress and externally applied stress.

Figures 8 and 9 also show that with delamination between the first aluminium layer and the rest of the strap, β values are increased along with crack growth rates and the crack growth retardation becomes less effective. The assumed circular delamination produced the least retardation.

3.3 Calculated SERR at the delamination crack tip
The model is for the case of adhesive failure at the interface between FM94/S2-prepreg and aluminium. The calculated maximum strain energy release rate for the circular and elliptical shaped delaminations due to the combined opening modes I and II, under the applied substrate load, are shown in Fig. 10. This illustrates the locations on the delamination front of the positions of maximum SERR due to mode I and to mode II.
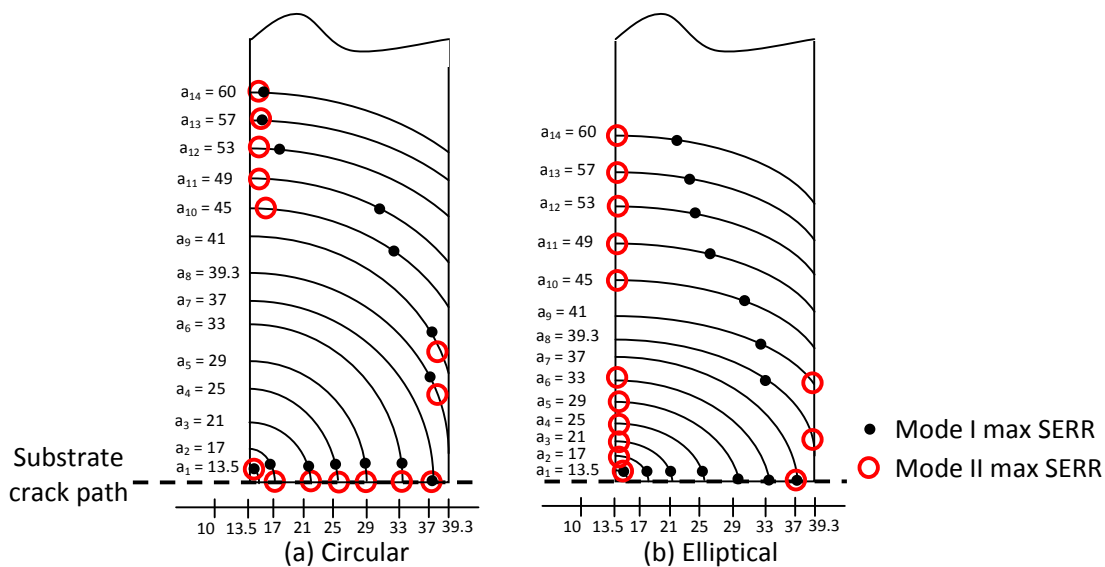
The maximum SERR due to mode I delamination for both circular and elliptical delaminations are located near the substrate crack path when the crack is underneath the strap with a SERR gradually varying from 22 J/m^2 to a maximum of 198 J/m^2 for the circular shape and from 22 to 152 J/m^2 for the elliptical case as the crack is growing in the substrate. Once the crack tip has passed the strap, the maximum moves away from the crack path and is located at the points of emergence of the delamination front at the edge of the strap bond. The values are much lower, decreasing from 5.5 J/m^2 to 0.18 J/m^2 for the circular shape and from 9.76 J/m^2 to 4.37 J/m^2 for the elliptical shape as the crack is growing in the substrate.

For mode II, the results are quite different from one delamination assumption to the other. For the circular shape, the trend is almost the same as for the mode I. The maximum SERR due to mode II is gradually increasing from 0.0 J/m^2 to a maximum of 319 J/m^2 as the crack is growing underneath the strap. Once the crack has passed the strap the SERR is increasing again from 109 J/m^2 to 253 J/m^2. For the elliptical case the maximum SERR are observed at the maximal delamination length except for cases of crack length near the end of the strap where the mode II SERR locations are near the crack path. As the crack is growing underneath the strap, the SERR is varying between 0.0 J/m^2 and 314 J/m^2. It reaches a maximum of 1006 J/m^2 when the crack has reached the edge of the strap. Once the crack has passed the end of the strap, it varies between 174 J/m^2 and 353 J/m^2.

These maximum SERR indicate where the delamination is most likely to extend, either in the direction of the substrate crack (*x*-direction) or in the loading direction (*y*-direction), e.g. for the circular delamination case delamination is more likely to extend in the *x*-direction, for the substrate crack situated underneath the strap and once the crack has reached the end of the strap, delamination is more likely to happen in the *y*-direction. For the elliptical case, further investigation is needed on the delamination growth behavior before the substrate crack has reached the end of the strap, but the model suggests that once the crack has passed the strap, delamination growth is more likely to happen in the loading direction. Therefore, the model suggests that before the crack has passed the strap, delamination is expected in the x-direction while it is expected to grow in the y-direction after the crack has passed the strap.

Toughness data obtained from static load tests of FM94/S2-prepreg and aluminium 2624-T351 using double cantilevered beam specimens are: G_{IC} = 2000 J/m² for a cohesive failure (failure within the FM94/S2-prepreg), G_{IC} = 1500 J/m² for adhesive failure (failure at the interface FM94/S2-prepreg and aluminium) [22]. From our model (Fig. 10), the maximum SERR occurs when the half crack length is 37 mm (i.e. 2 mm before the strap edge). At this crack length, the maximum SERR for mode I opening are 198 J/m^2 and 319 J/m^2 respectively for the circular delamination and the elliptical one. The SERR for the mode II opening are respectively 152 J/m^2 and 1006 J/m^2. Hence calculated strain energy release rates are much smaller than measured toughness values.

In future work implementation of the delamination will be revised. The delamination occurring at the interface between the reinforcement and the structure will be modeled to grow under cyclic fatigue. The substrate fatigue crack front and the delamination front will interact. In the model above, fatigue crack and fatigue delamination were implemented in a quasi-static manner. A major improvement will be to grow the substrate fatigue crack and the delamination in fatigue and thus develop the correct substrate crack and delamination profiles. Hence a subroutine with both fatigue crack growth and fatigue delamination growth implemented through the use of material data will constitute a more realistic model.

Figure 10 Assumed profiles of strap delamination crack fronts for a range of substrate crack lengths a, showing the location on the front of the point of maximum SERR due to Mode I and mode II loading components for (a) circular and (b) elliptical delaminations.

4   Conclusions

A 3D finite element model has been developed to simulate fatigue crack growth of an M(T) specimen made of aluminium alloy 2624-T351 reinforced with bonded Glare-2 6/5 (0.4) straps. The model predicts that the strap will cause reduction of stress intensity of substrate cracks at the bonded face of between 25 and 75% and a slight enhancement of stress intensity on the unbonded substrate face. These changes in stress intensity in turn promote predicted reductions of substrate fatigue crack growth rates of up to a factor of 5-10 in the presence of a delamination at the strap interface.

Acknowledgements

References

[1] Heinimann, M, Bucci, R, Kulak, M, Garratt, M. Improving damage tolerance of aircraft structures through the use of selective reinforcement, *Proc. 23rd Symposium of Int Committee on Aeronautical Fatigue, ICAF 2005*, Hamburg, June 2005, pp. 197-208.

[2] X. Zhang, D. Figueroa-Gordon, M. Boscolo, G. Allegri, P. E. Irving, Improving fail-safety of aircraft integral structures through the use of bonded crack retarders, in: Proceedings 24th Symposium of International Committee on Aeronautical Fatigue (ICAF), Naples, 2007.

[3] P E Irving, X Zhang, J Doucet, D Figueroa-Gordon, M Boscolo, M Heinimann, G Shepherd, M E Fitzpatrick, D Liljedahl, Life Extension Techniques for Aircraft Structures – Extending Durability and Promoting Damage Tolerance through Bonded Crack Retarders, *Proc. 26th Symposium of Int Committee on Aeronautical Fatigue, ICAF 2011*, Montreal, June 2011.

[4] Ehrström J-C, Muzzolini R, Arsène S, Van der Veen S. Improving damage tolerance of integrally machined panels. In: Proceedings of the 23rd symposium of international committee on aeronautical fatigue, ICAF 2005, Hamburg; 2005. p. 79–90.

[5] Hosseini-Toudeshky, H., Saber, M., & Mohammadi, B. (2009). Finite element crack propagation of adhesively bonded repaired panels in general mixed-mode conditions. *Finite Elements in Analysis and Design, 45*(2), 94-103.

[6] Krueger, R (2004). Virtual crack closure technique: History, approach, and applications. *Applied Mechanics Reviews, 57*(1-6), 109-143.

[7] Richard, HA, Buchholz, F, Kullmer, G, & Schöllmann, M (2003). *2D and 3D-mixed mode fracture criteria*, Key Engineering Materials, 251-252, 251[8] Hosseini-toudeshky, H, Mohammadi, B, & Bakhshandeh, S (2007). Mixed-mode fatigue crack growth of thin aluminium panels with single-side repair using experimental and numerical methods. *Fatigue and Fracture of Engineering Materials and Structures, 30*(7), 629-639.

[9] Gu, L, Kasavajhala, ARM, & Zhao, S (2011). Finite element analysis of cracks in aging aircraft structures with bonded composite-patch repairs. *Compos B: Engineering, 42*(3), 505-510.

[10] Umamaheswar, TVRS, & Singh, R (1999). Modelling of a patch repair to a thin cracked sheet. *Engng Fracture Mechanics, 62*(2-3), 267-289.

[11] Boscolo, M., & Zhang, X. (2010). A modelling technique for calculating stress intensity factors for structures reinforced by bonded straps. part I: Mechanisms and formulation. *Engng Fracture Mechanics, 77*(6), 883-895. [12] Boscolo, M., & Zhang, X. (2010). A modelling technique for calculating stress intensity factors for structures reinforced by bonded straps. part II: Validation. *Engng Fracture Mech, 77*(6), 896-907. [13] Xie, D., & Biggers Jr., S. B. (2006). Strain energy release rate calculation for a moving delamination front of arbitrary shape based on the virtual crack closure technique. part I: Formulation and validation. Engng Fracture Mech, 73(6), 771-785. [14] Xie, D., & Biggers Jr., S. B. (2006). Strain energy release rate calculation for a moving delamination front of arbitrary shape based on the virtual crack closure technique. part II: Sensitivity study on modeling details. Engineering Fracture Mechanics, 73(6), 786-801. [15] Harper, PW, & Hallett, SR (2010). A fatigue degradation law for cohesive interface elements - development and application to composite materials. *Int Journal of Fatigue, 32*(11), 1774-1787.

[16] Hosseini-Toudeshky, H, Jasemzadeh, A, & Mohammadi, B (2011). Fatigue debonding analysis of repaired aluminium panels by composite patch using interface elements. *Applied Composite Materials, 18*(6), 571-584.

[17] Bagnoli, F, Bernabei, M, Figueroa-Gordon, D, & Irving, PE (2009). The response of aluminium/GLARE hybrid materials to impact and to in-plane fatigue. Materials Science & Engng A, 523(1-2), 118-124.

[18] Abaqus Analysis User's Manual: 11.4.3 crack propagation analysis. http://abaqus.civil.uwa.edu.au:2080/v6.10/books/usb/default.htm. Accessed April 2012

[19] Fatigue crack growth rate data for aluminium 2624-T351, Alcoa Inc. (private communication).

[20] Rooke, DJ, Cartwright DP. Methods of determining stress intensity factors. Farnborough: Royal Aeronautical Establishment, 1973. RAE/TR-73031.

[21] Bonded reinforcement and crack retarders in integral aluminium aircraft structures, Final Report (unpublished), Cranfield University, 2010.

[22] Doucet, J (2012), Cranfield Internal Report, Cranfield University

A discussion on fracture mechanics crack growth-based fatigue life prediction applied to a notched detail

Hélder FSG Pereira[1], José AFO Correia[1], Abílio MP de Jesus[1,2]

[1]IDMEC-Pólo FEUP, Rua Dr. Roberto Frias, Porto, Portugal, *hfpereira@hotmail.com; jcorreia@utad.pt*
[2]School of Sciences and Technology, University of Tras-os-Montes e Alto Douro, Vila Real, Portugal; *ajesus@utad.pt*

Abstract Several methods for fatigue life prediction of structural components have been proposed in literature. The Fracture Mechanics crack growth-based fatigue prediction has been proposed to assess the residual fatigue life of components, which requires the definition of an initial flaw. Alternatively, Fracture Mechanics crack growth-based fatigue predictions may be used to simulate the whole fatigue life of structural components assuming that there are always initial defects on materials, acting as equivalent initial cracks. This latter approach is applied to a notched plate made of P355NL1 steel. Fatigue crack growth data of the material is evaluated using CT specimens, covering several stress R-ratios. Also, S-N fatigue data is available for the double notched plate, covering stress R-ratios equal to 0, 0.15 and 0.3. An estimate of the equivalent initial flaw size is proposed, using a back-extrapolation calculation. The crack propagation model takes into account stress ratio effects, account for propagation threshold and a correction for plasticity. Stress intensity factors are computed using the J-integral technique. The performances of predictions are analysed and deviations discussed.

1 Introduction

Fatigue modelling may be performed based on several alternative approaches such as the global S-N approaches, the local strain-life or stress-life approaches and the fracture mechanics based approaches. The global S-N approaches relate directly a global definition of a stress range with the total number of cycles to failure. The extrapolation of this kind of approaches for other structural details in in general limited. The experimental data, in the form of S-N curves, is usually applied to a limited group of details.

The local strain-life or stress-life approaches uses fatigue resistance data from fatigue test of smooth specimens. These approaches may be potentially applied to any structural detail, as long as the local stress or strain histories at potential cracking sites are known. While the stress-based approach is more suitable for high-cycle fatigue, the strain-based approach is more adequate for low- to medium cycle fatigue. However, the strain-life approach may be also applied for high-cycle fatigue, both approaches being perfectly equivalent for elastic loading. The local approaches are usually associated with local failure modes, such as the macroscopic crack initiation. However, the definition of the macroscopic crack initiation is neither easy nor consensual and usually a crack initiation criteria is postulated, such a crack of 0.25 mm depth.

Fracture Mechanics based fatigue approaches may be used to model fatigue crack propagation from an initial size to final dimensions responsible by the fracture of the component. The experimental fatigue crack growth rates of the material should be known in advance as well as the stress intensity factor histories for the actual structural detail. The fracture mechanics is naturally well suited for the evaluation of residual fatigue lives of structural components knowing the initial defects. This approach may be used to complement the local strain-life approaches, modelling the crack propagation from the initial crack to the critical dimensions leading to component collapse.

Fracture Mechanics based fatigue approaches may be further extended to simulate the global fatigue life of components, using the Equivalent Initial Flaw Size (EIFS) concept [2]. The material is assumed to include defects acting like initial flaws. Therefore, the fatigue life of the component is assumed as the number of cycles required to propagate these initial defects until critical dimensions.

This paper proposes the application of the Fracture Mechanics to model the total fatigue life of a rectangular notched plate made of P355NL1 steel. Fatigue crack growth data was evaluated for distinct stress R-ratios, using CT specimens. This data was used to compute the fatigue life of the notched plate, and results are compared with available S-N data. Experimental data was evaluated previously by some of the authors of this paper [7].

2   Experimental details

The present research is based on an experimental data derived for the P355NL1 steel supplied with 5 mm thick plates [7]. This steel is intended for pressure vessel applications and is a normalized fine grain low alloy carbon steel. Table 1 summarizes the mechanical properties of this steel.

Table 1 - Mechanical properties of the P355NL1 steel

Ultimate tensile strength, σ_{UTS} [MPa]	568
Monotonic yield strength, σ_y [MPa]	418
Young's modulus, E [GPa]	205.2
Poisson's ratio, ν	0.275
Cyclic hardening coefficient, K' [MPa]	777
Cyclic hardening exponent, n'	0.1068
Fatigue strength coefficient, σ'_f [MPa]	840.5
Fatigue strength exponent, b	-0.0808
Fatigue ductility coefficient, ε'_f	0.3034
Fatigue ductility exponent, c	-0.6016

Notched plates made of P355NL1 steel were fatigue tested under constant remote stress amplitude. Specimens are double notched rectangles extracted in the longitudinal/lamination direction of the steel sheets. The geometry of the specimens is illustrated in Figure 1. Peterson [1] proposes for this geometry an elastic stress concentration factor, K_t, equal to 2.17. Three test series were performed covering three distinct stress ratios, namely $R=0$, $R=0.15$ and $R=0.3$. Figure 2 presents the S-N fatigue data.
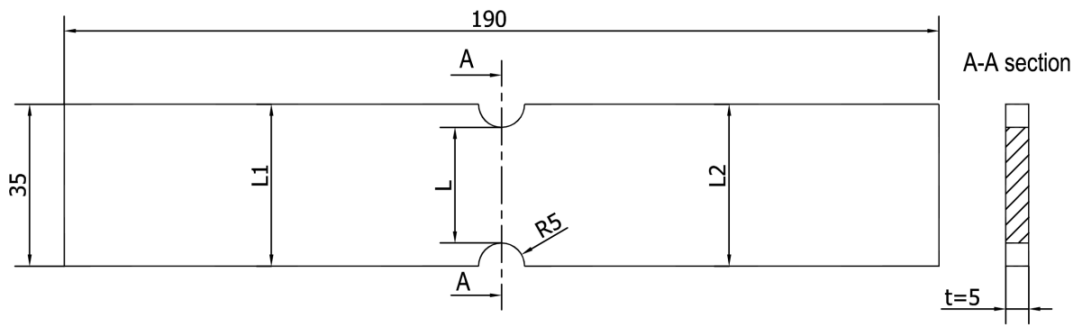
***Figure 1** – Notched rectangular plate (dimensions in mm)*
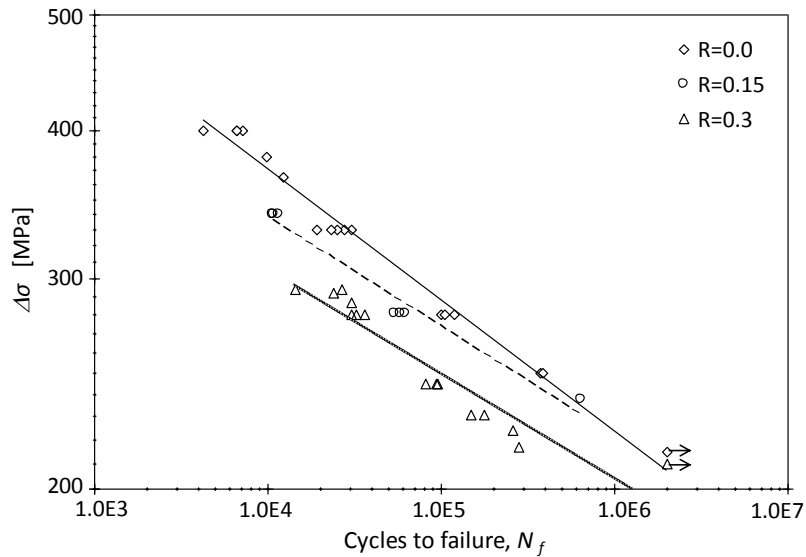
***Figure 2** – S-N fatigue data of the notched plate.*

In addition to the fatigue tests of notched plates, fatigue crack propagation tests were performed using Compact Tension specimens with the same thickness as the notched plates and width, W=40. A total of five specimens were tested under constant loading amplitude, covering three distinct stress ratios, namely R=0, R=0.5 and R=0.7. Figure 3 illustrates the resulting fatigue crack propagation data. The analysis of the results shows that they are approximately linear in the log-log presentation, meaning that propagation regime II was covered by the experiments. The propagation regime I, the near threshold propagation regime was not covered by the tests.
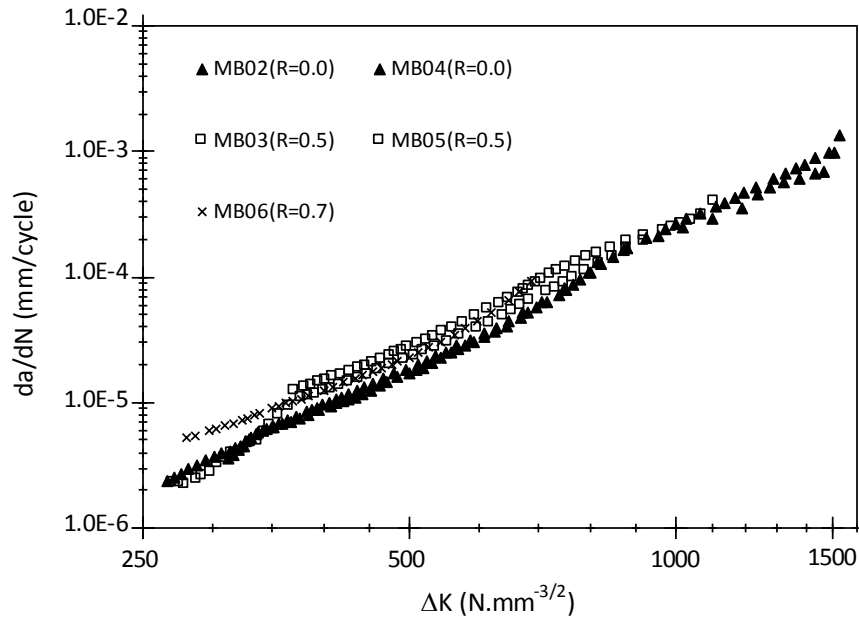
Figure 3 – *Crack propagation data for the P355NL1 steel.*

3   Fracture mechanics based fatigue modelling

The fracture mechanics based fatigue modelling is supported by material crack propagation laws, which have the following general form:

$$\frac{da}{dN} = f(\Delta K) \tag{1}$$

where *da*/*dN* is the fatigue crack growth rate, *ΔK* represents the stress intensity factor range and *f* is a function of the stress intensity factor, *K*. The number of cycles to failure may be computed by integrating the crack propagation law between the initial crack size, a_i and the final crack size a_f:

$$N = \int_{a_i}^{a_f} \frac{da}{f(\Delta K)} \tag{2}$$

In order to allow the computation of the global fatigue life of the component, the initial crack size a_i, is assumed a material characteristic and represents the EIFS of the material. The material is assumed to present internal defects acting like initial cracks. In general, the EIFS may be estimated by an inverse (back-extrapolation) analysis. Some authors try do estimate directly the EIFS using the Kitagawa–Takahashi diagram [2]:

$$a_i = \frac{1}{\pi}\left(\frac{\Delta K_{th}}{\Delta \sigma_f Y}\right)^2 \tag{3}$$

where *ΔK$_{th}$* is the stress intensity threshold, *ΔK$_f$* is the fatigue limit and *Y* is the geometric function that allows the computation of the stress intensity factor, as follows:

$$K = \sigma Y \sqrt{\pi a} \tag{4}$$

In this study, the back-extrapolation method is used since there is no precise data available for the material properties in Eq. (3).

Other key issue on fatigue modelling using the Fracture Mechanics, besides the definition of the EIFS, is the selection of the appropriate fatigue crack propagation laws. The Paris relation was the first one proposed in literature correlating the fatigue crack growth rate with the stress intensity factor range [3]:

$$\frac{da}{dN} = C\Delta K^m \tag{5}$$

where C and m are material constants. This relation gives a good description of the crack propagation regime II. However, this relation does not model the other propagation regimes and does not account for mean stress effects. Many other propagation models have been proposed in literature, with higher performance and complexity, requiring a significantly high number of constants [4]. In this paper, the Paris law is applied as a base crack propagation model. In addition, the modification of the Paris relation to account for stress ratio effects is also assumed, as proposed by Walker [5]:

$$\frac{da}{dN} = C\left[\frac{\Delta K}{(1-R_\sigma)^{1-\gamma}}\right]^m = C\overline{\Delta K}^m \tag{6}$$

where C, m and γ are constants. Also, an extension of the Paris relation, to account for crack propagation regime I, is adopted:

$$\frac{da}{dN} = C\left(\overline{\Delta K} - \Delta K_{th}\right)^m \tag{7}$$

On effect, the crack growth in the propagation regime I is very life consuming, which requires an accurate definition of the crack growth in this regime. The crack propagation threshold, ΔK_{th} is itself influenced by the stress ratio [6]. In reference [6], experimental evidence is given, showing a linear relation between the crack propagation threshold and the stress ratio. Figure 4 illustrates that dependency for several materials.
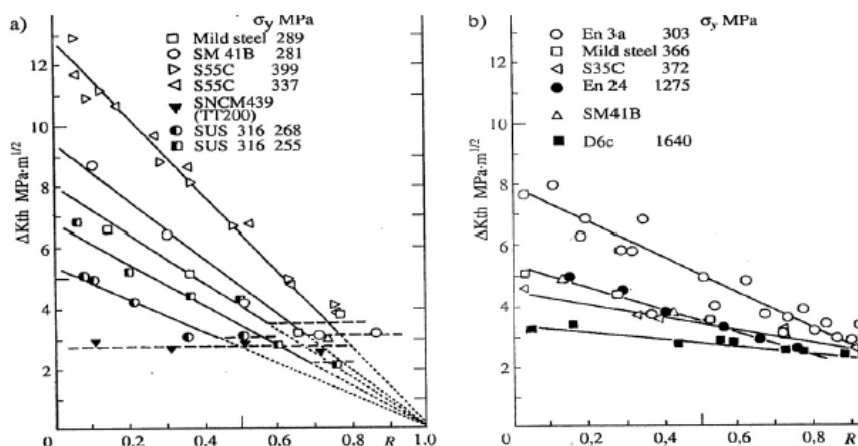
***Figure 4** – Influence of stress ratio R on the threshold value ΔK_{th}. Open symbols relate to ferritic-perlitic steels, filled symbols-for martensitic steels whereas semi-filled symbols-for austenite steels [6].*

In order to allow the application of the fracture mechanics based approach in S-N curves prediction covering low- to high-cycle fatigue regimes, the procedure presented before needs a further correction in order to account for plastic effects. One possibility is to use the elastic equivalent crack size, which results from the actual crack size added to the crack tip plastic zone size. This will lead to an updated/equivalent stress intensity factor range, as:

$$K_{eq} = \sigma Y \sqrt{\pi \cdot (a + \rho)} = \sigma Y \sqrt{\pi \cdot a_{eq}} \qquad (8)$$

In this paper, a numerical integration of the propagation laws is adopted. The integral of Equation (2) is replaced by the following approximation:

$$N = \sum_{a_i}^{a_f} \frac{\Delta a}{f(\Delta K)} \qquad (9)$$

where Δa is a discrete crack increment which is kept in a very small value, bellow the EIFS.

4 Results and dicussion

The crack propagation data presented in Figure 3 was first correlated using the Paris relation, resulting the constants presented in Table 2. In addition, the Walker relation was used to correlate the experimental data. Table 3 summarizes the parameters of the Walker relation. In the predictions proposed in this paper, the Walker relation was used to model the crack propagation on region I. The maximum stress intensity factor ranges from Table 2 were used to define the maximum crack sizes in the simulations. Since the thickness of the CT specimens and the notched plates are the same, these maximum stress intensity factors are a good estimation of the material toughness in the detail. Also, the stress ratios tested in the notched plates are distinct of the stress ratios tested in the CT specimens. Therefore, an extrapolation was carried out to evaluate the maximum stress intensity factors for the notched plate.

Table 2 – Paris crack propagation constants.

R	C^*	m	ΔK_{max} [N.mm$^{-1.5}$]
0.0	7.1945E-15	3.4993	1498
0.5	6.2806E-15	3.5548	1013
0.7	2.0370E-13	3.0031	687

*da/dN in mm/cycle and ΔK in N.mm$^{-0.5}$

Table 3 – Walker relation constants.

| C^*	m	γ
7.1945E-15	3.4993	0.92

*da/dN in mm/cycle and ΔK in N.mm$^{-0.5}$

Concerning the estimation of the crack growth rates in the propagation regime I, the Equation (7) was used. This equation requires the definition of the propagation threshold, which was estimated using the following linear relation:

$$\Delta K_{th} = 152 - 90.252R \quad (N.mm^{-1.5}) \tag{10}$$

where the value 152 N.mm$^{-1.5}$ corresponds to the propagation threshold for R=0. This value is very consistent with the threshold value point out in Figure 4 for the mild steel with yield stress of 366 MPa. It was decided to use distinct relations for the propagation regimes I and II, since the use of a single relation (Equation (7)) did not produced satisfactory results. On effect, the single use of Equation (7) leads to a poor correlation of the experimental data in the propagation regime II and also tends to underestimates the propagation threshold. Despite using two distinct crack propagation laws, they gave a continuous representation of the crack propagation data at the crack propagation I-II regimes transition.

Figure 5 illustrates the fatigue propagation laws adopted in this investigation for each stress ratio tested in the structural detail.
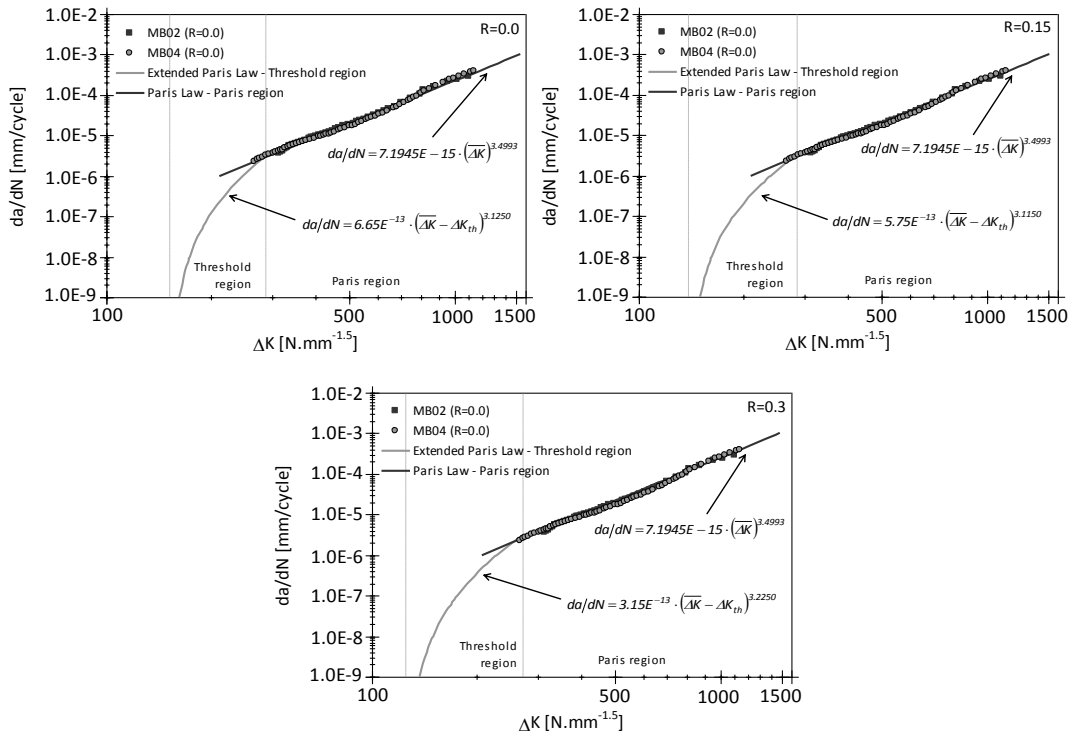

**Figure 5** – *Fatigue crack growth data correlations using two relations.*

The crack was assumed to propagate asymmetrically in one side of the specimens, starting at the notch root, as it was verified in the experimental program. Also, through thickness cracks were assumed. This situation was also observed for many cases in the experimental program. The required stress intensity factor was evaluated using a finite element model of the notched plate and adopting the J-integral method. Figure 6 represents a normalized stress intensity factor function obtained for the notched plate.

Figure 7, finally presents the estimations of the S-N curves for the notched plate for the tested stress ratios. It is clear that the procedure produced very satisfactory correlation of the experimental data. For this purpose, the EIFS was assumed equal to 2.25 μm. The crack

increment used in the numerical integration was 1/10 of the EIFS. The procedure was able to account for the stress ratio effects. Also, the model was able to produce a satisfactory prediction of the fatigue limit regions.
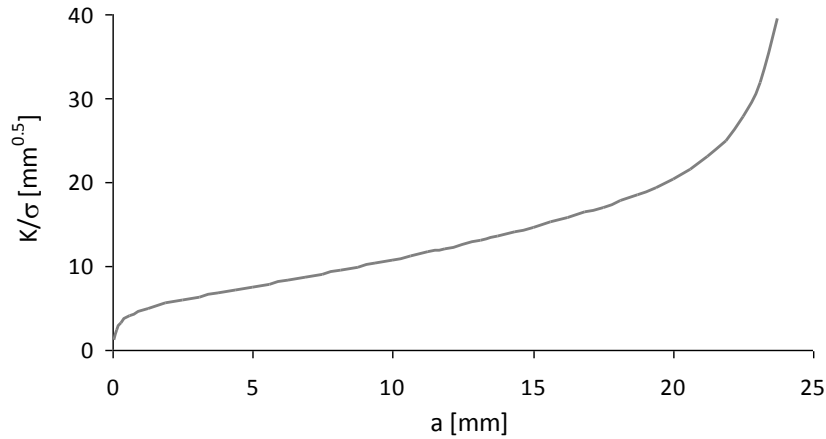
Figure 6 *– Stress intensity factor evolution for the notched plate, obtained using the J-integral approach.*
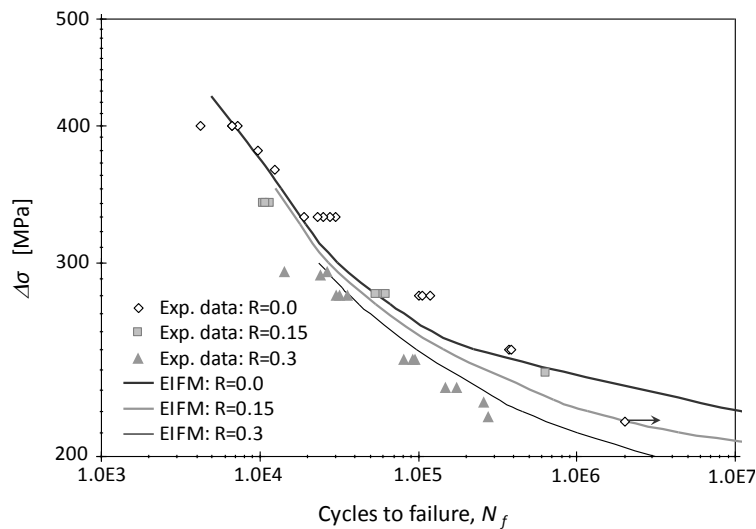
Figure 7 *– S-N curves prediction using a Fracture Mechanics based method and the EIFS.*

5   Concluding remarks

A Fracture Mechanics based fatigue model was assessed in this paper using experimental data available for the P355NL1 steel. The total fatigue life was modelled assuming a crack propagation process, from an initial equivalent flaw size. Experimental fatigue crack propagatio data was used to calibrate the crack propagation relations. Two relations were used instead of a unique relation to improve the predictions, since a single crack propagation relation tends to reduce the correlation in the crack propagation region II and to underestimates the fatigue threshold.

The prediction of the S-N data available for a notched detail made of P355NL1 steel showed a very good agreement between predictions and experimental data. The model was able to acoount for stress ratio effects and the fatigue limite region was fairly estimated. The EIFS was estimated to be 2.25 μm. The crack propagation thresholds, depite estimated in this paper, it was very consistent with data published in the literature for similair materials.

6   References

[1]   R.E. Peterson, "*Notch Sensitivity*", Metal Fatigue, Sines, G. and Waisman, J.L., edition, McGraw-Hill Book Company, Inc., New York, pp. 293-306, 1959.

[2]   Y. Xiang, Z. Lu, Y. Liu, "*Crack growth-based fatigue life prediction using an equivalent initial flaw model. Part I: Uniaxial loading*", Intenational Journal of Fatigue, Vol. 32, Num. 2, pp. 341-349, 2010.

[3]   P.C. Paris, F. Erdogan, "A critical analysis of crack propagation laws", Transactions of The ASME. Series E: Journal of Basic Engineering, Vol. 85, pp. 528-534, 1963.

[4]   S.M. Beden, S. Abdullah, A.K. Ariffin, "Review of Fatigue Crack Propagation Models for Metallic Components", European Journal of Scientific Research, Vol. 28, pp. 364-397, 2009.

[5]   N.E. Dowling, "Mechanical Behaviour of Materials – Engineering Methods for Deformation, Fracture and Fatigue", Second Edition, Prentice Hall, New Jersey, USA, 1998.

[6]   M. Szata, G. Lesiuk, "Algorithms for the estimation of fatigue crack growth using energy method", Archives of Civil and Mechanical Engineering, Vol. IX, Num. 1, pp. 119-134, 2009.

[7]   H.F.S.G. Pereira, A.M.P. de Jesus, A.S. Ribeiro, A.A. Fernandes, "*Fatigue Damage Behavior of a Structural Component Made of P355NL1 Steel under Block Loading*", Journal of Pressure Vessel Technology, Vol. 131, Num. 2, pp. 021407 (9 pages), 2009.

Use of Laser Peening for Fatigue Life Extension of Pre-fatigued Components

Thomas J. Spradlin[1], Kristina Langer[2]

[1]*Universal Technology Corporation, AFRL/RBSM, 2790 D Street, Wright-Patterson Air Force Base, OH, 45433, United States,Thomas.spradlin@ctr.wpafb.af.mil*

[2]*Air Force Research Laboratory, AFRL/RBSM, 2790 D Street, Wright-Patterson Air Force Base, OH, 45433, United States, kristina.langer@wpafb.af.mil*

Military aircraft worldwide are currently being pushed further into, and past, their initial design fatigue lives, the result being continually growing fleets of aging aircraft. This trend has lead to the research and development of surface residual stressing technologies as fatigue life mitigation tools. One such technology, Laser Peening (LP), can induce high-magnitude compressive residual stresses deep into the surface of metallic components. Extensive testing has been conducted to demonstrate the fatigue life extension garnered by LP for a variety of specimen shapes, loadings, and materials. However, the entirety of this testing has been conducted on coupons manufactured from fresh material which has not yet accumulated cyclic fatigue damage.

In this paper, we study the application of LP for specimens that have expended a significant portion of their average fatigue life. The goal is to investigate both the overall fatigue response as a function of pre-fatigue percentage and the interaction with pre-existing damage such as dislocation concentrations and fatigue cracks. Al 2024 specimens were designed and fatigue cycled under three-point bending in a self-aligning fixture. Geometric variations and surface roughness were minimized using careful machining and polishing tolerances (±0.005 and 10 μ-in., respectively). Three levels of pre-fatigue were used: 0, 25, and 50% of the mean total fatigue life of the specimen, as determined by cycling un-peened specimens to failure. After fatigue cycling to the desired amount of pre-fatigue, the specimens were laser peened in the fatigue critical zone using a basic overlapping raster pattern with two layers. The specimens were then replaced into the fatigue frame and cycled until failure.

The failure data was analyzed using a computer intensive statistical re-sampling technique known as bootstrapping to better understand observed trends regarding fatigue scatter, confidence intervals, and life enhancement. Simulation based fatigue life estimations were conducted to evaluate current fatigue life algorithms and their ability to capture both residual stress and pre-fatigue effects. Using experimental, statistical, and physics-based analytical approaches, the effects of pre-fatigue on the effectiveness of LP as a fatigue life mitigation tool will be ascertained.

Structural performance of a lifeboat craft under the application of static and dynamic loadings

M. S. Santos[1], Rui F. Martins[1,2], Paulo P. Silva[3], António R. Mateus[4]

[1]*Faculdade de Ciências e Tecnologia, Universidade Nova de Lisboa, UNIDEMI, Departamento de Engenharia Mecânica e Industrial, Campus de Caparica, 2829-516 Caparica, Portugal, rfspm@fct.unl.pt*

[2]*ICEMS-IST, Av. Rovisco Pais, 1, 1049-001 Lisboa, Portugal*

[3]*Missão de Acompanhamento e Fiscalização - Lanchas de Fiscalização Costeira, Marinha Portuguesa, Base Naval de Lisboa, 2800-001 Alfeite, Portugal*

[4]*Marinha Portuguesa, Direcção de Navios, Base Naval de Lisboa, 2800-001 Alfeite, Portugal*

Abstract The main purpose of this paper is to present the structural response of a lifeboat craft when subjected to the effect of slamming on its bow, but also when submitted to a hypothetical flooding of watertight compartments located in between bulkheads no. 17 and 20 and in the engine and water jet's compartments, separately. The studies were accomplished using the Finite Element Method (FEM) and non-linear FE analyses were performed, which allowed considering large deformations together with material models that included hardening and plasticity. The modes and frequencies of vibration of the high speed craft were also determined to check for structural resonance problems due to slamming induced loads, considering the sea conditions where the craft operates.

The results of the structural analyses revealed that the maximum stress induced in the structure, due to typical in-service load conditions, was, in average, the order of 50% of the Yield Strength of the materials used in the production of the high speed lifeboat, namely the aluminium alloys 5083-H111 e 6082-T6.

1   Introduction

The vessel under study is a high speed, light craft (HSLC) that complies with the speed requirement V≥25knots [1], and was designed to operate in a sea state 8, with significant wave height between 9 and 14 meters, wind force 10 and self-righting ability (Figure 1) [2].


Figure 1 - *Self-righting ability of the HSLC under study, that was designed, fabricated and is successfully operating in Portugal*

The lifeboat can transport up to twelve castaways and is propelled by two *Scania* diesel engines which drive two water-jets. The main characteristics of the lifeboat are summarised in Table 1.

Table 1 – *Main characteristics of the lifeboat craft*

Length of the craft, L, in metres, defined as the distance between perpendiculars	13,45m
Greatest moulded breadth, B, in metres	4,3m
Fully loaded displacement, Δ, in tonnes, in salt water	18t
Fully loaded draught, T, in metres, with the craft floating at rest in calm water	0,8m
Maximum speed, V, in knots	≥25knots
Motors/Water jets: Scania DI 12 43M 2x 478 KW/ *Ultradynamics* UJ 376	

The lightweight craft was built from two aluminium alloys used in shipbuilding, namely the 5083-H111 aluminium alloy and the heat-treated aluminium alloy 6082-T6, this last used in the reinforcements of the hull, in order to obtain lightweight stiffened panels (Figure 2a). The figures 2b and 2c show stress/strain curves for the 5083-H111 and 6082-T6 aluminium alloys, respectively, obtained from axial tensile tests [3] that were used to define the material models in the Finite Element (FE) computer code during the numerical analyses performed thereafter.

a) b) c)
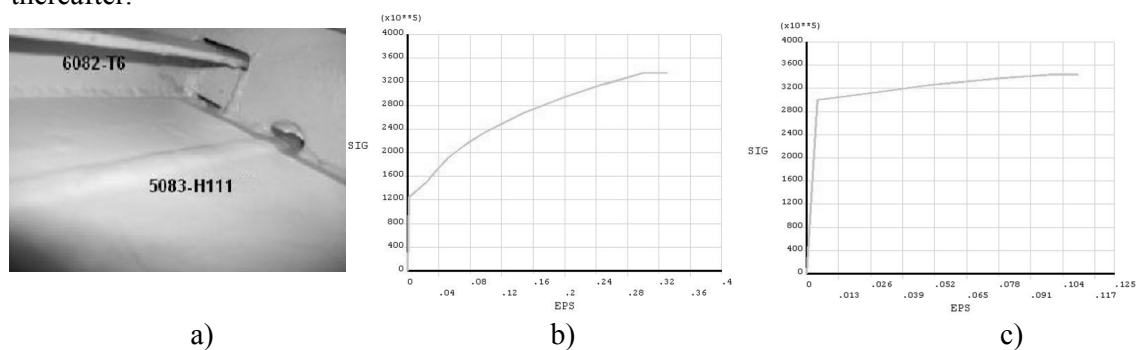
Figure 2 – *a) View of a lightweight reinforced panel showing a plate and reinforcement. b) Stress [Pa]-strain curve of the 5083-H111 aluminium alloy. c) Stress [Pa]-strain curve of the 6082-T6 aluminium alloy*

2   Modelling Finite Element Analysis (FEA)

The high speed, light craft under study was modelled (Figure 3a) and, due to symmetry, half of the structure was analysed using the FE computer code ANSYS. A shell element type was used during the structural and modal analyses performed and the non-linear large deflection theory was always considered.
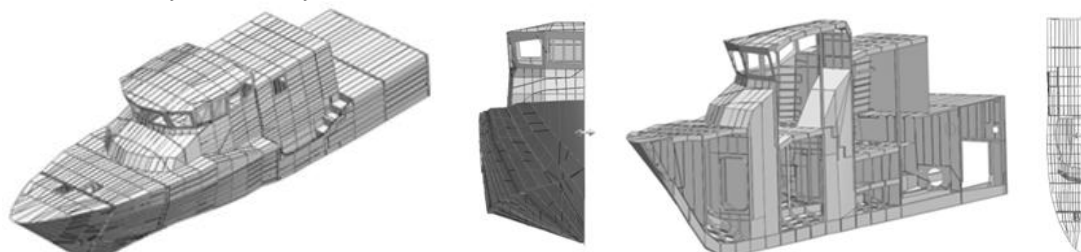
Figure 3 - *Overall view of the lifeboat modelled*

The design of aluminium speed crafts considers the classic approach of the structural longitudinal strength of the primary structure, as well as local loads of high frequency, as it is the case of slamming. These loads are usually determinant in the structural design of an

aluminium craft, where the bulkheads constitute an essential element of resistance submitted to compressive in-plane loads (because of "slamming") and a hydrostatic load due to hypothetical case of flooding of adjacent compartments. The bulkheads have a very small thickness (5 mm), associate with 3 mm thickness small "L" shape reinforcement scantlings.

3   Finite Element Analyses (FEA): loadings and restraints

The in-plane dynamic load was estimated according to the "Rules and Regulations for the Classification of Special Service Craft" [4], taking into account the length between perpendiculars of the lifeboat (13.45 metres), its fully load displacement (18 t), the aluminium monohull type of craft, with a waterline length of 12.5 metres, a significant wave height of 10 metres and a maximum breadth of 4 metres. The slamming pressure was applied on the outside shells of the hull's model, near bulkhead no. 20 (bow). In addition, pressure due to slamming effect depends on the encounter frequency (ω_e) of the waves on the hull, expressed by equation (1), where U defines the speed of the craft, g is the acceleration of gravity (9.81 m/s^2), ω corresponds to the wave frequency and θ is the angle of the wave's direction relative to the ship's speed vector [5].

$$\omega_e = \omega - \frac{\omega^2}{g}.U.\cos\theta \ [rad/s] \tag{1}$$

Varying U between 1 and 15 m/s (0,51 e 29,2 knots) and θ between 0º (stern seas) and 180º (bow seas), encounter frequencies, ω_e, between 0 rad/s and 3,136 rad/s (0 and 0,50 Hz) were calculated (Table 2). The maximum value obtained corresponds to a speed of 29 knots and an encounter angle of π rad (180º).

Table 2 – Encounter frequencies [rad/s]

Encounter Angle (º)	Speed of the Craft (knots)						
	1,94	3,89	5,83	…	25,27	27,21	29,16
	Encounter Frequencies (rad/s)						
0	1,009	0,876	0,743	…	**0,000**	**0,000**	**0,000**
1	1,009	0,876	0,743	…	**0,000**	**0,000**	**0,000**
2	1,009	0,876	0,743	…	**0,000**	**0,000**	**0,000**
3	1,009	0,876	0,744	…	**0,000**	**0,000**	**0,000**
…	…	…	…	…	…	…	…
177	1,010	0,878	0,745	…	2,868	3,001	3,133
178	1,009	0,877	0,744	…	2,869	3,002	3,135
179	1,009	0,876	0,743	…	2,870	3,003	**3,136**
180	1,009	0,876	0,743	…	2,870	3,003	**3,136**
Maximum	1,275	1,408	1,541	…	2,870	3,003	**3,136**
Minimum	1,009	0,876	0,744	…	**0,000**	**0,000**	**0,000**

In addition, design rules require watertight bulkheads to resist a hypothetical overflow of one of the adjacent compartments. The lateral design load to be applied to bulkheads was calculated according [4] - Part 5 Chap. 3ʳᵈ, which suggests the application of a uniformly distributed pressure given by equation (2), where h is the height of the bulkhead, instead of a hydrostatic load. This approach will induce higher deflections and stresses in the bulkhead than the application of a true hydrostatic pressure (ρgh).

$$P = 7.2 \times h \ (kPa) \tag{2}$$

Moreover, for unrestricted service, the wave coefficient, Cw, is given by equation (3) [1], which allows the calculation of the pressure acting on the craft's bottom, side (including superstructure side) and weather decks, for load point below design waterline (eq.4) [1]:

$$Cw=0.08\times L \text{ for } L \leq 100m \text{ (see Table 1 for L)} \tag{3}$$

$$p=10h_0+(k_s-1.5\times h_0/T).C_W \text{ (kN/m}^2) \tag{4}$$

where, k_s equals 7.5 aft amidships and h_0 is the vertical distance, in metres, from the waterline at draught T (Table 1) to the load point [1].

The loads were applied to the HSLC lifeboat's model (Figure 4) and results are presented in Figure 5.

a)

b)

c)

d)
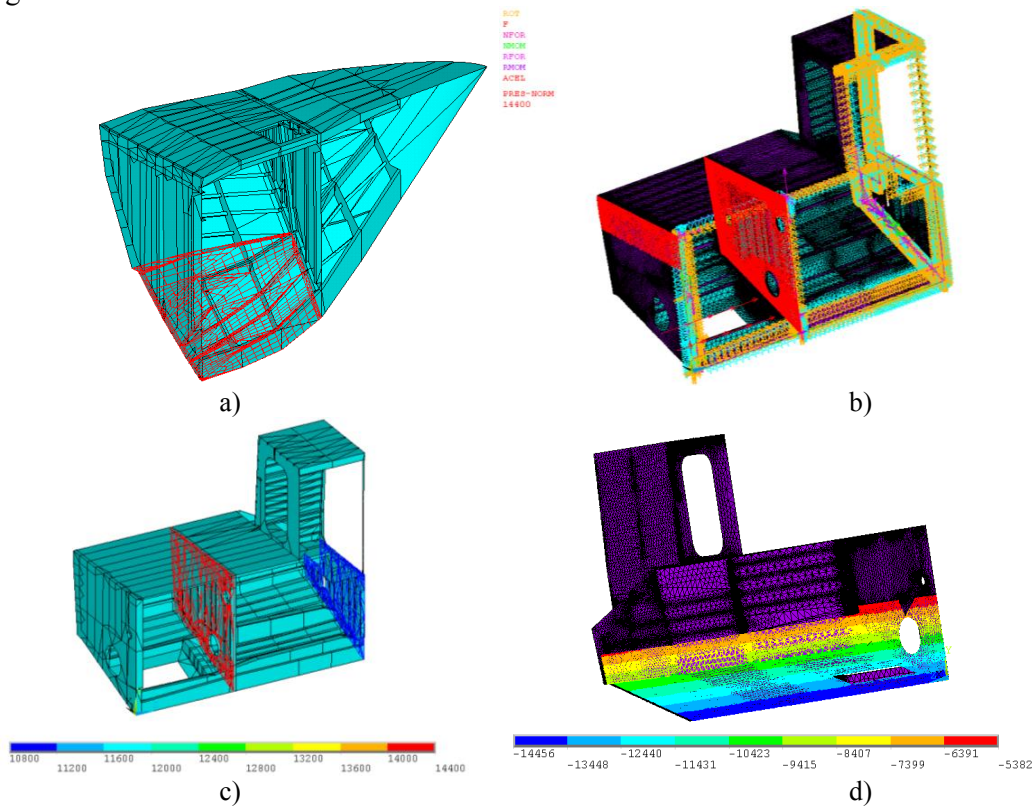
Figure 4 – a) Areas considered in the FEA for the application of the slamming pressure; b) Simulation of the hypothetical flooding of water-jets compartment; c) Simulation of the hypothetical flooding of motors compartment d) Pressure acting on the craft's bottom (stern)

4   Results and discussion

The slamming pressure applied on the bow during the performed FEA revealed that the Von Mises stress values induced in the structure were lower than the Yield Strength of the bow plates' material (Figure 5a); the stiffeners also remained in the elastic regime (Figure 5a). In addition, the maximum deflection calculated was approximately 11.5 mm (Figure 5b).

In what concerns the hypothetical flooding of the motors and jet's compartments, results shown (Figures 5c and d) that the Von Mises stresses induced in the majority of the stiffened bulkheads remained below 30MPa (yield strength safety factor, SF, higher than 4). Only in one point, namely in a stiffener near an opening, the maximum Von Mises stress induced was about 250MPa, which reveals a safety factor of 1.2. In a bulkhead's plate, also near the larger

opening existent there, the stresses calculated were in the order of 140MPa, which are slightly higher than the Yield Strength of the plate's material (120MPa). Nevertheless, for flooding structural design it may be assumed permanent deformation (material working on the plastic zone) [6].

When considering the dynamic and hydrostatic pressures applied on the hull's plates, the maximum stress induced on the plates and on the stiffeners, near stress concentration regions, will be approximately 60MPa (SF=2) and 180 MPa (SF=1.7), while in the other regions – plates and stiffeners – the von Mises stresses remained lower than 21 MPa (SF=5.7) and 63 MPa (SF=4.7), respectively.
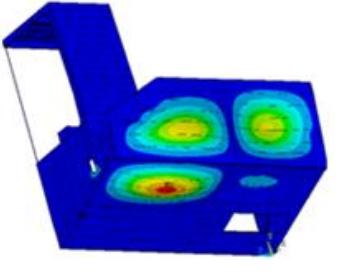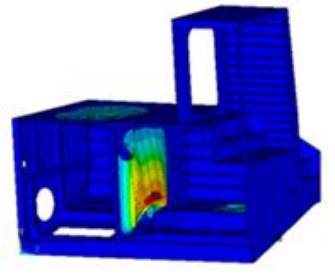

a)

b)

c)

d)

e)
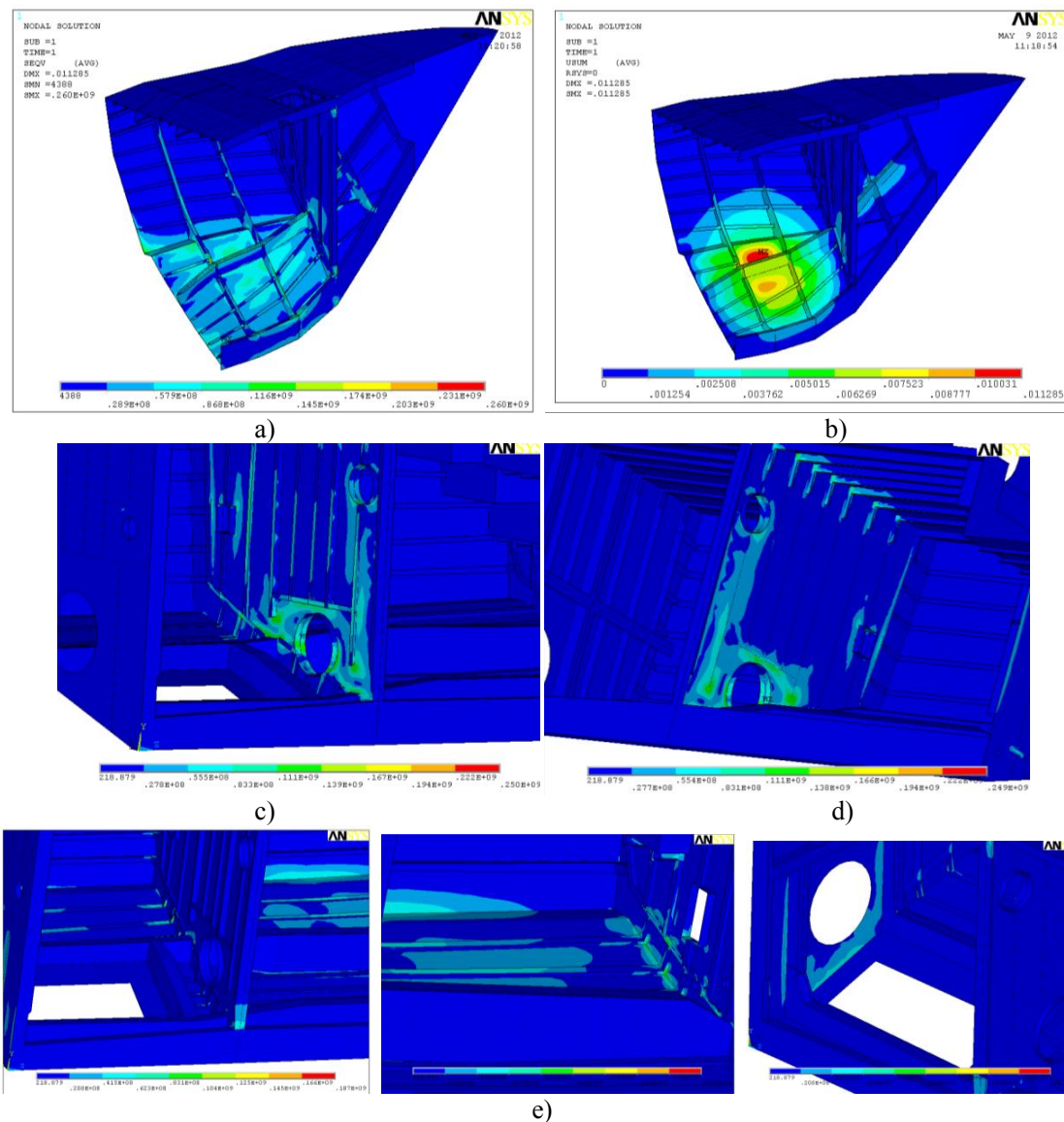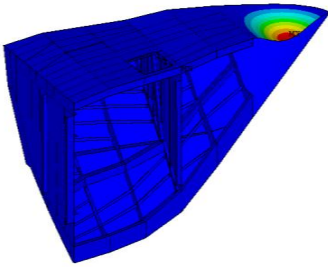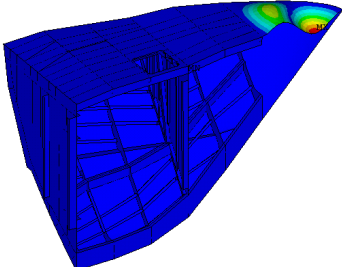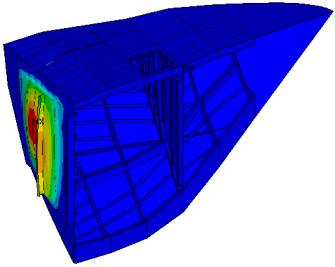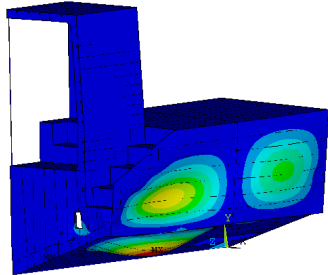
Figure 5 – *a, b) Von Mises stresses and displacements induced on the reinforced bow due to the application of the slamming pressure, respectively; c,d) Von Mises stresses induced in the structure due to the hypothetical flooding of water-jets compartment and motor's compartment, respectively; e) Von Mises Stresses induced on the stern due to pressure acting on the craft's bottom*

In addition, the first few frequencies and corresponding modes of vibration of the lifeboat were calculated for the bow and stern (Table 3), showing how far they are from the encounter frequencies presented in Table 2 (maximum encounter frequency equals 0.5Hz), thus with a very low probability of resonance occurrence.

Table 3 – First frequencies and modes of vibration of the bow and stern

Bow		
1ˢᵗ frequency of vibration (26.52Hz)	2ⁿᵈ frequency of vibration (57.51Hz)	3ʳᵈ frequency of vibration (68.49Hz)

Stern		
1ˢᵗ frequency of vibration (44.36Hz)	2ⁿᵈ frequency of vibration (45.69Hz)	3ʳᵈ frequency of vibration (48.16Hz)

5 Conclusions

The Von Mises stresses induced in the sections of the bow and stern analysed showed sufficient resistance to the loads expected in normal operation and in case of an incident flooding. The HSLC also has shown an almost nonexistent probability of occurrence of structural resonance phenomena due to slamming loads.

6 References

[1] Rules for classification of high speed, light craft and naval surface craft: structures, equipment, Part 3-Chapter 1: Design principles, design loads, *Det Norske Veritas*, 2005

[2] www.revistademarinha.com

[3] Matias, C., Mechanical behaviour of two aluminium alloys used in shipbuilding when applied in naval structures", MSc. (in Portuguese), FCT/UNL, 2008

[4] Rules and Regulations for the Classification of Special Service Craft, Lloyds Register of Shipping (1999)

[5] Perez, Tristan; Ship Motion Control: Cruise Keeping and roll stabilization using rudder and fins; Springer, 2005

[6] Chalmers, D.W; Design of ships' structures; HMSO, London, 1993

Application of alternative lightweight structures to support a helicopter's flight deck

Eduardo H. Vieira[1], Rui F. Martins [1,2], Paulo P. Silva[3]

[1]*Faculdade de Ciências e Tecnologia, Universidade Nova de Lisboa, UNIDEMI, Departamento de Engenharia Mecânica e Industrial, Campus de Caparica, 2829-516 Caparica – Portugal*

[2]*ICEMS/IST, Av. Rovisco Pais, 1, 1049-001 Lisboa - Portugal*

[3]*Portuguese Navy, Directorate of Ships, Naval Base of Lisbon, 2800-001 Alfeite – Portugal*

Abstract   The main purposes of this article consist in analyzing the possibility of implementing tubular structural elements in secondary and tertiary ship structures in order to obtain significant weight reduction and simultaneously maintain or increase its structural resistance. For that purpose, it was verified the possibility of replacing the beams and girders that support the flight deck of a frigate of the Portuguese Navy, simulating the impact load caused by an emergency landing of a "Super Lynx 300" helicopter over the flight deck. Several analyses were performed, varying the load application point, in order to determine the stress distribution induced in the different elements that compose the structure, both in current and alternative models.

The numerical simulations were performed using the Finite Element Method (FEM) on the current flight deck and its support structure, as well as alternative support structures. It was considered that none of the modeled structural elements would suffer permanent deformation driven by the applied load. Comparing the stress distribution throughout the different models, it was possible to obtain several alternative structures with weight reduction that could go up to 17% when considering a load safety factor of 1.5.

1   Introduction

The *Vasco da Gama Class* frigate (Figure 1a) started operating in 1991, being the first Portuguese ship equipped with missile launching systems: surface-surface and surface-air [1]. In addition, besides several innovations regarding the propulsion, weapons, sensors and communication systems, each ship integrates two "Super Lynx 300" helicopters (Figure 1b), which perform anti-submarine, anti-surface and area interdiction missions [2]. They also perform secondary missions like transport, surveillance, search and rescue. In figure 1c are shown the main dimensions of the helicopter and its mass.
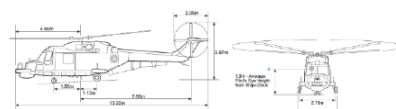
Maximum all up mass (MAUM): 5330 kg

a)   b)   c)

Figure 1 – *a) Vasco da Gama Class frigate; b) Flight deck; c) Helicopter's main dimensions and mass*

The flight deck is the frigate's area where the "Super Lynx 300" helicopters operate. It is situated on the ship's stern and has an area of 16 by 19 meters. According with the ship's drawings, the flight deck is situated above two compartments, separated by a bulkhead (Figure 2), which provides structural support to the structure in conjunction with four columns (Figure 2). All the referred elements contribute to maintain the structural integrity of the flight deck and have been modeled and considered on the study. The current flight deck and the bulkhead plates weigh approximately 24 000 kg, while the beams and girders weigh 12 700 kg. The total mass of the structure is approximately 37 000 kg.
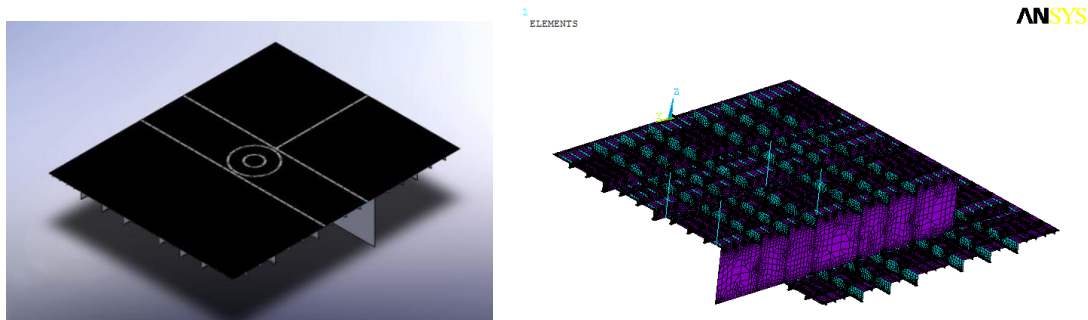

***Figure 2** – Three-dimensional model of the flight deck and finite element mesh of the current structure*

2   Finite element analysis of the current flight deck

The ANSYS® software was used to generate the numerical model shown in Figures 2 and 3, which tried to accurately represent the current flight deck. To achieve that purpose, detailed drawings of the ship were analyzed in order to obtain the correct position and geometry of all the different beams and girders. Moreover, the ANSYS' command *Smartsize* was used during the mesh generation stage with the purpose of obtaining a very well balanced and refined mesh. The *SmartSizing* algorithm first computes the edges' length of the finite elements for all lines of the areas to be meshed; then it tries to set an even number of line's divisions around each area so that a mapped mesh could be obtained. Finally, the lines located near the stress concentration details are refined, in order to improve the mesh density and allow the convergence of the results independently of the number of finite elements used. The structural finite element type "SHELL 63" was used to model the girders, the flight deck's plates and the bulkhead, while the four columns present in the current structure were modeled using the structural element designated as "PIPE 16". In Figure 3a it is possible to visualize the connectivity established between the finite elements belonging to adjacent areas. In Figure 3b are represented the footprints induced by the wheels of the helicopter simulated where the different load pressures were applied.
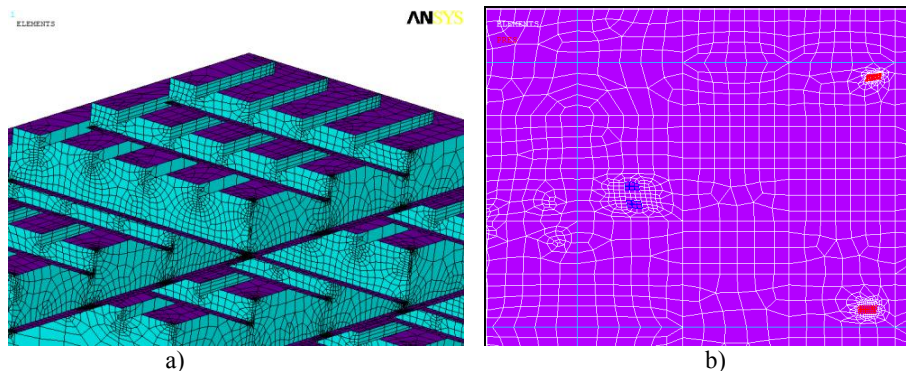

a)   b)

***Figure 3**– a) Detail view of the meshed structure; b) Dimensions of the areas where load pressures were applied*

254

For the calculation of the load pressure caused by the landing of the helicopter, it was considered the weight of the aircraft, together with the critical location of the center of gravity and footprint areas of the wheels, all multiplied by a specific load safety factor. According to Chalmers [3], for the landing maneuver, a load safety factor of 1.5 should be used for beams and girders and of 1.2 for the plates. In the studies performed [4], it was considered a load safety factor of 2 [5]. In addition, a fixed restraint condition was imposed at the support edges of the deck, at the bulkhead's edge and at the base of the columns.

The material used to build the flight-deck was a NV D36 high-strength steel (as designated by *Det Norske Veritas* Classification Society), which is characterized by the chemical composition and the mechanical properties presented in Table 1 and 2 [6], respectively. The steel, furnished in the normalized condition, is extensively used in shipbuilding and presents good weldability and low hardening effect after welding, due to the low probability of martensitic transformation during cooling [6]. A linear elastic and isotropic material model, with a longitudinal elasticity modulus of 210 GPa, was defined in all the numerical simulations performed, once it was considered that none of the modeled structural elements would suffer permanent deformation driven by the applied loadings.

The highest *Von Mises* equivalent stresses induced in the structure are shown in Table 3 and in one case the stress calculated is similar, although lower, to the Yield Strength. However, the numerical simulation correspond to a critical and non-usual load case where the centre of gravity of the helicopter was considered coincident with the center of the area of the flight deck, comprehended between the stern of the ship and the bulkhead (Table 3); in the standard landing position the centre of gravity of the helicopter and the centre of the flight deck are coincident and the induced stresses are lower. In addition, the maximum equivalent stress values calculated were always registered in the plates of the flight deck and never at the supporting girders, enabling, the removal and substitution of any plates with permanent deformation, but ensuring that the girders work inside the elastic limit.
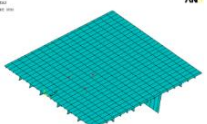
Table 1 - *Chemical composition of the NV D36 shipbuilding steel grade type*

C [%]	Si [%]	Mn [%]	P [%]	S [%]	Al [%]
0.18	0.5	≥0.7	0.035	0.035	≥0.02

Table 2 - *Mechanical properties of NV D36 shipbuilding steel grade type*

Yield Strength [MPa]	Tensile Strength [MPa]	Elongation [%]
≥355	490-620	≥21

Table 3 - *Maximum Von Mises stresses induced in the current structure due to a critical landing position. Load safety factor: 2*

Landing position	In the plate under the nose leg	In the plate, under a rear wheel	In the girders closest to the nose/rear wheels	In the bulkhead
	344 MPa	250 MPa	154 MPa	29 MPa

3   Alternatives configurations studied for the flight deck

To determine the lightest structure with the lowest equivalent stresses induced, several alternative structures were modeled and analyzed. All of them with the same constraints and load conditions applied to structure described in section 2. Initially, circular and triangular cut-offs (Figure 4) were introduced in the main support girders and were analyzed, having been calculated *Von Mises* stress values below the material's Yield Strength. However, the weight reduction achieved by these solutions was very small (maximum reduction value of 3.7%), when compared with the high amount of work and costs evolved in its production. For this reason, it was decided to model a new structure built with tubular elements (Figure 5), based on the results obtained in a topological optimization analysis of a simply-supported beam submitted to a middle span applied load.

The numerical simulations were performed considering different values for the thickness and external diameter of the tubular structural members (Table 4).
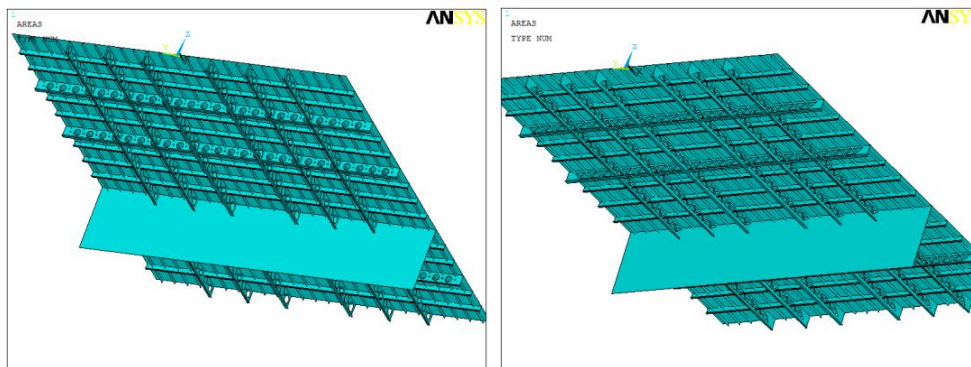

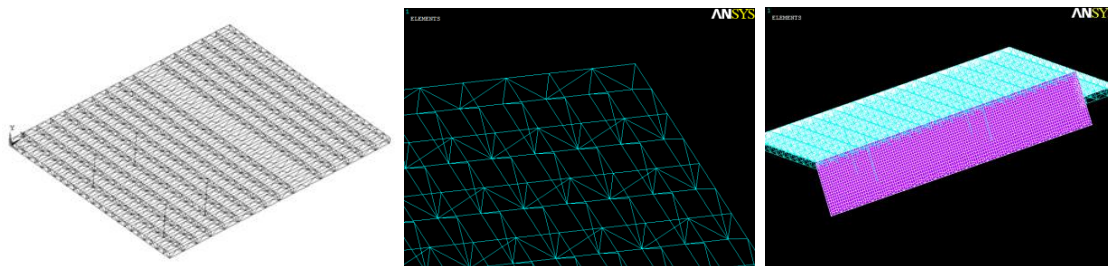***Figure 4**– Alternatives structures with circular and triangular cut-offs*

***Figure 5**– Tridimensional truss of tubular elements proposed to support the flight deck*

***Table 4 -** Dimensions of the tubular elements considered in the analyses*

Alternative structure no.	Commercial ref.	External diameter (")	Thickness (")	Area (mm^2)	Moment of inertia (mm^4)
1	3''	3,500	0,300	1 948,2	1,63x10^6
2	2''	2,375	0,154	693,3	2,77x10^5
3	1 ½''	1,900	0,145	515,8	1,29x10^5
4	1 ¼''	1,660	0,140	431,3	8,10x10^4
5	1''	1,315	0,133	318,6	3,64x10^4
6	¾''	1,050	0,113	214,6	1,54x10^4
7	½''	0,840	0,109	161,5	7,11x10^3

4   Analysis and discussion of results

The maximum *Von Mises* stress values induced at several critical locations of some structures under study (Table 4) are presented in Table 5, namely in alternative structures numbers 3 and 4, in the plates under the front and rear wheels of the helicopter, in the tubular structure near the columns and in the tubular structure near the landing zone. As can be observed in Table 6, neither all the structures studied remained in the elastic regime nor led to a mass reduction of the structure, as it is the case of alternative structures numbers 1, 2, 5, 6 and 7. In fact, only in case of alternative structures numbers 3 and 4 a mass reduction of 6% and 11%, respectively, was enabled, when compared with the current structure's mass, and the stresses calculated remained lower the Yield Strength of the material. In addition, these structures present both slightly higher deflection values than the verified in the current structure. Moreover, the stresses induced in tubular structure number 4 were higher than those induced in tubular structure number 3, due to the smaller section of the tubular elements that constitutes the later structure.

The frequencies and modes of vibration of the existing and new structures were calculated, as well as the buckling resistance of the support columns. It was verified that the columns won't present any structural instability.

If a load safety factor of 1.5 [3] have been applied instead, an alternative structure would allow a mass reduction of 17% (30575 kg), maintaining a stress and strain levels lower than structure number 4 analyzed considering a safety factor of 2. Finally, the possibility of reducing the plate's thickness of the flight deck (10 mm) was not considered, once it was demonstrated in a previous study that in certain critical locations that procedure would not be acceptable.

Table 5 - *Maximum Von Mises stresses induced in two alternatives structures due to a critical landing position. Load safety factor: 2*

Alternative structure no.	In the plate under the nose leg	In the plate, under a rear wheel	On the tubular structure closest to the nose/main wheels	At the connection of the tubular structure with a column
3	287 MPa	259 MPa	207 MPa	122 MPa
4	294 MPa	270 MPa	252 MPa	138 MPa

Table 6 – *Maximum deflection and stresses induced in the alternatives structures due to a critical landing position (load case no. 2). Load safety factor: 2*

Structure no.	Deflection (mm)	Maximum *Von Mises* stresses (MPa)	Mass (kg)	Mass variation (%)
Current	10	344	36892	-
1	7	267	62934	+70
2	9	279	38276	+4
3	11	287	34501	-6
4	13	294	32875	-11
5	15	389	30575	-17
6	19	441	28510	-23
7	23	469	27446	-26

5   Conclusions

The numerical simulations performed have demonstrated that two alternative geometries to the current flight deck configuration are capable of supporting the loading imposed by the landing operation of the helicopter (when a load safety factor of 2.0 was considered), presenting a mass reduction of 6% or 11% and simultaneously showing induced stresses lower than the Yield Strength of the material used to build the structure.

If a load safety factor of 1.5 was considered instead of 2.0, the mass reduction could be approximately of 17% and the stresses and strains induced in the structure would remain lower than the values obtained for the alternative structure number 4 (Table 6), which allowed a mass reduction of 11%.

6   References

[1] http://www.marinha.pt/PT/amarinha/meiosoperacionais/superficie/classevascoda gama/

[2]   http://www.agustawestland.com/products01_01.php?id_product=24

[3]   Chalmers, D. W., "*Design of Ships' Structures*", H M S O – Ministry of Defense

[4]   Vieira, E. H., "*Grelhas estruturais de elementos tubulares para aplicação em estruturas secundárias de navios*", MSc. Thesis (in Portuguese), FCT-UNL, 2010

[5]   Lloyd, Germanischer, "*Rules for Classification and Construction*", III Naval Ship Technology s.l.: Germanischer Lloyd, 2004.

[6]   *Det Norske Veritas*, Offshore Standard DNV-OS-B101, Metallic Materials, April 2009

Estimation of structural damage on helicopter tail boom in case of harsh landing events

G. Vallone, C. Sbarufatti, A. Manes and M. Giglio

Politecnico di Milano, Dipartimento di Meccanica
Via la Masa 1, 20156 Milano, ITALY
Tel: +39 02 2399 8203
e-mail: giorgio.vallone@mail.polimi.it

Abstract

Investigation about structural damage on helicopter components in case of harsh landing is poorly described in literature. Most of the studies are focused on the performance of skid gears, covering two main topics: the gear integrity after harsh landing and passenger safety. More studies may be found in the case of aircrafts, with similar purposes.

Nevertheless, the overloads due to unusual landing conditions may lead to distributed damages on the whole frame: in particular the tail boom can be severely exposed to the inertial loads caused by a harsh landing. At present those cases require a maintenance event to assess the integrity of the structure. The ability to detect the onset of damage with a proper sensor system may permit to avoid a similar circumstance, developing a condition based maintenance approach thus reducing the idle time of the machine. With this in mind, the present work focuses on the evaluation, through the use of Finite Element Model, of the stress due to harsh landing acting into the tail boom of a medium-weight helicopter, equipped with wheeled landing gear. Different conditions are considered, studying their influence on stresses, and a monitoring strategy is proposed.

1 Introduction

Harsh landing events may generate damage and/or zones affected by high plasticization into the helicopter structure. A scenario of particular interest is the one of the landing over ship's deck. As the seaway is virtually universally accepted as unpredictable ([1]), a vertical motion of the ship may generate a harsh landing event. In particular safe landing can be expected if the probability that it occurs during the lull time is sufficiently high. If, for some reasons, the landing does not happen during lull time the probability to have some damage is correlated to the relative speed between the helicopter and the ship's deck ([2]).

When an event is judged by some criteria as harsh, current approach provides mandatory maintenance. Two problems arise: first, to evaluate the effective harshness of the landing event to establish when a maintenance event is necessary or not. Second, to find zones where the damage is likely to occur. The knowledge of when and where to inspect the helicopter can be of great advantage. In a condition based maintenance (CBM) scenario, this may generate advantage for the final user in terms of maintenance accuracy, safety and idle time [3]. Furthermore, also in design phase (see, for example, [4]) great advantages may occur because of the increased knowledge of the helicopter behavior under contingent loads. Also not using directly a CBM approach, this methodology allow to inspect some locations judged more
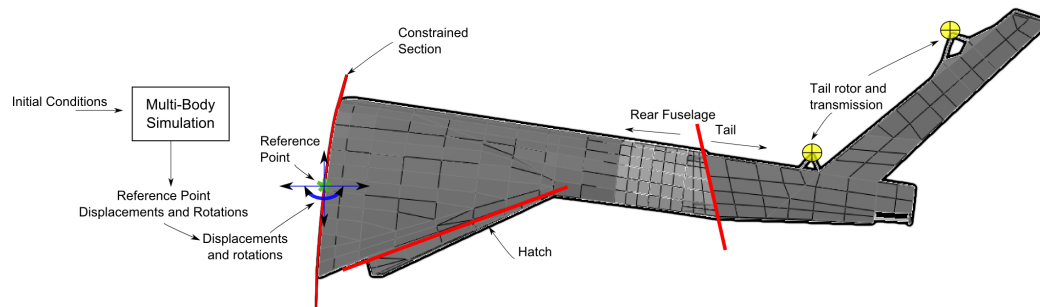
Figure 1 – *Schematization of simulation approach used.*

critical according previous analyses first, thus increasing the effectiveness of such inspections.

The present article does not consider in detail how to exploit reported advantages, but focus on establish if it is possible to estimate landing damage with some sensor techniques, at present used for structural health monitoring (SHM) applications. With this aim in mind a harsh landing scenario is simulated using a mixed multi-body and finite element analysis. The tail boom was identified as a part of interest: this because while the attention may be posed on the landing gear for localized damage, some damage may occur into the tail due to the great inertia loads experienced and propagate during flight. Moreover a complete inspection of this part may be time-expensive.

Few studies of helicopters harsh landing events may be found in literature and those are generally concentrated on skid gear case. An example is the one found in [5], where a dynamic drop simulation is conducted considering different landing scenarios. A rigid body is considered for the helicopter fuselage while a deformable model is used for the skid gear. The aim is to obtain a tool helping the design of the skid gear itself. Similar approach may be found in [6], [7], focusing one more time on landing gear design and [8], this time considering the landing forces on the occupants of the helicopter. An interesting study, basically for the similar topic, is [9]: here the attention is posed on the possibility of identifyng the damage on the skid row to enable CBM.

All these studies never focus on the deformability of the fuselage, while an example in this direction may be found in [10], where a FE model for the fuselage of a landing airplane is developed.

2   Simulation approach

The approach proposed to study the impact during landing, is divided in two subsequent steps:

- A multibody analysis of the landing not considering the fuselage deformability Figure 2;
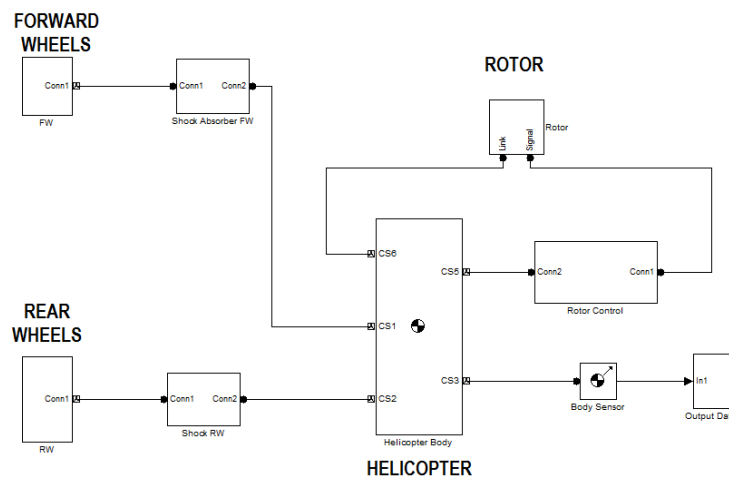
Figure 2 – *Multi-body block diagram.*

- FEM analysis of the entire tail boom, Figure 3.

Referring to Figure 1, initial conditions in terms of drop height, drop attitude and pilot behavior are given in input to the multi-body simulation: the helicopter is considered as a rigid body interacting with the land through shock absorbers and tires, whose mass and vertical deformations are considered. Displacements and rotations at a representative point near the rear fuselage are exported from the multi body and given as a time-dependent constrain to the FE model. In this model the law of motion obtained by multibody is given to a constrained section, assumed as rigid. This approach is considered adequate as may be found in [11], in particular if the zone investigated is not too near to the time-dependent constrain zone. Notice that, as our aim is to evaluate what happens when loads exceed design values, drop speeds were chosen considering the limit drop test impact speed identified by the technical standard.

2.1   Multibody analysis

Multibody model is developed in Matlab Simulink using SimMechanics package. A top-level schematization of the problem can be found in Figure 2: the helicopter body is linked to the rotor, controlled by a block elaborating the motion signal trough a pilot simulation. The bottom of the helicopter is connected to a deformable model of the wheels by the shock absorbers. Those are implemented as embedded functions controlled by relative displacement and speed, outputting a force over tire or helicopter body mass. A particular viscoelastic law is considered, with classical polytrophic compression and velocity-squared damping equations. The shock absorber force is considered composed by the sum of elastic, viscous and
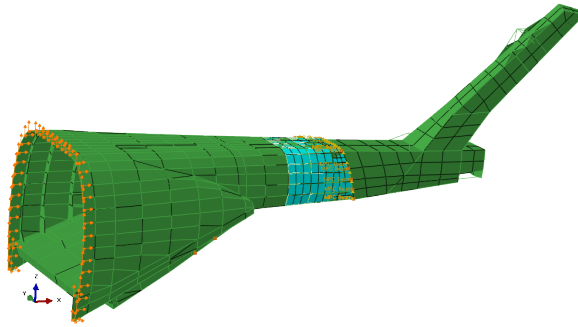
Figure 3 – *Mesh and applied boundary conditions and constrains between various helicopter tail boom parts.*
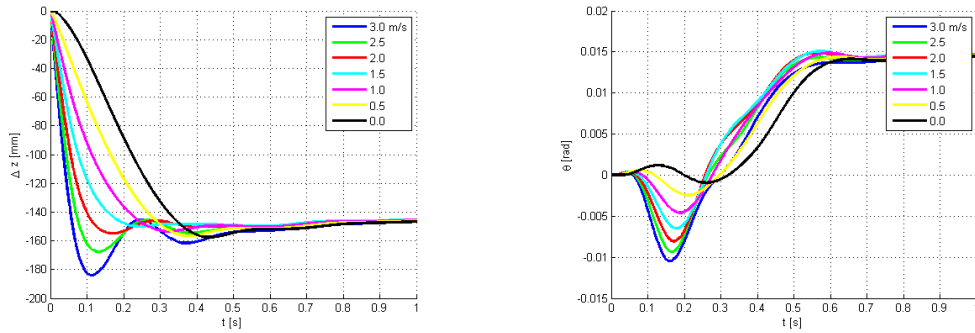
Figure 4 – *Vertical displacement at the reference point and pitch angle during landing*

friction components F_e, F_v and F_f:

$$
\begin{aligned}
F_e &= A_s p_{s0} \left(\frac{V_{s0}}{V_{s0}C_i - A_s s} \right)^{\gamma_s} \\
F_v &= \frac{1}{2}\rho A_h^3 \frac{|\dot{s}|\dot{s}}{A_0^2 C_d^2} \\
F_f &= \mu \tanh\left(\frac{\dot{s}}{\dot{s}_{ref}} \right) F_e
\end{aligned}
\tag{1}
$$

Where A_s, A_h, A_0 are the shock absorber gas, hydraulic and orifice area, ρ is the hydraulic fluid density, p_{s0} and V_{s0} the shock absorber gas reference pressure and volume, C_d the orifice discharge coefficient, and C_i the gas stroke ratio, s the stroke, γ_s the polytrophic exponent and μ is the friction coefficient.

The sum results in the total reaction force F_{tot}, considering the appropriate sign, accounting speed and displacement direction, of each component:

$$
F_{tot} = F_e + F_v + F_f
\tag{2}
$$

Regarding wheels, many models were developed for studying tire deformation during ground interaction. See for example the work in [12], [13]. Here the GRAAL

model, developed at Politecnico of Milan for landing impact analysis is used (see [14]). This considers the vertical force F_z using a polytrophic compression based on the intersection volume of a torus with the ground:

$$
\begin{aligned}
F_z &= A_t p_t \left(1 + \tanh \left(\frac{\dot{l}}{\dot{l}_{ref}} \right) \right) \\
p_t &= p_{t0} \left(\frac{V_{t0}}{V_{t0} - A_t l/2} \right)^{\gamma_t} \\
A_t &= 3.7ab \frac{l}{R_t}
\end{aligned}
\tag{3}
$$

Where A_t is the tire footprint area, p_t and p_{t0} are tire internal pressure and internal reference pressure, V_{t0} the tire reference volume, l the tire vertical deflection, a and b the elliptic footprint axes, γ_t the tire polytrophic exponent and R_t the tire radius.

For further details see [15]. Similar approaches are perhaps found in [16] and [17], where also the motion of the surface is considered, although the considered motion is not due to landing but to shipboard helicopter maneuvers.

Longitudinal and lateral forces were considered unimportant at this early stage: the simulation will in fact initially only account for a drop from different heights in proper attitude of the helicopter where the contemporary impact of the three wheels is achieved.

Some of the results obtained with multy-body model are reported in Figure 4, for various vertical speeds of the center of mass at the impact instant. Those were chosen near the value of $2\ m/s$, obtained starting from the drop test height considered by the technical standard [11], that should be considered as design speed. Every landing exceeding this condition should be considered as harsh.

In particular, displacements and inclination angle at the reference point considered are reported. The pitch angle remains into a limited range, this because the initial landing attitude considered while the vertical displacement shows a proper damped behavior till the speed remains bounded near the design value.

2.2   FE model

Global FE model of the tail boom was made of shell for skin and beam elements for stringers. Tail drive shaft system was assimilated to concentrated masses constrained to the tail using beams (refer to Figure 3 and Figure 1). Notice as actually the tail boom is composed of three main parts: the rear fuselage, the hatch (in aluminum) and the properly called tail, in carbon fiber, linked together using proper MPC constraints and contact.

As found in [9], [8], [6], [7] and [5], the usage of an explicit analysis is a consolidated way to explore structure deformation during landing. The movement of the tail was imposed writing, using Python scripts, a time-dependent boundary condition for a set of points of the FE model (constrained section in Figure 1). This section is forced to perform only rigid motions, obtained exploiting the data from multy-body simulation.

In Figure 3 the used mesh is reported: the zone near the interface of the rear fuselage and the tail was found in preliminary analyses more stressed. For this reason a refined mesh was used in this zone.
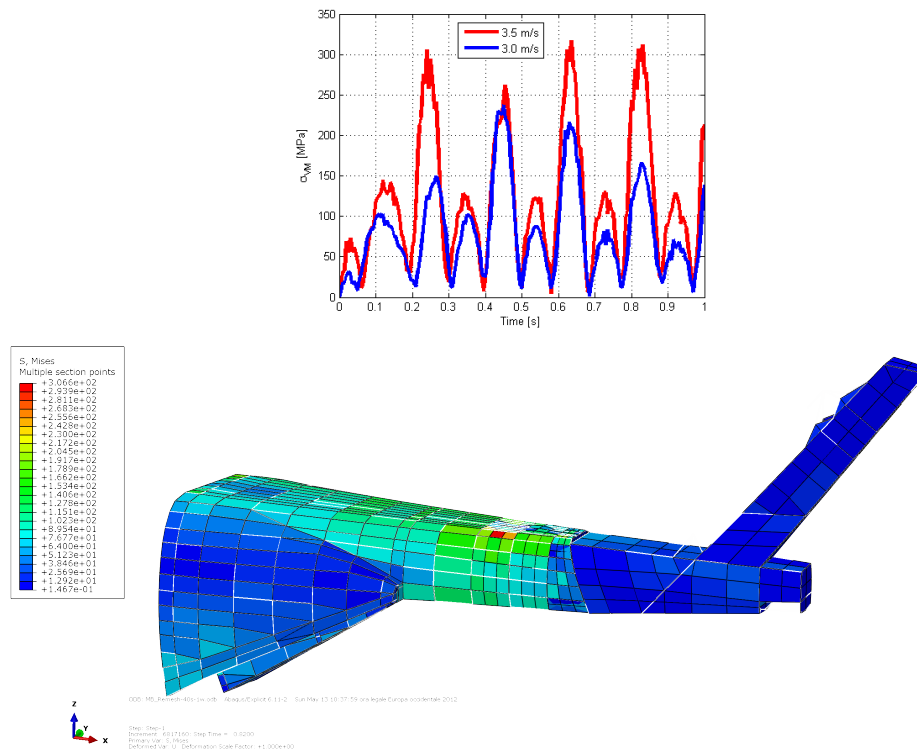
Figure 5 – *Stress distribution and history in the critical element.*

3   Results

FE model results are reported in Figure 5 in terms of stress spatial distribution and time law for the most dangerous element, according to Von Mises Criteria. Notice the asymmetry in the stress distribution due to the geometry of the helicopter and consequent mass distribution. In particular this is generating a horizontal motion, as is shown in Figure 6. A critical zone may be identified near the maximum stressed (see red zone in Figure 5, up). The maximum stress reached is near 300 MPa, for the maximum drop speed considered. The elastic limit of the aluminum used for the considered structure is near to 350 MPa (thus not reached during analysis). Nevertheless, the actual value is considerable: because the used FE modelization lacks of details that may ingenerate some stress concentration, is realistic to expect some damage in those high stressed zones. In particular a detailed submodel of the critical zone identified should be made to quantify and locate precisely the damage, if present.

The existence of a critical zone inside the structure is a good premise to the exploitation of results into a SHM scenario: some deformation sensors applied in this zone may guarantee a satisfactory probability of detection of the damage without the great costs necessary to monitor the whole fuselage.
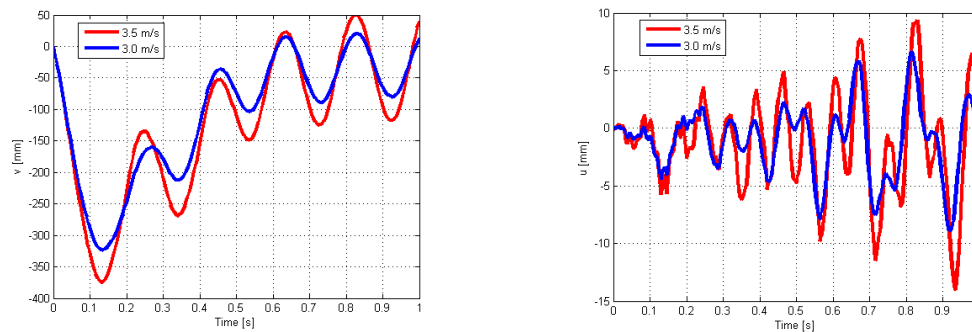
Figure 6 – *Vertical (left) and horizontal (right) displacements in function of time of the center of the back section of the tail.*

4 Conclusion

In this paper a mixed methodology allowing to investigate the damage due to harsh landing events of helicopters in case of rolling gear was presented. Results show that in those events inelastic deformations may occur into the fuselage and permit to identify a critical area where this phenomenon may occur, enabling the possibility to explore some SHM applications.

Further research should first consider a submodel evaluating the entity of damage, considering for example the actual shape of stringers and their joint with the skin by rivets, whose shape is typically capable of generating some stress concentration ([18]).

Second, in a damage tolerant approach the possibility to fly of the damaged helicopter should be investigated. The capability to sustain fly loads and subsequent landing loads should be evaluated. These aspects are strongly important in the evaluations necessary for a CBM approach: the possibility to fly with damaged structures should be quantified in terms of time to fail and safety. The data obtained may be exploited evaluating maintenance necessity after a harsh landing.

References

[1] B. Ferrier and T. Manning. Simulation and testing of the landing period designator (lpd) helicopter recovery aid. *Naval Engineers Journal*, pages 189–205, 1998.

[2] E. Suhir. Helicopter landing ship: Undercarriage strength and the role of the human factor. *Journal of Offshore Mechanics and Arctic Engineering*, 132:011603–011608, 2010.

[3] Tumer Mehr W. Chen and C. Hoyle. On quantifyng cost-benefit of ishm in aerospace systems. *IEEE Aerospace Conference*, 6:1–7, 2007.

[4] C. Boller and M. Buderath. Fatigue in aerostructures- where structural health monitoring can contribute to a complex subject. *Phil. Trans. R. Soc.*, 365:561–587, 2007.

[5] C.-H.Tho C. E. Sparks A.K. Sareen M. R. Smith C. Johnson. Efficient helicopter skid landing gear dynamic drop simulation using lsdyna. *Journal of the American Helicopter Society*, pages 483–492, 2004.

[6] K. Shorotri D. Schrage. Composite skid landing gear design feasibility. *Journal of the American Helicopter Society*, 54:42204–42004–13, 2009.

[7] K. Shorotri D. Schrage. Composite skid landing gear performance and laminate tailoring for reduced load factor under limit loads. *Journal of the American Helicopter Society*, 54:42205–42005–13, 2009.

[8] Y. T. Fuchs and K.E. Jackson. Vertical drop testing and analysis of the wasp helicopter skid gear. *Journal of the American Helicopter Society*, 56:12005–12005–10, 2011.

[9] O. T. Sagi D. Maynard and E. Enikov. Capacitive transducer for condition based maintenance after harsh landing events. *AUTOTESTCON, IEEE*, 2011.

[10] W.G. Luber E. Dill K. Kainz. Dynamic landing loads on combat aircraft with external stores using finite element models. *2007 IMAC-XXV*.

[11] European Aviation Safety Agency. Certification specifications for large rotorcraft cs-29, 2007.

[12] *Frictional and retarding forces on aircraft tyres. In ESDU, volume 5 of Performance*. ESDU, 1971.

[13] H.Sakai. Theoretical and experimental studies on the dynamic proprerties of tyres, part 3: Calculation of the six components of force and moment of a tyre. *International Journal of Vehicle Design*, 2:335–372, 1981.

[14] G. Ghiringhelli and M. Boschetto. Design landing loads evaluation by dynamic simulation of flexible aircraft. *AGARD CP-484 Landing Gear Design Loads*, 1990.

[15] S. Gualdi P. Masarati M. Morandini and G.L. Ghiringhelli. A multibody approach to the analysis of helicopter-terrain interaction. *European Rotorcraft Forum*, pages 72.1–12, 2002.

[16] D. R. Linn and R. G. Langlois. Development and experimental validation of a shipboard helicotper on-deck maneuvering simulation. *Journal of Aircraft*, 43:895–906, 2006.

[17] Z. H. Zhu M. LaRosa and J. Ma. Fatigue life estimation of helicopter landing probe based on dynamic simulation. *Journal of Aircraft*, 46:1533–1543, 2009.

[18] GS. Wang. Analysing the onset of multiple site damage at mechanical joints. *Int J Fract*, 2000.

Structural integrity assessment
for a component of the bucket-wheel excavator

Anghel Cernescu[1], Liviu Marsavina[2], Ion Dumitru[3]

[1]*Politehnica University of Timisoara,* *anghelcernescu@yahoo.com*

[2] *Politehnica University of Timisoara,* *lmarsavina@yahoo.com*

[3]*Politehnica University of Timisoara,* *dion@clicknet.ro*

Abstract. This paper presents a methodology for assessing the structural integrity of a tie member from a bucket-wheel excavator, ESRC 470 model, which were in operation for about 20 years. The tie member is made of S355J2N structural steel. Following the period of operation, the occurrence of microcracks which can propagate by fatigue is almost inevitable. It is therefore necessary to analyze the structural integrity and the remaining life of the component analyzed. In principle, the assessment methodology is based on three steps: 1. The evaluation of mechanical properties of the material component. 2. A FEM analysis using FRANC 3D software package to estimate the evolution of the stress intensity factor based on crack length and applied stress. 3. Risk factor estimation and remaining fatigue life predictions based on FAD diagram and Fatigue Damage Tolerance concept. Following the evaluation procedure were made predictions of failure risk factor and remaining fatigue life function of crack length and variable stress range, for a high level of confidence. As results of this analysis was implemented a program for verification and inspection of the tie member for the loading state and development of small cracks during operation.

1   Introduction

Safely operation of high capacity excavators used for extraction of lignite from the surface quarries is a very important issue regarding the rhythmic supply of the thermal power plants with coal.

Special conditions in which works like equipments require a series of controls and periodic inspections to assess the damage state, especially for those parts subjected to high loadings in the presence of additional shocks and the environment corrosive action. Operation for a long time in overloading mode associated with breach of conditions related to periodic review of load and displacement limiters have led to a failure in which was involved a giant bucket wheel excavator, ESRC 470, fig. 1.

The expert opinion on this excavator concluded that the element which gave up under the conditions of brittle fracture was one of the central tie-rods that support the bucket ladder on which is mounted the bucket wheel boom head. The breaking of the tie-rod, which caused the failure of the entire excavator, was determined by the presence of undetected cracks after non-destructive controls and which were extended up to achieve a critical length.

Based on above was initiated a program to verify all of the metallic constructions of tie-rods which are installed in a similar type ESRC 470 excavators. The paper presents some results of this study. These were related primarily to the analysis of material behavior at static and dynamic loadings in the absence or presence of fatigue cracks. In the second part of the paper is analyzed the possibility of tracing the FAD diagrams based on which it can be appreciated the damage level by using the nondestructive controls results. Finally it is

proposed a model for the assessment of tie-rod durability considering the fatigue crack propagation based on the variable amplitude loading spectra obtained for different functioning conditions of such equipment.

Figure 1 – *The collapse of a bucket wheel excavator ESRC 470*

2   Material and methods

2.1. The analysis of the bucket wheel boom tie rod from the ESRC 470 excavator

Bucket wheel excavators present the backbone of the open pit coal mining system. At present, Romania has in operation a large number of bucket wheel excavators, only in the mining basin of Oltenia region are four types of excavators: BWE SRs 2000 – 4 pieces; BWE ERC 1400 – 60 pieces; BWE SRs 1300 – 8 pieces; BWE ESRC 470 – 28 pieces.

When are in operating mode, they are exposed to a significantly strong effect of dynamic loads, which are furthermore stochastic. Continuous exploitation in severe operating conditions enhances the possibility for the occurrence of fatigue cracks. Their propagation in the vital parts of the support structure, such as tie-rods (of the bucket wheel boom, counterweight arm and portal) and their supports can lead to catastrophic consequences.

The bucket wheel excavators types ESRC 470 have registered in operation many defects at almost all mechanisms. The studies presented in this paper refer to one of the vital elements of the support structure, namely the bucket wheel boom tie-rod. The tie-rods of bucket wheel boom are made of S355J2 + N and have two areas with high risk of fracture: the eye-plates and the welded connections of the tie-rod bodies and eye-plates, fig. 2. The results of non-destructive testing of the analyzed tie-rod showed that the density and arrangement of gas pores type flaws and the linear and isolated slag inclusions are within the limits of acceptability for a class B welded joint, according to [2] and [3]. Instead, on the edge of the hole from eye-plate was detected a scratch that initiated a crack, fig. 3. Because in this case there was no standardization rule to check the safety of the tie-rod, was imposed an analysis on the structural integrity.
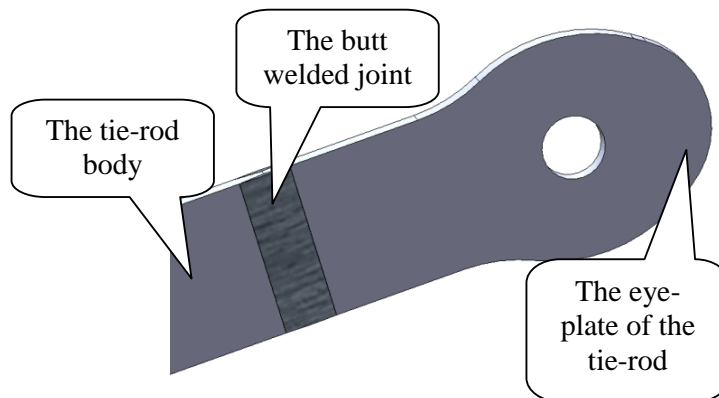
Figure 2 *- The bucket wheel boom tie-rod from BWE ESRC 470*
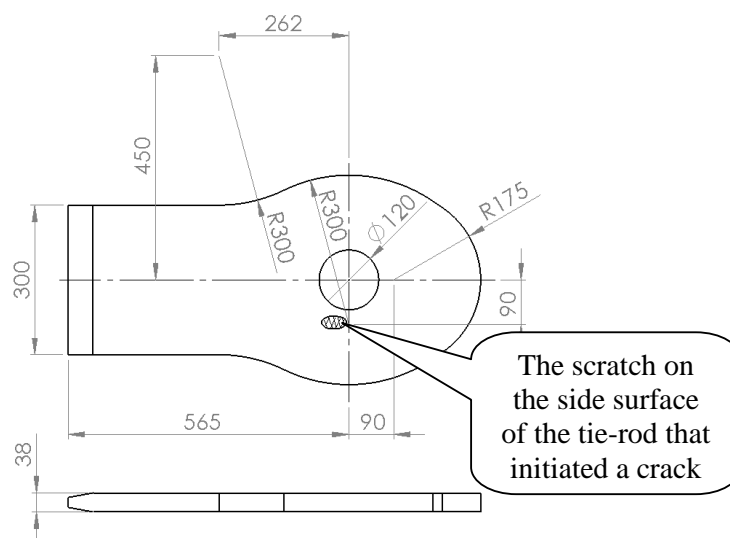
Figure 3 *– The eye-plate of the tie-rod and exfoliation that caused the crack initiation*

2.2. Mechanical properties of the tie-rod material

According to the technical documentation, the tie-rod material is S355J2+N, being usual steel for mechanical constructions. The J2 grade means that the minimum impact Charpy energy of 27 J corresponds to a temperature of -20 °C (T_{27J}), [4]. For the structural integrity analysis of the bucket wheel boom tie-rod, material samples were taken from a similar tie-rod to that analyzed, from an excavator removed from operation, in the same mining exploitation. The results of the experimental tests on samples steel were compared with standard SR EN 10025:2 – 2004 prescriptions for S355J2 steel, [5].

In table 1 are given the results of chemical analysis performed on the sampled material compared with the standard prescriptions. Tensile tests were performed on the sampled material, according to SR EN 10002-1 and the results are given in table 2.

Based on the results and considering that the material was sampled from a used tie-rod (about 12 years of operation), there is a tendency of strengthening of the material characterized by a slight increase in yield strength and a decrease in elongation.

For the evaluation of fracture toughness of the sampled material were used Chevron type specimens, fig. 5, according to ASTM E 1221-02, [6]. The main advantage of using the Chevron method is that it ensures the plain strain conditions in samples with small dimensions. The tests were performed at the temperature of 20 °C and the Chevron fracture toughness was $K_{IV} = 104.28$ MPa $\sqrt{m}$.

Table 1. The chemical composition of the material

Material	C [%]	Mn [%]	P [%]	S [%]	Si [%]	Others [%]
Sampled material	0.173	1.62	0.075	0.024	0.572	Al - 0.015
S355J2 SR EN 10025	0.12 – 0.2	0.59 – 1.6	0.003 – 0.04	0.003 – 0.04	0.5	Al – 0.025

Table 2. The mechanical properties of the bucket wheel boom tie-rod material

Material	Ultimate tensile strength [MPa]	Yield strength [MPa]	Elongation [%]
Sampled material	567	434	20
S355J2 SR EN 10025	470 - 630	355 - 480	24.5 - 32
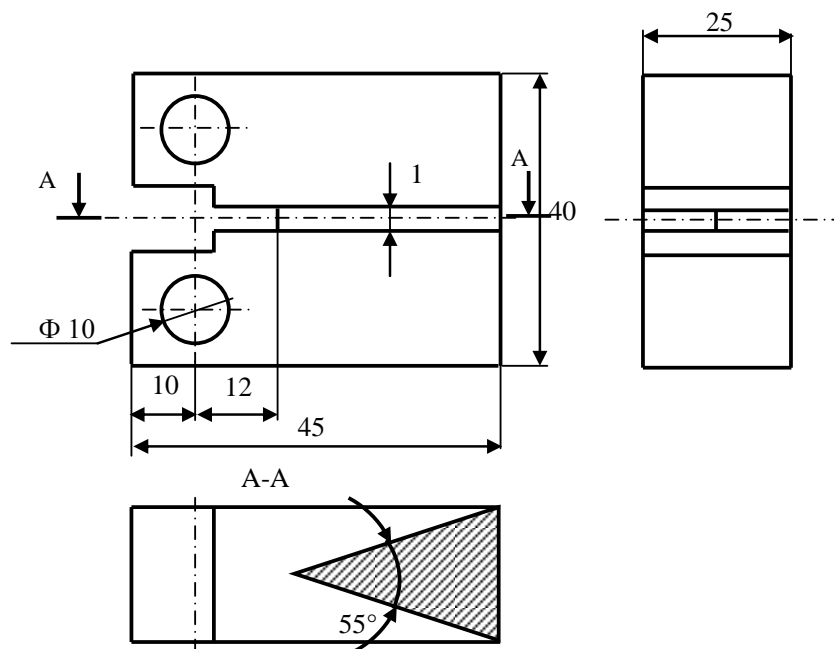
***Figure 4** - The Chevron type specimen for fracture toughness evaluation*

On the other hand, because the tie-rod is exposed to both static and dynamic loads, but also that works in a fairly wide temperature range, it was necessary to assess the material behavior in the presence of these factors. Therefore, the resilience tests have been performed on V-notch samples with cross-sectional dimensions of 10 x 10 mm, based on which was determined the Charpy impact energy at the temperature of 20 °C. The tests have been carried out according to SR EN ISO 148-1, [7] and the mean value of Charpy impact energy was 66.3 J.

By using the concept of Master Curve method, [8], described in FITNET FFS procedures, [9], was determined the fracture toughness transition curve depending the temperature that works the material:

$$K_{mat} = 20 + \{11 + 77 \cdot \exp[0.019(T - T_{27J} + 3°C)]\}\left(\frac{25}{B}\right)^{0.25} \cdot \left(\ln\frac{1}{1 - P_f}\right)^{0.25} \tag{1}$$

where: B is the crack front length or the specimen thickness and was considered to be 25 mm; T is the working temperature of the tie-rod in the range of -30 °C to +40 °C; T_{27J} is the temperature at which the Charpy energy is 27 J (in °C, and measured in a standard 10 x 10 mm Charpy V specimen) and P_f is the probability that the fracture toughness is lower than K_{mat}.

In figure 6 is given the material fracture toughness variation function of the working temperature for three different confidence levels:
-   $P_f = 0.05$ – the probability that the real fracture toughness of the material is lower than that calculated K_{mat} is only 5 %, meaning a 95 % of confidence level.
-   $P_f = 0.95$ – the probability that the real fracture toughness of the material is lower than the calculated K_{mat} is 95 %, meaning a 5 % of confidence level.
-   $P_f = 0.5$ is a medium probability.

For the analysis of the structural integrity of the tie-rod will be take into account the curve corresponding to the 95 % confidence level ($P_f = 0.05$). It also notice that the Chevron fracture toughness experimentally determined is located in the field considered for analysis (5 − 95 % confidence).
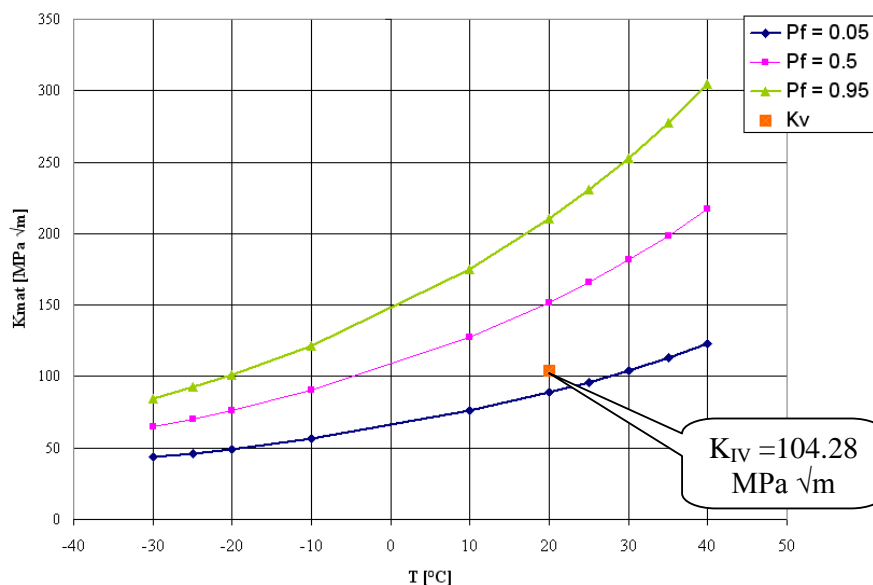
Figure 5 - The material fracture toughness function of the working temperature

2.3. The finite element analysis of the cracked eye-plate

Due to the scratch which appeared on the side surface of the tie-rod, close to the hole from eye-plate, on the edge of the hole was detected a crack with a quarter-ellipse shape. The crack had a length of 2.5 mm on the lateral surface of the eye-plate and about 1.8 mm on the inner surface of the hole. For this case was performed a FEM analysis using the software package FRANC 3D, [10]. Within this analysis was evaluated the stress and strain state from the eye-plate of the tie-rod, in the presence of crack, and also were evaluated the stress intensity

factors on the crack front. The FEM analysis was performed for a loading corresponding to the maximum force of 555.66 kN, applied to the inner surface of the hole.
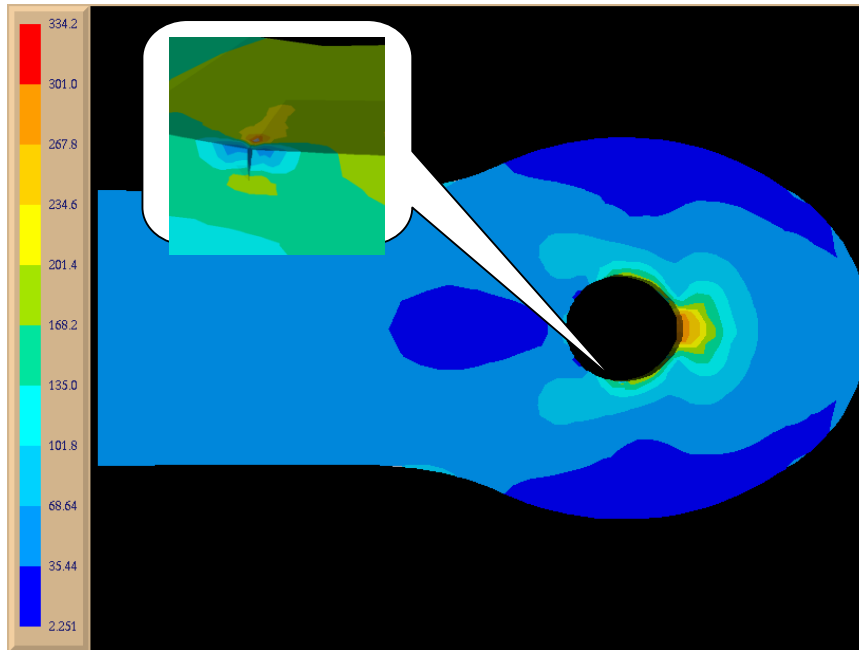
***Figure 5** – The von Mises stress distribution for initial crack*
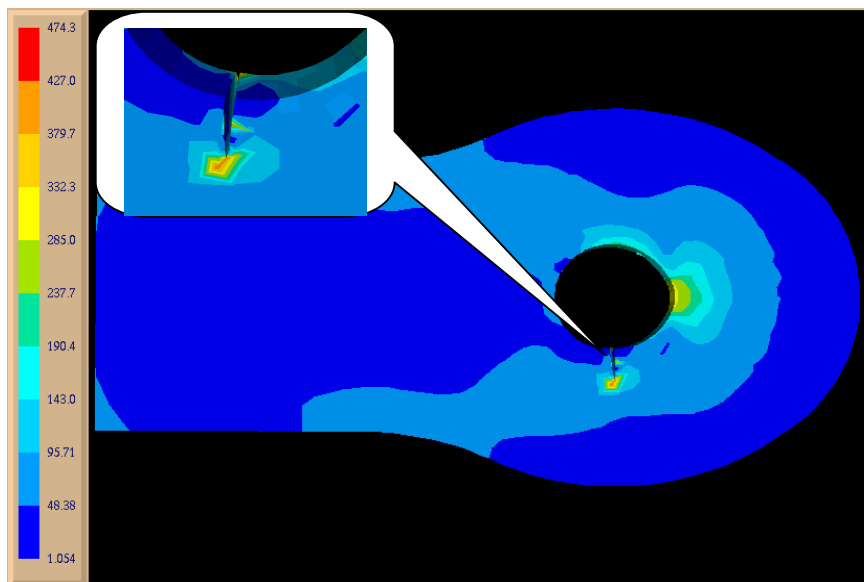

***Figure 6** – The von Mises stress distribution for the final stage of the crack*

3   Results and conclusions

On the FEM analysis, the initial crack was extended over several steps, until reaching the unstable state corresponding to maximum load, fig. 7. For each of extension step were determined the surface crack, the crack front length and respectively the stress intensity

factors on the crack front (K_I, K_{II} and K_{III}). The crack extension was based on a criterion that takes into account the maximum value of K_I.
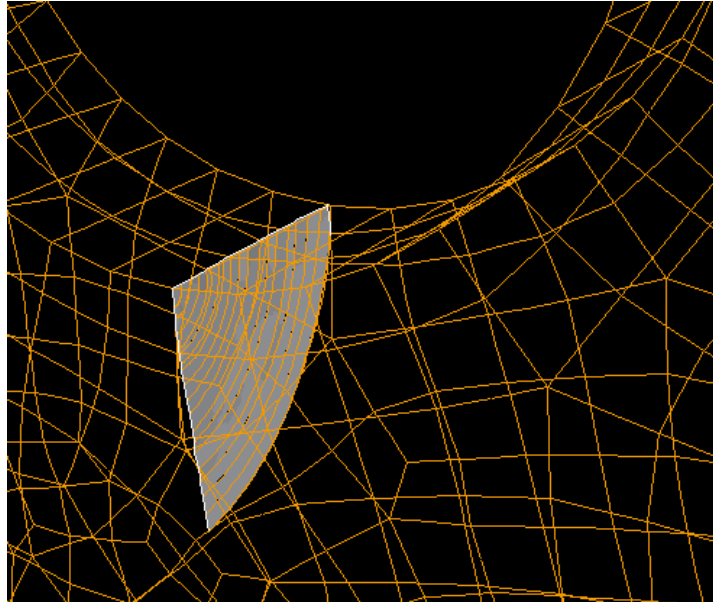
Figure 7 *– The initial crack extension*

In the figure 8 is given the variation of stress intensity factor, K_I, according to the root of crack surface, corresponding to maximum load. This chart indicates the critical crack size.
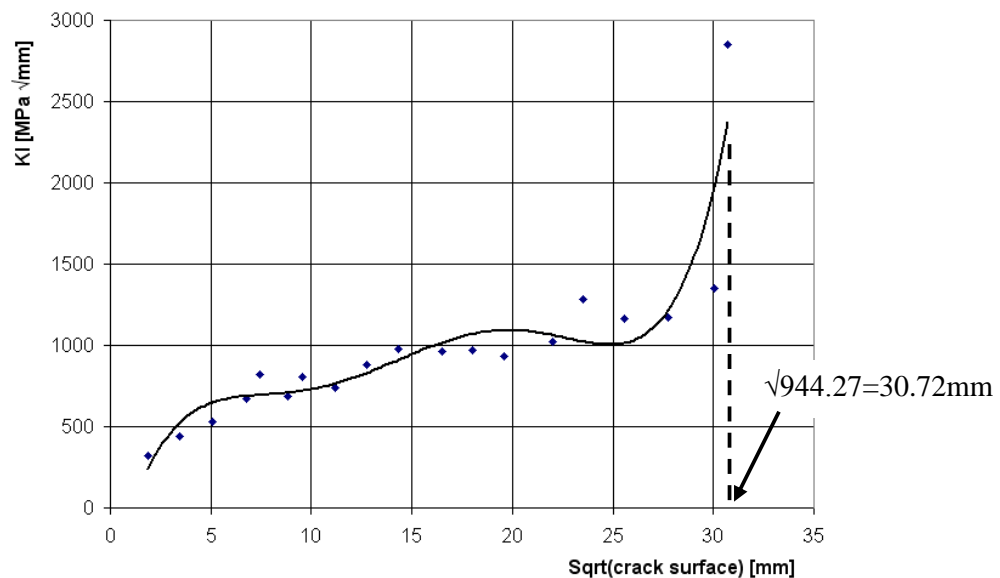
Figure 8 - *The variation of stress intensity factor K_I function of root of crack surface*

Assuming that K_I is dominant in crack extension and applying the FAD concept (Failure Assessment Diagram), was made an analysis of the tie-rod eye-plate in the conditions of a crack with size: $\sqrt{(2.5 \times 1.8)} = 1.876$ mm. On the basis of registrations conducted with strain gauges applied in the area of the hole from eye-plate, it was established the stress and strain state of the tie-rod member due to the weight that it supports and respectively, during excavation. Thus were established the limits of loading: $\sigma_{min} = 87.8$ MPa and $\sigma_{max} = 176$ MPa.

For materials which display or may be expected to display a lower yield plateau the FAD diagram is defined by the following relation, [11]:

$$K_r = S_r \left[\frac{8}{\pi^2} \cdot \ln \sec \left(\frac{\pi}{2} \cdot S_r \right) \right]^{-0.5} , \text{ for } S_r \leq 1 \tag{2}$$

where $K_r = K_I/K_{mat}$ and $S_r = \sigma_{appl}/\sigma_p$ (σ_{appl} – the value of applied stress, σ_p – the proof stress)

$$\sigma_p = \frac{YS + UTS}{2}$$

In the figure 9 is shown the FAD diagram of the structure and the two points corresponding to minimum and maximum applied stress.
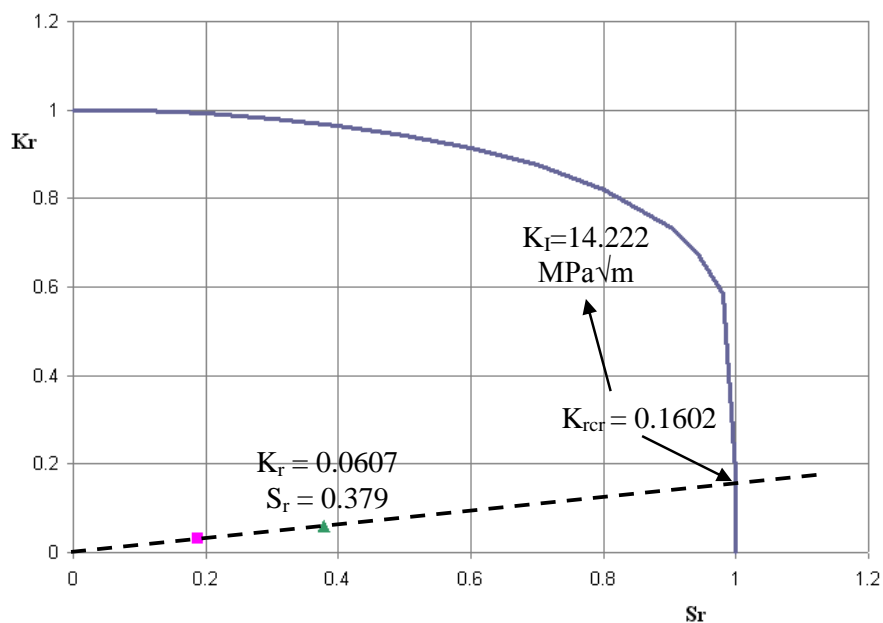
Figure 9 *– The FAD diagram of the analyzed tie-rod eye-plate (K_{mat} = 88.77 MPa√m – 20 °C)*

As regards the loading level related to the initial crack size, the analysis structure presents a good safety degree, pointed based on a safety factor, $c_f = K_{rcr}/K_r = 2.63$. The problem rises further, is related to the time when the structure reaches the critical state of instability, in the current conditions. On the FEM analysis, Franc3D software allows a calculation of a durability based on a defined loading spectrum and knowing the propagation constants. The loading spectrum was defined based on strain gauge records, fig. 10, and the propagation constants were determined based on experimental determinations on plate samples with central hole, presented in references [12] and [13]: C = 4.24718·10⁻¹⁴, n = 3.19125 (for R = 0); C = 1.52338·10⁻¹⁴, n = 3.41902 (for R = 0.5) and C = 0.87784·10⁻¹³, n = 2.886 (for R = -1). Therefore, by repeating the loading sequence in figure 10, was determined the number of cycles until the initial crack reaches the critical size. In the figure 11 is shown the curve between the crack size and number of cycles.
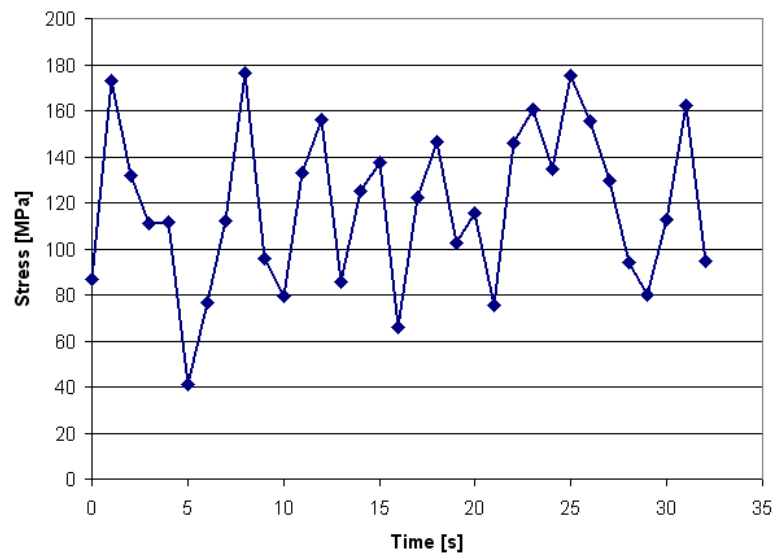
Figure 10 *– Loading sequence during an excavation*
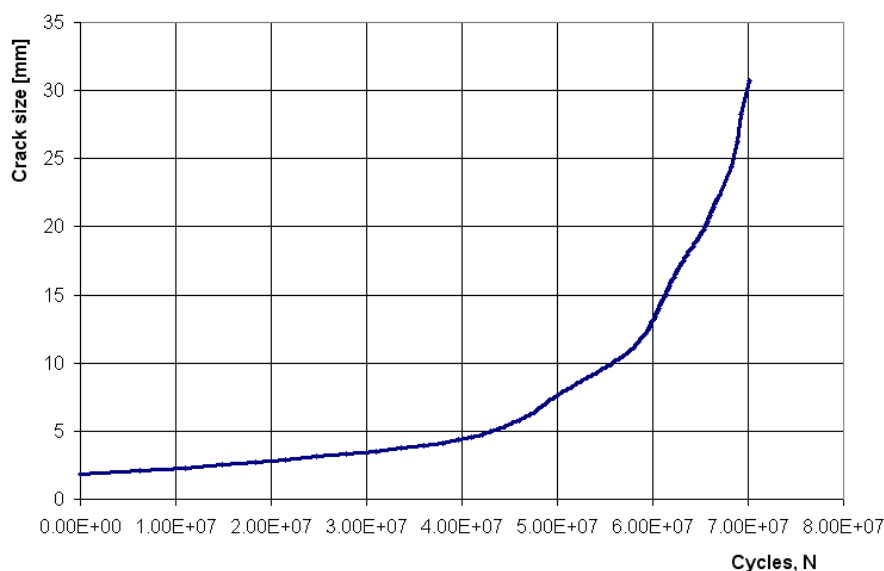
Figure 11 *– The curve of variation between the crack size and number of cycles*

As can be seen in figure 11, the instability of the eye-plate is reached after about 71 million cycles. The loading sequence from figure 10 is repeated during an excavation of about 500 times. Based on a calculation of the technological flow of excavation was determined a total number of excavations per year of about 7850000. Reporting the total number of cycles to the total number of excavation per year results in a remaining life of about 9 years.

Based on this evaluation, in the analyzed case were set inspection intervals as follows: in the first three years after assessment were set three inspections at intervals of a year, in the next two years were conducted four inspections at every 6 months and in the sixth year after evaluation, was decided to replace the tie-rod because it becomes more difficult to operate with the excavator.

This work is a part of a complex system of assessment and rehabilitation of the bucket wheel excavators from Romania. The process of assessment presented enroll entirely in the line of

assessment methodologies at European and worldwide level (SINTAP, FITNET FFS, R5, etc.)

Acknowledgements

References

1. Dr. Miodrag, A. Arsic - *Methodological approach to integrity assessment and determination of remaining fatigue life for welded structures of the bucket-wheel excavators*, International Conference "Structural integrity of welded structures", ISIM Timisoara, 2011;
2. EN ISO 5817 - *Welding – fusion – welded joints in steel, nickel, titanium and their alloys (beam welding excluded) – quality levels for imperfection*. EUROPEAN COMMITTEE FOR STANDARDIZACION, 2007;
3. EN 1714./prA. *Non destructive examination of welds – ultrasonic examination of welded joints*. EUROPEAN COMMITTEE STANDARDIZACION, 1997/ 2001;
4. SR EN 10027-1 – *Designation systems for steels – Part 1: Steels names*, European Standard, 2007;
5. EN 10025-2 – *Hot rolled products of structural steels – Part 2: Technical delivery conditions for non-alloy structural steels*, European Standard, 2004;
6. ASTM E 1221-02 – *Determining Plane-Strain (Chevron-Notch) Fracture Toughness of metallic materials*;
7. SR EN ISO 148-1 – *Metallic materials – Charpy pendulum impact test – Part 1: Test method*, 2011;
8. *Master Curve approach to monitor fracture toughness of reactor pressure vessels in nuclear power plants*, IAEA-TECDOC, 2009;
9. M. Kocak, S. Webster, J. Janosch et al - *FITNET FFS – Procedure – Fracture, Fatigue, Creep, Corrosion*, vol. I, 2008;
10. Franc3D - http://www.cfg.cornell.edu/software/franc3d_osm.htm;
11. T.L. Anderson – *Fracture Mechanics – Fundamentals and applications*, second edition, Department of Mechanical Engineering, Texas A&M University, College Station, Texas, CRC Press, 1995;
12. J.I. Hanel – *Schwingfestigteit und Ribfortschreitung von eigenspannungsbehafteten Ribstaben an St52 unter Eihstufenbelastung*, Darmstadt, 1972;
13. H. Saal – *Der Einflub von Formshal und Spannungsverhaltnis auf die Zeit und Dauerfestigkesten und Ribfortschreitung bei Flachstaben aus St52*, Darmstadt, 1972;
14. T. Babeu, I. Dumitru, L.Marsavina et al. – Analiza si incercari de rezistenta pentru evaluarea duratei de viata a utilajelor grele, Mirton publishing, Timisoara, 1999;
15. L. Marsavina – *Metode numerice in calculul parametrilor din Mecanica Ruperii* – PhD thesis, 1998;
16. F. Gutierez-Solana, S. Cicero - *FITNET FFS procedure: A unified European procedure for structural integrity assessment*, Engineering Failure Analysis, 16(2009), 559-577.

Turbomachines blades integrity and seal materials interactions - Dynamic experimental analyses.

R. Mandard[1,2], S. Baïz[1,2,3], J.-F. Witz[2] , X. Boidin[1,2], Y. Desplanques[1,2],

J. Fabis[3], R. Ortiz[3], E. Deletombe[3]

[1]Ecole Centrale de Lille, Cité Scientifique, 59650 Villeneuve d'Ascq (France),
romain.mandard@centraliens-lille.org

[2]Laboratoire de Mécanique de Lille (LML), UMR CNRS 8107,
Cité Scientifique, 59650 Villeneuve d'Ascq (France)

[3]ONERA, The French Aerospace Lab, Bd Paul Painlevé, 5, 59000 Lille (France)

Abstract Abradable seals are used in jet engines to minimize clearance between rotor blade tips and casing, and hence optimize the compression efficiency. Blade-seal interferences occur during engine operation, which may lead to severe blade-casing sealing deterioration or blade failure. In order to improve the mechanical design of the engine, the coupling between blade dynamics and seal material wear mechanisms has to be experimentally studied. A dedicated and original test rig has been developed to produce blade-seal interactions which are representative to jet engine compressor stage conditions. The reversed curvature configuration – compared to compressor conditions – allows an accurate instrumentation of the blade-seal interaction area (displacements, force and high-speed images). The analysis of the interaction between a titanium alloy (TA6V) blade and an AlSi-hBN abradable seal shows that blade dynamics correlates well with the macroscopic wear profile of the seal. A time-frequency decomposition is used to go further into dynamic measurement interpretation. This analysis shows the superposition of blade-seal interaction dynamics and test rig eigenmodes, which are known thanks to an experimental modal analysis.

1 Introduction

The gap between rotating blade tips and stationary casing in jet engines compressor stages affects directly the compression efficiency. An abradable seal is sprayed on the casing; then the seal grinding during the first engine revolutions set a minimal clearance between blades and casing. Reduced clearance, dynamical and thermo-mechanical loadings lead to blade-seal interferences [1]. The abradable casing liner is designed to be worn preferentially to the blade. Nevertheless severe abradable seal wear and blade cracks due to fatigue may occur [2]. Severe seal wear raises blade-casing clearance, leading to compressor surge and engine stall while blade failure is critical for the engine integrity. The main issue to establish models of these phenomena is the lack of knowledge of the blade-seal interaction forces and their connection with the abradable seal wear.

Industrial test rigs have been developed to characterize seals abradability and quantify blade and seal wear rates [3], [4] in representative conditions of engine operation (relative blade-seal velocity from 100 to 450 $m.s^{-1}$, seal temperature up to 1200°C and blade-seal interference from 2 to 2000 μm). A rotating blade rubs against a translating sample of abradable material. Laboratory devices are used to identify blade-seal interaction forces at relative speed up to 100 $m.s^{-1}$[5] and 270 $m.s^{-1}$ [6]. In this case, the blade-seal relative velocity is created by launching the abradable sample toward a rigid blade using a pneumatic air gun. The test rig developed by Padova [7] is also used to measure force components at the blade tip during the interaction between a rotating blade and a coated static casing. [6] and [7] implement the same method for forces identification which is based on the inversion of the frequency response function matrix of the force measurement device.

The original test rig presented in this paper has been developed in order to study the coupling between flexible blade dynamics and abradable seal wear mechanisms [8], accounting the following needs: being representative of compressor stage operation conditions, quantifying seal wear at macro and micro-scales, allowing the identification of the interaction forces and having a more easy access for the instrumentation of the blade and interaction zone compared to a classical rotating blade rig. In the third and fourth parts of the paper data analysis of reference testing are processed. The third part presents the correlation between time-varying measurements done during blade-seal interaction – representative of blade dynamics – and post-mortem wear profile of the abradable seal. The fourth part investigates a time-frequency decomposition of the measurements that is used to interpret their modal content.

2   Experimental approach

2.1   Test rig

The test rig has been developed to produce blade-seal interaction tests with the main following requirements for the blade-seal configuration (fig. 1):

- To be able to instrument and interpret the short-duration interactions;

- To be representative of the in-service conditions of first compressor stages in terms of blade-seal tangential relative speed.

To that end it has been designed with a simplified and flexible blade and in a reversed curvature configuration compared to the compressor condition. The tangential relative speed is created by spinning a cylinder (300 mm diam.) with abradable seal material coating (vs. rotating blade in the compressor). The interaction is set up by translating the flexible blade (fastened on a mobile unit moved with a piezoelectric actuator) toward the rotating seal. The cylinder width provides 10 testing tracks: after one experiment, the incursion cell can be moved along the x axis (fig. 1 b) to set up the blade in front of a virgin track to start another experiment. The reversed curvature configuration presents several advantages:

- The blade-seal interaction area is non-rotating. A rotating blade – as in compressor real case – is complex to instrument and actuate in order to create interactions with a static casing. Our test rig enable an easy observation of the blade dynamics and blade-seal interaction (part 2.2);

- The centrifugation makes it possible to evacuate the abradable debris and avoids the debris to be accumulated on the testing track. During the compressor operation this evacuation is done by the gas flow that carries the worn debris away.

One can object to this configuration the following points: first, contrary to the real case (abradable on the static casing), the abradable coating is here centrifuged and the effect on the radial stress in the seal is unknown. Second, the non-rotation of the blade does not take into account the centrifugal stiffening effect, which may modify the contact forces between the blade and the abradable seal [2].

Blade-seal interaction experiments presented in this paper were performed with a plasma-sprayed AlSi-hBN abradable coating (Metco 320NS). Flexible blade was designed taking into account material and dynamical features of blades used in compressor stages. The material used is a titanium alloy TA6V and the chosen geometry (60x10x2 mm) gives a first bending eigenfrequency at 450 Hz.
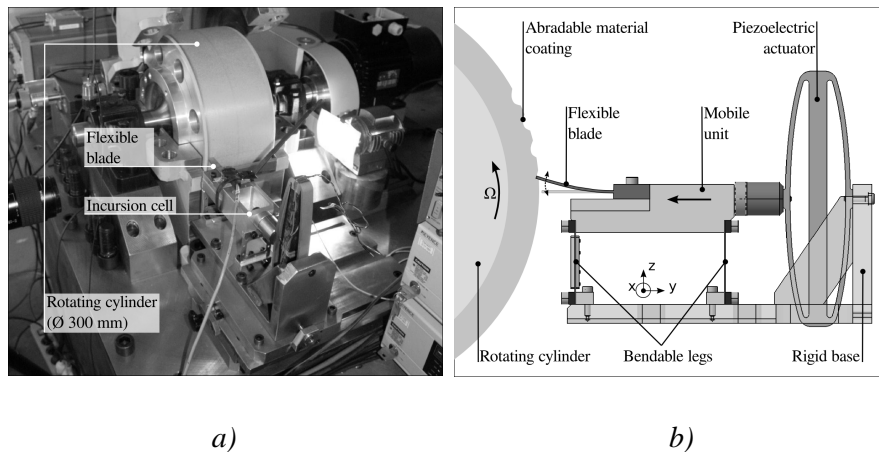
a)   b)

Figure 1 *– Test rig a) Picture b) Scheme of the incursion cell*

2.2 Experimental strategy

As previously demonstrated the main advantage of the reversed curvature configuration is that the blade-seal interaction zone is non-rotating and the incursion cell can be equipped with dynamic instrumentation (fig. 2a). The inlet parameters of the interaction test are the seal tangential speed V_s, (i.e. cylinder rotational speed Ω), the apparent incursion δ_y (i.e. mobile unit displacement, up to 500 μm) and apparent incursion speed V_y (i.e. mobile unit speed, up to 50 mm.s^{-1}).

During an interaction test the global dynamic response of the incursion cell is measured in terms of apparent incursion δ_y, actuator force F_y, blade deflection D_z (close to the tip), blade deformation ε_{yy} (close to the end-restraint and measured on the upper side, let ε_{yy} be ε). A laterally placed high-speed camera captures blade-seal interaction at 4000 frames per second.

Raw data of a reference experiment are presented in fig. 2 b). The chosen inlet parameters are the following ones: $V_s = 19$ m.s^{-1}, $\delta_y = 200$ μm and $V_y = 40$ mm.s^{-1}. The blade-seal interaction has a 8.5 ms duration (within the dotted-lines frame).

In this paper, the proposed strategy consists in investigating the results of this reference experiment and aims for:

- Interpreting the raw signals that are apparently easily legible in the time domain (D_z and ε) and correlating theses signals with the video frames and a macroscopic analysis of the abradable seal wear;

- Interpreting more complex measurements – such as F_y – with an adequate analysis in the time-frequency domain. Despite the distance between the F_y measurement and the blade tip – where the contact forces are researched in order to characterize the rub – this signal is a significant information about the global interaction between the incursion cell and the abradable seal.
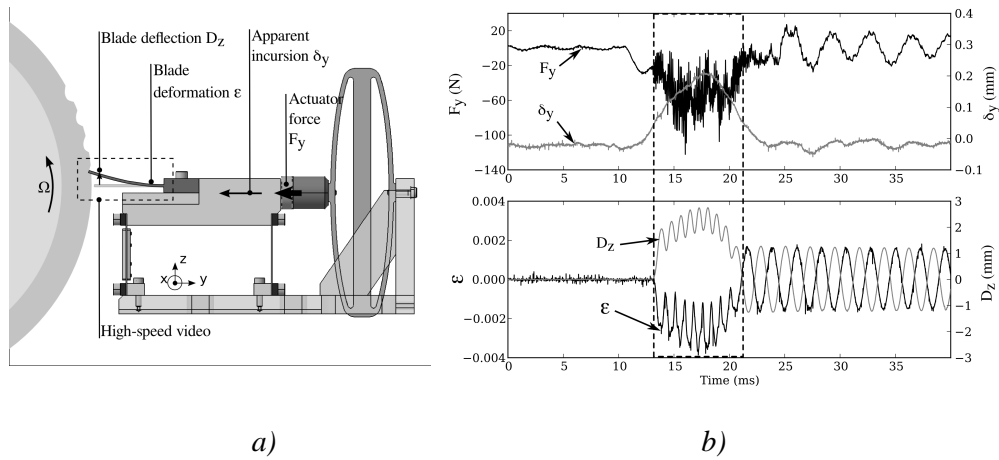
Figure 2 – Data acquisition during blade-seal interaction a) Localization on incursion cell b) Raw data vs time (blade-seal interaction within dotted lines)

3   Data analysis – Part I: time-space correlation of raw data

3.1   Macroscopic wear of the abradable track

After blade-seal interaction testing, the wear marks are visible for most of abradable tracks (fig. 3a). For the reference experiment the track is worn over a 60° sector, corresponding to the 8.5 ms interaction duration at 1200 rpm rotation speed (fig. 3b). It is possible to identify 9 wear marks with a simple visual inspection thanks to a texture modification of the abradable. A profile measurement has been carried out in order to evaluate the depth of the wear marks. For this measurement the cylinder is mounted and centered on a low-speed rotating spindle. A laser displacement sensor facing the middle of the track is used to record the track profile over the complete cylinder perimeter. Figure 3c shows the measured track profile (solid line) relative to the average profile of the complete track (dotted line). The maximal wear depth is about 50 μm. The maximum wear depth is obtained at the maximum apparent incursion $\delta_y = 200$ μm. Owing to the blade dynamics, the connection between δ_y and the abradable wear depth is not direct. In the literature the wear mechanisms of casing materials are often quantified by the prescribed incursion of the blade (i.e. apparent incursion) [7], which may be irrelevant considering the blade flexibility. In our case there is an absolutely need to process a post-mortem profile measurement which can be correlated to the blade dynamics.
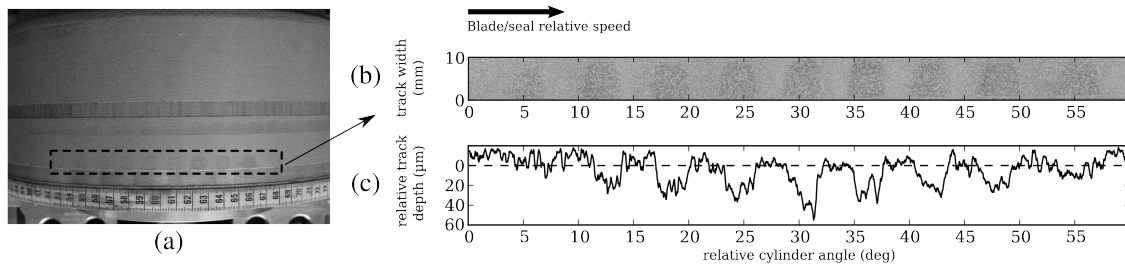
Figure 3 – a) Global view of the 10 tracks on the cylinder b) Reference experiment track wear (sector of interaction with the blade) c) Track wear profile

3.2 Correlation between wear and blade dynamics raw signals

According to the blade deflection D_z and deformation ε measurements (fig. 2) – which are in phase – the 8.5 ms interaction is a series of bounces – at 1200 Hz – of the blade on the abradable coating. Knowing the exact revolution speed of the cylinder during the interaction (thanks to an optical tachometer) it is possible to plot the blade deformation signal versus the covered rotation angle. Figure 4 presents the blade deformation and track profile plotted versus cylinder angle. For this analysis a manual shift-translation of the curves has been done considering observations made on the high-speed video: the blade wears the abradable coating out when the compression of upper side of the blade increases (i.e. when ε decreases). According to figure 4 this is an relevant interpretation: the angular intervals noted as 'W' corresponding to the track grooves match the intervals of negative slope of the ε curve.
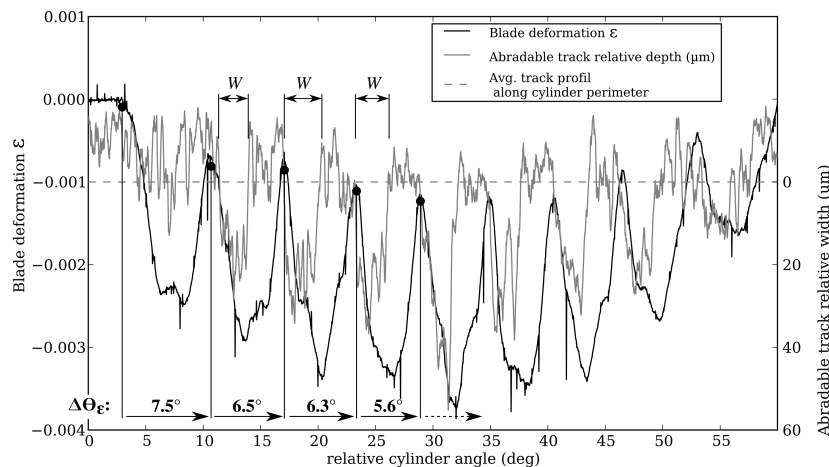

***Figure 4** – Blade deformation vs abradable track profile*

The high-speed video is also a source of information regarding the abradable track wear. 4000 frames per second at 1200 rpm provides a 1.8° cylinder rotation between two frames. A fine observation of the expelled abradable debris very close to the contact area makes it possible to distinguish when the blade bounces start. Figure 5 illustrates the series of the four first blade bounces of the experiment. *Frame 00* is the last frame before the interaction starts; no debris is visible at the blade tip. *Frame 01* corresponds to the first blade-seal contact: a small amount of abradable debris expelling is visible. During the contact the debris flow increases (*frame 02*) until the blade tip detaches from the abradable seal; the contact starts again *frame 05* (small debris flow is visible). The third contact starts between *frames 08* (no debris flow) and *09* (large debris flow). Fourth et fifth contacts start respectively *frames 12* and *15*. In this way one can calculate the cylinder rotation $\Delta\theta_{video}$ between two contact starts (i.e. during one blade bounce) – with a resolution of 0.9° – and compare it to the rotation $\Delta\theta_\varepsilon$ during one bounce measured on the deformation ε curve (fig. 4). The difference between the measured $\Delta\theta$'s is less than 0.5° cylinder rotation which is satisfactory considering the rotation speed Ω and the interaction duration.
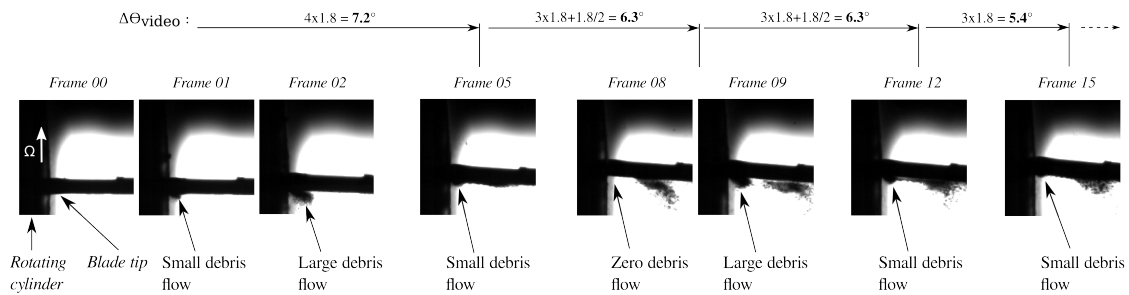
Figure 5 – *Blade bounces visualization on high-speed video frames*

4 Data analysis – Part II: decomposition in the time-frequency domain

4.1 Experimental modal analysis of the test rig incursion cell

During the interaction experiment a global dynamic response of the incursion cell was measured. In order to clearly understand the blade dynamics it becomes necessary to know the unavoidable contribution of the incursion cell (actuator, mobile unit) on the measured signals. An experimental modal analysis [9] of the incursion cell has been carried out to identify its vibration modes with a free condition at the blade tip. The structure was excited with an impulse hammer in the y and z directions (fig. 1b). The response of the structure was measured on 21 points on the blade using a laser velocity sensor and 21 points on the mobile unit using an accelerometer. After the frequency response function acquisition, the computation of the modes has been done with a dedicated software (LMS). The nature and frequencies of the incursion cell vibration modes in the blade tip free condition and in the [0-10 kHz] frequency band are presented table 1. Two low-frequency translation modes in the y axis T_y^1 and T_y^2 have been identified at 150 and 280 Hz and are the consequence of the flexibility of the actuator and of the two bendable legs that link the mobile unit to the rigid base. Two rotation modes R_z and R_y at 850 and 2200 Hz and a translation mode T_z at 1400 Hz characterize also the incursion cell dynamics.

Table 1 – *Experimental modes of the incursion cell*

Free condition at blade tip			
Mode	Nature	Axis	Frequency (Hz)
T_y^1	Translation	y	150
T_y^2	Translation	y	280
R_z	Rotation	z	850
T_z	Translation	z	1400
R_y	Rotation	y	2200

A supplementary modal analysis of the isolated blade with free and contact conditions at the tip has given its bending eigenmodes of which frequencies are shown table 2. In parallel to this theoretical and analytical modal analysis based on the Euler-Bernoulli [10] and Timoshenko [11] beam models has been achieved for validating a blade bending model that will be used in a coming work. Theoretical frequencies of the three first bending modes are shown table 2. They are in a good agreement with experiment. This complete modal analysis of the incursion cell gives a mode database that will be used to interpret in the frequency domain the measured signals during blade-seal interaction experiment.

Table 2 – Experimental and theoretical blade bending eigenfrequencies

	Free / Contact condition at blade tip		
Mode #	Experimental	Euler-Bernoulli beam model	Timoshenko beam model
$B^1_{free/contact}$	450 / 1935	447 / 1961	447 / 1953
$B^2_{free/contact}$	2795 / 6335	2802 / 6355	2787 / 6283
$B^3_{free/contact}$	7735 / 12130	7846 / 13259	7742 / 12974

### 4.2 Signal interpretation using time-frequency decomposition

In our study a time-frequency decomposition is needed for several reasons. The first one is the seeming superposition of modal contributions in recorded signals – following the example of the reference experiment force measurement F_y. The second one is the transient nature of the observed dynamics. Two methods have been investigated, the Short-Time Fourier Transform (STFT) and the Continuous Wavelet Transform (CWT). Both are used to plot a spectrogram of the signal, with the time on the abscissa, the frequency on the ordinate and the transform result amplitude represented with a color map. The principle of the STFT is the application of the Fast Fourier Transform (FFT) to a part of the signal centered at a time t. The width of the window that select the signal part must reach a compromise between time and frequency resolution [12]. The best compromise found for the studied signal for highlighting phenomenas is a 5 ms wide window. Figure 6a presents the SFTF of F_y with the classical plotting of the absolute value of the FFT.

The CWT is a reversible operation (vs non-reversible for the STFT) that projects the signal onto a base of complex and non-stationary functions (vs stationary for the STFT) called wavelets [13]. The resulting transformation decomposes the signal on scales which are fractional powers of two, instead of Fourier frequencies for the STFT. It is however convenient in our case to convert the scales into Fourier frequencies for two reasons: making possible the comparison with the STFT and enabling the identification of the incursion cell modes in the signal. The CWT has been computed using the tool kit of Torrence [13] with a Morlet wavelet (*p=6* as wavelet parameter) and plotting the real part of the transform (fig. 6c).

The first difference is the time resolution. The effect of the window width for the STFT is visible: the high frequency close to 8 kHz appears before the blade-seal interaction (fig. 6a). On the contrary the occurrence of this frequency for the CWT is much more time-resolved

(fig. 6c). Thanks to the fine time resolution of the CWT one can distinguish the positive and negative parts of the oscillation at a given frequency, for instance in the case of the main free vibration observed after the interaction. Note also that this low frequency – visible with a low amplitude on the raw signal – is detected before the interaction with the CWT but not with the STFT. One could imagine observing the same positive and negative parts of the oscillations using the STFT and plotting its real part (instead of the absolute value) to get a phase information (fig 6b). It makes unfortunately the time-frequency visualization less clear. The main disadvantage of the CWT plotted with a frequency ordinate axis is that the frequency resolution is lower than for the STFT. This is due to the scale-to-frequency transform which expands the spectrogram along the frequency axis. Note that the spectrogram color maps limits have been set to improve the visualization of modal content. Figure 7 shows a plot of the cross-section (in absolute value) of the figure 6 spectrograms at $t = 16\ ms$, what illustrates objectively the peaks localization and frequency resolution of the time-frequency transforms. The CWT is finally the adopted method for the time-frequency decomposition because of the time resolution, the amount of viewable dynamics content and the reversibility feature that will be use in a coming work of signal reconstruction. FFT of the complete signal is however used in parallel for its frequency resolution advantage – as shown figure 8.
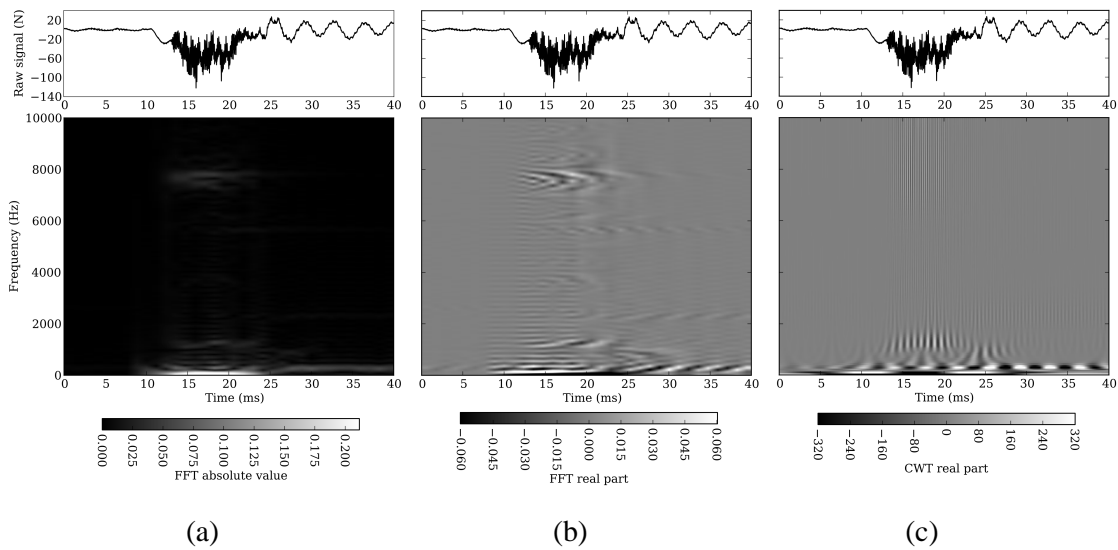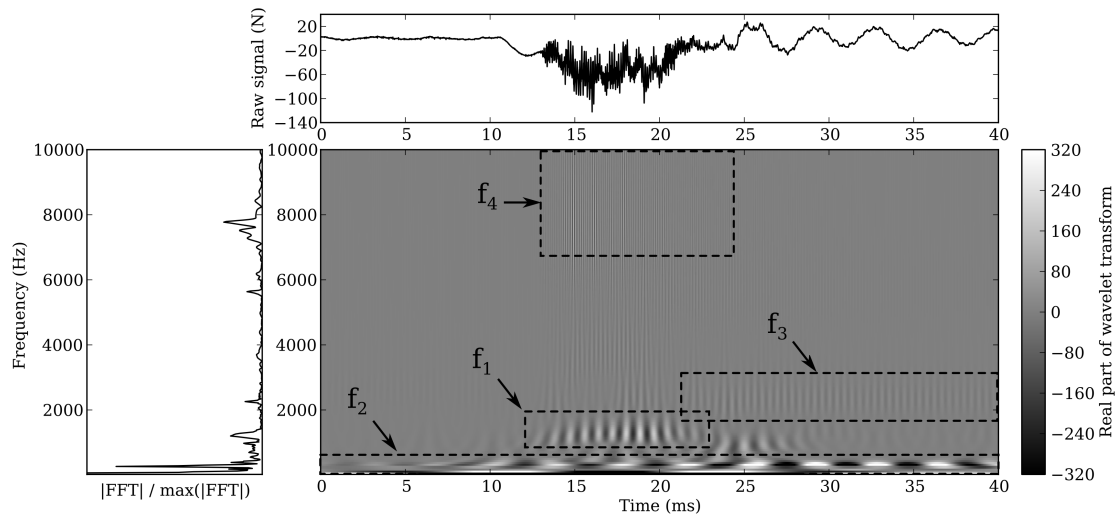

Figure 6 – *Spectrograms of F_y force measurement using a) STFT (absolute value) b) STFT (real part) c) CWT*
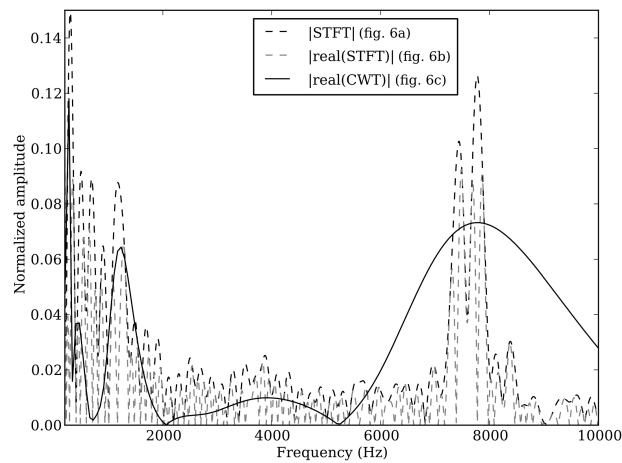
***Figure 7** – Cross-sections of fig. 6 spectrograms at t = 16 ms*

Figure 8 is used in order to identify the modal contents of the F_y force measurement. The main feature of the time-frequency decomposition is the $f_1 = 1200\ Hz$ frequency, which is the flexible blade bounce frequency linked to the macroscopic track wear profile. Despite that the F_y sensor location is distant (fig. 2a) from the blade-seal contact the measured signal contains a quantitative and time-localized information linked to the track wear. $f_2 = 300\ Hz$ and $f_3 = 2200$ are respectively the incursion cell modes T_y^2 and R_y (table 1). R_y is mainly activated after the interaction and may not have a significant influence of the measured force amplitude. On the other hand T_y^2 is detected before, during and after the interaction with a variable level of amplitude. This vibration is not a contribution of the blade-seal interaction – but a contribution of the incursion cell intrinsic dynamics – and may have a significant influence of the measured force amplitude. The fourth identified modal component is $f_4 = 7.8\ kHz$ which corresponds to the third bending mode of the blade with a free tip condition (B^3_{free}, see table 2). This mode is activated during the blade-seal interaction. In contrast to f_2 and f_3, f_4 is a modal component of the signal that is relevant in our framework – because it is representative of the blade and interaction dynamics. Note that the first and second bending modes B^1 are B^2 are not detected in the signal.

***Figure 8** – Spectrogram of F_y force measurement: identification of modal components*

5   Conclusion

Blade-seal dynamic interaction experiments have been achieved on an original test rig, specifically designed to allow an accurate instrumentation of the blade-seal interaction area. Data analysis (blade deformation, blade tip high-speed video, post-mortem wear measurement) of the reference experiment show that the blade dynamics can be directly connected to the abradable seal macroscopic wear. In this experiment, apparent incursion can not be considered as blade tip incursion since the blade interacts with the abradable seal by bouncing. During the experiment a force measurement is done along the apparent incursion direction: a time-frequency analysis is investigated since raw data are not explainable as such. By coupling a modal analysis of the rig incursion cell and blade and the time-frequency analysis one can identify the contributions of blade-seal interaction (bounces frequency), blade dynamics (bending modes) and intrinsic modal properties of the incursion cell. This analysis is a preliminary work that will be used for the interaction forces identification at the blade tip and the correlation with abradable seal micro- and macroscopic wear mechanisms. In parallel to that improvements on the test rig will be achieved in order to reach higher blade-seal tangential relative speed and perform experiments at compressor in-service temperature.

6   References

[1]   Giovannetti I., Bigi M., "*Clearance reduction and performance gain using abradable material in gas turbines*", ASME Conf. Proc. 2008, GT2008-50290, pp.555-563, 2008

[2]   Millecamps A., Brunel J.-F., "*Influence of thermal effects during blade-casing contact experiments*", ASME Conf. Proc. 2009, DETC2009-86842, pp.855-862, 2009

[3]   Dorfman M., Erning U., "*Gas turbines use 'abradable' coatings for clearance-control seals*", Sealing Technology, Vol. 2002, Num. 1, pp.7-8, 2002

[4]   Chupp R.E., Ghasripoor F., "*Applying abradable seals to industrial gas turbines*", GE Global Research Technical Report, 2002

[5]   Sutter G., Philippon S., "*Dynamic analysis of the interaction between an abradable material and a titanium alloy*", Wear, Vol. 261, pp.686-692, 2006

[6]   Cuny M., Philippon S., "*Etude expérimentale des interactions dynamiques aube/carter*", 20ème Congrès Français de Mécanique, 2011

[7]   Padova C., Dunn M.G., "*Casing treatment and Blade-Tip configuration effects on controlled gas turbine blade tip/shroud rubs at engine conditions*", Journal of Turbomachinery, Vol. 133, 011016 (12 pages), 2011

[8]   Baïz S, "*Etude experimentale du contact aube/abradable : Contribution à la caractérisation mécanique des matériaux abradables et de leur interaction dynamique sur banc rotatif avec une aube*", PhD Thesis, Ecole Centrale de Lille (France), 2011

[9]   Venizelos G., "*Vibrations des structures*", Ellipses, 2002

[10]   Le Tallec P., "*Introduction à la dynamique des structures*", Ellipses, 2002

[11]   Van Rensburg N.F.J., Van der Merwe A.J., "*Natural frequencies and modes of a Timoshenko beam*", Wave Motion, Vol. 44, pp.58-69, 2006

[12]   Gurley K., Kareem A., "*Applications of wavelet transforms in earthquake, wind and ocean engineering*", Engineering Structures, Vol. 21, pp.149-167, 1999

[13]   Torrence C., Compo G.P., "*A practical guide to wavelet analysis*", Bulletin of the American Meteorological Society, Vol. 79, pp.61-78, 1998

A novel test method for durability evaluation of an adhesively bonded joint between CFRP and CFRP sandwich components under surface loading

Stefan Ladisch[1], Martin Rinker[1], Benjamin Teich[2], Hélène Tchambo[3], Alexander Goldstein[1],

Matthias Petersilge[1], Ralf Schlimper[1] and Ralf Schäuble[1]

[1]*Fraunhofer Institute for Mechanics of Materials IWM*

Walter-Huelse-Strasse 1, 06120 Halle, Germany

*stefan.ladisch@iwmh.fraunhofer.de*

[2]*Airbus Operations GmbH, Stade, Germany*

[3]*Assystem GmbH, Bremen, Germany*

Abstract Due to the damage-free pre-treatment of the jointed components and the areal load distribution, adhesive bonding is an eminently suitable joining technology for composite materials. Adhesively bonded joints between fibre reinforced composite parts are commonly used, such as in wind turbine rotor blades or in the ship building and automotive industry. In consequence of the increasing number of Carbon Fibre Reinforced Polymer (CFRP) components, adhesively bonding becomes more and more relevant also for aircraft structures. This work deals with the durability evaluation of an adhesively bonded joint between a CFRP frame rib and a CFRP sandwich shell of an aircraft component under surface loading. For this purpose, a water pressured test rig introducing the surface load into the test component by an elastomeric membrane was designed and sized via numerical simulation of the membrane draping behaviour. Based on this calculation the needed water volume for the test was determined. Afterwards the components were tested under quasi-static and fatigue loading. During the tests thermography measurements as well as novel Structural Health Monitoring techniques (Comparative Vacuum Monitoring) were used to determine the damage initiation and propagation.

1 Introduction

Sandwich structures exhibit a high bending stiffness and strength to weight ratio and are particularly suited for use in structures sensitive to buckling. Sandwich structures are commonly used for lightweight secondary aircraft components and their suitability for use in primary aircraft structures is investigated more and more [1]. Within the German aeronautics research programme a novel primary aircraft sandwich structure was developed for the centre box of a vertical tail plain of a commercial aircraft. The major characteristics of the box structure are the lenticular CFRP/Foam core sandwich side panels joined to CFRP frame ribs [2]. A potential design approach for the joining is adhesively bonding. Within preliminary numerical studies based on global Finite Element Analysis of the aircraft the aerodynamic surface pressure load normal to the sandwich panel was figured out to cause the most critical peeling load case for the rib/sandwich joint. Considering this load case, a test method for the reliability evaluation of the bonded component under quasi-static and fatigue loading is presented in this paper.

Figure 1 shows the specimen design, which represents a 653 mm long half box section. The 1200 mm wide sandwich shell has a lenticular outer shape and a plane inner side. The sandwich is closed at the front and rear end. Near to the front and rear end the CFRP front and rear spars of the centre box are riveted to the monolithic ends of the sandwich panel. For the tested half box section, the spars are cut not in the middle plane of the box but 20 mm alongside, because the spar centre lines are used to fix the specimen to the test rig. The half frame rib is bonded to the plane inner side of the sandwich shell. The rib starts with a straight side behind the front spar and ends in front of the rear spar with a slope side. At the rear end the outer rib flange ranges through the rear spar up to the shell edge.
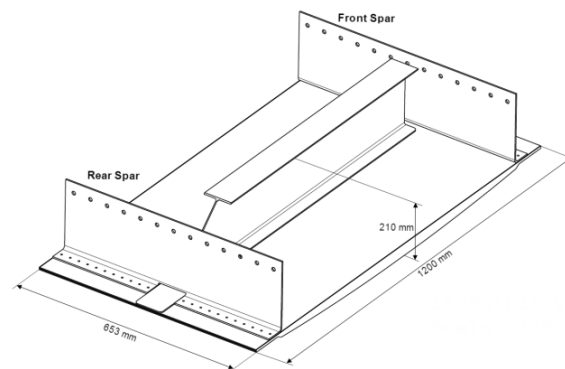
Figure 1 - *Specimen scheme of adhesive bonded rib to a curved sandwich panel with fixing*

The sandwich core consists of the closed cell PMI foam ROHACELL® 71RIST having a maximum thickness of 28.5 mm in the middle of the panel. The face sheets are composed of non-crimped carbon fibre fabrics consisting of three individual layers and have the overall stacking sequence $[(+45/0/-45)_s]_2$ (1.5 mm). The sandwich was manufactured by using open mould liquid composite moulding (LCM) technology at CTC GmbH Stade [3]. The CFRP spars and the rib are manufactured by pultrusion and have a stacking sequence of $[(90/-45/90/45/90/-45/0/45)_s]$ (4.0 mm) and $[(45/0/-45)_s]_2$ (3.0 mm). Epibond® 1590 A/B epoxy adhesive is used for the investigated bonding between rib and sandwich shell.

As already mentioned, the specimen is fixed to the test rig at the spar centre lines. The surface load has to be applied uniformly on the lenticular outer sandwich side. Water filled pressure cushions have been used effectively to apply lateral pressure loads on flat sandwich panels [4, 5]. In contrast to these investigations the loaded panel side of the investigated component is not flat but lenticular, making a uniformly contact behaviour more complicated. Thus, an alternative novel test rig was developed. A thin and flexible elastomeric membrane (EPDM) is spanned on a water tank with variable and controllable volume and pressure, shown in ***Figure 2***. The specimen itself is completely fixed to the test rig and not moved during testing. The uniform membrane contact is achieved already at low pressure loads, which are controlled directly by the pressure in the tank. The test rig has to resist at least 0.02 MPa and 0.03 MPa in the quasi-static test and 0.01 MPa during the fatigue test. These loads are driven by the centre box design loads and correspond to Limit Load (LL = 0.02 MPa) and Ultimate Load (UL = 0.03 MPa).

2   Test Rig – Design and Sizing
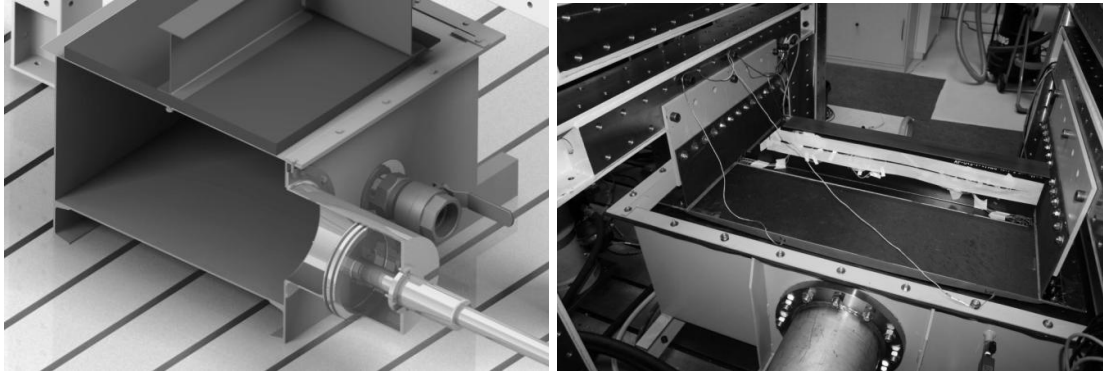
Figure 2 *– Cross section of the test rig model with specimen on top (left) and realized test rig with specimen (right)*

Since the test rig should be used not only for quasi-static but also for fatigue tests under alternating load, the contact behaviour between membrane and specimen becomes in particular important. On the one hand, the membrane needs to be as thin and flexible as possible to achieve a complete surface contact already at low loads. On the other hand, a thin and flexible membrane is highly loaded in areas not pressing on the specimen or on other stiff parts of the test rig. Furthermore, excessive membrane bulging results in a high water volume needed to be moved into and out of the tank during the fatigue test, which in turn causes the need for a high volume pump - or an alternative tank design.

Finite Element calculations were performed to evaluate the optimal membrane thickness and the optimal distance between the specimen edges and the tank, where a uniform contact is achieved already at low pressure loads. The geometric nonlinear model (shown in ***Figure 3*** left) was built in ANSYS® using solid elements for the foam core, the EPDM membrane and the steel tank and laminate solid elements for the sandwich face sheets, the rib and the spars. Material data were used from [6, 7]. The contact between membrane and sandwich was modelled with surface based contact formulation. The contact status plots were used to evaluate the contact behaviour for each configuration. The optimal design was found with a 3 mm thick membrane and a distance of 25 mm between specimen and tank edges. Finally, the additional volume needed to achieve contact and pressure was calculated based on the nonlinear deformation analysis to about 10 litres at 0.05 MPa pressure load. To move 10 litres into and out of the tank at 2 Hz test frequency, a hydraulic cylinder was designed and flanged on the tank side instead of a water pump. The hydraulic cylinder itself is actuated by a servohydraulic test system.
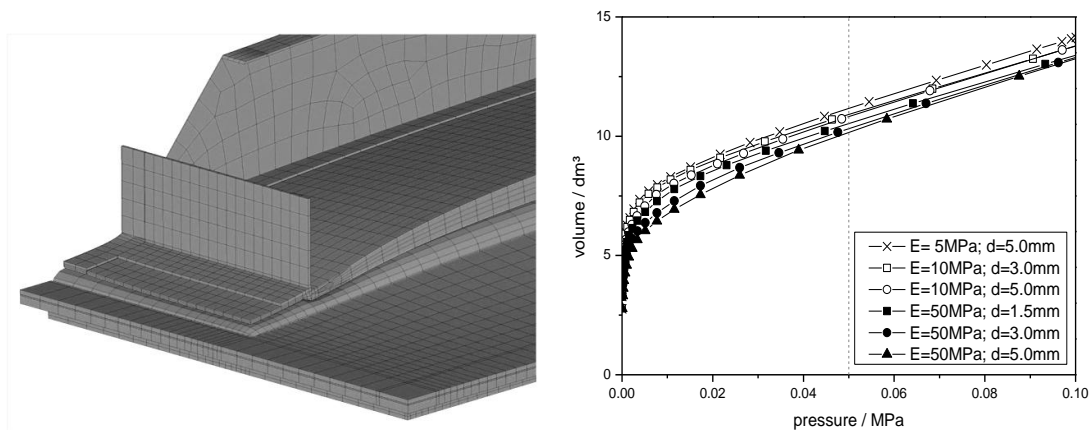
Figure 3 – FEA model for the test rig sizing (left) and calculated additional volume needed to increase the tank pressure for different membrane moduli and thicknesses (right).

3   Experimental Results

The specimen deformation behaviour was measured with the Digital Image Correlation system (DIC) ARAMIS developed by GOM mbH. The monitored area was located on the top flange of the rib in the centre of the specimen. Furthermore, strain gauges were used to measure the strain of both the top and bottom rib flange in the middle of the specimen (see *Figure 4* left). The novel SHM technique CVM-TTT (Comparative Vacuum Monitoring – Trough The Thickness) was used to detect damages in the adhesive layer and their propagation [9] (see *Figure 4* right). Additionally, thermography measurements were performed to visualize damage progression.
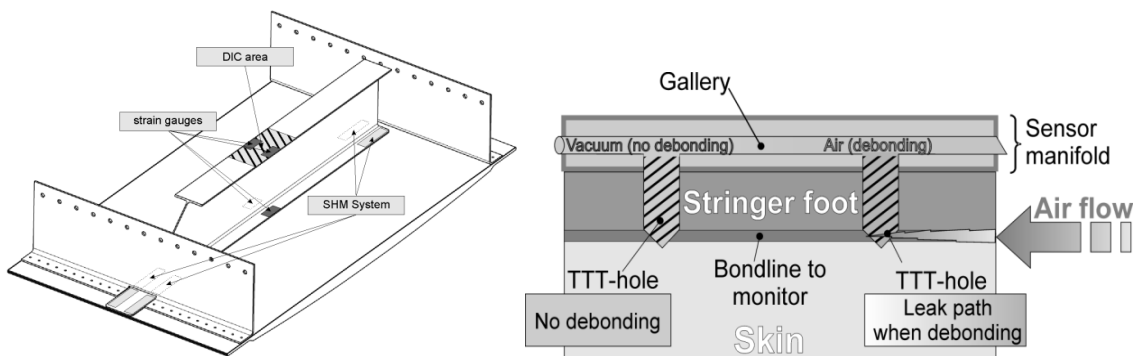
Figure 4 – Specimen scheme with applied measurement systems (left) and sketch of principle of the SHM-System CVM-TTT (right)

The first step of the experimental program was a quasi-static test up to LL = 0.02 MPa. During this test the specimen showed no audible or visible damage. Both the strain curves and the displacement curve are shown in *Figure 5*. The strain of the upper flange of the rib rises almost linear with the increasing pressure. Because of the location near to the neutral axis of the specimen, the strain of the lower flange is very low with a slightly negative slope. The bending of the specimen in the centre rises up to 2.2 mm. During this test the SHM system showed no indication of any damage of the adhesive layer. This was also proven by the thermography investigation.
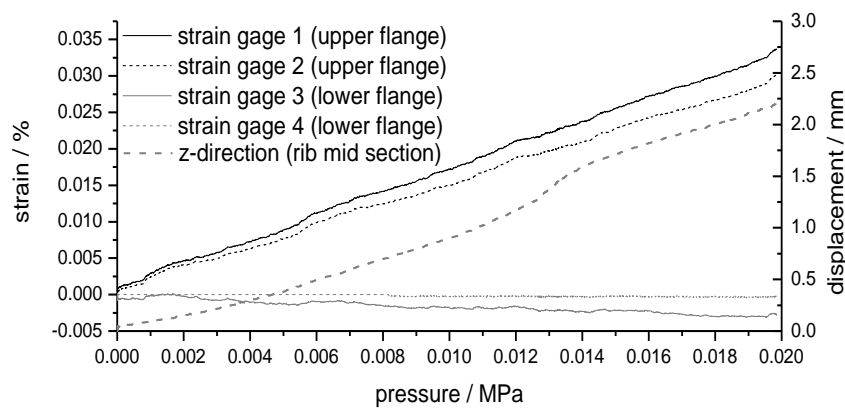
Figure 5 *– Strain and displacement curves of the quasi-static LL test up to 0.02 MPa*

After the quasi-static limit load test the specimen was loaded by a fatigue sequence of 120,000 load cycles at the maximum load of 0.5 x LL = 0.01 MPa with a load ratio of R = 0.1 and a test frequency of 2 Hz. The maximum strain - load cycle - curves of the upper flange are shown in ***Figure 6*** (left). After every 10,000 cycles the test was interrupted in order to inspect the specimen, visible by strain drops in the diagram at every interruption. Between load cycle number 10,000 and 30,000 some errors occurred during the strain measurement resulting in unusable strain values especially of strain gauge 1. However, except this drop the maximum strain of the rib flange is nearly constant for the overall testing time. The CVM-TTT system was connected to the servohydraulic test system, so that the test was stopped automatically when one of the sensors measured a damage occurrence. These stops are marked in the diagram with the numbers 1 to 6. The corresponding crack propagation map is shown in ***Figure 6*** (right). Initial leaky sensors (unusable) are marked with "0". As expected, the peeling load caused by the bending of the specimen becomes most critical at the straight end of the rib. After an initial damage occurred, the crack propagated under fatigue loading in the adhesive bonding along the rib with the direction to the middle of the specimen. However, the crack propagation was too small to cause an impact on the overall specimen deformation behaviour and to be visible in the strain-load cycle-curves.
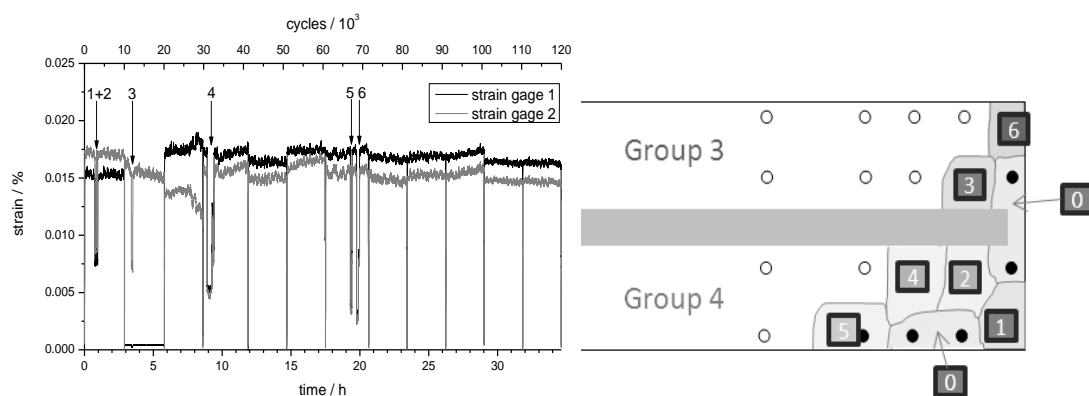
Figure 6 *– Maximum strain in the upper rib flange as a function of the load cycles during the first fatigue test (left) and crack propagation map from top view at the front spar (right)*

The next load type was a quasi-static test up to UL = 0.03 MPa. The CVM-TTT system detected two more damage events at 0.025 MPa and 0.026 MPa, increasing the crack at the straight rib end. Because of sealing problems of the SHM system after the last damage event,

the test was interrupted for 45 minutes while the testing actuator was kept in position. Thus, the strain and deformation curves proceed in a loop-like manner (***Figure 7***).
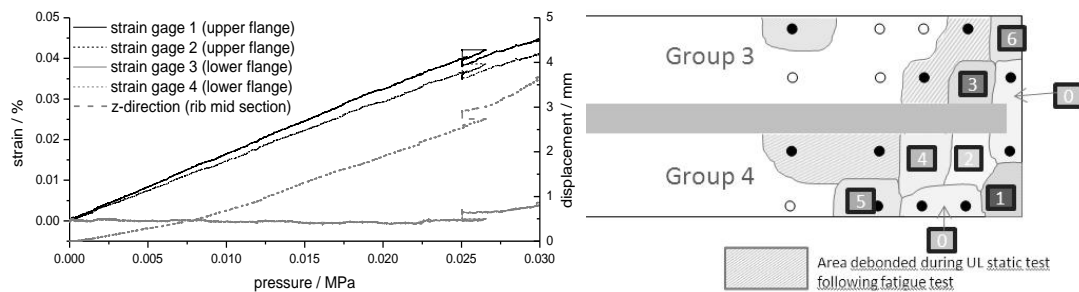
Figure 7 *– Strain and displacement curves of the quasi-static UL test up to 0.03 MPa (left) and crack propagation map from top view at the front spar (right)*

After the ultimate load test another fatigue test was performed over 60,000 load cycles. Maximum load, load ratio and test frequency were the same as in the first fatigue test. ***Figure 8*** shows the maximum strain curves of the upper rib flange for the whole test program. In the diagram the quasi-static ultimate load test is marked with "UL". After the ultimate load test the maximum strain became slightly lower which is potentially caused by the load release in the rib due to the increased delamination from the sandwich shell. During this fatigue sequence the SHM system showed no additional damages in the adhesive layer. Like in the previous tests, the damage detection of the SHM system correlated well with the thermography images.
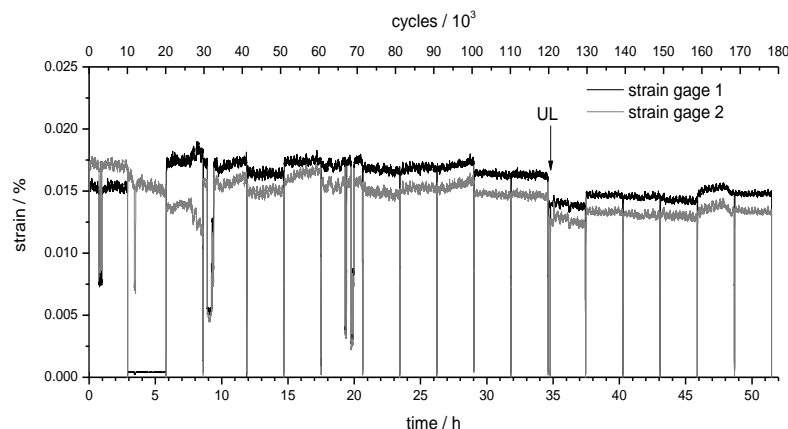
Figure 8 *– Maximum strain in the upper rib flange as a function of the load cycles during the first and the second fatigue test*

4   Conclusion

A novel test rig was designed, built up and put into operation to apply a homogenous surface load on a curved, in this case lenticular, sandwich structure. The rig is based on a water filled tank with an elastomeric membrane spanned over the top side. The design and sizing process was supported by nonlinear FEA taking particularly into account the contact behaviour between the membrane and the sandwich panel. Afterwards, an adhesively bonded joint between a CFRP frame rib and a CFRP sandwich shell of an aircraft component was tested under quasi-static and fatigue loading. The damage initiation and propagation could be monitored using thermography and the CVN-TTT

system. Except for small stable damage propagation at the straight rib end, the adhesive bonding sustained the whole test program based on the design loads of the component. Future work will be focused on the simulation of the rib/sandwich debonding behaviour.

5   References

[1]   A. S. Herrmann, P. C. Zahlen and M. I. Zuardy, "*Sandwich Structures Technology in Commercial Aviation: Present Applications and Future Trends*", Sandwich Structures 7: Advancing with Sandwich Structures and Materials, Part 1, pp. 13-26, 2005

[2]   M. I. Zuardy and A. S. Herrmann, "*An advanced centre box of a vertical tail plane with a side panel from CFRP foam-core sandwich structure*", CEAS Aeronautical Journal Vol. 2, pp. 253-269, 2011

[3]   P. C. Zahlen, M. Rinker and C. Heim, "*Advanced manufacturing of large, complex foam core sandwich panels* ", Proceedings of the 8th International Conference on Sandwich Structures, Porto, Portugal, p. 606–23, 2008

[4]   P. Jolma, S. Segercrantz and C. Berggreen, "*Ultimate Failure of Debond Damaged Sandwich Panels Loaded with Lateral Pressure – An Experimental and Fracture Mechanics Study*", Journal of Sandwich Structures and Materials, Vol. 9, pp. 167-196, 2007

[5]   D. A. Crump, J. M. Dulieu-Barton and J. Savage, "*Design and commission of an experimental test rig to apply a full-scale pressure load on composite sandwich panels representative of an aircraft secondary structure*", Meas. Sci. Technol., Vol. 21, 015108 (16pp), 2010

[6]   M. Rinker, "*Bruchmechanische Bewertung der Schadenstoleranz von CFK-Schaum-Sandwichstrukturen*", Phd Thesis, TU Braunschweig, Germany, 2011

[7]   JURIMA GmbH, EPDM Technical Datasheet

[8]   H. Stehmeier and H. Speckmann, "*Comparative Vacuum Monitoring (CVM): Monitoring of fatigue cracking in aircraft structures*", Proceedings of the 2th European Workshop on Structural Health Monitoring, Munich, Germany, 2004

Cohesive zone modeling of the DCB test in cortical bone tissue

F.A.M. Pereira[1], J.J.L. Morais[1], N. Dourado[1], M.F.S.F. de Moura[2], M.I.R. Dias[3]

[1]CITAB/UTAD, Departamento de Engenharias, Quinta de Prados, 5001-801

Vila Real, Portugal

[2]Faculdade de Engenharia da Universidade do Porto, Departamento de Engenharia Mecânica, Rua Dr. Roberto Frias, 4200-465 Porto, Portugal

[3] UTAD, Departamento de Ciências Veterinárias, Quinta de Prados, 5001-801

Vila Real, Portugal

Abstract   Fracture characterization of bovine cortical bone tissue has been performed in hydrated and dehydrated specimens using the double cantilever beam test (DCB). The aim was to analyze how the presence/absence of water influences the material fracture. Resistance-curves were obtained experimentally using two different methods: the Compliance Based Beam Method (CBBM) and the Modified Experimental Compliance Method (MECM). Both provided consistent results, revealing that toughness in hydrated bone is three times as big as in dehydrated one. Based on experimental data, parameters of the bilinear softening damage law were also determined for hydrated and dehydrated bone using an inverse method based on a developed genetic algorithm. Significant differences were observed on the shape of the cohesive laws as well as on the respective parameters, thus being concluded that water plays a fundamental role on bone fracture behavior.

Keywords: Bone, Fracture characterization, Mode I, Double Cantilever Beam test.

1   Introduction

Fracture characterization of bone is fundamental in order to deal with fracture risks and its dramatic social and economical consequences. As a result, the development of a suitable fracture tests to characterize bone fracture under mode I loading acquires special relevancy. There are several difficulties that should be taken into account, as is the case of a non-negligible process zone ahead of the crack tip [1] and the restrictions on specimen dimensions that are possible to get from bone.

In this work, a miniaturized version of the DCB test is developed in order to characterize bone fracture under mode I loading. This test is used to assess the influence of water on bone fracture properties, i.e. fracture toughness and failure modes. Additionally, the cohesive laws of hydrated and dehydrated bovine cortical bone were obtained through cohesive zone modelling (CZM).

2. Experiments

Bone specimens were harvested from fresh bovine femora of young animals (nearly eight months) within one day post-mortem period. Specimens were cut from the mid-diaphysis following the anatomic orientations illustrated in Figure 1. A total number of twenty

specimens were prepared. Half of them were hydrated and the other half dehydrated just before performing flexure and fracture tests.
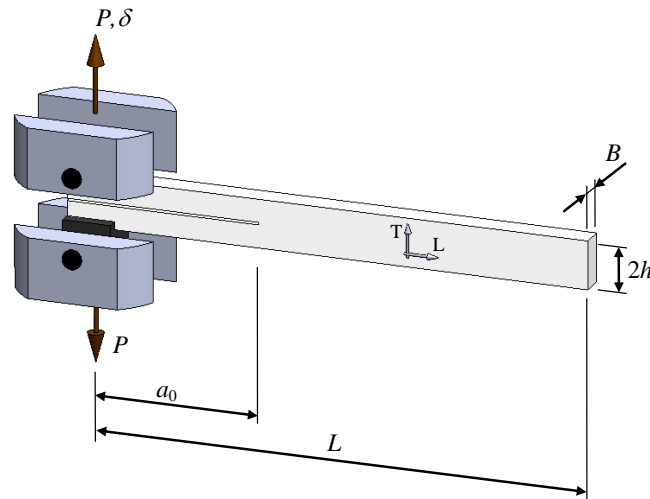
Figure 1. *Schematic representation of the DCB test (L: longitudinal direction; and T: tangential direction of the femur).*

The nominal sample dimensions are L=60 mm, B = 2.7 mm, $2h$ = 6 mm and a_0 = 18.6 mm. Experimental tests (Figure 2) were performed using a servo-electrical testing system (Micro-Tester INSTRON 5848) under displacement control, imposing an actuator velocity of 0.2 mm/min, in order to induce smooth crack propagation. Load-displacement (P-δ) curves were registered with an acquisition rate of 5 Hz.

Figure 2. *DCB test in bone.*

3. Data reduction schemes

Two different data reduction schemes providing Resistance-curves (R-curves) were used to evaluate bone fracture energy under mode I loading. The first one is the Modified Experimental Compliance Method (MECM), which requires experimental compliance calibration as a function of the crack length. The second one, named Compliance Based Beam Method (CBBM), is a method based on beam theory and crack equivalent concept.

3.1 Modified Experimental Compliance Method (MECM)

The MECM is based on a power law establishing an empirical relationship between compliance (C= δ/P) and crack length a,

$$C = ka^n \tag{1}$$

being k and n constant parameters to be determined experimentally by fitting. Combining Eq.

(1) with the Irwin-Kies relation

$$G_I = \frac{P^2}{2B}\frac{dC}{da} \tag{2}$$

leads to

$$G_I = \frac{nP\delta}{2Ba} \tag{3}$$

To overcome the limitation related to crack length monitoring during propagation, experimental compliance calibration considering different initial crack lengths a_0 should be carried out. Therefore, from Eq. (1), it can be written,

$$\log_{10} C_0 = n\log_{10} a_0 + \log_{10} k \tag{4}$$

where n and k can be determined through linear regression. The compliance calibration curve is obtained considering five initial crack lengths a_0 introduced consecutively, and ranging between 19 and 23 mm. In the fracture tests the compliance calibration curve is used to estimate the equivalent crack length during the course of the test.

3.2 Compliance Based Beam Method

Using the Timoshenko beam theory the compliance versus crack length becomes

$$C = \frac{8a^3}{E_L Bh^3} + \frac{12a}{5BhG_{LT}} \tag{5}$$

being G_{LT} the shear modulus in the LT plane (Figure 2). In order to account for root rotation at the crack tip a correction to the crack length must be considered [2]

$$\Delta = h\sqrt{\frac{E_f}{11G_{LT}}\left[3 - 2\left(\frac{\Gamma}{1+\Gamma}\right)^2\right]} \tag{6}$$

where

$$\Gamma = 1.18\frac{\sqrt{E_f E_T}}{G_{LT}} \tag{7}$$

Since some variability is always present in natural materials like bone, the longitudinal elastic modulus can be estimated considering the initial conditions (C_0, a_0)

$$E_f = \left(C_0 - \frac{12(a_0 + |\Delta|)}{5BhG_{LT}}\right)^{-1}\frac{8(a_0 + |\Delta|)^3}{Bh^3} \tag{8}$$

During crack growth an equivalent crack length (a_e) can be estimated solving equation (5) as a function of the current compliance using the MAtlab® software [3]. The R-curve ($G_I = f(a_e)$) can be obtained combining Eqs. (2) and (5),

$$G_I = \frac{6P^2}{B^2 h}\left(\frac{2a_e^2}{h^2 E_f} + \frac{1}{5G_{LT}}\right) \tag{9}$$

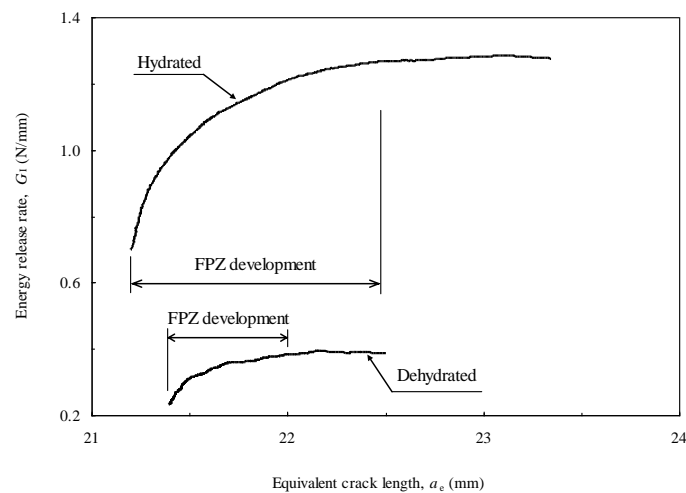## 4. Fracture energy

Load-displacement curves obtained during the DCB tests were registered for hydrated and dehydrated bone (Figure 3). The dehydrated bone presents a typical brittle behaviour, instead of the hydrated one that shows a typical ductile behaviour.
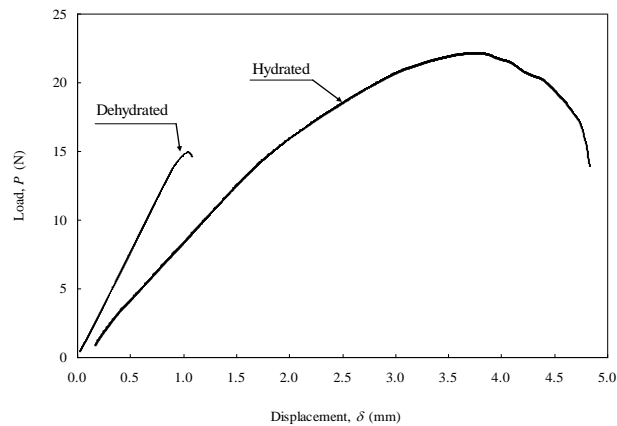
Figure 3. *Typical P-δ curves of hydrated and dehydrated young bovine bone.*

The resulting R-curves also highlight the different behaviour between these two different cases. The differences reflect on the values of toughness as well as in the size of the FPZ, which are both bigger in the hydrated material.

Figure 4. Typical R-curves of hydrated and dehydrated young bovine bone.

Table 1 present the summary of the fracture energies for hydrated and dehydrated young bovine bone. The remarkable difference on toughness emphasizes the important role of water on the fracture behaviour of bone.

Table 1 – Longitudinal flexure modulus and fracture energy of hydrated and dehydrated bone.

Hydrated			Dehydrated		
E_L (GPa)	G_{Ic} (N/mm) MECM	G_{Ic} (N/mm) CBBM	E_L (GPa)	G_{Ic} (N/mm) MECM	G_{Ic} (N/mm) CBBM
22.07	1.67	1.80	22.07	1.67	1.80
20.46	1.25	1.26	20.46	1.25	1.26
19.07	1.96	1.97	19.07	1.96	1.97
20.22	1.56	1.49	20.22	1.56	1.49
20.75	2.65	2.59	20.75	2.65	2.59
22.08	1.82	1.84	22.08	1.82	1.84
19.69	1.95	1.93	19.69	1.95	1.93
21.08	1.55	1.68	21.08	1.55	1.68
21.56	1.44	1.47	21.56	1.44	1.47
21.84	1.73	1.68	21.84	1.73	1.68
Average					
20.88	1.76	1.77	20.88	1.76	1.77
CoV (%)					
5	22	21	5	22	21

4. Cohesive laws

Cohesive laws (CL) representative of fracture behaviour of hydrated and dehydrated bone can be obtained through an optimization strategy involving an inverse method and a genetic algorithm [4]. A bilinear cohesive damage law (Figure 5) was used to simulate typical bone fracture behaviour performing finite element analysis of the DCB bone specimens. The optimization strategy consists on the determination of the cohesive law that minimizes the differences between numerical and experimental load-displacement curves.
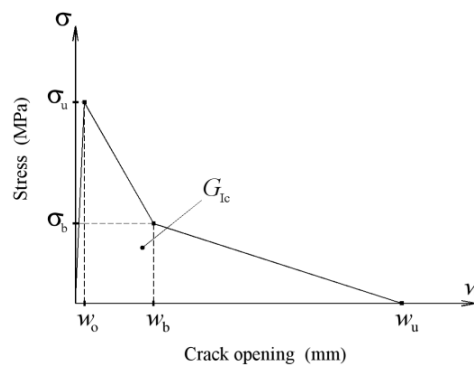
Figure 5 – Bilinear cohesive law.

Cohesive laws obtained for hydrated and dehydrated bones are shown in figure 6. The transverse local strength (σ_u) of the dehydrated bone is approximately the double of the hydrated one. On the other hand, the ultimate relative displacement (ω_u) of the hydrated bone is approximately an order of magnitude higher than the dehydrated case. These two aspects clearly emphasize the different performance of the two cases, i.e., the

hydrated bone is much more ductile than the dehydrated one that clearly denotes a significant brittle behaviour.
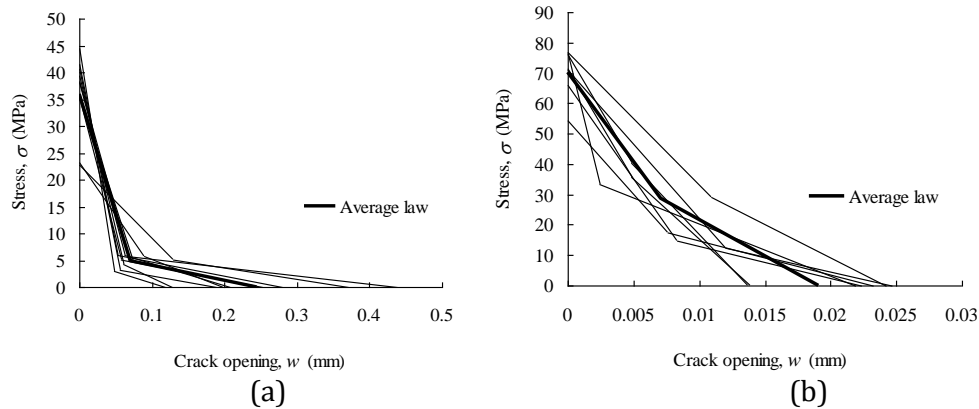

Figure 12 – Cohesive laws of the (a) hydrated and (b) dehydrated bone.

6. Conclusions

A miniaturized version of the DCB test was applied to bone fracture characterization under pure mode I loading. The testing method associated with a suitable data reduction scheme based on crack equivalent concept proved to be adequate for the purpose. Fracture tests were performed on hydrated and dehydrated bones in order to assess the influence of water on the material fracture behaviour. Cohesive laws allowing simulating the bone fracture were determined for both cases and pronounced differences were obtained. It was concluded that water has a remarkable influence in which concerns fracture properties and global fracture behaviour of bone.

Acknowledgements

References

[1] J. J. L. Morais, M. F. S. F. de Moura, F. A. M. Pereira, J. M. C. Xavier, N. Dourado, M. I. R. Dias, J. M. T. Azevedo, The Double Cantilever Beam Test Applied to Mode I Fracture Characterization of Cortical Bone Tissue, Journal of the Mechanical Behaviour of Biomedical Materials 3:446–453, 2010.

[2] Hashemi S, Kinloch AJ, Williams JG. The analysis of interlaminar fracture in uniaxial fibre–polymer composites. P Roy Soci A-Math Phy 1990;427:173–99.

[3] de Moura MFSF, Morais JJL, Dourado N. A new data reduction scheme for mode I wood fracture characterization using the double cantilever beam test. Eng Fract Mech 2008;75:3852–3865.

[4] Dourado N, Morel S, de Moura MFSF, Valentin G, Morais J. Comparison of fracture properties of two wood species through cohesive crack simulations. Compos Part A-Appl S 2008;39:415–427.

Effects of the Shear Strain Rate on the Torsion of Trabecular Bone

A.C. Vale[1,2], J. Faustino[1,2], L. Reis[1,3], A. Lopes[2], B. Vidal[2], J. Monteiro[4], J.E. Fonseca[2,5],

H. Canhão[2,5], M.F. Vaz[1,3]

[1]*Instituto de Ciência e Engenharia de Materiais e Superfícies, Instituto Superior Técnico, T.U. Lisbon, Av. Rovisco Pais, Lisbon, Portugal*
Email: ana_cvale@hotmail.com

[2]*Rheumatology Research Unit, Instituto de Medicina Molecular, Faculdade de Medicina da Universidade de Lisboa, Lisbon, Portugal*

[3]*Departamento de Engenharia Mecânica, Instituto Superior Técnico, Av. Rovisco Pais, Lisbon, Portugal*

[4]*Serviço de Ortopedia, Hospital de Santa Maria, Lisbon, Portugal*

[5]*Serviço de Reumatologia e Doenças Ósseas Metabólicas, Hospital de Santa Maria, Lisbon, Portugal*

Abstract As one of the major functions of bone is to provide structural support for the musculoskeletal system, it is important to evaluate its mechanical strength. Bones may be subjected to multiaxial stresses due to bone pathologies, accidental loads which may lead to hip, wrist fracture or to a prosthetic joint replacement. Torsional loading may lead to fractures, especially involving long bones from lower limbs. The aim of this work was to study the effect of the strain rate on the shear properties of trabecular bone, with a particular emphasis to old female osteoporotic patients (from 56 to 91 years). Cylindrical samples were core drilled from human femoral heads along the primary trabecular direction. The cylinder's ends were polished and embedded in blocks of polymer material which fit the grips of the testing device. Deformation rates of 0.005, 0.01 and 0.05 s^{-1} were applied. From the torque-angular displacement curves, the shear stress-strain curves were obtained. The maximum shear strength and the shear modulus (*i.e.* the slope of the linear region) were determined. The results showed that the strain rate increase is reflected in an increase of the shear stress. The same effect was not detected on the shear modulus.

1   Introduction

Skeletal fragility is an important orthopaedic concern due to its association with an increased risk of fracture. Advanced age and bone diseases, such as, osteoporosis, are factors that increase the fracture risk. In order to understand the osteoporosis and its treatment it is necessary to analyze the mechanical behaviour of the trabecular bone tissue. Trabecular bone is enclosed in compact bone at the end of epiphyses, or at the core of flat and small bones, and it consists of a network of rods or plates.

Less attention is given to the torsional behaviour of trabecular bone in comparison with compression or bending [1]. However, the bones are required to respond to multiaxial stress due to bone pathologies, to accidental loads or to joint replacement [2]. Torsional tests measure the shear stress applied to bone during movements of the body. Few authors have studied the shear properties of human trabecular bone [2, 3], while several torsional tests were conducted on animals, such as, rat [4], bovine [5] or ovine [6].

In order to perform a torsion test, the extremities of the bone sample are embedded in blocks of polymer material which fit the grips of the testing device [1, 7].

Previous investigation of the viscoelastic behaviour of trabecular bone was performed on animal vertebrae, without any disease. Deformation rates of 0.002, 0.015 and 0.05 s^{-1} were applied. The shear modulus and the shear strength were found to increase with the strain rate [6]. To our knowledge, the influence of the shear rate on the shear properties of the human osteoporotic trabecular bone was never performed.

The goal of this work was to study the mechanical behaviour in torsion of the human trabecular bone. A particular emphasis is given to the determination of the effect of the strain rate on the shear properties of human osteoporotic bone. Samples from femoral heads of old female osteoporotic patients (from 56 to 91 years) of three age-groups were tested in pure torsion. Scanning electron microscopy (SEM) analysis was performed on samples before and after the tests, to observe the damage caused by torsion.

2 Materials and methods

In this study, 29 femoral heads were collected from female patients who underwent total hip replacement surgery as a consequence of fragility fracture of the femoral neck at the Orthopaedic Department of Hospital de Santa Maria. After the surgery, samples were stored at -80ºC. From each femoral head, two cylindrical samples were extracted in the highest *in vivo* loading direction, using a perforating drill. The two samples, one for the torsion test and another for the SEM analysis, have diameters of approximately 10mm. The cortical shell was removed. Bone cylinders were de-fatted for three hours using a solution of methanol and chloroform (1:1), and were hydrated overnight in phosphate buffered saline solution (PBS). The samples for the torsion test were used one day after this procedure while the samples for SEM observations were stored at -20ºC.

Both extremities of the torsion samples were embedded in a mixture of resin and hardener (Mecaprex MA2) in the proportion of 100g to 12g, respectively. Careful mounting was needed to guarantee the alignment between polymer and bone. The diameter and height of the cylinder between two extremities of polymer was measured.

During a test, the specimen is subjected to a torque that originates its torsion. Torsion tests were performed until failure, in a universal test machine Instron model 8874 (Instron Corporation, Canton, USA), with a load cell 25 kN which also allows a torque of 100Nm (Figure 1a). The strain rates used were 0.005, 0.01 and 0.05 s^{-1}. The torque, T (Nm) and the angular displacement ϕ (rad) are obtained during the test. In general, the curve of the torque in function of the angle per unit length ($\theta = \phi/L$) is represented. A typical torque-angular displacement curve is shown on Figure 2a, showing the maximum torque, T_{max}, and the torsional stiffness, K which is the slope of the linear region. The shear strain, γ (%) is calculated as equation (1), where r and L are the radius and the length of the sample between polymeric extremities, respectively. On the trabecular bone torsion tests, there are, at least, two procedures proposed for determining the shear stress, τ. Nazarian et al. [7, 8], use equation (2). Other authors [2, 5, 6] calculate the shear stress by the equation (3), proposed by Nadai [9] for an isotropic material, where dT/dθ is the slope of the torque-angle per unit length curve. To calculate this derivative, the experimental torque curve is fitted to an exponential expression $A(1 - B\exp(-C\theta))$ [2]. The slope is calculated from the fitted points by a linear regression. The calculated value of dT/dθ is used in equation (3) to obtain the shear stress-strain curve (Figure 2b). The shear modulus, G, is calculated as the slope of the $\tau - \gamma$

curve in the initial zone [2] as in Figure 2b. From each test, K, τ_{max} and G were calculated. We calculated the shear modulus by the two procedures, and the differences were less than 0.2 %, which lead us to choose the Nazarian procedure due to its simplicity.

$$\gamma = \left(\frac{r\phi}{L} \right) \times 100 \qquad (1)$$

$$\tau = \frac{2T}{\pi r^3} \qquad (2)$$

$$\tau = \frac{1}{2\pi r^3} \left[\theta \frac{dT}{d\theta} + 3T \right] \qquad (3)$$

Figure 1b) presents a photograph of a sample after the torsion test. Prior to SEM observations, bone samples were glued to an aluminium plate and coated with a conductivity layer. SEM analysis was carried out in a field emission gun scanning electron microscope FEG-SEM (model 7001F, JEOL) using an accelerating voltage of 10 kV. The images were acquired with backscattered electrons.

a) *b)*
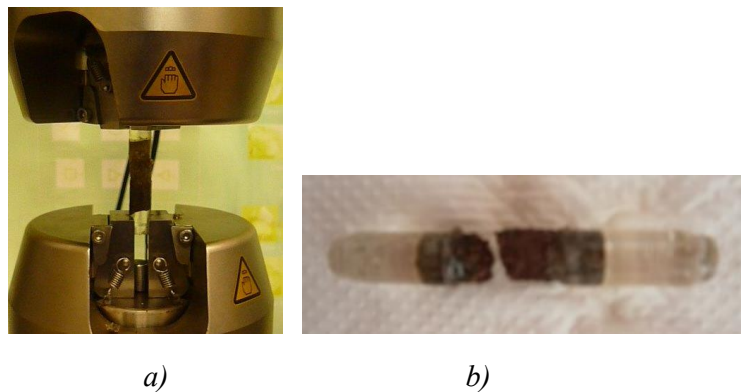
Figure 1 – *Photographs of: a) torsion test setup and b) sample after torsion failure.*

a) *b)*
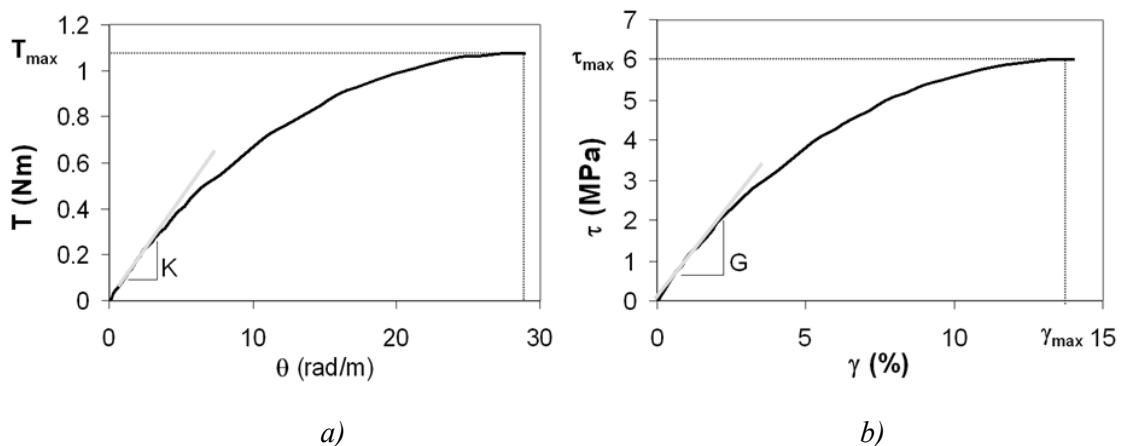
Figure 2 – *Torsion curves: a) experimental torque T versus angular deformation θ curve; b) calculated shear stress τ as a function of the shear strain γ.*

3   Results

All torque-angle per unit length curves exhibit the behaviour of Figure 2a. The curves shear stress-shear strain also had the same aspect of Figure 2b. On the majority of the cases, we found that failure occurred in directions that are oblique to the axial direction (Figure 1b).

The mean torsion properties were torsional stiffness 11.68±5.60 Nmrad^{-1}, maximum shear stress 5.94±2.98 MPa, ultimate shear strain 7.77±3.03 % and shear modulus 139.73±60.17 MPa. Figure 3 presents the results of the mean values of K, τ_{max}, and G, for the three strain rates used, while Figure 4 exhibits the results of the same parameters as a function of age. The mean values of torsional stiffness and maximum shear stress increase with the strain rate. The same effect is not detected on the shear modulus, where for the strain of 0.01 s^{-1}, a slight decrease is detected. No clear trends of the shear properties are detected with the aging.

a)   *b)*   *c)*
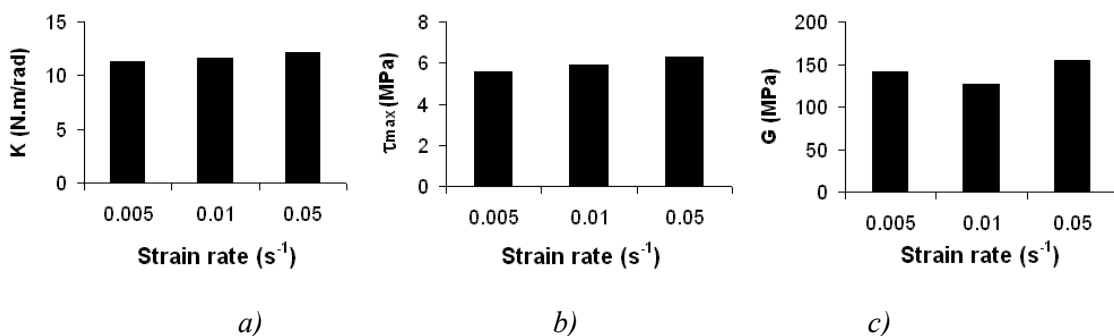
Figure 3 – *Mean values of: a) torsional stiffness, b) maximum shear stress and c) shear modulus as a function of the strain rate.*

a)   *b)*   *c)*
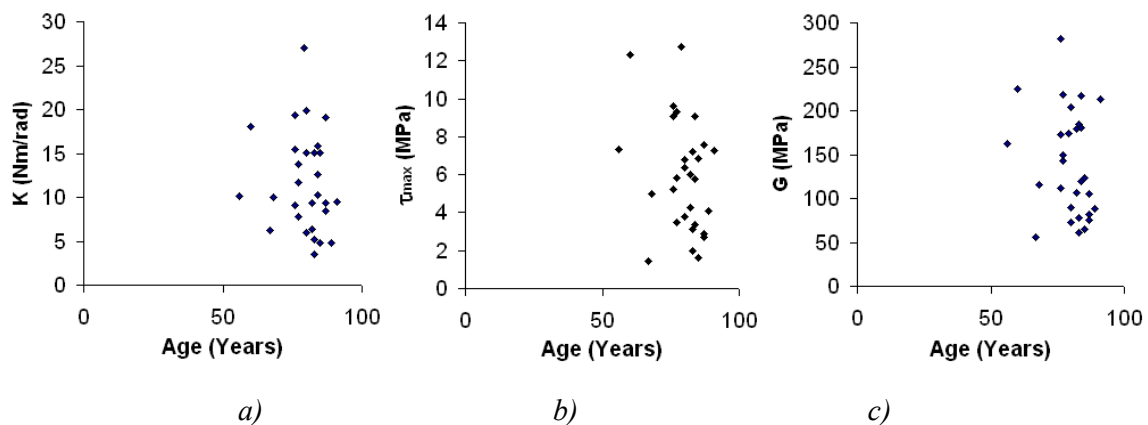
Figure 4 – *Experimental values of: a) torsional stiffness, b) maximum shear stress and c) shear modulus as a function of age.*

Figure 5 shows two micrographs taken in the scanning electron microscope of the same sample before and after the torsion tests. It was observed that, after the mechanical tests, the trabeculae are fractured and separated in two parts. The fracture surface exhibits a rough topology where the presence of shear effect due to applied torque can be identified.

a)   b)
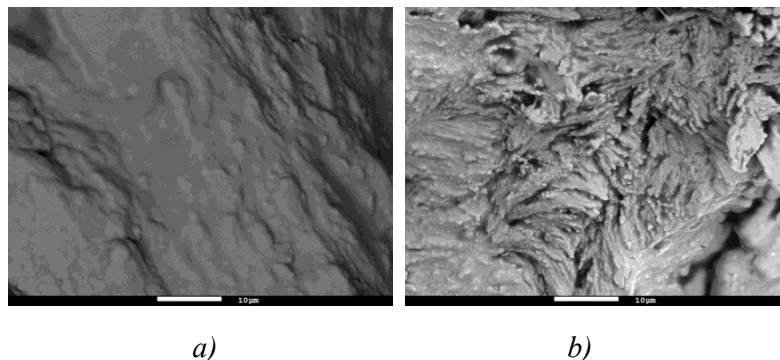
Figure 5 – *Scanning electron microscopy photographs, obtained with backscattered electrons, of the sample BM346: a) before and b) after the torsion test.*

4   Discussion/Remarks

The knowledge of the shear failure properties is essential on the prediction of trabecular bone failure for prosthesis design and fracture risk assessment.

On human femoral trabecular bone, the mean shear modulus was found to be 289 MPa [2], which is similar to the values obtained for animal trabecular bone [6]. Other torsion properties were τ_{max} =6.1±2.7 MPa, γ_{max} =4.6±1.3 % [2]. Our mean maximum shear stress value 5.94±2.98 MPa is close to the values obtained for human healthy bone, that have τ_{max} =6.1±2.7 MPa [2]. However, the values of the shear modulus that we obtained for osteoporotic bone are much lower than the values obtained with healthy bone.

The shear modulus increases with the maximum shear stress (Figure 6), evidenced with a positive Spearman correlation coefficient (ρ =0.746) with a significant correlation (p<0.0001). This is in accordance with the findings of Garnier et al. [2] for healthy trabecular bone.
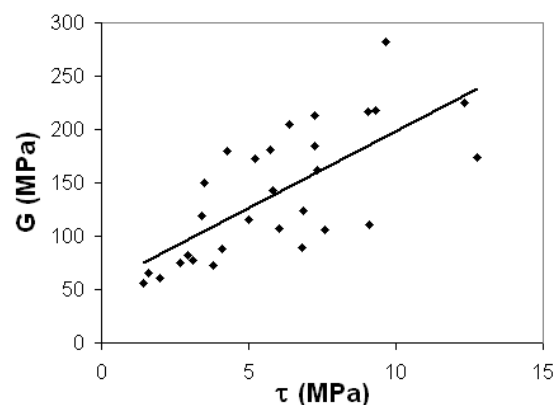
Figure 6 – *Shear modulus as a function of the maximum shear stress for all samples tested.*

While the shear stress increases with the strain rate, the shear modulus does not seem to exhibit the same behaviour. This is probably related to the effect of the disease on the torsion mechanisms, as osteoporosis affects the shear modulus, but does not have an effect on the shear strength.

Our results also provided new insights into the damage mechanisms responsible for torsional deformation. The trabecular bone walls, or trabeculae, have an arrangement of lamellae that are planar arrangements (3-7 µm) formed by groups of collagen fibers (1µm)

[10]. Before testing, the lamellae were parallel aligned (Figure 5a) in a very organized way. However, after being subjected to torsion, we observed a breakage of the collagen fibers (Figure 5b) and probably of the lamellae. It seems that the trabecular walls twist during the test, given rise to fracture of some of its components.

Acknowledgements

5   References

[1] Sharir, A. ,Barak, M., Shahar, R., "*Whole bone mechanics and mechanical testing*", Veter J, Vol.177, Num.1, pp. 8-17, 2008.

[2] Garnier, K., Dumas, R., Rumelhart, C., Arlot, M., "*Mechanical characterization in shear of human femoral cancellous bone: torsion and shear tests*", Med Eng Phys, Vol.21, Num.9, pp. 641-649, 1999.

[3] Rincón-Kohli, L., Zysset, P.K., "*Multi-axial mechanical properties of human trabecular bone*", Biomech Model Mechanobiol, Vol. 8, pp.195–208, 2009.

[4] Lind, P. M., Lind, L., Larsson, S., Örberg, J., "*Torsional Testing and Peripheral Quantitative Computed Tomography in Rat Humerus*", Bone, Vol.29, Num.3, pp. 265-270, 2001.

[5] Ford, C.M., Keaveny, T.M., "*The dependence of shear failure properties of trabecular bone on apparent density and trabecular orientation*", J Biomech, Vol. 29, Num. 10, pp. 1309-1317, 1996.

[6] Kasra, M., Grynpas, M., "*On the shear properties of trabecular bone under torsional loading: effects of bone marrow and strain rate*", J Biomech, Vol.40, Num.13, pp. 2898-2903, 2007.

[7] Nazarian, A., Meier, D., Müller, R., Snyder, B., "*Functional dependence of cancellous bone shear properties on trabecular microstructure evaluated using time-lapsed micro-computed tomographic imaging and torsion testing*", J Orthop Res, Vol.27, Num.12, pp. 1667-1674, 2009.

[8] Nazarian, A., Bauernschmitt, M., Eberle, C., Meier, D., Müller, R., Snyder, B.D., "*Design and validation of a testing system to assess torsional cancellous bone failure in conjunction with time-lapsed micro-computed tomographic imaging*", J Biomech, Vol. 41, pp. 3496–3501, 2008.

[9] Nadai A., "*Torsion of a round bar. The stress–strain curve in shear. In: Theory of flow and fracture of solids*". New York: McGraw- Hill, 1950, pp. 347–349.

[10] Vaz, M.F., Canhão, H., Fonseca, J.E., "*Bone: A Composite Natural Material, Advances in Composite Materials - Analysis of Natural and Man-Made Materials*", Pavla Tesinova (Ed.), Rijeka, InTech, 2011.

Fracture characterization of cortical bone tissue under mode II loading

using the end loaded split and the end notched flexure tests

F.A.M. Pereira[1], J.J.L. Morais[1], N. Dourado[1], M.F.S.F. de Moura[2], M.I.R. Dias[3]

[1]CITAB/UTAD, Departamento de Engenharias, Quinta de Prados, 5001-801

Vila Real, Portugal

[2]Faculdade de Engenharia da Universidade do Porto, Departamento de Engenharia Mecânica, Rua Dr. Roberto Frias, 4200-465 Porto, Portugal

[3] UTAD, Departamento de Ciências Veterinárias, Quinta de Prados, 5001-801

Vila Real, Portugal

Abstract   In this work, a comparison between the End-Loaded Split (ELS) and the End Notched Flexure (ENF) tests is made concerning their adequacy to evaluate mode II fracture properties of cortical bone tissue [1]. In both tests, two slight longitudinal grooves were machined in each lateral side of the specimen to provide self-similar crack propagation along the longitudinal specimen direction. To overcome the difficulties intrinsic to crack length monitoring during its propagation, equivalent crack methods were adopted as data reduction schemes. These methods do not need crack length measurement during the course of the tests, and provide the assessment of the equivalent crack extent as a function of the current specimen compliance using the beam theory. Both tests provided consistent results. This work showed that the ENF test presents some advantages when compared to the ELS in which concerns the identification of mode II fracture properties in bone.

1   Introduction

The study of bone fracture is an important research topic, since it can contribute to understand the fundamentals of bone failure induced by disease, age, drugs and exercise. In fact, fracture mechanics measurements can be viewed as a valuable method to characterize the toughness of bone, providing a quantitative determination of its fracture resistance. In this context, the definition of appropriate testing methods to evaluate fracture properties of bone is fundamental.

The majority of studies found in literature are dedicated to bone mode I fracture [1, 2], and much less attention has been dedicated to mode II fracture in bone. The fundamental reasons are related to experimental difficulties, namely the definition of an appropriate test method. The solutions proposed in literature are not adequate owing to difficulties related to specimen dimensions and spurious mode mixity instead of a pure mode II loading [1, 3].

In this work, miniaturized versions of the ELS and ENF tests are proposed for fracture characterization of bone. Data reduction schemes based on beam theory, specimen compliance and crack equivalent concept were used to overcome the difficulties inherent to crack monitoring during its propagation. Although some differences were

obtained, both tests provided consistent results concerning the measurement of the fracture energy under mode II loading. The advantages and drawbacks of each test are thoroughly discussed in the present work. Design guidelines are provided in order to get appropriate measurements of fracture properties under mode II loading.

2. ELS test

2.1. Experiments

Seven specimens were prepared from fresh bovine femora of young animals (aged about 8 months) within one day post-mortem. The initial crack length a_0 is constituted by a notch (0.3 mm thick) performed with a circular saw, and a small crack (0.25 mm length) executed with a sharp blade. As observed in Fig. 1, specimens were conceived in order to provide propagation in the TL fracture system (i.e., the normal to the crack plane is the tangential direction of mid-diaphysis and the crack propagation direction is the longitudinal direction of mid-diaphysis). Prior to the pre-crack execution the longitudinal modulus (E_L) was determined for each specimen before introducing the pre-crack, by means of three-point bending test. Fracture tests were performed under displacement control (0.5 mm/min) using a servo-electrical material testing system (MicroTester INSTRON 5848), with a 2 kN load-cell, for an acquisition frequency of 5 Hz. During the test, the applied load (P) and displacement (δ) were registered. Since the experimental praxis during the ELS tests revealed that crack frequently deviates from its initial plane ($z = 0$ in Fig. 2), two slight longitudinal grooves have been machined in each lateral side of the specimen to diminish the width (b instead of B in Fig. 2) of the ligament area, thus compelling crack advance to occur along the L-axis. The nominal dimensions were: $L_1 = 60$, $L = 50$, $d = 3$, $a_0 = 20$, $2h = 6$, $b = 2.3$, $B = 3.3$ and $t = 1$ (dimensions in mm). As observed in Fig. 3 the fixture testing device includes a linear guidance system which allows horizontal translation of the clamping grip during the loading process.
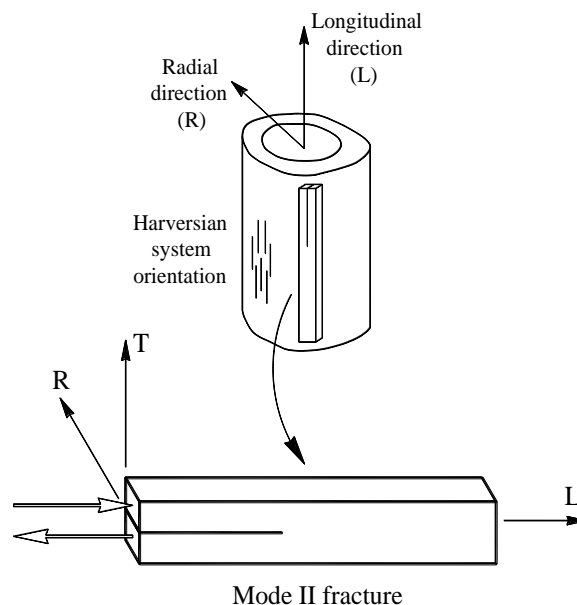
Figure 1. *Schematic diagram of a bone femur showing the location where samples can be harvested.*
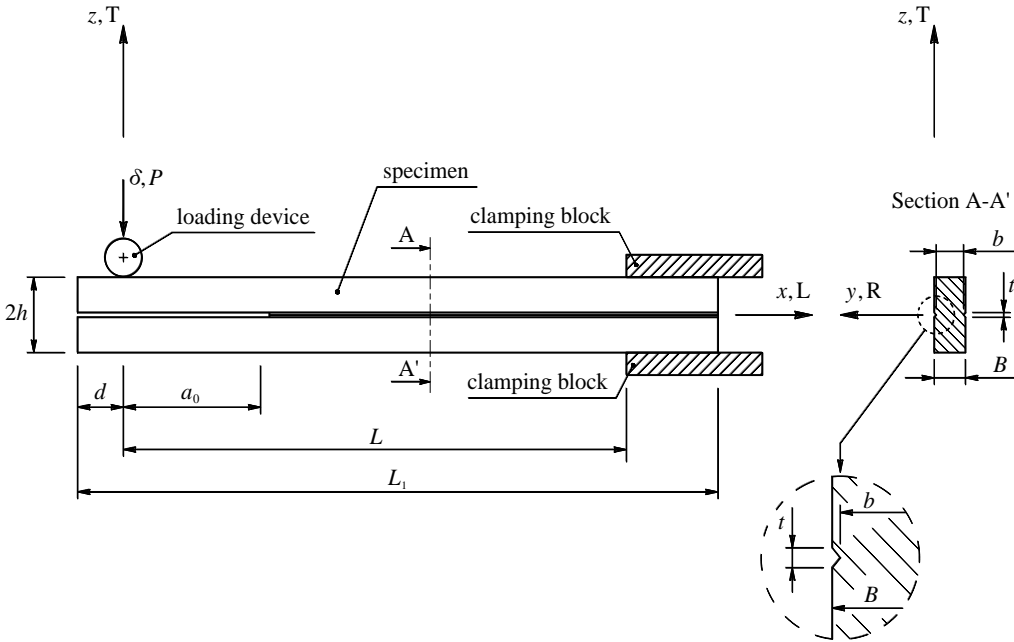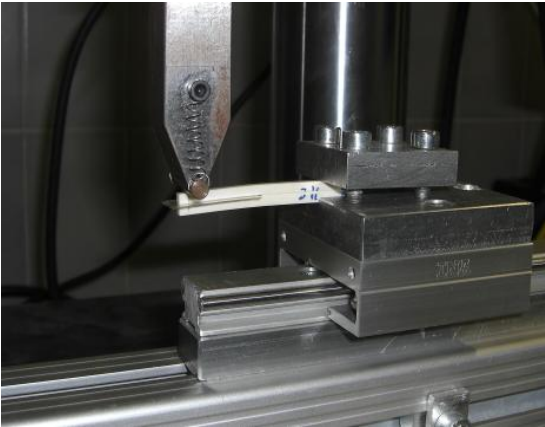
Figure 2. *Schematic representation of the ELS test.*

Figure 3. *ELS test in bone*

2.2 Data reduction scheme - ELS

Considering the Timoshenko beam theory, the specimen compliance (C) is [4]

$$C - \frac{3a^3}{2Bh^3E_L} = \frac{L^3}{2Bh^3E_L} + \frac{3L}{5BhG_{LT}}$$

(1)

In the ELS test there is a source of variability related with the clamping conditions that are never perfect. This difficulty can be overcome considering the initial conditions (C_0, a_0)

$$C_0 - \frac{3a_0^3}{2Bh^3E_L} = \frac{L_{ef}^3}{2Bh^3E_L} + \frac{3L_{ef}}{5BhG_{LR}}$$

(2)

where L_{ef} is the effective specimen length. From Eqs. (1) and (2) the equivalent crack length (instead of a) during propagation becomes

$$a_e = \left[(C - C_0)\frac{2Bh^3E_L}{3} + a_0^3 \right]^{1/3}$$

(3)

which does not depend on parameter L_{ef}. The fracture energy in mode II (G_{II}) can now be obtained from Eqs. (3) and the Irwin-Kies relation

$$G_{II} = \frac{P^2}{2b}\frac{dC}{da}$$

(4)

It should be noted that due to the presence of the longitudinal grooves (Fig. 2) the width of the ligament section is b, instead of B. Therefore,

$$G_{II} = \frac{9P^2a_e^2}{4bBh^3E_L}$$

(5)

The $G_{II}=f(a_e)$ relationship provides the R-curve, whose plateau defines the fracture energy under mode II loading [5].

3. ENF test

3.1. Experiments

Seven ENF specimens were prepared as described in the previous section. The size restrictions lead to the following specimen dimensions (Fig. 4a): $2L_1 = 65$ mm, $2L = 60$ mm, $a_0 = 21$ mm, $2h = 6$ mm, $B = 3.3$ mm and $b = 2.3$ mm. The tests were performed using a servo-electrical testing system (MicroTester INSTRON 5848), with constant displacement rate of 0.5 mm/min (Fig. 4b). A 2 kN load-cell was used, considering an acquisition frequency of 5 Hz.

(a)

(b)
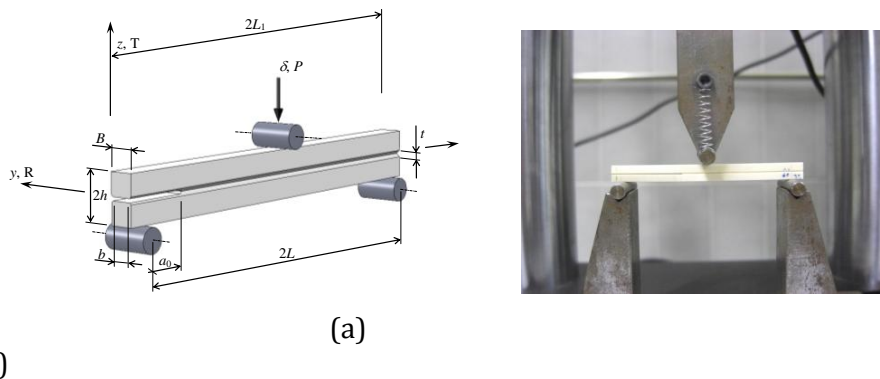
Figure 4. *Schematic representation (a) and a photography (b) of the ENF test.*

3.2 Data reduction scheme – ENF

By means of the Timoshenko beam theory the specimen compliance is,

$$C = \frac{3a^3 + 2L^3}{8Bh^3E_L} + \frac{3L}{10BhG_{LT}} \tag{6}$$

where E_L and G_{LT} are the elastic longitudinal and shear moduli, respectively. In order to avoid the previous measurement of the longitudinal modulus as performed in the ELS test, the initial conditions (C_0, a_0) can be used to estimate the equivalent elastic modulus (E_f)

$$E_f = \frac{3a_0^3 + 2L^3}{8Bh^3}\left(C_0 - \frac{3L}{10BhG_{LT}}\right)^{-1} \tag{7}$$

During crack growth the current compliance C is used to estimate an equivalent crack length a_e through Eqs. (6 and 7),

$$a_e = \left[\frac{C_c}{C_{0c}}a_0^3 + \frac{2}{3}\left(\frac{C_c}{C_{0c}}-1\right)L^3\right]^{1/3} \tag{8}$$

where $C_c = C - \dfrac{3L}{10BhG_{LT}}$; $C_{0c} = C_0 - \dfrac{3L}{10BhG_{LT}}$ $\qquad$ (9)

Combining equations (6, 7 and 5) G_{II}=f(a_e) can be obtained as

$$G_{II} = \frac{9P^2a_e^2}{16bBh^3E_f} \tag{10}$$

Following this procedure, it is not necessary to monitor crack length during its growth and the determination of the elastic modulus before the fracture test, which is an advantage of the ENF test relatively to the ELS.

4. Results

Figures 5 and 6 present the typical load-displacement curves and the corresponding R-curves obtained in the ELS and ENF tests. In both cases a plateau value is achieved on the R-curves thus demonstrating that both tests are able to be applied for fracture characterization of bone under mode II loading. The global results of the fracture energies are presented in Table 1. As it can be seen, both tests present consistent results owing to the natural variability of bone.
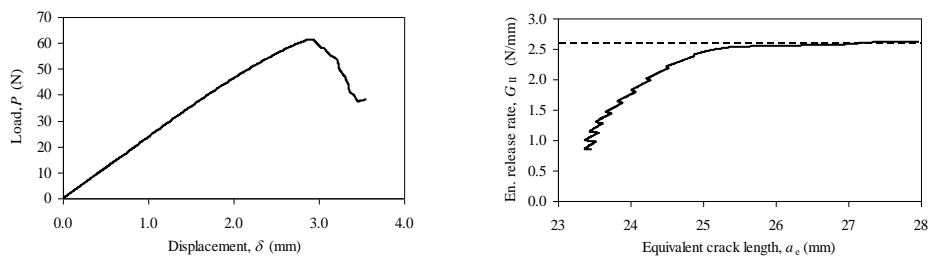
Figure 5. *Typical load-displacement curve and the corresponding R-curve obtained in the ELS test.*
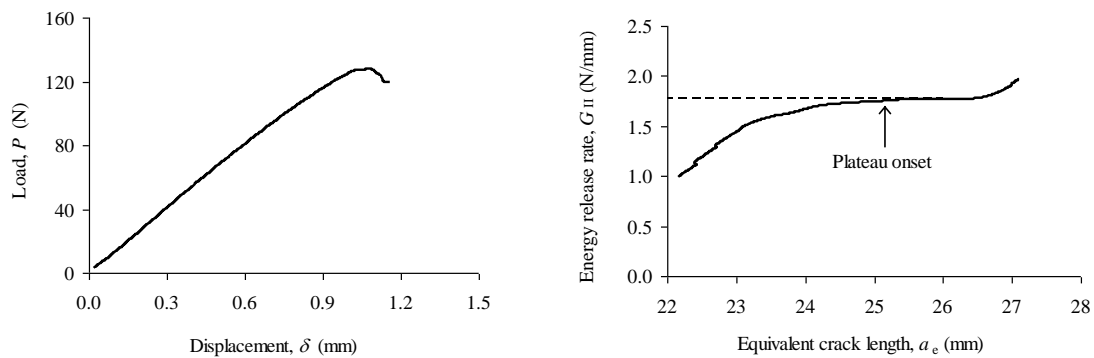
Figure 6. *Typical load-displacement curve and the corresponding R-curve obtained in the ENF test.*

Table 1. *Resume of fracture energies (G_{IIc} (N/mm))*.

	ELS	ENF
	2.55	2.90
	2.65	2.40
	2.45	2.32
	2.38	1.77
	2.64	2.30
	2.75	1.95
	2.4	2.10
Average	2.55	2.25
CoV (%)	5.5	16.2

5. Conclusions

Miniaturized versions of the ELS and ENF tests were used to fracture characterization of bone under mode II loading. It was verified that with a judicious selection of the specimen dimensions both tests can provide valuable measurements of this important property in bone. Additionally, appropriate data reduction schemes based on beam theory, specimen compliance and crack equivalent concept were developed in order to overcome several difficulties inherent to a suitable application of the proposed tests.

Acknowledgements

References

[1] Norman, T.L., Nivargikar, V., Burr, D.B., 1996. Resistance to crack growth in human cortical bone is greater in shear than in tension. Journal of Biomechanics 29, 1023–1031.

[2] Phelps, J.B., Hubbard, G.B., Wang, X., Agrawal, C.M., 2000. Microstructural heterogeneity and the fracture toughness of bone. Journal of Biomedical Materials Research 51, 735–741.

[3] Zimmermann, E.A., Launey, M.E., Barth, H.D., Ritchie, R.O., 2009. Mixed-mode fracture of human cortical bone. Biomaterials 30, 877–5884.

[4] M. F. S. F. de Moura, N. Dourado, J. J. L. Morais, F. A. M. Pereira, Numerical Analysis of the ENF and ELS Tests Applied to Mode II Fracture Characterization of Cortical Bone Tissue, Fatigue and Fracture of Engineering Materials & Structures 34:149–158, 2011.

[5] F. A. M. Pereira, J. J. L. Morais, N. Dourado, M. F. S. F. de Moura, M. I. R. Dias, Fracture Characterization of Bone under Mode II Loading Using the End Loaded Split Test, Journal of the Mechanical Behavior of Biomedical Materials 4:1764–1773, 2011.

Compressive Fatigue Tests on Trabecular Bone

C. Palma[1,2], A.C. Vale[1,2], P.M. Amaral[1,3], L.G. Rosa[1,3], A. Lopes[2], J. Monteiro[4], J.E. Fonseca[2,5], H. Canhão[2,5], M.F. Vaz[1,3]

[1]*Instituto de Ciência e Engenharia de Materiais e Superfícies, Instituto Superior Técnico, T.U. Lisbon, Av. Rovisco Pais, Lisbon, Portugal, Email: catarina.palma@ist.utl.pt*

[2]*Rheumatology Research Unit, Instituto de Medicina Molecular, Faculdade de Medicina da Universidade de Lisboa, Lisbon, Portugal*

[3]*Departamento de Engenharia Mecânica, Instituto Superior Técnico, Av. Rovisco Pais, Lisbon, Portugal*

[4]*Serviço de Ortopedia, Hospital de Santa Maria, Lisbon, Portugal*

[5]*Serviço de Reumatologia e Doenças Ósseas Metabólicas, HSM, Lisbon, Portugal*

Abstract An understanding of the mechanical behaviour of bone is extremely important, as it provides structural support for the musculoskeletal system. Bone is loaded in fatigue as a result of prolonged exercise and repetitive activities, which may lead to a reduction in stiffness and a consequent increase of the risk of fracture. Nevertheless, there are few studies on the fatigue behaviour with human specimens. The aim of our work was to characterize the fatigue behaviour of trabecular human bone. Patients with severe hip osteoarthritis are frequently submitted to total hip replacement surgery. In this study, trabecular bone cylinders extracted from human femoral heads were loaded under compressive fatigue. Prior to fatigue tests, samples were compressed monotonically and were preconditioned for twenty compression cycles under load control. The initial secant elastic modulus, E_0, was determined from the slope of the 20th cycle. The initial modulus was used to normalize the interval of applied stress, which was set to $\Delta\sigma/E_0 = 0.0015$. The fatigue test was performed at a frequency of 2Hz (physiological frequency) and tests were stopped after reaching a residual strain of 0.8% or the fracture of the sample. In general, the fatigue behaviour of trabecular bone is characterized by an increase on the residual strain, a broadening of the hysteresis loops, and by a decrease of the secant modulus.

1 Introduction

Bones are subjected to fatigue in response to cyclic repetitive loading, being one of the primary causes of human bone fracture [1]. During the last decade there was an increase in the number of studies intended to understand the fatigue of hard tissues of the skeletal system, in order to predict and prevent failures. Although the majority of the works on fatigue of bone found in the literature describe results from animal testing [1-5], there are a few studies on fatigue of human trabecular bone [2, 3, 6, 7]. Fatigue fractures may occur both in cortical and in trabecular bone. Cortical bone is found on the outer shell of bones and is dense in comparison with the interior trabecular bone which is regarded as a cellular solid with a larger porosity. Trabecular bone consists in a network of trabeculae, *i.e.*, rods and plates of bone tissue.

In response to cyclic loading, bone will fail at stresses below the values that the material can sustain under static loading. Fatigue fractures, known as stress fractures, may be a result

of daily activities or prolonged and intense exercise, which may occur in young adults as for example, athletes [1, 4, 5]. The fatigue fractures denoted as fragility fractures happen in elderly patients with osteoporosis and occur on the femur or on vertebrae, where most of the load is supported by trabecular bone [1, 4]. However, the works performed on the fatigue of trabecular bone are rare. Fatigue microdamage occurs due to the accumulation of micro-cracks. Micro-cracks on the trabeculae may be repaired through bone remodelling (metabolism). However if the patients are old the remodelling process does not repair the damaged sites, micro-cracks are accumulated and coalesce, leading to a decrease in bone stiffness and to an increase of the fracture risk [4, 7]. Latest observations revealed that micro-cracks appear more frequently on trabeculae that are already damaged, instead of trabeculae that were not previously injured [7].

The objective of this study was to assess the compressive fatigue behaviour of human trabecular bone. Bone cylinder samples were extracted from human femoral heads belonging to patients with hip osteoarthritis that were subjected to hip replacement surgery. To our knowledge, there are no works published on the cyclic behaviour of osteoarthritis bone. Samples were subjected to compressive fatigue loading and the microdamage after the mechanical test was evaluated by scanning electron microscopy.

2   Materials and methods

Trabecular bone was obtained from patients who suffered from hip osteoarthritis and underwent total hip replacement surgery at the Orthopaedic Department of Hospital de Santa Maria. Five donors (one male, BM453, and four females) were studied with age, in the range 56-72 years (Table 1). After the surgical procedure, the femoral epiphyses were stored at -80ºC. Before testing, the material was defrosted at room temperature. A cylinder of trabecular bone was removed from each femoral head, using a drill with a diameter of 15 mm, in the highest *in vivo* loading direction. The cortical shell was cut off, and the sample height was approximately 30mm. The cylinders extremities were polished with a 800 grade silicon carbide paper under water flow to make them parallel. Bone cylinders were de-fatted for three hours using a chloroform and methanol solution (1:1 ratio) and were hydrated overnight in phosphate buffered saline (PBS) solution.

Specimens were tested using a three-step protocol, in a servo-hydraulic testing machine (model 8502, Instron Corp., Canton MA) with a load cell of 100 kN. An extensometer was attached to the extremities of the cylinder using rubber elastic bands (Figure 1a). As fatigue tests may take a long time, samples must be kept wet and, in our experiments they were sprayed with a saline solution. In the first part of the mechanical test, the bone cylinder was tested in monotonic compression in order to obtain the load $F_{strain0.15}$, at which the strain was 0.15 %. This value of strain was chosen taken into account that daily activities may attain a maximum strain of 0.3%, it was below the yield strain (around 0.7%) and was not expected to create damage. On the second step, the specimen was preconditioned by loading for 20 cycles in load control, using a sinusoidal waveform at a frequency of 2 Hz. The applied loads varied between $F_{min} = 50$ N and the value of $F_{strain0.15}$ determined on the first stage. The aim of the second step is to calculate the initial secant elastic modulus, E_0, which is determined from the slope of the 20th cycle. Fatigue tests are carried out under normalized stress defined as $\Delta\sigma/E_0$, where $\Delta\sigma$ is the interval of applied stress, i.e., $\Delta\sigma=\sigma_{max}-\sigma_{min}$. As we are using non-healthy bone, a value of $\Delta\sigma/E_0 =0.0015$ was chosen, which is lower than the values found in the literature. With the values of the modulus E_0, determined in the preconditioned step, the maximum stress σ_{max} and consequently F_{max}, were calculated for each specimen. The minimum load was, again, set to $F_{min} = 50$ N. The final step or the fatigue tests consisted of N

cycles (loading and unloading) under the applied normalized stress. Tests were conducted until fatigue failure, which may be defined to occur when the residual strain reaches the value of 0.8% [7] or when we observe the fracture of the sample.

From fatigue tests, stress-strain curves are obtained (Figure 1b). We measured the initial secant modulus E_i, which is the secant's slope of the first stress-strain loops after the stabilization of the machine and the final secant modulus, E_f, at the end of the test. We also registered the changes in the plastic strain for a cycle $\Delta\varepsilon_{pl}$, the residual strain after final unloading ε_{res}, and the maximum strain ε_{max}.

After fatigue testing, scanning electron microscopy (SEM) was used to analyze the degree of damage within the trabeculae. SEM analysis was carried out in a field emission gun scanning electron microscope (FEG-SEM) (model 7001F, JEOL) using an accelerating voltage of 25 kV. Prior to microscopic analysis, the samples were mounted in resin, polished, and then coated with a gold film.

a)   *b)*
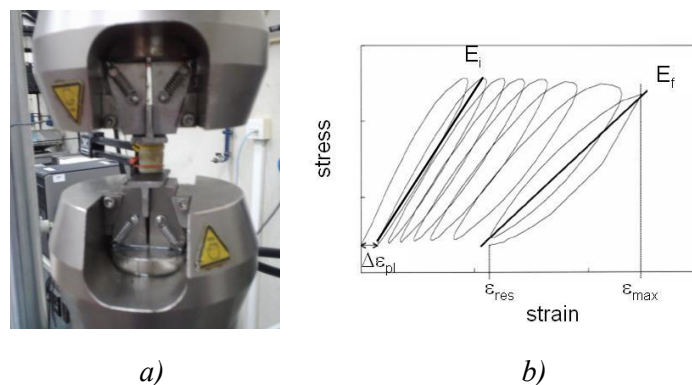
Figure 1 – *a) Photograph of the compressive fatigue testing setup and b) schematic representation of a typical stress-strain curve (adapted from [4]).*

3   Results

Table 1 lists the results of the monotonic tests, *i.e.*, the load $F_{strain0.15}$, that was further used on the preconditioning step. The initial elastic modulus E_0 calculated from the preconditioning tests varied from 878 to 1772 MPa for different patients (Table 1), which indicates different mechanical characteristics among specimens. As a consequence, the maximum applied force F_{max} on the fatigue tests is different for each sample (Table 1).

Table 1 – *Results from the monotonic and from the preconditioning tests*

Sample	Age (years)	$F_{strain0.15}$ (N)	E_0 (MPa)	F_{max} (N)
BM439	68	447	1275	388
BM440	64	129	878	282
BM448	72	258	1149	354
BM453	56	362	1579	469
BM478	59	319	1772	520

Figure 2a exemplifies a stress-strain curve obtained from the fatigue tests of a bone sample. Only a selected number of cycles was represented. An analysis of the plot of Figure 2a reveals a decrease in the elastic secant modulus with the increase of the number of cycles.
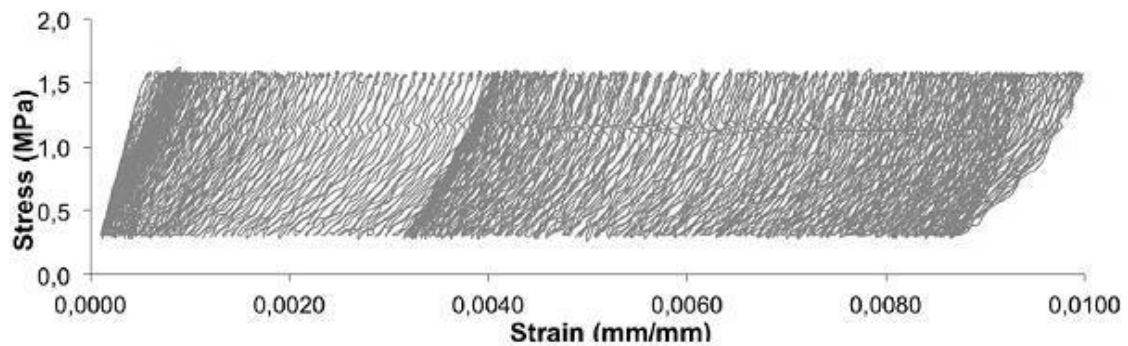
a)
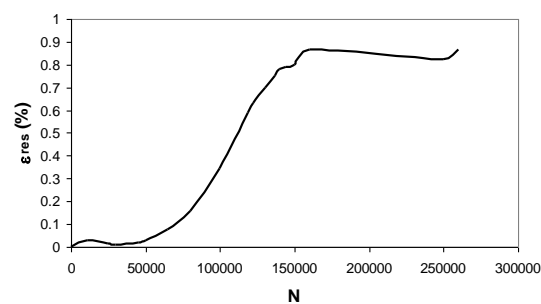
b)

Figure 2 – *a) Stress-strain curves obtained with compressive fatigue test; b) residual strain as a function of the number of cycles N (sample BM440).*

Figure 2b exhibits the residual strain as a function of the number of cycles. There is an increase in ε_{res} until N ≈160000, after which the residual strain attains a plateau. Table 2 summarizes the results of the fatigue tests for all the samples. The number of cycles to failure was in the range 171000 to 396000. With the exception of sample BM453, the secant elastic modulus E_f, at the end of the test, is lower than the initial secant modulus E_i. The width of the hysteresis loop may be evaluated by $\Delta\varepsilon_{pl}$. In three of the samples it was observed a broadening of the loop, with $\Delta\varepsilon_{plf} > \Delta\varepsilon_{pli}$, while samples BM440 and BM478 showed a lower value of $\Delta\varepsilon_{plf}$ than the $\Delta\varepsilon_{pli}$.

Table 2 – *Results from the fatigue tests*

Sample	N	E_i (MPa)	E_f (MPa)	ε_{res} (%)	ε_{max} (%)	$\Delta\varepsilon_{pl\ i}$	$\Delta\varepsilon_{pl\ f}$
BM439	221000	2325	2260	0.68	0.76	1.04×10^{-5}	3.54×10^{-5}
BM440	260000	1787	1005	0.87	0.99	5.21×10^{-5}	4.16×10^{-5}
BM448	396000	1284	1170	0.42	0.56	2.29×10^{-5}	8.54×10^{-5}
BM453	283000	1176	1316	0.52	0.69	8.10×10^{-5}	1.17×10^{-4}
BM478	171000	1773	1199	1.77	1.99	6.43×10^{-5}	4.38×10^{-5}

Figure 3 shows two micrographs taken in the scanning electron microscope of the same sample before and after the fatigue tests. We observed that, after the mechanical tests, the trabeculae are damaged with several micro-cracks.

a)	*b)*
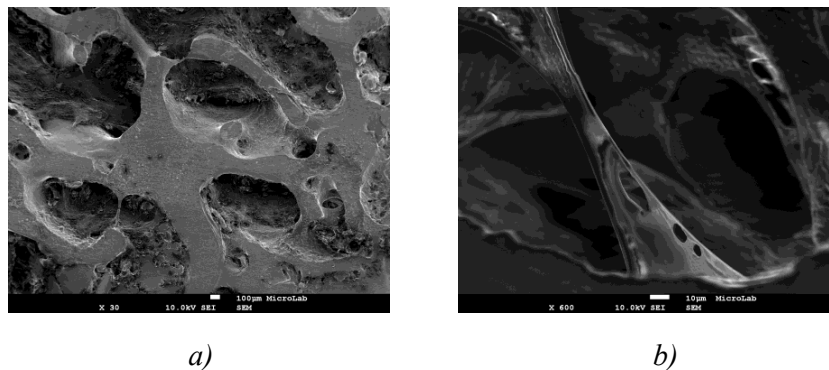
Figure 3 –*Scanning electron microscopy photographs of the sample BM478: a) before and b) after the fatigue test (magnifications of a) and b) are very different).*

4 Discussion

The understanding of the fatigue behaviour of trabecular bone is of great awareness on the prevention of failures. However, the studies found in the literature are rare. In this paper, we developed a preliminary work on the fatigue failure of bone from femoral heads belonging to patients with hip osteoarthritis. The definition of failure in a fatigue test is arbitrary, but we choose it to occur when the residual strain reaches 0.8 %, or when there is the fracture of the sample. The fatigue limit may be set based on a decrease in the secant elastic modulus of 10%. Figure 4 shows the evolution of the normalized modulus E_f/E_i as a function of N for the entire tests. The plot clearly shows an initial decrease in the secant modulus for four samples, with the exception of sample BM439, where there is an initial increase in E_f/E_i followed a decreased step. For most of the cases, the fatigue test could have been stopped after the decrease in the secant modulus. The continuation of the test could eventually be misleading, as in the case of sample BM453. On this specimen's test, the prolongation of the experiment, beyond the minimum of E_f/E_i, lead to an increase in the modulus until the end of the test reaching an higher value in comparison with the initial one (Table 2). Using the criterion of the decrease in the elastic modulus of 10%, four samples suffered from fatigue failure, being only the sample BM439 the one that showed a different behaviour. Some cases of an increase of the normalized modulus during the fatigue tests are reported on the literature for healthy trabecular bone [7]. This is probably the result of an underestimation of stiffness in the preconditioning cycles [4, 7].

Taken into account the results of Figure 2b, for residual strains less 0.8%, we may observe that deformation follows the three classical stages of fatigue [2]. An initial transient behaviour with a rapid increase in strain in the first cycles, is followed by a second stage with a strain saturation. The third step consists of a fast increase of the deformation until fatigue failure. However, as we performed the tests for a larger number of cycles, N>130000, there was an accumulation of strains, characterized by another plateau, which may be due to time-dependent or creep damage [4].

The normalized modulus E_f/E_i was also plotted as a function of the maximum strain and of the age of the patients (Figure 5). Figure 5a shows a tendency for a decrease of E_f/E_i with ε_{max}, which is in accordance with the published studies, which have concluded that the post-mechanical properties were most dependent on the maximum compressive strain [1, 4].
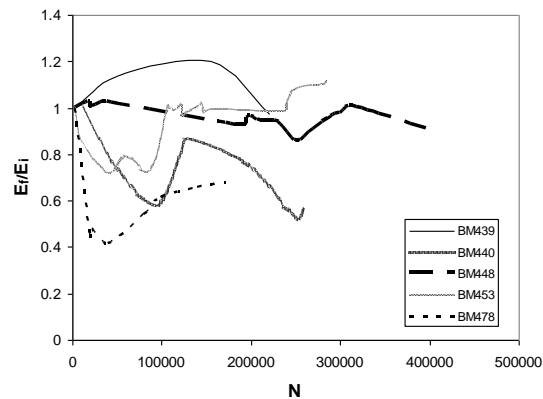
***Figure 4** –Normalized modulus E_f/E_i as a function of the number of cycles, N.*

Figure 5b shows a plot of the normalized modulus versus the age of the patients. As the number of samples is very small we may not take conclusions, but we may state that there is a tendency for a decrease of E_f/E_i with the age. It is possible that the micro-crack density, after fatigue loading, increases with the patient's age, which may lead to a decrease in bone stiffness.
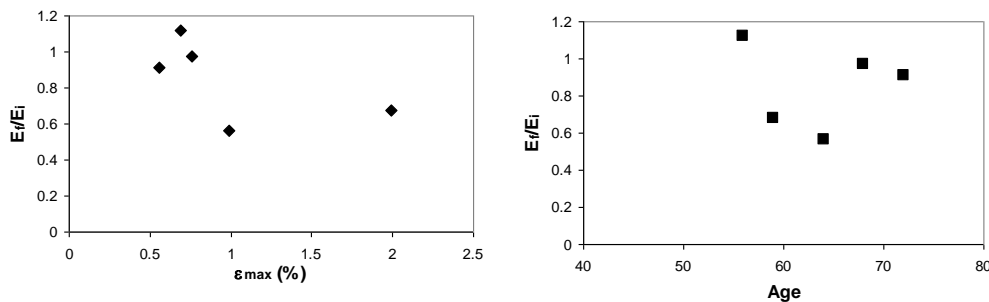
***Figure 5 – a)** Normalized modulus E_f/E_i as a function of a) the maximum strain, ε_{max} and b) the age of the patients.*

Cycling loading of trabecular bone result in highly non-uniform deformations, as evidenced by our SEM observations. We observed several micro-cracks on the same trabeculae which is in accordance with the findings of Green et al. [7], that states that micro-cracks appear more frequently on trabeculae that are already damaged, instead of non-injured trabeculae.

Consistent with the data reported in literature for healthy trabecular bone, the cyclic data for bone with osteoarthritis, showed, in the majority of the cases, progressive decrease of secant modulus and accumulation of strain with an increase in the residual strains. Our results show that at the moment of hip replacement, bones still possess fatigue resistance and could support cycling loading until a certain number of cycles. The major difficulties in fatigue testing are the unknown conditions of number of cycles at different stress and the amount of unrepaired damage accumulated. The repair linked with the remodelling process is hard to establish. These issues are challenges towards the prediction of bone failure and will be the focus of future works.

Acknowledgements

5   References

1] Ganguly, P., Moore, T.L.A., Gibson, L.J., *"A phenomenological model for predicting fatigue life in bovine trabecular bone"*, J Biomech Eng, Vol.126, Num.3, pp.330-339, 2004.

[2] Dendorfer, S., Maier, H., Hammer, J., *"Fatigue damage in cancellous bone: An experimental approach from continuum to micro scale"*, J Mech Beha Biomed Mater, Vol. 2, Num. 1, pp. 113-119, 2009.

[3] Haddock, S.M., Yeh, O.C., Mummaneni, P.V., Rosenberg, W.S., Keaveny, T.M., *"Similarity in the fatigue behaviour of trabecular bone across site and species"*, J Biomech, Vol.37, Num.2, pp. 181-187, 2004.

[4] Moore, T.L.A., Gibson, L.J., *"Fatigue of bovine trabecular bone"*, J Biomech Eng, Vol.125, Num.6, pp. 761-768, 2003.

[5] Moore, T.L.A., Gibson, L.J., *"Fatigue microdamage in bovine trabecular bone"*, J Biomech Eng, Vol.125, Num.6, pp. 769-776, 2003.

[6] Rapillard, L., Charlebois, M., Zysset, P.K., *"Compressive fatigue behavior of human vertebral trabecular bone"*, J. Biomech, Vol.39, Num.11, pp. 2133-2139, 2006.

[7] Green, J.O., Wang J., Diab, T, Vidakovic, B., Guldberg, R.E., *"Age-related differences in the morphology of microdamage propagation in trabecular bone"*, J. Biomech, Vol.44, Num.15,pp. 2659-2666, 2011.

The use of nanomaterials
in the control and prevention of Legionella bacteria

Geraldes, M.J.O.[1], Rodrigues, P.A.F. [1], Belino, N.J.R.[1], Ferraz, C.A. [2], Sousa, S.I.V. [2]

[1]Beira Interior University, Covilhã, Portugal,geraldes@ubi.pt

[2]Porto University, Porto, Portugal

Abstract Legionnaires`disease or legionellosis is an infection caused by a bacteria belonging to the Legionella kind.. The infection caused by Legionella pneumophila presents two differents forms: the Legionnaire`s Disease and the Pontiac Fever wich is a less severe form of the disease. Legionnaire`s Disease has increased over the time due to the use of central air conditioning, affecting population groups that are vulnerable due to the age or due to their health, like insufficient immune systems. So, in places as hospitals (unit intensive care, covers, emergencies), homes, nursing homes, etc, the implementation of preventive measures, as the application of air filters, is fundamental. As the usual filters used in those places are not completely secure, new filters must be developed. New textile materials will be selected and produced as hydrophobic nanofibers, with an appropriate antimicrobial agent incorporated to control Legionella pneumophila. The nano-filter layer should have a good moisture permeability, a good air permeability, and appropriate porosity and thickness.

1   Introduction

The Legionnaire`s disease is a term used to describe all forms of infection caused by bacterias of the genus Legionella. This pneumonia affects 2-5% of exposed persons (1), within 5 to 15% tend to die. Usually is acquired by inhalation or aspiration of Legionella bacteria, from contaminated environments. The inhaled particles must be sufficiently small size, 1-3 micrometres, to penetrate and be retained in the lungs (alveoli), and they can be suspended in the air for longs periods, being designated aerosols particles (2). The severity of the infection caused by Legionella in humans, depends on the type of exposure by the human, the more or less susceptibility, as well the own strain of Legionella.This bacterial infection can be of two types: a less severe called Pontiac Fever, and a severe clinical manifestation called Legionnaire`s disease. This one, in hospitals arises in patients with some health problems like chronic obstructive pulmonary disease (COPD), alcoholism, transplantation or immunosuppression problems. Also, the pacients visitors with certain predisposing conditions may be at risk of contracting the disease (3,4).

Currently, High Efficiency Particulate Air (HEPA) filters are the most used to capture microorgamims in ventilation, filtration and air conditioning systems. However, they are not completly secure. So, new filters should be developed.

2 Objective

The aim of this work is the development of a nanofilter, more exactly a bioactive nanofilter, from a non-woven structure based on hydrophobic fibres, in wich one layer is a nano layer incorporating appropriate biocides to control Legionella pneumophila.

The non-woven industry generally considers nanofibers as having a diameter less than one micron, although the NationalScience Foundation (NSF) defines nanofibers as having at least the dimension of 100 nanometer (NM) or less. Generally, nanofibers are produced through an electrospinning process, wich is a process that produces fibers of diameters from 10nm to several hundred nanometers. The electrospinning process is knowed since 1934 when the first patent on electrospinning was filed. Fibers properties depend of several parameters like: field uniformity, polymer viscosity, electric field strengh and the distance between nozzle and collector (DCD).

3 Methodology

This project involves several steps like:

a) Production of nanofibers by electrospinning process, such as polyester, polyamide, polypropilene and other hydrophobic nanofibers ;
b) Production of a nanofilter from a textile non-woven structure;
c) Selection of the antimicrobiane agent;
d) Incorporation of the antimicrobiane agent in the differents nonwovens textile structures;
e) Experimental laboratory performance evaluation of the produced bioactive nanofilters (microbiological testing and air quality).

The electrospinning process allows to obtain fibers with thickness between 0 and 200 nm. It is a method wich use an electric field to get nano.fibers from a polymer solutiom, being applied a voltage to get a ject of solution to be drawn into the collector panel. By evaporation, the jet forms very thin polymer fibers, wich will be the base of the filter nanolayer (5).

Indeed, the non-woven textile fabrics are used in a great variety of filtration systems, due to its structures, thickness and filtration efficience.

The non-woven stuctures with nano-fibers have advantages relatively to the conventional non-wovens with microfibers used in conventional filtration systems , due to its low frictional forces, lower pressure drop, higher permeability and greater particle capture (6). Another advantage is the increase of interactions between fibers, when compared with fibers processed at a macro scale, since nano-fibers presents a high surface area, increasing the contact between them.

About antimicrobial agents, they must present a large spectrum of antimicrobial activity, and they must prevent infection by pathogenic microorganisms, control the spread of

microorganisms, reduce the formation of odours and be compatible with the textiles structures were are applied (7).

As refered before, the experimental evaluation of the bioactive nano-filters produced will be done trough microbiological testings and air quality, according specifics standards.

4 Conclusions

The textile materials, specially non-woven structures are used in a great variety of filtration systems due the materials, kind of structure and thickness, wich increases the filter performance.

There are a lot of antimicrobial solutions applied in air filtration systems. The HEPA filters are the most widely commercialized in filters ventilation systems and air conditioning.

The ISO 20743:2007 "Determination of antibacterial activity of antibacterial finished products" defines a quantitative method to the determination of antibacterial activity in textiles, including non-woven structures, and it is possible to choose the most appropriate method to evaluate antimicrobial actiivity. Indoor air quality and meteorological parameters are analyzed specialy to evaluate the filter performance with respect to control Legionella, more exactly Legionella pneumophila.

This work is still at an early stage, but we believe in the efficiency of these new bioactive nanofilters.

5 References

(1) Brief, R., & Bemath, T.," Indoor Pollution :Guidelines for Prevention and Control fo Microbiological Respiratory Hazards Associated with Air Conditioning and Ventilation Systems, 3 (1), 5-10;

(2) The determination of Legionella bacteria in water and others environmental Samples – Part 1 –Ratinale of surveying and sampling. Environment Agency, 2005;

(3) Armstrong, T. W., & Haas, C. N., " Legionnaires disease: evaluation of a quantitative microbial risk assessment model", Journal of Water and Health, 2008;

(4) Comission for occupacional safety and health. CODE OF PRACTICE PREVENTION AND CONTROL OF LEGIONNAIRES DISEASE, 2010;

(5) Rodrigues, P. A. F., Sousa, S. I. V., Geraldes, M. J., Alvim-Ferraz, M. C. M. , Martins, F.G., " Bioactive Nano-filters to Control Legionella on I door Air", Advanced Materials Research,vol 506, pp 23-26, 2012;

(6) Igwe, G. J.,, " Surfaces structures of Needle-Felted Gas Filter. New York: Ellis Horwood Limited, 1988,

(7)   Michielsen, S., "Surface Modification of fibres via graft-side amplifying polymers". Geprgia Institute of Tecnhology, pp. 41-45, 2004.

Evaluation of Hysteretic Behavior of Eccentrically Braced Frames With Zipper-Strut Upgrade

Seyed Mehdi Zahrai[1], Milad Pirdavari[2], Hamid Momeni Farahani[3]

[1]*Associate Professor, Center of excellence for Management and Engineering of civil Infrastructures, Department of Civil Engineering, Faculty of Engineering, The Univ. of Tehran, P.O.Box 11365/4563 Tehran, Iran*

[2] *Department of Civil Engineering, Azad University, Central Tehran Branch, Tehran, Iran*

[3] *Department of Civil Engineering, Amir Kabir University, Tehran, Iran*

Abstract This paper describes the seismic behavior of the upgraded eccentrically braced frames (EBF) using zipper-struts which connect the mid-point of shear links in all stories. By adding zipper struts to the conventional EBF system, the unbalanced shear force is distributed among all stories due to the added continuity between shear links. This results in the extension of the structure's displacement capacity in Immediate Occupancy and Life Safety acceptance criteria. Moreover, a noticeable delay occurs until shear links experience enough rotation to meet Collapse Prevention acceptance criteria. Consequently, the structure may experience higher levels of displacement in comparison to the conventional EBFs.

The numerical modeling of the zipper-strut-equipped model is conducted using finite-element method software and the hysteretic behavior of the system is analyzed under cyclic load, with the goal of evaluating the continuity of the rotation between shear links, along with close observation of shear behavior of the links throughout the steps of the analysis. The hysteretic response of the upgraded EBF system is compared to that of a similar prototype without the new modification. The interaction of shear link and zipper-struts are also studied in this paper. Furthermore, the prototypes are subjected to nonlinear static (Pushover) analysis in two configurations; one with moment-resisting connections and one with pinned connections. The acceptance criteria of these structures are studied and the extension of these zones is determined. Finally, the increase of ductility coefficient for the prototypes with zipper-strut is observed, which is calculated in accordance with the maximum displacement of the structure at Collapse Prevention stage.

Joining technologies for hybrid materials consisting of sheet metal and carbon fibre reinforced plastics

C. Lauter[1], M. Sarrazin[1], T. Troester[1]

[1] *University of Paderborn, Chair for Automotive Lightweight Construction (LiA), Pohlweg 47-49, 33098 Paderborn, Germany, christian.lauter@uni-paderborn.de*

Abstract The attempt for enhanced security, lean production and the need for a more economical consumption of resources during the process of production and operation of automobiles require new approaches and new solutions in lightweight construction. One promising approach is the combination of sheet metal and fibre reinforced plastics (FRP) to form hybrid structures. Here, the wall thickness of the metallic structure is reduced and afterwards a local FRP reinforcement is applied to heavily loaded sections of the construction. In this way it is possible to produce load-adapted lightweight structures that are up to 35 % lighter than mere steel solutions.

Current research work within the scope of a collaborative research project at the Chair for Automotive Lightweight Construction (LiA) at the University of Paderborn concentrates on the investigation of hybrid materials and their processing. In particular, new manufacturing processes like the prepreg press technology are developed to make hybrid components attractive and available for automotive mass production. This includes, for example, trimming process chains, reducing cycle times and thus a reduction of process steps and costs. This is amongst other things realised by using the epoxy matrix resin as an adhesive.

Current research results in the field of hybrid materials are presented in this paper. First, the prepreg press technology to manufacture automotive structural components in hybrid design is illustrated. In particular the advantages of this technology compared to conventional processing methods for FRP are highlighted, such as a reduction of cycle times from more than 15 minutes to below 5 minutes. Afterwards the joining of the steel and the FRP component by the use of the epoxy matrix resin as an adhesive is discussed. The bonding was investigated on the basis of relevant standards and various influences on the bond strength, such as different surface treatments, curing times and temperatures. In addition, results for the bond strength are compared to a typical epoxy-based crash-stable adhesive for automotive applications. It is shown that the bond strength of conventional prepreg epoxy matrix resins reaches over 90 % of the strength of structural adhesives for quasistatic shear tensile loads. Besides a significant reduction of costs could be realised by skipping an additional bonding process. Hereafter it is pointed out that the orientation of fibres in the boundary layer has a decisive influence on the bond strength of prepreg pressed samples. Finally, appropriate solutions and design informations are proposed.

1 Introduction

Due to economical and ecological constraints the development of lightweight concepts becomes extremely important. These apply in particular to developing crash-relevant structures. In addition, the automotive industry must develop innovative and integral approaches for lightweight construction to meet future regulations in climate protection. For example, by reducing the vehicle weight by 100 kg, a reduction of CO_2 emissions of about

8.5 g/km respectively a reduction of fuel consumption of about 0.3 l/100 km can be realised. Nevertheless the average weight of automobiles increased over the past years mainly because of safety and comfort requirements.

Currently, there are three main trends in automotive lightweight construction: The use of high-strength metal alloys, substituting metals by composites, and the combination of hybrid materials. By using high-strength metal alloys the wall thickness of structures can be reduced. However, once a critical minimum thickness is reached designers can expect stability problems. Thus, the potential of high-strength materials for lightweight construction is limited. The second approach: substituting conventional construction materials by carbon fibre reinforced plastics (CFRP) allows considerable weight savings [1] [2], but is restricted to high-priced vehicles because of long cycle times and high material costs. Hence, structural components realised in multi-material design are an interesting alternative [3] [4]. In this context, the manufacturing of components consisting of sheet metal blanks made of steel with a local CFRP reinforcement is being investigated. These hybrid structures should allow manufacturers to produce safety-relevant vehicle components, such as b-pillars, at lower costs compared to components made of mere CFRP [5] [6].

2   Hybrid structures: sheet metal with local FRP reinforcements

Hybrid materials consist of a sheet metal basic layer, a locally applied fibre reinforced plastic (FRP) reinforcement layer and an optional sheet metal covering layer. The layered structure offers the possibility to tailor components to their expected loading (Figure 1).
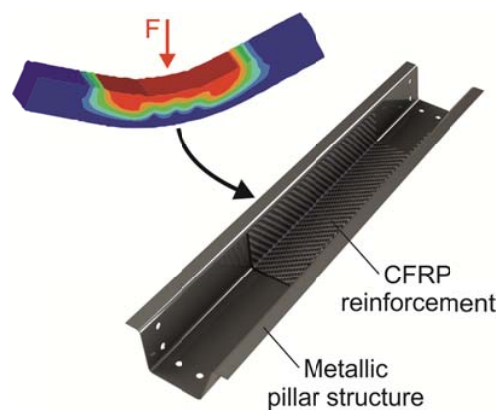
Figure 1 - *Tailored hybrid pillar structure consisting of sheet metal and local CFRP reinforcement*

Such tailored structures do not only bear a high potential for lightweight design but also show an optimised use of the expensive FRP materials, which finally leads to cost-optimized lightweight constructions. Amongst others press hardened steels can be used as sheet metals. Due to the FRP reinforcements, the wall thickness of the steel parts can be reduced. Hybrid components can easily be integrated into existing processes of vehicle production, because their metallic surface enables the use of conventional joining technologies like spot welding or clinching. The integration into existing body constructions is also possible because of the metallic basic structuce.

3 Prepreg press technology

The prepreg press technology is one approach to produce hybrid structural automotive parts in large volumes. The process can be divided into four main parts (Figure 2). First, prepregs (pre-impregnated, semi-finished fibre products) are produced continuously on special machines and shipped on coils. The layer structure is realised according to the expected loads in the component, for example a b-pillar. The laminate is cut corresponding to the later structure geometry. Second, a robot handles the prepregs. After inserting an already formed steel structure into a heated steel tool, the prepreg is applied to the steel structure by automated handling. Then the tailored prepreg is pressed onto the sheet metal by a heated punch. As the epoxy resin functions as an adhesive the joining of sheet metal and CFRP is realised in this third step, too. After a pre-curing of about 90 to 120 seconds, depending on the thickness of the prepreg, the hybrid component is removed by a robot and stacked. The post-curing of the components is realised during a downstream cataphoretic painting process.
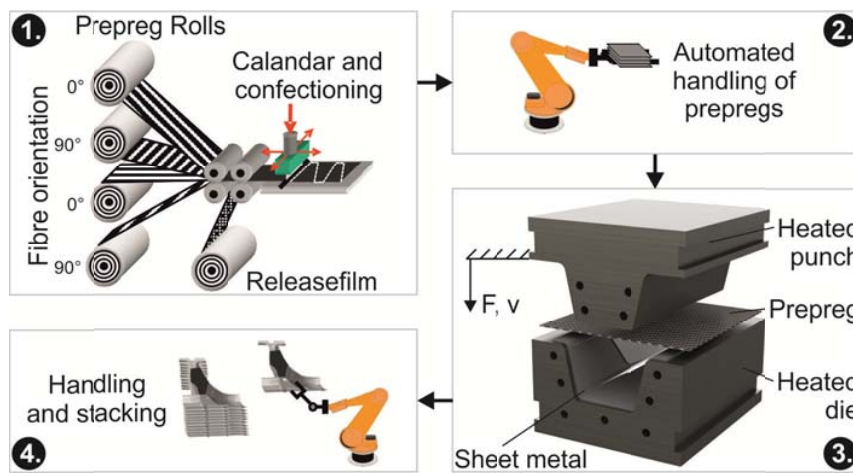
Figure 2 - *Process steps for prepreg-pressing to produce hybrid automotive structural parts, for example a b-pillar*

4 Materials and testing methods

The joining technology between CFRP and sheet metal is a decisive factor for the functioning and strength of hybrid materials. In order to characterise the joining properties single lap-shear specimens were investigated accoring to DIN EN 1465:2009. For the investigation four different joining technologies were used: a) epoxy resin matrix as adhesive, b) adhesive Dow Betamate 1620, c) blind rivets and d) thread cutting screws (Figure 3).
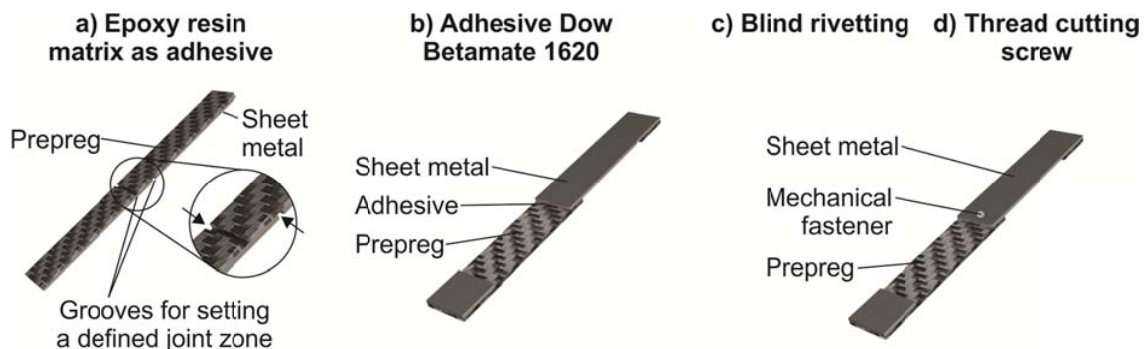
Figure 3 – *Sample geometry for different joining technologies*

The samples constisted of sheet metal and CFRP. For the metal component a S235JR with a thickness of t = 2 mm was used. The prepregs were standard semi-finished products from SGL. The epoxy resin from SGL (Type E201) embeds carbon fibres in a symmetric 9 layer bidirectional scrim (0/90/0/90/0/90/0/90/0°). The prepregs were manufactured by prepreg press technology as descirbed in chapter 4. For the bonding with epoxy resin as an adhesive the prepreg was directly pressed on the metallic surface. The CFRP of the samples joined by Dow Betamate 1620, blind rivetting (Gesipa PolyGrip 6.4 x 15 mm) and thread cutting screws (DIN 7513 M4 x 10 mm) were first pressed and cured. Afterwards the CFRP was joined onto the sheet metal.

To find an optimum solution of the conflict between economical aims and the strength of the joint time and temperature for consolidation during the prepreg-press process was varied according to the reaction-velocity temperature rule (Arrhenius equation). The temperature was varied between 120 °C and 200 °C. The prepreg-pressed samples were compared with adhesive-bonded samples and the influence of different types of surface treatment was investigated.

5   Results

A comparison of maximum force and tensile energy absorption of the different joining technologies is shown in figure 4. The epoxy resing matrix reaches slightly smaller values than the Dow Betamate for both parameters. The advantage of the use of the epoxy resin as an adhesive is, that the complex and cost intensive joining process can be omitted. The values for the mechanical fasteners are significantly worse because of high stress concentration at the joining element. This leads to failure of the CFRP.
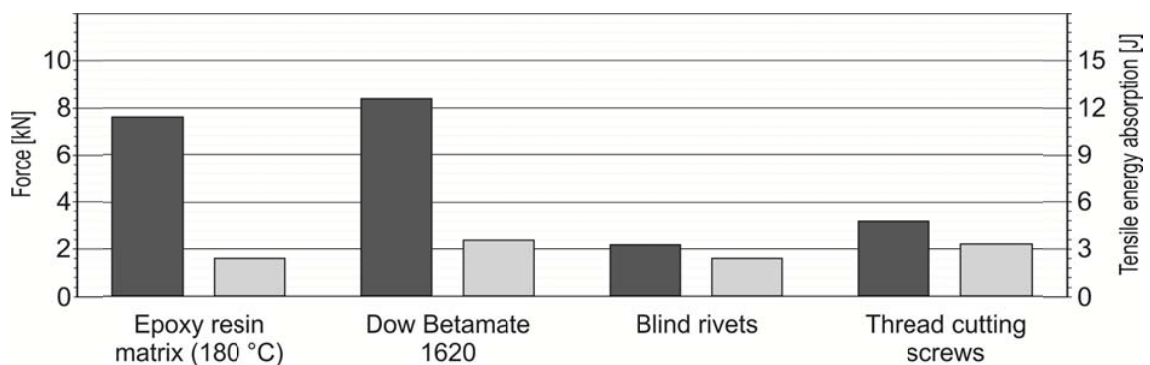
Figure 4 *– Comparison of maximum force and tensile energy absorption of different bonding technologies for hybrid structures*

The analysis of failure behaviour of the different bonding technologies showed some characteristics (Figure 5). While for the pressed samples failure occurred in between the boundary layer and the second fibre layer of the CFRP, the adhesive-bonded samples failed due to delamination of the first fibre layer. The joint area itself remained undamaged. The mechanical fasteners were predominantly pulled out of the CFRP component.

| Epoxy resin matrix (180 °C) | Dow Betamate 1620 | Blind rivets | Thread cutting screws |
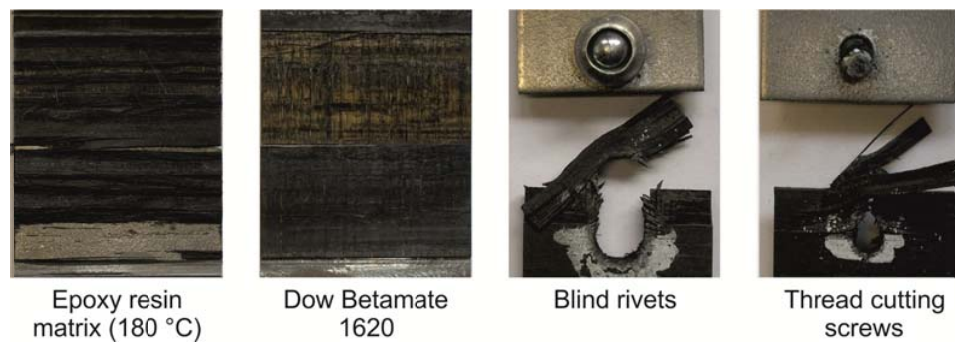
Figure 5 – Characteristic failure behaviour of different bonding technologies

The fibre orientation of the boundary layer had the greatest influence on the properties of the joint (Figure 6). Samples with fibres vertical to the direction of loading (90°) had the highest strength. The elastic matrix material dominated the mechanical properties close to the boundary layer. The fibres only bear a small part of the load. Thus, the laminate can absorb local tension peaks like a bond line. Samples with fibres parallel to loading, in the contacted layer, failed with 75 % of the load applied.

Adhesive: epoxy resin (SGL, Type E201); CFRP-Prepreg: 9 layer; steel-surface: oiled; temperature: 180 °C; time: 210 s (EP)

| $\alpha = 0°$ $\tau_K = 18{,}1$ MPa | $\alpha = 45°$ $\tau_K = 14{,}3$ MPa | $\alpha = 90°$ $\tau_K = 24{,}2$ MPa |
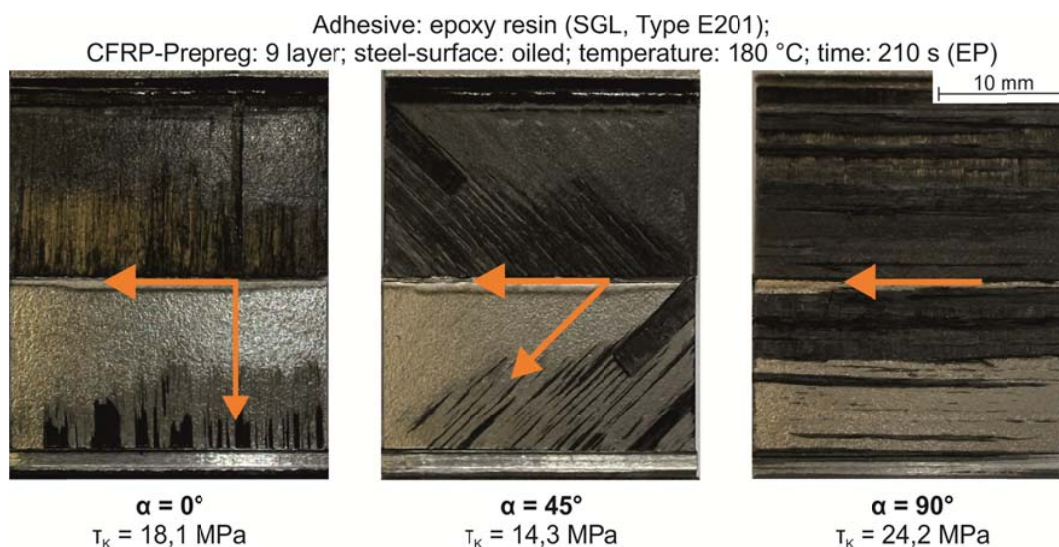
Figure 6 – Influence of fibre orientation of the contacted layer on the bond strength

The inhomogeneous structure of CFRP is reflected in the properties of the joint. Special properties of such materials need to be considered in the design of hybrid structures in order to achieve the intended properties of the compound.

6   Conclusions

Hybrid structures consisting of sheet metal and fibre reinforced plastics offer a major potential for lightweight design in the automotive industry. The prepreg press technology allow a significant reduction of process steps as well as process time. By using prepreg-press-technology CFRP prepregs are formed into steel structures. In the paper four different bonding technologies were investigated. For hybrid structures joining technologies promise the greatest benefit. The joining can be realised for example by the use of a structural adhesive or by the use of the epoxy resin as an adhesive. The adhesive bonded samples reaches a sligtlhy better performance under quasistatic loads. On the other hand the advantage

of the use of the epoxy resin as an adhesive is, that the complex and cost intensive joining process can be omitted. These cost savings might be more interesting for large volume processing.

7 Acknowledgements

8 References

[1] A. Horoschenkoff, "Statt Stahl und Aluminium", Kunststoffe, Num. 5, pp. 50-54, 2010

[2] D. Lutz, "Chassis lightweight design exemplified on a suspension strut – State of the art and potential", 11th Aachen Colloquium Automobile and Engine Technology, Aachen, pp. 437-455, 2002

[3] Gu. Kopp, R. Schöll, Ge. Kopp, "Neuartige Leichtbau-Fahrzeugkonzepte durch Hybrid3-Strategie", Lightweight Design, Num. 1, pp. 36-40, 2008

[4] H. Al-Zubaidy, R. Al-Mahaidi, X.-L. Zhao, "Experimental investigation of bond characteristics between CFRP fabrics and steel plate joints under impact tensile loads", Composite Structures, Vol. 94, Num. 2, pp. 510-518, 2012

[5] F. Möller, C. Thomy, F. Vollertsen, P. Schiebel, C. Hoffmeister, A. S. Herrmann, "Novel method for joining CFRP to aluminium", Physics Procedia, Num. 5, pp. 37-45, 2010

[6] J. G. Broughton, A. Beevers, A. R. Hutchinson, "Carbon-fibre-reinforced plastic (CFRP) strengthening of aluminium extrusions", International Journal of Adhesion and adhesives, Vol. 17, Num. 3, pp. 269-278, 1997

Evaluation of Modelling Capability of K-PAW Fabrication of Thin Structures of Titanium Alloy

W. Sun[1], M.B. Mohammed[1], L. Xu[1], T.H. Hyde[1], D.G. McCartney[1] and S.B. Leen[2]

[1]*Department of Mechanical, Materials and Manufacturing Engineering, University of Nottingham, University Park, NG7 2RD, UK, W.Sun@nottingham .ac.uk*

[2]*Department of Mechanical and Biomedical Engineering, Nun's Island, National University of Ireland, Galway, Republic of Ireland, Sean.Leen@nuigalway.ie*

Abstract The predictions of distortions and residual stresses are of great significance in welded structures. This is because distortions can lead to unacceptable levels of inaccuracies while residual stresses can trigger in-service defects. Both distortions and residual stresses are subject to the evolution of thermal strains in the regions near the molten/weld pool during welding and cooling. Therefore, the prediction of thermal histories is essential. On the other hand, dividing the weld bead into several seams that are welded sequentially is one of the most cost effective and easy to implement distortion and residual stress mitigation strategy in the robotic welding industry. However, the determination of the sequence by which these seams are welded is challenging due to the large number of possible options. Therefore, a fully automated optimization tool is needed to solve this combinatory problem. This paper reports a comprehensive piece of research work focused on the development, validation and application of finite element (FE) modelling capability for the prediction and optimization of robotic keyhole plasma arc welding (K-PAW) of titanium-based (Ti-6Al-4V) thin structures.

1   Introduction

Distortions and residual stresses are major concerns in welded structures [1]. This is because distortions can lead to unacceptable inaccuracies, particularly in thin structures, while residual stresses can trigger in-service defects [2]. The evolutions of both distortions and residual stresses are directly influenced by the thermal strain variations resulting from shrinkage during cooling [3, 4]. Therefore, distortions and residual stresses mitigation strategies are based on counter-acting these shrinkage effects [5, 6]. These mitigation strategies are generally categorized into design-related, such as weld joint details and mechanical clamping, and process-related, such as welding torch travel speed and heat input. In practice, combinations of both strategies are implemented. The experimental characterization of the optimum set of design-related and process related strategies requires very lengthy lead times and most importantly is extremely costly. Therefore, the finite element modelling of welding processes is of crucial importance in characterizing design and candidate process parameters and reasonably approximating their limitations. However, experimental investigations are initially required to develop the finite element FE model and assess the accuracy of its predictions.

Dividing the weld bead into several seams that are welded sequentially in a specific order is one of the most cost effective and practical distortion and residual stress mitigation strategies in the robotic welding industries [6]. This is because its implementation cuts on costs associated with additional process arrangements as it only requires coding the optimum

welding sequence into the welding robot control system. However, determining the optimum welding sequence requires solving the combinatory problem associated with the large number of possible options resulting from rearranging the orders and directions of seams. Investigating all possible sequence options also requires very lengthy times which makes it substantially expensive. Therefore, welding industries tend to opt for small improvement and abandon the search for the ultimate optimum welding sequence. However, the effectiveness of the search for an optimum welding sequence can be significantly improved via the implementation of a suitable optimization algorithm.

The potential for the application of keyhole plasma arc welding (K-PAW) process in the fabrication of the sophisticated aero-engine structures is very promising. This is because K-PAW process has a relatively high power density closer to those in laser and electron beam welding processes while K-PAW process is more cost effective and more tolerant of joint preparation [7]. The heat input required to establish the keyhole welding mode in plasma arc welding process is achieved by forcing plasma arc though a fine-bore nozzle at high velocities and high temperatures. The challenge in K-PAW process is however the determination of the process parameters envelops for stabilizing the keyhole welding mode. There are three primary process parameters in total, being transverse speed, current and plasma gas flow rate (PGFR) [8]. The determination of these envelops requires initial experimental investigations which can then be complemented by the use of FE and/or analytical models.

This paper reports a comprehensive piece of research work on the experimental and computational investigations that were carried out to characterize, develop, optimize and validate numerous aspects of the FE modelling of K-PAW process of typical aero-engine titanium-based (Ti-6Al-4V) thin structures. The experimental investigations include the determination of K-PAW processes parameters envelops using robotic welding facilities and the measurements of thermal histories, distortions, residual stresses, weld pool and heat affected zone (HAZ) dimensions. Several thin structures and welding methodologies were exploited in the course of these experimental investigations. The computational investigations on the other hand, include the development and validation of a full 3D FE models using the welding-specific commercial software SYSWELD as well as the development and validation of a fully automated welding sequence optimization tool using genetic algorithm approach that was integrated with FE in a MATLAB platform. Finally, the application of the developed FE modelling capability in the fabrication of a typical thin aero-engine Ti-6Al-4V structure is demonstrated.

2   Robotic KPAW Process of Thin Ti-6Al-4V Structures

The K-PAW process was carried out using the six-axis robotic system in Figure 1 – (a) in order to maintain the welding processes consistency and to demonstrate the suitability of K-PAW process in the demanding robotic welding industry. The plasma arc welding torch assembly was mounted on the robot wrist and consisted of a non-consumable tungsten electrode, an inner constricting nozzle, an outer shielding nozzle, and gas flow systems, as shown in Figure 1 – (b). The plasma gas passes through the constricting nozzle and couples with the arc generated by the electrode to generate the constricted plasma arc beam [9]. The shielding gas protects the weld pool from oxidation [10].

(a)   (b)
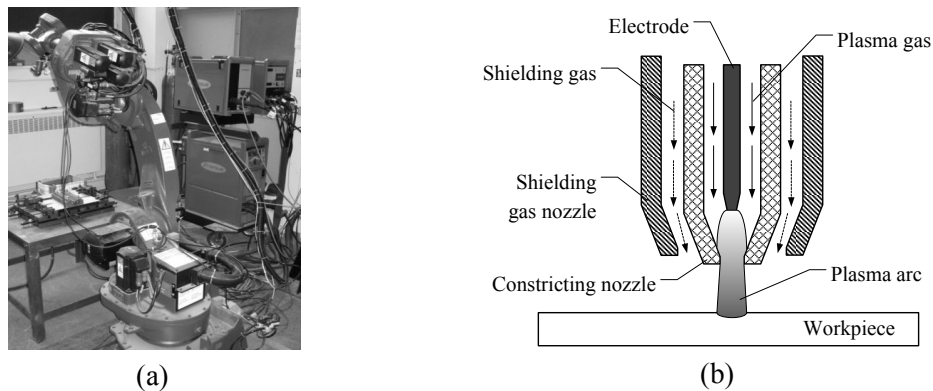
Figure 1 *- (a) Robotic K-PAW Kit (b) Schematic of K-PAW torch in operation*

Three thin Ti-6Al-4V structures were welded using the robotic K-PAW arrangements described above to develop and validate the K-PAW FE modelling capability, being the flat plate, flat T-joint and curved T-joint, as shown in Figure 2. These structures were all cut from the same batch of 2.1 *mm* thick standard Ti-6Al-4V industrial sheets.

(a)   (b)

(c)
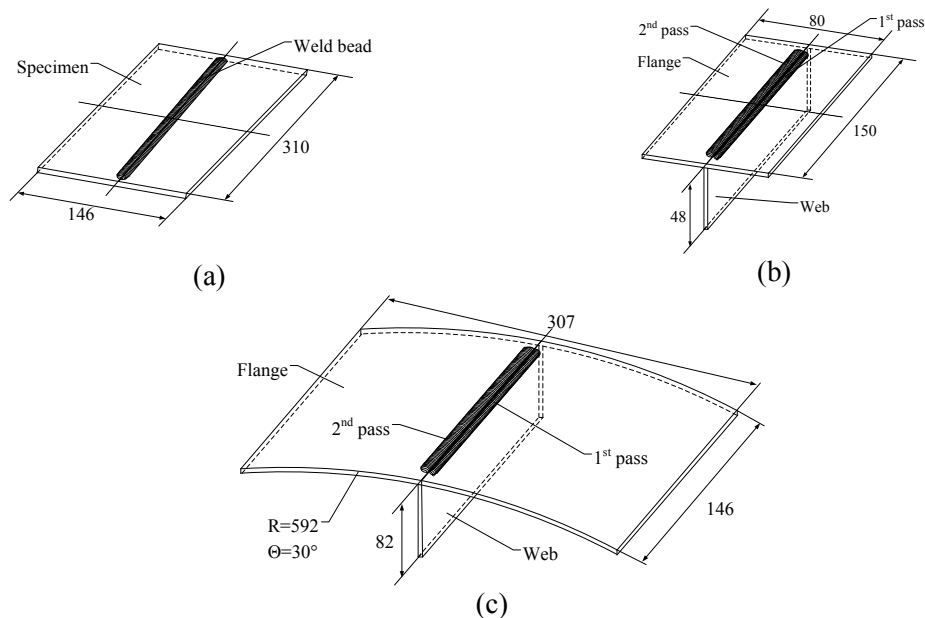
Figure 2 *– Welded Ti-6Al-4V thin structures (a) flat plate (single pass) (b) flat T-joint (2-parallel passes) (c) curved T-joint (2-parallel passes)*

2.1   Keyhole Welding Mode Parameters Envelop

There are three primary parameters in the K-PAW process that determines the heat input rate required to stabilize the key-hole welding mode. These parameters are current, transverse speed and PGFR. Identifying the field envelope for these parameters is of significant importance from structural integrity point of view as excessing or lessening the heat input rate compromises the weld joint integrity as a result of over-penetration or partial-penetration, respectively (Figure 3). The field envelope for these primary K-PAW process parameters were characterized experimentally by systematically varying these parameters and examining their effects on the persistence of the keyhole welding mode. The welding of the thin plate structure shown in Figure 2 – (a) was used for the purpose.
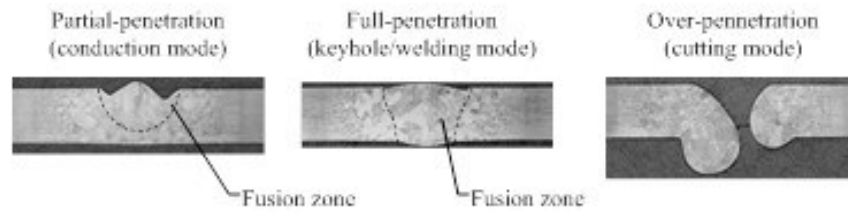
Figure 3 - Weld modes in plasma arc welding

2.2   Experimental Measurements and Characterisations

A number of measurements and characterizations techniques were implemented to support the experimental work as well as the development and validation of the FE modelling capability. These include optical microscopic investigations by which the dimensions of the molten and heat-affected zones were determined. The thermal history was also captured by recoding the change in temperature with time during welding and cooling stages using type-K thermocouples. The distortions induced by the welding process were measured using a three-dimensional coordinate-measuring machine (CMM) in which the coordinates of the thin structures are accurately scanned using a contact probe before and after welding [11]. Finally, the residual stresses were measured using synchrotron X-ray diffraction technique in which the strains induced by the residual stresses are measured at crystallographic planes levels. These strains are then used to evaluate the nature and magnitude of these residual stresses [12].

3   FE Modelling of K-PAW of Thin Ti-6Al-4V Structures

The FE modelling was carried out using the full 3D brick elements available in the welding specific FE software SYSWELD. The heat input and distribution from the welding torch was modelled using the 3D conical Gaussian heat source function shown in Figure 4 and described by Equ 1 in which Q is the total heat flux, Q_0 is the maximum heat flux, r_e is the radius of the fusion zone on the welding torch side (z_e) and r_i is the radius of the fusion zone on the opposite side of the welding torch (z_i). The clamping conditions were defined by constraining the three velocity components (Ux, Uy and Uz) of the nodes in the clamped areas on the thin structures. Heat transfer by convection and radiation were also accounted for as presented in the work of Deshpande *et al.* [13].
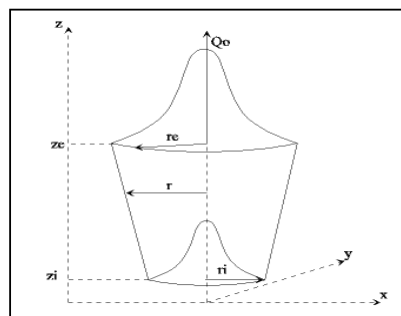
Figure 4 – 3D heat source function for heat input and distribution from welding torch

$$Q\left(x, y, z\right) = Q_0 \exp\left(-\frac{x^2 + y^2}{r_o^2}\right), \; r_o = r_e - \left(r_e - r_i\right)\left(\frac{z_e - z}{z_e - z_i}\right) \qquad \textit{Equ 1}$$

A very thin layer (0.25 mm thick) of "chewing gum elements" was defined at the adjoining surfaces of the welded structures as illustrated in Figure 5. These chewing gum elements have no stiffness, hence the name, and it undergoes transition from the no stiffness state to the state of taking on the mechanical behaviour of the Ti-6Al-4V once their temperature exceeds the melting point. This allows for the representation of the local mechanical interlocking between the welded structures as a result of the occurrence of fusion.
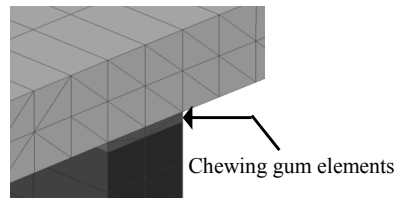
Figure 5 – *Chewing gum elements for representation of welding at adjoining surfaces*

4   Optimization of Welding Sequence

Genetic algorithms (GA) was coded in MATLAB to search for an optimized welding sequence using the mechanics of natural selection and natural genetics developed by Goldberg [14]. The welding seams for a given welding process were defined as a string of genes that can undergo evolution by means of cross-over and mutation operations as illustrated in Figure 6 below. A number of boundary conditions and checks were however defined in the optimization code in order to ensure solutions feasibility, e.g. the number of seams/genes. The FE software was used to evaluate the optimized solution in every optimization iteration by integrating it into GA. This integration was also developed in MATALB platform as shown in Figure 7.
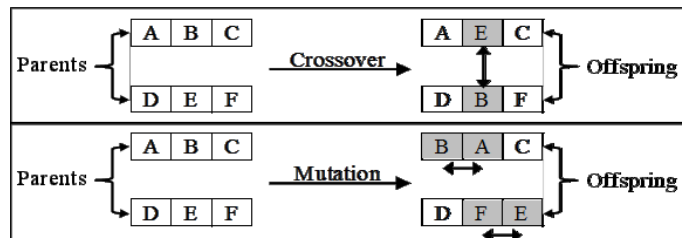
Figure 6 – *Genetic evolution operations in optimization using genetic algorithm*
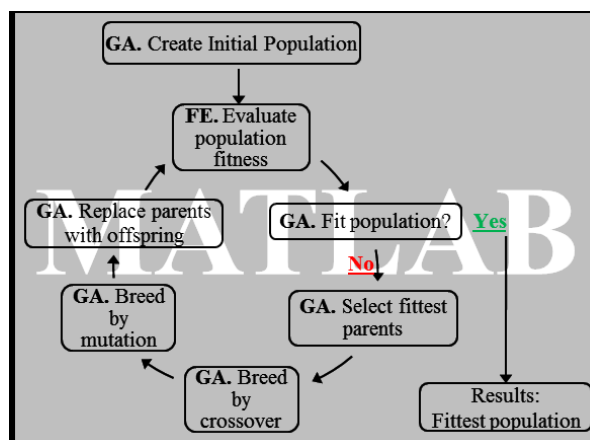
Figure 7 – *Principles of seams welding sequence optimization using genetic algorithm*

5   Results and Discussions

The primary K-PAW process parameters, i.e. current, transverse speed and PGFR, envelop was characterized by systematically varying the values of these parameters. For example, Figure 8 – (a) shows the field envelop for transverse speed and current at a constant PGFR of 1.0 l·min⁻¹. The variations in the microstructural characteristics in the specimens used in investigating the parameters envelop were then used to determine the dimensional profiles of the fusion and heat-affected zones using optical microscopy as shown in Figure 9. This information was used in conjunction with the values of Ti-6Al-4V melting temperature (1650˚C [15]) to develop and validate the 3D conical Gaussian heat source function described previously in Figure 4 and Equ 1. The validation of the heat source function is demonstrated in the experimental/FE comparison of the fusion and heat affected zones dimensions shown in Figure 9. This development in the heat source function definition was then utilized to complement the process parameters field envelop investigation of the 2.1 mm thick Ti-6Al-4V plates as shown in Figure 8 – (b).

(a)   (b)
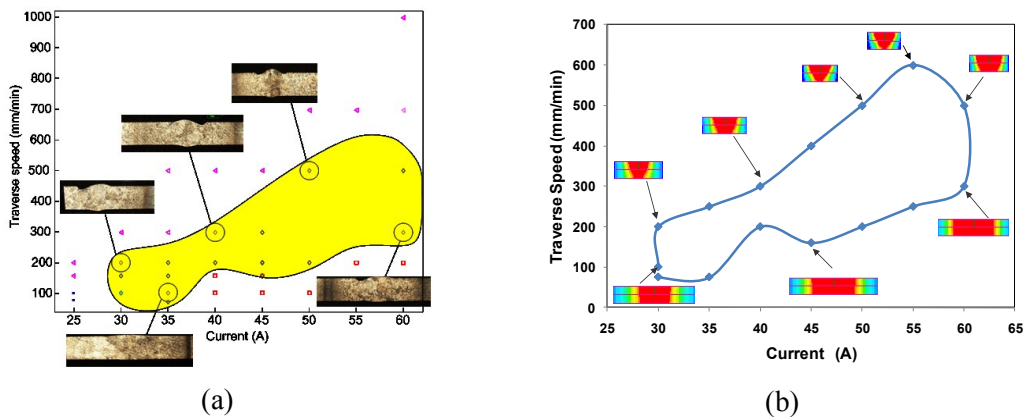
Figure 8 – Investigation and validation of K-PAW process envelop for 2.1 mm thick Ti-6Al-4V plate (a) experimental (b) numerical (FE)
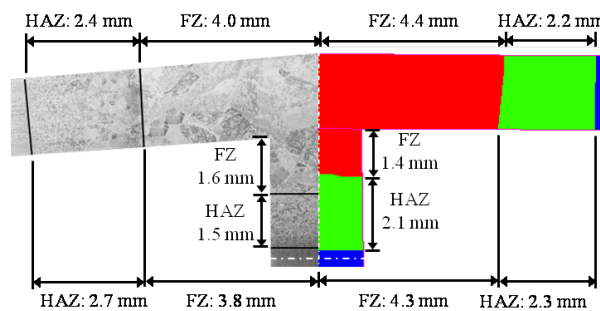
Figure 9 – FE calibration of heat source function using microstructural characteristics

Three temperature histories were measured during the welding of the flat plate using type-K thermocouples that were positioned at approximately 4, 4.5 and 5 mm (TC1, TC2, TC3, respectively) from the centre of weld pool (Figure 10 – (a)). Figure 10 – (b) demonstrates how well the measured and FE predicted temperature histories are in agreement for TC3 in this case. This improved the confidence over the heat source developed above and in the FE predictions of thermal induced strains which are the key in the evolutions of distortions and residual stresses.
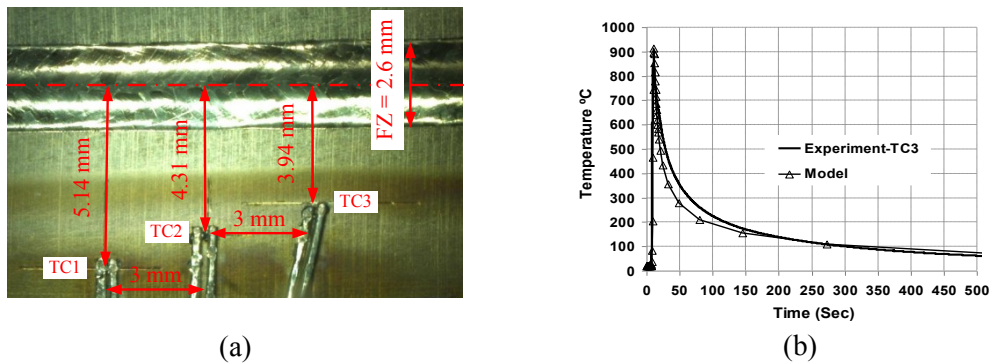
(a)   (b)

***Figure 10** – (a) Experimental (b) Measured and FE predicted temperature histories*

Figure 11 – (b) shows a comparison between the distortion on the front edge of the curved T-joint extracted from CMM measurements (Figure 11 – (a)) and FE predictions. It is evident from the figure that the predicted distortion trends are in very good agreement with the measured ones; however, there are variations in the magnitude of distortions. These variations are very likely to be as a result of the incomprehensive set of mechanical properties available for Ti-6Al-4V which is planned to be addressed in future developments.

(a)   (b)
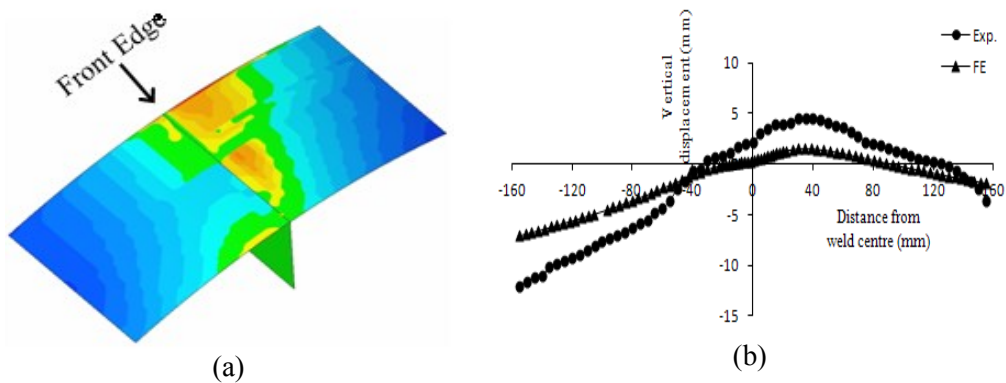
***Figure 11** - (a) Experimental (b) Comparison of measured and FE predicted distortions*

The residual stresses predicted by the FE models are also in very good agreement in terms of both trends and magnitudes with the experimentally measured ones in the region near the fusion and heat-affected zones as can be seen in Figure 12 – (b).

(a)   (b)
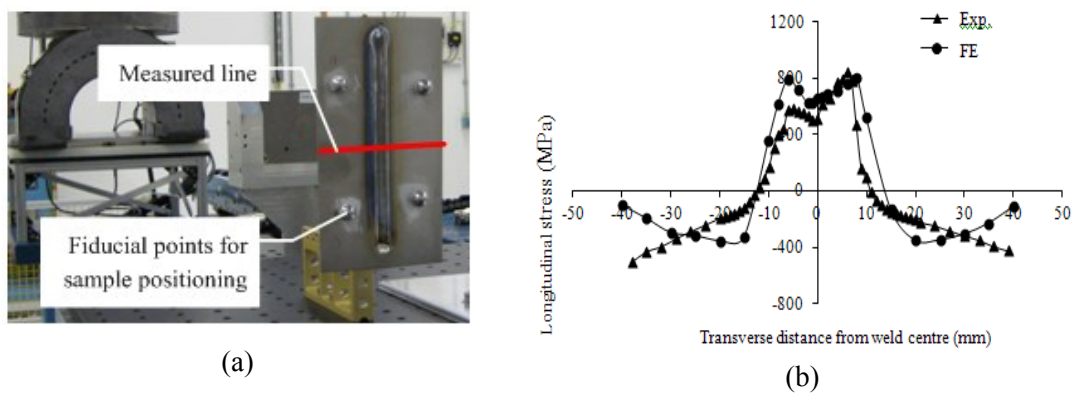
***Figure 12** - (a) Experimental (b) Measured and FE predicted residual stresses*

Figure 13 – (b) shows an example of the results obtained from the optimization procedure described in section-4 above for the 4-seams welding sequence problem shown in Figure 13 – (a). Both the order and the direction of the seams can change in this problem resulting in a total of 192 possible welding sequence options. The optimization procedure was able to identify the second best optimum welding sequence (+1 -4 -2 -3) in the 6th iteration as shown in Figure 13 – (b). This resulted in minimizing distortions by about 70% by investigating only about 3% of all possible welding sequence options.

(a)   (b)
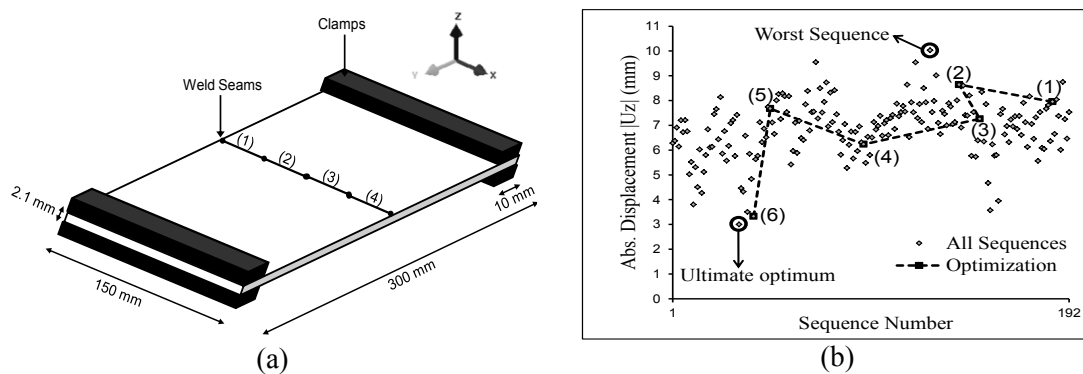
Figure 13 – *4-seams welding sequence optimization problem (a) problem definition (b) optimization results*

6   Application of K-PAW FE Modelling Capability

The simplified replica of a Ti-6Al-4V aero-engine casing shown in Figure 14 – (a) was developed to demonstrate a typical application for the K-PAW FE modelling capability developed in this comprehensive piece of research work. As can be seen in the figure, this aero-engine casing replica is composed of 12 identical portions. The welding scenario is that each portion has 4 seams as shown in Figure 14 – (b). The aim is to minimize distortion in the entire casing structure (global optimization) by minimizing the distortion in each of the portions (local optimization). This can be achieved by optimizing the 4-seam welding sequence problem for each portion using the GA optimization procedure.

(a)   (b)
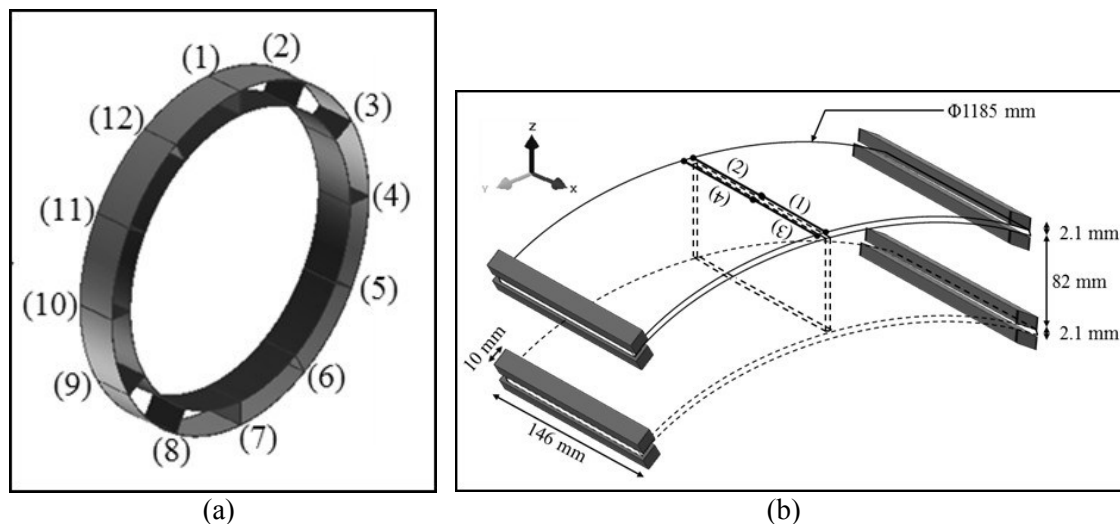
Figure 14 – *Simplified replica of an aero-engine casing structure (a) global (b) local*

The results of the optimization for the simplified replica of a portion of an aero-engine casing are shown in Figure 15 – (a). The optimum welding sequence (+1 -4 +2 -3) was identified in the ninth iteration and produced a maximum distortion of 1.27 mm. Identifying an optimized welding sequence in the ninth iteration implies that about 98% of time required for the FE modelling of all possible welding sequences (384 sequences) was saved while achieving about 40% reduction in welding induced distortion. Figure 15 – (b) shows the global casing distortion which has been optimized by optimizing the distortion in the local structure.

(a)   (b)
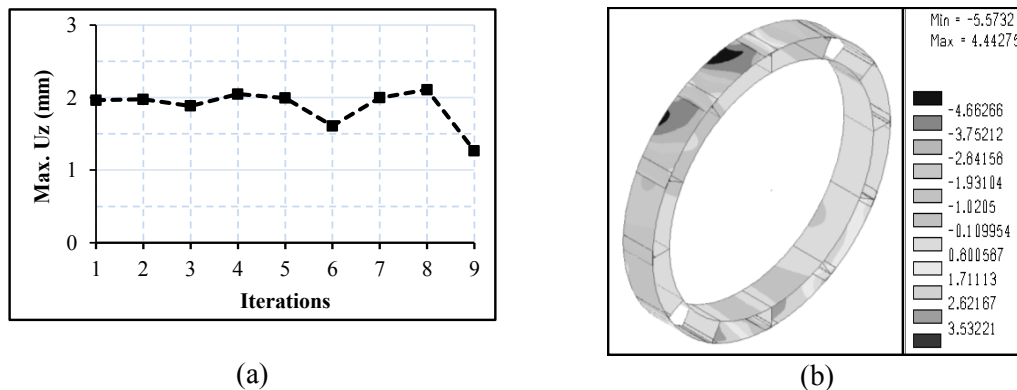
Figure 15 *– (a) Optimization results (b) Global distortion*

7   Conclusions and Future Work

This paper reported a comprehensive piece of experimental and computational based research work on the development of a finite element modelling capability for the prediction and optimization of K-PAW process of thin (2.1 mm) Ti-6Al-4V structures. FE predictions include temperature histories, distortions, residual stresses and the dimensions of the fusion and heat affected zones. The FE predictions of the aforementioned behaviours were in very good agreement with the experiments. Slight differences in trends and values have appeared in the predictions of distortions and residual stresses; however these are possibly due to the incomprehensive set of the mechanical properties available for the titanium-based Ti-6Al-4V alloy. The improvement in these FE predictions is anticipated to greatly enhance predictions of in-service behaviours of such fabricated structures. Moreover, it is anticipated to enhance the design of the process and relevant post-welding processes such as heat treatments.

On the other hand, the examples of the developed GA-based optimization procedure presented in this paper demonstrated the power of this tool in minimizing distortion in very limited number of iterations. This optimization tool has a huge potential to be conveniently modified to suite other optimization objectives and or welding processes.

The developed welding process modelling capability on K-PAW of Ti-6Al-4V, reported in this paper, will provide a useful guidance and generic methodologies for optimum design of thin and complex light weight structures, such as aeroengine casings. In addition, the current research will form a basis for the establishment of a frame work on structural integrity assessment and component lifing of welding fabricated thin structures, which is the aim of our future research on this topic.

8   Acknowledgments

9   References

1.   Damsbo, M. and Ruhoff, P.T., An evolutionary algorithm for welding task sequence ordering, in *Artificial Intelligence and Symbolic Computation, International Conference AISC'98*, 16-18 September 1998, New York, United States.

2.   Damsbo, M. and Ruhoff, P.T., An evolutionary algorithm for welding tasl sequence ordering. *AISC'98, LNAI*, 1998, **1476**: p. 120-131.

3.   Kadivar, M.H., Jafarpur, K., and Baradarn, G.H., Optimizing welding sequence with genetic algorithm. *Journal of Computational Mechanics*, 2000, **26**: p. 514-519.

4.   Tsai, C.L., Park, S.C., and Cheng, W.T., Welding distortion of a thin-plate panel structure. *Welding Research Supplement*, 1999: p. 156-165.

5.   Tsai, C.L., Park, S.C., and Cheng, W.T., Welding distortion of a thin-plate panel structure. *Welding Journal*, 1999, **78**(5): p. 156S-165S.

6.   Nnaji, B.O., Gupta, D., and Kim, K.Y., Welding distortion minimization for an aluminum alloy extruded beam structure using a 2D model. *Transactions of the ASME*, 2004, **126**: p. 52-63.

7.   Wu, C.S., Hu, Q.X., and Gao, J.Q., An adaptive heat source model for finite-element analysis of keyhole plasma arc welding. *Computational Materials Science*, 2009, **46**: p. 167-172.

8.   Norrish, J., *Advanced Welding Processes*, 1992, Bristol: IOP Pubilishing.

9.   Lucsa, W., *TIG and Plasma Welding*, 1990, Cambridge: Abington Publishing.

10.   Althouse, A.D., Turnquist, C.H., and Bowditch, W.A., *Modern Welding*, 9th ed., 2000, London: GoodGoodheart-Wilcox.

11.   Xu, L., Sun, W., McCartney, D.G., Deshpande, A.A., and Hyde, T.H., Distortion measurement of bead-on-plate and t-joint keyhole plasma arc welds of thin titanium alloy sheets, in *The International Conference ESIA11 on Engineering Structural Integrity Assessment*, 24-25 May 2011, Manchester, United Kingdom.

12.   Fitzpatrick, M.E. and Lodini, A., Eds. *Analysis of Residual Stress by Diffraction by Using Neutron and Synchrotron Radiation*, 2003, Taylor and Francis: London.

13.   Deshpande, A.A., Short, A.J., Sun, W., McCartney, D.G., Xu, L., and Hyde, T.H. *Parameter idnetification for stable keyhole plasma arc welding of a Ti-6Al-4V sheet*, in *AeroMat* 2010. Bellevue, WA, USA.

14.   Goldberg, D.E., *Genetic Algorithms in Search, Optimization, and Machine Learning*, 1989: Addison-Wesley Publishing Company, Inc. 412.

15.   Collings, E.W., *Materials Properties Handbook: Titanium Alloys*, 1994, Ohio: ASM International.

Accuracy of adhesive joint strength predictions by finite element analyses

R.D.S.G. Campilho[1,2], M.D. Banea[3], L.F.M. da Silva[3]

[1]*Faculdade de Economia e Gestão, Universidade Lusófona do Porto,*

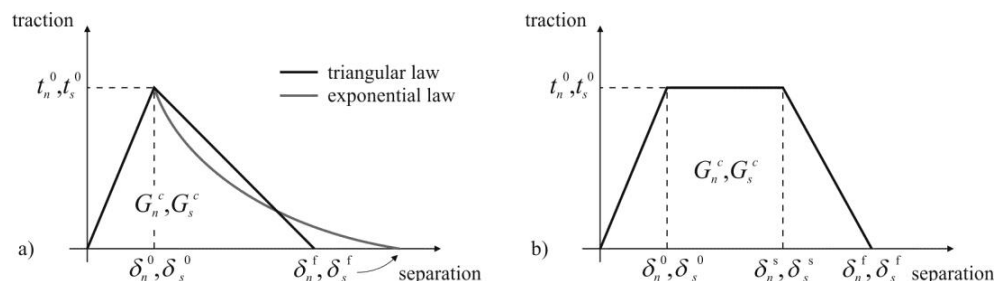*Rua Augusto Rosa, 24, 4000-098 Porto, Portugal*

[2]*Departamento de Engenharia Mecânica, Instituto Superior de Engenharia do Porto*

Rua Dr. António Bernardino de Almeida, 431, 4200-072 Porto, Portugal

[3]*Departamento de Engenharia Mecânica, Faculdade de Engenharia da Universidade do*

Porto, Rua Dr. Roberto Frias, s/n, 4200-465 Porto, Portugal

Abstract Adhesively-bonded joints are extensively used in several fields of engineering, as an easy and efficient method to join components. Cohesive Zone Models (CZM) have been used in the last decade for the strength prediction of adhesive joints, as an add-in to Finite Element (FE) analyses that allows simulation of damage growth within bulk regions of continuous materials or interfaces between different materials, by consideration of energetic principles. Compared to conventional FE, a much more accurate prediction s achieved, as this technique provides an accurate representation of the entire failure process. A useful feature of CZM is that different shapes can be developed for the cohesive laws, depending on the nature of the material or interface to be simulated, allowing a faithful representation of the fracture processes. The triangular and trapezoidal CZM shapes are most commonly used for strength prediction of typical structural materials. This work studies the influence of the CZM shape (Fig. 1) used to model a thin adhesive layer in single-lap adhesive joints, for an estimation of its influence on the strength prediction under different material conditions. As a result of this study, some conclusions were established to assess the importance of using a CZM shape for a given adhesive that faithfully represents its behaviour, under different material behaviours (a brittle and a ductile adhesive were tested). The viability of using a triangular CZM that is easier to use, without compromising the accuracy of the results, was also assessed.

Figure 1 - *CZM laws with triangular, exponential and trapezoidal shapes available in Abaqus®*

Study and optimization of the T-peel joint using the finite element method

P.F.P. Afonso[1], R.D.S.G. Campilho[1,2], A.M.G. Pinto[1]

[1]Departamento de Engenharia Mecânica, Instituto Superior de Engenharia do Porto

Rua Dr. António Bernardino de Almeida, 431, 4200-072 Porto, Portugal

[2]Faculdade de Economia e Gestão, Universidade Lusófona do Porto,

Rua Augusto Rosa, 24, 4000-098 Porto, Portugal

Abstract The most traditional methods of joining components are bolting, riveting, welding or adhesive-bonding. Adhesive bonds don't require holes and distribute the load over a larger area than mechanical connections. However, they tend to develop a peak tension pullout and shear stresses near the ends of the overlap because of the differential effect of the substrates deformation and asymmetry of the transmitted load. As such, premature rupture may occur, especially a brittle adhesive is used. In addition, adhesive bonds are very sensitive to surface treatment, operating temperature, moisture, aging and other environmental extremes. The combination of adhesive bonding with spot welding allows some competitive advantages to traditional adhesive bonds and also increased resistance (especially for brittle adhesives), decreased weight, increased stiffness, better resistance to tearing and fatigue, and easier manufacturing because a positioning device during curing of the adhesive is not required. This technique dates back to the 70's [1], although the process remained unattended until recently due to lack of systematic theoretical and experimental research. Nonetheless, in the last decade this scenario progressively changed through the accomplishment of experimental and theoretical investigations [2]. This paper presents an experimental and numerical study of T-peel hybrid joints (adhesive and spot welded) subjected to tensile and bending loads, compared to traditional adhesive and spot welded joints. The numerical work will be performed by the finite element method (FEM) package Abaqus® using cohesive damage models (CDM) for the simulation of damage onset and growth within the adhesive bond and spot welds. A parametric study will be held considering a few design variables, which will allow the optimization of hybrid joints. As a result of this study, the advantages of the proposed hybrid technique are discussed, compared to the purely bonded or welded equivalent joints, and some design principles are proposed in light of the studied optimization variables. The suitability of the chosen predictive technique for the specific purpose of designing bonded/welded joints is also assessed.

References

1. Jones, T.B. A future for weldbonding sheet steel. Welding and Metal Fabrication 1978, 46, 415.
2. Charbonnet, P.; Clad, A.; Fant-Jaeckels, H.; Thirion, J.L. Weldbonding: A very well adapted joining technique to decrease the weight of steel structures. La Revue de Métallurgie – CIT 2000, April; 543.

Mixed-Mode Fracture Toughness Determination
Using Non-conventional Techniques

Filipe J.P. Chaves[1], L.F.M. da Silva[2], M.F.S.M de Moura[2], D. Dillard[3]

[1]*IDMEC- Pólo FEUP,* Faculdade de Engenharia da Universidade do Porto, Rua Dr. Roberto Frias, 4200-465 Porto, Portugal, chaves.filipe@fe.up.pt
[2]*DEMec,* Faculdade de Engenharia da Universidade do Porto
[3] Engineering Science and Mechanics Department, Virginia Tech

Abstract

The focus of this work is to understand the effect of the adhesive thickness and adhesive ductility on the mixed mode loading of double cantilever beam (DCB) joints. After some extensive testing in pure modes (I and II), some other tests with a ratio of mixed modes using single leg bending (SLB), asymmetric DCB and the dual actuator loading (DAL) frame were done to obtain enough data to support the design of an apparatus that uses DCB steel specimens to obtain the fracture envelope for adhesives.

Using this apparatus, a ductile epoxy was characterized and the fracture envelope is presented. A data reduction scheme that does not require the crack length (a) measurement for the determination of the strain energy release rate (G) is also presented.

1   Introduction

Bonded joints in service are usually subjected to mixed-mode conditions due to geometric and loading complexities. Consequently, the fracture characterization of bonded joints under mixed-mode loading is a fundamental task.
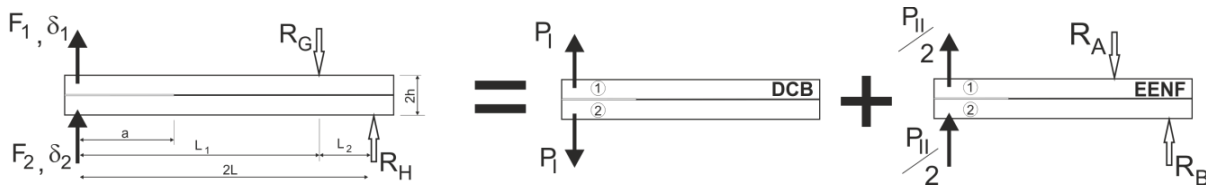
There are some conventional tests proposed in the literature concerning this subject, as is the case of the ADCB, the SLB and the cracked lap shear (CLS). Nevertheless, these tests are limited in which concerns the variation of the mode-mixity, which means that different tests are necessary to cover the fracture envelope in the G_I-G_{II} space [1]. After proposing a data reduction scheme for the DAL [2], a new test jig, based on the Spelt jig [3] was designed allowing to obtain the fracture envelope for an adhesive, using a DCB specimen.

2   Data reduction scheme

The classical data reduction scheme proposed by Spelt et al. [3] requires crack length monitoring. This can be considered an important limitation in cases where crack tip is not easily identified, which is the case of mode II predominant loading cases, since the crack tends to close during propagation. On the other hand, when the fracture process zone (FPZ) ahead of the crack tip is non-negligible (as is the case of adhesives with some ductility) the

energy dissipation in the FPZ must be taken into account, which does not happen when the crack length is used as a fracture parameter. In order to overcome these drawbacks, an alternative data reduction scheme based on specimen compliance, beam theory and crack equivalent concept is proposed. Using Timoshenko beam theory, the strain energy of the specimen (Fig. 1) due to bending and including shear effects is:

$$U = \frac{(F_1 + F_2)^2}{2\,E\,I\,L_2^2} \int_{L_1}^{L_1+L_2} \left(L_1 + L_2 - x\right)^2 dx + \int_0^a \frac{\frac{P_{II}^2}{4} x^2}{\frac{E\,I}{8}}\, dx + \int_a^{L_1} \frac{P_{II}^2\, x^2}{2\,E\,I}\, dx$$

$$+ \int_{L_1}^{2L} \frac{P_{II}^2\, L_1^2\, (2L-x)^2}{2\,E\,I\,(2L-L_1)^2}\, dx \tag{1}$$

Figure 1 *– Spelt Jig loading scheme.*

The Spelt jig test can be viewed as the combination of a DCB and an equivalent end notch flexure (EENF) test, as shown in Figure 1, with the reaction forces:

$$R_G = \frac{(F_1+F_2)2\,L}{2L-L_1} \text{ and } R_H = \frac{(F_1+F_2)\,L_1}{2L-L_1} \tag{2}$$

$$R_A = \frac{2\,L\,P_{II}}{2L-L_1} \text{ and } R_B = \frac{P_{II}L_I}{2L-L_1} \tag{3}$$

The loadings are:

$$P_I = \frac{F_1-F_2}{2} \tag{4}$$

$$P_{II} = F_1 + F_2 \tag{5}$$

And the displacements:

$$\delta_I = \delta_1 - \delta_2 \tag{6}$$

$$\delta_I = \frac{\delta_1+\delta_2}{2} \tag{7}$$

Assuming $G = \frac{E}{2(1+\upsilon)}$, the pure compliances become:

$$C_I = \frac{8a^3}{Ebh^3} + \frac{24 \cdot a(1+\upsilon)}{5Ebh} \tag{8}$$

$$C_{II} = \frac{1}{E\,I}\left(a^3 + \frac{2}{3}\,L\,L_1^2\right) + \frac{12\,L_1\,L\,(1+\upsilon)}{5\,E\,b\,h\,(2L-L_1)} \tag{9}$$

These equations take into account the specimen behaviour, however, the stress concentrations, root rotation and the existence of a non-negligable FPZ require the calculation af an equivalent crack length for mode I ($a_{e,\,I}$) and mode II ($a_{e,\,II}$):

$$\alpha\,a_{eI}^3 + \beta\,a_{eI} + \gamma = 0 \tag{10}$$

Where

$$\alpha = \frac{8}{E_f bh^3}\;;\; \beta = \frac{24\,(1+\vartheta)}{5\,E_f b\,h};\gamma = -C_I \tag{11}$$

Using Matlab® software and only keeping the real solution, one obtains

$$a_{\mathrm{eI}} = \frac{1}{6\alpha}\,A - \frac{2\beta}{A} \tag{12}$$

where

$$A = \left(\left(-108\gamma + 12\sqrt{3\left(\frac{4\beta^3 + 27\gamma^2\alpha}{\alpha}\right)}\right)\alpha^2\right)^{\frac{1}{3}} \tag{13}$$

In mode II, the equivalent crack length (a_{eII}) can be straightforwardly obtained from Equation (9)

$$a_{e,II} = \left[\left(C_{II} - \frac{12\,L\,L_1(1+\upsilon)}{5\,E_{f,II}b\,h\,(2L-L_1)}\right)E_{f,II} \cdot I - \frac{2}{3}\,L\,L_1\right] \tag{14}$$

The equivalent rigidity for the system in mode I is:

$$E_{f,I} = \frac{8\,(a_0+\Delta)}{C_{O\,II,corr} \cdot I}\left[\frac{\left(a_0 + \Delta\right)^2}{h^2} + \frac{3(1+\upsilon)}{5}\right] \tag{15}$$

And for mode II:

$$E_{f,II} = \frac{a_0^3 + \frac{2}{3}\,L\,L_1^2}{C_{O\,II} \cdot I} \cdot \frac{12L_1L(1+\upsilon)}{5\,C_0 b\,h\,(2L-L_1)} \tag{16}$$

The strain energy release rate components can be determined using the Irwin-Kies equation

$$G = \frac{P^2}{2B}\frac{dC}{da} \tag{17}$$

For mode I, the combination of equations leads to

$$G_I = \frac{12\,P_I^2}{E_{f,I}b^2h}\left(\frac{a_{eq,I}^2}{h^2} + \frac{1+\upsilon}{5}\right) \tag{18}$$

The strain energy release rate in mode II is obtained from Equations (9) and (17)

$$G_{II} = \frac{3\,P_{II}^2\,a_{e,I}^2}{2\,E_{f,II}\cdot I} \tag{19}$$

3 Numerical analysis

To verify the performance of the test and the adequacy of the data reduction scheme, a numerical analyisis was carried out including a cohesive damage model. The specimen geometry and mechanical properties are presented in Figure 2 and Table 1.

h = 12.7 mm

2L = 260 mm

L₂ = 35 mm

b = 25 mm
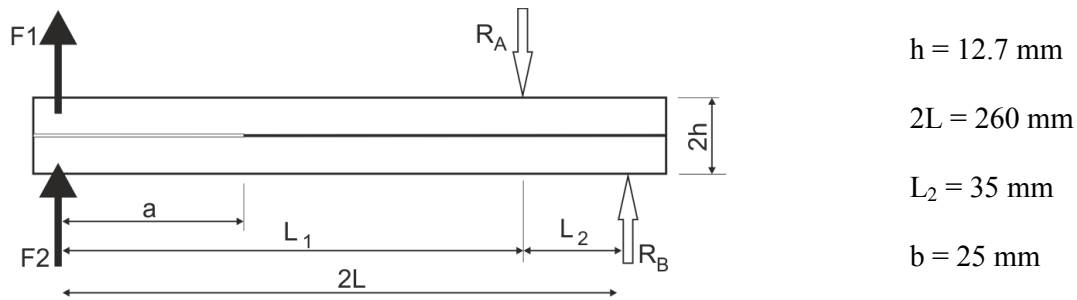
Figure 2 – Specimen geometry.

Table 1 – Elastic and cohesive properties

Elastic properties (Steel)		Cohesive properties (Adhesive)			
E (GPa)	G (MPa)	$\sigma_{u,I}$ (MPa)	$\sigma_{u,II}$ (MPa)	G_{Ic} (N/mm)	G_{IIc} (N/mm)
210	80.77	23	22.8	0.43	4.7

The simulation was done in ABAQUS® with 3600 plane strain 8-node quadrilateral elements and 280 6-node interface elements with null thickness placed at the mid-plane of the bonded specimen. The Spelt apparatus was modelled with Beam and Link Multi Point

Constraints allowing the variation of arm length with the jig parameters (S1, S2, S3 and S4), as shown in Figure 3.
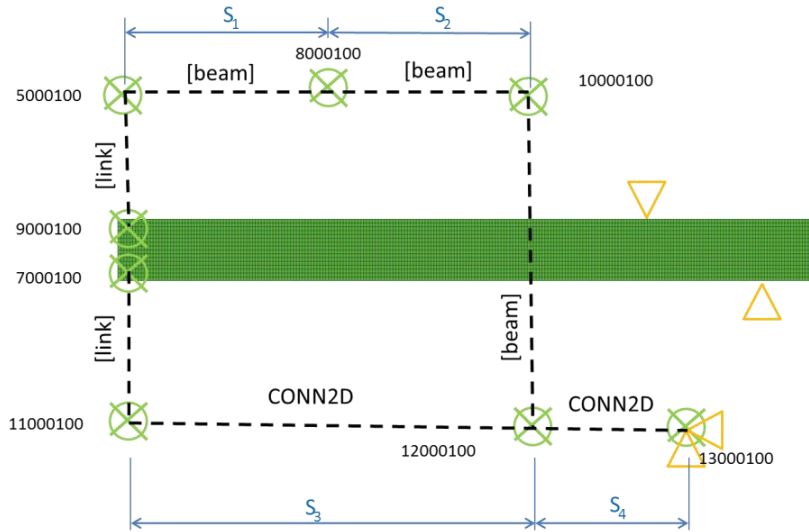
Figure 3 – ABAQUS® model for the Spelt Jig.

A trapezoidal cohesive law was used, as shown in Figure 4, in order to obtain a better agreement with the adhesive ductile behaviour.
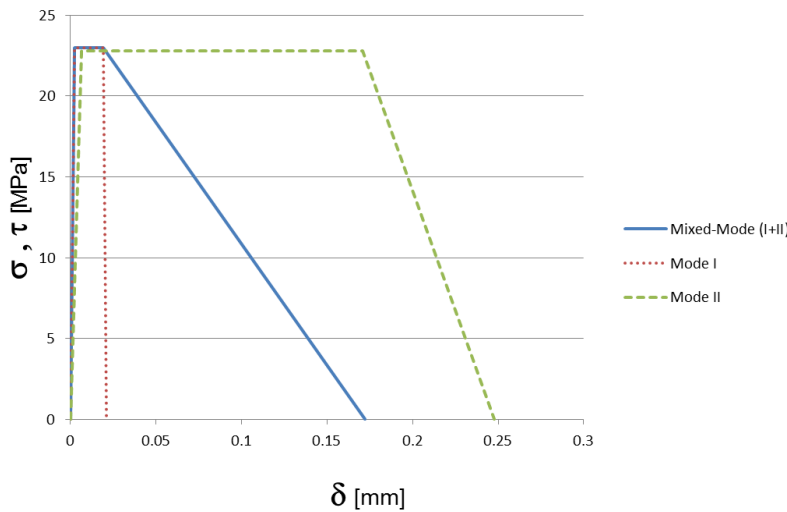
Figure 4 – Mixed-Mode cohesive softening law.

The cohesive model is based on a mixed-mode linear softening law (Figure 4). It uses the quadratic stress criterion

$$\left(\frac{\sigma_{\mathrm{I}}}{\sigma_{\mathrm{u,I}}}\right)^2 + \left(\frac{\sigma_{\mathrm{II}}}{\sigma_{\mathrm{u,II}}}\right)^2 = 1$$

(20)

to simulate damage initiation and the linear energetic criterion

$$\left(\frac{G_{\mathrm{I}}}{G_{\mathrm{Ic}}}\right)+\left(\frac{G_{\mathrm{II}}}{G_{\mathrm{IIc}}}\right)=1$$

(21)

to deal with damage growth.

54 model scenarios were studied by variation of S_1, S_2, S_3 and S_4, allowing to plot the envelope shown in Figure 5. Figure 6 shows two different scenarios obtained from ABAQUS® for combination P6 (S1= 60, S2= 100 , S3=160, S4= 80) on the top and P54 (S1= 40, S2= 40 , S3=80, S4= 180) on the bottom.
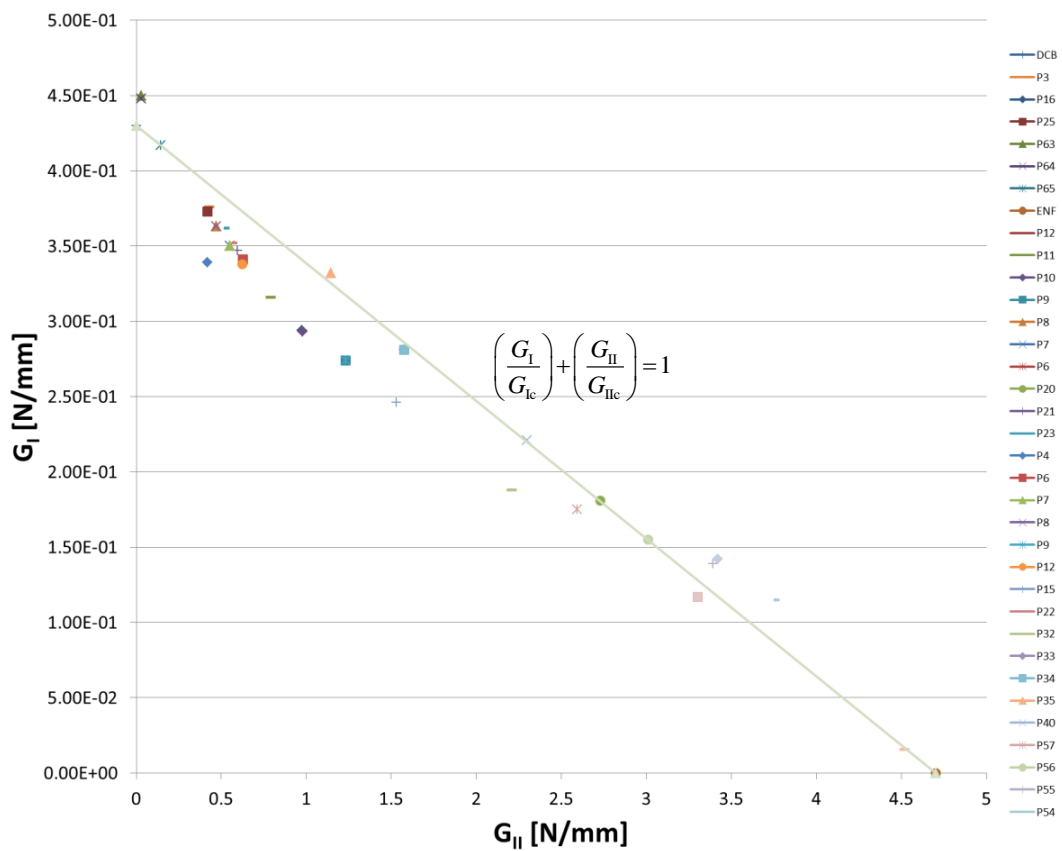
Figure 5– Fracture envelope plot.
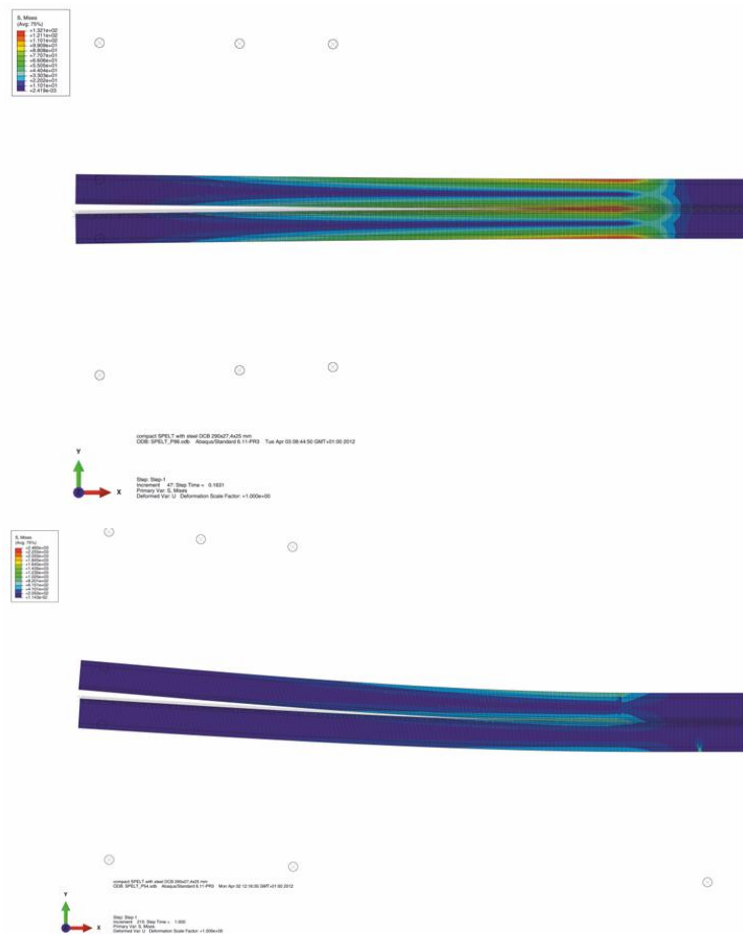
Figure 6 *– Von Mises stress plot for the two scenarios P6 (top) and P54 (bottom) .*

4   Conclusions

The fracture envelope (Figure 5) shows a fairly good accordance with the energetic criterion for fracture growth defined in Equation (21). There are, however, some mixed-mode ratios that are more reliable for testing purposes. It was also noted that the pure mode I (DCB) was in good accordance with the G_{Ic} value. The model was not able to comply with pure mode II (ENF), instead it gives a very close approximation with a very small amount of mode I. The numerical analysis already done gives a good information for the experimental testing that should confirm the suitability of the Spelt jig to obtain the fracture envelope for adhesive joints.

5   References

[1]   L.F.M. da Silva,V.H.C. Esteves, F.J.P. Chaves. "Fracture toughness of a structural adhesive under mixed mode loadings", Mat.-wiss. u.Werkstofftech., 42, No. 5 , pp.460-470, 2011.

[2]   Filipe J.P. Chaves, M.F.S.F. de Moura , L.F.M. da Silva , D.A. Dillard, "Numerical analysis of the dual actuator load test applied to fracture characterization of bonded joints", International Journal of Solids and Structures, 48 , pp.1572–1578, 2011

[3]   G. Fernlund and J. K. Spelt, "Mixed–Mode Fracture Characterization of Adhesive Joints", Composites Science and Technology, 50, pp. 441-449, 1994.

Mechanical Characterization of a High Temperature Epoxy Adhesive

Mariana D. Banea[1], Lucas F.M. da Silva[2], Raul D.S.G. Campilho[3]

[1] *Instituto de Engenharia Mecânica (IDMEC), 4200-465, Porto, Portugal, mbanea@fe.up.pt*

[2] *Departamento de Engenharia Mecânica, Faculdade de Engenharia, Universidade do Porto,*

Rua Dr. Roberto Frias, 4200-465 Porto, Portugal, lucas@fe.up.pt

[3] *Faculdade de Economia e Gestão, Universidade Lusófona do Porto,*

Rua Augusto Rosa, 24, 4000-098 Porto, Portugal, raulcampilho@gmail.com.

Abstract: It is well known that in order to properly design a joint the adhesive behaviour has to be characterized. Thus, to determine the stresses and strains in adhesive joints in a variety of configurations, it is necessary to know the adhesive mechanical properties. In this work, the performance of a high temperature epoxy adhesive has been studied through bulk specimens and adhesive joint tests. In order to obtain a tensile strength profile of the adhesive, bulk specimens of cured adhesive were produced and tested in tension at RT and high temperatures (100ºC, 125ºC, 150ºC). The Thick Adherend Shear test (TAST) was performed in order to measure the shear properties. The double cantilever beam (DCB) for opening pure mode I loading and the end-notched flexure (ENF) for sliding pure mode II loading were used to get the mode I and II adhesive fracture toughness. Results showed that the failure loads of both the bulk test and joint test specimens vary with temperature and this needs to be considered in any design procedure.

1   Introduction

In order to properly design a joint, the adhesive behaviour has to be characterized. Hence, to determine the stresses and strains in adhesive joints in a variety of configurations, it is necessary to know the adhesive mechanical properties. Furthermore, to predict the joint strength, the stress distribution and a suitable failure criterion are essential. One of the simplest failure criteria is that based on a stress or strain limit state, i.e. based on a continuum mechanics approach for which the availability of the stress–strain curve of the adhesive is sufficient. However, for the more realistic and sophisticated methods such as progressive damage methods, damage laws of adhesives to be used under different temperatures are necessary. A cohesive zone model (CZM), used to model the progressive damage and failure, models the fracture process extending the concept of continuum mechanics by including a zone of discontinuity modelled by cohesive zones, thus using both strength and energy parameters to characterize the debonding process. The parameters that define the damage law are the fracture toughness (G_c) and the maximum stress (σ_c^0) for each fracture mode.

The majority of adhesively-bonded assemblies fracture characterization under pure mode I is performed using the DCB specimen [1]. In a fracture mechanics analysis of this specimen, the crack is predicted to propagate when the energy release rate for mode I crack growth (G_I) becomes equal to the toughness of the adhesive or the adhesive's critical energy release rate (G_{Ic}). The main advantages of this test method include its simplicity and the possibility to

obtain the fracture toughness mathematically using the beam theory for brittle materials. Several techniques can be used to derive the fracture toughness of structural adhesives from fracture characterization tests. The most common methodologies for analysis are based on Linear-Elastic Fracture Mechanics (LEFM). The Compliance Calibration Method (CCM) is based on the Irwin-Kies equation [2], requiring the calculation of the compliance, C, ($C=\delta/P$, where δ is the displacement and P is the applied load) relative to the crack length during crack growth. The Direct Beam Theory (DBT), based on elementary beam theory, and the Corrected Beam Theory (CBT), including the effects of crack tip rotation and deflection, are also available within the scope of LEFM. The Compliance-Based Beam Method (CBBM) was recently developed by de Moura et al. [3] and is based on the crack equivalent concept, depending only on the specimen's compliance during the test.

For the determination of the toughness in mode II there are various test methods available: the end notched flexure (ENF) test, the end loaded split (ELS) test and the four-point notched flexure (4ENF) test. The ELS test presents large displacements and is sensitive to the clamping device. The 4ENF is more sophisticated but has problems of friction due to the loading mode in the pre-crack region. Therefore, the most suitable testing method for mode II appears to be the ENF test. The ENF test is essentially a three-point flexure test on a pre-cracked specimen causing a shear mode loading in the adhesive.

In this work, the performance of a high temperature epoxy adhesive has been studied through bulk specimens and adhesive joint tests. In order to obtain a tensile strength profile of the adhesive, bulk specimens of cured adhesive were produced and tested in tension at RT and high temperatures (100ºC, 125ºC, 150ºC). The Thick Adherend Shear test (TAST) was performed in order to measure the shear properties. The double cantilever beam (DCB) for opening pure mode I loading and the end-notched flexure (ENF) for sliding pure mode II loading were used to get the mode I and II adhesive fracture toughness.

2   Experimental details

2.1. Materials
The adhesive investigated in this study was a one-component high temperature paste epoxy adhesive XN1244, supplied by Nagase ChemteX (Japan). The characterization tests for XN1244 adhesive were carried out under tension and shear considering three specimens for each condition, which allowed the determination of the strengths and moduli in both loadings. The tensile properties (mode I loading) of XN1244 adhesive were determined using "dogbone" tensile specimens in a previous study [4]. The Thick Adherend Shear Test (TAST) was performed in order to measure the shear properties (mode II loading) of the adhesive according to standard ISO 11003-2:1999, using steel substrates of dimensions 110mm x 25mm x 12mm. The joint surfaces were grit blasted and degreased with acetone prior to the application of the adhesive. The bondline thickness was nominally 0.7 mm and the length of the overlap test section was 5 mm. Two spacers (1.5 mm thick) were inserted in the gaps between the adherends after the application of the adhesive and prior to curing in order to provide the necessary spacing between the two adherends. These spacers were removed after the adhesive was cured. The joints were cured in a hot press following the manufacturer's suggested curing conditions (1 h at 140ºC). TAST tests were performed at RT on a MTS servo-hydraulic machine, model 312.31, at a constant crosshead rate of 0.1 mm/min. The displacement was measured with two methods: a 25 mm length MTS extensometer and a non-contact method (video microscopy). As the extensometer is mounted in the metallic substrate,

the extensometer measures not only the displacement of the adhesive, but also the displacement of the adherend. Therefore, it is necessary to apply a correction to the measured displacements. At the same time, a video microscopy was used to record the displacements, which gives only the adhesive displacement. The strains were calculated using the spatial correlation method developed by Chousal [5].

A characteristic shear stress-strain curve of XN1244 adhesive measured by the two methods (MTS extensometer and video microscopy) at RT is shown in Fig 1. The XN1244 adhesive has a shear modulus of 2.15±0.10 [GPa], shear failure strength of 31.61±2.83 [MPa] and a maximum shear strain of 8.05±1.2 [%]. The shear modulus was determined from the stress-strain curve measured by the video microscopy method (the 'adhesive' curve). The shear strength is coincident for the two curves. The shear strain to failure presented in the text was obtained from the 'steel + adhesive' curve because it is not always possible to get the last part of the curve by spatial correlation due to image focus problems at break point.

Hard tool steel DIN 40CrMnMo7 substrates were used for the DCB and ENF specimens, in order to assure an elastic behaviour of the adherends.
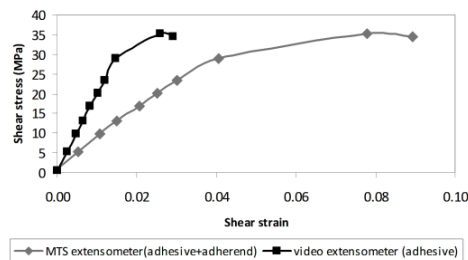
Figure 1 - *Typical XN1244 adhesive shear stress-strain curve measured by the two methods (MTS extensometer and video microscopy).*

2.2. Specimen fabrication

The DCB and ENF joint surfaces were grit blasted and degreased with acetone prior to the application of the adhesive. The specimen geometry and the loading are shown in Fig. 2 (the width b of the specimen is 25 mm). The bondline thickness was nominally 0.2 mm. Spacers (calibrated steel bars of 0.20 mm) were inserted between the adherends before the application of the adhesive in order to control the bondline thickness. These spacers were removed after the adhesive was cured. A sharp pre-crack in the adhesive layer mid-thickness was assured using a razor blade. A mould with spacers for the correct alignment of the adherends was used. The DCB and ENF joints were cured at 140ºC for 1 hour.

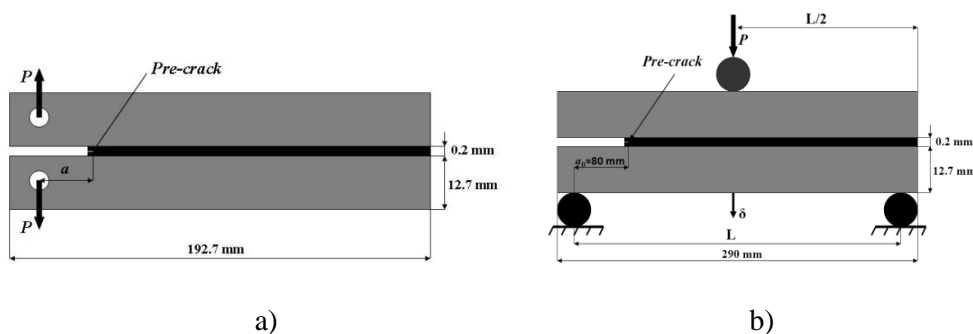a)   b)

Figure 2 – *DCB (a) and (b) ENF specimens*

2.3. Test procedure

The DCB and ENF specimens were tested at RT and high temperatures (100, 150 and 200ºC) using a universal testing machine Instron® model 8801 (Instron Co., USA) with a 100kN load cell, under a constant crosshead rate of 0.5 mm/min. The load–displacement (*P–δ*) curve was registered during the tests. The DCB specimens set-up is shown in Fig. 3a., while the ENF specimens set-up is shown in Fig.3b. A thermocouple was applied to the specimen in order to assure that the air temperature inside the chamber was equal to the specimen's temperature. The tests were always performed after approximately 10 min. of achieving the test temperature in the specimens, to ensure a steady-state temperature throughout the specimen prior to testing.

a)   b)
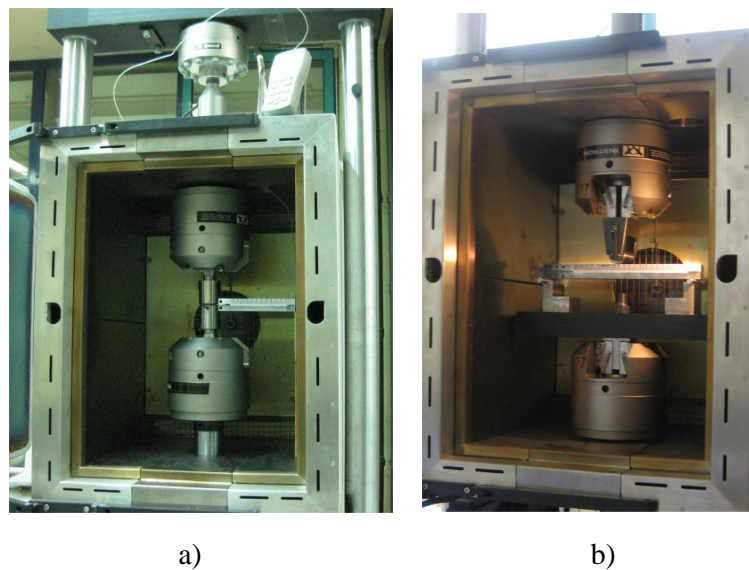
Figure 3 *- DCB (a) and ENF (b) specimens set-up.*

2.4. Data analysis

DCB data analysis

The Compliance-Based Beam Method (CBBM) was recently developed by de Moura et al. [3] and is based on the crack equivalent concept, depending only on the specimen's compliance during the test. G_{Ic} can be obtained by the following expression:

$$G_{Ic} = \frac{6P^2}{b^2 h} \left(\frac{2a_{eq}^2}{h^2 E_f} + \frac{1}{5G} \right) \qquad (1)$$

a_{eq} is an equivalent crack length obtained from the experimental compliance and accounting for the fracture process zone (FPZ) at the crack tip, h is the specimen height, E_f is a corrected flexural modulus to account for all phenomena affecting the *P-δ* curve, such as stress concentrations at the crack tip and stiffness variability between specimens, and G is the shear modulus of the adherends.

ENF data analysis

Similar to DCB, the Compliance-Based Beam Method (CBBM) which was developed by de Moura *et al.* [6] was used to evaluate G_{IIc}. This method is based on the crack equivalent concept, depending only on the specimen's compliance during the test. Thus, it does not require crack length monitoring during crack growth which was observed to be very difficult to perform with accuracy in the ENF test. In addition, the equivalent crack length, a_{eq}, accounts for the FPZ effects at the crack tip, which is not taken into account when the real crack length is considered. G_{IIc} can be obtained by the following expression:

$$G_{IIc} = \frac{9P^2 a_{eq}^2}{16b^2 E_f h^3} \qquad (2)$$

where P is applied load, E_f is an equivalent flexural modulus calculated from the initial compliance and initial crack length, thus avoiding the influence of specimen variability on the results; b is the specimen width; a_{eq} is the equivalent crack length and h is the adherend thickness. The readers are referred to Ref. [6] for the detailed formulations of the CBBM method.

3. Results: Determination of G_{Ic} and G_{IIc}

Representative experimental $P–\delta$ curves of the DCB and ENF specimens as a function of temperature are presented in Fig. 4. The critical fracture energy in mode I and II, G_{Ic} and G_{IIc}, were evaluated using the CBBM method presented in Section 2.4.
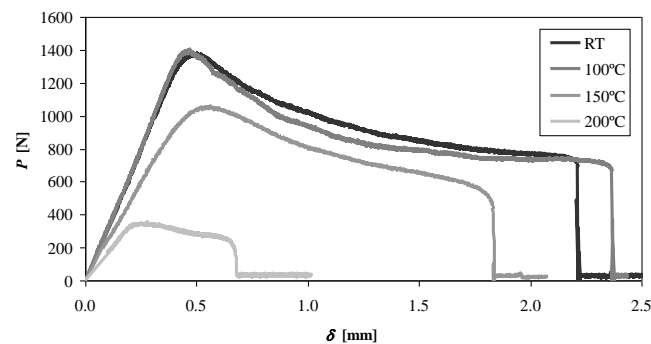

a)
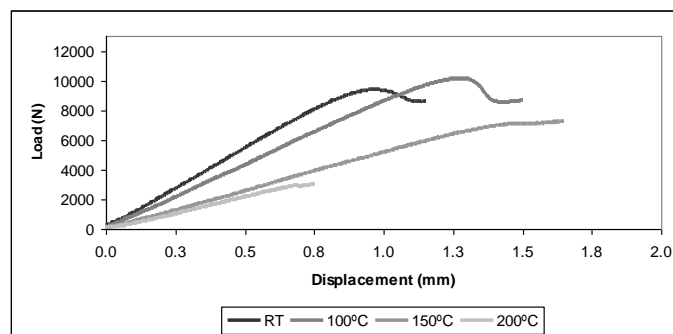
b)

Figure 4 - *Representative P–δ curves of the DCB (a) and ENF (b) specimens as a function of temperature.*

For the DCB specimens, the slopes and maximum loads were almost the same at RT and 100ºC, but a slightly increase in displacement can be seen at 100ºC. The maximum load slightly decreased at 150ºC, while at 200ºC, a dramatic drop in maximum load and displacement was observed (Fig. 4a).

For the ENF specimens (Fig. 4b), the load increases until the crack initiation process is completed. After that, the crack tip starts propagating. A continuous drop in the force is seen as the crack continuously propagates until the crack reaches the ENF specimen's middle (at the time the crack approaches the loading cylinder, the load starts to increase due to the compression near the crack tip, which obstruct propagation because of friction effects). The maximum loads increased at 100ºC and decreased at 150ºC, while a significant increase in displacement can be seen at both temperatures. At 200ºC, a dramatic drop in maximum load and displacement was observed.

The effect of temperature on the fracture toughness, G_{Ic}, is presented in Fig. 5. At 100ºC the fracture toughness, G_{Ic}, of the adhesive slightly increased (by approximately 10%). This can be explained by the fact that, as the temperature increases, the strength decreases but the ductility increases giving an additional plastic deformation at the crack tip, hence an increase in toughness. At 150ºC, G_{Ic} is slightly lower indicating the vicinity to the T_g. However, it can be concluded that at temperatures below T_g, the fracture toughness, G_{Ic}, seems to be insensitive to temperature. Moreover, a drastic drop in fracture toughness was observed at 200ºC. This was expected as the testing temperature overpasses the T_g of the adhesive.
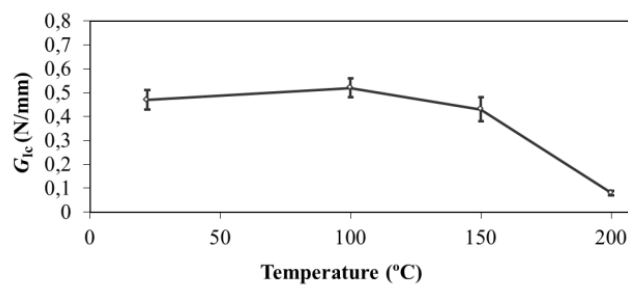
Figure 5 *- Fracture toughness G_{Ic} as a function of temperature.*

The effect of temperature on the fracture toughness, G_{IIc}, is presented in Fig. 6. At 100ºC, the fracture toughness, G_{IIc}, of the adhesive increased by approximately 33% in relation to the value at RT. This can be explained by the fact that, as the temperature increases, the strength decreases but the ductility increases giving an additional plastic deformation at the crack tip, hence an increase in toughness. At 150ºC, G_{IIc} decreased by approximately 22%, indicating the approach to the T_g. Nevertheless, a drastic drop in G_{IIc} was observed at 200ºC. This was expected as the testing temperature overpasses the T_g of the adhesive.

The relation G_{IIc}/G_{Ic} is presented in Table 1. It can be seen that the G_{IIc} follows the same trend as G_{Ic} as a function of temperature, but the increase in ductility with the increase of temperature affects more G_{IIc} as shear deformation involves more plastic work of the adhesive.
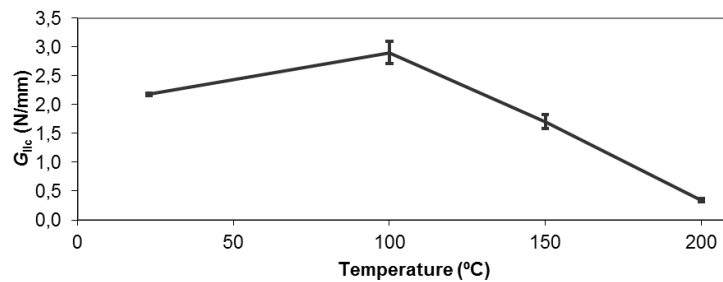
Figure 6 *- Fracture toughness G_{IIc} as a function of temperature.*

In the literature, the most common is to assume a value of 2 for G_{IIc}/G_{Ic} when the value of G_{IIc} is unknown [7]. On the other hand, there are studies that found higher values for G_{IIc}/G_{Ic}, such as, 14 for a brittle epoxy adhesive and 22 for a ductile adhesive [8], while in [9] the value found is approximately 10. Therefore, it is important to test not only in mode I but also in mode II for a complete and accurate characterization of an adhesive bond.

Table 1 *- Comparison of the fracture toughness in mode I (G_{Ic}) and mode II (G_{IIc}) as a function of temperature (average values).*

	Mode I G_{Ic}(N/mm)	Mode II G_{IIc}(N/mm)	G_{IIc}/G_{Ic}
RT	0.47	2.18	4.68
100ºC	0.50	2.90	5.80
150ºC	0.42	1.70	4.04
200ºC	0.07	0.34	4.25

4. Conclusions

Pure mode I DCB adhesive fracture toughness (G_{Ic}) tests were performed at room and high temperatures (100ºC, 150ºC and 200ºC). The results showed that the value of G_{Ic} was relatively insensitive to temperature up to T_g, while above T_g (at 200ºC) a drastic decrease in G_{Ic} was found.

Pure mode II ENF adhesive fracture toughness (G_{IIc}) tests were performed at room and high temperatures (100ºC, 150ºC and 200ºC). The mode II fracture toughness was found to increase at 100ºC and decrease at 150ºC, as the temperature approaches T_g. Moreover, a drastic drop in fracture toughness was observed at 200ºC, when the T_g of the adhesive was overpassed.

A database of mechanical properties of the high temperature adhesive studied was established which will be used in finite element (FE) analysis to simulate the deformations at different testing conditions.

5. References

[1]. Andersson, T. and U. Stigh, *"The stress-elongation relation for an adhesive layer loaded in peel using equilibrium of energetic forces"*. International Journal of Solids and Structures 41(2), pp. 413-434, 2004.~

[2]. Kanninen M.F and Popelar CH., *"Advanced Fracture Mechanics",* Oxford University Press, Oxford, UK, 1985.

[3]. de Moura, M.F.S.F., Campilho R.D.S.G., and Gonçalves J.P.M., *"Crack equivalent concept applied to the fracture characterization of bonded joints under pure mode I loading"*. Composites Science and Technology, 68, pp. 2224-2230, 2008.

[4]. Banea MD., de Sousa FSM., da Silva LFM., Campilho RDSG., de Bastos Pereira AM., *"Effects of Temperature and Loading Rate on the Mechanical Properties of a High Temperature Epoxy Adhesive"*, Journal of Adhesion Science and Technology, 25(18), pp. 2461-2474, 2011.

[5]. Chousal, J.A.G., Gomes J. F., in: Proc. M2D, 3rd International Conference on Mechanics & Materials in Design, Orlando, FL, 2000.

[6]. de Moura, M.F.S.F. and A.B. de Morais, *Equivalent crack based analyses of ENF and ELS tests*. Engineering Fracture Mechanics, 75(9), pp. 2584-2596, 2008.

[7]. da Silva, L.F.M., Rodrigues, T.N.S.S., Figueiredo, M.A.V., de Moura, M.F.S.F., Chousal, J.A.G., *Effect of Adhesive Type and Thickness on the Lap Shear Strength,* Journal of Adhesion, 82(11), pp. 1091-1115, 2006.

[8]. da Silva L.F.M., de Magalhães F.A.C.R.G., Chaves F.J.P. and de Moura M.F.S.F*., Mode II fracture toughness of a brittle and a ductile adhesive as a function of the adhesive thicknes*s, Journal of Adhesion, 86(9), pp. 889-903, 2010.

[9]. Campilho, R.D.S.G., de Moura, M.F.S.F., Ramantani, D.A., Morais, J.J.L., and Domingues, J.J.M.S., *"Tensile behaviour of three-dimensional carbon-epoxy adhesively bonded single- and double-strap repairs"*, International Journal of Adhesive and Adhesion, 29(6), pp. 678–68, 2009.

The enriched natural neighbour radial point interpolation method for the analysis of crack tip stress fields

S. Moreira[1], J. Belinha[1], L.M.J.S. Dinis[2], R.M. Natal Jorge[2]

[1]*Instituto de Engenharia Mecânica (IDMEC-FEUP), Rua Dr. Roberto Frias, s/n 4200-465 Porto PORTUGAL {em08163@fe.up.pt ; jorge.belinha@fe.up.pt}*

[2]*Faculdade de Engenharia da Universidade do Porto, Department of Mechanical Engineering, Rua Dr. Roberto Frias, s/n 4200-465 Porto PORTUGAL ldinis@fe.up.pt ; rnatal@fe.up.pt*

Abstract: Meshless Methods were created and developed in order to answer to some drawbacks and limitations found in the Finite Element Method (FEM). In the last few years meshless methods enlarge their application field, and are today a competitive and alternative numerical method in structural analysis. In this work a meshless method is used to study several solid mechanics benchmark examples considering an elasto-static analysis. Generally, in meshless methods the nodes discretizing the problem domain can be randomly distributed, since the field functions are approximated within a flexible influence domain rather an element, and the influence domains may and must overlap each other, in opposition to the no-overlap rule between elements in the FEM. In this work a radial interpolator meshless method is used to analyse the stress field around the crack tip. In this meshless method the nodal connectivity and the background integration mesh, totally dependent on the nodal mesh, are achieved using mathematic concepts, such as Voronoï Diagrams and the Delaunay tessellation. The obtained interpolation functions, used in the Galerkin weak form, are constructed with the Radial Point Interpolators and possess the delta Kronecker property. Due the organic procedure employed to impose the nodal connectivity the displacement and the stress field are smooth and accurate.

1 Introduction

Applied to different engineering fields and to distinct applied sciences, the Finite Element Method (FEM) is a well-known numerical method [1]. Small elements divide the problem domain and the field function is interpolated within each element by simple interpolation functions, the so called shape functions. However in the case of complex geometries the generation of highly distorted elements is common. The distortion of elements causes low quality shape functions which can affect the performance of the method.

Since the field functions are approximated within an influence domain rather than an element, in the meshless methods [2] the nodes can be arbitrary distributed. In opposition to the no-overlap rule between elements in the FEM, in meshless methods the influence domains may and must overlap each other. The Diffuse Element Method (DEM) [3] was the first meshless method using the moving least square approximants (MLS) in the construction of the approximation function. Proposed by Lancaster and Salkauskas [4], the MLS was firstly used for surface fitting. Belytschko evolved the DEM and developed one of the most popular meshless method, the Element Free Galerkin Method (EFGM) [5]. The Smooth Particle

Hydrodynamics Method (SPH) [6], which is one of the oldest, it is in the origin of the Reproducing Kernel Particle Method (RKPM) [7]. Other meshless methods such as the meshless local Petrov-Galerkin method (MLPG) [8], the Finite Point Method (FPM) [9] and the Method of Finite Spheres (FSM) [10] were developed as well. Although these meshless methods have been successfully applied in computational mechanics there are several problems not completely solved. One of these problems, and perhaps the most important unsolved issue, is the imposition of essential and natural boundary conditions, due to the lack of the delta Kronecker property. This is the immediate consequence, in the referred meshless methods, of using approximation functions instead of interpolation functions.

To address the above problem several new meshless methods were developed in the last few years, the Point Interpolation Method (PIM) [11], the Point Assembly Method [12], the Natural Neighbour Finite Elements Method (NNFEM) [13] or Natural Element Method (NEM) [14] and the Meshless Finite Element Method (MFEM) [15]. The PIM is a very attractive method. The approximation functions are in fact interpolation functions, consequently generating shape functions with the delta Kronecker property. The construction of the shape functions is simple, compared with the EFGM, and its derivatives are easily obtained. The PIM evolved, and instead of using the original polynomial basis function, it was proposed in [16] and successfully applied in [17], the use of the radial basis function for solving partial differential equations. This combination allows the generation of the Radial Point Interpolation Method (RPIM). The radial basis functions used in these early works were the Gaussian and the multiquadric radial basis functions. Initially the radial basis function was developed for data surface fitting, and later, with the work developed by Kansa [18], the radial basis function was used for solving partial differential equations. However the RPIM uses, unlike Kansa's algorithm, the concept of "influence domain" instead of "global domain", generating sparse and banded stiffness matrices, more adequated to complex geometry problems. The NEM is currently one of the most popular and discussed meshless method. In the NEM the trial and test functions are constructed using natural neighbour interpolants [19]. The natural neighbour interpolants represent a multivariate data interpolation scheme which has been initially used in data fitting. To construct the interpolation function the natural neighbour interpolants rely on geometrical and mathematical concepts such as the Voronoï diagrams [20] and the Delaunay tessellation [21]. Another important issue is the need of a background mesh for integration purposes. In fact a meshless method is not a truly mesh free method, if it relies in a secondary background integration mesh. Nevertheless the general idea [22] is that truly meshless methods, methods that do not require any mesh at all, are less stable and less accurate.

Recently an improved meshless method was developed, the Natural Neighbour Radial Point Interpolation Method (NNRPIM) [23, 24]. The NNRPIM uses mathematic concepts, such as Voronoï Diagrams and the Delaunay tessellation, to construct the influence-cells, the basic structure of the nodal connectivity in the NNRPIM, and the background integration mesh, totally dependent on the nodal mesh. Unlike the FEM, where geometrical restrictions on elements are imposed for the convergence of the method, in the NNRPIM there are no such restrictions, which permits a random node distribution for the discretized problem. The NNRPIM interpolation functions, used in the Galerkin weak form, are constructed with the Radial Point Interpolators (RPI). The NNRPIM interpolation functions possess the delta Kronecker property and its construction is simple and its derivatives are easily obtained. The radial basis function (RBF) used in the RPI is the multiquadric RBF. Although the NNRPIM is a recent developed meshless method it has been extended to many fields of the computational mechanics, such as the static analysis of isotropic and orthotropic plates [25] [26] and the functionally graded material plate analysis [27], the 3D shell-like approach [28]

for laminated plates and shells [29]. The dynamic analysis of several solidm echanic problems was also studied [30-32]. The NNRPIM was also tested in more demanding applications, such as the material nonlinearity [25] and the large deformation analysis [33]. More recently the NNRPIM was successfully extended to the bone tissue remodelling analysis [34]. In this work the NNRPIM is used to analyse the stress field around the crack tip. The interpolation functions, used in the Galerkin weak form, are enriched and the effect on the stress field around the crack tip is studied.

2   Meshless Method

The NNRPIM uses the Voronoï diagrams and the Delaunay triangulation, which are useful mathematical tools, in the determination of the natural neighbours for each node belonging to the global nodal set $N=\{n_1,n_2,...,n_N\}$. This theory is applicable to a n-Dimensional space. The Voronoï diagram of N is the partition of the domain defined by N in sub-regions V_I, closed and convex. The nodal connectivity is imposed by the overlap of the influence-cells, similar to the influence domain concept, which are obtained from the Voronoï cells. The cell formed by n nodes that contributes to the interpolation of the interest point x_I is called "influence-cell", which is obtained with the following procedure. A point of interest, x_I, searches for its neighbour nodes following the Natural Neighbour Voronoï construction (first natural neighbours of x_I), then, based on a previous construction of the Voronoï diagram for the node mesh, the natural neighbours of the first natural neighbours of x_I are added to the influence-cell. In an initial phase, after the domain discretization in a regular or an irregular nodal mesh, the Voronoï cells of each node are constructed. These cells can be considered as a background mesh for integration purpose, being determined the influence-cell for each one of these integration points. Using the Voronoï tessellation and the Delaunay triangulation small areas or volumes, respectively for the two-dimensional case and for the three-dimensional case, are established. These areas or volumes can be isoparameterized and the Gauss-Legendre quadrature scheme applied. In this work the Gauss-Legendre quadrature scheme was used: 1x1 for two-dimensional cases; 1x1x1 for three-dimensional cases. These two integrations schemes are sufficient for the used meshless formulation.

Consider a function $u(x)$ defined in the domain Ω, which is discretized by a set of N nodes. In the present meshless formulation the function $u(x)$ passes through all nodes using a Euclidean functional. It is assumed that only the nodes within the influence-cell of the point of interest x_I have effect on $u(x)$. The value of function $u(x_I)$ at the point of interest x_I is obtained by,

$$u(x_I)=\sum_{i=1}^{n}R_i(x_I)\ a_i(x_I)=R(x_I)\ a(x_I)$$ **Di:**

where $R_i(x_I)$ is the radial basis function, n is the number of nodes inside the influence-cell of x_I. The coefficients $a_i(x_I)$ are non constant coefficients of $R_i(x_I)$. Eq.(1) can be written in the matricial form, $u_s=R_G\cdot a$, solved in order to a and by back substitution on eq.(1),

$$u(x_I)=R(x_I)R_G^{-1}u_s=\varphi(x_I)u_s$$ **Di:**

The partial derivative of the interpolation function can be easily obtained. Early works on the radial point interpolators sustain that these interpolation functions possess the delta Kronecker property and also that the partition of unity is satisfied. In two-dimensional (2D) linear elastic fracture mechanics (LEFM) the mode-I crack tip fields are expressed as,

$$\begin{Bmatrix} u_1 \\ u_2 \end{Bmatrix} = \frac{K_I}{2\mu}\sqrt{\frac{r}{2\pi}} \begin{Bmatrix} \cos(\theta/2)\left[\kappa - 1 + 2\sin^2(\theta/2)\right] \\ \sin(\theta/2)\left[\kappa + 1 - 2\cos^2(\theta/2)\right] \end{Bmatrix} ; \begin{Bmatrix} \sigma_{11} \\ \sigma_{22} \\ \sigma_{12} \end{Bmatrix} = \frac{K_I}{\sqrt{2\pi r}}\cos(\theta/2) \begin{Bmatrix} 1 - \sin(\theta/2)\sin(3\theta/2) \\ 1 + \sin(\theta/2)\sin(3\theta/2) \\ \sin(\theta/2)\sin(3\theta/2) \end{Bmatrix} \quad (3)$$

Being K_I the stress intensity factor for mode-I dependent on the crack length, the domain geometry and the applied load, and (r,θ) are the cylindrical coordinates of a point with the origin located at the crack tip and the positive angle measured counterclockwise from the axis of the crack. κ is the Kolosov constant defined as $\kappa = (3-\upsilon)/(1+\upsilon)$. Considering eq. (3) it is possible to insert new terms in eq. (1), enriching the interpolation function.

3   Results and Conclusions

Several elasto-static benchmark examples were studied with the proposed meshless method. An edge-cracked rectangular plate with the dimension 10x10mm^2 subjected to a uniformed tension of f=1.0N is considered. The plane stress condition is considered, and the material properties are E=1000Pa and υ=0.25. The problem domain is discretized in the nodal mesh presented in figure 1(a). With the meshless analysis the stress field presented in figure 1(b), (c) and (d) was obtained.

(a)   (b)   (c)   (d)
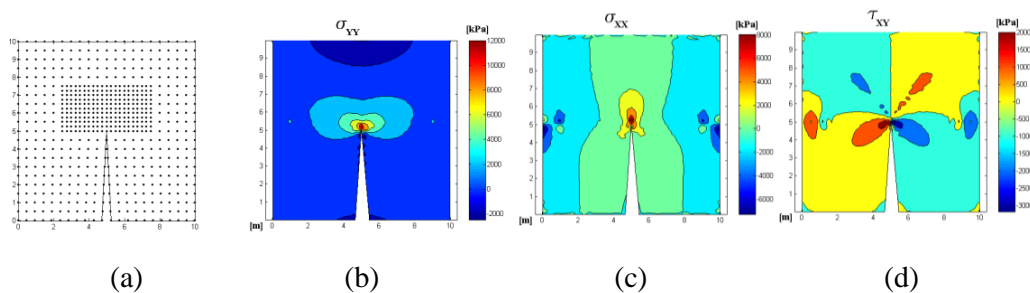
Figure 1 - *Domain nodal discretization and obtain stress field*

In this work NNRPIM was extended to analise the the stress field around the crack tip. With this meshless method the obtained variables fields are always smooth and accurate.The NNRPIM proved to be a flexible and accurate numerical method with great potential in more demanding problems, such as large deformation problems and moving discontinuities.

4   References

[1.]   Bathe K.J., *Finite Element Procedures*. (1996): Prentice-Hall: Englewood Cliffs, NJ.

[2.]   Belytschko T., Krongauz Y., Organ D., Fleming M., and Krysl P., *Meshless Methods: an overview and recent developments.* Computer Methods in Applied Mechanics and Engineering, (1996). **139**(1): p. 3-47.

[3.]   Nayroles B., Touzot G., and Villon P., *Generalizing the Finite Element Method: Diffuse Approximation and Diffuse Elements.* Computational Mechanics, (1992). **10**: p. 307-318.

[4.]   Lancaster P. and Salkauskas K., *Surfaces Generation by Moving Least Squares Methods.* Mathematics of Computation, (1981). **37**: p. 141-158.

[5.]   Belytschko T., Lu Y.Y., and Gu L., *Element-Free Galerkin Method.* International Journal for Numerical Methods in Engineering, (1994). **37**: p. 229-256.

[6.]   Monaghan J.J., *Smoothed Particle Hydrodynamics: Theory and Applications to Non-Spherical Stars.* Monthly Notices of the Astronomical Society, (1977). **181**: p. 375-389.

[7.]   Liu W.K., Jun S., and Zhang Y.F., *Reproducing Kernel Particle Methods.* International Journal for Numerical Methods in Fluids, (1995). **20**(6): p. 1081-1106.

[8.]   Atluri S.N. and Zhu T., *A new meshless local Petrov-Galerkin (MLPG) approach in computational mechanics.* Computational Mechanics, (1998). **22**(2): p. 117-127.

[9.]   Oñate E., Idelsohn S., Zienkiewicz O.C., and Taylor R.L., *A Finite Point Method in Computational Mechanics - Applications to Convective Transport and Fluid Flow.* International Journal for Numerical Methods in Engineering, (1996). **39**: p. 3839-3866.

[10.]   Bathe K.J. and De S., *Towards an Efficient Meshless Computational Technique: The Method of Finite Spheres.* Engineering Computations, (2001). **18**: p. 170-192.

[11.]   Liu G.R. and Gu Y.T., *A Point Interpolation Method for Two-Dimensional Solids.* International Journal for Numerical Methods in Engineering, (2001). **50**: p. 937-951.

[12.]   Liu G.R., *A Point Assembly Method for Stress Analysis for Two-Dimensional Solids.* International Journal of Solid and Structures, (2002). **39**: p. 261-276.

[13.]   Traversoni L., *Natural Neighbour Finite Elements.* Int. Conf. on Hydraulic Engineering Software, Hydrosoft Proc., Computational Mechanics Publications, (1994). **2**: p. 291-297.

[14.]   Braun J. and Sambridge M., *A numerical method for solving partial differential equations on highly irregular evolving grids.* Nature, (1995). **376**: p. 655-660.

[15.]   Sergio R., Idelsohn S., Oñate E., Calvo N., and Del Pin F., *The Meshless Finite Element Method.* International Journal for Numerical Methods in Engineering, (2003). **58**(6): p. 893-912.

[16.]   Wang J.G. and Liu G.R., *A Point Interpolation Meshless Method based on Radial Basis Functions.* International Journal for Numerical Methods in Engineering, (2002). **54**: p. 1623-1648.

[17.]   Wang J.G. and Liu G.R., *On the Optimal Shape Parameters of Radial Basis Functions used for 2-D Meshless Methods.* Computer Methods in Applied Mechanics and Engineering, (2002). **191**: p. 2611-2630.

[18.]   Kansa E.J., *A scattered data approximation scheme with applications to computational fluid-dynamics - I & II.* Computers and Mathematics with Applications, (1990). **19**: p. 127-161.

[19.]   Sibson R., *A brief description of natural neighbor interpolation.* Interpreting Multivariate Data, in V. Barnett (ed.), (Wiley, Chichester), (1981): p. 21-36.

[20.]   Voronoï G.M., *Nouvelles applications des paramètres continus à la théorie des formes quadratiques.* Deuxième Mémoire: Recherches sur les parallélloèdres primitifs, J. Reine Angew. Math., (1908). **134**: p. 198-287.

[21.]   Delaunay B., *Sur la sphére vide. A la memoire de Georges Voronoï.* Izv. Akad. Nauk SSSR, Otdelenie Matematicheskih i Estestvennyh Nauk, (1934). **7**: p. 793-800.

[22.]   Liu G.R., *Mesh Free Methods, Moving beyond the Finite Element Method*. (2002): CRC Press.

[23.]   Dinis L.M.J.S., Jorge R.M.N., and Belinha J., *Analysis of 3D solids using the natural neighbour radial point interpolation method.* Computer Methods in Applied Mechanics and Engineering, 2007. **196**(13-16): p. 2009-2028.

[24.] Belinha J., *The Natural Neighbour Radial Point Interpolation Method - Solid Mechanics and Mechanobiology Applications.* PhD Thesis, Faculdade de Engenharia da Universidade do Porto, 2010: p. 280.

[25.] Dinis L.M.J.S., Jorge R.M.N., and Belinha J., *Analysis of plates and laminates using the natural neighbour radial point interpolation method.* Engineering Analysis with Boundary Elements, 2008. **32**(3): p. 267-279.

[26.] Dinis L.M.J.S., Jorge R.M.N., and Belinha J., *Static and Dynamic Analysis of Laminated Plates Based on an Unconstrained Third Order Theory and Using a Radial Point Interpolator Meshless Method.* Computers and Structures, 2011. **89**(19-20): p. 1771–1784.

[27.] Dinis L.M.J.S., Jorge R.M.N., and Belinha J., *An Unconstrained Third-Order Plate Theory applied to Functionally Graded Plates using a Meshless Method.* Mechanics of Advanced Materials and Structures, 2010. **17**: p. 1-26.

[28.] Dinis L.M.J.S., Jorge R.M.N., and Belinha J., *A 3D Shell-Like approach using a Natural Neighbour Meshless Method: isotropic and orthotropic thin structures.* Composite Structures, 2010. **92**(5): p. 1132-1142.

[29.] Dinis L.M.J.S., Jorge R.M.N., and Belinha J., *Composite Laminated Plates: A 3D natural neighbour radial point interpolation method approach.* Journal of Sandwich Structures and Materials, 2010. **12**(2): p. 119-138.

[30.] Dinis L.M.J.S., Jorge R.M.N., and Belinha J., *The Natural Neighbour Radial Point Interpolation Method: Dynamic Applications.* Engineering Computations, 2009. **26**(8): p. 911-949.

[31.] Dinis L.M.J.S., Jorge R.M.N., and Belinha J., *The dynamic analysis of thin structures using a radial interpolator meshless method*, in *Vibration and Structural Acoustics Analysis*, Vasques C. and Rodrigues J., Editors. 2011, Springer. p. (in press).

[32.] Dinis L.M.J.S., Jorge R.M.N., and Belinha J., *A Natural Neighbour Meshless Method with a 3D Shell-Like Approach in the Dynamic Analysis of Thin 3D Structures.* Thin-Walled Structures, 2011: p. DOI: 10.1016/j.tws.2010.09.023.

[33.] Dinis L.M.J.S., Jorge R.M.N., and Belinha J., *Large Deformation Applications with the Radial Natural Neighbours Interpolators.* Computer Modelling in Engineering and Sciences, 2009. **44**(1): p. 1-34.

[34.] Belinha J., Jorge R.M.N., and Dinis L.M.J.S., *A meshless microscale bone tissue trabecular remodelling analysis considering a new anisotropic bone tissue material law.* Computer Methods in Biomechanics and Biomedical Engineering, 2012: p. 10.1080/10255842.2012.654783.

Aplication of Isogeometric Analysis
to simulate a sheet metal forming operation
using the Finite Element code LS-DYNA

J. Monteiro, M.P.L. Parente, R.M. Natal Jorge, A.A. Fernandes

IDMEC - Faculdade de Engenharia da Universidade do Porto
{dem09020,mparente,rnatal,aaf }@fe.up.pt

Abstract   A new computational method called Isogeometric Analysis (IGA) [1] is currently being developed, with the goal of integrating computer aided design (CAD) and finite element analysis (FEA). The main idea behind its development is to reuse the mathematical description for the geometry produced in the design stage (CAD) to conduct the numerical analysis studies (FEA). Currently, Non-Uniform Rational B-Splines (NURBS) are being used as basis functions in many Isogeometric analyses [2], since this geometrical representation is one of the most widely used in engineering design systems.

1. Introduction

This work presents the basic ideas of Isogeometric analysis using the Finite Element package LS-DYNA to simulate sheet metal forming process. The results were compared with the normal procedure, using a standard Finite Element formulation, based on Lagrange polynomials.
In order to compare the two methods it was used a benchmark automotive crashworthiness evaluation.
The simulation focus in a square tube buckling on accordion mode, this is considered as a benchmark test of the strength of a shell element under large deformations. This work compares the results of the application of NURBS elements, with the FEM analysis.

2. Material and Methods

The definition of the different parameters required for the numerical simulation were obtained from the work of Benson et al [5], namely the geometry dimensions, material parameters, boundary conditions, perturbation location and loads.
The displacement of the upper edge is forced at a constant velocity at one extremity of the tube, while the opposite end of the tube was kept fixed, due to symmetry conditions only a quarter of the tube was modeled.

It was applied a geometric imperfection in both simulations with an amplitude of 0.05 mm, as shown in Figure 1, in order to trigger the buckling of the tube at a height of 67.5 mm from the base. This imperfection is implemented by perturbing the initial coordinates of the nodes, or control points, along a line on the y-z face by 0.05 mm in the x direction and on the x-y face by 0.05 mm in the z direction.
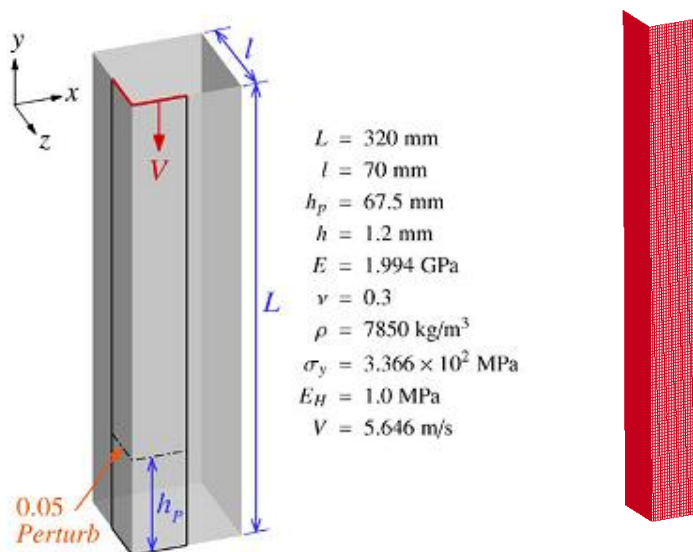
Figure 1 - Typical problem of a square tube buckling: problem description and the mesh. Only one quarter of the geometry is modeled with appropriate symmetry boundary conditions.

The following Figure 2 represents the buckling of the tube simulated with the Finite Element Method. From this simulation there will be obtained values which are going to be used as a term of comparison between the two elements NURBS versus FEM.

Based on future results, it will be possible to analyze the efficiency of one method in comparison with the other.

The aim of this study is to determine if the use of NURBS on LS-DYNA is an effective and accurate way to simulate the buckling of square tubes when compared to FEM. Several concepts such as computational time, better geometrical representation and geometrical compatibility will be used as a method of comparison.
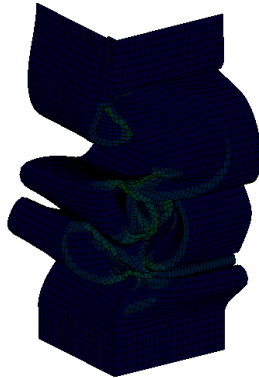
Figure 2 – Deformed mesh obtained from the FEM simulation, showing the distribution of the equivalent plastic strain.

3. Conclusions

The simulation shows that the deformation of the tube shows the same buckles as the ones represented with NURBS in the work of Benson et al [5].

References

[1] Cottrell, J.A., Hughes, T.J.R., Bazilevs, Y.: "Isogeometric Analysis – Toward Integration of CAD and FEA", John Wiley & Sons, Ltd, 2009.

[2] Hughes, T.J.R., Cotrell, J.A., Bazilevs, Y.: "Isogeometric analysis: CAD, finite elements, NURBS, exact geometry, and mesh refinement", Computer Methods in Applied Mechanics and Engineering, 194, 2005, 4135-4195.

[3] T.J.R.Hughes, J.A. Cottrell and Y.Bazilevs, Isogeometric analysis; CAD, finite elements, NURBS, exact geometry and mesh refinement. *Computer Methods in Applied Mechanics and Engineering, 194:4135-4195,2005.*

[4] J.B.R.F.P. Monteiro, M.P.L. Parente, R.M. Natal Jorge, A.A. Fernandes, Análise das componentes da base com elementos isogeométricos para problemas envolvendo incompressibilidade, 2011.

[5] D.J. Benson et al, Isogeometric shell analysis: The Reissner–Mindlin Shell 2010.

Coupled-Multi Scale Models: Advantages and limitations

F. J. P. Reis[1], F. M. Andrade Pires[1]

[1]DEMec - Department of Mechanical Engineering
Faculty of Engineering, University of Porto
Rua Dr. Roberto Frias 4200-465 Porto, Portugal
dem09012@fe.up.pt

Abstract The behavior of a material is inevitably a reflection of its micro-structure. As a consequence, the development of new materials, which has to satisfy the increasingly severe requirements, demands the manipulation of their microstructure.

The numerical tools are a vital ally on the developement and desing of performant structures where the selection of the material is itself a huge challenge. Conventionally, the modeling of different materials has been performed by means of continuous constitutive models where the characterization of the main effects which take place at their micro-structure is established by differential equations. Although remarkable results were achieved with this procedure, in widely heterogeneous materials this approach has shown clear limitations.

As a result, a new approach has recently aroused a great interest either in scientific or industrial communities: coupled multi-scale models. This approach stands out due to the fact that, each spatial domain where relevant and crucial effects occurs (void growth, crack propagation, damage, phase transformation among several others) may be conveniently modeled by means of a representative volume element (RVE). By definition, the deformation of the micro-structure is driven by a macroscopic deformation tensor and, the stress at the macro-scale is a consequence of the global behavior of the RVE.

However, the use of this formulation requires some caution since, there are some pathologies that this kind of models suffers. In general these pathologies are inherent with the definition of the RVE as well as with the mesh dependence that these models suffers.

In this context, the main goal of this paper is twofold: point out the limitations of coupled-multi scale models and suggest some improvements in order to circumvent them.

.

Application of Finite Element formulation to solid-shell structures for the analysis of time reduction

N. Mukunthamani, M.P.L. Parente, A.A. Fernandes, R.M. Natal Jorge

IDMEC – Faculdade de Engenharia, Universidade do Porto
Rua Dr. Roberto Frias, 4200-405, Porto,Portugal
E-mail: nickilsrivatsan@gmail.com

IDMEC – Faculdade de Engenharia, Universidade do Porto
Rua Dr. Roberto Frias, 4200-405, Porto,Portugal
{mparente, aaf, rnatal}@fe.up.pt

Abstract

The Enhanced Assumed Strain Method [1] is a procedure in the finite element method by which a number of internal variables is added to the strain field in order to enhance it, originating more deformation modes. This technique has proved effective in preventing volumetric and transverse shear locking in 3-D shell elements [2]. The technique yields productive results even with coarse meshes (lesser number of elements during analysis), which can result in reducing the manipulation time. The developed element HCiS12 was developed and tested with static structures and it was validated with established examples [3]. This has proved that HCiS12 element helps in obtaining the results with minimum number of elements (coarse mesh) and thus reduces time consumed.

In the present work the developed element is applied to shell structures to analyse the dynamics of the structures. A few other elements are also tested with the structures to compare the results. Structures with different mesh sizes, starting from a coarse mesh to a finer mesh are modelled and tested. The structure is then excited with a particular frequency range and the displacement in "Z" direction is found. The behaviour of the elements at different frequencies with different mesh sizes is obtained. From the results it has been proved that EAS has behaved well in the dynamic analysis of the shell structures

1. Enhanced assumed strain Technique

Finite Element analysis has been a very effective and primitive method of studying the mechanical structures in great detail. It helps to provide solutions for complicated engineering problems with either the theoretical method or a much easier computational methods with the help of commercial software. There are numerous methods in FEA to solve different engineering problems, of which Enhanced Assumed Strain Method is a notable technique.

The enhanced strain method is a powerful technique, in the sense that permits the inclusion of more or less additional variables for the enhanced strain field. Thus, it is possible to construct a formulation with good behavior both in bending and near incompressible situations.

However, the number of additional variables in the enhanced field is a crucial matter. If increasing the number of additional variables, and consequently, modes of deformation, normally improves the element performance, it can also leads to instabilities, numerical inefficiency and large CPU costs, due to complications in manipulating large matrices. Using the classical 8 GP numerical integration, the objective is therefore to reach the dimension 23 for the base of the subspace of incompressible deformations.

The formulation thus obtained by,

$$\boldsymbol{\varepsilon} = \boldsymbol{\varepsilon}_d + \boldsymbol{\varepsilon}_\alpha = \begin{bmatrix} \mathbf{B}_d^e & \mathbf{B}_\alpha^e \end{bmatrix} \begin{bmatrix} \mathbf{d}^e \\ \boldsymbol{\alpha}^e \end{bmatrix}$$

where,

The first part $\mathbf{B}_d^e$ is the standard strain displacement differential operator, which is the function of the linear shape functions.

$\mathbf{B}_\alpha^e$, is the enhanced variable field ($\boldsymbol{\alpha}$).

2. Element developed based on EAS

The element EAS was previously developed by IDMEC, Portugal for static analysis. This element was tested for static analysis and had proved reliable in reducing the time consumed by the CPU during the analysis. In the static analysis the shell structure was applied a load and the displacement is found. The different formulations were also tested with the shell which included EAS element type.

The objective of this research is to use this EAS element for a dynamic analysis of shell structures. To begin with the element was tested with simple shell structures like thin plate with minimum thickness. Later it was tested with a real automotive part provided by BMW.

This analysis is carried out to find if EAS element helps in time reduction during dynamic analysis.

3. Results based on the plate structure

The results obtained were plotted and are given below. The "X" axis of the graph contains frequency range and the "Y" axis is maximum displacement
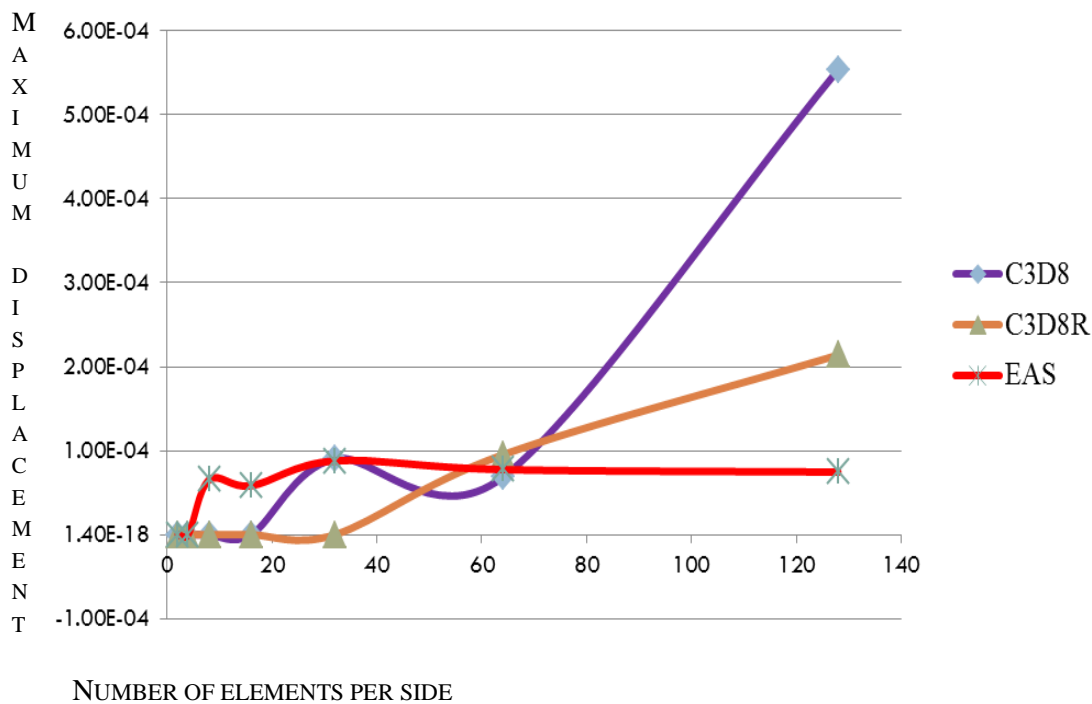
Graph 1- *Displacement in "Z" direction for element types tested*

The graphs show that the EAS has a constant displacement value independent of the mesh size. But the other formulations vary according to the mesh sizes.

The results could be obtained on a theoretical basis where the different formulations tend to converge at a point towards the more refined mesh size.

The graph shows that most of the formulations tend to converge at a point and if this could be validated, it can be said that EAS element arrives much closer to the result even with minimum number of elements. It shows that it does not depend on the mesh size, but exhibits uniform displacement for all the mesh sizes.

This shows that the results obtained at the fine mesh is very close to the results obtained at coarse mesh. So this element helps in reducing the manipulation time by reducing the time taken by CPU.
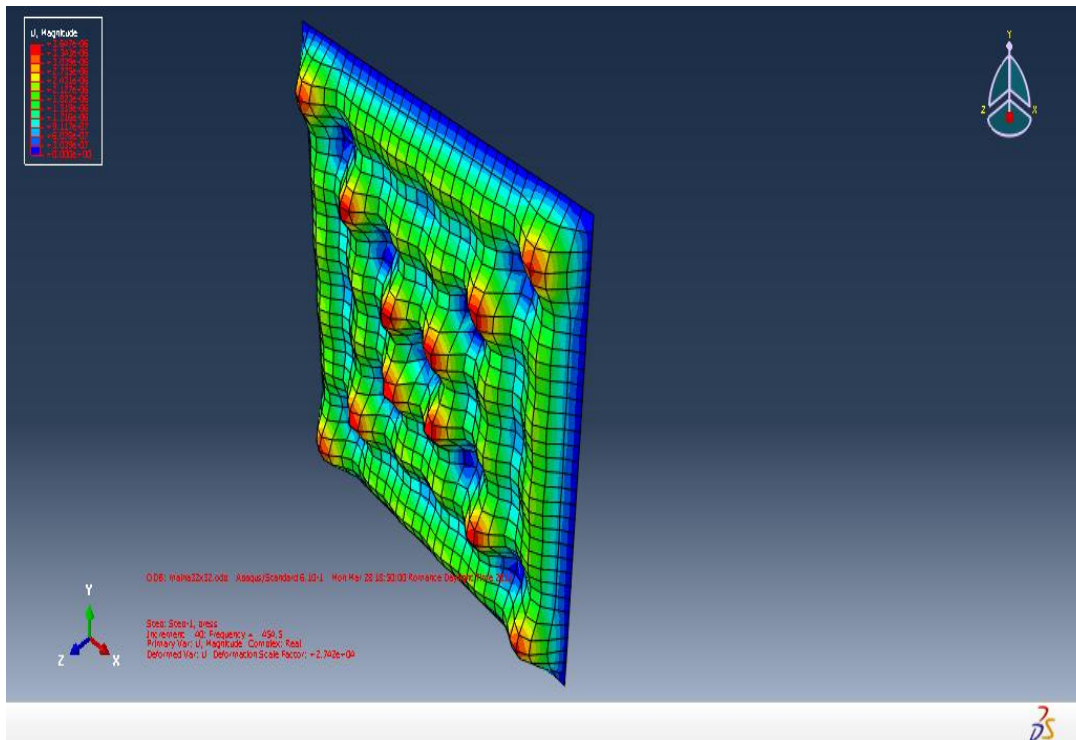
Figure 1*-Deformed plate structure after the implementation of the Element*

4. Time consumed by the plate structure during analysis for 1mm and 0.5 mm thickness

Time consumption during this analysis was calculated and the time consumed for the analysis for the plate structure could be seen in the Table.1

Number of elements per side	C3D8 (In sec)	EAS (In sec)
2	5.3	19.9
4	6.9	8.1
8	12.5	17.8
16	41	58.1
32	166.9	278.30
64	706.9	923.6

Table 1*- Time consumption for the 1mm plate*

Number of elements per side	C3D8 (In Sec)	EAS (In Sec)
2	5.4	5.4
4	6.8	8.2
8	12.5	17.8
16	40	57.3
32	157.5	216.7
64	638	871.3

***Table 2**- Time consumption for the 0.5mm plate*

For the plate with 1 mm thickness the deformations obtained by 64 elements with C3D8 is achieved with just 32 elements using EAS formulation.The time saved in this case is 428.6 seconds.

For the Plate with 0.5 mm thickness the deformation obtained by EAS with 32 elements per side is equal to the deformation obtained by C3D8 with 64 elements. The time saved in this case is 421.3 seconds

5. Results based on Natural frequencies of the Plate structures

Number of elements per side
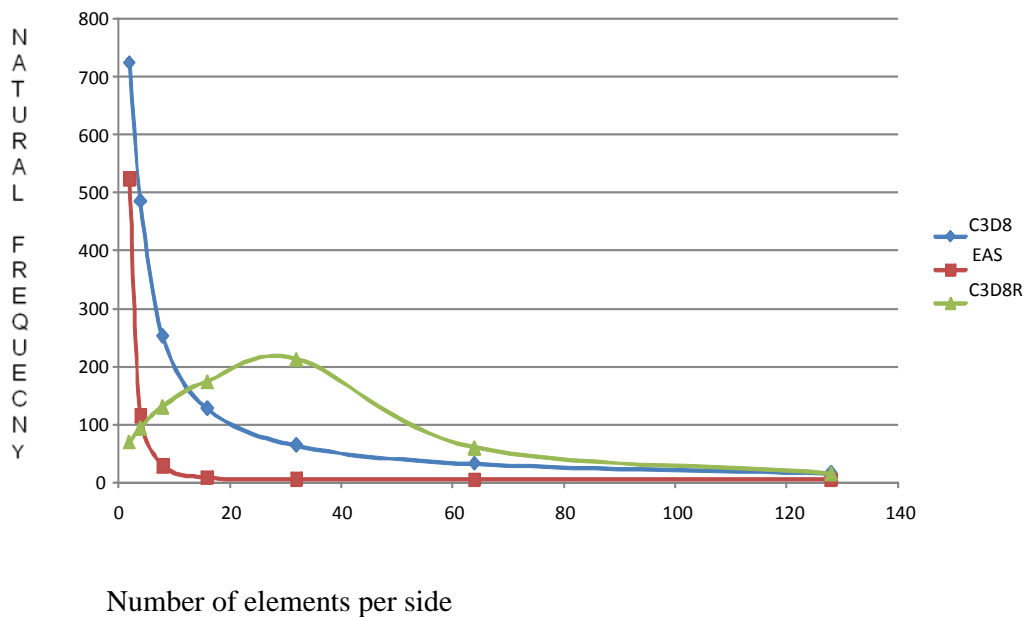
Graph 2- Results based on the Natural Frequencies

The behaviour of the element could also be understood from these results. The first five Natural frequency values are taken for three different elements and plotted in the graph. The shown above is the first Natural frequency value for three different element formulations. The behaviour of the elements is very similar to that of the maximum displacement graphs. All the elements converge nearly to one frequency value which is 14 Hz.

It could be assumed that since, all the element formulations converge nearly to this point we can take it as a reference value. This value is achieved by EAS element with just 16 elements per side. This shows that the results using EAS element formulation could be obtained with minimum number of elements per side which helps in time reduction.

6. Conclusions

The testing of the element type EAS element has given significant results with both the simple shell structure and also with the real automobile part. For the simple shell plate the maximum displacement values and the Natural frequency values shows that the final result could be obtained with the minimum number of elements per side.

Whereas the results from the other element formulations vary according to the number of elements per side which shows they are dependent on the mesh sizes as well. The EAS element shows a uniform deformation irrespective of the mesh sizes or the number of elements per side. The results obtained from the Natural frequency values also shows that the EAS element does not vary with the mesh size. The final frequency value at which all the formulations converged was 14 Hertz and EAS element has values very close to this final value with a minimum number of elements per side.

Acknowledgements

References

[1] JC Simo, MS Rifai, "A class of mixed assumed strain methods and the method of incompatible modes", Int. J. Num. Meth. Eng., 29:1595-1638, 1990.

[2] RJ Alves de Sousa, RM Natal Jorge, RA Fontes Valente, JMA César de Sá, "A new volumetric and shear locking-free 3D enhanced strain element", Engineering Computations, 20:896-925, 2003.

[3] RA Fontes Valente, RJ Alves de Sousa, RM Natal Jorge, "An enhanced strain 3D element for large deformation elastoplastic thin-shell applications", Computational Mechanics, 34:38-52, 2004.

[4] Scordelis AC, Lo KS. Computer analysis of cylindrical shells. Journal of American Concrete Institute 1969; 61:539–561.

[5] S. Ahmad, B.M. Irons, O.C. Zienkiewicz, Analysis of thick and thin shells structures by curved finite elements, International Journal for Numerical Methods in Engineering, 2:419-451, 1970.

[6] O.C. Zienkiewicz, R.L. Taylor and J.M. Too, Reduced integration techniques in general analysis of plates and shells, International Journal for Numerical Methods in Engineering, 3:275-290, 1979.

[7] E. Ramm, A plate/shell element for large deflections and rotations, In: K.J. Bathe, J.T. Oden, W. Wunderlich (eds) Formulations and Computational Algorithms in Finite Element

A primal closest point projection algorithm for Magnesium alloys

S.H.Wu[1], F.M. Andrade Pires[1], Abel D. Santos[1], A. Barata da Rocha[1]

[1]Faculty of Engineering, University of Porto

Rua Dr. Roberto Frias 4200-465 Porto, Portugal

Email:shwoo2001@gmail.com

Abstract: Due to their high strength-to-weight ratio, Magnesium alloys offer a great potential to reduce weight and have been widely used in the automotive and aerospace industries. However, their hexagonal close packed (HCP) crystallographic structure, with a c/a ratio of 1.624, has a very limited number of active slip systems at room temperature, which are not enough to accommodate plastic deformation without the activation of twinning. The polar nature of deformation twinning promotes a strong asymmetry between yielding in tension and compression, usually known as strength differential effect (SD). Conventional phenomenological constitutive models of plasticity [1, 3] such as Hill *et al*., Barlat *et al*., Karafillis and Boyce (1993) fail to capture this unconventional mechanical behavior. Therefore, Cazacu and Plunkett [2] have proposed a generic yield criteria, by using the transformed principal stress, to account for the initial plastic anisotropy and SD effect simultaneously. In this contribution, the Cazacu model is briefly described and implemented using a primal Closest Point Projection Method (CPPM) within an implicit quasi-static finite element environment. The accuracy of the algorithm is assessed by means of iso-error maps.

1   Introduction

The continuously increasing requirement of fuel efficiency and the reduction of CO_2 emissions have fostered the study of new materials that have high strength-to-weight ratios. Among them, Magnesium alloys have shown considerable promise and have a high potential of being applied in the automotive and aerospace industries. However, their Hexagonal Closed Packed (HCP) crystallographic structure promotes a very different mechanical behavior when compared to other metals with FCC and BCC structures, such as steel, aluminum etc [4, 8]. At room temperature, there are a limited number of adequate basal and non-basal slip systems to be activated and the activation of the twinning mechanism plays an important role to accommodate the deformation. The polar nature of deformation twinning promotes a strong asymmetry between yielding in tension and compression, usually known as strength differential effect (SD). In addition, the cold rolled magnesium sheet also shows a strong anisotropy because of the evolution of crystallographic texture leaded by the rolling process. The yield surface evolution can be seen in Fig.1. In order to accurately simulate sheet metal forming, a correct description of the material constitutive behavior is essential. In recent years, numerous studies [2, 5] have been conducted with the elasto-viscoplastic crystal plasticity finite element method (CP-FEM) in order to understand the micro-mechanisms involved and capture the macro mechanical behavior. But its high computational cost limits its application to real sheet metal forming. Phenomenological yield surface functions are still a good choice in metal forming finite element simulations.

Although numerous yield criteria [5] such as Hill from 1948 and 1979, Hosford, Barlat , or Barlat and Lian , Karafillis *et al* have been proposed, all of them fail to capture this unconventional mechanical behavior. Therefore, Cazacu and Plunkett [2] have proposed generic yield criteria, by using the transformed principal stress with a 4th-order linear transformation operator on the Cauchy stress tensor, to account for the initial plastic anisotropy and SD effect simultaneously. The evolution of the yield surface of this criteria can fit the experimental results very well, which can be seen in Figure 1.
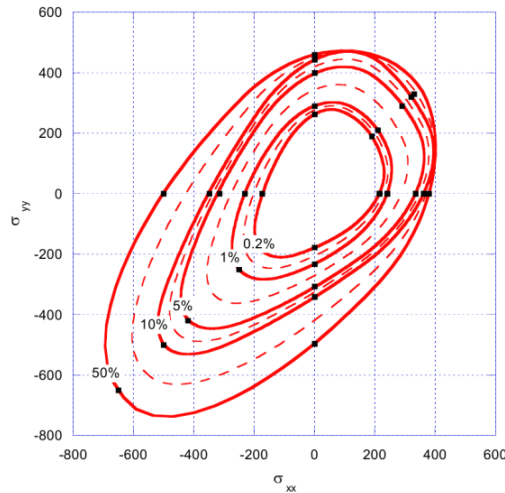
Figure 1 – Yield surface of Magnesium alloys (AZ31B) [5]

In this contribution, the Cazacu formulation is briefly described, and implemented using a primal Closest Point Projection Method (CPPM) within an implicit quasi-static finite element environment. For the assessment of the accuracy of this numerical stress integration algorithm, iso-error maps at different stress state are analysed.

2   Constitutive formulation

To extend an isotropic yield function to an orthotropic one, a 4ᵗʰ order linear transformation is multiplied by the stress deviator S to obtain the transformed tensor Σ, which can be defined as:

$$\Sigma = \mathbf{L}S, \tag{1}$$

where $\mathbf{L}$ is a 4ᵗʰ order tensor, which includes 9 independent anisotropy coefficients for three dimensional stress conditions. It is worth noting that although the transformed tensor is not deviatoric, the orthotropic criterion is insensitive to hydrostatic pressure and thus the condition of plastic incompressibility is satisfied.

It can be expressed as 6×6 matrix as

$$
\begin{bmatrix} \Sigma_{11} \\ \Sigma_{22} \\ \Sigma_{33} \\ \Sigma_{12} \\ \Sigma_{23} \\ \Sigma_{13} \end{bmatrix} =
\begin{bmatrix}
L_{11} & L_{12} & L_{13} & 0 & 0 & 0 \\
L_{12} & L_{22} & L_{23} & 0 & 0 & 0 \\
L_{13} & L_{23} & L_{33} & 0 & 0 & 0 \\
0 & 0 & 0 & L_{44} & 0 & 0 \\
0 & 0 & 0 & 0 & L_{55} & 0 \\
0 & 0 & 0 & 0 & 0 & L_{66}
\end{bmatrix}
\begin{bmatrix} S_{11} \\ S_{22} \\ S_{33} \\ S_{12} \\ S_{23} \\ S_{13} \end{bmatrix}. \tag{2}
$$

Then, the transformed stress can be calculated as

$$\Sigma = \begin{bmatrix} \phi_1\sigma_{11} + \varphi_1\sigma_{22} + \psi_1\sigma_{33} \\ \phi_2\sigma_{11} + \varphi_2\sigma_{22} + \psi_2\sigma_{33} \\ \phi_3\sigma_{11} + \varphi_3\sigma_{22} + \psi_3\sigma_{33} \\ C_{44}\sigma_{12} \\ C_{55}\sigma_{23} \\ C_{66}\sigma_{13} \end{bmatrix}, \tag{3}$$

where,

$$\phi_1 = (2L_{11} - L_{12} - L_{13})/3, \phi_2 = (2L_{12} - L_{22} - L_{23})/3, \phi_3 = (2L_{13} - L_{23} - L_{33})/3 \tag{4}$$

$$\varphi_1 = (-L_{11} + 2L_{12} - L_{13})/3, \varphi_2 = (-L_{12} + 2L_{22} - L_{23})/3, \varphi_3 = (-L_{13} + 2L_{23} - L_{33})/3 \tag{5}$$

$$\psi_1 = (-L_{11} - L_{12} + 2L_{13})/3, \psi_2 = (-L_{12} - L_{22} + 2L_{23})/3, \psi_3 = (-L_{13} - L_{23} + 2L_{33})/3 \tag{6}$$

To describe the strength differential effect between tension and compression, a material parameter k is introduced and the proposed orthotropic criterion [5] can be expressed by

$$F = B[(|\Sigma_1| - k\Sigma_1)^a + (|\Sigma_2| - k\Sigma_2)^a + (|\Sigma_3| - k\Sigma_3)^a]^{1/a}, \tag{7}$$

where Σ_1, Σ_2, Σ_3 are the principal values of Σ. In order to ensure the convexity of yield function, the introduced parameter, k, should be within the range of $k \in [-1,1]$. When the transformed matrix $\mathbf{L}$ is equal to the identity matrix, the proposed formulation can reproduce, as a limiting case, the von Mises yield criteria. The scalar B is

$$B = \left[\frac{1}{(|\phi_1| - k\phi_1)^a + (|\phi_2| - k\phi_2)^a + (|\phi_3| - k\phi_3)^a} \right]^{1/a} \tag{8}$$

Since the effective stress σ_{eq} is the first order homogeneous function in stresses, from the work equivalence principle it follows that the law of evolution for the effective plastic strain (associated with σ_{eq}) reduces to $\dot{\bar{\varepsilon}}^p = \lambda$. The loading-unloading conditions can be expressed in Kuhn-Tuckner form as

$$F \leq 0, \ \dot{\lambda} \geq 0, \ \dot{\lambda}F = 0. \tag{9}$$

The phenomenon of hardening describes the changes in yield stress that result from plastic straining and the flow stress, σ_Y, represents the size of the yield function during deformation.

Table.1 - *Material parameter of AZ31B [4].*

	ρ (g/cm³)	Modulus E (GPa)	Poisson's Ratio υ	Flow Curve (MPa)		
				K(MPa)	ε_0	n
Mg AZ31	1.77	45	0.35	406.8	0.0078	0.187

An appropriate equation describing changes in the flow stress of the material depends on deformation conditions. To describe the uniaxial true stress-strain curve response at rolling direction, a Swift´s work hardening law is used in the current paper, which can be expressed by

$$\sigma_Y = K(\varepsilon_0 + \bar{\varepsilon})^n. \tag{10}$$

All the mechanical parameters employed in the simulations can be seen in Table.1 The coefficients evolution for the Cazacu yield criteria have been obtained from the paper [5], and are listed in Table 2.

Table 2 - *AZ31B coefficients corresponding to the yield surface evolution [5].*

	a	k	L_{12}	L_{13}	L_{22}	L_{23}	L_{33}	L_{44}	L_{55}	L_{66}
0.002	2	0.2941	0.1724	-0.0701	1.0503	0.0552	0.7723	0.7547	1.2899	1.0641
0.01	2	0.2290	0.0091	-0.1160	1.1598	0.0585	1.2048	1.6770	2.1879	1.2230
0.05	2	0.3575	-0.0014	0.0342	1.1384	0.1493	1.2361	1.9628	2.2370	1.5302
0.1	2	0.4097	-0.0551	0.0177	1.1270	0.1506	1.2578	1.9373	2.0409	1.5667
0.5	2	0.2995	-0.2387	0.4351	1.2409	0.6143	2.2740	2.2647	2.6521	1.6595

3. Integration algorithm

Within the infinitesimal elasto-plastic finite element context, the elastic strains are usually much smaller than the plastic strains, and hence an additive decomposition of the total strain rate $\dot{\boldsymbol{\varepsilon}}$ into an elastic part $\dot{\boldsymbol{\varepsilon}}^e$ and a plastic part $\dot{\boldsymbol{\varepsilon}}^p$ is usually considered. Thus, the constitutive equations can be written in a rate form as

$$\dot{\boldsymbol{\varepsilon}} = \dot{\boldsymbol{\varepsilon}}^e + \dot{\boldsymbol{\varepsilon}}^p. \tag{11}$$

The elastic stress-strain relationship is given by

$$\dot{\boldsymbol{\sigma}} = \mathbf{D}^e : \dot{\boldsymbol{\varepsilon}}^e, \tag{12}$$

where $\mathbf{D}^e$ denotes the fourth order elasticity tensor.

The incremental solution of the initial boundary-value problem for elasto-plasticity problems requires a discrete time integration of the constitutive equations of the model over a time increment, from a known state at time t_n to the unknown state at t_{n+1}, given the total strain increment $\Delta\varepsilon$. The stress and updated variables, which characterize the inelastic response of the material, are pursued for a given strain increment and the previous values of the internal variables [6]. The numerical integration of elasto-plasticity constitutive equations is typically carried out by means of the so-called elastic predictor return mapping schemes. A fully implicit elastic predictor return mapping algorithm for Cazacu and Plunkett model [2], which is called Closest Point Projection Method (CPPM), is implemented within an implicit quasi-static finite element environment. In the algorithm, a trial stress is made to relax to the closest point on the yield surface. A summary of the implicit CPPM, developed in their work, for Cazacu model is presented in Box.1.

4. Results and discussion
4.1 Benchmark test

In order to show the applicability of the proposed integration algorithm and verify if the anisotropic behavior is caputred by Cazacu´s model, a cup drawing benchmark test is performed for the magensium alloy AZ31B. A schematic diagram of the problem can be seen in Figure 2 and the specific dimension can be found in Reference [7].

Box.1 - *Fully implicit closest point projection method (CPPM) for Cazacu model*

(i)   Elastic predictor. Given $\Delta\boldsymbol{\varepsilon}$ and the state variables at t_n, evaluate the elastic trial state:

$$\boldsymbol{\varepsilon}_{n+1}^{e\ trial} = \boldsymbol{\varepsilon}_n^e + \Delta\boldsymbol{\varepsilon}\ ;\ \bar{\varepsilon}_{n+1}^{p\ trial} = \bar{\varepsilon}_n^p$$

$$P_{n+1}^{trial} = K\varepsilon_{v\ n+1}^{e\ trial};\ \boldsymbol{S}_{n+1}^{trial} = 2G\boldsymbol{\varepsilon}_{d\ n+1}^{e\ trial};\ \boldsymbol{\sigma}_{n+1}^{trial} = \boldsymbol{S}_{n+1}^{trial} + P_{n+1}^{trial}\boldsymbol{I}$$

$$\boldsymbol{\Sigma}_{n+1}^{trial} = \mathbf{L}:\boldsymbol{S}_{n+1}^{trial};$$

$$J_{2\ n+1}^{0\ trial} = \frac{1}{2}tr(\boldsymbol{\Sigma}_{n+1}^{trial\ 2})\ ;J_{3\ n+1}^{0\ trial} = \frac{1}{3}tr(\boldsymbol{\Sigma}_{n+1}^{trial\ 3})\ ;$$

$$\Sigma_1^{trial} = 2cos(\theta_1)\sqrt{\frac{J_{2\ n+1}^{0\ trial}}{3}} + \frac{P_{n+1}^{trial}}{3};$$

$$\Sigma_2^{trial} = 2cos\left(\theta_1 - \frac{2\pi}{3}\right)\sqrt{\frac{J_{2\ n+1}^{0\ trial}}{3}} + \frac{P_{n+1}^{trial}}{3},$$

$$\Sigma_3^{trial} = 2cos\left(\theta_1 + \frac{2\pi}{3}\right)\sqrt{\frac{J_{2\ n+1}^{0\ trial}}{3}} + \frac{P_{n+1}^{trial}}{3};$$

$$cos(3\theta_1) = \frac{J_{3\ n+1}^{0\ trial}}{2}\left(\frac{3}{J_{2\ n+1}^{0\ trial}}\right)^{3/2}$$

$$\sigma_{eq\ n+1}^{trial} = B\left[\left(\left|\Sigma_1^{trial}\right| - k\Sigma_1^{trial}\right)^a + \left(\left|\Sigma_2^{trial}\right| - k\Sigma_2^{trial}\right)^a + \left(\left|\Sigma_3^{trial}\right| - k\Sigma_3^{trial}\right)^a\right]^{1/a};$$

(ii)   Check Plastic admissibility

$$\text{If}\ \ F = \sigma_{eq\ n+1}^{trial} - \sigma_Y(\bar{\varepsilon}_{n+1}^{p\ trial}) \le 0$$

Then set $(\ )_{n+1} = (\ )_{n+1}^{trial}$ and EXIT

(iii) Return mapping. Solve the system of eight equations using the Newton-Raphson iterative method

$$\begin{Bmatrix}\boldsymbol{\varepsilon}_{n+1}^e - \boldsymbol{\varepsilon}_{n+1}^{e\ trial} + \Delta\gamma\boldsymbol{N}_{n+1} \\ \bar{\varepsilon}_{n+1}^p - \bar{\varepsilon}_n^p - \Delta\gamma \\ F = \sigma_{eq} - \sigma_Y\end{Bmatrix} = \begin{Bmatrix}\boldsymbol{0} \\ 0 \\ 0\end{Bmatrix}$$

$$\boldsymbol{N}_{n+1} = \frac{\partial F}{\partial \boldsymbol{\sigma}}$$

The solution is found for $\boldsymbol{\varepsilon}_{n+1}^e$, $\bar{\varepsilon}_{n+1}^p$ and $\Delta\gamma$. The stress tensor can be obtained by

$$\boldsymbol{\sigma}_{n+1} = \mathbf{D}^e:\boldsymbol{\varepsilon}_{n+1}^e$$

(iv)   EXIT
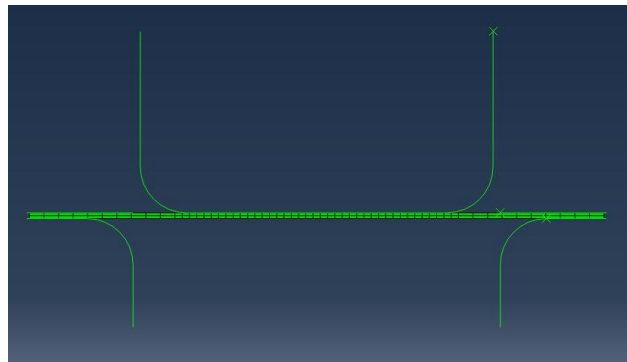
Figure 2 - *Schematic section view of cup test drawing*

The Punch, die and blank holder are considered as rigid surfaces in the simulation. The cicular blank is meshed with the fully integrated 8-noded brick element C3D8. In order to avoid the occurence of wrinking during drawing, the constant blankholder force of 30KN is applied to the blank. The final shape and the equivaleng plastic strain contour after the drawing operation are shown in Figure 3. It is possible to observe a pronounced earing effect, and the plastic deformation primariliy occurs at the neighboring place of the earing. This result suggests that Cazacu´s model can be used to model the ansitropic mechanical behavior between the rolling direction and transverse direction.
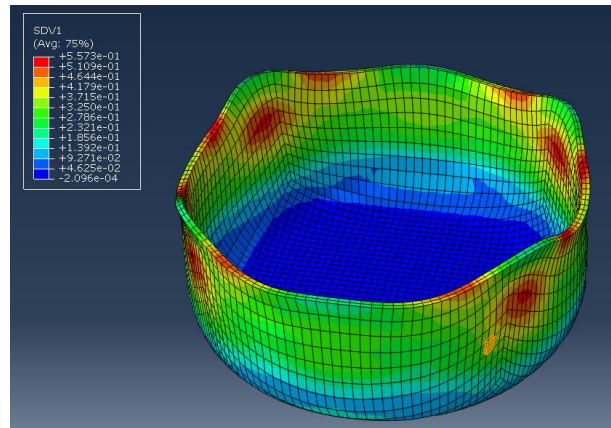
Figure 3 *– equivalent plastic strain contour*

4.2 Iso-error maps

In order to assess the accuracy of the stress integration algorithm, iso-error maps are drawn by standard numerical testing procedure [36]. A sequence of strain increments is applied that correspond to specified normalised elastic trial stress increments of the form

$$\Delta\sigma^{trial} = \frac{\Delta\sigma_T}{\sigma_{eq}}\boldsymbol{T} + \frac{\Delta\sigma_N}{\sigma_{eq}}\boldsymbol{N}, \tag{13}$$

where, $\boldsymbol{N}$ and $\boldsymbol{T}$ are, respectively, the unit (in Euclidean norm) normal and tangent vectors to the yield surface and σ_{eq} is the equivalent stress.

Applying increments of trial stress in the tangential and normal direction to the yield surface, the error is evaluated by

$$ERROR(\%) = \frac{\sqrt{(\sigma_N - \sigma_{EXACT}):(\sigma_N - \sigma_{EXACT})}}{\sqrt{\sigma_{EXACT}:\sigma_{EXACT}}}, \tag{14}$$

where, $\boldsymbol{\sigma}_N$ is numerical solution, $\boldsymbol{\sigma}_{EXACT}$ is the exact solution. Here, due to the lack of an analytical solution, $\boldsymbol{\sigma}_{EXACT}$ is assumed to be the stress obtained by subincrementation of each stress increment into 1000 steps.

When the transformed tensor, **L**, is equal to the identity tensor and the material parameter *c* vanishes, the model should reproduce the von Mises model. In Figure 4, the iso-error map for this limiting scenario is depicted and it is possible to conclude that the results are in complete agreement with the iso-error maps of von Mises.
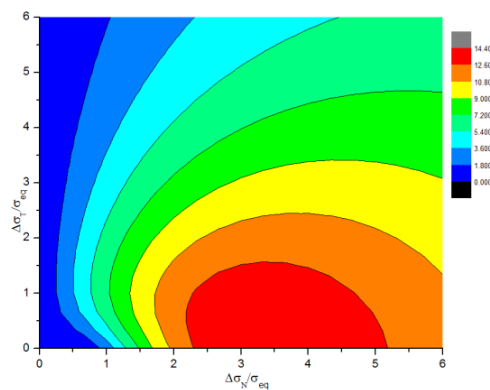
***Figure 4 –** Iso-error maps when L is equal to identity tensor and c vanishes*

To show the behavior of algorithm for a representative set of stress states, iso-error maps are plotted at six representative stress points on the yield surface: (A) uniaxial tensile in the rolling direction, (B) Biaxial tensile state, (C) uniaxial tensile in transverse direction, (D) compressive in rolling direction, (E) biaxial compressive state (F) compressive in transverse direction, as shown in Figure 5.
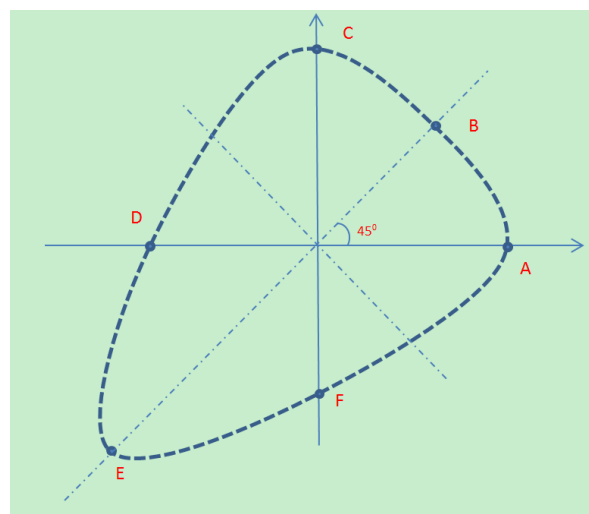
***Figure 5 –** Error representation*

In Figure 6, the hatched pattern regions of the iso-error map represent the regions where no convergence is achieved after more than 200 iterations. It can be seen that the region where convergence is not achieved at iso-error map of point A is located for larges value of normal direction (right side of the Figure 6(a)). In contrast, the region where convergence is not achieved for point D is located at top region where the value of $\Delta\sigma_T$ is higher (top side of the Figure 6(D)). This result indicates that the iso-error maps of compressive state is defintely different from the tensile stress state, which is justified by the strength differential effect. A similar behavior also occurs in the transverse direction, by comprasion of the iso error maps between tensile and compressive states in the transverse direction, it is found that although the iso-error value at compressive stress state is a little higher than tensile stress state, the region where convergence is not achieved is obviously smaller than the tensile stress state, which is mainly located at top-left of iso-error map. The regions also occur in the biaxial stress state. All of them indicate that with large incremental steps it is easy not to achieve convergence during the numerical stress integration.

Uniaxial tensile in rolling direction (Point A)

(A)

Uniaxial tensile in transverse direction (Point C)

(B)

Baxial tensile state (Point B)

(C)

Compressive in rolling direction (Point D)

(D)

Compressive in transverse direction (Point F)

(E)

Biaxial compressive state (Point E)

(F)
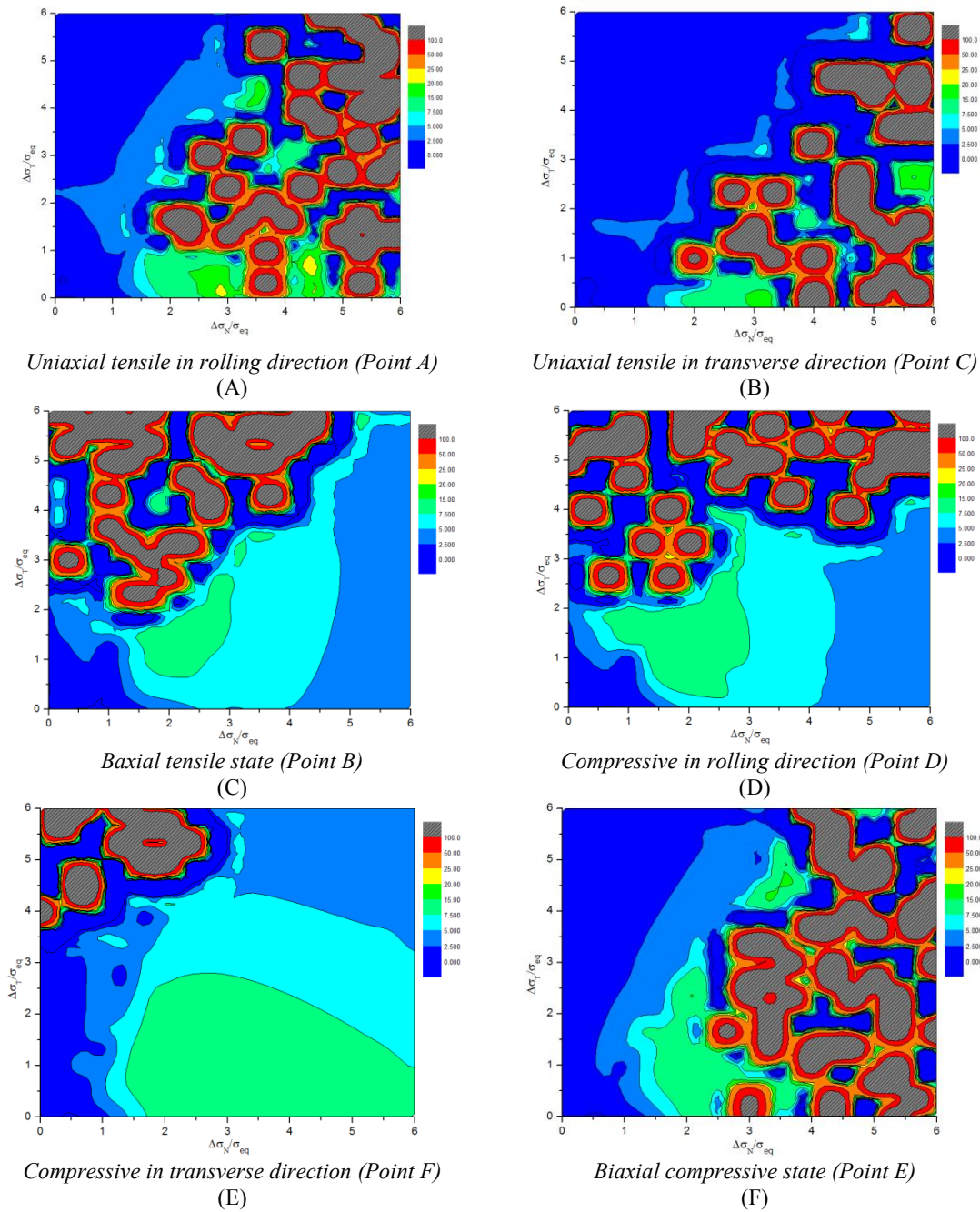
Figure 6 – *Iso-Error maps at different stress state*

5. Conclusions

In this paper, the HCP Cazacu´s model is described and used to model the mechanical behavior of Mangesium alloy AZ31B. A fully implicit integration algorithm based on the Closest Point Projection Method(CPPM) is implemented within an implicit enviroment. A benchmark test-cup drawing is performed to validate the model and the simulated results are able to show that the model caputures the earing phenomenon after drawing the AZ31B sheet, which has a good agreement with the experimental results. Finally, Iso-error maps at six representative stress states of the AZ31B yield surface have been drawn. It is shown that the

statbility at tensile and compressive stress states have a pronounced difference and large increments can not be employed due to the loss of convergence promoted by the model.

Acknowledgements

References:

[1] Nixon, M. E., O. Cazacu, et al. (2010). Anisotropic response of high-purity α-titanium: Experimental characterization and constitutive modeling. International Journal of Plasticity 26(4): 516-532.

[2] Cazacu, O., B. Plunkett, et al. (2006). Orthotropic yield criterion for hexagonal closed packed metals. International Journal of Plasticity 22(7): 1171-1194.

[3] EA de Souza Neto, D Peric, and DRJ Owen. Computational methods for plasticity theory and applications. John Wiley & Sons Ltd, 2008.

[4] Nguyen Duc-Toan, Park Jin-Gee, Kim Young-Suk. (2010). Combined kinematic/isotropic hardening behavior study for magnesium alloy sheets to predict ductile fracture of rotational incremental forming. International Journal material forming. Vol.3 Suppl:939-942.

[5] Brian W. Plunkett. Plastic anisotropy of hexagonal closed packed metals. Ph.D. dissertation in University of Florida (2005).

[6] S.W.Lee, J.W.Yoon, and D.Y.Yang. (1998).A stress integration algorithm for plane elastoplasticity and its applications to explicit finite element analysis of sheet metal forming processes. Computers & Structure. Vol(66):301-311.

[7] Yoon, J. W., F. Barlat, et al. (2000). "Earing predictions based on asymmetric nonquadratic yield function." International Journal of Plasticity 16(9): 1075-1104.

[8] Dirk Steglich, Wolfgang Brocks, Jan Bohlen, Frederic Barlat. (2011).Modelling direction-dependent hardening in magnesium sheet forming simulations. International Journal material forming. Vol.4:243-253

Application of CDM models for the simulation of the mechanical behavior of Ti-6Al-4V titanium alloy.

N.Allahverdizadeh[1], A.Manes[1], M.Giglio[1]

[1]*Politecnico di Milano, Dipartimento di Mecanica, Via la Masa 1, Milano 20156, Italy.*

Abstract. Simulation of the mechanical behavior of the materials is a key factor in the design process. Continuum damage mechanics is one of the most influential frameworks which have been proposed and extended to simulate the mechanical and failure behavior of materials. In this paper, using finite element simulations, a CDM model, calibrated with a simple specimen, has been applied on the different specimen geometries in order to verify the geometrical transferability of the calibration. The tested material is Ti-6Al-4V titanium alloy which is one the most commonly used materials in the aerospace structures. The predictions which have been made by the numerical simulations were compared with the experimental results obtained by Giglio et al.[1]. Two different specimen geometries has been considered and the accuracy of the CDM models in the simulations of the experimental results have been investigated.

1   Introduction

Knowing the mechanical behaviour of material is necessary in order to have a efficient design. Calibration of the mechanical behavior of materials has a significant importance in the design aspects. Damage Mechanics is a powerfull framework which tries to simulate the behavior of materials up to the failure. During the last decades a lot of researches has been done to make failure models more comprehensive and more reliable. Generally damage mechanics can be categorazied in three different groups. Phenomenological models are the first and simplest group. From the application point of view, these models are the most popular models also. It is easy to apply these models however, because of the simple nature of phenomenological models they try to reproduce the phenomenon of the failure and not the physics behind. Ricetracey [2], McClintock [3], LeRoy [4], Bao. Bai and Wierzbiki [5, 6, 7] are some of the most important phenomenological models. The second group is porosity models. These kind of models are based on the micromechanical concepts. Gorson[8], Tvergaard and Needleman [9] are considered as the founders of the the porosity models. Having a nomerous number of model parameters which has to be determined for each material (by means of experimental tests), makes application of the prosity models difficult and restricts their applicability. The last group is continuum damage mechanics (CDM) models. These models has a common point with prosity models. In the both of these models there is a coupling between damage evolution and plasticity. This assumption makes them more realistic and complex. In 1958 Kachanov [10] proposed the idea of equivalent stress. Lemaitre [11] used this concept and proposed the first CDM model. Different CDM models have been proposed after the Lemaitre's model. However, the main concept in all of these models is the same and the difference is related to the assumed damage evolution function for the model.[12, 13, 14, 15]. Initially Lemaitre developed his model for ductile damage. However, different authors have tried to extend the application of the CDM models and modify them inorder to obtain models which are proper for the other types of failure such as creep. Bhattacharya [16], Jing et al.[17] and Hayust [18] proposed models for the creep. In the Lemaitr's model the isotropic distribution was considered for the damage. In some cases this assumption is not satisfying and more complex models are needed. There are also some models which consider the anisotropic distribution for damage. [19, 20, 21]. Authors of the

present work have done some researches before inorder to identify the Lemaitre's models parameters for Ti-6Al-4V titanium alloy [22]. Ti-6Al-4V titanium alloy has an extensive usage in the aerospace structures. In the present study, based on the previous work of authors, Lemaitre's CDM model has been applied on more complex geometries in order to understand the geometry transferability of the Lemaitr's model in this cases. This is the first step to warrant the exploitation of such models in more complex numerical simulations aimed to the reproduction of real critical component or system subjected to extreme load.

2   Lemaitre's CDM model

According to the CDM models, damage is defined as a thermodynamic state variable which characterizes the deterioration of the material. Due to the increment in the number and size of defects inside the material during the loading, deterioration of material occurs. Damage is a variable which shows the amount of this deterioration. The load carrying capacity of the material consequently decreases with the evolution of the damage. As mentioned before, Lemaitre assumed an isotropic distribution for the damage and difined the damage parameter for a reference volume element by the following quation:

$$D = 1 - \frac{A_{ef}}{A_0} \tag{1}$$

Where D is damage, A_{ef} is the effective resisting area and A_0 is the nominal area before damage. CDM models generally are based on the strain equivalence hypothesis which means that the value of strain in the damaged material is equal to the value of the strain in the undamaged material with the effective stress. Effective stress is defined by the following equation:

$$\sigma_{eff} = \frac{\sigma}{1-D} \tag{2}$$

Where σ_{eff} is the effective stress and σ is the stress value in the damaged material. Total dissipation potentials can be determined by the superposition of the effects of the plasticity and damage dissipation potentials.

$$F = F_p(\sigma, R, X, D) + F_D(Y, D) \tag{3}$$

Where F, F_p, F_D are respectively total, plastic and damage dissipation energies. R and X are isotropic and kinematic hardening stresses and Y is a damage associated variable. Lemaitre supposed a linear relationship for the damage evolution function and defined the F_D as the following equation:

$$F_D = \frac{S_0}{s_0+1} \left(\frac{-Y}{S_0}\right)^{s_0+1} \dot{P} \tag{4}$$

Where S_0 and s_0 are the material parameters. According to the above formulation damage evolution function obtains from th following equation:

$$\dot{D} = \left(\frac{K^2}{2ES_0} \left[\frac{2}{3}(1+v) + 3(1-2v)\left(\frac{\sigma_H}{\sigma_{eq}}\right)^2\right] p^{\frac{2}{M}}\right)^{s_0} \dot{p} \tag{5}$$

σ_H and σ_{eq} are hydrostatic and equivalent vonmises stresses, p is the total equivalent accumulated plastic strain, v and E are respectively Poisson's ratio and modulus of elasticity and K is material constant related to isotropic hardening. Thus it is necessary to solve a set of damage evolution and plasticity equations inorder to apply the lemaitre's model.

3 De Souza Neto's Algorithm

In the CDM models there is a coupled relationship between the damage evolution and plasticity. Therefore in order to apply the CDM models it is necessary to solve a series of equations. From the numerical point of view, for the application of the CDM model in the finite element models an algorithm is needed in order to guaranty the proper application and fast convergence of the model. There are some proposed algorithms for the application of the Lemaitre's model. The most complete algorithm is Doghri's [23] algorithm. To apply this algorithm, it is necessary to solve a series of 14 equations. Thus application of this algorithm is not so strightforward. There are some other algorithms with some assumptions to simplify the application procedure. Teng [24] and De Souza Neto [25] have proposed algorithms for the case of isotropic hardening. In the absence of the cyclic loading this is a good assumption. De Souza Neto used the elastic predictor/return mapping method to drive the equations. By using this method, De Souza Neto simplified Doghri's algorithm to the solution of one nonlinear equation. The whole procedure of the derivation of this equation and step by step algorithm can be found in [25]. In the present study De Souza Neto's algorithm has been used for the application of the Lemaitre's model.

4 Numerical Model & Ressults

Recently Giglio et al.[1] has published a paper about the calibration of the mechanical behavior of Ti-6Al-4V titanium alloy using a phenomenological model (as fa as ductile failure is concerned). They have done comprehensive experiments and numerical simulations on the different specimen geometries. In the present study, two of the specimens which have been tested by Giglio et al.[1] has been chosen in order to apply Lemaitre's model and making the comparison between the results. Figure 1 shows the geometry of this two specimen. Figure 2 shows the stress triaxiality-PEEQ and load angle-PEEQ diagrams for the simple cubic specimen which previously have been used by authors [22] and the two new specimens. Aim of this work is in fact to asses the goemetry transferability of the CDM calibration when aplied to diiferent lonading conditions (triaxility, lode angle). For each specimen the element most involved by PEEQ has been choosen and the evolution of the stress triaxiality and lode angle with PEEQ has been extracted from the FE results (hereafter described). As it can be seen from the figure 2, different regions of stress triaxiality and load angle are included in the specimens which are a good test to show the transferability of the calibrated CDM model.
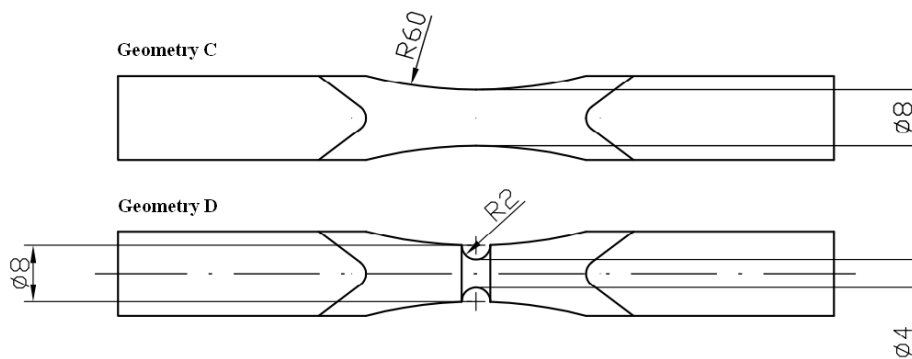
Figure 1 - Specimen Geometry
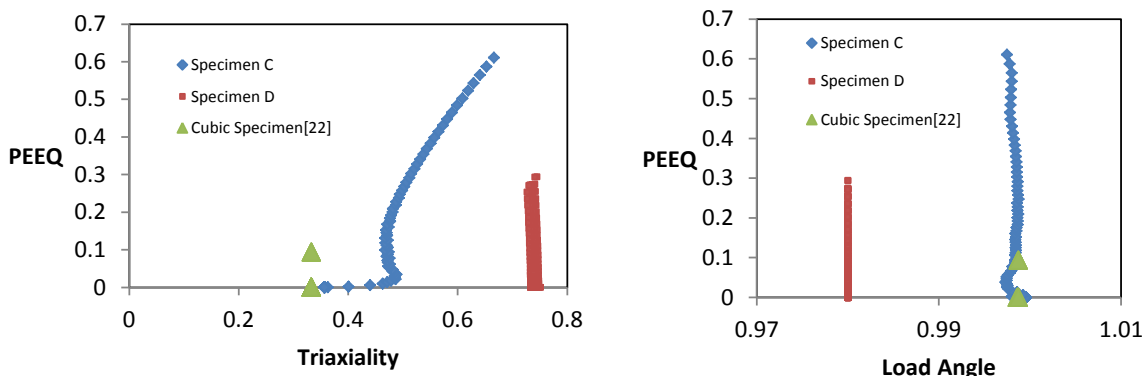
Figure 2 - *Triaxiality-PEEQ and Load Angle-PEEQ.*

In particular, in the previous simple specimen which was used for the calibration a simple cube), the value of stress triaxiallity was exactly 0.33. Therfore in the present study the new specimens with different stress triaxiallities (up to almost 0.8) achieved during the test, are choosen to cover the difirent domains in sthe stste of stress (stress tensor).

The numerical models are made in abaqus v6.10. 3D mesh with C3D8R elements have been used in the model. Traction load has been applied on the specimens. The type of analysis is explicit. Continuum damage mechanics models are not included in the damage models which are available in the abaqus. Therefore, in order to apply Lemaitre's model it is necessary to write a subroutine. In the present study according to the De Souza Neto's algorithm and by using Fortran language a VUMAT subroutine has been written and imported into abaqus. Figure 3 shows the meshed specimen D. Lemaitre's model parameters for Ti-6Al-4V titanium alloy have been identified by authors in the previous article [22]. In the present study this values have been used in order to apply Lemaitre's model.

Figure 3 - *Meshed Specimen D.*

Table 1 – *Material Properties*
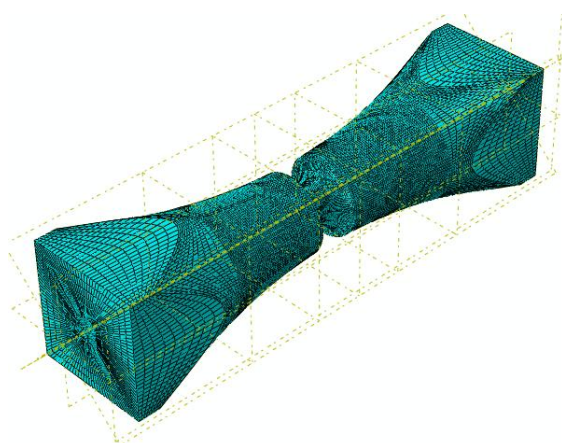
Modulus of elasticity	$110×10^3$ MPa
Shear modulus	41670 MPa
Poisson's ratio	0.32
Bulk modulus	101852 MPa
S_0	2.52 MPa
Hardening coefficient	700 MPa
Hardening power	0.6683
Yield stress	930 MPa
D_{cr}	0.35

Figures 3 and 4 show the load-displacement experimental behavior of the specimens according to the Giglio et al's[1] results and CDM model's predictions from numerical models (using the calibration recently found in [22]). Thus aim of this comparison is to evaluate the capability of the model (calibrated in a single loading condition) to reproduce corectly the behaviour of the material in diferent loading conditions. As it can be seen CDM model is partially able to reproduce the plastic behavior of the material in the different loading conditions. The maximum difference between the value of the load at a constant displacement in two models is 11% which is acceptable. This difference can be reduced by some modifications inside the code or by changing the model parameters in order to reach to the better results. Obtaining the model parameter from the experimental data has some uncertenities. It is common in the literature to find the model parameters by the try and error method in a way that by changing the model parametrs it is possible to be closer to the experimental results and then use these new parameters for the further simulations.
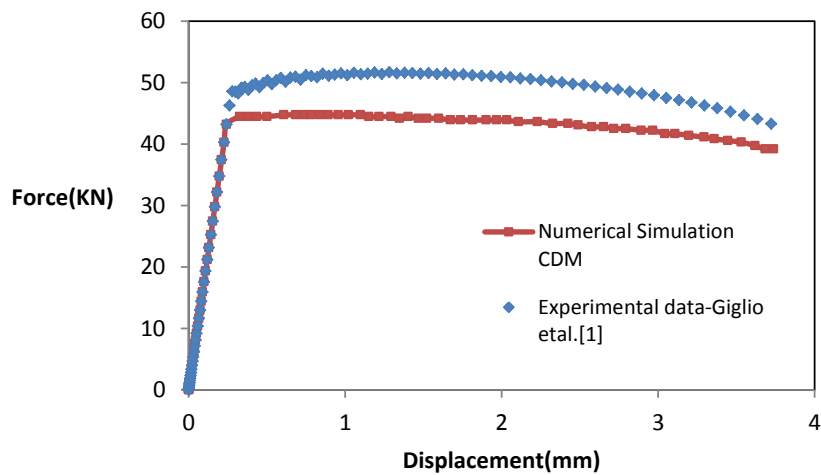
Figure 3 - Load-Displacement, Specimen C, see Figure 1.
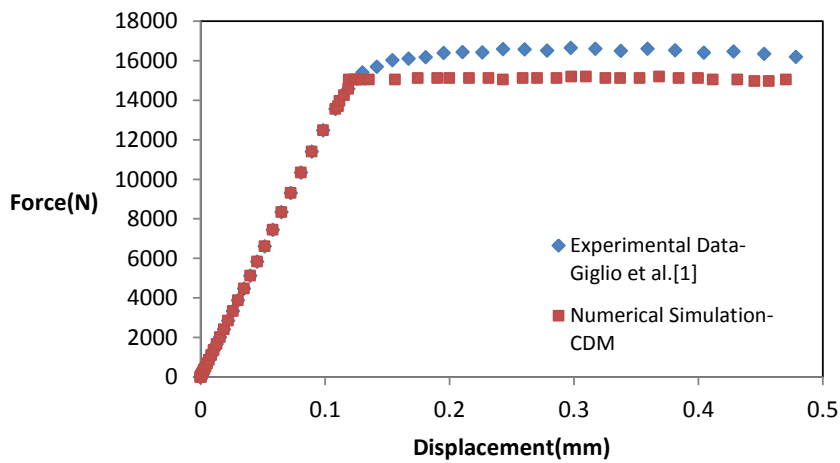
Figure 4 - Load- displacement, Specimen D, see Figure 1.

According to the simulation results it seems that the value of 0.35 for the critical damage is conservative. The critical value of damage is not affected the plastic area but it has an important effect on the failure point. By using the value of 0.35 for the critical damage, failure occurs before the real failure. By incresing the value of the critical damage to 0.4-0.6 better predictions for the failure point can be obtained. The above results have been obtained by this new modified values for thecritical damage.

5   Conclusion

Lemaitre's Continuum damage mechanics model has been applied on some complex specimens. Testing material is Ti-6Al-4V titanium alloy. CDM model parameters for this material have been identified before by authors [22]. Simple cubic specimen was used for the calibration. In the present study 2 new specimens with the different loading condition have been choosen in order to verify the transferability of the calibrated model. Load-displacement data obtained from numerical simulations has been compared with the experimental load-displacement data obtained by Giglio et al.[1]. The results are fairy good. However further investigations can be made to impove the understanding of the model CDM model behaviour in order to increase the reliability in geometry transferability.

References

[1]   M.Giglio, A.Manes, F.Vigano, "Ductile fracture locus of Ti–6Al–4V titanium alloy", International Journal of mechanical sciences, Vol.54, pp121-135, 2012.

[2]   J.R.Rice, D.M.Tracey, "On the ductile enlargement of voids in triaxial stress fields", Journal of mechanics and physics of solids, Vol.3, pp.201-217, 1969.

[3]   F.A.McClintock, "A criterion of ductile fracture by the growth of the holes", Journal of applied mechanics, Vol. 35, pp. 363-372, 1963.

[4]   G.Leroy, J.D.Embury, G.Edward and M.F.Ashby, "A model of ductile fracture based on the nucleation and growth of voids", Acta metallurgica, Vol.29, pp. 1509-1522, 1981.

[5] Y.Bao, T.Wierzbicki, "On the fracture locus in the equivalent strain and stress triaxiality space", International journal of mechanical sciences, Vol46, pp. 81-98, 2004.

[6]   Y.Bai, T.Wierzbicki, "A new model of metal plasticity and fracture with pressure and lode dependence", International journal of plasticity, Vol.24, pp. 1071-1096, 2008.

[7]   Y.Bai, T.Wierzbicki, "Application of Extended Mohr-Coulomb criterion to ductile fracture", International journal of fracture, 161, pp.1-20, 2010.

[8] A.L.Gurson, "Continuum theory of ductile rupture by void nucleation and growth: Part I-Yield criteria and flow rules for porous ductile media", Journal of engineering materials and technology, Vol.99, pp. 2-15, 1977.

[9] V.Tvergaard, A.Needleman, "Three dimensional micro structural effect of plane strain ductile crack growth", International journal of solids and structures, Vol.45, pp. 6165-6179, 2006.

[10] L.M.Kachanov, "Time of the rupture process under creep condition", TVZ Akad, S.S:r., OTD Ted Nauk, Vol. 8, 1958.

[11]   J.Lemaitre, "A continuous damage mechanics model for ductile fracture", Journal of engineering materials and technology, Vol.107, pp. 83-90, 1989.

[12]   S.Chandrakanth and P.C.Pandey, "An isotropic damage model for ductile material engineering", Engineering fracture mechanics, Vol.50, pp. 457-465, 1995.

[13] N.Bonora, "A nonlinear CDM model for ductile failure", Engineering fracture mechanics, Vol.58, p. 11-28, 1997.

[14] W.Tai and b.X.Yang, "A new damage mechanics criterion for ductile fracture", Engineering fracture mechanics, Vol.27, pp. 371-378, 1987.

[15] H.W.Tai, "Plastic damage and ductile fracture in mild steels", Engineering fracture mechanics, Vol. 36, pp. 853-880, 1990.

[16] B.Bhattacharya and B.Ellingwood, "A new CDM-based approach to structural deterioration", International journal of solids and structures, Vol.36, pp. 1757-1779, 1999.

[17] J.Jing, G.Meng, Y.Sun, S.Xia, "An effective damage mechanics model for creep-fatigue life assessment of a steam turbine rotor", International journal of pressure vessles piping, Vol. 80, pp. 389-396, 2003.

[18] D.R.Hayhurst, F.Vakili-Tahami and J.Q.Zhou, "Constitutive equations for time independent plasticity and creep of 316 stainless steel at 550℃" , International journal of pressure vessels and piping, Vol.80, pp. 97-109, 2003.

[19]   C.L.Chow C.L and j.Wang, "Anisotropic theory of continuum damage mechanics for ductile fracture", Engineering fracture mechanics, Vol.27, pp. 547-558, 1987.

[20]   G.Z.Voyiadjis, T.Park, "Kinematics of damage for finite strain elasto-plastic solids", International journal of engineering science, Vol.37, pp. 803-830, 1999.

[21]   J.Lemaitre, "Anisotropic damage law of evolution", Eauropean journal of mechanics, Vol.19, pp. 187-208, 2000.

 [22]   N.Allahverdizadeh, A.Manes, M.Giglio, "Identification of damage parameters for Ti-6Al-4v titanium alloy using continuum damage mechanics", MATERIALS SCIENCE AND ENGINEERING TECHNOLOGY (Materialwissenschaft undWerkstofftechnik), Vol.43,pp.435-440, 2012.

[23] I.Doghri, "Numerical implementation and analysis of a class of metal plasticity models coupled with ductile damage", international journal of numerical methods in engineering, Vol.38, 3403-3431, 1995.

[24] X.Teng, "Numerical Prediction of slant fracture with continuum damage mechanics", Engineering fracture mechanics, Vol.75, pp.2020-2041, 2008.

[25] EA.De Souza Neto, "A fast one-equation integration algorithm for Lemaitre ductile damage model". Communications in numerical methods in engineering, Vol.18, pp.541-554, 2002.

Structural Geometry Optimization of Passenger Railway Car Platform

V. Infante, M. de Freitas, B. Li and L. Reis

ICEMS – Instituto de Ciência e Engenharia de Materiais e Superfícies, Instituto Superior Técnico, TULisbon, Av. Rovisco Pais, 1049-001 Lisboa, Portugal

Abstract The main objective of the project LighTRAIN is to study an improvement in the design and manufacture of passenger railway car platform (floor). The new solution of the platform designed during the project may exhibit a significant change compared with the original platform. The manufacture of the new solution involves appropriate methodologies and tools.

The study developed included the modelling of original platform, the modelling of optimized solutions and the comparison of the improved solutions with original platform.

The results obtained for the original platform showed a maximum deflection of 1.225 mm, a maximum tensile stress of 15 MPa and the total mass is 522.5 kg.

The modelling of optimized solutions present an optimisation of the triangulation using an irregular distribution of the triangles with the same bars thickness as the original platform simulation. For each type of configuration was modelling 4 different triangles distribution.

The best configuration (Figure 1) has a total mass of 469.7 kg which represents a weight reduction of 10.1% in comparison with the original platform. This configuration shows a maximum deformation of 1.293 mm (Figure 2) and a maximum tensile stress of 23.6 MPa.he main objective of the project LighTRAIN is to study an improvement in the design and manufacture of passenger railway car platform (floor), including the comparison of the improved solution with the original platform.

The new solution of the platform designed during the project may exhibit a significant change compared with the original platform. The manufacture of the new solution involves appropriate methodologies and tools.
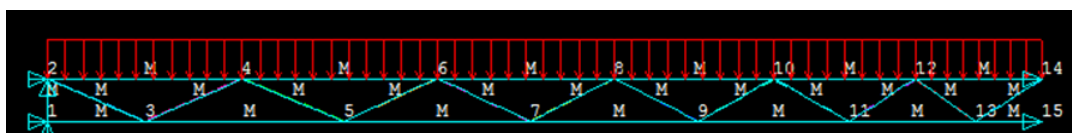
Figure 1 - Loads and boundary conditions of improved platform
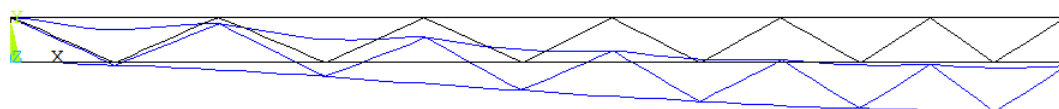
Figure 2 - Deflection of improved platform.

Acknowledgements

Structural solutions for underframe/floor of passenger railway car: initial steps

João P. A. Dias[1], Daniel F. O. Braga[1], Paulo M. S. T. de Castro[2], Sérgio M. O. Tavares[2], Pedro M.G. P. Moreira[1]

[1]*INEGI—Rua Dr. Roberto Frias, 400, 4200-465 Porto, Portugal*
[2]*FEUP—Rua Dr. Roberto Frias, s/n, 4200-465 Porto , Portugal*

Abstract The LighTRAIN project aims at the development of novel solutions for the underframe/floor of passenger railway cars, seeking to obtain improved life cycle costs through light-weighting and/or reduced fabrication costs, whilst ensuring compliance with the applicable design requirements such as deflection behavior and weight.

Structural solutions based on double-skin bodyshells are nowadays frequent and used by most of the manufacturers of railway passenger cars. In this work several solutions using different shape reinforced profiles were studied, considering large hollow extrusions as commonly found at present, *e.g.* [1,2], but also alternatives manufactured by joining skins and reinforcements using different manufacturing techniques as frictions stir welding and laser beam welding among others. The poster will present some of the progress made in this recently initiated project.

a)   *b)*
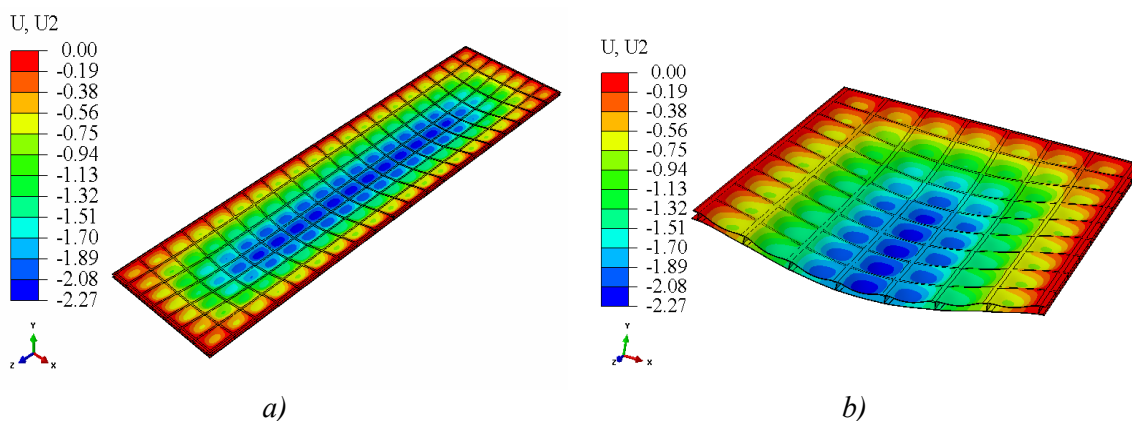
Figure 1 – *example of deflection analyses: deflection for solution using Z profile reinforcements; a) general view, b) half structure.*

References
[1]   Meysam Mahdavi Shahri, Rolf Sandström, 'Fatigue analysis of friction stir welded aluminium profile using critical distance', International Journal of Fatigue, vol.32, 2010, pp.302–309
[1]   Meysam Mahdavi Shahri, Rolf Sandström, Wojciech Osikowicz, 'Critical distance method to estimate the fatigue life time of friction stir welded profiles', International Journal of Fatigue, vol.37, 2012, pp.60-68

Mode II Fracture Characterization of *Pinus pinaster* Wood

M. F. S. F. de Moura[1], M. A. L. Silva[2], J. J. L. Morais[2],
A. B. de Morais[3], J. M. Q. Oliveira[4]

[1]*FEUP, Faculty of Engineering, University of Porto, R. Dr. Roberto Frias, 4200-465 Porto, Portugal*
[2]*CETAV/UTAD, Engineering Department, Quinta de Prados, 5000-801 Vila Real, Portugal*
[3]*University of Aveiro, Department of Mechanical engineering, Campus Santiago, 3810-193 Aveiro, Portugal.*
[4]*Instituto Politécnico de Viseu, Departamento de Engenharia de Madeiras, Viseu, Portugal.*

Abstract The present work describes experimental and numerical studies on the application of the End Notched Flexure (ENF) and End Loaded Split (ELS) tests to mode II wood fracture characterization. In this context, ENF and ELS specimens were used to determine GIIc of a clear Pinus pinaster wood in the RL system, which is the most relevant for structural design. In mode II fracture tests the crack faces are in contact, thus hindering a rigorous visualization of the crack tip. This makes classic methodologies based on crack length measurement during experimental tests inadequate, since they induce significant errors on the mode II fracture properties.

To overcome this experimental problem a Compliance Based Beam Method (CBBM) is developed. This new data reduction scheme does not require the crack length monitoring and includes the effects of the Fracture Process Zone (FPZ) ahead of crack tip.
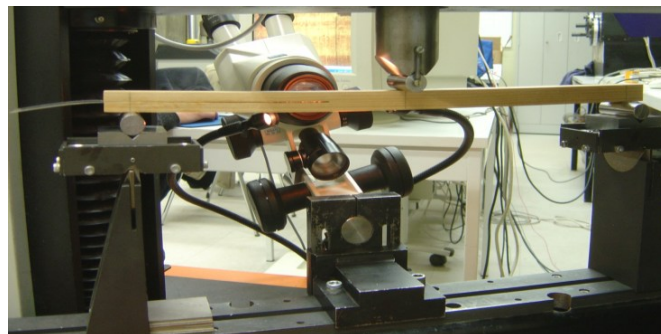
Figure 1 - *The ENF experimental set-up*

Fatigue Assessment of Old Riveted Metallic Bridges

A.M.P. de Jesus[1,2], A.A. Fernandes[2,3] A.L.L. da Silva[2,3], J.A.F.O. Correia[2]

[1]ECT, Universidade de Trás-os-Montes e Alto Douro, Vila Real, Portugal

[2]IDMEC – Pólo FEUP, Porto, Portugal

[3]DEM, Faculdade de Engenharia da Universidade do Porto, Porto, Portugal

Abstract The fatigue behavior of metallic bridges is a major concern of modern design since these structures are subjected to variable amplitude loading, which may be significant due to heavy traffic and long operational periods (expected/past), mainly in railway bridges. There are an important number of old metallic bridges that are susceptive to present significant damage levels but their full immediate replacement is not feasible due to economic restriction. The rehabilitation of those structures is usually the option, which requires comprehensive fatigue studies in order to guarantee a safe operation. Authors have been involved in National (Fatigue Behaviour of Riveted Connections from Old Steel Bridges) and European projects (FADLESS – Fatigue Damage Control and Assessment for Railway Bridges) aiming the experimental fatigue characterization of materials from metallic bridges (see example in Figure 1) and local fatigue modeling of bridge details (see Figure 2). S-N, local and fracture mechanics based approaches have been proposed to assess the fatigue behavior of complex bridge details. Deterministic and probabilistic approaches have also been investigated.
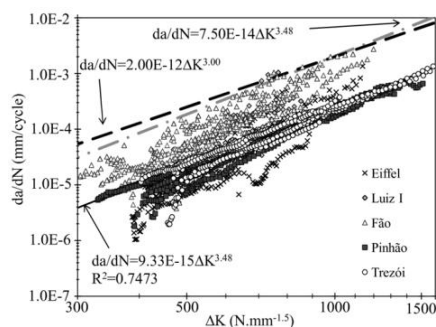
Figure 1 – da/dN data from five Portuguese bridges.
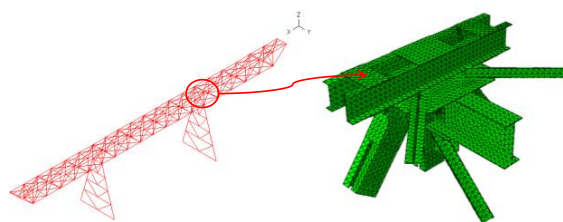
Figure 2 – Global-local FE model of a bridge node.

References

A.M.P. De Jesus, H. Pinto, A. Fernández-Canteli, E. Castillo, J.F.O. Correia, 2010, "Fatigue Assessment of a Riveted Shear Splice Based on a Probabilistic Model", *International Journal of Fatigue*, Vol. 32, No.2, pp. 453-462.

A.M.P. de Jesus, A.L. Silva, M.V. Figueiredo, José A. Correia, A.S. Ribeiro, A.A. Fernandes, 2011, "Strain-Life and Crack Propagation Fatigue Data From Several Portuguese Old Metallic Riveted Bridges", *Engineering Failure Analysis*, Vol. 18, No. 1, pp. 148-163.

J.A.F.O. Correia, Abilio M.P. de Jesus, Alfonso Fernández-Canteli, 2012, "A procedure to derive probabilistic fatigue crack propagation data*", International Journal of Structural Integrity*, Vol. 3 No. 2, pp. 158-183.

Index

blank